

Peter Lugner *Editor*

# Vehicle Dynamics of Modern Passenger Cars



International Centre  
for Mechanical Sciences



Springer

# **CISM International Centre for Mechanical Sciences**

## **Courses and Lectures**

### **Volume 582**

#### **Series editors**

##### **The Rectors**

Friedrich Pfeiffer, Munich, Germany

Franz G. Rammerstorfer, Vienna, Austria

Elisabeth Guazzelli, Marseille, France

Wolfgang A. Wall, Munich, Germany

##### **The Secretary General**

Bernhard Schrefler, Padua, Italy

##### **Executive Editor**

Paolo Serafini, Udine, Italy



The series presents lecture notes, monographs, edited works and proceedings in the field of Mechanics, Engineering, Computer Science and Applied Mathematics. Purpose of the series is to make known in the international scientific and technical community results obtained in some of the activities organized by CISM, the International Centre for Mechanical Sciences.

More information about this series at <http://www.springer.com/series/76>

Peter Lugner  
Editor

# Vehicle Dynamics of Modern Passenger Cars



Springer

*Editor*

Peter Lugner

Institute of Mechanics and Mechatronics

TU Wien

Vienna

Austria

ISSN 0254-1971

ISSN 2309-3706 (electronic)

CISM International Centre for Mechanical Sciences

ISBN 978-3-319-79007-7

ISBN 978-3-319-79008-4 (eBook)

<https://doi.org/10.1007/978-3-319-79008-4>

Library of Congress Control Number: 2018937684

© CISM International Centre for Mechanical Sciences 2019

This work is subject to copyright. All rights are reserved by the Publisher, whether the whole or part of the material is concerned, specifically the rights of translation, reprinting, reuse of illustrations, recitation, broadcasting, reproduction on microfilms or in any other physical way, and transmission or information storage and retrieval, electronic adaptation, computer software, or by similar or dissimilar methodology now known or hereafter developed.

The use of general descriptive names, registered names, trademarks, service marks, etc. in this publication does not imply, even in the absence of a specific statement, that such names are exempt from the relevant protective laws and regulations and therefore free for general use.

The publisher, the authors and the editors are safe to assume that the advice and information in this book are believed to be true and accurate at the date of publication. Neither the publisher nor the authors or the editors give a warranty, express or implied, with respect to the material contained herein or for any errors or omissions that may have been made. The publisher remains neutral with regard to jurisdictional claims in published maps and institutional affiliations.

Printed on acid-free paper

This Springer imprint is published by the registered company Springer International Publishing AG  
part of Springer Nature

The registered company address is: Gewerbestrasse 11, 6330 Cham, Switzerland

# Preface

At the CISM course “Vehicle Dynamics of Modern Passenger Cars”, a team of six international distinguished scientists presented advances regarding theoretical investigations of the passenger car dynamics and their consequences with respect to applications.

Today, the development of a new car and essential components and improvements are based strongly on the possibility to apply simulation programmes for the evaluation of the dynamics of the vehicle. This accelerates and shortens the development process. Therefore, it is necessary not only to develop mechanical models of the car and its components, but also to validate mathematical–mechanical descriptions of many special and challenging components such as e.g. the tire. To improve handling behaviour and driving safety, control schemes are integrated, leading to such properties as avoiding wheel locking or torque vectoring and more. Future developments of control systems are directed towards automatic driving to relieve and ultimately replace most of the mundane driving activities.

As a consequence, this book and its six sections—based on the lectures of the mentioned CISM course—aim to provide the essential features necessary to understand and apply the mathematic–mechanical descriptions and tools for the simulation of vehicle dynamics and its control. An introduction to passenger car modelling of different complexities provides basics for the dynamical behaviour and presents the vehicle models later used for the application of control strategies. The presented modelling of the tire behaviour, also for transient changes of the contact patch properties, provides the needed mathematical description. The introduction to different control strategies for cars and their extensions to complex applications using, e.g., state and parameter observers is a main part of the course. Finally, the formulation of proper multibody code for the simulation leads to the integration of individual parts. Examples of simulations and corresponding validations will show the benefit of such a theoretical approach for the investigation of the dynamics of passenger cars.

As a start, the first Chapter “[Basics of Vehicle Dynamics, Vehicle Models](#)” comprises an introduction to vehicle modelling and models of increasing complexity. By using simple linear models, the characteristics of the plane vehicle

motion (including rear wheel steering), driving and braking and the vertical motion are introduced. Models that are more complex show the influence of internal vehicle structures and effects of system nonlinearities and tire-road contact. Near Reality Vehicle Models, an assembly of detailed submodels, may integrate simple models for control tasks.

Chapter “[Tire Characteristics and Modeling](#)” first presents steady-state tire forces and moments, corresponding input quantities and results obtained from tire testing and possibilities to formulate tire models. As an example, the basic physical brush tire model is presented. The empirical tire model known as Magic Formula, a worldwide used tire model, provides a complex 3D force transfer formulation for the tire-road contact. In order to account for the tire dynamics, relaxation effects are discussed and two applications illustrate the necessity to include them.

Chapter “[Optimal Vehicle Suspensions: A System-Level Study of Potential Benefits and Limitations](#)” starts with fundamental ride and handling aspects of active and semi-active suspensions presented in a systematic way, starting with simple vehicle models as basic building blocks. Optimal, mostly linear-quadratic (H2) principles are used to gradually explore key system characteristics, where each additional model DOF brings new insight into potential benefits and limitations. This chapter concludes with practical implications and examples including some that go beyond the traditional ride and handling benefits.

Chapter “[Active Control of Vehicle Handling Dynamics](#)” starts with the principles of vehicle dynamics control: necessary basics of control, kinematics and dynamics of road vehicles starting with simple models, straight-line stability. The effects of body roll and important suspension-related mechanics (including the Milliken Moment Method) are presented. Control methods describing steering control (driver models), antilock braking and electronic stability control, all essential information for an improvement for the vehicle handling, are provided.

In Chapter “[Advanced Chassis Control and Automated Driving](#)”, it is stated first that recently various preventive safety systems have been developed and applied in modern passenger cars, such as electronic stability system (ESS) or autonomous emergency braking (AEB). This chapter describes the theoretical design of active rear steering (ARS), active front steering (AFS) and direct yaw moment control (DYC) systems for enhancing vehicle handling dynamics and stability. In addition to recently deployed preventive safety systems, adaptive cruise control (ACC) and lane-keeping control systems have been investigated and developed among universities and companies as key technologies for automated driving systems. Consequently, fundamental theories, principles and applications are presented.

Chapter “[Multibody Systems and Simulation Techniques](#)” starts with a general introduction to multibody systems (MBS). It presents the elements of MBS and discusses different modelling aspects. Then, several methods to generate the equations of motion are presented. Solvers for ordinary differential equation (ODE) as well as differential algebraic equation (DAE) are discussed. Finally, techniques for “online” and “offline” simulations required for vehicle development including real-time applications are presented. Selected examples show the connection between simulation and test results.

The application of vehicle and tire modelling, the application of control strategies and the simulation of the complex combined system open the door to investigate a large variety of configurations and to select the desired one for the next passenger car generation. Only conclusive vehicle tests are necessary to validate and verify the simulation quality—an advantage that is utilized for modern car developments.

To summarize these aspects and methods, this book intends to demonstrate how to investigate the dynamics of modern passenger cars and the impact and consequences of theory and simulation for the future advances and improvements of vehicle mobility and comfort. The chapters of this book are generally structured in such a way that they first present a fundamental introduction for the later investigated complex systems. In this way, this book provides a helpful support for interested starters as well as scientists in academia and engineers and researchers in car companies, including both OEM and system/component suppliers.

I would like to thank all my colleagues for their great efforts and dedication to share their knowledge, and their engagement in the CISM lectures and the contributions to this book.

Vienna, Austria

Peter Lugner

# Contents

<b>Basics of Vehicle Dynamics, Vehicle Models</b> . . . . .	1
Peter Lugner and Johannes Edelmann	
<b>Tire Characteristics and Modeling</b> . . . . .	47
I. J. M. Besselink	
<b>Optimal Vehicle Suspensions: A System-Level Study of Potential Benefits and Limitations</b> . . . . .	109
Davor Hrovat, H. Eric Tseng and Joško Deur	
<b>Active Control of Vehicle Handling Dynamics</b> . . . . .	205
Tim Gordon	
<b>Advanced Chassis Control and Automated Driving</b> . . . . .	247
Masao Nagai and Pongsathorn Raksincharoensak	
<b>Multibody Systems and Simulation Techniques</b> . . . . .	309
Georg Rill	

# Basics of Vehicle Dynamics, Vehicle Models



Peter Lugner and Johannes Edelmann

**Abstract** For the understanding and knowledge of the dynamic behaviour of passenger cars it is essential to use simple mechanical models as a first step. With such kind of models overall characteristic properties of the vehicle motion can be investigated. For cornering, a planar two-wheel model helps to explain understeer-oversteer, stability and steering response, and influences of an additional rear wheel steering. Another planar model is introduced for investigating straight ahead acceleration and braking. To study ride comfort, a third planar model is introduced. Consequently, in these basic models, lateral, vertical and longitudinal dynamics are separated. To gain insight into e.g. tyre-road contact or coupled car body heave, pitch and roll motion, a 3D-model needs to be introduced, taking into account nonlinearities. Especially the nonlinear approximation of the tyre forces allows an evaluation of the four tyre-road contact conditions separately—shown by a simulation of a braking during cornering manoeuvre. A near reality vehicle model (NRVM) comprises a detailed 3D description of the vehicle and its parts, e.g. the tyres and suspensions for analysing ride properties on an arbitrary road surface. The vehicle model itself is a composition of its components, described by detailed sub-models. For the simulation of the vehicle motion, a multi-body-system (MBS)-software is necessary. The shown fundamental structure of the equations of motion allows to connect system parts by kinematic restrictions as well, using closed loop formulations. A NRVM also offers the possibility for approving a theoretical layout of control systems, generally by using one of the simple vehicle models as observer and/or part of the system. An example demonstrates the possibility of additional steering and/or yaw moment control by differential braking.

**Keywords** Vehicle dynamics • Vehicle handling • Basic models  
Non-linear models

---

P. Lugner (✉) · J. Edelmann

Institute of Mechanics and Mechatronics, TU Wien, Vienna, Austria  
e-mail: peter.lugner@tuwien.ac.at

## 1 Introduction

Important features of modern passenger cars with respect to vehicle dynamics are easy handling for normal driving, appropriate ride comfort, and support of the driver by control systems e.g. for lane keeping or in critical situations.

In addition to investigate the fundamental dynamic behaviour of the vehicle, theoretical methods support the engineer in an early stage of vehicle development in order to define basic vehicle layout properties, where no experiments are available, and also for understanding detailed dynamic properties of (sub) systems. Thereby the use of models of different complexity comprises the understanding of basic properties as well as the interaction with (human) control systems, by applying simulations with multi-body-system (MBS) programs, see Lugner (2007), Rill (2012). With the obtained results, the overall characteristics of the car can be interpreted and recommendations for details of components can be given, as well as the potential for future developments and improvements demonstrated.

Which kind of mathematical–dynamical vehicle model is needed/will be used is obviously a matter of the demanded degree of detail with respect to the investigated ride/handling quality. For the understanding and characterization of the basic behaviour with respect to the longitudinal and lateral dynamics and vertical motion, different linearized models may be used, see e.g. Mitschke and Wallentowitz (2014), Plöchl et al. (2015).

More complex models, including proper nonlinear descriptions of the tyre behaviour, are necessary to describe the spacial carbody motion and tyre–road contact to consider higher accelerations.

For the layout of vehicle components and their kinematic and dynamic interaction, detailed MBS-models including full nonlinearities are used to establish a near reality vehicle model (NRVM). Such a model also provides the possibility to investigate the behaviour of control systems in a theoretical environment—a necessity for the tuning of structures and parameters for a later realisation.

## 2 Simple (linear) Vehicle Models

By using basic (planar) linear models with a low number of degrees of freedom (DoF), the equation of motions may decouple with regard to lateral, longitudinal and vertical vehicle motion. Thus, cornering, longitudinal dynamics and vertical dynamics can be investigated independently.

## 2.1 Cornering, x-y-plane Motion

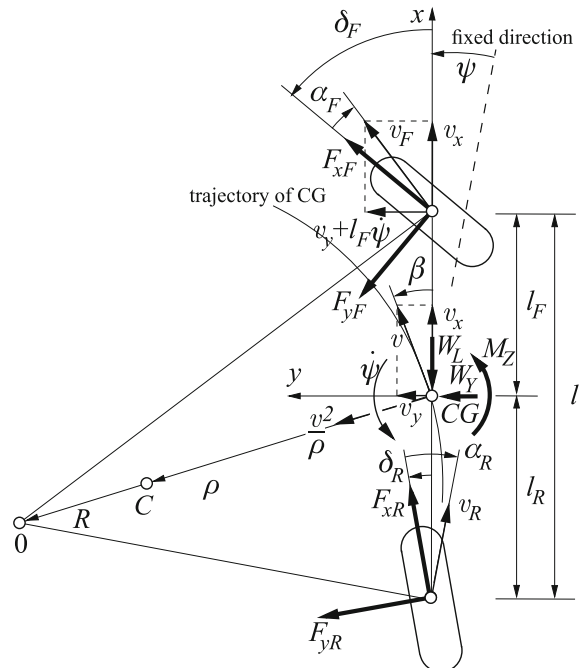
This well known simplified model of the vehicle is based on merging both wheels of an axle to a substitutive wheel (axle characteristics) in the centre of this axle, see Fig. 1. Furthermore, it is assumed that the whole model—called two-wheel model (or bicycle model)—may move in the  $x$ - $y$ -plane only. Since the model is planar, the  $CG$  will also move in this plane only, e.g. Plöchl et al. (2015), Plöchl et al. (2014), Abe (2009), Popp and Schiehlen (2010). For the nomenclature and explanation of state variables see also DIN ISO 8855 (2013).

The relevant DoF for this model are the longitudinal and lateral motion and the rotation about a vertical axis, represented by the velocities  $v_x$  and  $v_y$  (or  $v$  and side slip angle of the vehicle  $\beta$ ), and yaw rate  $\dot{\psi} = r$ , see Fig. 1.

With front and rear steering angles  $\delta_F$  and  $\delta_R$  as inputs to the vehicle, the kinematic description of the motion of the car provides the side slip angles of front and rear substitutive wheels with

$$\begin{aligned}\alpha_F &= \delta_F - \frac{v_y + l_F \dot{\psi}}{v_x} \\ \alpha_R &= \delta_R - \frac{v_y - l_R \dot{\psi}}{v_x}\end{aligned}\quad (1)$$

**Fig. 1** Planar vehicle model



A linear model as basic description of the lateral tyre/axle forces

$$F_{yi} = C_i \alpha_i \quad i = R, F \quad (2)$$

is applied, where the cornering stiffness  $C_i$  comprises properties of the tyres and the suspension stiffnesses.

With the aerodynamic forces  $W_L$ ,  $W_Y$  and the aerodynamic moment  $M_Z$  the equations of motion are

$$x : \quad m(\dot{v} - a_q \beta) = (F_{xF} - F_{yF} \delta_F) + (F_{xR} - F_{yR} \delta_R) - W_L \quad (3)$$

$$y : \quad m(a_q + \beta \dot{v}) = (F_{xF} \delta_F + F_{yF}) + (F_{xR} \delta_R + F_{yR}) + W_Y \quad (4)$$

$$z : \quad I_Z \ddot{\psi} = (F_{xF} \delta_F + F_{yF}) l_F - (F_{xR} \delta_R + F_{yR}) l_R + M_Z \quad (5)$$

The lateral acceleration can be expressed by using the radius  $\rho$  of the curvature of the path of the *CG*

$$a_q = \frac{v^2}{\rho} \quad (6)$$

Considering the steering angles  $\delta_F$ ,  $\delta_R$  and the longitudinal tyre/axle forces  $F_{xF}$ ,  $F_{xR}$  (provided by the drive train and brake system) as input quantities, Eqs. (1)–(5), will describe the motion of the car by  $v(t)$ ,  $\psi(t)$ ,  $\rho(t)$ .

With the restriction of the linear description of the lateral tyre forces, neglecting the influence of the longitudinal force transfer and assuming small accelerations  $\dot{v}$  or steady state conditions, Eqs. (4) and (5) are sufficient to describe the in-plane-motion of the vehicle.

For basic investigations of the cornering behaviour a constant longitudinal velocity is considered, leading to

$$v \cong v_x = \text{konst} \quad ; \quad v = (\dot{\beta} + \dot{\psi})\rho \quad (7)$$

$$a_q \cong a_y = v(\dot{\beta} + \dot{\psi}) \quad (8)$$

Moreover, for constant velocity  $v$  the longitudinal tyre forces will be small. Thus the expressions  $F_{xi} \delta_i$  in (4) and (5) can be neglected. and the linear matrix equation of the linear two-wheel model is derived by

$$\dot{x} = \mathbf{F}x + \mathbf{G}\delta \quad (9)$$

$$x = \begin{bmatrix} v_y \\ \dot{\psi} \end{bmatrix} = \begin{bmatrix} v_y \\ r \end{bmatrix}, \quad \delta = \begin{bmatrix} \delta_F \\ \delta_R \end{bmatrix},$$

$$\mathbf{F} = \begin{bmatrix} -\frac{C_F + C_R}{mv_x} & -\frac{(l_F C_F - l_R C_R)}{I_Z mv_x} - v_x \\ -\frac{(l_F C_F - l_R C_R)}{I_Z v_x} & -\frac{l_F^2 C_F + l_R^2 C_R}{I_Z v_x} \end{bmatrix}, \quad \mathbf{G} = \begin{bmatrix} \frac{C_F}{m} & \frac{C_R}{m} \\ \frac{l_F C_F}{I_Z} & \frac{l_R C_R}{I_Z} \end{bmatrix}$$

Another way to describe the system is to transfer (9) into a second-order-system, Kortüm and Lugner (1994)

$$\ddot{\beta} + 2K_1\dot{\beta} + K_2\beta = \frac{C_F}{mv_x}\dot{\delta}_F - \frac{C_F(l_F mv_x^2 - C_R l_R l)}{I_Z mv_x^2}\delta_F + \frac{C_R}{mv_x}\dot{\delta}_R - \frac{C_R(-l_R mv_x^2 - C_F l_F l)}{I_Z mv_x^2}\delta_R \quad (10a)$$

$$\ddot{r} + 2K_1\dot{r} + K_2r = \frac{l_F C_F}{I_Z}\dot{\delta}_F + \frac{C_F C_R l}{I_Z m v_x}\delta_F - \frac{l_R C_R}{I_Z}\dot{\delta}_R - \frac{C_F C_R l}{I_Z m v_x}\delta_R \quad (10b)$$

with

$$K_1 = \frac{I_Z(C_R + C_F) + m(C_F l_F^2 + C_R l_R^2)}{2I_Z m v_x} > 0 \quad (11)$$

$$K_2 = \frac{l^2 C_F C_R + (C_R l_R - C_F l_F) m v_x^2}{I_Z m v_x^2} \gtrless 0 \quad (12)$$

Here it becomes immediately obvious that the expression

$$(C_R l_R - C_F l_F) m v_x^2 \quad (13)$$

is responsible for the sign of  $K_2$  and the possibility for larger velocities  $v_x$  that  $K_2 < 0$ . This is indicating an unstable steady-state motion of the system. To increase the range of stable behaviour, it will help to put CG closer to the front  $l_F < l_R$  and/or ‘softer’ substitutive tyres at the front  $C_F < C_R$  (e.g. applying a stiffer torsion bar at the front axle).

## 2.2 Steady State Cornering Without Rear Wheel Steering ( $\delta_R = 0$ )

In general the common passenger car layout does not have additional rear wheel steering, but this feature may be used for control purposes in the near future. An essential information regarding the vehicle behaviour with respect to the influence of the cornering radius and the velocity is provided by the steady state condition,

where the cornering radius is equal to the curvature radius  $\rho = R$  and

$$v = \text{const.} \quad (14)$$

$$\dot{\psi} = r = v/R \quad (15)$$

$$a_y = v^2/R \quad (16)$$

The steady state values for the steering angle and the side slip angle of the car derive directly from (10a) and (10b) with (14) and with  $\delta_R = 0$ :

$$\delta_{F,st} = \delta_{Fo} + \frac{C_R l_R - C_F l_F}{C_R C_F l} m a_{y,st} \quad (17)$$

$$\beta_{st} = \beta_o - \frac{l_F}{C_R l} m a_{y,st} \quad (18)$$

Using the condition  $v \rightarrow 0$  the corresponding values of side slip angle and steering angle (also denoted Ackermann angle  $\delta_a$ ) are, see Fig. 2:

$$\beta_o = \frac{l_R}{R}, \quad \delta_a = \delta_{Fo} = \frac{l}{R} = \frac{l}{v_x^2} a_{y,st}, \quad \beta_o = \frac{l_R}{l} \delta_{Fo} \quad (19)$$

To characterize the steering behaviour, an understeer gradient is used:

$$K_{US} = \frac{m(C_R l_R - C_F l_F)}{C_R C_F l} \gtrless 0 \quad (20)$$

Consequently (17) can be modified, and with the sign of  $K_{US}$  the increase/decrease of the necessary steering angle with increasing values of velocity or acceleration can be explained.

$$\frac{\delta_{H,st}}{i_s} = \delta_{F,st} = \delta_{Fo} + K_{US} a_{y,st} \quad (21)$$

As indicated in (21) also the hand wheel steering angle  $\delta_{H,st}$  together with the steering system ratio  $i_s$  is introduced. Thus, (21) and  $K_{US}$  may be used to characterise the steering behaviour of the vehicle:

$$K_{US} > \text{understeer behaviour}$$

$$K_{US} = \text{neutral steering}$$

$$K_{US} < \text{oversteer behaviour}$$

For a graphical presentation of a typical behaviour two kinds of figures are common. With the data given in Table 1 for an oversteer vehicle A and an understeer vehicle B the Fig. 3 shows the change of steering angle  $\delta_F$  for constant velocity as function of

**Fig. 2** Driving condition  
for  $v \rightarrow 0$

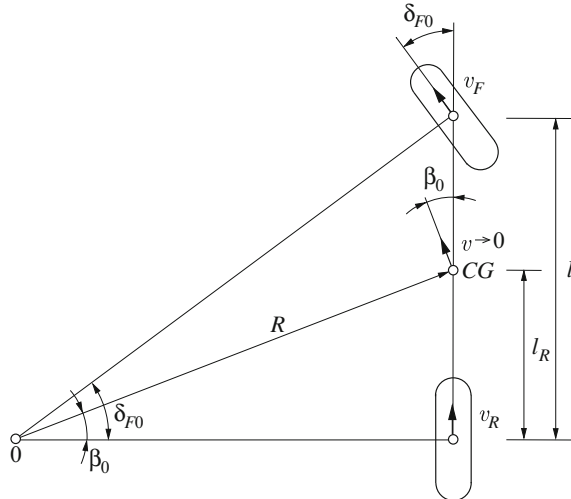


**Table 1** Vehicle data for the linear 2-wheel models used for the demonstration examples: two different steering characteristics

Vehicle	A	B
$m$	1900 kg	
$I_Z$	$2900 \text{ kgm}^2$	
$l_F$	1.44 m	
$l_R$	1.36 m	
$C_F$	$90\,000 \text{ N rad}^{-1}$	$60\,000 \text{ N rad}^{-1}$
$C_R$	$80\,000 \text{ N rad}^{-1}$	$110\,000 \text{ N rad}^{-1}$
$K_{US}$	$-1.95 \cdot 10^{-3} \text{ s}^2 \text{m}^{-1}$	$+6.50 \cdot 10^{-3} \text{ s}^2 \text{m}^{-1}$
Steering characteristics	oversteer	understeer

lateral acceleration  $a_y$  (for variation of  $R$ ) and constant radius  $R$  as function of lateral acceleration  $a_y$  (for variation of  $v$ ), Lugner (2007).

For the oversteer vehicle A with increasing  $a_y$  the necessary steering angle  $\delta_F$  decreases. Consequently an increasing sensitivity of the driver is necessary for proper steering. The understeer vehicle B needs increasing steering angles  $\delta_F$  with increasing  $a_y$ , a property that for the driver fits to the expected behaviour. Though the steering behaviour is quite different for vehicles A and B, the side slip angle  $\beta$  characteristics do not show greater differences with increasing  $a_y$ . For both vehicles the  $\beta < 0$  indicates an inward turned attitude during cornering.

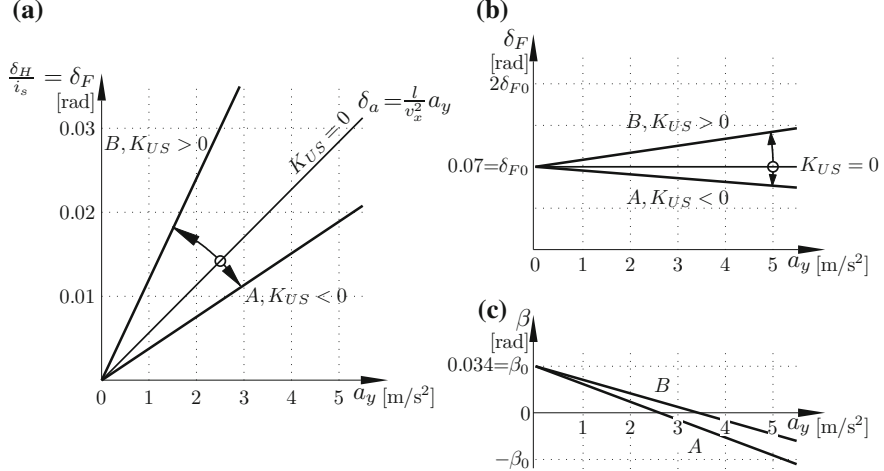


**Fig. 3** Steady state steering characteristics, data corresponding to Table 1: **a** for  $v = \text{constant} = 80 \text{ km/h}$ ; **b** for  $R = \text{constant} = 40 \text{ m}$ ; **c** side slip angles to **(b)**

### 2.3 Steady State Cornering with Rear Wheel Steering $\delta_R \neq 0$

The effects of additional rear wheel steering, representing an additional system input, make it possible to change/improve the steering behaviour or the side slip angle of the car.

For cornering with very low speed ( $v \rightarrow 0$ ), Fig. 4 provides

$$\frac{l}{R} = \delta_{Fo} - \delta_{Ro} \quad (22)$$

$$\beta_{Ro} = \frac{l_R}{l} \delta_{Fo} + \frac{l_F}{l} \delta_{Ro} = \frac{l_R}{R} + \delta_{Ro} \quad (23)$$

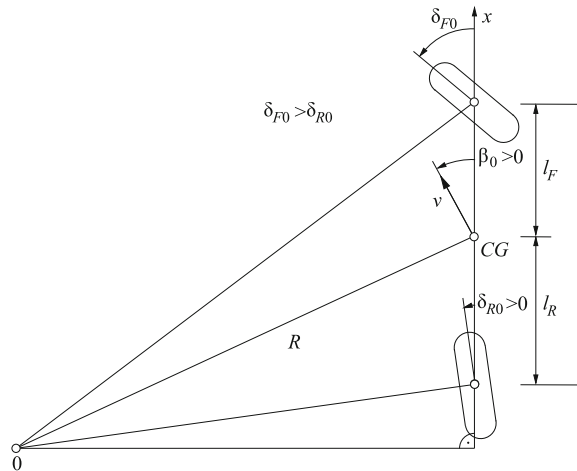
according to the relation of these two steering inputs. So  $\delta_{Ro}$  may be chosen in such a way that  $\beta_{Ro} = 0$  for left/right cornering.

For velocities or accelerations larger than zero the equation corresponding to (17) becomes

$$\delta_{F,st} - \delta_{R,st} = \delta_{Fo} - \delta_{Ro} + \frac{C_R l_R - C_F l_F}{C_F C_R l} m a_{y,st} \quad (24)$$

It is obvious that for constant  $\delta_{Fo} - \delta_{Ro}$  and no further change of the rear wheel steering angle (e.g.  $\delta_{R,st} = 0$ ), the characterisation for under-, neutral- and oversteer behaviour is the same as before. On the other hand, if  $(\delta_{R,st} - \delta_{Ro})$  is used as a variable input—e.g. by a control system—one may achieve an arbitrary steering behaviour.

**Fig. 4** Additional rear wheel steering: steady state cornering with  $v \rightarrow 0$



Assuming that there is no change of the initial rear wheel steering angle  $\delta_{R0}$ , and  $\delta_{R,st} = 0$ , the side slip angle of the vehicle will become

$$\beta_{R,st} = \beta_{Ro} + (\delta_{R,st} - \delta_{Ro}) - \frac{l_F}{C_R l} m a_{y,st} \quad (25)$$

Compared to (19), this relation indicates a shift in  $\beta_{st}$  only.

In contrast to (10a) it can be shown that, with a proper control, the side slip angle  $\beta$  of the car can be held at  $\beta_{st} = 0$ —as considered to be desirable in literature.

$$\beta_{st} = 0 = \delta_F \left( \frac{l_R}{l} - \frac{C_F l_F m v_x^2}{l^2 C_F C_R} \right) + \delta_R \left( \frac{l_F}{l} + \frac{C_R l_R m v_x^2}{l^2 C_F C_R} \right) \quad (26)$$

Especially in tight curves with  $v_x \rightarrow 0$  this control aim may help the driver regarding the orientation of the vehicle motion and the direction of his/her view. If it is wanted to have both a given steering (wheel) characteristic for the driver and the side slip angle  $\beta = 0$ , an additional front wheel steering  $\Delta\delta_F$  or a variable steering ratio  $i_s$  need to be used.

## 2.4 Stability

Under certain conditions the motion of the car—represented by the linear differential equations (9) or (10)—can become unstable. Even small disturbances at steady state driving conditions will result in uncontrolled motions, e.g. Mitschke and Wallentowitz (2014), Rill (2012).

The eigenvalues of the equations of motion characterize the stability behaviour. As well known, the eigenvalues  $\lambda_{1,2}$  can be derived from the homogenous part of the differential equations (9) or (10) by

$$\det(\mathbf{F} - \lambda \mathbf{E}) = 0 \quad (27)$$

(where  $\mathbf{E}$  represents the unity matrix) or

$$\lambda^2 + 2K_1\lambda + K_2 = 0 \quad (28)$$

From (28) the eigenvalues follow immediately with

$$\lambda_{1,2} = -K_1 \pm \sqrt{K_1^2 - K_2} \quad (29)$$

In general, stability is given as long as the real parts of the eigenvalues are smaller than zero. The system will show an unstable behaviour if  $K_2 < 0$ . To determine the sign of  $K_2$  Eq. (12) leads to

$$\begin{aligned} l^2 C_F C_R + (C_R l_R - C_F l_F) m v_x^2 &\gtrless 0 \\ l + \frac{(C_R l_R - C_F l_F)}{l C_R C_F} m v_x^2 &\gtrless 0 \end{aligned} \quad (30)$$

So it is immediately obvious that the expression (see (13))

$$(C_R l_R - C_F l_F) m v_x^2 \quad (31)$$

is responsible for the sign of  $K_2$  and the possibility for larger velocities  $v_x$  that  $K_2 < 0$  indicates the instability of the system.

Using (20) Eq. (30) can be expressed by

$$\delta_{F0} + K_{US} a_{y,st} \gtrless 0; \quad (32)$$

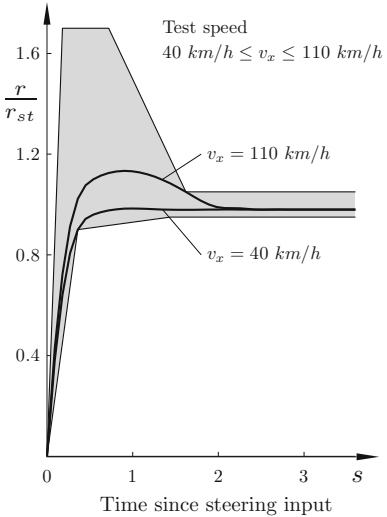
which is identical with the right hand side of (21). So the sign of the understeer gradient  $K_{US}$  is also informative regarding the stability. An oversteer vehicle can become unstable for higher velocities/accelerations.

Since only the homogenous equations are employed for the determination of the stability, the criterion (32) for a car with additional rear wheel steering needs to be modified due to (24) to

$$\delta_{F0} - \delta_{R0} + K_{US} a_{y,st} \gtrless 0 \quad (33)$$

Since  $\delta_{R0} \gtrless 0$  the lateral acceleration  $a_{y,st}$  for the stability limit can be changed compared to pure front wheel steering.

**Fig. 5** Steering step input limits defined by ESV (Experimental Safety Vehicle): with two examples of a passenger car (step input  $\dot{\delta}_H \cong 500^\circ/\text{s}$ , final steady state lateral acceleration  $a_{y,st} \cong 0.4g$ )



## 2.5 Step Steering Input

In critical situations it may happen that the driver will introduce a step like steering input. Then the response of the vehicle can be characterized e.g. by the yaw velocity  $r$  which will reach the steady state value  $r_{st}$  after the transient phase following the input. Figure 5 shows accepted limits for  $r(t)$ .

The corresponding steady state straight ahead driving yaw velocity gain (see (10b)) is defined by

$$G_{r,st} = \frac{r}{\delta_H/i_s}_{st} = \frac{v_x}{l + K_{US}v_x^2} \quad (34)$$

where the denominator is already introduced with (30).

For an understeer vehicle  $K_{US} > 0$  the gain  $G_{r,st}$  will have a maximum at a characteristic speed  $v_{ch}$  that can be obtained by

$$\begin{aligned} \frac{\partial G_{r,st}}{\partial v_x} &= \frac{l - K_{US}v_{ch}^2}{(l + K_{US}v_{ch}^2)^2} = 0 \\ v_{ch}^2 &= \frac{l}{K_{US}}, \quad K_{US} > 0 \end{aligned} \quad (35)$$

In contrast, the oversteer vehicle  $K_{US} < 0$  will have an unlimited yaw response for the critical speed  $v_{crit}$

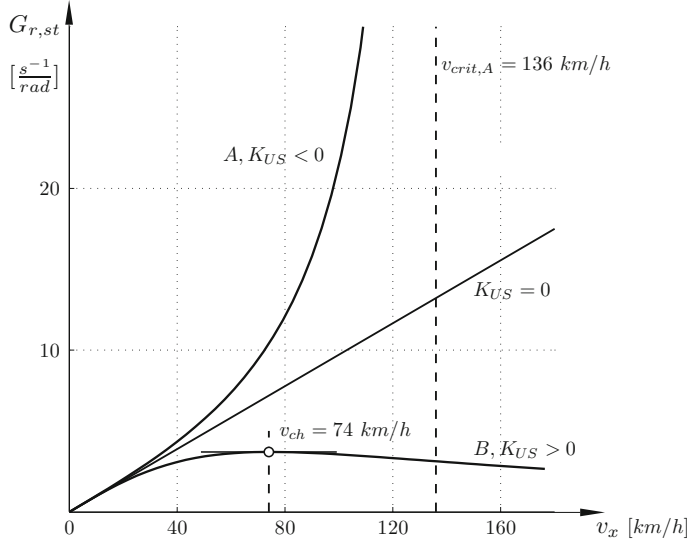


**Fig. 6** Behaviour of oversteer, neutral and understeer vehicle with respect to the static yaw velocity gain; vehicle data for A, B according Table 1

$$\begin{aligned} G_{r,s} &\Rightarrow \infty \\ v_{crit}^2 &= -\frac{l}{K_{US}}, \quad K_{US} < 0 \end{aligned} \quad (36)$$

Figure 6 shows for the already introduced vehicles A and B (see Table 1) the yaw velocity gains. The understeer vehicle B shows a nearly equal response for 40 km/h and more—a driver friendly behaviour. The increasing response of vehicle A will be a challenge for the driver even for velocities smaller than the critical one.

The corresponding acceleration response is shown in Fig. 7. With the steady state acceleration

$$a_{y,st} = r v_x$$

the lateral acceleration response

$$\frac{a_y}{\delta_H/is}_{st} = G_{ay,st} = \frac{v_x^2}{l + K_{US}v_x^2} \quad (37)$$

has the same structure as the yaw response. The understeer vehicle B has a limitation for the  $a_{y,st}$  while even a neutral steering vehicle tends to have nonlinear increasing values of  $G_{ay,st}$ .

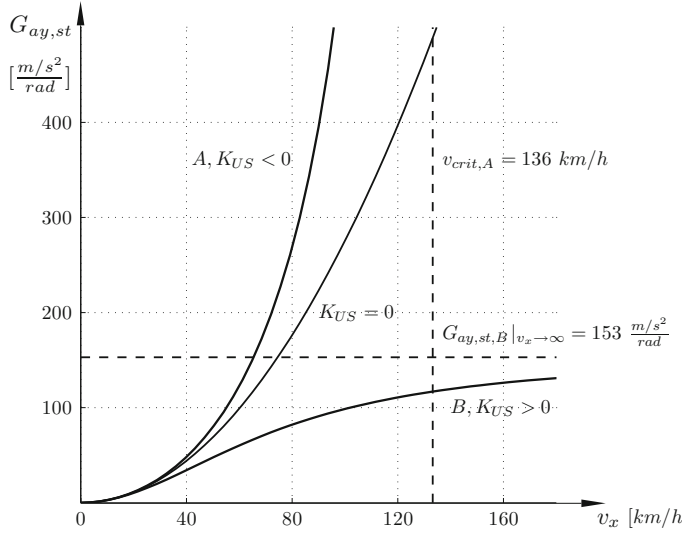


**Fig. 7** Steady state lateral acceleration gain for oversteer  $K_{US} < 0$ , neutral steer  $K_{US} = 0$  and understeer vehicle  $K_{US} > 0$ ; vehicle data for A, B according to Table 1

## 2.6 Frequency Response

To provide an information for an alternating steering the vehicle reaction to harmonic inputs of different frequencies can be considered. It is assumed that the driver starts the harmonic input at straight ahead driving; no rear wheel steering is taken into account.

The yaw velocity frequency response for frequency  $\nu$  results again from Eq. (10):

$$G_r(iv) = \left(\frac{r}{\delta_F}\right)|_{iv} = G_{r,st} \frac{1 + T_Z(iv)}{1 + \frac{2D}{\omega_o}(iv) - \frac{\nu^2}{\omega_o^2}} \quad (38)$$

with

$$\begin{aligned} T_Z &= \frac{mv_x l_F}{C_R l} \\ \omega_o^2 &= K_2 = \frac{C_F C_R l^2}{I_Z m v_x^2} \left(1 + \frac{K_{US} v_x^2}{l}\right) \\ D\omega_o &= K_1 \end{aligned}$$

The response for the lateral acceleration can be calculated using also (10) and

$$a_y = v_x(r + \dot{\beta})$$

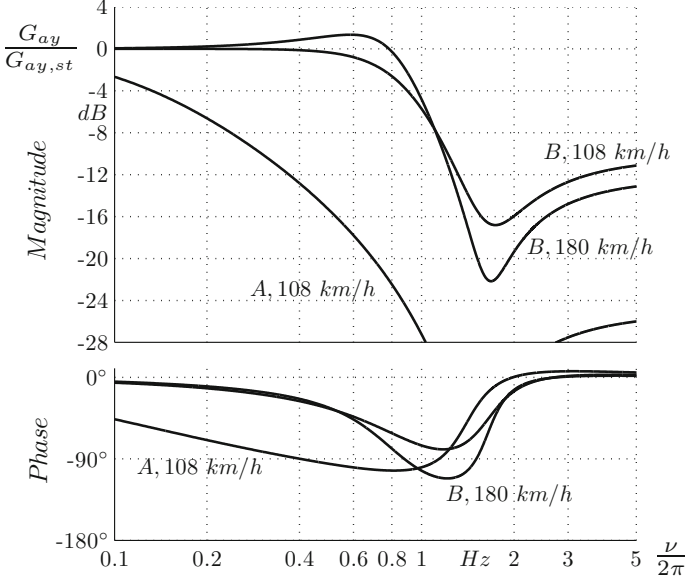


**Fig. 8** Normalized acceleration frequency response of the oversteer vehicle A and the understeer vehicle B (Table 1). No response of vehicle A for  $v > v_{crit} = 136$  km/h

$$\frac{a_y(iv)}{\delta_F(iv)} = v_x \left[ \frac{r(iv) + iv\beta(iv)}{\delta_F(iv)} \right]$$

$$G_{ay}(iv) = \left( \frac{a_y}{\delta_F} \right) = G_{ay,st} \frac{1 + T_1(iv) - T_2 v^2}{1 + \frac{2D}{\omega_o}(iv) - \frac{v^2}{\omega_o^2}} \quad (39)$$

with

$$T_1 = \frac{l_R}{v_x} \quad , \quad T_2 = \frac{I_z}{C_R l}$$

and  $D, \omega_0$  corresponding to (38).

With Fig. 8 it can be noticed that for the lateral acceleration gain in the region of normal steering till about 1 Hz the oversteer vehicle shows a strongly frequency dependent response with large phase angles compared to the driver friendly behaviour of vehicle B. The low steering response behaviour about 1–2 Hz is a generally accepted feature.

Examples for measured frequency responses are shown in Fig. 9 for an understeer vehicle.

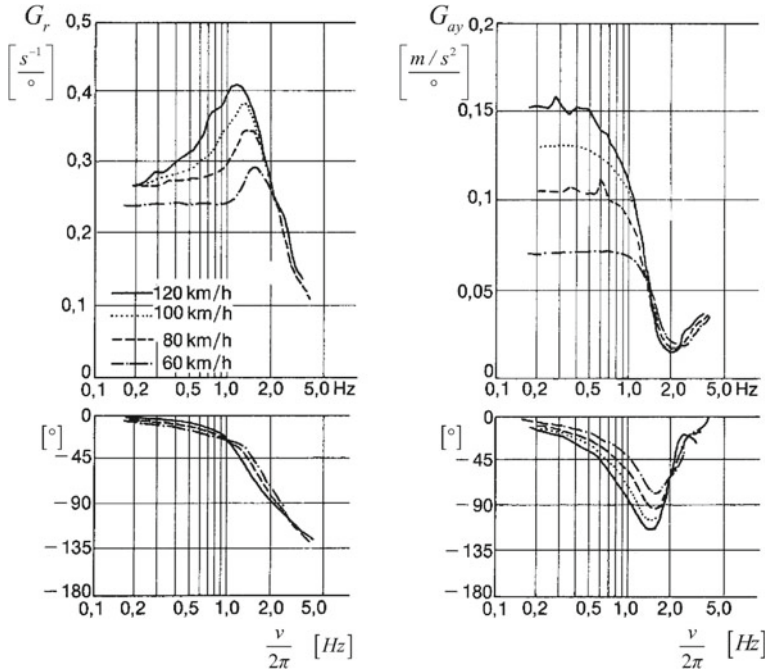


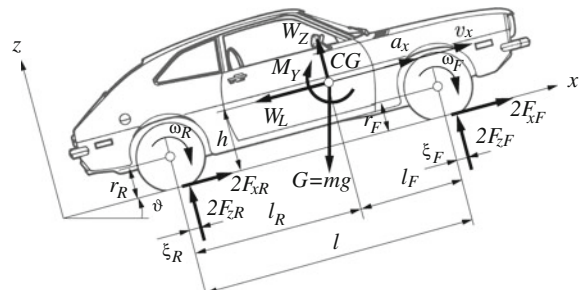
**Fig. 9** Measurements of yaw velocity and lateral acceleration responses of an understeer vehicle ( $K_{US} = 0.0062 \text{ s}^2 \text{m}^{-1}$ ,  $v_{ch} = 76 \text{ km/h}$ ) similar to vehicle A for different driving velocities, Lugner (2007)

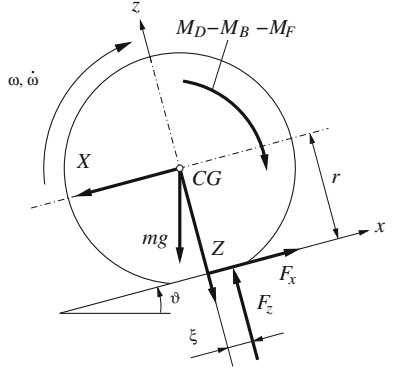
## 2.7 Longitudinal Dynamics, x-z-plane

To investigate the influences of braking or accelerating a plane vehicle model like Fig. 10 is introduced, Plöchl et al. (2015), Lugner (2007). Thereby no heave and pitch motions are taken into account.

If the individual rotations of the wheels are included further extensions with respect to the configuration of the drive train (four-wheel drive, electric hub drive,

**Fig. 10** Plane vehicle model for longitudinal dynamics; symmetry to central x-z-plane



**Fig. 11** Model of a wheel

etc.) and at least the sticking and slipping of a wheel can be considered. Correspondingly Fig. 11 shows the essential features of the wheel motion. It is assumed that in the wheel hub—also the CG of the wheel—the forces  $X, Z$  are transferred to the axle. The normal force  $F_z$  has an offset, the pneumatic trail  $\xi$ , which represents the rolling resistance.  $M_D, M_B, M_F$ , are driving torque, braking torque and friction moment by the wheel bearing.

For the kinematics, the simplification that the tyre radius  $r$  is equal to the rolling radius is assumed.

The equations of motion for the vehicle Fig. 10 now can be established:

$$ma_x = 2F_{xF} + 2F_{xR} - W_L - G \sin \vartheta \quad (40)$$

$$0 = 2F_{zF} + 2F_{zR} + W_Z - G \cos \vartheta \quad (41)$$

$$2I_F\dot{\omega}_F + 2I_R\dot{\omega}_R = 2F_{zR}(l_R - \xi_R) - 2F_{zF}(l_F + \xi_F) - 2(F_{xF} + F_{xR})h + M_Y \quad (42)$$

With the aerodynamic components  $W_L, W_Z, M_Y$ , the moments of inertia  $I_F, I_R$  of the wheels with respect to their axes and the whole vehicle mass  $m$ . The angular acceleration of e.g. the rear wheel can be calculated by

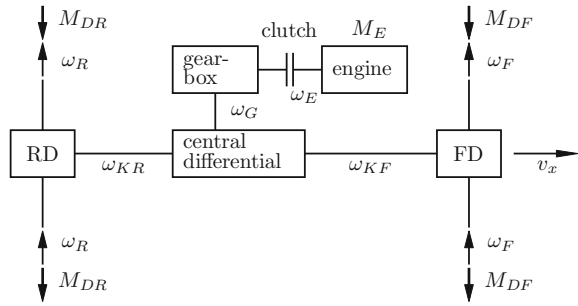
$$I_R\ddot{\omega}_R = M_{DR} - M_{BR} - M_{FR} - F_{zR}\xi_R - F_{xR}r_R \quad (43)$$

with the drive torque  $M_{DR}$ , the braking moment  $M_{BR}$  and possible small friction effects with  $M_{FR} \approx 0$ .

To determine the effects of the drive train configuration by Eqs. (40)–(43), the longitudinal acceleration  $a_x$  initiated by the drive/brake forces has to be considered. Assuming pure rolling of the wheels and

$$\begin{aligned} r_R\omega_R &= r_F\omega_F = r\omega = v_x \\ r\dot{\omega} &= a_x \end{aligned} \quad (44)$$

**Fig. 12** Structure of a drive train with axle and central differentials



the longitudinal acceleration of the vehicle becomes

$$(m + \frac{2I_R}{r^2} + \frac{2I_F}{r^2})a_x = \frac{M_D}{r} - \frac{M_B}{r} - W_{ges} \quad (45)$$

with the substitutes

$$\begin{aligned} W_{ges} &= \frac{M_F}{r} + W_R + W_L + W_G \\ \xi_F/r &= \xi_R/r = f_R \\ W_R &= f_R(2F_{zR} + 2F_{zF}) = f_R(G \cos \vartheta - W_Z) \\ W_G &= mg \sin \vartheta \\ M_F &= 2(M_{FR} + M_{FF}) \approx 0 \\ M_D &= 2M_{DR} + 2M_{DF} \\ M_B &= 2M_{BR} + 2M_{BF} \end{aligned}$$

A drive train configuration with symmetric structure, angular velocity  $\omega_E$  of the engine and  $\omega_{KR}$ ,  $\omega_{KF}$  for the front and rear drive shafts is established with Fig. 12.

With the transmission ratio  $N_{Gn}$  of the gear box and the ratio  $N_D$  of the axle differentials and the torque splitting of the central differential with  $v_F$ ,  $v_R$ , the kinematics become

$$\begin{aligned} \omega_E &= \omega_G N_{Gn}, \\ \omega_G &= v_R \omega_{KR} + v_F \omega_{KF} \\ \omega_{KR} &= N_D \omega_R, \quad \omega_{KF} = N_D \omega_F \end{aligned} \quad (46)$$

and the torques for the different kind of drives

$$\begin{aligned}
2M_{DF} &= M_D v_F, \quad 2M_{DR} = M_D v_R \\
&\text{with } v_F + v_R = 1 \\
&\text{for rear wheel drive : } v_R = 1 \\
&\text{for front wheel drive : } v_F = 1 \\
&\text{for 4WD with equal distribution : } v_R = v_F = 0.5
\end{aligned} \tag{47}$$

The torque transfer from the engine torque  $M_E(\omega_E)$  to the wheels, using (44), can be written by

$$\begin{aligned}
M_D &= (2M_{DF} + 2M_{DR}) = \\
&\eta M_E(\omega_E)N - r \left[ \frac{\Theta_E N^2}{r^2} + \frac{(I_C + I_{DR} + I_{DF})}{r^2} N_{Gn}^2 \right] a_x
\end{aligned} \tag{48}$$

with

$$N = N_{Gn} N_D$$

$\eta$  coefficient of efficiency  
 $\Theta_E$  substitutive moment of inertia for the engine  
 $I_C$  moment of inertia for parts of gears and central differential  
 $I_{DF}, I_{DR}$  moments of inertia: parts of differentials and shafts.

Consequently (45) can be transformed to

$$(m + m_r)a_x = \frac{\eta M_E \omega_E N}{r} - \frac{M_B}{r} - W_{ges} \tag{49}$$

with the reduced mass for the rotational parts:

$$m_r = \frac{1}{r^2} \left[ \Theta_E N^2 + (I_C + I_{RD} + I_{FD}) N_{GN}^2 + (2I_R + 2I_F) \right]$$

To determine the normal forces  $F_{zF}$  and further on the friction limits for the force transfer of the tyres, again Eqs. (41) and (42) are used. With the simplification of pure rolling (44) and equal values  $\xi_R = \xi_F = \xi$ , these equations can be written in the form

$$\begin{aligned}
2F_{zF} + 2F_{zR} &= G \cos \vartheta - W_z \\
-2l_F F_{zF} + 2l_R F_{zR} &= \left[ \left( \frac{2I_F}{r} + \frac{2I_R}{r} \right) a_x + (ma_x + W_L + G \sin \vartheta)h \right. \\
&\quad \left. + M_Y + \xi(G \cos \vartheta - W_Z) \right]
\end{aligned} \tag{50}$$

Linearization and neglecting small terms and aerodynamic components leads to

$$\begin{aligned} M_Y &\cong 0, \quad W_Z \cong 0 \\ \xi(G \cos \vartheta) &\ll (ma_x + W_L + G \sin \vartheta)h \\ (2I_F + 2I_R)/r &\ll mh \end{aligned}$$

$$\begin{aligned} \frac{F_{zF}}{G} &= \frac{l_R}{l} \cos \vartheta - a^* \frac{h}{l} \\ \frac{F_{zR}}{G} &= \frac{l_F}{l} \cos \vartheta + a^* \frac{h}{l} \end{aligned} \quad (51)$$

$$\begin{aligned} \text{with } a^* &= \left( \frac{a_x}{g} + \sin \vartheta + \frac{W_L}{mg} \right) \\ q &= 100 \cdot \tan \vartheta \text{ in \%} \end{aligned} \quad (52)$$

If the inclination angle  $\vartheta$  is small (road grade  $q$  less than about 10%), then the sine-function can be linearized too.

With the determination of the normal forces, the rolling resistance  $W_R$ , see (45), can be calculated. Corresponding to Fig. 11 without  $M_D, M_B, M_F$  and no grade  $\vartheta = 0$ , the longitudinal force due to tyre flexibility and energy dissipation can be written with

$$F_x = -\frac{\xi}{r} F_z = -f_R F_z \quad (53)$$

Some examples for typical values of the rolling resistance coefficient  $f_R$  are shown in Fig. 13, see e.g. Plöchl et al. (2014). As expected the energy dissipation increases at higher speeds, but in the limits by traffic regulations it is nearly constant.

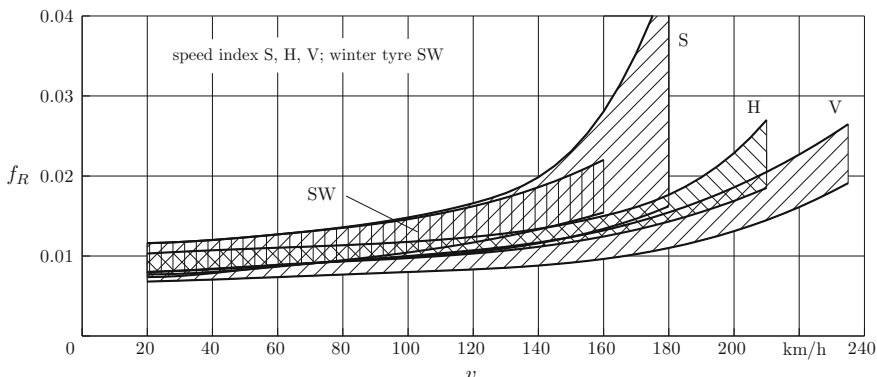


**Fig. 13** Rolling resistance coefficient  $f_R$  for different types of passenger car tyres

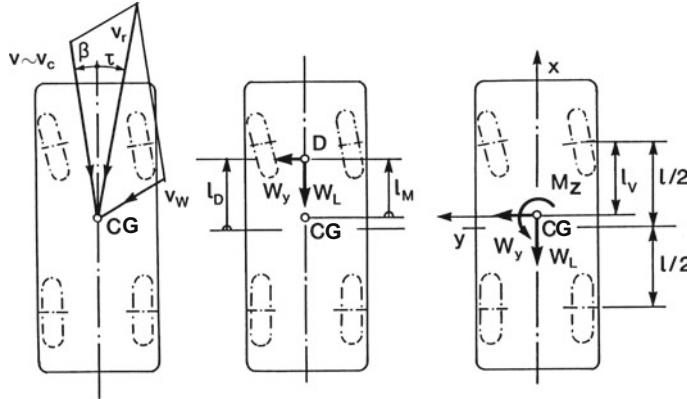


**Fig. 14** Aerodynamic forces  $W_y$ ,  $W_L$  and moment  $M_Z$  by running speed  $v_c$  and ambient wind  $v_w$ ; plane motion

The consequences of the aerodynamics for a vehicle running with  $v$  and ambient wind  $v_w$ , are shown in Fig. 14, Mischke and Wallentowitz (2014), Kortüm and Lugner (1994).

With the cross section area  $A$  and aerodynamic coefficients  $c_i$ , the forces are presented by

$$\begin{aligned} W_L &= W_X = c_x(\tau)A \cdot \frac{v_r^2 \rho}{2} \\ W_Y &= c_y(\tau)A \cdot \frac{v_r^2 \rho}{2} \\ M_Z &= c_M(\tau)l_M A \cdot \frac{v_r^2 \rho}{2} \end{aligned} \quad (54)$$

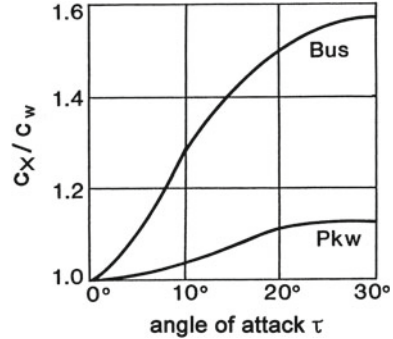
The coefficients are determined by experiments in a wind tunnel or/and also by software packages calculating the aerodynamic flow.

To take into account the angle of attack  $\tau$ , the coefficients are considered to be functions of  $\tau$ . Defining the coefficient for calm air with  $c_w = c_x(\tau = 0)$  as an example, Fig. 15 shows the normalized value  $c_x(\tau)/c_w$ , Kortüm and Lugner (1994). The values of the coefficient vary depending on the shape of the car body and will be about  $c_w \sim 0.3$  for passenger cars. The position for point D can be estimated with  $l_D \cong 0.3l$  for passenger cars and  $l_D \cong 0.17l$  for more squared like shapes.

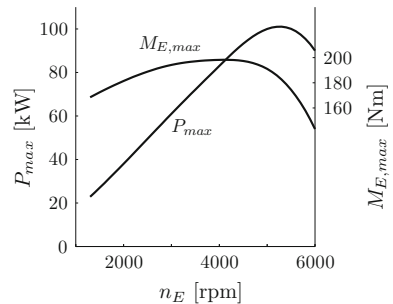
To provide driving performance information with respect to available engine torque  $M_E$ , transferred to the wheels or corresponding longitudinal forces, the engine characteristics and drive train structure have to be known.

Figure 16 shows the typical maximal driving torque  $M_{E,max}(n_E)$  and power  $P_{max}(n_E)$  of a gasoline engine as function of the engine speed  $n_E = 60(\omega_E/2\pi)$  for steady state conditions, Lugner (2007).

**Fig. 15** Normalized drag coefficient  $c_x(\tau)/c_w$  as function of the angle of attack  $\tau$



**Fig. 16** Maximum torque  $M_{E,max}$  and power  $P_{max}$  of a gasoline combustion engine



Considering the influence of the throttle position  $\lambda_T$  and the engine drag  $M_{E,d}(n_E)$  an approximation for the available engine torque can be formulated. For low velocities/engine speeds, due to the fuel injection, at  $\lambda_T = 0$  the drag  $M_{E,d}(n_E) > 0$ . In the range of operation,  $M_{E,d}$  is approximated by a linear function of  $n_E$ .

$$M_E = (M_{E,max} - M_{E,d})f(\lambda_T) + M_{E,d}, \quad 0 \leq f(\lambda_T) \leq 1 \quad (55)$$

So with the knowledge of  $f(\lambda_T)$  and the characteristics for  $M_{E,max}$  and  $M_{E,d}$  the whole performance volume of the engine can be presented. Furthermore the transmission ratio  $N$  can be introduced. With the effective driving force  $K_E$  and  $W_{ges}$ —see (49)—the vehicle driving performance becomes

$$\begin{aligned} m\lambda a_x &= K_E(v, N) - W_{ges}(v, N) \\ \lambda &= \frac{m + m_R}{m} \end{aligned} \quad (56)$$

$$K_E = \frac{\eta M_E(n_E) N_D N_{Gn}}{r}, \quad K_{Emax} = \eta \frac{M_{Emax}(n_E)}{r} N_D N_{Gn} \quad (57)$$

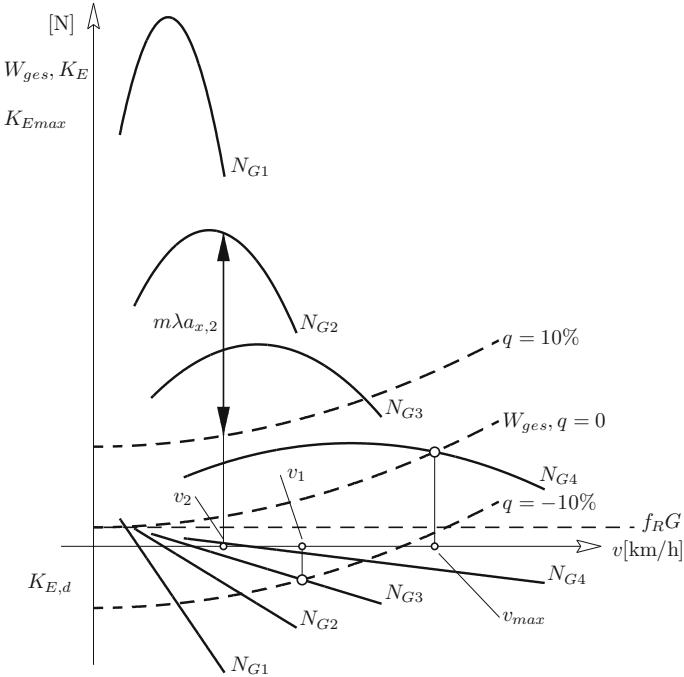


**Fig. 17** Driving characteristics of a passenger car: max engine driving forces  $K_{E,max}$  and drag forces  $K_{E,d}$  with 4 gears  $N_{Gi}$  and driving resistances  $W_{ges}$  for different grades  $q$

Now using the engine characteristics Eq. (55), limit values for the principal driving behaviour of a gasoline engine vehicle with 4 gears can be depicted in Fig. 17.

For a road without grade,  $q = 0$ ,  $v_{max}$  is determined by the intersection of the resistances with  $K_{E,max}$  of the fourth gear ( $N_{G4}$ ). The velocity  $v_1$  results from a downhill run ( $q = -10\%$ ) without throttle activation. If the car is operated at  $v_2$  with the second gear ( $N_{G2}$ ) on an uphill road with  $q = 10\%$ , the (still) available driving force  $m\lambda a_{x,2}$  can be used for accelerating the car.

So Fig. 17 represents an overall diagram for the creation of the effective driving force  $K_E$  by engine and drive train transmission to the wheels. In principle, similar diagrams will also be valid for other kinds of drive train and engines when using characteristics equivalent to  $K_{E,max}$  and  $K_{Ed}$ .

Alternative propulsion systems in operation today are hybrid systems with a combination of electric engine(s) and combustion engine, and full electric systems. The latter may have a centrally placed engine or wheel hub motors, with the possibility to provide individual torques to each wheel, Chan (2007). To fully utilize such kinds of propulsion, control systems have to be introduced, and the individual tyre-road contacts need to be considered generally in combination with more complex vehicle models. Examples of such drive trains are investigated e.g. in Galvagno et al. (2013).

To investigate the braking performance, Eq. (52) needs to be considered again. For inclination angle  $\vartheta$  and aerodynamic resistance  $W_L$  the normalized deceleration  $\beta$  of the car can be written by

$$\begin{aligned}\beta &= -\left(\frac{a_x}{g} + \sin \vartheta + \frac{W_L}{mg}\right) \\ \beta &= \left(-\frac{2F_{xF}}{mg}\right) + \left(-\frac{2F_{xR}}{mg}\right)\end{aligned}\quad (58)$$

$$\beta = (-\bar{F}_{xF}) + (-\bar{F}_{xR}) \quad (59)$$

In case of large  $\vartheta$  and aerodynamic drag it may happen that  $\beta < 0$  despite of  $a_x < 0$ , meaning downhill acceleration.

Using (51), the normalized tyre forces can be expressed by

$$\begin{aligned}\bar{F}_{zF} &= \bar{l}_R + \beta \bar{h} \\ \bar{F}_{zR} &= \bar{l}_F - \beta \bar{h} \\ \bar{l}_R &= \frac{l_R}{l}, \quad \bar{l}_F = \frac{l_F}{l}, \quad \bar{h} = \frac{h}{l}\end{aligned}\quad (60)$$

Limitations resulting from the force transfer (tyre–road) will be approximated using constant friction coefficients

$$\mu_{max} = \mu_{R,max} = \mu_{F,max} \quad (61)$$

$$|\bar{F}_{xi}| \leq \mu_{max} \bar{F}_{zi} \quad i = F, R$$

With (59) and (61) the maximum deceleration  $\beta_{max} = \beta_{ideal}$  is achieved when both axles are at the limit of locking

$$\begin{aligned}|\bar{F}_{xi}| &= \mu_{max} \bar{F}_{zi} \quad i = F, R \\ \beta_{max} &= \beta_{ideal} = \mu_{max}\end{aligned}\quad (62)$$

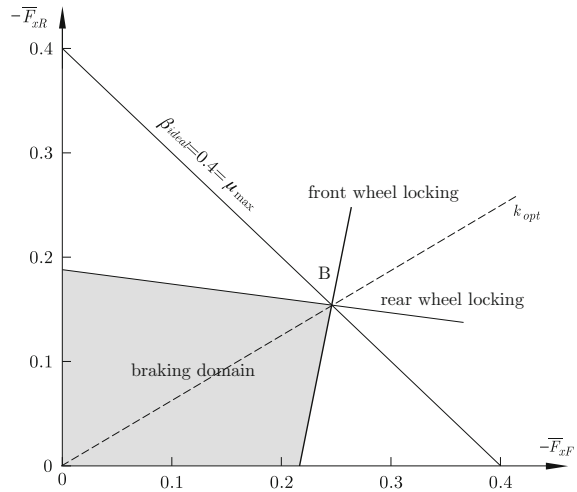
and with (59) follows

$$(-\bar{F}_{xF}) + (-\bar{F}_{xR}) = \mu_{max} \quad (63)$$

A break force balance  $k$  by the design of the brake system is defined by (the negative sign is used to indicate the direction of action of the forces):

$$k = \frac{-\bar{F}_{xF}}{-\bar{F}_{xR}} \quad (64)$$

**Fig. 18** Example of the braking capability for  $\mu_{max} = 0.4$ , symmetric arrangement, optimal brake balance  $k_{opt}$ ,  $\beta > 0$



To utilize the maximum deceleration, that is achieved when both the front and rear wheels are at their friction limit, the brake balance has to be, using (60):

$$\frac{(-\bar{F}_{xF})}{(-\bar{F}_{xR})} = \frac{\bar{l}_R + \bar{h}\mu_{max}}{\bar{l}_F - \bar{h}\mu_{max}} = k_{opt}. \quad (65)$$

Further on relations can be established between  $\bar{F}_{xF}$ ,  $\bar{F}_{xR}$  for the cases that only front or rear wheels are locking.

$$\begin{aligned} (-\bar{F}_{xF}) &= \mu_{max}\bar{F}_{zF}; \quad (-\bar{F}_{xR}) = (-\bar{F}_{xF}) \frac{1 - \bar{h} \cdot \mu_{max}}{\bar{h} \cdot \mu_{max}} - \frac{\bar{l}_R}{\bar{h}} \\ (-\bar{F}_{xR}) &= \mu_{max}\bar{F}_{zR}; \quad (-\bar{F}_{xF}) = -(-\bar{F}_{xR}) \frac{1 + \bar{h}\mu_{max}}{\bar{h}\cdot\mu_{max}} + \frac{\bar{l}_F}{\bar{h}} \end{aligned} \quad (66)$$

Choosing e.g.  $\mu_{max} = 0.4$ , Eq. (66) will define a breaking domain: within this area the vehicle can brake without reaching the friction limits at one of its wheels/axles, Fig. 18. In point B all wheels are at the friction limit corresponding to (62). The diagonal line  $\beta = \mu_{max} = 0.4$  is provided by relation (63). With (65), the brake balance  $k_{opt}$  will cross the line of  $\mu_{max}$  in point B, indicating the utilization of the maximum braking forces at both axles.

The brake performance diagram, Fig. 19, Lugner (2007), shows the braking domains for  $\mu_{max} = 0.3$  and  $\mu_{max} = 0.8$  for loaded and unloaded conditions,  $\beta > 0$ . The curves (a) and (b) represent the points B for all possible  $\mu_{max}$  values. As an example: point A on (c), which represents the design brake balance, corresponds to a normalized deceleration of  $\beta = 0.4$  determined by the intersection of  $\beta = \text{constant}$

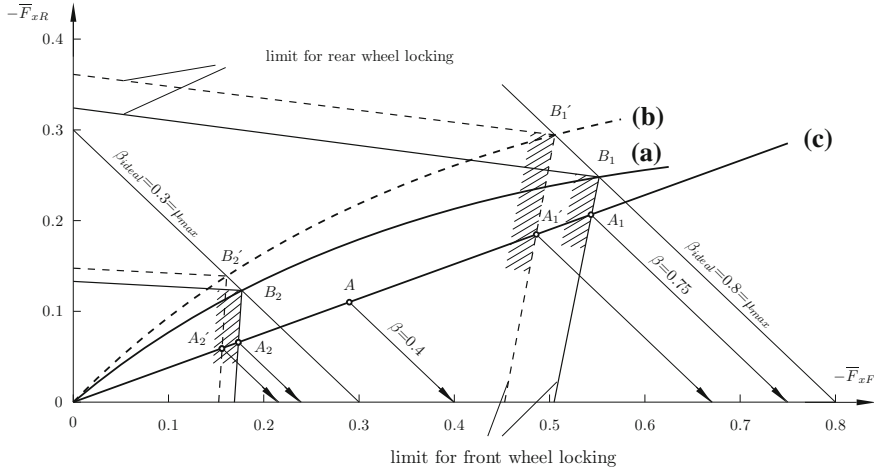


**Fig. 19** Brake force distribution diagram for a passenger car with 2 loading conditions: **a**  $\bar{l}_F = 0.47$ ,  $\bar{h} = 0.2$ ; **b**  $\bar{l}_F = 0.52$ ,  $\bar{h} = 0.19$ ; design brake balance, **c**  $\bar{F}_{xF}/\bar{F}_{xR} = k = 2.63$

with the  $x$ -axis. The brake balance  $k$  is chosen in a way that the front wheels will lock first for all possible  $\mu_{max}$ . Generally, if front wheel locking will occur, the vehicle will just move straight ahead, without starting yaw motion. The points  $A'_i$ ,  $A_i$  and the corresponding  $\beta$ -diagonals define the achieved decelerations using (59).

With a more complex brake system lay out there may be a brake balance factor different for different deceleration sections thereby better using the corresponding braking domains.

The consequences/area of action of an ABS system are indicated by the shaded areas in Fig. 19. But not only the more or less improvement in deceleration but especially the avoidance of a wheel locking is essential!

To get some information with respect to  $\mu$ -split conditions—the wheels of one side encounter low friction values—a simple extension of the plane longitudinal vehicle model, Fig. 20, together with a drive train configuration similar to Fig. 12, and  $v = v_R = v_F = 0.5$  according to (47) can be used. Thereby no grade or aerodynamic drag are taken into account but the height of the CG above the ground is considered. Different cases of the locking of the central differential  $C$  or axle differentials I, II induce yaw moments  $W^*$  which may result in a spinning of vehicle if there is no proper reaction by the driver. A DSP (dynamic stability program) will avoid such a yaw moment and will correspond to the case A in the considered configuration.

As expected the all wheel drive with all differentials locked AC I II will utilize the maximum  $\mu$ -value at each wheel providing the largest acceleration  $a_{x,max}$  but also the largest yaw moment  $W^*$ . For other configurations of the drive train  $a_{x,max}$  is reached if one or more wheels are at their friction limits. E.g. for a standard rear wheel drive RD the limit is defined by the slipping of wheel 4 while both wheels of the rear axle

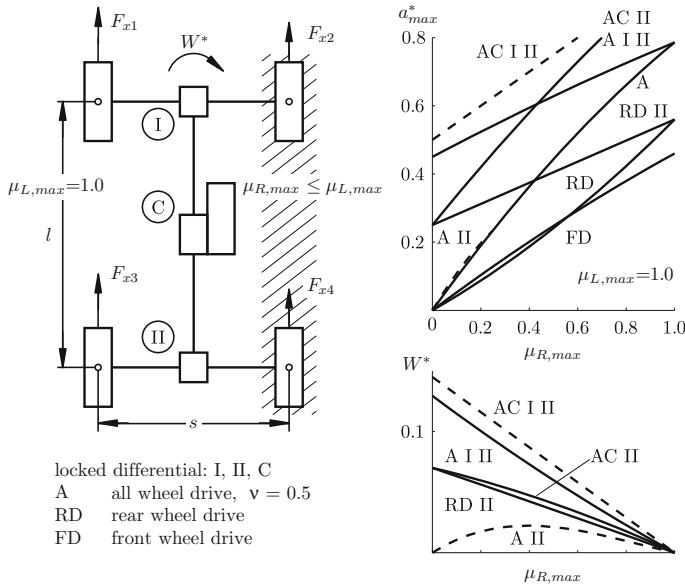


**Fig. 20** Different drive train configurations with  $\mu$ -split conditions, maximum possible acceleration  $a_{x,max}$  and yaw moment  $W^* = [(F_{x1} - F_{x2}) + (F_{x3} - F_{x4})](s/2)$

transfer the same longitudinal force. No yaw moment  $W^*$  is generated. Now locking the rear axle differential, configuration RD II allows the left wheel 3 to transfer a higher longitudinal force  $F_{x3} > F_{x4}$  resulting in higher  $a_{max}$  but also providing a yaw moment. When no axle differential is locked—cases RD, FD, A—, no yaw moment will occur.

## 2.8 Vertical Motion

Mainly the vertical motion of the car body by heave and pitch resulting from the road surface structure is responsible for the ride comfort of the passengers. For further details please refer to the following chapter of this book: D. Hrovath, H.E. Tseng, J. Deur: *Optimal Vehicle Suspensions: A System-level Study of Potential Benefits and Limitations*. In general, the root mean square value of the body acceleration  $a_{RMS}$  is used as comfort measure, with additionally taking into account the human sensitivity for vibrations.

The human sensitivity was determined by vibration experiments where different frequencies and vertical/horizontal accelerations are applied onto a person. The results are standardized in VDI 2057, ISO 2631-1. For a stochastic input the signal passes a standardized form filter to provide a weighed  $a_{RMS}$ -value as a sensitivity measure for the effect of vibrations on the whole human body. In Fig. 21, VDI

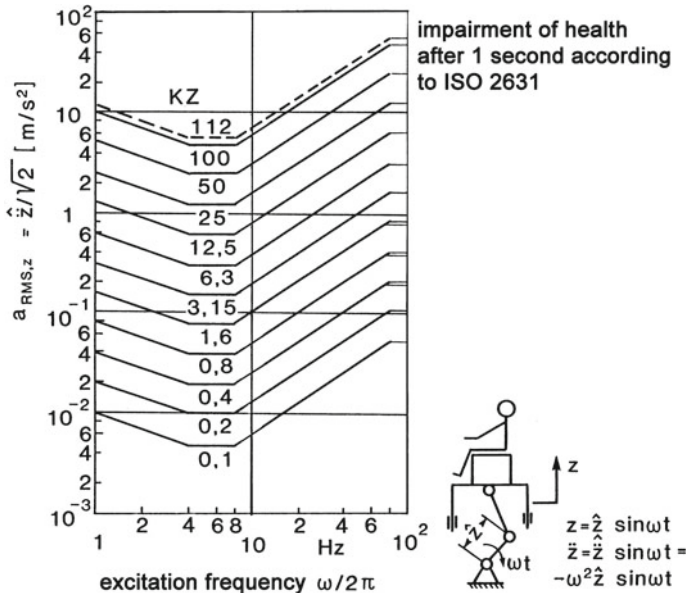


**Fig. 21** Human sensitivity to harmonic excitation by the value of KZ

2057 edition 1979, larger KZ-values indicate less tolerance to the vibration and less duration without comfort reduction or pain, Kortüm and Lugner (1994), Popp and Schiehlen (2010). Obviously in the range of 4–8 Hz the human body with its internal structure is most sensitive.

For the necessary stochastic input  $\zeta$  of the road, profile approximations by white noise and form filter, standard profiles or (more expensive) measurements are used. Very often the vehicle itself is represented by a simple vibration system, e.g. Popp (2014), Zhao (2017).

Such a vehicle model with 4 DoF is shown in Fig. 22, Kortüm and Lugner (1994). The aim is to determine the vertical acceleration  $a_{RMS,z}$  to evaluate the impact of the stochastic input to the wheels by the road excitations  $\zeta_F(t)$  and  $\zeta_R(t) = \zeta_F(t - \frac{\lambda}{v})$ . The distance  $\lambda$  characterises the position on the car body.

The linearized equation of motion with constant coefficients and the stochastic vector  $h$  is

$$\mathbf{M}\ddot{\mathbf{y}} + \mathbf{D}\dot{\mathbf{y}} + \mathbf{K}\mathbf{y} = h \quad (67)$$

$$z = \begin{bmatrix} z_C \\ \theta \\ z_F \\ z_R \end{bmatrix} = z_s + y = z_s + \begin{bmatrix} y_C \\ \theta \\ y_F \\ y_R \end{bmatrix}$$

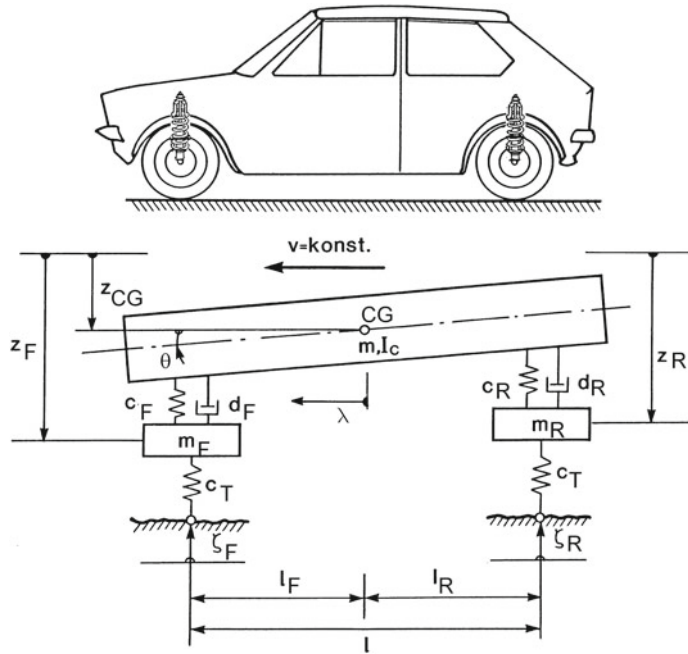


**Fig. 22** Plane vehicle model for the determination of the vertical accelerations

$$\mathbf{D} = \begin{bmatrix} d_F + d_R & d_F l_F - d_R l_R & -d_F & -d_R \\ d_F l_F - d_R l_R & d_F l_F^2 + d_R l_R^2 & -d_F l_F & d_R l_R \\ -d_F & -l_F d_F & d_F & 0 \\ -d_R & l_R d_R & 0 & d_H \end{bmatrix}$$

$$\mathbf{M} = \begin{bmatrix} m & 0 & 0 & 0 \\ 0 & I_C & 0 & 0 \\ 0 & 0 & m_F & 0 \\ 0 & 0 & 0 & m_R \end{bmatrix}$$

$$\mathbf{K} = \begin{bmatrix} c_F + c_R & c_F l_F - c_R l_R & -c_F & -c_R \\ c_F l_F - c_R l_R & c_F l_F^2 + c_R l_R^2 & -l_F c_F & l_R c_R \\ -c_F & -l_F c_F & c_F + c_T & 0 \\ -c_R & l_R c_R & 0 & c_R + c_T \end{bmatrix}$$

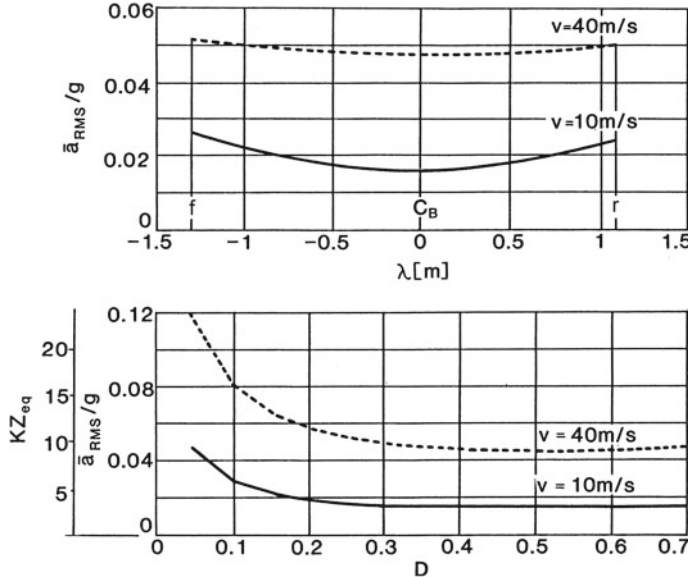


**Fig. 23** Comfort measure  $KZ_{eq}$  and normalized vertical root mean square value  $\bar{a}_{rms}/g$  for different positions  $\lambda$  at the car body ( $D = 0.3$ ) and as function of the suspension damping  $D$  for different forward velocities  $v$

$$h = \mathbf{H}\zeta = \begin{bmatrix} 0 & 0 \\ 0 & 0 \\ -c_T & 0 \\ 0 & -c_T \end{bmatrix} \begin{bmatrix} \zeta_F \\ \zeta_R \end{bmatrix}$$

As can be noticed, the small quantities  $y_F, y_R$  are the deviations from the steady-state wheel positions and  $y_C$  that from the *CG* of the car body. The pitch angle for steady state is assumed to be  $\theta = 0$ .

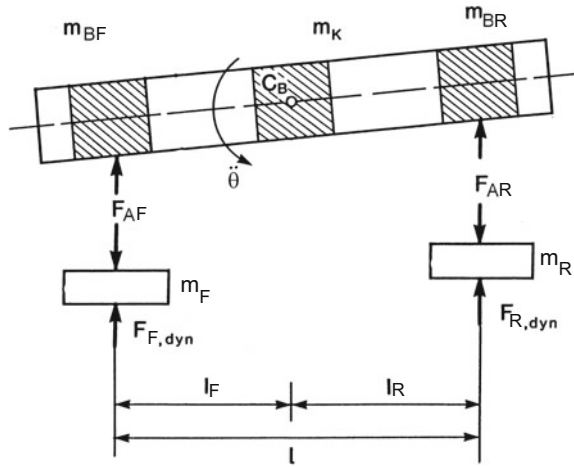
Using the covariance analysis and the comfort measure presented in Fig. 21, the relevant  $\bar{a}_{RMS}/g$ -values and  $KZ_{eq}$ -values can be determined, where the natural damping  $D$  and respective damping constants are related by

$$\begin{aligned} d_F &= 2D\sqrt{c_F ml_R/l} \\ d_R &= 2D\sqrt{c_R ml_F/l} \end{aligned} \tag{68}$$

Figure 23 shows that  $\bar{a}_{RMS}/g$  is lowest near to the centre of the vehicle and the natural damping needs to be about  $D \geq 0.2$  to guarantee a reasonable vertical comfort.

To simplify the 4 DoF model, an assumption with respect to the distribution of the car body mass can be used.

**Fig. 24** Substitution of the car body by 3 concentrated masses



The car body is presented by 3 substitutive masses, see Fig. 24, which need to fulfill the conditions

$$\begin{aligned} m_{BF} + m_{BR} + m_K &= m, \\ m_{BF}l_F &= m_{BR}l_R, \\ m_{BF}l_F^2 + m_{BR}l_R^2 &= I_C = mi_C^2 \end{aligned} \quad (69)$$

with the whole body mass  $m$  and the moment of inertia  $I_C$ , like before.

By (69) the substitutive masses become

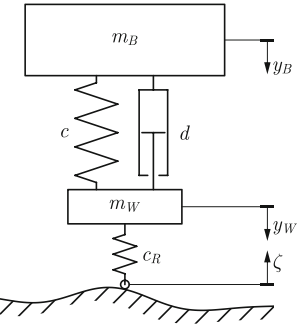
$$\begin{aligned} m_K &= m \left( 1 - \frac{i_C^2}{l_F l_R} \right) \cong 0, \\ m_{BF} &= m \frac{i_C^2}{l_F l} \cong m \frac{l_R}{l}, \\ m_{BR} &= m \frac{i_C^2}{l_R l} \cong m \frac{l_F}{l} \end{aligned} \quad (70)$$

As indicated with the first equation, if  $i_C \sim \sqrt{l_F l_R}$ —which is valid in most passenger cars—the vehicle model can be reduced to two separate 2 mass models, Fig. 25—a well known and investigated approach, e.g. Zhao (2017), Hrovat et al. (2014).

The two equations of motion, in the similar form like (67), taking into account the deviations from the static positions, are

$$\mathbf{M}\ddot{\mathbf{y}} + \mathbf{D}\dot{\mathbf{y}} + \mathbf{K}\mathbf{y} = h \quad (71)$$

**Fig. 25** Vertical two mass model: proportional body mass  $m_B$ , wheel mass  $m_W$



$$\mathbf{y} = \begin{bmatrix} y_B \\ y_W \end{bmatrix}, \quad \mathbf{M} = \begin{bmatrix} m_B & 0 \\ 0 & m_W \end{bmatrix}$$

$$\mathbf{D} = \begin{bmatrix} d & -d \\ -d & d \end{bmatrix}, \quad \mathbf{h} = \begin{bmatrix} 0 \\ -c_R \zeta \end{bmatrix}$$

$$\mathbf{K} = \begin{bmatrix} c & -c \\ -c & c + c_R \end{bmatrix}$$

Using (71) and typical parameters, the frequency response function for the body acceleration with harmonic road excitation  $\zeta = \zeta_a \cos \omega t$  shows the typical two peaks near the eigenfrequencies of the system, Fig. 26. Taking into account the human sensitivity in the range 4–8 Hz (shaded area), the suspension design has to avoid eigenfrequencies in that area.

### 3 Extended Nonlinear Models

The linear vehicle models provide useful insight with respect to the overall behaviour of the system. They are often the basis for control design as well as for observers. But they do not provide e.g. a realistic (high-frequency) information of the force transfer between tyre and road. Only narrow limits may be taken into account, see e.g. (62). To determine the normal tyre forces  $F_{zi}$ , the effects of the suspension system need to be considered, generally by the combined roll, pitch and heave motion. Additionally for the calculation of the lateral tyre forces  $F_{yi}$  besides the side slip angles (lateral slip) the longitudinal slip or/and the longitudinal tyre forces  $F_{xi}$ , provided by braking or accelerating, have to be known. Then an approximation for the tyre behaviour like

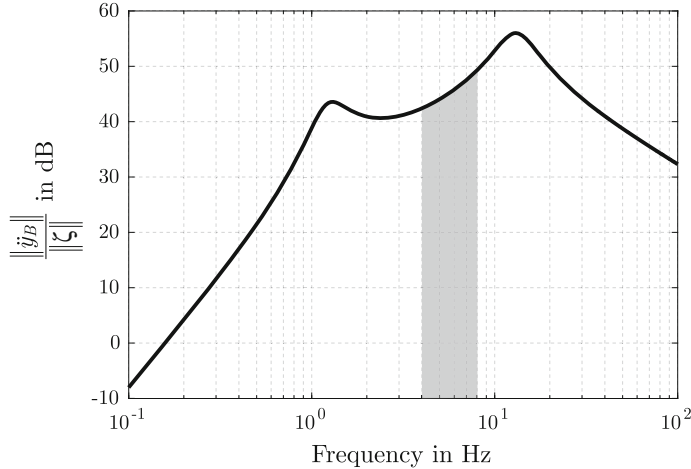


**Fig. 26** Frequency response function of body acceleration for typical  $m_B, m_W$

**Fig. 27** Example of a tyre-force characteristic of a passenger car tyre

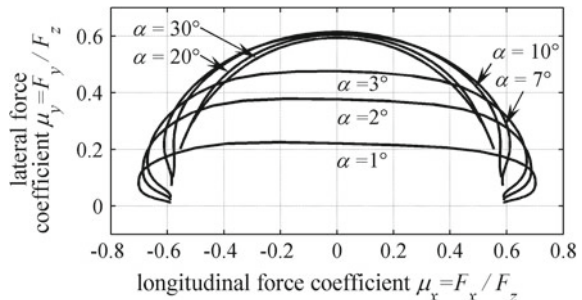
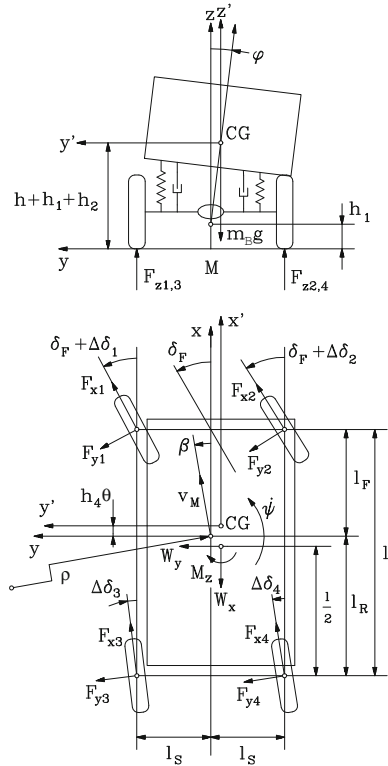


Fig. 27, Edelmann et al. (2008) completes the essential characteristics of the tyre-road force transfer, e.g. Pacejka (2014), see also the chapter *Tire Characteristics and Modeling* written by I.J.M. Besselink in this book.

A vehicle model that provides the possibility to investigate a 3D-motion and relative motion of the car body is shown in Fig. 28, Plöchl (1995). Since this model also comprises the individual tyre-road contact, it is necessary to use a tyre characteristic like Fig. 27 to match the model complexity of the vehicle.

The equations of motion for this system may be still established by hand. E.g. by neglecting small terms, especially within the Euler equations, the structure of these equations for horizontal surface can be presented in the form:

**Fig. 28** 3D-vehicle model  
with relative car body  
motion and individual  
tyre-road contact



$$\left. \begin{array}{l} x : m \frac{dv}{dt} \cos \beta - m \frac{v^2}{\rho} \sin \beta + m_B h_4 \ddot{\varphi} = f_x(F_{xi}, F_{yi}, \delta_i + \Delta \delta_i, W_x) \\ y : m \frac{dv}{dt} \sin \beta + m \frac{v^2}{\rho} \cos \beta - m_B h_2 \ddot{\varphi} = f_y(F_{xi}, F_{yi}, \delta_i + \Delta \delta_i, W_y) \\ z : m_B \dot{h} = f_z(F_{zi}, (m - m_B)g) \\ x : I_x \ddot{\varphi} = g_x(F_{xi}, F_{yi}, F_{zi}, \delta_i + \Delta \delta_i, W_y) \\ y : I_y \ddot{\theta} = g_y(F_{xi}, F_{yi}, F_{zi}, \delta_i + \Delta \delta_i, W_x) \\ z : I_z \ddot{\psi} = I_z \ddot{r} = g_z(F_{xi}, F_{yi}, \delta_i + \Delta \delta_i, M_W) \\ i = 1 \div 4, \quad v_M \approx v \end{array} \right\} \quad (72)$$

The whole vehicle mass  $m$  comprises body mass  $m_B$  and the masses of the wheels and parts of their suspensions. For the moment of inertia  $I_z$ , also the whole vehicle mass distribution is considered. By  $\sin \beta$  and  $\cos \beta$  it is indicated that there is no restriction to small side slip angles. The distances  $h_2$  and  $h_4$  indicate the possibility to take into account roll and pitch axes. The additional steering angles  $\Delta \delta_i$  indicate the possibility to consider additional control inputs.

To determine the normal forces  $F_{zi}$ , spring and damper properties are essential. With the knowledge of  $F_{zi}$ , the side slip angles  $\alpha_i$  and the longitudinal slip  $s_{Li}$  or  $F_{xi}$  (depending on the input of the drive/brake system and respective mechanical

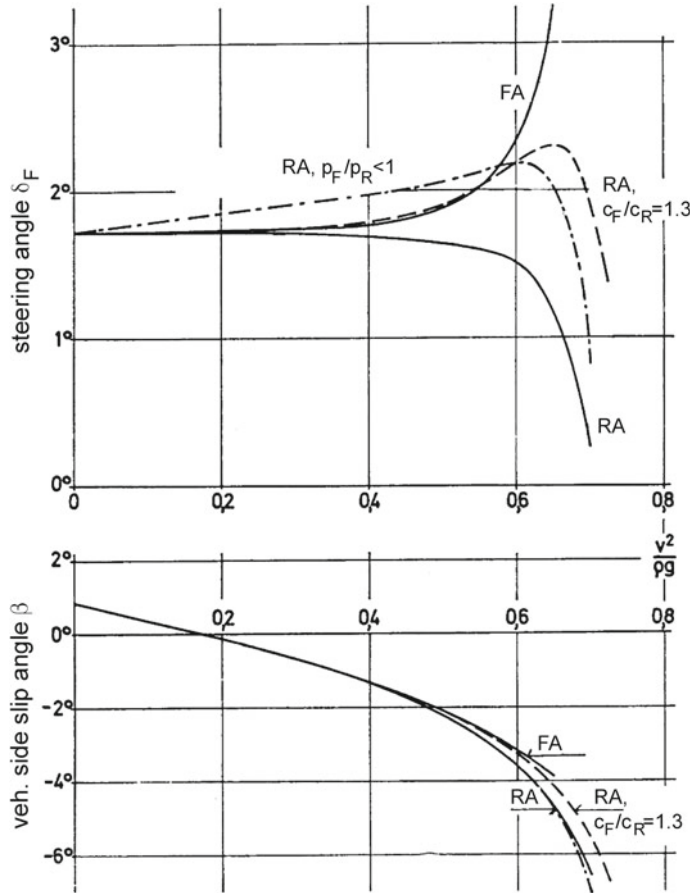


**Fig. 29** Steady-state cornering,  $R = 100$  m, mean front steering angle  $\delta_F$  and vehicle side slip angle  $\beta$ : front wheel drive FA, rear wheel drive RA, suspension stiffness ratio front/rear  $c_F/c_R$ , tyre pressure distribution  $p_F/p_R$

modelling), the lateral tyre forces  $F_{yi}$  can be calculated using an approximation of the tyre characteristics.

$$\begin{aligned} F_{zi} &= p_{zi}(h, \varphi, \theta, \dot{h}, \dot{\varphi}, \dot{\theta}, (m - m_B)g) \\ F_{xi} &= p_{xi}(s_{Li}(\text{drive/brake}), F_{zi}) \\ \alpha_i &= f_\alpha(v, \beta, r, \delta_i + \Delta\delta_i) \\ F_{yi} &= p_{yi}(F_{xi}, F_{zi}, \alpha_i) \end{aligned} \quad (73)$$

For  $F_{yi}$  and  $F_{xi}$ , the road surface condition needs to be taken into account. E.g. for Fig. 27, the outer envelope of the curves corresponds to about  $\mu_{max} = 0.6$  in lateral direction and 0.7 in longitudinal direction.

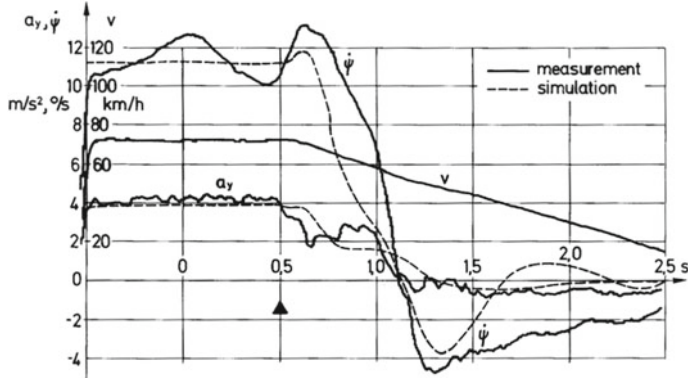


**Fig. 30** Emergency braking during cornering

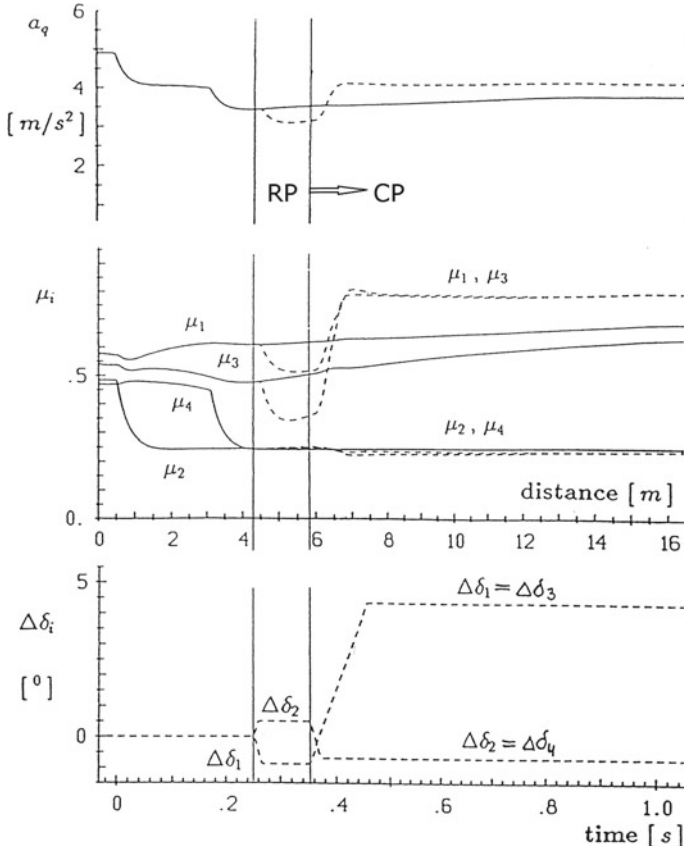
The principal consequences of the complex model with its nonlinearities can already be investigated for steady-state cornering. The corresponding extension of Fig. 3 results in Fig. 29 for a vehicle with neutral steering  $K_{US} = 0$  for  $v = 0$ . The oversteer–understeer characteristics change significantly at higher accelerations for different vehicle layouts. For the side slip angle  $\beta$ , the system modifications have a limited influence.

A simulation of an emergency braking during cornering needs to be done at least with a model of such complexity, Fig. 30. However, the comparison with the measurement also indicates that higher frequency responses cannot be mapped with this model. In addition, not ideal initial conditions lead to further deviations.

To demonstrate the possibility to investigate the impact of different local friction conditions at each wheel, cornering with passing a  $\mu$ -split area is shown in Fig. 31, Lugner et al. (1988). The stepwise decrease of the lateral acceleration  $a_y$  is caused by encountering a  $\mu$ -split condition. To detect, which wheels are running on low  $\mu$ , in the recognition phase RP an additional steering of inner wheels  $\Delta\delta_1=\Delta\delta_3 < 0$  is applied, while outer wheels  $\Delta\delta_2=\Delta\delta_4 > 0$  steer less taking into account the higher values of  $F_{zi}$  at the outer wheels. Thereby, the tyre side slip angles slightly change. Since the lateral acceleration  $a_y$  still decreases more, the influence of the increasing side slip angles at the outer wheels do not change the transferred tyre side forces considerably, as they work near their friction potential. Consequently,  $\Delta\delta_1$  and  $\Delta\delta_3 > 0$  can be used to compensate partially for the lower friction coefficient at the outer track in the control phase CP, using a feed forward control.

## 4 Near Reality Vehicle Model (NRVM)

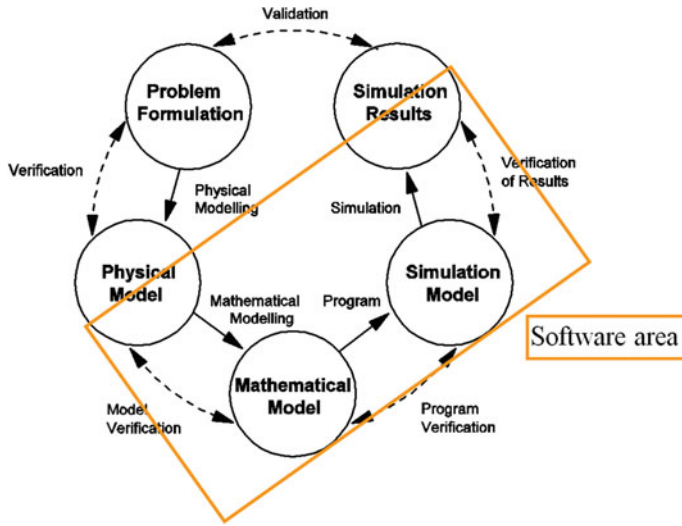
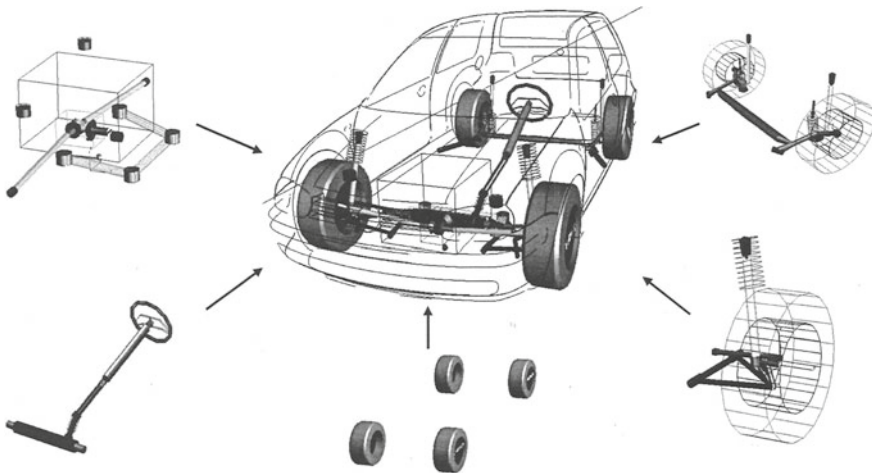
Though the extended nonlinear model provides quite a lot of details and insight with respect to tyre–road contact to investigate the impact of design details on vehicle han-



**Fig. 31** Cornering with lower friction at the outer wheels 2 and 4 ( $\mu_{max} = 0.25$ ); friction values  $\mu_i$  of the tyre-road contact,  $\delta_R = 0$ : Recognition phase RP, feed forward control CP

dling, the vehicle components (e.g. steering system) need to be modelled with corresponding complexity. Thereby ‘corresponding complexity’ means that the investigated model of the vehicle or parts of it have (nearly) the same depth in the modelling regarding their subsystems. Thus, for the reliability of simulation results, it will be essential to have a tuned and also verified model of the different vehicle parts, including a proper knowledge of the necessary parameters or nonlinear properties, see Bub and Lugner (1992).

For the simulation of the vehicle as a whole or parts of it (e.g. for experiments at testing rigs), multi-body system (MBS) simulation programmes are used. For such a simulation the preparation of the system structure and the input process is essential—as well as the interpretation of logically expected results, indicated as ‘Validation’ in Fig. 32, that visualizes this overall process, Kortüm and Lugner (1994). The nowadays available software covers most of the (otherwise necessary) steps in

**Fig. 32** Structure of simulation process**Fig. 33** Assembly of component models to the overall vehicle model

the progress of establishing a simulation (environment) of the behaviour of a complex system.

The set up of the physical model is indicated in Fig. 33, Lugner (2007). In most cases the integration of the components and their interconnection to build the overall vehicle model can be done by software packages. Also models of the components themselves are generally established with the use of MBS software.

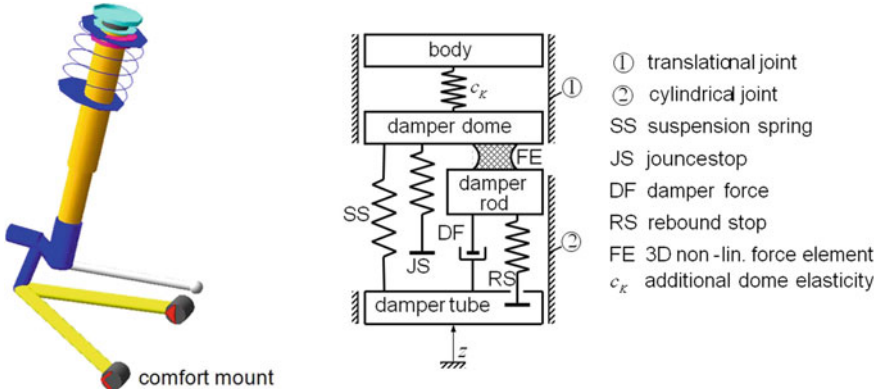


**Fig. 34** Detailed physical model of a McPherson-type suspension

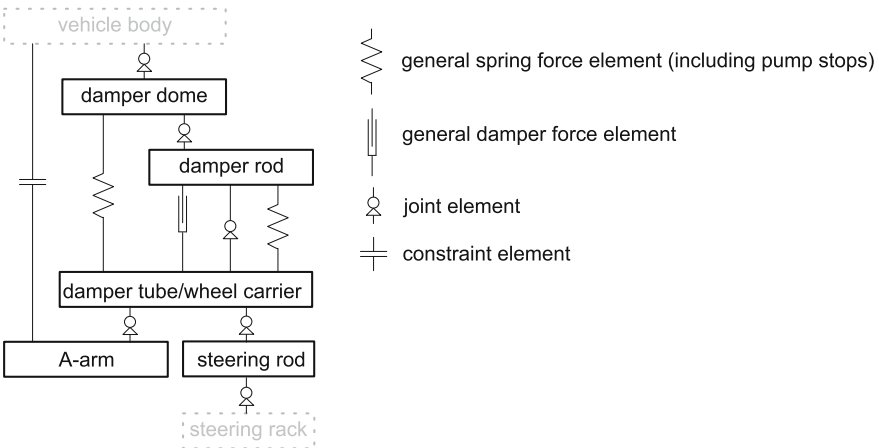


**Fig. 35** Software structure to Fig. 34

An example of a detailed modelling of a McPherson front suspension strut is shown in Fig. 34, Lugner (2007). This kind of model will also be used for tests on a virtual test rig. Figure 35 demonstrates how the corresponding software structure looks like. The connection to the main model and the kinematic constrains have to be introduced after the physical sub-model is defined.

For the now general motion of the NRVM a 3D kinematic description is necessary, Kortüm and Lugner (1994). In a first step the position and orientation of a body fixed frame  $x_B, y_B, z_B$  with respect to the inertial system  $x_I, y_I, z_I$  will be established Fig. 36.

In the next step the motion of the wheel coordinate system  $x_1, y_1, z_1$ , with respect to the body fixed frame is defined. The position/contact of the wheel with the road surface, described in the inertial system, closes the ‘loop’, Fig. 37.

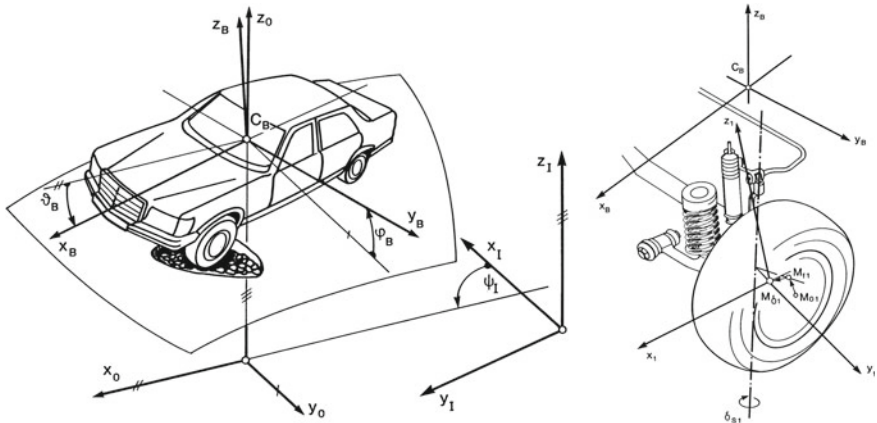


**Fig. 36** 3D description of car body and relative position of wheel to car body

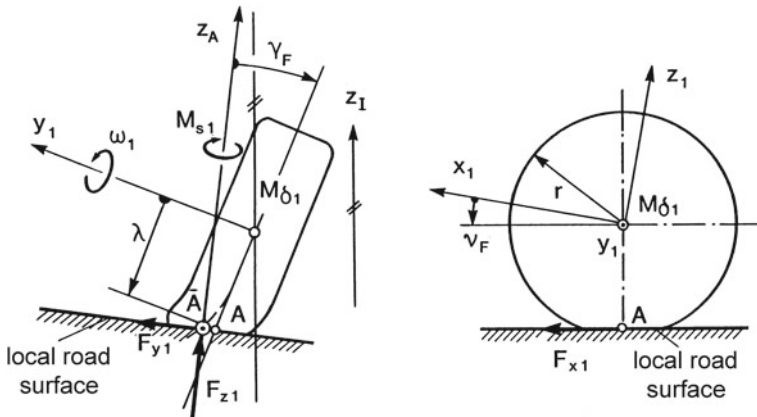


**Fig. 37** Kinematics of tyre road interface

The connection between the system parts are springs and dampers (bushings), fixed connections or special force elements like the tyre-force characteristics, Fig. 27. Naturally, the sequence of the time derivatives of the degrees of freedom of the parts and their connections provide the necessary velocities and accelerations—which is done by the MBS software. The road surface itself as an input quantity can be modelled e.g. by using a measured spectral density, Fig. 38, Lugner (2007). According to the complexity of the tyre–road contact and force transfer, the detailed structure of the surface has to be created with the corresponding complexity. A more sophisticated tyre model, e.g. with a belt structure, has to/may be used for rough road or single obstacle crossing simulations. An example of such a model is shown in Fig. 39, see also Oertel et al. (1998), Lugner (2007). An interesting overview of (complex) tyre models, as well as their applications can be seen in Gruber and Sharp (2015).

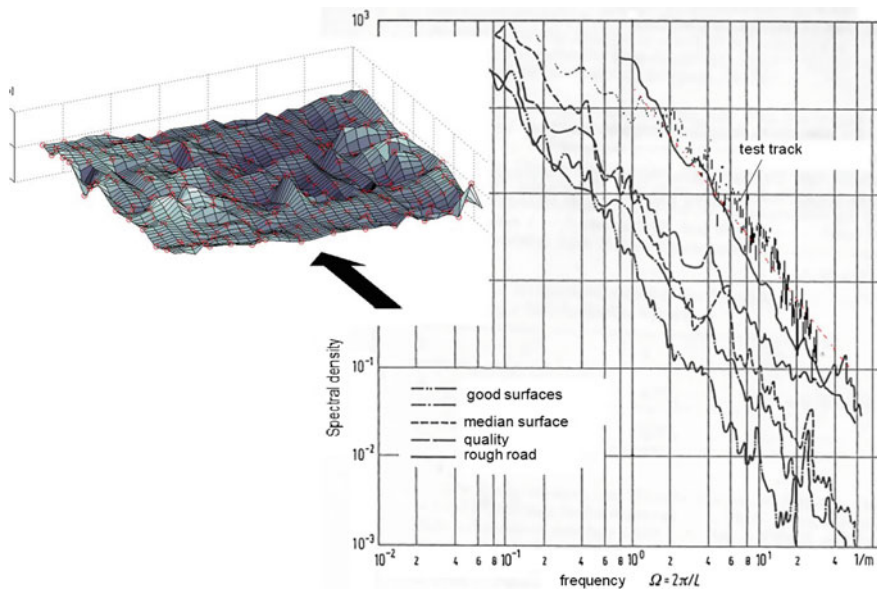


**Fig. 38** Digitalized road surfaces based on measured power spectral densities

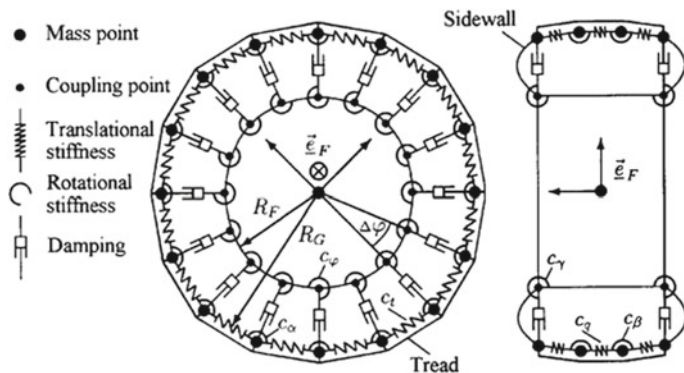


**Fig. 39** Tyre model RMOD-K

The system equations for the mathematical processing principally look like

$$\begin{aligned}
 \dot{p}(t) &= T(p)v(t); \\
 M(p)\dot{v} &= f(p, v, t) + G^T(p)\lambda; \\
 g(p) &= 0 \\
 \dot{g}(p, v) &= \frac{\partial g(p)}{\partial p}T(p)v = G(p)v = 0 \\
 \ddot{g}(p, v, \dot{v}) &= G(p)\dot{v} + G(p, v)v = 0 \tag{74} \\
 p \in R^{n_p} &: \text{generalized coordinates} \\
 v \in R^{n_p} &: \text{generalized velocities} \\
 M(p) \in R^{n_p \times n_p} &: \text{generalized mass matrix} \\
 f(p, v, t) \in R^{n_p} &: \text{generalized forces, inertia and gyro expressions} \\
 \lambda \in R^{n_z} &: \text{Lagrange multiplier} \\
 g(p) \in R^{n_z} &: \text{position constraints}
 \end{aligned}$$

It is indicated that there may be constraints due to structural (kinematic) loops. The kind and number of constraints very much depends on the choice of coordinates of the system parts.

More details on how to establish the system equations can be found in the contribution of G. Rill: *Multibody Systems and Simulation Techniques* within this book.

The possibilities for detailed investigations of the behaviour of the vehicle and its components may be indicated with Fig. 40. The vehicle may move on a rough road and the motion of the wheels, car-body and steering wheel for straight ahead driving can be calculated and observed. Moreover, the internal forces and relative motion of the system (parts), e.g. the steering system, are provided.

A particular field of application of NRVM is the design of control systems within the car—a more and more important challenge in modern passenger cars, see the

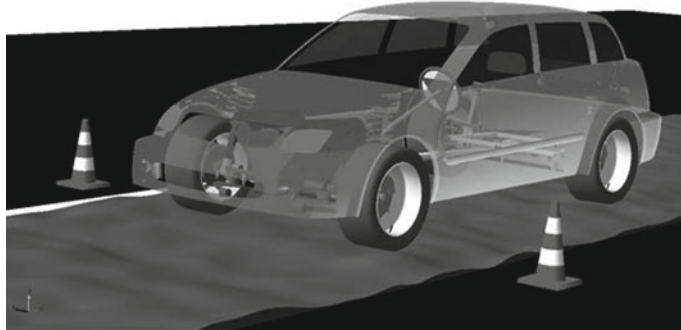


**Fig. 40** Symbolical picture for a NRVM moving straight ahead on a rough road

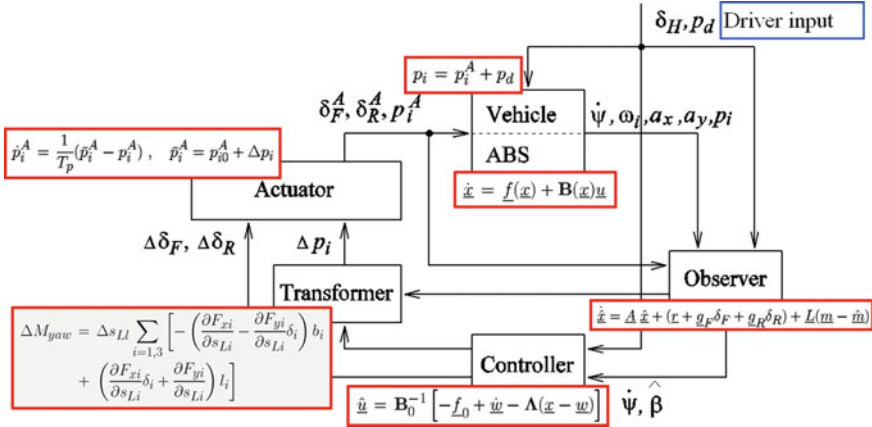


**Fig. 41** Example of a control loop for additional steering and braking (yaw moment control): the ‘Observer’ is based on a basic model, the ‘Vehicle’ is represented by a NRVM

respective chapters of this book: T. Gordon: *Active Control of Vehicle Handling Dynamics* and M. Nagai, P. Raksincharoensak: *Advanced Chassis Control and Automatic Driving*.

For such investigation the NRVM is introduced into the control loop as ‘virtual prototype’, e.g. in order to check different vehicle configurations. A possible observer or the description of properties of vehicle components are mainly based on simple (linear) vehicle models or more complex models, if needed.

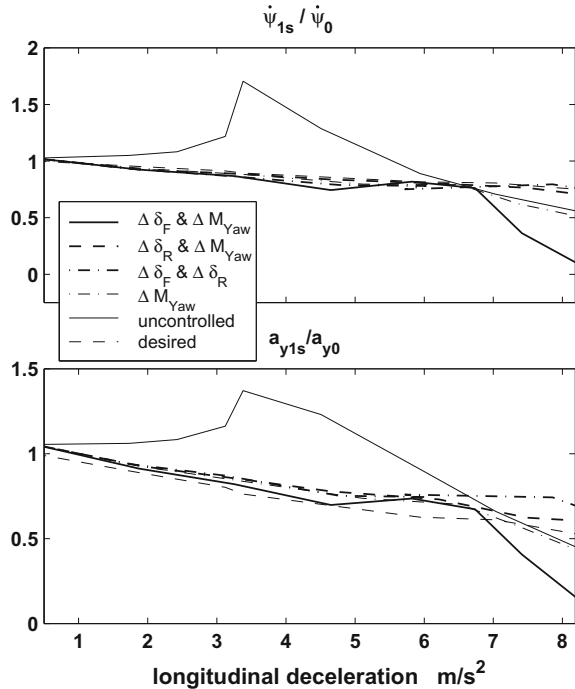
An example of a control structure configuration for the application of additional steering or/and individual braking to generate a desired yaw moment is shown in Fig. 41, Heinzl et al. (2002), Lugner (2007).

In order to study the overall system behaviour, as essential feature the ‘vehicle’ has to be represented by a NRVM or at least a detailed model, otherwise the impact of brake pressure changes  $\Delta p$  and additional steering  $\Delta \delta_F, \Delta \delta_R$  cannot be mapped properly. For the ‘observer’, here a state estimator, a simple 2-wheel model (or a basic 4-wheel model) is used. With the controller, the feed back for yaw and side slip of the vehicle are calculated additionally, using the respective expression for a correction of the yaw moment  $\Delta M_{yaw}$ . The drivers’ inputs are steering wheel angle  $\delta_H$ , corresponding to the desired trajectory, and brake pressure  $p_d$ . Additional inputs are yaw rate  $\dot{\psi}$ , angular velocity  $\omega_i$  of the wheels, the longitudinal and lateral accelerations  $a_x, a_y$ , and the brake pressure  $p_i$  at the wheels (possibly altered by an ABS-system, van Zanten et al. (1994)). These quantities are assumed to be measured or/and provided by the NRVM.

How different control strategies, based on the scheme of Fig. 41, can improve the manoeuvre ‘braking during cornering’ with constant positioning of the steering wheel is demonstrated in Fig. 42, for a high friction surface.

The desired vehicle behaviour will be that the vehicle stays on the demanded track with constant radius of curvature, independent of the amount of longitudinal

**Fig. 42** Results example to control scheme Fig. 41;  
Braking in a curve 1 s after starting to brake: normalized yaw velocity and lateral acceleration for different controls



deceleration. In Fig. 42, the normalized values of the lateral acceleration and yaw velocity 1 s after the starting of the braking indicate the motion tendency of the vehicle. E.g. increased deceleration and yaw velocity correspond to the car turning to the inside of the curve with increased yaw motion—which becomes essential for the uncontrolled car for longitudinal decelerations larger than  $3 \text{ m/s}^2$ . The different control strategies with additional steering or yaw moment control by individual braking minimize the deviations over the whole range up to a deceleration of about  $8 \text{ m/s}^2$ . Only the combination of yaw moment stabilization and additional front wheel steering indicates an outward turning of the vehicle for higher decelerations. It may be necessary to change the tuning of the control loop, especially for such a combination of the control inputs.

## 5 Conclusion and Consequences

To improve understanding of the fundamental dynamic characteristics of a passenger car, it is possible to consider (almost independent) linear vehicle models for each of the main motion directions separately. The 3 DoF-model for yaw and plane motion may explain the cornering properties. For acceleration and braking, a linear one directional model shows the main influences of drive train and brake system.

To estimate the impact of an excitation due to road unevenness on ride comfort and safety, a model describing the vertical and pitch motions only can be used to calculate comfort measures for the driver and the road holding capability represented by the tyre's normal forces.

For a more detailed insight into the dynamics of vehicles and the interaction of tyre and road, 3D-motion of the carbody and suspension properties, and especially a nonlinear description of the tyre forces needs to be considered. Then, e.g. the utilized friction between tyre and road of individual wheels can be calculated, and limit manoeuvres, induced by changing road conditions, studied. This kind of models can already be used as virtual prototypes to check simple control strategies, designed on the basis of one or more of the linear models.

As its name indicates, the near reality vehicle models (NRVM) integrate a detailed modelling of components and vehicle parts into a full system model, aiming at representing the dynamics of the vehicle and its components in detail and up to higher frequencies. A component description has to take into account the whole range of nonlinearities and motion limitations—in particular for the tyres. The separate modelling of components, e.g. the wheel suspension, also makes it possible to test and verify their dynamic behaviour on test-rigs before an integration into the whole vehicle model. The kinematic and dynamic motion range of the NRVM than has no restrictions w.r.t its application. Moreover, such a complex model might be needed to validate control systems, often based on more basic (linear) models, as well as their parameters. To simulate the motion of the vehicle, its parts and their kinematic and dynamic interaction, typically available MBS software packages will be used. However, one aspect needs to be taken into account: the accuracy of the model strongly correlates to the accuracy of parameters and nonlinearities; often, they are/have to be tuned corresponding to the investigated problem. In addition, a check and comparison between results derived by NRVM and basic (linear) models is recommended.

## References

- Abe, M. (2009). *Vehicle handling dynamics* (2nd ed.). Elsevier.
- Bub, W., & Lugner, P. (1992). *Systematik der Modellbildung Teil 1: Konzeptionelle Modellbildung, Teil 2: Verifikation und Validation.*, VDI Berichte Nr. 295.
- Chan, C. C. (2007). The state of the art of electric hybrid and fuel cell vehicles. *Proceedings of the IEEE*, 95(4).
- DIN ISO 8855 (2013). *Straßenfahrzeuge – Fahrdynamik und Fahrverhalten – Begriffe*.
- Edelmann, J., Plöchl, M., Lugner, P., Mack, W., & Falkner, A. (2008). Investigations on the power slide of automobiles. In *Proceedings of AVEC'08*.
- Galvagno, E., Morina, D., Sorniotti, A., & Velardocchia, M. (2013). Drivability analysis of through-the-road-parallel hybrid vehicles. *Meccanica*, 48, 351–366.
- Gruber, P., & Sharp, R. S. (2015). In *Proceedings of the 4th International Tyre Colloquium: Tyre Models for Vehicle Dynamics Analysis*, April, 20–21, 2015. University of Surrey, Guildford, United Kingdom.
- Heinzl, P., Lugner, P., & Plöchl, M. (2002). Stability control of a passenger car by combined additional steering and unilateral braking. *Vehicle System Dynamics Supplement*, 37.

- Hrovat, D., Tseng, E., Fodor, M., & Asgari, J. (2014). Active and semiactive suspension systems. In G. Mastinu & M. Plöchl (Eds.), *Handbook road and off-road vehicle dynamics*. CRC Press.
- Kortüm, W., & Lugner, P. (1994). *Systemdynamik und Regelung von Fahrzeugen*. Springer.
- Lugner, P., Mittermayr, P., & Endlicher, K. O. (1988). *Theoretical investigations on the behaviour of a car with additional four-wheel steering at  $\mu$ -split conditions C440/88*. IMechE.
- Lugner, P. (2007). Tyre models, propulsion and handling of road vehicles. In W. Schielen (Ed.), *Dynamical analysis of vehicle systems: CISM courses and lectures* (Vol. 497). Springer.
- Mitschke, M., & Wallentowitz, H. (2014). *Dynamik der Kraftfahrzeuge* (5th Auflage). Springer.
- Oertel, C. H., Eichler, M., & Faudr, A. (1998). *RMOD-K Version 5.2, Manual*. CA Entwicklung, gedas GmbH.
- Pacejka, H. B. (2014). Tire as a vehicle component. In G. Mastinu & M. Plöchl (Eds.), *Handbook road and off-road vehicle dynamics*. CRC Press.
- Plöchl, M. (1995). *Zusammenwirken von allradgelenktem Fahrzeug und Fahrer in kritischen Fahrsituationen*, Dissertation, TU Wien.
- Plöchl, M., Lugner, P., & Edelmann, J. (2014). Basics of longitudinal and lateral vehicle dynamics. In G. Mastinu & M. Plöchl (Eds.), *Handbook road and off-road vehicle dynamics*. CRC Press.
- Plöchl, M., Endlicher, K.-O., & Lugner, P. (2015). *Grundlagen der Fahrzeugdynamik, Teil 1*. Skriptum: Institut für Mechanik, TU Wien.
- Popp, K., & Schiehlen, W. (2010) *Ground vehicle dynamics*. Springer.
- Popp, K. (2014). Ride comfort and road holding. In G. Mastinu & M. Plöchl (Eds.), *Handbook road and off-road vehicle dynamics*. CRC Press.
- Rill, G. (2012). *Road vehicle dynamics: Fundamentals and modeling*. CRC Press.
- van Zanten, A., Erhardt, R., & Pfaff, G. (1994). *FDR—Die Fahrdynamikregelung von Bosch ATZ96*.
- Zhao, L. et al. (2017). An analytical formula of driver RMS acceleration response for quarter-car considering cushion effects. *Vehicle System Dynamics*, 55(9). Taylor & Francis.

# Tire Characteristics and Modeling



I. J. M. Besselink

**Abstract** Tires are the interface between vehicle and road. The forces and moments generated by the tires determine the motion of a road vehicle. Dedicated tire tests provide insight in these forces and moments and their dependency on slip, inclination angle and vertical force. The brush tire model can explain the measured characteristics qualitatively, the Magic Formula is a semi-empirical tire model to quantitatively describe them. To account for tire dynamic behavior, relaxation effects are discussed and modeled.

**Keywords** Tire mechanics • Brush tire model • Magic Formula • Tire dynamics

## 1 Introduction

### 1.1 Scope

Road vehicles have been equipped with pneumatic tires for many years. Over these years there have been improvements in the construction and materials being used, but apart from a gradual decrease of the aspect ratio and changes of the tread pattern not too much appears to have changed for the casual observer. Nevertheless, the importance of tires should not be underestimated: tires provide the interface between vehicle and road and will affect all aspects of vehicle dynamics, for example: ride comfort, handling behavior and braking performance. The forces and moments generated by the tire will determine the motions of a road vehicle. Tires also play an important role in the energy consumption of a road vehicle and the noise produced by it, but these two aspects are outside the scope of this chapter.

Research on tire behavior, analyzing and modeling the forces and moments generated for various operating conditions in particular, has a long history. Dedicated test equipment has been developed to do tire testing in a laboratory environment or

---

I. J. M. Besselink (✉)

Faculty of Mechanical Engineering, TU Eindhoven, Eindhoven, The Netherlands  
e-mail: I.J.M.Besselink@tue.nl

to monitor the tires on a vehicle while driving. With the massive increase in computing power over the years vehicle and tire simulation models have become ever more complex, together with increasing requirements on their accuracy. For a review on tire modelling reference is made to Pacejka and Sharp (2007).

Despite all efforts, no physics based tire simulation model is available to date that can predict tire behavior for all possible operating conditions. The friction phenomena between tire and road are rather complex and dependent on for example sliding velocity, temperature, road roughness, the presence of water or snow, etc. Furthermore, the tire may experience complex deformations, for example when driving over a rutted road. The forces and moments cannot be predicted accurately yet for these conditions by existing models. Tire simulation models still rely on full scale tire measurements for model development, parametrization and validation.

In this chapter the emphasis will be on describing results obtained from tire measurements and accompanying tire modeling. Most of the theory and tire models described here, have been developed at the Delft University of Technology under the supervision of professor Hans Pacejka. For a more elaborate discussion on tire modeling reference is made to the book “Tire and Vehicle Dynamics” by Pacejka (2012). Here the aim is to provide a concise overview and consistent approach to modeling the tire in the context of full vehicle simulations. This implies that the focus is on the overall tire behavior, describing and modeling these characteristics. A detailed description of the physics governing rubber friction on a road surface is outside the scope of this chapter. Also the complexity of the tire models will be limited, e.g. finite element tire models will not be discussed.

## 1.2 Sign Conventions and Slip Definitions

A sign convention is adopted and a contact point is defined to describe the forces and moments acting at the tire-road interface. A commonly accepted definition is the ISO sign convention as shown in Fig. 1, see ISO (1991). The wheel is considered to be an infinitely thin disk and the road is assumed to be locally flat. The distributed forces that are present between tire and road across the contact patch are lumped into three forces and moments that act at the contact center  $C$ . The location of this contact center  $C$  is defined by the intersection of three planes:

1. the road plane
2. wheel center plane through the plane of symmetry of the wheel
3. the plane through the wheel spin axis  $y'$  and normal to the road.

Three axis are defined at the contact center  $C$ . The  $x$ -axis is defined by the intersection of plane 1 and 2 and positive in the forward driving direction. The  $y$ -axis is defined by the intersection of plane 1 and 3 and positive to the left. The  $z$ -axis is normal to the road plane and positive upwards. The forces and moments that are generated between tire and road are assumed to act at the contact center  $C$  and are expressed in the  $x$ ,  $y$  and  $z$ -axis of the wheel as defined here.

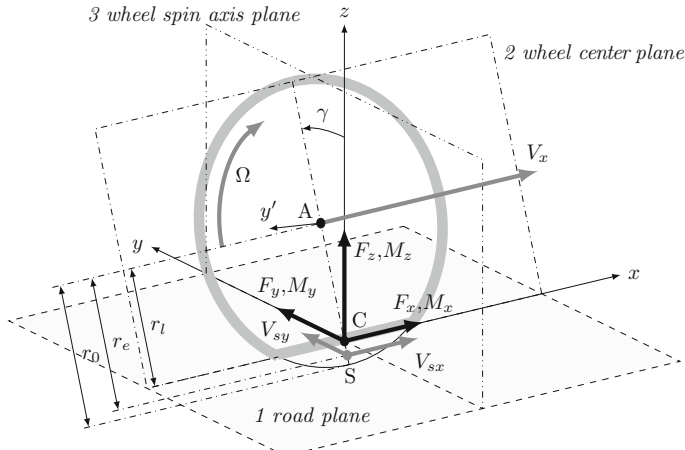


**Fig. 1** ISO sign convention with adapted inclination angle  $\gamma$

Three forces and three moments can be distinguished:

- longitudinal force  $F_x$
- lateral force  $F_y$
- vertical force (or normal force)  $F_z$
- overturning moment  $M_x$
- rolling resistance moment  $M_y$
- self-aligning moment  $M_z$ .

It should be noted that in practice the forces and moments are measured at the wheel center  $A$  using a measuring hub or wheel equipped with strain gauges. In order to calculate the forces at contact center  $C$ , both the location of the contact center and inclination angle  $\gamma$  are required.

Different tire radii may be distinguished. The free tire radius  $r_0$  equals the radius of the undeformed tire. The loaded radius  $r_l$  equals the distance between the wheel center  $A$  and contact point  $C$ . The effective rolling radius  $r_e$  relates the angular velocity of the wheel  $\Omega$  about the wheel spin axis  $y'$  with the forward velocity  $V_x$  for a freely rolling tire according to

$$r_e = \frac{V_x}{\Omega}. \quad (1)$$

Both the loaded radius  $r_l$  and effective rolling radius  $r_e$  are dependent on the vertical force  $F_z$ , as is illustrated in Fig. 2. The loaded radius  $r_l$  decreases almost linearly with increasing vertical force  $F_z$ , whereas the effective rolling radius  $r_e$  shows a smaller dependency on  $F_z$ . A point  $S$  may be defined, which corresponds to the instant center of zero velocity for the freely rolling tire. The distance between point  $S$  and the wheel center  $A$  equals the effective rolling radius  $r_e$ .

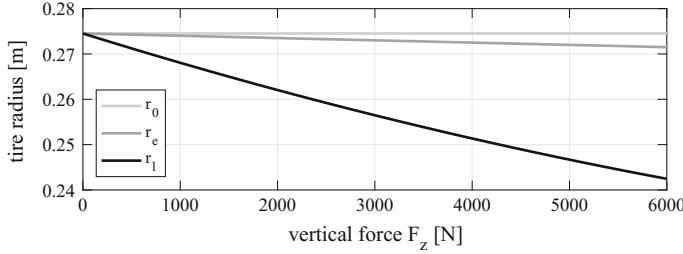


**Fig. 2** Dependency of the effective and loaded tire radius,  $r_e$  and  $r_l$ , on the vertical force  $F_z$

The longitudinal slip  $\kappa$  of the tire is defined as

$$\kappa = -\frac{V_{sx}}{|V_x|} = -\frac{V_x - \Omega r_e}{|V_x|}, \quad (2)$$

where  $V_{sx}$  equals the longitudinal sliding velocity of point  $S$ ,  $V_x$  equals the longitudinal velocity of the wheel center  $A$  and  $\Omega$  equals the angular velocity of the wheel. Note that for a freely rolling wheel  $\kappa$  and  $V_{sx}$  are equal to zero by definition. When the wheel is locked and does not rotate ( $\Omega = 0$ )  $\kappa$  will be equal to  $-1$ . The tire behavior can be considered to be linear for small values of longitudinal slip  $\kappa$ , i.e. the longitudinal force  $F_x$  increases linearly with the longitudinal slip  $\kappa$ ,

$$F_x = C_{F\kappa} \kappa \quad (3)$$

where  $C_{F\kappa}$  equals the longitudinal slip stiffness.

The side slip angle (or drift angle)  $\alpha$  of the tire is defined as

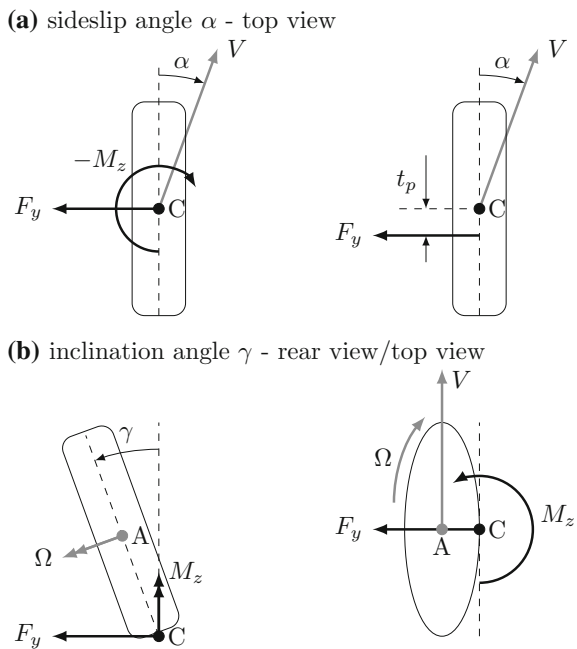
$$\tan(\alpha) = -\frac{V_{sy}}{|V_x|}, \quad (4)$$

where  $V_{sy}$  equals the lateral sliding velocity of point  $S$ . The inclination angle  $\gamma$  is the angle between the normal to the road plane and the wheel center plane. In the sign convention adopted here a positive inclination angle  $\gamma$  corresponds to a rotation about the  $x$ -axis in the negative direction, as shown in Fig. 1. For small angles, up to a few degrees, the lateral force  $F_y$  and self-aligning moment  $M_z$  depend linearly on the side slip angle  $\alpha$  and inclination angle  $\gamma$  according to

$$\begin{aligned} F_y &= C_{F\alpha} \alpha + C_{F\gamma} \gamma \\ M_z &= -C_{M\alpha} \alpha + C_{M\gamma} \gamma, \end{aligned} \quad (5)$$

where  $C_{F\alpha}$  equals the cornering stiffness,  $C_{M\alpha}$  the self-aligning stiffness,  $C_{F\gamma}$  the camber stiffness and  $C_{M\gamma}$  the camber torque stiffness. With the adopted sign convention of Fig. 1 and (5) these stiffness are all positive for regular tires. An exception

**Fig. 3** Lateral force  $F_y$  and self-aligning moment  $M_z$  resulting from a side slip angle  $\alpha$  (a) and inclination angle  $\gamma$  (b)



is the camber stiffness  $C_{F\gamma}$ , which may be zero or even negative for some truck tires. The pneumatic trail  $t_p$  relates the self-aligning moment  $M_z$  to the lateral force  $F_y$ , according to

$$t_p = -\frac{M_z}{F_y}. \quad (6)$$

The pneumatic trail  $t_p$  can be interpreted as the moment arm of the lateral force  $F_y$  to produce a self-aligning moment  $M_z$ ; this is illustrated in Fig. 3. This figure also shows the effect of an inclination angle  $\gamma$  on the lateral force  $F_y$  and self-aligning moment  $M_z$ . Note that for a positive side slip angle  $\alpha$  and positive inclination angle  $\gamma$  the contributions to the self-aligning moment  $M_z$  have opposite sign.

Based on the preceding definitions, it is clear that the tire forces and moments are a function of various slip quantities and inclination angle. In a way the tire can be considered as a non-linear function with multiple inputs and outputs, as illustrated by Fig. 4. In the next sections the focus will be on the relation between the inputs  $\kappa, \alpha, \gamma, F_z$  and outputs  $F_x, F_y$  and  $M_z$ . As already indicated in Fig. 4 there are many additional factors that have an influence on the tire forces and moments, but they all will be assumed to be constant. In Sects. 2, 3 and 4 the steady-state relations between the inputs and outputs will be considered. Thereafter the dynamic behavior of the tire will be discussed in Sect. 5.

**Longitudinal slip definition** In some literature a different definition for the longitudinal slip is used. Brake slip is defined as:

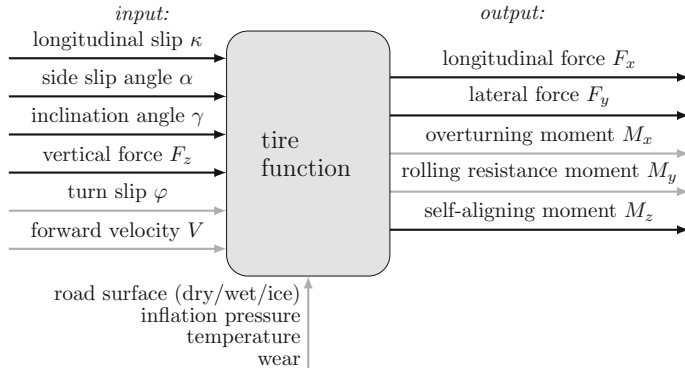


**Fig. 4** The tire considered as a non-linear function

$$s_{xb} = \frac{V_x - \Omega r_e}{V_x} \cdot 100\%, \quad (7)$$

and drive slip is defined as:

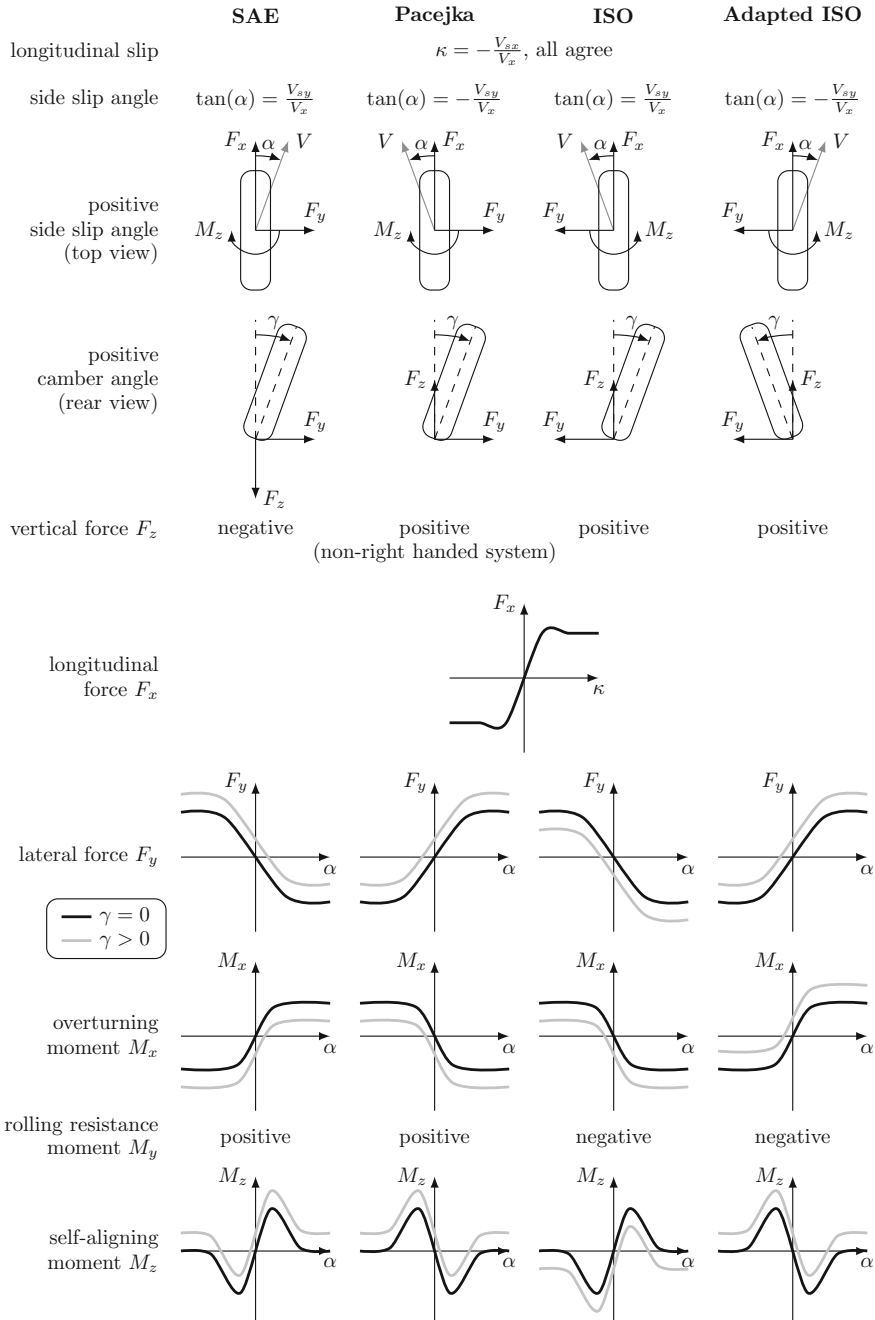
$$s_{xd} = \frac{\Omega r_e - V_x}{\Omega r_e} \cdot 100\%. \quad (8)$$

Both brake and drive slip have a value between 0 and 100%. For modeling purposes a continuous descriptions as given by (2) is more convenient. The effective rolling radius  $r_e$  may also be referred to as the dynamic tire radius in some literature. Note that all definitions of longitudinal slip, (2), (7) and (8), will result in a division by zero, when the vehicle is standing still ( $V_x = 0, \Omega = 0$ ), which is undesirable from a computational point of view. In Sect. 5 this will be discussed further.

**Sign conventions** Over time various sign conventions and axis systems have been used and standardized. The SAE and ISO sign convention use the same definition for the  $x$ -axis, but have opposite definitions of the  $y$  and  $z$ -axis. Both SAE and ISO define the tire side slip angle as

$$\tan(\alpha) = \frac{V_{sy}}{V_x}. \quad (9)$$

Furthermore SAE and ISO define a positive inclination angle  $\gamma$  corresponding to a rotation about the positive  $x$ -axis. Though this may seem intuitive at first, a positive side slip or inclination angle will then result in a lateral force in the negative  $y$ -direction. This makes the definition and interpretation of the cornering and camber stiffness cumbersome, as they will be negative for a regular tire. In the SAE sign convention the vertical force  $F_z$  will be negative when the tire is loaded, which is also not very intuitive.

**Fig. 5** Comparison of tire sign conventions and slip definitions

Adopting the ISO sign convention for expressing the tire forces and moments and adding a minus sign to the ISO definitions for side slip and inclination angle results in an intuitive set of tire characteristics, as illustrated by Fig. 5. This figure was first published by Besselink (2000). Note that with this sign convention a positive slip value ( $\kappa, \alpha$ ) generally results in a positive force or moment and that a positive inclination angle  $\gamma$  results in an upward shift of the force or moment curve.

## 2 Tire Force and Moment Measurements

### 2.1 Test Equipment and Measurement Program

Dedicated test equipment exists to measure the relations between tire forces and moments as a function of slip, inclination angle and vertical force. A distinction can be made between indoor and outdoor testing. For indoor testing traditionally an external or internal drum is used, but the curvature of the drum surface will affect the results obtained. To circumvent this problem the Flat-Trac tire testing machine has been developed, as shown in Fig. 6. In essence it can be considered as a scaled up version of a belt grinder and the tire fixture allows to prescribe the desired vertical force, longitudinal slip, camber and side slip angle. In this way experiments can be executed in a controlled laboratory environment. On the other hand, the sandpaper surface may not accurately reflect the road surface characteristics and measurements on snow or ice are not possible. To avoid these issues tire test trailers have been developed to measure force and moment characteristics on an actual road surface. As an example the TASS tire test trailer is shown in Fig. 7. Though it allows to do testing on different road surfaces, it is difficult to precisely control the environmental conditions (e.g. temperature, humidity, water film depth, etc.) and some processing of the measurement results is necessary to account for road irregularities.

As shown in Fig. 4, the tire may be considered as a non-linear function with multiple inputs and outputs. In a traditional force and moment measurement program typically only one input is varied, while the other inputs are kept constant. Furthermore a distinction can be made between “pure” and “combined” slip conditions. Pure slip conditions refer to cases where only longitudinal slip or a side slip angle is applied, so braking in a straight line ( $\alpha = 0^\circ, F_y \approx 0 \text{ N}$ ) or drifting of a freely rolling tire ( $\kappa = 0, F_x \approx 0 \text{ N}$ ). In the case of combined slip both  $\kappa$  and  $\alpha$  are unequal to zero and a combination of longitudinal and lateral forces will arise. An example of a traditional tire testing program is listed in Table 1, the results will be discussed next. The dimensions of the tire under consideration are 195/65 R15 and the inflation pressure equals 2.0 bar.



**Fig. 6** IABG Flat-Trac tire force and moment testing machine



**Fig. 7** TASS tire test trailer

**Table 1** Tire force and moment measurement program

	$\kappa$ (-)	$\alpha$ (°)	$\gamma$ (°)	$F_z$ (kN)
<i>Pure slip</i>				
Alpha sweep	0	-15 to 15	-5/0/5	2.0/4.5/7.0
Kappa sweep	0 → -1	0	-5/0/5	2.0/4.5/7.0
<i>Combined slip</i>				
Kappa sweep	0 → -1	-2/2/5/9	0	2.0/4.5/7.0

## 2.2 Alpha Sweep Results

In an alpha sweep measurement the side slip angle  $\alpha$  is varied using a triangular wave signal. In the tests discussed it varies between -15 and 15° and the absolute rate of change is equal to 1 deg/s. The test is executed at a forward velocity of 60 km/h. The choice of the forward velocity and rate of change of the side slip angle will affect the heat development in the tire and will influence the results obtained in these tests, experience has shown that the values mentioned here result in representative tire force and moment characteristics.

The measured lateral force characteristics for different vertical forces and inclination angles are shown in Fig. 8a. Near the origin the linear relation between the side slip angle  $\alpha$  and lateral force  $F_y$  can be observed. As already introduced in (5), this slope known as the cornering stiffness  $C_{F\alpha}$ , the unit is N/deg. or N/rad. It is defined as

$$C_{F\alpha} = \frac{\partial F_y}{\partial \alpha} \Big|_{\kappa=0, \alpha=0, \gamma=0}. \quad (10)$$

It is clear that this slope dependents on the vertical force  $F_z$ , as shown in Fig. 9a. Note that the cornering stiffness does not increase linearly with the vertical force, but reaches a maximum for a specific vertical force and then decreases again.

The lateral force  $F_y$  saturates and its magnitude reaches a maximum for large positive and negative side slip angles, at this point the tire is sliding laterally. It can be seen from Fig. 8a that the increase of the lateral force when changing  $F_z$  from 2000 to 4500 N is bigger compared to the increase when changing from 4500 to 7000 N. This implies that magnitude of the maximum lateral force does not increase linearly with the vertical force. The fiction coefficient  $\mu_y$  relates the maximum magnitude of the lateral force to the vertical force,

$$\mu_y = \frac{\max(|F_y|)}{F_z}. \quad (11)$$

The dependency of the lateral friction coefficient  $\mu_y$  on the vertical force  $F_z$  is shown in Fig. 9e. A linear decrease with the vertical force  $F_z$  is seen.

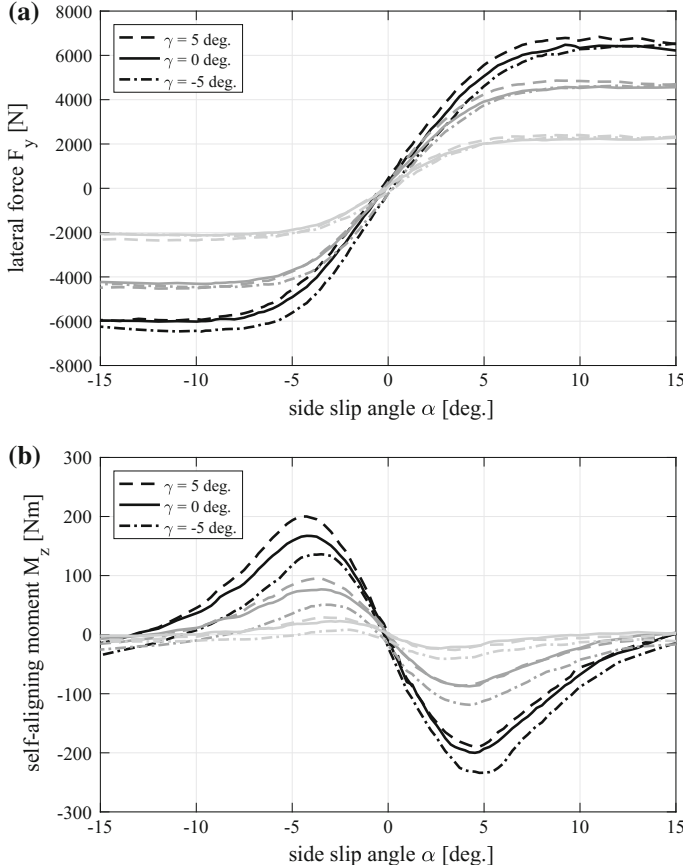


**Fig. 8** Measured lateral force (a) and self-aligning moment (b) characteristics, pure side slip—free rolling tire ( $\kappa = 0$ ). Legend: black  $F_z = 7000$  N, gray  $F_z = 4500$  N, light gray  $F_z = 2000$  N

The measured self-aligning moment characteristic for different vertical forces and inclination angles is shown in Fig. 8b. The self-aligning moment  $M_z$  reaches a maximum before it decreases to zero for large side slip angles. The magnitude of the peak increases progressively with the vertical force  $F_z$ . Near the origin of the graph the self-aligning moment decreases linearly with an increase of the side slip angle  $\alpha$ . The self-aligning stiffness  $C_{M\alpha}$  is defined as

$$C_{M\alpha} = - \frac{\partial M_z}{\partial \alpha} \Big|_{\kappa=0, \alpha=0, \gamma=0}. \quad (12)$$

Note that a minus sign is necessary in (12) to obtain a positive stiffness value due to the adopted sign convention. The dependency of  $C_{M\alpha}$  on the vertical force  $F_z$  is shown in Fig. 9b. The pneumatic trail  $t_p$  can be calculated using (6) and the results

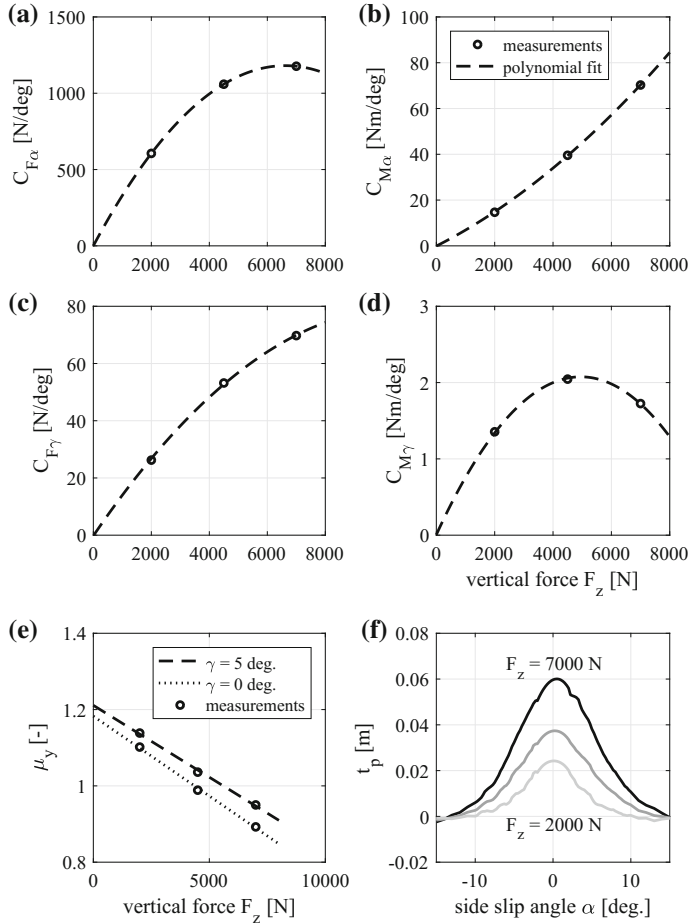


**Fig. 9** Tire characteristics, cornering stiffness  $C_{F\alpha}$  (a), self-aligning stiffness  $C_{M\alpha}$  (b), camber stiffness  $C_{F\gamma}$  (c), camber torque stiffness  $C_{M\gamma}$  (d), lateral friction coefficient  $\mu_y$  (e) and pneumatic trail  $t_p$  (f)

are shown in Fig. 9f. The pneumatic trail decreases with increasing magnitude of the side slip angle. Increasing the vertical force  $F_z$  results in an increase of the pneumatic trail.

The effect of an inclination angle  $\gamma$  on the lateral force  $F_y$  and self-aligning moment  $M_z$  is also shown in Fig. 8. A positive inclination angle results in an upward shift of both curves, a negative inclination angle moves them downwards. It is also clear that the application of a 5° inclination angle has far less influence on the lateral force and self-aligning moment compared to introducing 5° of side slip angle. This is also reflected in the camber stiffness  $C_{F\gamma}$  and camber torque stiffness  $C_{M\gamma}$ . Since the measurements are only done for discrete values of the inclination angle  $\gamma$

( $-5, 0$  and  $5^\circ$ ), the camber stiffness is approximated by

$$C_{F\gamma} = \frac{\Delta F_y}{\Delta \gamma} \Big|_{\kappa=0, \alpha=0}. \quad (13)$$

The camber torque stiffness is calculated as

$$C_{M\gamma} = \frac{\Delta M_z}{\Delta \gamma} \Big|_{\kappa=0, \alpha=0}. \quad (14)$$

In these equations  $\Delta F_y$  is the difference in lateral force for  $\gamma$  equal to  $5$  and  $-5^\circ$ ,  $\Delta M_z$  is the difference in the self-aligning moment for  $\gamma$  equal to  $5$  and  $-5^\circ$  and  $\Delta \gamma$  is equal to the range of  $10^\circ$ . The dependency of  $C_{F\gamma}$  and  $C_{M\gamma}$  on the vertical force  $F_z$  is shown in Fig. 9c, d respectively. The most important observation here is that for this particular tire the camber stiffness  $C_{F\gamma}$  is a factor 15–20 smaller compared to the cornering stiffness  $C_{F\alpha}$ . For the camber torque stiffness  $C_{M\gamma}$  this factor ranges from 10 to 40 when comparing to the self-aligning stiffness  $C_{M\alpha}$ . These numbers indicate that an inclination angle change has only a limited influence on the lateral force  $F_y$  and self-aligning moment  $M_z$ . But as can be seen from Fig. 8a, the maximum lateral force  $F_y$  increases when an inclination angle is applied. Calculating the lateral friction coefficient  $\mu_y$  for this part of the curve, an increase of approximately 5% can be seen when an inclination angle of  $5^\circ$  is applied in comparison to zero inclination angle. This is also shown in Fig. 9e.

When looking carefully at the measurement results, it can be seen that the lateral force  $F_y$  and self-aligning moment  $M_z$  are not exactly zero when the sideslip angle  $\alpha$  and inclination angle  $\gamma$  are zero. This is not necessarily a measurement error, but it can be caused non-symmetry of the tire construction. There are two effects:

- **plysteer** is determined by the construction and build-up of the carcass layers of the tire. The lateral force due to plysteer changes sign when reversing rolling direction of the tire, so e.g. when going from forward to backward rolling. Plysteer may be interpreted as a “pseudo” side slip angle,  $\alpha_{ply}$ .
- **conicity** is determined by the shape of the tire and/or carcass. The lateral force due to conicity does not change sign when reversing the rolling direction of the tire. Conicity may be interpreted as a “pseudo” camber angle,  $\gamma_{con}$ .

The magnitude of the “pseudo” side slip angle,  $\alpha_{ply}$  is about  $0.1^\circ$ , the “pseudo” camber angle,  $\gamma_{con}$  reaches values up to  $0.5^\circ$  for the tire under consideration.

## 2.3 Kappa Sweep Results

In a kappa sweep measurement the longitudinal slip of the tire is varied by modulating the brake pressure. This results in a reduction of the angular velocity  $\Omega$ , while the forward velocity  $V_x$  is kept constant at 60 km/h. The longitudinal force  $F_x$  as a

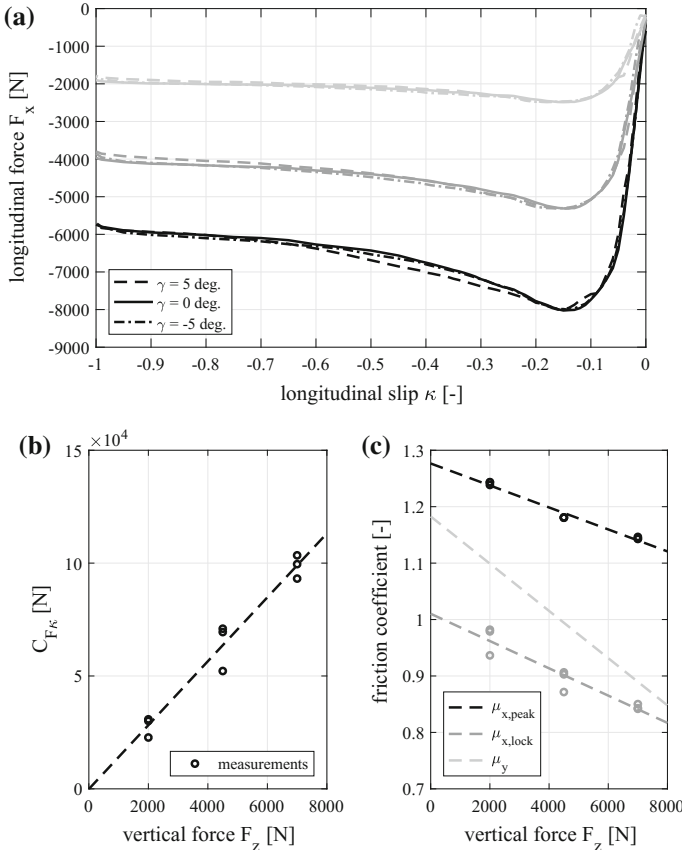


**Fig. 10** Measured longitudinal force characteristics (a), slip stiffness  $C_{F_k}$  (b) and friction coefficients (c). Legend graph a: black  $F_z = 7000 \text{ N}$ , gray  $F_z = 4500 \text{ N}$ , light gray  $F_z = 2000 \text{ N}$

function of longitudinal slip  $\kappa$  for a number of kappa sweep experiments is shown in Fig. 10a. For small values of slip the relation between  $F_x$  and  $\kappa$  is linear, the slope of this curve is known as the longitudinal slip stiffness  $C_{F_k}$ , which is defined as:

$$C_{F_k} = \left. \frac{\partial F_x}{\partial \kappa} \right|_{\kappa=0, \alpha=0, \gamma=0}. \quad (15)$$

The longitudinal slip stiffness is almost linearly dependent of the vertical force  $F_z$ , as shown in Fig. 10b. Furthermore it can be observed that the magnitude of the longitudinal force reaches a maximum when the longitudinal slip  $\kappa$  is in the order of  $-0.15$ . When the wheel is locked ( $\kappa = -1$ ) the magnitude of the longitudinal force  $F_x$  that can be transmitted is reduced in comparison to the maximum value. For both the maximum force and locked wheel situation a friction coefficient may be defined,

$\mu_{x,peak}$  and  $\mu_{x,lock}$  respectively, the are defined as

$$\mu_{x,peak} = -\frac{\min(F_x)}{F_z}, \quad (16)$$

and

$$\mu_{x,lock} = -\left.\frac{F_x}{F_z}\right|_{\kappa=-1}. \quad (17)$$

The dependency of these friction coefficients on the vertical force is shown in Fig. 10c. It can be seen that both decrease with increasing vertical force  $F_z$ . Furthermore it can be noted that the lateral friction coefficient is  $\mu_y$ , as previously shown in Fig. 9e, is more sensitive to changes of the vertical force. A final remark with respect to Fig. 10a is that the longitudinal slip characteristics are hardly affected by an inclination angle.

So far braking in a straight line has been discussed, where the side slip angle  $\alpha$  is equal to zero. For combined slip conditions, a kappa sweep is executed while a fixed side slip angle is applied. Some results are shown in Fig. 11a. The introduction of a side slip angle has a marked influence on the longitudinal slip characteristics. The slope at the origin, the longitudinal slip stiffness  $C_{F_K}$ , is reduced. Also the magnitude of the maximum longitudinal force is reduced. The longitudinal force for a locked wheel situation ( $\kappa = -1$ ) remains unchanged.

The measured lateral force  $F_y$  is shown in Fig. 11b. For a freely rolling tire ( $\kappa = 0$ ) the introduction of a side slip angle  $\alpha$  will result in a lateral force  $F_y$ . As the magnitude of the longitudinal slip  $\kappa$  is increased, the lateral force decreases and becomes almost zero when the wheel is locked ( $\kappa = -1$ ). Another way of plotting the lateral force  $F_y$  is shown in Fig. 12a. The curve obtained from the alpha sweep is plotted. The lateral force for specific values of longitudinal slip are extracted from Fig. 11b and added to this graph. Obviously the values for free rolling ( $\kappa = 0$ ) correspond quite well with the alpha sweep results, the differences may be caused by tire temperature effects. When braking the wheel and increasing the magnitude of  $\kappa$ , the maximum lateral force  $F_y$  is reduced and the same is true for the slope near the origin, the cornering stiffness  $C_{F_\alpha}$ . So mutual interactions exist when considering combined slip:

- The introduction of a side slip angle  $\alpha$  results in a reduction of the longitudinal slip stiffness  $C_{F_K}$  and peak longitudinal force.
- The introduction of longitudinal slip  $\kappa$  results in a reduction of the cornering stiffness  $C_{F_\alpha}$  and magnitude of the lateral force.

Another way of plotting combined slip measurement results is shown in Fig. 13, where  $F_y$  is plotted as a function of  $F_x$  for different vertical forces and side slip angles. It is clear that the maximum forces that can be transmitted are limited by a friction ellipse. The self-aligning moment for combined slip conditions is difficult to measure accurately, Fig. 12b shows the measurement results.

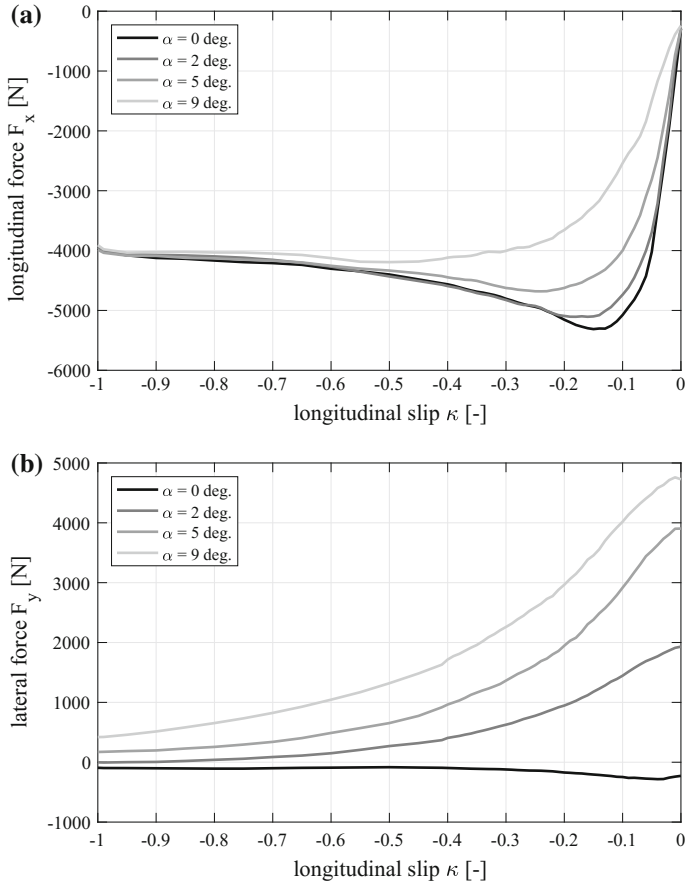


**Fig. 11** Measured longitudinal force (a) and lateral force (b) characteristics for combined slip conditions ( $F_z = 4500$  N,  $\gamma = 0^\circ$ )

**Wheel dynamics during braking** Figure 14 shows the wheel being braked, while the forward velocity  $V_x$  remains constant. The equation of motion governing the rotational dynamics of the wheel is given by

$$I_{yy}\dot{\Omega} = -M_b - r_l F_x(\kappa), \quad (18)$$

where  $I_{yy}$  equals the mass moment of inertia of the wheel about the  $y$  axis,  $M_b$  equals the brake moment and  $r_l$  equals the loaded tire radius. Reformulating the longitudinal slip Eq. (2) gives

$$\kappa = \frac{\Omega r_e}{V_x} - 1. \quad (19)$$

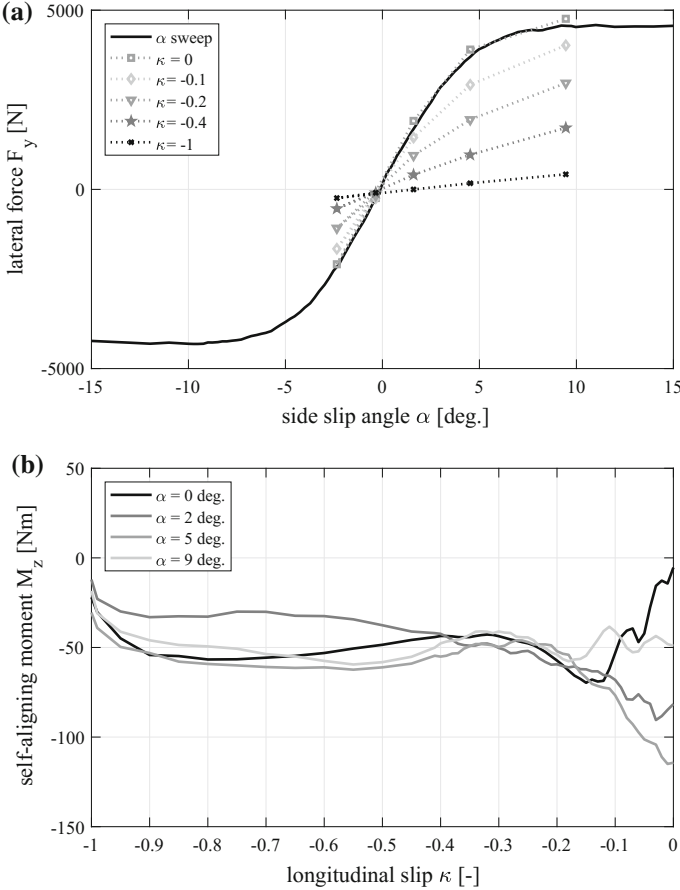


**Fig. 12** Measured lateral force characteristics (a) and self-aligning moment ( $F_z = 4500$  N,  $\gamma = 0^\circ$ )

When increasing the brake moment  $M_b$  the angular acceleration  $\dot{\Omega}$  becomes negative and thus the angular velocity  $\Omega$  is reduced. As the forward velocity  $V_x$  remains constant, the longitudinal slip  $\kappa$  will become negative. This results in a negative longitudinal force  $F_x$  that counteracts the brake moment  $M_b$ . When the brake moment is kept constant, the system will settle for equilibrium and the angular acceleration  $\dot{\Omega}$  becomes zero. However when the brake moment  $M_b$  exceeds the maximum moment that can be developed by the tire,  $F_z \mu_{x,peak} r_l$ , no stable equilibrium can be found, the wheel will quickly slow down until the angular velocity becomes zero. In a kappa sweep the brake moment  $M_b$  is increased linearly over time until wheel lock occurs

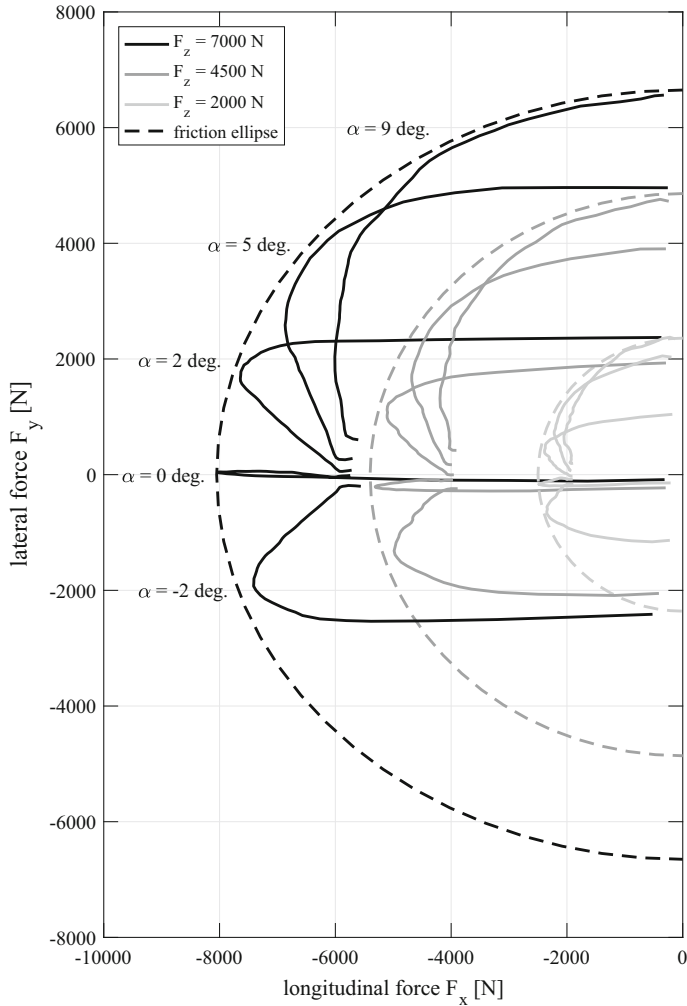


**Fig. 13** Measured combined slip characteristics ( $\gamma = 0^\circ$ )

and the brake moment is made zero again, an example is shown in Fig. 15. After passing the peak of the longitudinal force for  $\kappa = -0.15$ ,  $\kappa$  quickly decreases to  $-1$ . It will be therefore be difficult to precisely measure the tire characteristics for the  $\kappa$  range between  $-0.15$  and  $-1$ . Considering the short time frame in which this process takes place, the assumption of steady-state behavior may also be questionable. To circumvent some of these issues, kappa-sweep measurements are typically repeated three times and the results are averaged to produce graphs like Fig. 10a.

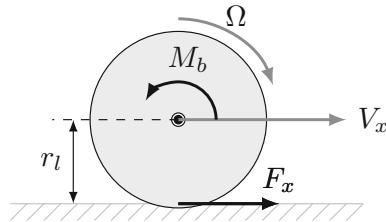


**Fig. 14** Force and moment acting on a wheel being braked

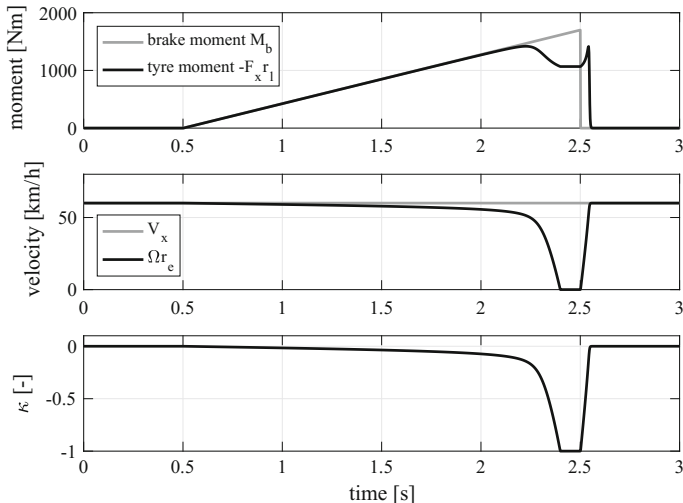


**Fig. 15** Simulation results of a  $\kappa$ -sweep

### 3 The Brush Tire Model

#### 3.1 Introduction

In the previous section the results of force and moment testing are presented without providing an explanation why the characteristics have a specific shape. The brush tire model is a comparatively simple physical model, that can be used to qualitatively explain tire behavior. The brush tire model was first described by Fromm, according to Pacejka (2012).

Before discussing the brush tire model, the fundamentals of this tire model will be explained by developing a model of a brush, as shown in Fig. 16. The brush is equipped with bristles that touch the surface. When a vertical force  $F_n$  is applied, and assuming static equilibrium, a distributed vertical force per unit of length  $q_z(x)$  will be present between the bristles and surface. The origin of the brush fixed axis system is defined at the center of the base of the bristles and the contact length is

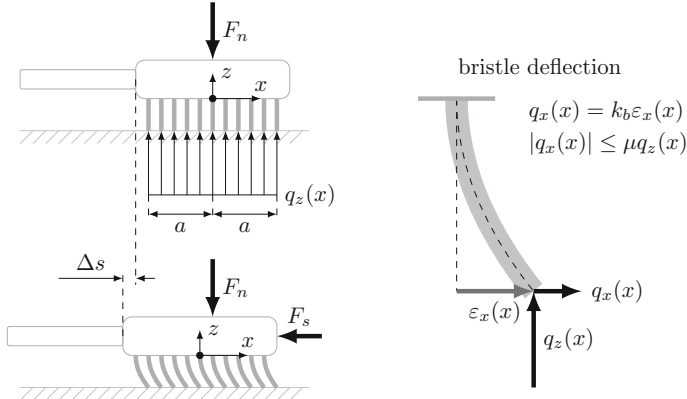


**Fig. 16** Model of a brush

equal to  $2a$ . The vertical force then equals

$$F_n = F_z = \int_{-a}^a q_z(x) dx. \quad (20)$$

Assuming that  $q_z(x)$  is constant the following expression is obtained

$$q_z = \frac{F_z}{2a}. \quad (21)$$

Note that the unit of  $q_z$  is N/m and since the tire does not stick to the road  $q_z(x)$  can not become negative.

The bristles are compliant and can deflect. The bristle deflection  $\epsilon_x$  is considered to be positive when moving in the positive  $x$ -direction, as shown in Fig. 16. The bristle stiffness per unit of length equals  $k_b$ , the unit of  $k_b$  equals N/m<sup>2</sup>. The relation between the longitudinal force per unit of length  $q_x(x)$  and bristle deflection  $\epsilon_x(x)$  equals

$$q_x(x) = k_b \epsilon_x(x). \quad (22)$$

Furthermore a friction coefficient  $\mu$  is present between the tip of the bristle and surface. The magnitude of the longitudinal force per unit of length  $q_x(x)$  is limited according to

$$|q_x(x)| \leq \mu q_z(x). \quad (23)$$

This limits the maximum possible deflection of the bristle to:

$$|\epsilon_{x,max}(x)| = \frac{\mu q_z(x)}{k_b} = \frac{\mu F_z}{2ak_b}. \quad (24)$$

Starting with undeflected bristles and moving the brush over a small distance  $\Delta s$  towards the left in the negative  $x$ -direction, all bristles will start to deflect. The magnitude of the bristle deflection  $\varepsilon_x(x)$  will be the same for all bristles and equal to  $\Delta s$ . A force  $F_s$  is required to move the brush to the left and this force is in equilibrium with the force developed by the bristles,

$$F_s = F_x = \int_{-a}^a q_x(x)dx = k_b \int_{-a}^a \varepsilon_x(x)dx = 2ak_b\Delta s. \quad (25)$$

Obviously the magnitude of  $F_x$  increases linearly with the deflection of the bristles  $\varepsilon_x$  and displacement  $\Delta s$ . When  $\Delta s$  is increased further and the maximum bristle deflection will be reached and all bristles will start to slide at the same instance. The longitudinal force  $F_s$  is then given by:

$$F_s = F_x = \int_{-a}^a q_x(x)dx = k_b \int_{-a}^a \varepsilon_{x,max}(x)dx = \mu F_z \quad (26)$$

A plot of the force  $F_s$  as a function of the displacement  $\Delta s$  is shown in Fig. 17, where  $\Delta s = 0$  corresponds to undeflected bristles. For small displacements the bristles are in adhesion with the surface and the force  $F_s$  increases linearly with the bristle deflection. For large displacements all bristles will reach their maximum deflection and slide with respect to the surface. The force  $F_s$  is then equal to the friction coefficient multiplied by the vertical force. When reversing the direction of  $\Delta s$  the bristles will be in adhesion at first, when the displacement is large enough in the opposite direction they will start to slide again, as shown in Fig. 17.

Figure 18 gives an impression of the brush tire model and bristle deflection when a side slip angle  $\alpha$  is applied. Differences between the brush and brush tire mode are:

- In the brush tire model a parabolic distribution of the vertical force per unit of length  $q_z(x)$  is assumed instead of a constant  $q_z$ .

**Fig. 17** Force as a function of the displacement  $\Delta s$  for the brush model

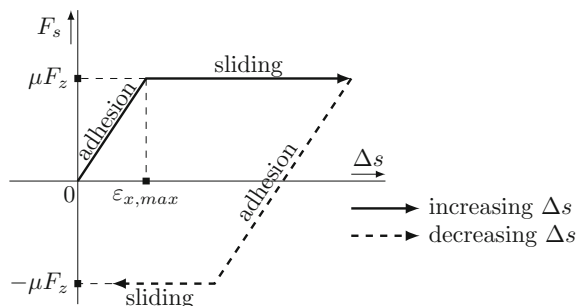
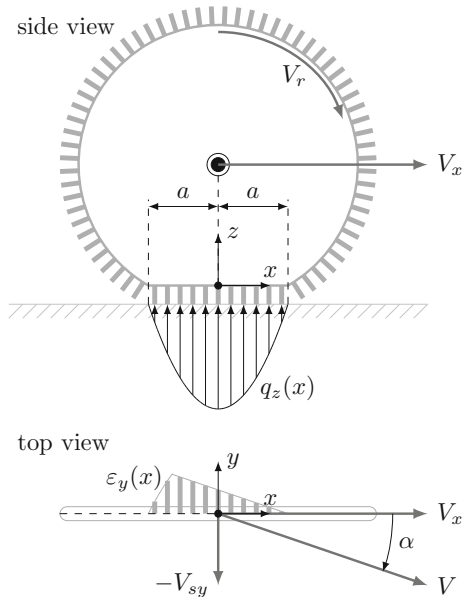


**Fig. 18** The brush tire model



- In the brush tire model the bristle deflection in the lateral direction  $\varepsilon_y(x)$  is also considered.
- In the brush tire model the wheel rotates, meaning that undeformed brushes enter the contact region and brushes will leave the contact region again. This causes the bristle deformation pattern to be more complex, both adhesion and sliding may occur in the contact zone.

In the brush tire model the wheel is represented by a thin disk, which is equipped with a single row of bristles around the circumference. The bristles are compliant in the longitudinal and lateral direction, representing the combined stiffness of the tire carcass, belt and tread elements. The disk is flattened in the contact region and the bristles are in contact with the road for a distance known as the contact length, being equal to  $2a$ . As the wheel is rotating, a bristle element will enter and leave the contact region after a certain time. It is assumed that a bristle entering the contact region is undeformed and positioned perpendicular to the road surface. In the contact region a sliding velocity may be present between the disk and road surface, e.g. due to the presence of a side slip angle  $\alpha$ . This will cause the bristles to deflect and forces will develop in the contact region. The longitudinal force  $F_x$ , lateral force  $F_y$  and self-aligning moment  $M_z$  can be determined by summing the contributions of the individual bristle elements. Outside the contact region the bristles are undeflected and do not contribute to the forces and moment. In the next sections the brush tire model will be analyzed in detail for steady-state conditions, i.e. fixed values of  $\kappa$ ,  $\alpha$  and  $F_z$ .

### 3.2 Bristle Deflections

Figure 18 shows the brush tire model. The angular velocity of the wheel equals  $\Omega$  and at the circumference of the tire the velocity is equal to the rolling speed  $V_r$ , which is related to  $\Omega$  by

$$V_r = \Omega r_e, \quad (27)$$

where  $r_e$  equals the effective rolling radius. As shown in Fig. 18 a coordinate system is introduced at the center of the contact line and in agreement with earlier definitions given in Sect. 1.2. The  $x$ -coordinate is used to identify the position of a bristle in contact region. As the wheel is rotating, a bristle element will enter and move though the contact region, before leaving it again. The time increment  $\Delta T$  is introduced to denote the amount of time the bristle is in contact with the road after entering the contact zone. The following expression applies:

$$\Delta T = \frac{a - x}{V_r}. \quad (28)$$

In steady-state conditions the wheel has a fixed side slip angle  $\alpha$ . The velocity  $V$  of the wheel center can be projected on the wheel plane, which results in a longitudinal velocity component  $V_x$  and lateral sliding velocity  $V_{sy}$ .

$$V_x = V \cos(\alpha), \quad (29)$$

$$V_{sy} = -V \sin(\alpha), \quad (30)$$

When assuming a constant, non-time varying side slip angle  $\alpha$  the entire wheel has a lateral velocity of  $V_{sy}$ . Thus the lateral velocity of the base of the bristles in the contact region with respect to the road also equals  $V_{sy}$ . The longitudinal velocity of the base of the bristles in the contact zone with respect to the road equals

$$V_{sx} = V_x - V_r. \quad (31)$$

Combining (31) with the definition of longitudinal slip  $\kappa$  (2), the following expression is obtained

$$V_r = V_x(1 + \kappa). \quad (32)$$

When assuming that the bristle tip sticks to the road after the first contact is made, then the bristle deflection is calculated by multiplying the velocity with the time the bristle spends in the contact zone  $\Delta T$ . The longitudinal bristle tip deflection  $\varepsilon_x(x)$  and lateral tip deflection  $\varepsilon_y(x)$  then become

$$\varepsilon_x(x) = -V_{sx}\Delta T = -(V_x - V_r)\left(\frac{a - x}{V_r}\right) = (a - x)\frac{\kappa}{1 + \kappa} = (a - x)s_x \quad (33)$$

and

$$\varepsilon_y(x) = -V_{sy}\Delta T = -V_{sy} \left( \frac{a-x}{V_r} \right) = (a-x) \frac{\tan(\alpha)}{1+\kappa} = (a-x)s_y. \quad (34)$$

It should be noted that these expressions for the bristle tip deflections are only valid as long as the bristle tip is in adhesion with the road. To simplify the expressions the theoretical slip values  $s_x$  and  $s_y$  are introduced. The theoretical longitudinal slip  $s_x$  is defined as

$$s_x = \frac{\kappa}{1+\kappa} \quad (35)$$

and the theoretical lateral slip  $s_y$  is defined as

$$s_y = \frac{\tan(\alpha)}{1+\kappa}. \quad (36)$$

As already discussed in the previous section, the maximum bristle deflection will be limited by the friction coefficient  $\mu$ . A parabolic distribution of the vertical force per unit of length is assumed for the brush tire model, as shown in Fig. 18. The vertical force per unit of length  $q_z(x)$  is dependent on the longitudinal coordinate  $x$  and given by:

$$q_z(x) = \frac{3F_z}{4a} \left( 1 - \left( \frac{x}{a} \right)^2 \right) \quad (37)$$

Obviously the vertical force  $F_z$  is obtained when integrating expression (37) over the contact length, see (20). Since the friction coefficient  $\mu$  and bristle element stiffness  $k_b$  are assumed to be constant, the maximum possible bristle tip deflection  $\varepsilon_{max}$  will be dependent on  $q_z(x)$ , and thus be a function of the longitudinal coordinate  $x$ .

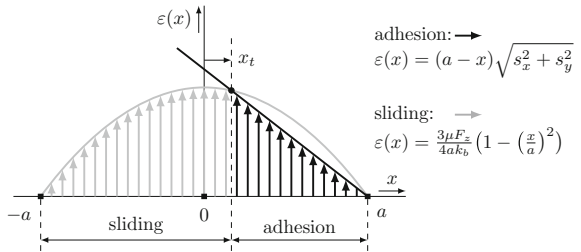
$$|\varepsilon_{max}(x)| = \frac{\mu q_z(x)}{k_b}. \quad (38)$$

The maximum possible bristle tip deflection will follow the parabolic shape of the pressure distribution. Both at the leading ( $x = a$ ) and trailing edge ( $x = -a$ ) of the contact region the maximum bristle deflection will be zero, since  $q_z(-a) = q_z(a) = 0$ . At the center of the contact region ( $x = 0$ ) the maximum possible bristle tip deflection will be reached.

As can be seen for the expressions of the longitudinal and lateral bristle tip deflection (33) and (34), the bristle deflection will increase linearly with its position in the contact region when moving backwards toward the end of the contact region. This can be generalized in the combined bristle deflection  $\varepsilon(x)$ , which is the vectorial sum of the longitudinal and lateral deflection

$$\varepsilon(x) = \sqrt{\varepsilon_x^2(x) + \varepsilon_y^2(x)} = (a-x) \sqrt{s_x^2 + s_y^2}. \quad (39)$$

**Fig. 19** The brush tire bristle deflection



A bristle tip initially sticks to the road when entering the contact region, thereafter the deflection builds up until a point where it starts to slide towards the end of the contact region. A transition point is defined where the bristle state changes from sticking to sliding, indicated by the coordinate  $x_t$ . This is illustrated by Fig. 19. At the transition point  $x_t$  the combined bristle deflection equals the maximum bristle deflection, thus  $\varepsilon(x_t) = \varepsilon_{max}(x_t)$ .

$$(a - x_t) \sqrt{s_x^2 + s_y^2} = \frac{3\mu F_z}{4ak_b} \left(1 - \left(\frac{x_t}{a}\right)^2\right). \quad (40)$$

This quadratic equation in terms of  $x_t$  has two solutions, a trivial solution  $x_t = a$  and a second solution

$$x_t = \frac{4k_b a^3}{3\mu F_z} \sqrt{s_x^2 + s_y^2} - a. \quad (41)$$

Obviously the transition point  $x_t$  has to be in a physically plausible range, so  $-a \leq x_t \leq a$ . It can be seen that for infinitely small theoretical slip values that (41) provides  $x_t = -a$  as a solution. As the theoretical slip increases,  $x_t$  will increase. The solution  $x_t = a$ , indicating that all bristles in the contact region are in the sliding state, is reached when the following condition is met

$$\sqrt{s_x^2 + s_y^2} \geq \frac{3\mu F_z}{2k_b a^2}. \quad (42)$$

For this condition all bristles in the contact region are sliding, there are no bristles in the adhesion state anymore.

### 3.3 Forces and Moment for Pure Slip Conditions

Before moving to the more complex combined slip case, pure side slip will be analyzed first. In this case the longitudinal slip  $\kappa$  will be zero and same applies to the longitudinal bristle deflection  $\varepsilon_x(x)$ . Using (34) the lateral bristle deflection then

becomes

$$\varepsilon_y(x) = (a - x) \tan(\alpha). \quad (43)$$

Considering the limit case, when the side slip angle  $\alpha$  is very small, the assumption can be made that all bristle elements in the contact region are in the adhesion state. To calculate the lateral force  $F_y$  the lateral force per unit of length  $q_y(x)$  has to be integrated over the contact length

$$F_y = \int_{-a}^a q_y(x) dx = k_b \int_{-a}^a \varepsilon_y(x) dx = k_b \tan(\alpha) \int_{-a}^a (a - x) dx \quad (44)$$

Since  $\alpha$  is small,  $\tan(\alpha) \approx \alpha$ , and solving the integral gives

$$F_y = 2k_b a^2 \alpha = C_{F\alpha} \alpha. \quad (45)$$

Note that we have obtained an expression for the cornering stiffness  $C_{F\alpha}$  of the tire, being dependent on the bristle stiffness  $k_b$  and contact length. To calculate the self-aligning moment  $M_z$  the moment arm  $x$  has to be taken into account and the expression becomes

$$M_z = \int_{-a}^a q_y(x) x dx = k_b \int_{-a}^a \varepsilon_y(x) x dx = k_b \tan(\alpha) \int_{-a}^a (a - x) x dx. \quad (46)$$

Solving the integral gives

$$M_z = -\frac{2}{3} k_b a^3 \alpha = -C_{M\alpha} \alpha. \quad (47)$$

The expression for the pneumatic trail  $t_p$  becomes

$$t_p = \frac{C_{M\alpha}}{C_{F\alpha}} = \frac{1}{3} a. \quad (48)$$

So far it has been assumed that the side slip angle  $\alpha$  is infinitely small. To handle larger values of the side slip angle both sticking and slipping of bristles in the contact region has to be considered. A generic expression for the transition point  $x_t$ , (41), has already been derived in the previous section. For pure side slip it reduces to

$$x_t = \frac{4k_b a^3}{3\mu F_z} |\tan(\alpha)| - a. \quad (49)$$

Sliding of all bristle elements will start to occur when  $x_t = a$ . The corresponding side slip angle  $\alpha_{sliding}$  is given by

$$|\tan(\alpha_{sliding})| = \frac{3\mu F_z}{2k_b a^2}. \quad (50)$$

To determine the lateral force  $F_y$  and self-aligning moment  $M_z$ , similar to (44) and (46), the lateral force per unit of length  $q_y(x)$  has to be integrated over the contact length. However part of the bristles in the contact region are in the adhesion state between  $x = x_t$  and  $x = a$ , and the other bristles are in the sliding state between  $x = -a$  and  $x = x_t$ . For both regions different expressions for  $q_y(x)$  are applicable. For the sliding part we have  $q_y(x) = \mu q_z(x)$ , for the adhesion part  $q_y(x) = k_b \varepsilon_y(x)$ . The integral to calculate  $F_y$  thus becomes

$$F_y = \frac{3\mu F_z}{4a} \int_{-a}^{x_t} \left(1 - \left(\frac{x}{a}\right)^2\right) dx + k_b \tan(\alpha) \int_{x_t}^a (a-x) dx. \quad (51)$$

For the self-aligning moment  $M_z$  the expression is very similar, but the moment arm  $x$  needs to be taken into account,

$$M_z = \frac{3\mu F_z}{4a} \int_{-a}^{x_t} \left(1 - \left(\frac{x}{a}\right)^2\right) x dx + k_b \tan(\alpha) \int_{x_t}^a (a-x)x dx. \quad (52)$$

Note that when  $|\alpha| \geq \alpha_{sliding}$  that  $x_t = a$  and second part of the integrals (51) and (52) disappears. For this condition the following expressions are obtained for the lateral force  $F_y$  and self-aligning moment  $M_z$ :

$$F_y = \mu F_z, \quad (53)$$

and

$$M_z = 0 \quad (54)$$

respectively. When  $|\alpha| \leq \alpha_{sliding}$  the integrals (51) and (52) have to be solved, and expression (49) is used to determine  $x_t$ . To simplify the expressions, the parameter  $\theta$  is introduced, it is defined as

$$\theta = \frac{2k_b a^2}{3\mu F_z} = \frac{1}{|\tan(\alpha_{sliding})|}. \quad (55)$$

The theoretical lateral slip  $s_y$  follows from (36), given that  $\kappa = 0$

$$s_y = \tan(\alpha). \quad (56)$$

By solving the integrals the expressions for  $F_y$  and  $M_z$  become

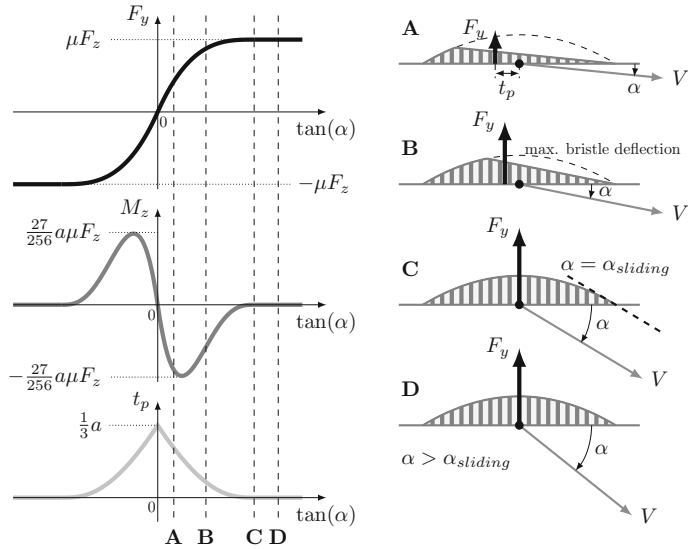


**Fig. 20** The brush tire model results for pure side slip

$$F_y = 3\mu F_z \theta s_y \left( 1 - |\theta s_y| + \frac{1}{3}(\theta s_y)^2 \right) \quad (57)$$

$$M_z = -\mu F_z a \theta s_y \left( 1 - 3|\theta s_y| + 3(\theta s_y)^2 - |\theta s_y|^3 \right). \quad (58)$$

Using these results, the following expression can be obtained for the pneumatic trail  $t_p$ ,

$$t_p = \frac{a}{3} \left( \frac{1 - 3|\theta s_y| + 3(\theta s_y)^2 - |\theta s_y|^3}{1 - |\theta s_y| + \frac{1}{3}(\theta s_y)^2} \right). \quad (59)$$

A graphical representation of the lateral force  $F_y$ , self-aligning moment  $M_z$  and pneumatic trail  $t_p$  is shown in Fig. 20. As the side slip angle  $\alpha$  increases the bristle deflection in the contact region increases, and thus the lateral force  $F_y$  increases, up to the level where all bristles have reached the maximum deflection. The self-aligning moment  $M_z$  is a result of the non-symmetric bristle deflection in the leading and trailing parts of the contact zone. For small side slip angles an increase of the side slip angle will result in a larger bristle deflection and increase of the self-aligning moment. For large values of side slip the asymmetry in the bristle deflection in the leading and trailing part of the contact zone is reduced and vanishes completely when all bristles are sliding. The pneumatic trail  $t_p$  corresponds to the centroid of the bristle deflection. It decreases monotonically with increasing side slip angle, until it becomes zero when all bristles in the contact zone are sliding.

The discussion of the pure longitudinal slip case is very similar to the pure lateral slip case. In this case  $\alpha$  is equal to zero thus  $\varepsilon_y(x)$  will be zero too, the expression for  $\varepsilon_x(x)$  is given by (33). The expression for the transition point  $x_t$  becomes

$$x_t = \frac{4k_b a^3}{3\mu F_z} \left| \frac{\kappa}{1 + \kappa} \right| - a = 2\theta a \left| \frac{\kappa}{1 + \kappa} \right| - a. \quad (60)$$

Again full sliding of all bristle elements in the contact zone will occur when  $x_t = a$ , thus the following condition has to be met

$$\left| \frac{\kappa_{sliding}}{1 + \kappa_{sliding}} \right| = \frac{1}{\theta}. \quad (61)$$

Two solutions exist for  $\kappa_{sliding}$ , for positive  $\kappa$

$$\kappa_{sliding} = \frac{1}{\theta - 1} \quad (62)$$

and for negative  $\kappa$

$$\kappa_{sliding} = -\frac{1}{\theta + 1}. \quad (63)$$

Note that the longitudinal slip  $\kappa$  where full sliding occurs is different for driving ( $\kappa > 0$ ) and braking ( $\kappa < 0$ ). The expressions for the bristle deflections  $\varepsilon_y(x)$  (34) and  $\varepsilon_x(x)$  (33) are very similar, the only difference being that  $s_y$  is replaced by  $s_x$ . This also implies that the function  $F_x(s_x)$  will be identical to  $F_y(s_y)$ . Thus the equation for the lateral force  $F_y$  (57) can also be used to calculate the longitudinal force  $F_x$  when replacing  $s_y$  by  $s_x$ . The theoretical slip  $s_x$  will be equal to the longitudinal slip  $\kappa$  for small values of slip. It allows to determine the longitudinal slip stiffness  $C_{F_K}$ , which equals

$$C_{F_K} = 2k_b a^2. \quad (64)$$

Note that the expression for the longitudinal slip stiffness  $C_{F_K}$  is identical to the cornering stiffness  $C_{F_\alpha}$  (45).

### 3.4 Forces and Moment for Combined Slip Conditions

In the case of combined slip, the bristles will deflect both in the longitudinal and lateral direction. The evaluation of the combined slip case is similar to the pure side slip case. Next a summary of the equations of the brush model is given, which can handle both pure and combined slip conditions.

$$s_x = \frac{\kappa}{1 + \kappa} \quad (65)$$

$$s_y = \frac{\tan(\alpha)}{1 + \kappa} \quad (66)$$

$$s_{comb} = \sqrt{s_x^2 + s_y^2} \quad (67)$$

$$\theta = \frac{2k_b a^2}{3\mu F_z} \quad (68)$$

When  $s_{comb} < 1/\theta$  then

$$F = 3\mu F_z \theta s_{comb} \left( 1 - |\theta s_{comb}| + \frac{1}{3}(\theta s_{comb})^2 \right) \quad (69)$$

$$t_p = \frac{a}{3} \left( \frac{1 - 3|\theta s_{comb}| + 3(\theta s_{comb})^2 - |\theta s_{comb}|^3}{1 - |\theta s_{comb}| + \frac{1}{3}(\theta s_{comb})^2} \right). \quad (70)$$

When  $s_{comb} \geq 1/\theta$

$$F = \mu F_z \quad (71)$$

$$t_p = 0 \quad (72)$$

The expressions for the longitudinal force  $F_x$ , lateral force  $F_y$  and self-aligning moment  $M_z$  are:

$$F_x = \frac{s_x}{s_{comb}} F \quad (73)$$

$$F_y = \frac{s_y}{s_{comb}} F \quad (74)$$

$$M_z = -t_p \cdot F_y \quad (75)$$

The required model parameters are the bristle stiffness per unit of length  $k_b$ , the friction coefficient  $\mu$  and half of the tire contact length  $a$ . The tire contact length  $2a$  depends on the vertical tire deflection  $\rho$ , which is dependent again on the vertical force  $F_z$ . Assuming the tire to behave as a linear spring in the vertical direction, see e.g. Fig. 2, the tire deflection  $\rho$  reads

$$\rho = \frac{F_z}{k_z}, \quad (76)$$

where  $k_z$  equals the vertical tire stiffness. A first estimate for the dependency of half of the contact length  $a$  on the tire deflection  $\rho$  can be made by assuming that the wheel is a rigid circular disk that penetrates the road. The next equation can be obtained for half of the contact length,

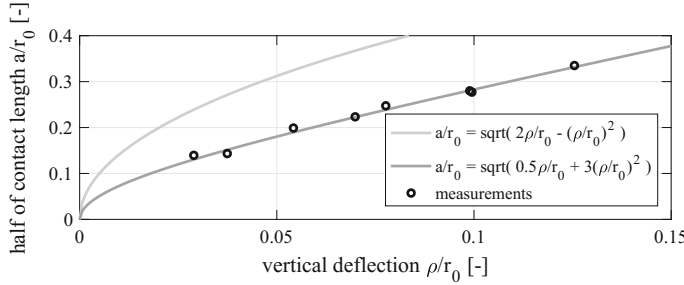


**Fig. 21** Experimental results and equations to describe half of the contact length  $a$

$$a = r_0 \sqrt{2\left(\frac{\rho}{r_0}\right) - \left(\frac{\rho}{r_0}\right)^2}, \quad (77)$$

where  $r_0$  equals the undeformed tire radius. A comparison with experimental results shows that this is not a very accurate representation, since in reality the contact length is much shorter, as shown in Fig. 21. By adapting the contact length equation in a pragmatic way, a better match with the measurement results can be obtained. The empirical equation for  $a$  then becomes

$$a = r_0 \sqrt{0.5\left(\frac{\rho}{r_0}\right) + 3\left(\frac{\rho}{r_0}\right)^2}. \quad (78)$$

**Implementation: divisions by zero** When programming the brush tire model equations, care has to be taken to avoid divisions by zero. This can occur at several instances:

- when both  $\kappa$  and  $\alpha$  are zero, the combined theoretical slip  $s_{comb}$  (67) will be zero, and a division by zero will occur in (73) and (74). A solution is modify the denominator in expressions (73) and (74). Since  $s_{comb} \geq 0$  it can be replaced by  $\max(s_{comb}, \epsilon)$ , where  $\epsilon$  is a small positive number and the function  $\max(a, b)$  returns  $a$  if  $a \geq b$  or  $b$  when  $b > a$ .
- The brush tire model equations are only valid when  $F_z \geq 0$ . When a wheel lifts off the ground the vertical tire force  $F_z$  will become zero and the calculation of  $\theta$  (68) becomes problematic. A solution is to evaluate  $\theta$  for a small positive vertical force, e.g.  $\max(F_z, \epsilon)$ . With this modification the forces  $F_x$ ,  $F_y$  and self-aligning moment  $M_z$  will still be zero when  $F_z = 0$  as a result of the multiplication with  $F_z$  in expression (69).
- When the wheel locks up, the angular velocity  $\Omega$  will be zero and the longitudinal slip  $\kappa$  will become  $-1$ . A division by zero will occur in the calculation of the theoretical slip  $s_x$  (65) and  $s_y$  (66). It can be noted that the brush tire model equations have been derived under the assumption that the wheel is rotating in the forward direction ( $\Omega > 0$ ) and that the bristles spend a certain time in the contact zone.

When the wheel is not rotating we basically get the brush model, as discussed in Sect. 3.1. The resulting force will be equals to  $\mu F_z$  and in the opposite direction of the sliding velocity

$$F_x = -\mu F_z \frac{V_{sx}}{\sqrt{V_{sx}^2 + V_{sy}^2}}, \quad F_y = -\mu F_z \frac{V_{sy}}{\sqrt{V_{sx}^2 + V_{sy}^2}}. \quad (79)$$

Assuming that  $\Omega$  and  $V_x$  cannot become negative, then  $\kappa \geq -1$ . The division by zero can be eliminated by modifying the denominator of expressions (65) and (66) to  $\max(1 - \kappa, \epsilon)$ . The results obtained then are still in agreement with (79).

**Implementation: forward and backward driving** The brush tire model equations have been derived for specific conditions, for example  $V_x > 0$  and  $\Omega \geq 0$ . When implementing the brush tire model in a vehicle model also other conditions may appear, e.g. driving backwards, vehicle sliding backwards while the driven wheels still rotate in the forward direction, vehicle standing still, etc. To handle these conditions, it is more convenient to use the sliding velocities  $V_{sx}$ ,  $V_{sy}$  and rolling velocity  $V_r$  to calculate the tire forces and moments, instead of  $\kappa$  and  $\alpha$ . The theoretical slip equations have to be adapted. The expressions become

$$s_x = -\frac{V_{sx}}{\max(|V_r|, V_{r,min})} \quad (80)$$

$$s_y = -\frac{V_{sy}}{\max(|V_r|, V_{r,min})} \quad (81)$$

where  $V_{r,min}$  is a lower boundary for the rolling speed. This value should not be selected too small (e.g. 1 m/s) as it will make the resulting differential equations numerically stiff, leading to long simulation times. It can also be verified that when the rolling speed  $V_r$  is equal to zero that (79) will be obtained. Furthermore the pneumatic trail  $t_p$  will change sign when switching from forward to backward driving, and it will be zero when the rolling speed  $V_r$  (or equivalently  $\Omega$ ) is equal to zero. This can be incorporated in a continuous way by modifying Eq. (75) to

$$M_z = -t_p F_y \tanh(10V_r). \quad (82)$$

### 3.5 Brush Model Validation

In Sects. 2.2 and 2.3 the results of steady-state force and moment measurements for a specific tire have been presented. Here a comparison will be made with the results obtained with the brush tire model. The parameters of the brush tire model are listed

**Table 2** Brush tire model parameters for a passenger car tire

Parameter	Symbol	Value	Unit
Free tire radius	$r_0$	0.315	m
Vertical stiffness	$k_z$	$2 \times 10^5$	N/m
Friction coefficient	$\mu$	1.0	—
Bristle stiffness	$k_b$	$7 \times 10^6$	N/m <sup>2</sup>

in Table 2. They have been selected to get the best possible match of the brush tire model with the measurements and expression (78) is used to calculate half of the contact length  $a$ .

First pure slide slip will be considered and a comparison is shown in Fig. 22 for the lateral force  $F_y$  and self-aligning moment  $M_z$ . It can be seen that the shapes are similar, but the magnitude of the self-aligning moment is largely underestimated. The same applies for the pneumatic trail  $t_p$ , as shown in Fig. 23a. The pure longitudinal slip case, consisting of straight line braking, is shown in Fig. 23b. It is clear that the brush tire model does not differentiate between a peak and locked wheel friction coefficient, so the match with the measurements is not that good. Furthermore it can be noted that the slope of the curve near the origin, the longitudinal slip stiffness  $C_{F_K}$ , is too low. Figures 24 and 25 show results for combined slip conditions. It can be seen that the brush tire model also displays the decrease of the longitudinal slip stiffness  $C_{F_K}$  with increasing magnitude of the side slip angle  $\alpha$ , see Fig. 24a. The lateral force  $F_y$  for combined slip conditions, as shown in Fig. 24b, is fairly accurate. The decrease of the magnitude of the lateral force with increasing magnitude of the longitudinal slip  $\kappa$  is captured well. The self-aligning moment  $M_z$  is shown in Fig. 25a. In the measurements  $M_z$  does not decrease to zero for large values of the longitudinal slip  $\kappa$ , so apparently some phenomena are not included in the brush model. Plotting  $F_y$  versus  $F_x$ , as is done in Fig. 25b, clearly shows the  $\mu F_z$  friction circle which limits the maximum shear forces. In this figure also the forces for the driving side are shown ( $\kappa > 0$ ), which have not been measured. For the smaller side slip angles some asymmetry can be observed: for the same magnitude of the longitudinal force  $F_x$ , the lateral force  $F_y$  is smaller when the wheel is driven in comparison to braking. This phenomenon is also seen in tire measurements.

The differences between model and measurements can also be quantified. The same combinations of inputs ( $\kappa$ ,  $\alpha$  and  $F_z$ ) as used in the measurements are applied to the brush tire model and a comparison can be made between the outputs of the model ( $F_x$ ,  $F_y$  and  $M_z$ ) and the measured quantities. The following error criterion is used to numerically assess the differences

$$\epsilon = \frac{\sum_{i=1}^n |(F_{model,i} - F_{meas,i})|}{\sum_{i=1}^n |F_{meas,i}|} \cdot 100\%, \quad (83)$$

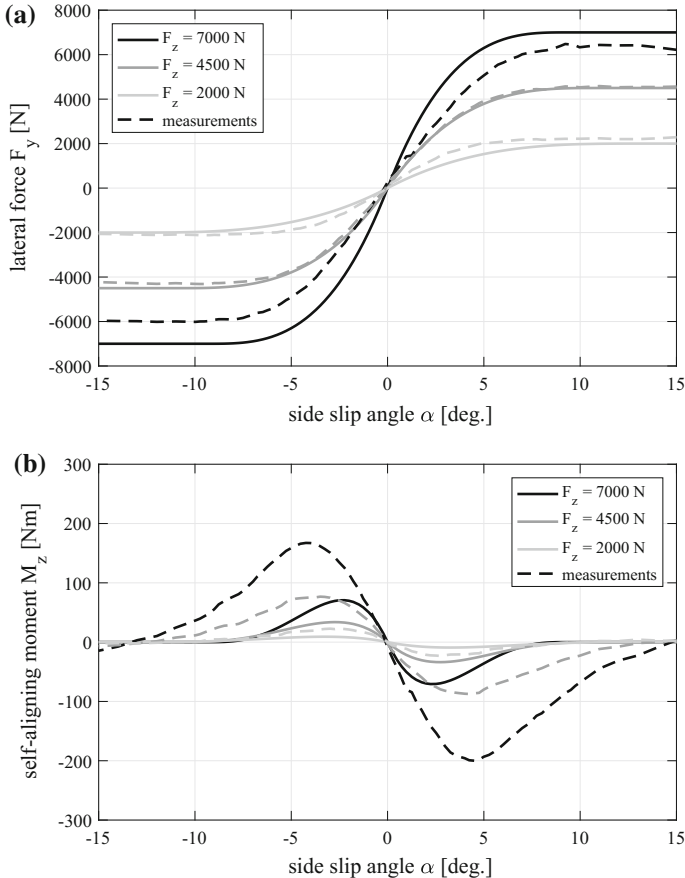


**Fig. 22** Comparison of brush tire model with measurements for pure side slip, lateral force  $F_y$  and self-aligning moment  $M_z$

where  $n$  is the number of measurement points,  $i$  an index to identify an individual measurement point,  $F_{model}$  the result of the model and  $F_{meas}$  the measurement result. For the different outputs of the brush tire model the error  $\epsilon$  has been calculated and the results are listed in Table 3. Based on Figs. 22, 23, 24 and 25 it can be seen that an error of 10% or larger indicates that the measurements are not modeled very accurately. It is obvious from the Figs. 22b and 25a that the self-aligning moment representation is very poor in particular.

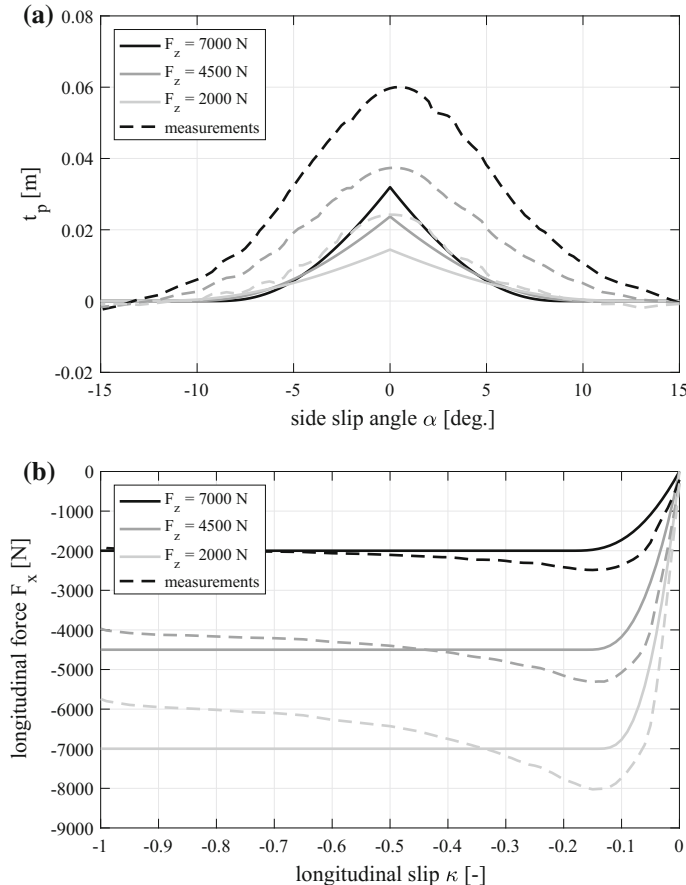


**Fig. 23** Comparison of brush tire model with measurements for pure side and longitudinal slip, pneumatic trail  $t_p$  and longitudinal force  $F_x$

**Table 3** Brush tire model errors

	Pure (%)	Combined (%)
$F_x$	11.4	9.7
$F_y$	15.3	16.6
$M_z$	73.3	97.0

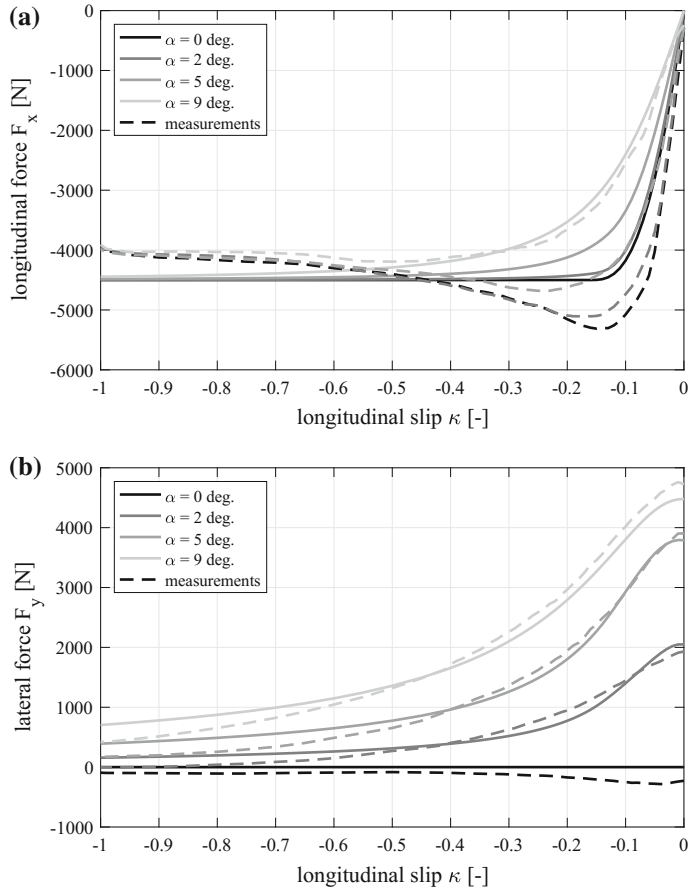


**Fig. 24** Comparison of brush tire model with measurements for combined slip,  $F_x$  and  $F_y$  ( $F_z = 4500$  N)

**Brush tire model improvements** The brush tire model is a relatively simple physical tire model, that allows to qualitatively describe the tire characteristics. There are various ways to improve the accuracy of the model:

- Separate the stiffness of tread elements and carcass. Introduction of a flexible carcass or rigid ring to which the flexible bristle elements are attached.
- Improve the accuracy of the distribution of the vertical force per unit of length, so that it better reflects the actual pressure distribution in the contact area.
- Introduce a more refined friction law, the friction coefficient  $\mu$  should be a function of sliding velocity and vertical force.
- Introduce multiple, parallel rows of bristles.

In Pacejka (2012) a more advanced brush tire model, called “Treadsim”, is described that includes most of the improvements listed here.

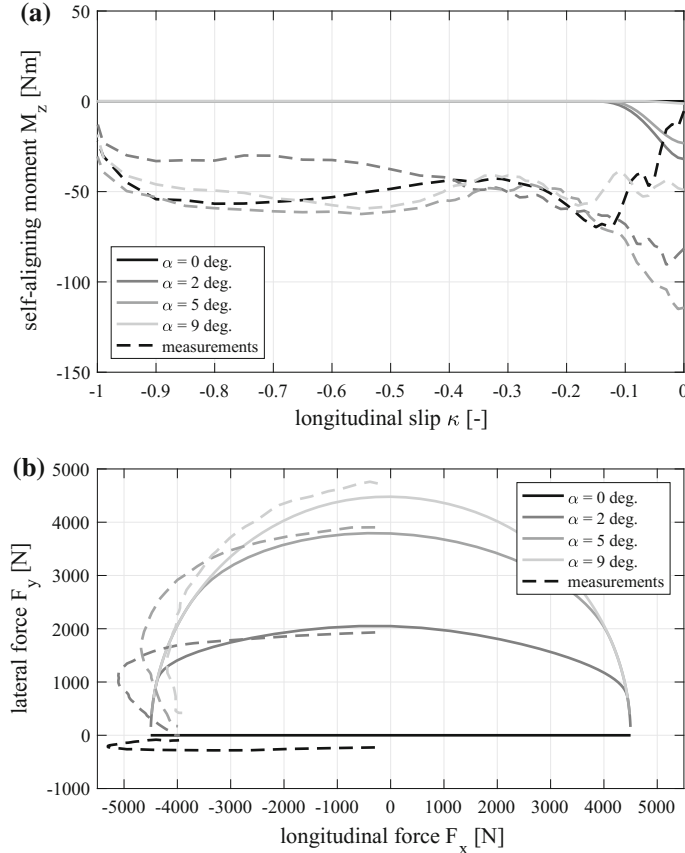


**Fig. 25** Comparison of brush tire model with measurements for combined slip,  $M_z$  and  $F_y$  versus  $F_x$ , ( $F_z = 4500$  N)

## 4 The Magic Formula Tire Model

### 4.1 Magic Formula Fundamentals

The brush tire model, as discussed in the previous section, is a physical model that is very useful to explain the shape of the measured tire force and moment characteristics. It is however not capable to accurately represent the measured force and moment characteristics. Although model enhancements are possible, experience has shown that a major effort is required to create a truly accurate physical tire model. Also the computational effort of such a detailed and refined physical tire model may be high, which will make them not suitable for full vehicle simulations.

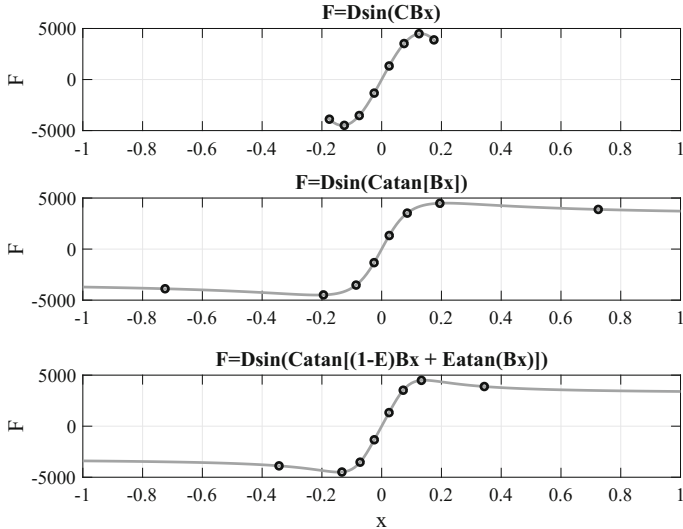


**Fig. 26** Stretching the sine function ( $B = 8$ ,  $C = 1.5$ ,  $D = 4500$ ,  $E = -2$ )

The tire characteristics do not necessarily have to be modeled using a physical approach, what we are looking for is a tire model, a “tire function”, that can represent the measured force and moment characteristics with sufficient accuracy. In a full vehicle simulation the inputs  $\kappa$ ,  $\alpha$ ,  $\gamma$  and  $F_z$  will vary continuously, so it should allow interpolation as the measurements are for example executed for a fixed vertical force  $F_z$ . Furthermore it should allow a plausible extrapolation, as during a full vehicle simulation conditions may be encountered that have not been tested.

Generic curve fitting techniques, e.g. using polynomials, may be used to capture the measured tire characteristics, but their performance is not considered to be adequate. The “Magic Formula” is a semi-empirical tire model that employs specifically designed functions to best represent the measured tire characteristics. The first version of this tire model was developed by Egbert Bakker of Volvo Cars Helmond and professor Pacejka of the TU Delft, Bakker and Pacejka (1987). As all model equations were published in the open literature from the start, the model rapidly became popular and it is one of the most used tire models worldwide in full vehicle handling simulations.

The observation was made is that the longitudinal, lateral and self-aligning moment characteristics have sinusoidal shape, with a stretched horizontal axis for large values of slip. This consideration is the base for the Magic Formula tire model. The accompanying equation reads

$$y = D \sin(C \arctan[(1 - E)Bx + E \arctan(Bx)]) \quad (84)$$

where  $x$  would represent a slip variable,  $\kappa$  or  $\alpha$  and  $y$  the force or moment. Figure 26 illustrates how the sine function is stretched. The atan function results in a saturation of the input to the sine function, the  $E$  parameter provides a way to influence the position of the peak.

Next to the sine version of the Magic Formula (84), also a cosine version is used to model specific aspects of the tire, for example the pneumatic trail  $t_p$ , as shown in Fig. 9f. The cosine Magic Formula is given by

$$F = D \cos(C \arctan[((1 - E)Bx + E \arctan(Bx))]). \quad (85)$$

Both sine and cosine Magic Formula are shown in Fig. 27, including the meaning of some parameters. We can observe that:

- $D$  determines the peak value
- $C$  determines the limit value when  $x$  is going to plus or minus infinity. For the sine Magic Formula

$$C = 2 - \frac{2}{\pi} \arcsin\left(\frac{y_\infty}{D}\right), \quad (86)$$

and for the cosine Magic Formula

$$C = 2 - \frac{2}{\pi} \arccos\left(\frac{y_\infty}{D}\right). \quad (87)$$

note that  $C \geq 1$ .

- For the sine Magic Formula the product  $BCD$  determines the slope at the origin.
- For the cosine Magic Formula the product  $BC$  determines the curvature near the origin.
- The parameters  $B$ ,  $E$  and  $C$  determine the location of the peak  $x_m$  for the sine Magic Formula and point where the curve crosses zero  $x_0$  for the cosine Magic Formula. The parameter  $E$  can be calculated by

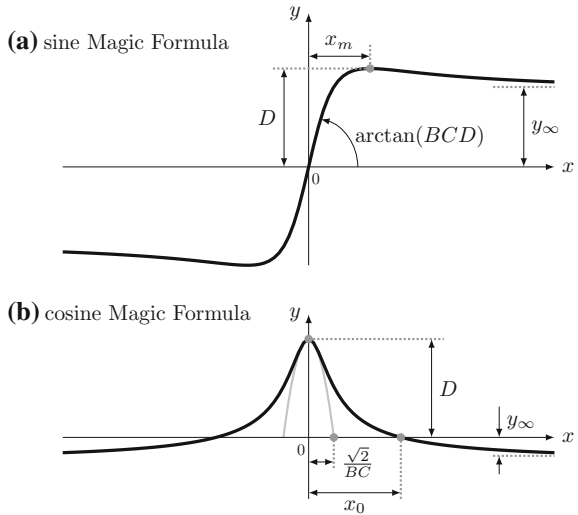
$$E = \frac{Bx - \tan(\pi/2C)}{Bx - \arctan(Bx)}, \quad (88)$$

where  $x$  is either  $x_m$  or  $x_0$ . Note that it should hold that  $E \leq 1$ , if  $E$  exceeds 1 unrealistic curves will be obtained.

Equations (84) and (85) provide the basic equations. To model a tyre accurately for different operating conditions the parameters are made dependent on for example the vertical force  $F_z$  and inclination angle  $\gamma$ . More details will be given in the next sections.

An iterative, non-linear, constrained optimization procedure is typically used to determine the Magic Formula tire model parameters. The objective of the optimization is to minimize the error criterion given by (83), while the constraints  $C \geq 1$  and  $E \leq 1$  are applicable. To start the optimization procedure an initial estimate has to be provided for the parameters. Thereafter the error criterion is reduced with every

**Fig. 27** Sine and cosine Magic Formula and illustration of the meaning of its parameters



iteration step, while the constraints are checked and maintained if necessary. The MATLAB function “fmincon”, which is part of the optimization toolbox, has been used successfully for this purpose.

In the next sections more details on the Magic Formula tire model will be introduced. Since its conception, different versions of the Magic Formula have been developed. The equations presented in the next sections reflect the version as described by Pacejka (2012) and implemented in the MF-Tyre 6.x software, TASS (2018). For educational reasons the effects of changes in tire inflation pressure have been omitted, these extensions have been developed at the TU Eindhoven and are described by Besselink et al. (2010). The same applies to parking and turn slip behavior, which is described in more detail in Pacejka (2012).

To make the Magic Formula parameters dimensionless, the following parameters are introduced:

- nominal vertical force  $F_{z0}$
- free radius of the non-rolling tire  $r_0$ .

The nominal vertical force  $F_{z0}$  should approximately reflect the static vertical tire force, in case of a passenger car tire it will be in the order of 4000 N. Its value only affects the magnitude of the Magic Formula parameters, but not the final accuracy of the model. As will be shown in the next sections, some parameters of the Magic Formula (e.g.  $D$  and  $E$ ) are dependent on the vertical force. To include these effects a dimensionless force increment  $d_{Fz}$  is introduced, defined as:

$$d_{Fz} = \frac{F_z - F_{z0}}{F_{z0}}. \quad (89)$$

Strictly speaking the free tire radius  $r_0$  used in the Magic Formula expressions does not have to reflect the actual free radius of the tire, it is just used to make the parameters in the expression for the self-aligning moment dimensionless. However in most tire modeling software  $r_0$  is also used in the loaded radius calculation and therefore should be defined precisely and reflect the actual tire dimension.

## 4.2 Longitudinal Force

The equations to describe the longitudinal force  $F_x$  for pure slip conditions,  $\alpha = 0$ , are given by Eqs. (90)–(99). In (90) the sine Magic Formula (84) can be recognized, with additional shifts both in the horizontal and vertical direction,  $S_{Hx}$  and  $S_{Vx}$  respectively. The peak friction coefficient is modeled by (94), a constant part  $p_{Dx1}$  and part linearly dependent on the vertical force  $p_{Dx2}$  can be recognized. They allow to capture the linear decrease of the peak friction coefficient  $\mu_{x,peak}$  with vertical force  $F_z$ , as shown in Fig. 10c. For many tires the dependency of  $\mu_{x,peak}$  on the inclination angle  $\gamma$  will be negligible, so  $p_{Dx3}$  may be set to zero in that case. The longitudinal slip stiffness  $C_{F_K} = K_{xK}$  is given by (96). In the measurement, see Fig. 10b, a linear dependency on the vertical force  $F_z$  is seen which can be captured by parameter  $p_{Kx1}$ . The parameters  $p_{Kx2}$  and  $p_{Kx3}$  allow to model a non-linear dependency on the vertical force  $F_z$ . However they should be used carefully, in particular  $p_{Kx3}$ , as extrapolation to very high vertical forces may result in physically impossible results when longitudinal slip stiffness  $K_{xK}$  becomes negative.

$$F_{xp} = D_x \sin(C_x \arctan[(1 - E_x)B_x \kappa_x + E_x \arctan(B_x \kappa_x)]) + S_{Vx} \quad (90)$$

$$\kappa_x = \kappa + S_{Hx} \quad (91)$$

$$C_x = p_{Cx1} \quad (92)$$

$$D_x = \mu_{x,peak} F_z \quad (93)$$

$$\mu_{x,peak} = (p_{Dx1} + p_{Dx2} d_{Fz})(1 - p_{Dx3} \gamma^2) \lambda_{\mu x} \quad (94)$$

$$E_x = (p_{Ex1} + p_{Ex2} d_{Fz} + p_{Ex3} d_{Fz}^2)(1 - p_{Ex4} \operatorname{sgn}(\kappa_x)) \quad (95)$$

$$K_{xK} = F_z (p_{Kx1} + p_{Kx2} d_{Fz}) \exp(p_{Kx3} d_{Fz}) \lambda_{KxK} \quad (96)$$

$$B_x = \frac{K_{xK}}{C_x D_x} \quad (97)$$

$$S_{Hx} = p_{Hx1} + p_{Hx2} d_{Fz} \quad (98)$$

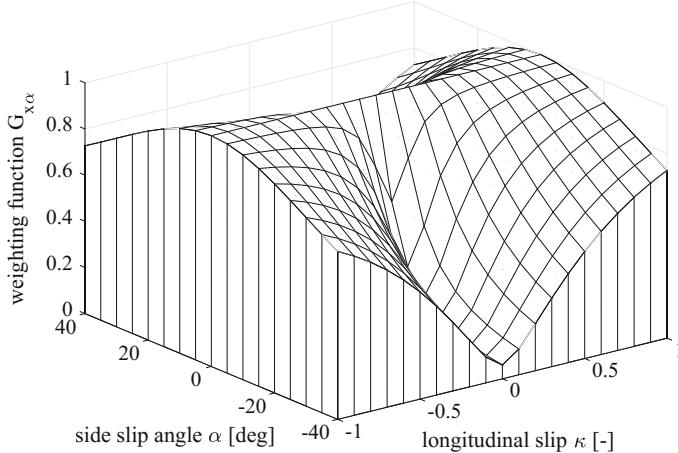


**Fig. 28** Combined slip weighting function  $G_{x\alpha}$  for the longitudinal force  $F_x$

$$S_{Vx} = F_z(p_{Vx1} + p_{Vx2}d_{Fz})\lambda_{\mu x} \quad (99)$$

To model the forces for combined slip conditions a weighting function  $G_{x\alpha}$  is introduced, as can be seen from (100). This weighting function has a value between 0 and 1. This is logical as the longitudinal force  $F_x$  is reduced for combined slip conditions in comparison to pure slip, which is illustrated by Fig. 11a. To model this weighting function  $G_{x\alpha}$  the cosine Magic Formula (85) is used, in (101) it appears both in the numerator as well as the denominator. It can be seen that  $G_{x\alpha}$  will always be equal to one when  $\alpha$  is equal to zero. For a given vertical force  $F_z$  and longitudinal slip  $\kappa$ , the weighting function  $G_{x\alpha}$  as a function of  $\alpha$  will have the cosine Magic Formula shape. The longitudinal slip  $\kappa$  affects  $B_{x\alpha}$  and changes the width of the cosine Magic Formula. Furthermore,  $B_{x\alpha}$  will be zero when  $\kappa$  goes to plus or minus infinity and the weighting function  $G_{x\alpha}$  equals one again. A plot of the weighting function  $G_{x\alpha}$  is shown in Fig. 28.

$$F_x = F_{xp}G_{x\alpha} \quad (100)$$

$$G_{x\alpha} = \frac{\cos(C_{x\alpha} \arctan[(1 - E_{x\alpha})B_{x\alpha}\alpha_s + E_{x\alpha} \arctan(B_{x\alpha}\alpha_s)])}{\cos(C_{x\alpha} \arctan[(1 - E_{x\alpha})B_{x\alpha}S_{Hx\alpha} + E_{x\alpha} \arctan(B_{x\alpha}S_{Hx\alpha})])} \quad (101)$$

$$\alpha_s = \alpha + S_{Hx\alpha} \quad (102)$$

$$B_{x\alpha} = (r_{Bx1} + r_{Bx3}\gamma^2) \cos(\arctan(r_{Bx2}\kappa)) \quad (103)$$

$$C_{x\alpha} = r_{Cx1} \quad (104)$$

$$E_{x\alpha} = r_{Ex1} + r_{Ex2}d_{Fz} \quad (105)$$

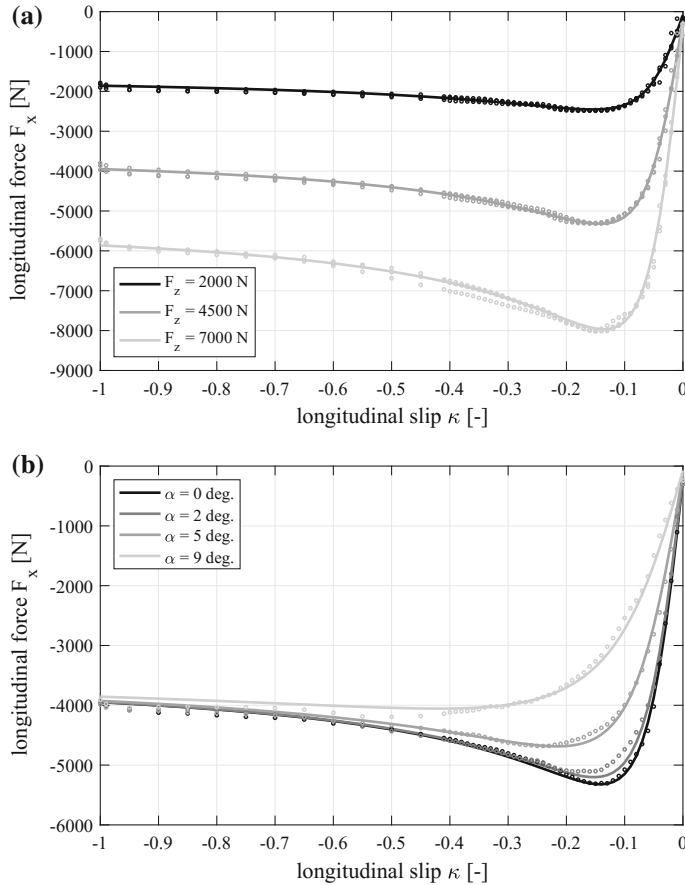


**Fig. 29** Magic Formula (solid lines) and measurements (dots) for the longitudinal force  $F_x$ , pure slip (a) and combined slip (b)

$$S_{Hx\alpha} = r_{Hx1} \quad (106)$$

The Magic Formula parameters have been determined for the measurements presented in Sect. 2.3 and are listed in Table 4. The difference between measurement and model  $e$  is also listed in this table, obviously the Magic Formula shows a much increased accuracy in comparison to the brush tire model (Table 3). The results can be checked visually in Fig. 29.

**Table 4** Longitudinal force Magic Formula parameters

Constants	$F_{z0} = 5000 \text{ N}$
$F_x$ pure	$p_{Cx1} = 1.5591$ $p_{Dx1} = 1.1752, p_{Dx2} = -0.0889, p_{Dx3} = 0$ $p_{Ex1} = 0, p_{Ex2} = -0.1182, p_{Ex3} = 0.1844, p_{Ex4} = 0$ $p_{Kx1} = 20.4330, p_{Kx2} = 0, p_{Kx3} = 0$ $p_{Hx1} = -0.0022, p_{Hx2} = 0$ $p_{Vx1} = 0, p_{Vx2} = 0$
$F_x$ combined	$r_{Bx1} = 15.9985, r_{Bx2} = 12.1522, r_{Bx3} = 0$ $r_{Cx1} = 1.0177$ $r_{Ex1} = 0.1783, r_{Ex2} = -0.2879$ $r_{Hx1} = 0$
Model error	Pure: $\epsilon = 1.33\%$ , combined: $\epsilon = 2.39\%$

### 4.3 Lateral Force

The equations to describe the lateral force  $F_y$  for pure slip conditions,  $\kappa = 0$ , are given by Eqs. (107)–(121). The basic approach is very similar to modeling the longitudinal force  $F_x$ . Again a sine Magic Formula is used, including a horizontal and vertical shift. The friction coefficient  $\mu_y$  is modeled by (111). When ignoring the contribution of  $\gamma$ , a linear dependency of  $\mu_y$  on the vertical force  $F_z$  can be seen, as also observed in the measurements, see Fig. 9e. Measurements indicate that the dependency of the cornering stiffness  $C_{F\alpha}$  on the vertical force  $F_z$  is different when compared to the longitudinal slip stiffness  $C_{F\kappa}$ , see Figs. 9a and 10b. The equation used modeling the cornering stiffness  $K_{ya}$  (113) is quite different from the expression for the longitudinal slip stiffness  $K_{x\kappa}$  (96). Note that the expression for  $K_{ya}$  includes the influence of the inclination angle  $\gamma$ , whereas  $\gamma$  is assumed to be zero in the definition of  $C_{F\alpha}$  (10). In earlier versions of the Magic Formula the value of  $p_{Ky4}$  was fixed to 2. Considering that a sine Magic Formula is used for modeling  $K_{ya}$  the value of  $p_{Ky4}$  should be equal or greater than 1 in any case.

The camber stiffness modeled by  $K_{yy}$  (114), this expression represents the measured camber stiffness  $C_{Fy}$ , as shown in Fig. 9c. In the measurements the  $F_y$  versus  $\alpha$  curve is shifted vertically as a result of an inclination angle  $\gamma$ , in the Magic Formula expressions this is taken into account by the vertical shift  $S_{Vyy}$  (121). A horizontal shift due to camber,  $S_{Hy\gamma}$  (118), ensures that when  $\alpha$  is equal to zero, that the desired lateral force is obtained. In earlier versions of the Magic Formula the contribution of the inclination angle  $\gamma$  was implicitly included in the horizontal shift. This did not allow to accurately model very large camber angles. With the equations presented here even motorcycle tire characteristics with inclination angles in excess of  $45^\circ$  can be accurately represented.

$$F_{yp} = D_y \sin(C_y \arctan[(1 - E_y)B_y \alpha_y + E_y \arctan(B_y \alpha_y)]) + S_{Vy} \quad (107)$$

$$\alpha_y = \alpha + S_{Hy} \quad (108)$$

$$C_y = p_{Cy1} \quad (109)$$

$$D_y = \mu_y F_z \quad (110)$$

$$\mu_y = (p_{Dy1} + p_{Dy2} d_{Fz})(1 - p_{Dy3} \gamma^2) \lambda_{\mu_y} \quad (111)$$

$$E_y = (p_{Ey1} + p_{Ey2} d_{Fz})(1 + p_{Ey5} \gamma^2 - (p_{Ey3} + p_{Ey4} \gamma) \operatorname{sgn}(\alpha_y)) \quad (112)$$

$$K_{y\alpha} = p_{Ky1} F_{z0} \sin \left( p_{Ky4} \arctan \left( \frac{F_z}{(p_{Ky2} + p_{Ky5} \gamma^2) F_{z0}} \right) \right) (1 - p_{Ky3} |\gamma|) \lambda_{Ky\alpha} \quad (113)$$

$$K_{y\gamma} = F_z (p_{Ky6} + p_{Ky7} d_{Fz}) \lambda_{Ky\gamma} \quad (114)$$

$$B_y = \frac{K_{y\alpha}}{C_y D_y} \quad (115)$$

$$S_{Hy} = S_{Hy0} + S_{Hy\gamma} \quad (116)$$

$$S_{Hy0} = p_{Hy1} + p_{Hy2} d_{Fz} \quad (117)$$

$$S_{Hy\gamma} = \frac{K_{y\gamma} \gamma - S_{V\gamma}}{K_{y\alpha}} \quad (118)$$

$$S_{V_y} = S_{V_y0} + S_{V_y\gamma} \quad (119)$$

$$S_{V_y0} = F_z (p_{V_y1} + p_{V_y2} d_{Fz}) \lambda_{\mu_y} \quad (120)$$

$$S_{V_y\gamma} = F_z (p_{V_y3} + p_{V_y4} d_{Fz}) \gamma \lambda_{Ky\gamma} \lambda_{\mu_y} \quad (121)$$

The model for combined slip conditions uses a weighting function  $G_{yk}$  to modify the pure slip characteristics. Furthermore a braking induced plysteer force  $S_{V_{yk}}$  is introduced.

$$F_y = F_{yp} G_{yk} + S_{V_{yk}} \quad (122)$$

The expressions for  $G_{yk}$ , given by (123)–(128), are almost identical to the expression for  $G_{x\alpha}$ , Eqs. (101)–(106). Basically  $\alpha$  and  $\kappa$  are exchanged and a few additional parameters are introduced in these expressions,  $r_{By3}$  and  $r_{Hy2}$ . Figure 30 gives an impression of the shape of the weighting function  $G_{yk}$ .

$$G_{yk} = \frac{\cos(C_{yk} \arctan[(1 - E_{yk}) B_{yk} \kappa_s + E_{yk} \arctan(B_{yk} \kappa_s)])}{\cos(C_{yk} \arctan[(1 - E_{yk}) B_{yk} S_{Hyk} + E_{yk} \arctan(B_{yk} S_{Hyk})])} \quad (123)$$

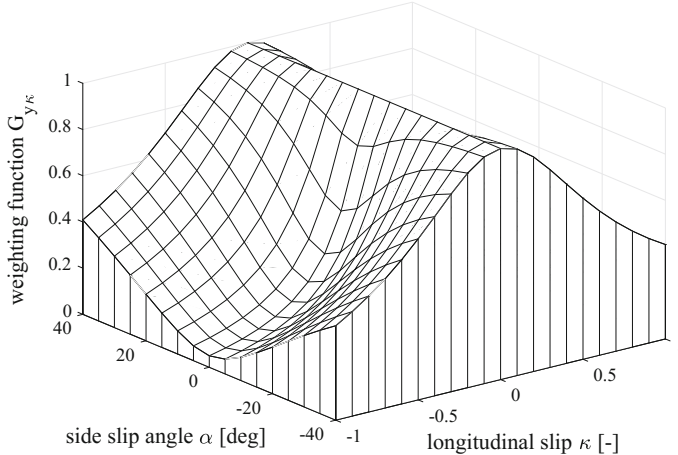


**Fig. 30** Combined slip weighting function  $G_{y\kappa}$  for the lateral force  $F_y$

$$\kappa_s = \kappa + S_{Hy\kappa} \quad (124)$$

$$B_{y\kappa} = (r_{By1} + r_{By4}\gamma^2) \cos(\arctan[r_{By2}(\alpha - r_{By3})]) \quad (125)$$

$$C_{y\kappa} = r_{Cy1} \quad (126)$$

$$E_{y\kappa} = r_{Ey1} + r_{Ey2}d_{Fz} \quad (127)$$

$$S_{Hy\kappa} = r_{Hy1} + r_{Hy2}d_{Fz} \quad (128)$$

A longitudinal force due braking or driving may introduce an additional plysteer angle. This results in an additional lateral force that is visible for small side slip angles in particular. This phenomenon is impossible to be modeled accurately using weighting functions, so an additional force  $S_{Vy\kappa}$  is introduced. In expression (129) a sine Magic Formula is used, thus parameter  $r_{Vy5}$  should be in the range between 1 and 2. In expression (130) a cosine Magic Formula is used, here it is important that  $r_{Vy4}$  is not too small to ensure that the braking induced plysteer force disappears for larger side slip angles.

$$S_{Vy\kappa} = D_{Vy\kappa} \sin(r_{Vy5} \arctan(r_{Vy6}\kappa)) \quad (129)$$

$$D_{Vy\kappa} = \mu_y F_z (r_{Vy1} + r_{Vy2}d_{Fz} + r_{Vy3}\gamma) \cos(\arctan(r_{Vy4}\alpha)) \quad (130)$$

The Magic Formula parameters and modeling error  $\epsilon$  have been determined for the measurements presented in Sects. 2.2 and 2.3, they are listed in Table 5. A comparison of measurement and Magic Formula tire model can be found in Fig. 31.

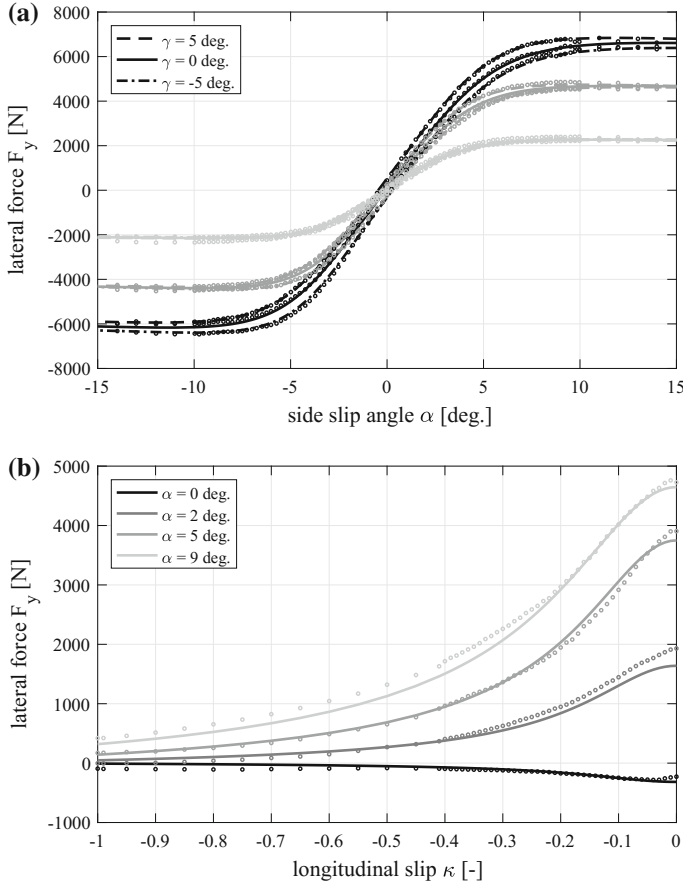


**Fig. 31** Magic Formula (solid lines) and measurements (dots) for the lateral force  $F_y$ , pure slip (a) and combined slip (b)

#### 4.4 Self-aligning Moment

In the Magic Formula the self-aligning moment  $M_z$  is described by the following equation

$$M_z = -t_p F_{yp0} G_{yk0} + M_{zr} + s_z F_x, \quad (131)$$

where  $t_p$  equals the pneumatic trail defined by Eqs. (132)–(139),  $F_{yp0} G_{yk0}$  is the combined slip lateral force for zero inclination angle ( $\gamma = 0$ ),  $M_{zr}$  is the residual moment defined by Eqs. (140)–(144),  $s_z$  equals the moment arm of the longitudinal force  $F_x$  and is defined by (145).

The pneumatic trail  $t_p$  is modeled using a cosine Magic Formula as expressed by (132), the final multiplication with  $\cos(\alpha)$  ensures that the pneumatic trail  $t_p$  will be

**Table 5** Lateral force Magic Formula parameters

Constants	$F_{z0} = 5000 \text{ N}$
$F_y$ pure	$p_{Cy1} = 1.2640$ $p_{Dy1} = 0.9894, p_{Dy2} = -0.1914, p_{Dy3} = 0$ $p_{Ey1} = -1.3186, p_{Ey2} = -0.7057, p_{Ey3} = 0.3278$ $p_{Ey4} = -3.5829, p_{Ey5} = 25.1493$ $p_{Ky1} = 13.2701, p_{Ky2} = 1.4990, p_{Ky3} = 0$ $p_{Ky4} = 2, p_{Ky5} = 0, p_{Ky6} = 0.7033, p_{Ky7} = 0$ $p_{Hy1} = -0.0019, p_{Hy2} = 0$ $p_{Vy1} = 0.0320, p_{Vy2} = 0, p_{Vy3} = 0.1853$ $p_{Vy4} = 0.4649$
$F_y$ combined	$r_{By1} = 6.8792, r_{By2} = 5.0932, r_{By3} = 0, r_{By4} = 0$ $r_{Cy1} = 1.0665$ $r_{Ey1} = -0.1376, r_{Ey2} = 0.7782$ $r_{Hy1} = 0, r_{Hy2} = 0$ $r_{Vy1} = 0, r_{Vy2} = 0, r_{Vy3} = -0.5938, r_{Vy4} = 20$ $r_{Vy5} = 2.1557, r_{Vy6} = 10$
Model error	Pure: $\epsilon = 1.92\%$ , combined: $\epsilon = 7.35\%$

zero when the side slip angle  $\alpha$  equals  $90^\circ$ . To handle combined slip conditions no additional equations are used, but an equivalent side slip angle is calculated,  $\alpha_{tp,eq}$  (133). This approach has some similarities with modeling combined slip in the brush tire model. Note that the expressions for the pneumatic trail  $t_p$  include the influence of the inclination angle  $\gamma$ . The pneumatic trail  $t_p$  is multiplied with a lateral force  $F_y$  that is evaluated for  $\gamma = 0$  (131).

$$t_p = D_{tp} \cos(C_{tp} \arctan[(1 - E_{tp})B_{tp}\alpha_{tp,eq} + E_{tp} \arctan(B_{tp}\alpha_{tp,eq})]) \cos(\alpha) \quad (132)$$

$$\alpha_{tp,eq} = \arctan \sqrt{\tan^2(\alpha_{tp}) + \left( \frac{K_{xk}}{K_{ya}} \right)^2 \kappa^2 \cdot \operatorname{sgn}(\alpha_{tp})} \quad (133)$$

$$\alpha_{tp} = \alpha + S_{Htp} \quad (134)$$

$$S_{Htp} = q_{Hz1} + q_{Hz2}d_{Fz} + (q_{Hz3} + q_{Hz4}d_{Fz})\gamma \quad (135)$$

$$B_{tp} = (q_{Bz1} + q_{Bz2}d_{Fz} + q_{Bz3}d_{Fz}^2)(1 + q_{Bz4}\gamma + q_{Bz5}|\gamma|) \frac{\lambda_{Ky\alpha}}{\lambda_{\mu y}} \quad (136)$$

$$C_{tp} = q_{Cz1} \quad (137)$$

$$D_{tp} = \frac{F_z r_0}{F_{z0}} (q_{Dz1} + q_{Dz2} d_{Fz}) (1 + q_{Dz3} \gamma + q_{Dz4} \gamma^2) \lambda_{tp} \quad (138)$$

$$E_{tp} = (q_{Ez1} + q_{Ez2} d_{Fz} + q_{Ez3} d_{Fz}^2) (1 + (q_{Ez4} + q_{Ez5} \gamma) \left( \frac{2}{\pi} \right) \arctan(B_{tp} C_{tp} \alpha_{tp})) \quad (139)$$

When the lateral force is equal to zero, the self-aligning moment does not necessarily have to be zero. The residual moment  $M_{zr}$  is introduced to incorporate this additional contribution to  $M_z$ .

$$M_{zr} = D_r \cos(\arctan(B_r \alpha_{r,eq})) \cos(\alpha) \quad (140)$$

$$\alpha_{r,eq} = \arctan \sqrt{\tan^2(\alpha_r) + \left( \frac{K_{xx}}{K_{ya}} \right)^2 \kappa^2 \cdot \text{sgn}(\alpha_r)} \quad (141)$$

$$\alpha_r = \alpha + S_{Hy} + \frac{S_{VY}}{K_{ya}} \quad (142)$$

$$B_r = q_{Bz9} \frac{\lambda_{Kya}}{\lambda_{\mu_y}} + q_{Bz10} B_y C_y \quad (143)$$

$$D_r = F_z r_0 [(q_{Dz6} + q_{Dz7} d_{Fz}) \lambda_r + (q_{Dz8} + q_{Dz9} d_{Fz}) \gamma \lambda_{Ky} \\ + (q_{Dz10} + q_{Dz11} d_{Fz}) \gamma |\gamma| \lambda_{Ky}] \lambda_{\mu_y} \quad (144)$$

For combined slip conditions the longitudinal force  $F_x$  may have a contribution to the self-aligning moment  $M_z$ . This can be easily imagined as the contact path having a lateral deflection with respect to the wheel plane of symmetry. In the Magic Formula the moment arm of longitudinal force  $s_z$  is modeled to take this effect into account.

$$s_z = r_0 \left( s_{sz1} + s_{sz2} \left( \frac{F_y}{F_{z0}} \right) + (s_{sz3} + s_{sz4} d_{Fz}) \gamma \right) \quad (145)$$

The Magic Formula parameters and modeling error  $\epsilon$  have been determined for the measurements presented in Sects. 2.2 and 2.3 and they are listed in Table 6. A comparison of measurement and the Magic Formula tire model can be found in Fig. 32.

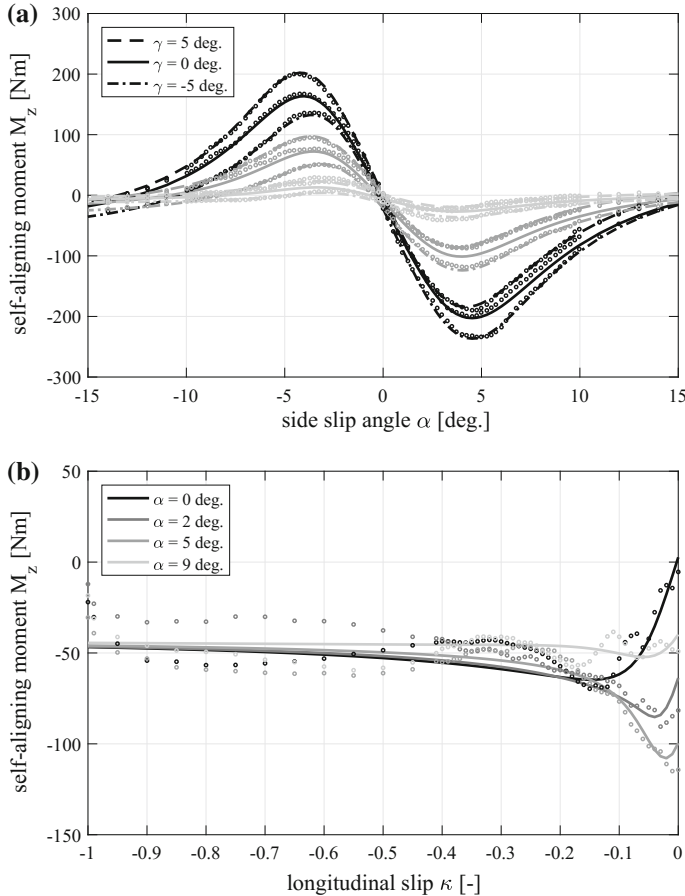


**Fig. 32** Magic Formula (solid lines) and measurements (dots) for the self-aligning moment  $M_z$ , pure slip (a) and combined slip (b)

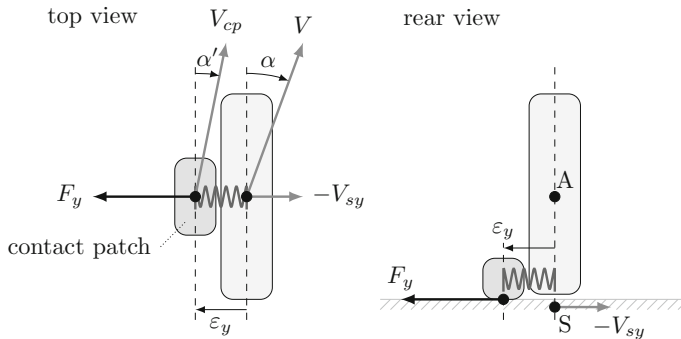
## 5 Tire Dynamics

### 5.1 Introduction to Tire Relaxation Behavior

In the previous sections the focus has been on analyzing and modeling the steady-state forces and moments. The tire is considered and modeled as a complex, non-linear function with multiple inputs and outputs as shown in Fig. 4. In the steady-state approach any change of an input will result in an instantaneous change of the outputs. As will be shown in this section, this is not how a real tire behaves in dynamic situations. Typically a tire responds with some delay on abrupt changes of the inputs. A model to illustrate these effects is shown in Fig. 33. The tire contact patch has a

**Table 6** Self-aligning moment Magic Formula parameters

Constants	$F_{z0} = 5000 \text{ N}$ , $r_0 = 0.315 \text{ m}$
$t_p$	$q_{Bz1} = 8.6117$ , $q_{Bz2} = -0.8357$ , $q_{Bz3} = -4.2173$ $q_{Bz4} = -0.2891$ , $q_{Bz5} = 0.6218$ $q_{Cz1} = 1.1423$
	$q_{Dz1} = 0.1231$ , $q_{Dz2} = 0.0071$ , $q_{Dz3} = 0$ , $q_{Dz4} = 9.6467$ $q_{Ez1} = -3.1431$ , $q_{Ez2} = 0.7236$ , $q_{Ez3} = -6.4258$ $q_{Ez4} = -0.3275$ , $q_{Ez5} = 0$
	$q_{Hz1} = -0.0067$ , $q_{Hz2} = 0$ , $q_{Hz3} = 0.1209$ , $q_{Hz4} = 0$
$M_{zr}$	$q_{Bz9} = 0$ , $q_{Bz10} = 0.2865$ $q_{Dz6} = -0.0037$ , $q_{Dz7} = 0.0068$ , $q_{Dz8} = 0.0610$ $q_{Dz9} = -0.0625$ , $q_{Dz10} = 0$ , $q_{Dz11} = 0$
$s_z$	$s_{sz1} = 0.0363$ , $s_{sz2} = 0.0102$ , $s_{sz3} = -0.5962$ $s_{sz4} = 0.2702$
Model error	Pure: $\epsilon = 7.82\%$ , combined: $\epsilon = 17.12\%$

**Fig. 33** Tire model with a lateral degree of freedom for the contact patch

lateral degree of freedom  $\dot{\varepsilon}_y$  with respect to the wheel, the stiffness associated with this degree of freedom is  $k_y$ . The contact patch can slide with respect to the road.

The relative velocity of the contact patch  $\dot{\varepsilon}_y$  with respect to the wheel plane has to be added to the absolute sliding velocity of point  $S$ ,  $V_{sy}$ , to obtain the side slip angle  $\alpha'$  of the contact patch. The side slip angle angle of the contact patch  $\alpha'$  becomes

$$\tan(\alpha') = -\frac{V_{sy} + \dot{\varepsilon}_y}{|V_x|}. \quad (146)$$

Note that in the regular definition of the tire side slip angle  $\alpha$  (4) that the wheel is considered as a rigid disk. Assuming linear tire behavior and neglecting the mass of the contact path, the spring force and lateral force due to side slip have to be in

equilibrium,

$$F_y = C_{F\alpha} \alpha' = k_y \varepsilon_y. \quad (147)$$

Assuming that  $C_{F\alpha}$  and  $k_y$  are independent of time, the following expression is obtained after differentiation with respect to time

$$\dot{\varepsilon}_y = \frac{C_{F\alpha}}{k_y} \dot{\alpha}'. \quad (148)$$

Substituting (148) in (146) results in

$$\frac{C_{F\alpha}}{k_y} \frac{1}{|V_x|} \dot{\alpha}' + \tan(\alpha') = \tan(\alpha). \quad (149)$$

The ratio between cornering stiffness  $C_{F\alpha}$  and lateral stiffness  $k_y$  is known as the relaxation length  $\sigma_y$ , thus

$$\sigma_y = \frac{C_{F\alpha}}{k_y}. \quad (150)$$

The longitudinal velocity  $V_x$  is approximately equal to the time derivative of the traveled distance  $s_t$ . For a positive longitudinal velocity and linearization for small values of the side slip angle, the following expression is obtained

$$\sigma_y \frac{dt}{ds_t} \frac{d\alpha'}{dt} + \alpha' = \sigma_y \frac{d\alpha'}{ds_t} + \alpha' = \alpha. \quad (151)$$

From this equation it becomes clear that the relaxation behavior of a tire is not dependent on time, but on the traveled distance  $s_t$ . Starting from an initial condition where  $\alpha'$  and  $\alpha$  are equal to zero and applying a step in the tire side slip angle  $\alpha$  with magnitude  $\alpha_{step}$ , the analytical solution of (151) equals

$$\alpha' = (1 - e^{-s_t/\sigma_y}) \alpha_{step}. \quad (152)$$

The lateral force  $F_y$  becomes

$$F_y = C_{F\alpha} (1 - e^{-s_t/\sigma_y}) \alpha_{step}. \quad (153)$$

Note that this expression is only valid under the assumption of linear tire behavior and small side slip angles.

As the tire relaxation behavior is a function of the traveled distance, the forward velocity does not play a role when doing measurements to assess the tire relaxation behavior and as a result this behavior can be measured at very low speeds. A measurement device that allows to execute relaxation length measurements is the flat plank tire tester as shown in Fig. 34. The wheel is mounted on a measurement hub



**Fig. 34** TU/e flat plank tire tester

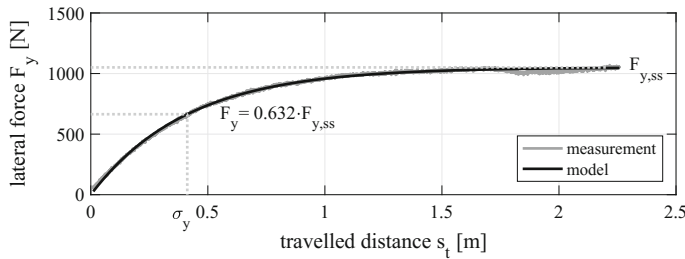


**Fig. 35** Tire response to a step in side slip angle ( $\alpha_{step} = 1^\circ$ ,  $F_z = 4000$  N,  $\sigma_y = 0.412$  m,  $C_{F\alpha} = 1050$  N/deg)

that allows to measure the forces and moments that occur at the wheel center. The road is represented by a plank with a length of approximately 7 m, which can move in the horizontal plane with a maximum velocity of 0.05 m/s. The measurement hub can move vertically allowing to press the tire against the plank and thus giving control over the vertical tire force  $F_z$ . Furthermore it can be rotated about the vertical axis allowing a steering angle to be applied to the wheel.

To apply a step in side slip angle the required steering angle is applied first, then the wheel is pressed against the plank and thereafter the plank is moved forward with a low, constant velocity. The lateral force as a function of traveled distance is shown in Fig. 35. In the same figure (153) is plotted, showing that it can accurately represent the measurement results. Note that the relaxation length  $\sigma_y$  for this experiment equals 0.412 m. In general the relaxation length corresponds to the distance traveled since the start of the application of the step in side slip angle, when 63.2% of the steady-state value of the lateral force  $F_y$  is reached. Note that the relaxation behavior of the tire is not dependent on time, but traveled distance. This also means that when the forward velocity is increased, that the tire force will respond more quickly since the distance traveled in the same amount of time will increase.

**Brush tire model** The brush tire model can be used to gain more insight in various aspects of tire relaxation behavior. Figure 36 shows the response of the brush tire model to a small step in side slip angle. In this example it is assumed that no sliding of the bristles will occur and that the steady-state deformation pattern of the bristles

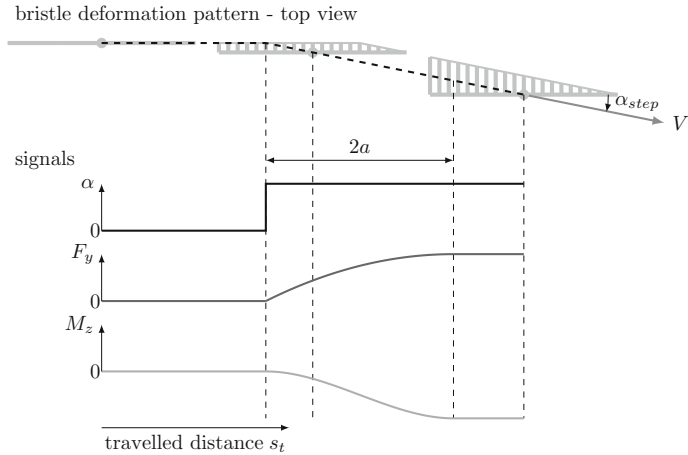


**Fig. 36** Brush tire model transient behavior on a step in side slip angle

is triangular. Initially all bristles are undeformed and upon the application of the side slip angle the tire needs to move forward over a distance  $2a$  to obtain the steady state deformation pattern. As a result the lateral force and self-aligning moment will develop as a function of the traveled distance and relaxation effects become visible. Various, qualitatively valid observations with respect to relaxation behavior can be made from the brush tire model step response:

- It can be noted that there is a difference in the response of the lateral force  $F_y$  and self-aligning moment  $M_z$ . Upon application of the step in side slip angle  $F_y$  starts to increase immediately, whereas the gradient of  $M_z$  is equal to zero. This behavior has also been observed for aircraft tires, for normal passenger car tires this phenomenon is hardly noticeable.
- For large side slip angles the tire will need to travel less than  $2a$  to obtain the steady state deformation pattern, as the bristles in the trailing part of the contact patch are already sliding. Thus the relaxation length is expected to decrease with increasing side slip angle.
- As the contact length  $2a$  increases with the vertical force, the relaxation length will also increase with the vertical force  $F_z$ .
- When the tire is running at a fixed side slip angle, a stepwise increase of the vertical force will also result in relaxation effects. The increase of the vertical force results in a longer contact length and increased maximum bristle deflections. The tire will need to travel over a certain distance before settling for a new steady-state deformation pattern.
- Since there is no fundamental difference between longitudinal and lateral bristle deformation, relaxation behavior will not only be present in the lateral direction but also in the longitudinal direction.

In the next section a pragmatic tire model will be developed, which includes all the aforementioned effects.

## 5.2 Modeling Tire Dynamics

The steady-state Magic Formula tire model will be extended with differential equations that capture the relaxation behavior up to large side slip angles, furthermore the model is modified to handle zero forward velocity. It can be noted that in the definitions of the longitudinal slip  $\kappa$  (2), side slip angle  $\alpha$  (4) that the longitudinal velocity  $V_x$  appears in the denominator. This implies that a division by zero will occur when  $V_x$  is equal to zero and the equations cannot be solved numerically. A possible solution is to introduce a lower limit for the longitudinal velocity  $V_{x,min}$ . The longitudinal slip is then by

$$\kappa = -\frac{V_{sx}}{\max(V_x, V_{x,min})}. \quad (154)$$

Though it solves the numerical problems, it is not correct from a physical point of view. For velocities below  $V_{x,min}$  and assuming linear tire behavior, the following expression is obtained for the longitudinal force

$$F_x = -\frac{C_{F\kappa}}{V_{x,min}} \cdot V_{sx}. \quad (155)$$

So actually a damper is modeled: the longitudinal force  $F_x$  is proportional and opposite to the sliding velocity  $V_{sx}$ . This makes it impossible to simulate for example a car being parked on a slope. The car would slowly move downwards as a sliding velocity is necessary to generate a longitudinal force, which does not correspond to the physical reality. The same phenomenon will occur in the lateral direction.

A solution to this problem can be found by multiplying expression (149) with  $|V_x|$  and using the definition of the side slip angle  $\alpha$ , as proposed by Zegelaar (1998). The following expression is obtained then

$$\frac{C_{F\alpha}}{k_y} \dot{\alpha}' + |V_x| \tan \alpha' = -V_{sy}. \quad (156)$$

When  $V_x$  is equal to zero, the following equation is obtained for  $\alpha'$ ,

$$\alpha' = -\frac{k_y}{C_{F\alpha}} \int V_{sy} dt. \quad (157)$$

Assuming linear tire behavior the lateral force  $F_y$  becomes

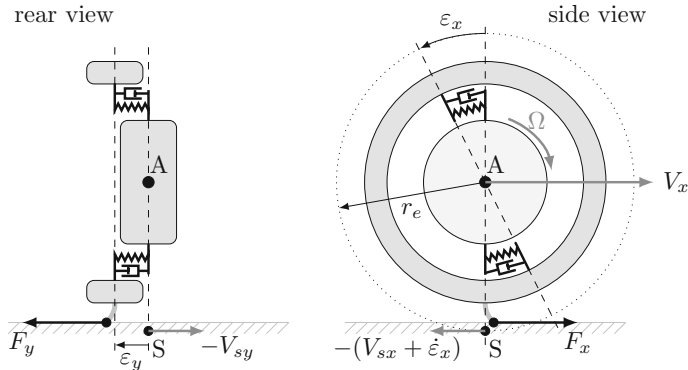


**Fig. 37** Dynamic tire model having a longitudinal and lateral degree ( $\epsilon_x$  and  $\epsilon_y$ ) of freedom to include motions of the tire belt with respect to the rim

$$F_y = C_{Fa} \alpha' = -k_y \int V_{sy} dt. \quad (158)$$

So by integrating the sliding velocity  $V_{sy}$  a deflection is obtained which is multiplied by the non-rolling lateral stiffness  $k_y$  to obtain the lateral force  $F_y$ . When  $V_x$  equals zero, the tire thus behaves as a spring which corresponds to physical reality. It should be noted when the tire starts sliding and  $\alpha'$  becomes very large that this approach does not yield physically correct results.

A pragmatic model is proposed to include the various observations made when analyzing the brush tire model transient behavior in a quantitatively correct way. The stiffness of the tire belt with respect to the rim is modeled separately from the relaxation behavior of the tread elements attached to the belt, this is illustrated in Fig. 37. The mass of the tire belt is assumed to be zero in the model described here, but it is also possible to split the mass of the wheel in two items: rim combined with tire bead and tire belt. In the lateral direction  $\epsilon_y$  reflects the displacement of the belt with respect to the rim. In the longitudinal direction the wheel can be considered to consist of two concentric rings, that can rotate with respect to each other. The deformation  $\epsilon_x$  represents the translation at the circumference of tire as a result of a relative rotation of the tire belt with respect to the rim. Note that differences between the effective and loaded tyre radius a neglected in this approach.

The force equilibrium in the longitudinal and lateral direction equals

$$d_x \dot{\epsilon}_x + k_x \epsilon_x = F_{x,MF}(\kappa', \alpha', \gamma, F_z) \quad (159)$$

$$d_y \dot{\epsilon}_y + k_y \epsilon_y = F_{y,MF}(\kappa', \alpha', \gamma, F_z) \quad (160)$$

where  $k_x$  ( $d_x$ ) and  $k_y$  ( $d_y$ ) represent the stiffness (damping) in the longitudinal and lateral direction,  $F_{x,MF}$  and  $F_{y,MF}$  are the longitudinal and lateral force calculated

using the Magic Formula. The relaxation behavior of the tread elements is described by the following equations

$$\sigma_c \dot{\kappa}' + |V_x| \kappa' = -V_{sx} - \dot{\epsilon}_x \quad (161)$$

$$\sigma_c \dot{\alpha}' + |V_x| \tan \alpha' = -V_{sy} - \dot{\epsilon}_y \quad (162)$$

where  $\sigma_c$  represents the relaxation length of the tread elements in contact with the road. The magnitude of  $\sigma_c$  is typically in the order of half of the contact length  $a$ . After rearranging (159)–(162) the following set of first order differential equations is obtained

$$\dot{\epsilon}_x = \frac{1}{d_x} (F_{x,MF}(\kappa', \alpha', \gamma, F_z) - k_x \epsilon_x), \quad (163)$$

$$\dot{\epsilon}_y = \frac{1}{d_y} (F_{y,MF}(\kappa', \alpha', \gamma, F_z) - k_y \epsilon_y), \quad (164)$$

$$\dot{\kappa}' = \frac{1}{\sigma_c} (-V_{sx} - \dot{\epsilon}_x - |V_x| \kappa'), \quad (165)$$

$$\dot{\alpha}' = \frac{1}{\sigma_c} (-V_{sy} - \dot{\epsilon}_y - |V_x| \tan \alpha'). \quad (166)$$

This model allows to accurately describe the non-linear dynamic behavior for large side slip angles. This is illustrated by Fig. 38, which shows a number of relaxation length measurements with different side slip angles. The non-linear dependency of the steady-state lateral force is modeled with the Magic Formula. It can be observed that for larger side slip angles the tire responds more quickly and the relaxation length is reduced. This effect is correctly captured with Eqs. (164) and (166). A more simple approach, whereby only the side slip angle is filtered using fixed relaxation length and equation similar to (149), is not able to show this behavior. In the next section it will also be shown that the tire response to vertical force variations is correctly captured by the model presented here.

### 5.3 Applications

This section will briefly discuss two examples showing the relevance of tire relaxation behavior. The shimmy stability of a wheel having a yaw degree of freedom will be analyzed first. The loss of side force due to vertical force variations will be discussed next.

**Shimmy** Shimmy is an instability, which is caused by the interaction of the dynamic behavior of the suspension and tire. It has been researched already for a long time, an early paper was written by Von Schlippe and Dietrich (1941). The unstable lat-

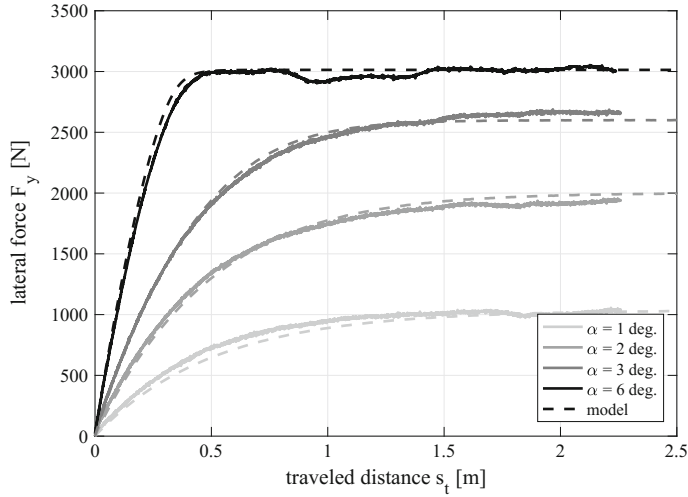
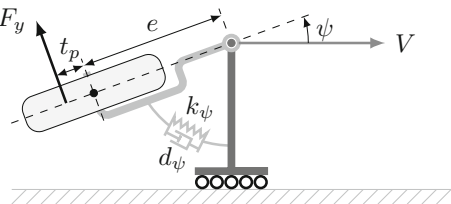


**Fig. 38** Comparison of measurements and model response for various steps in side slip angle ( $k_y = 130,000 \text{ N/m}$ ,  $d_y = 1300 \text{ Ns/m}$ ,  $\sigma_c = 0.05 \text{ m}$ )

**Fig. 39** Trailing wheel system (top view)



eral and yaw vibration of the wheel can reach considerable amplitudes resulting in a loss of control of the vehicle or even structural damage. The shimmy frequency is typically in the range of 5–25 Hz. The most simple system capable of showing the shimmy instability is the trailing wheel system, as seen in Fig. 39. Linear tire behavior will be assumed in the following analysis. The yaw equation of motion of this system is given by

$$(I_{zz} + me^2)\ddot{\psi} + d_\psi\dot{\psi} + k_\psi\psi = -C_{F\alpha}(e + t_p)\alpha'. \quad (167)$$

The relaxation behavior of the tire is described by

$$\sigma_y\dot{\alpha}' + V\alpha' = -V_{sy} = V\psi + e\dot{\psi} \quad (168)$$

In state-space form ( $\dot{\mathbf{x}} = \mathbf{Ax}$ ) the equations become

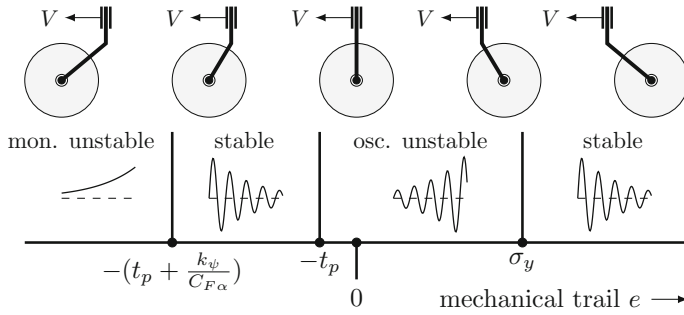


**Fig. 40** Trailing wheel system stability results ( $d_y = 0$ )

$$\begin{bmatrix} \ddot{\psi} \\ \dot{\psi} \\ \dot{\alpha}' \end{bmatrix} = \begin{bmatrix} -\frac{d_y}{I_t} - \frac{k_y}{I_t} - \frac{C_{Fa}(e+t_p)}{I_t} \\ 1 & 0 & 0 \\ \frac{e}{\sigma_y} & \frac{V}{\sigma_y} & -\frac{V}{\sigma_y} \end{bmatrix} \begin{bmatrix} \dot{\psi} \\ \psi \\ \alpha' \end{bmatrix}. \quad (169)$$

In these equations  $e$  equals the length of mechanical trail,  $k_y$  the yaw stiffness and  $d_y$  the yaw damping constant. The total moment of inertia about the swivel axis equals  $I_t = I_{zz} + me^2$ , with  $m$  being the mass and  $I_{zz}$  the yaw moment of inertia of the wheel, including the tire.

The stability of the system can be investigated by calculating the eigenvalues of the matrix  $\mathbf{A}$ . For a complex eigenvalue  $\lambda = a + ib$  the damped eigenfrequency  $f_d$  in [Hz] can be calculated by

$$f_d = \frac{b}{2\pi} \quad (170)$$

and the dimensionless damping ratio  $\zeta$  equals

$$\zeta = -\frac{a}{|\lambda|} \cdot 100\%. \quad (171)$$

Analytical expressions for the stability can be obtained for the system stability using the Hurwitz criterion when the yaw damping  $d_y$  is equal to zero. In this case the stability boundaries are independent of the forward velocity  $V$ . Results are shown in Fig. 40 and the length of the mechanical trail  $e$  appears to be a decisive factor. The trailing wheel system shows an oscillatory unstable behavior for small negative and positive values of the mechanical trail  $e$ .

By adding yaw damping, so  $d_y > 0$ , this instability can be suppressed. The stability results will become velocity dependent and no analytical expressions are available to describe the stability for this situation. The working principle of the yaw damper can be described as follows. When the yaw angle  $\psi$  changes the lateral tire force  $F_y$  responds with some delay due to the relaxation effects. This also implies that the tire yaw moment about the rotation axis has a delayed response with respect to the yaw

**Fig. 41** TU/e tire measurement tower



angle, which may result in an instability. The damper  $k_\psi$  produces a moment with a phase lead with respect to the yaw angle  $\psi$  and can thus counteract the tire yaw moment with a phase delay.

The shimmy stability of more complex systems has been analyzed by for example Besselink (2000), the influence of nonlinear tire behavior on shimmy stability has been researched by Ran (2016).

**Cornering on undulated roads** When a car is cornering the tires have to develop lateral forces to keep the car on the circular path. The lateral force that the tire can develop is influenced by the vertical force variations that may occur as a result of road irregularities. This phenomenon has been investigated with a lab set-up, as shown in Fig. 41, where a measurement tower is placed on top of a drum. The wheel is kept a constant side slip angle  $\alpha$  and a hydraulic actuator is used to prescribe the vertical position of the measurement hub. First experiments of this type were reported by Takahashi and Pacejka (1988) and later by Maurice (2000).

Tests have been executed with a forward velocity of 0.6 m/s and a fixed side slip angle of 5° to illustrate the contribution of tire relaxation effects. The vertical force  $F_z$  has an average value of 4000 N and changes sinusoidally with an amplitude of 2000 N and different excitation frequencies are used: 0.25, 0.5, 1 and 2 Hz. Since tire relaxation behavior is path dependent, it is convenient to use the wavelength  $\lambda$  to interpret the results, the following relation holds:

$$\lambda = \frac{V}{f}, \quad (172)$$

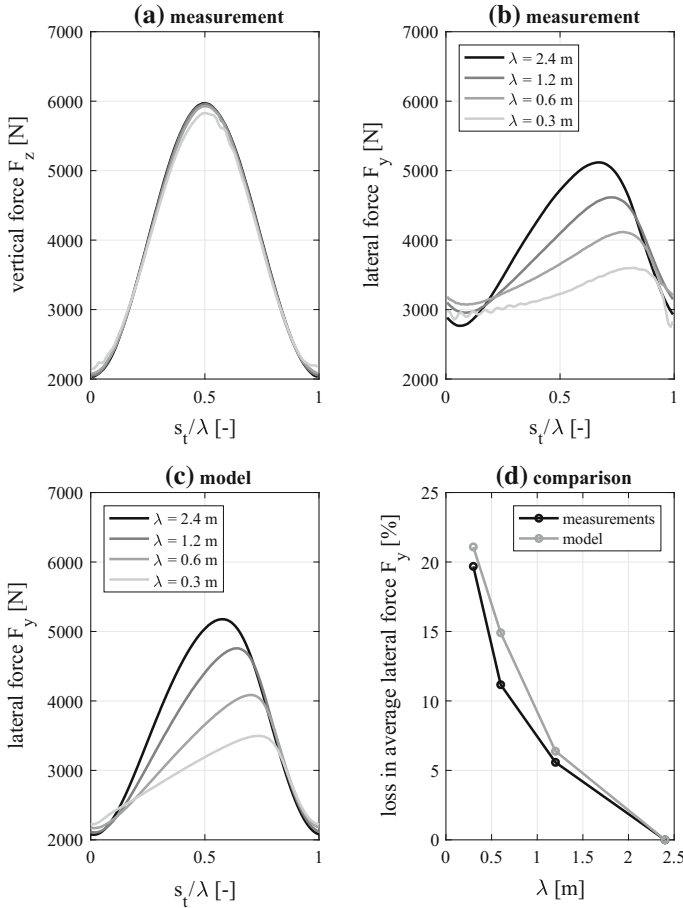


**Fig. 42** Tire relaxation effects due to sinusoidal vertical force changes ( $\alpha = 5^\circ$ ,  $V = 0.6 \text{ m/s}$ )

where  $V$  is the forward velocity and  $f$  the excitation frequency. So in the experiments the wavelength varies between 2.4 m ( $f = 0.25 \text{ Hz}$ ) and 0.3 m ( $f = 2 \text{ Hz}$ ). Figure 42 shows measurement results, on the horizontal axis the traveled distance, normalized with the wavelength, is plotted. From Fig. 42b it is clear that a major decrease of the average later force  $F_y$  occurs when the wavelength is reduced by increasing the excitation frequency. The tire relaxation effects are clearly visible: the lateral force  $F_y$  responds with some delay on an increase of the vertical force, whereas this not the case for a decreasing vertical force.

Simulations have been executed for the same conditions. The steady-state cornering characteristics are have been measured on the drum and are fitted using the Magic Formula. The following parameters have been used in dynamic model:  $k_y = 130,000 \text{ N/m}$ ,  $d_y = 1300 \text{ Ns/m}$  and  $\sigma_c = 0.02 \text{ m}$ . The simulated lateral force  $F_y$  is shown in

Fig. 42c. When comparing the simulations with the measurements it is clear that the main phenomena are captured well by the model, although differences exist. When comparing the reduction in the average side force and using  $\lambda = 2.4$  m as the baseline, it can be seen in Fig. 42d that the model shows the same trend and appears to be fairly accurate.

In the optimization process of automotive shock absorbers one of the criteria is to minimize the vertical tire force variations. Both measurements and simulations show the loss of average side force due to a varying vertical force when the tire is subjected to a fixed side slip angle. Though the experiments are executed at a low forward velocity (2.16 km/h) and the maximum excitation frequency is limited to 2 Hz, the results are still meaningful for road car cornering.

## References

- Bakker, E., Nyborg, L., & Pacejka, H. B. (1987). *Tire modeling for use in vehicle dynamics studies*. SAE Paper No. 870421.
- Besselink, I. J. M. (2000). *Shimmy of aircraft main landing gears*. Ph.D. Thesis, TU Delft.
- Besselink, I. J. M., Schmeitz, A. J. C., & Pacejka, H. B. (2010). An improved Magic Formula/Swift tyre model that can handle inflation pressure changes. *Vehicle System Dynamics*, 48(1), 337–352. <https://doi.org/10.1080/00423111003748088>
- ISO International Standard. (1991). *Road vehicles—Vehicle dynamics and road holding ability—Vocabulary*. ISO 8855:1991.
- Maurice, J. P. (2000). *Short wavelength and dynamic tyre behaviour under lateral and combined slip conditions*. Dissertation, TU Delft.
- Pacejka, H. B. (2012). *Tire and vehicle dynamics* (3rd ed.). Butterworth-Heinemann. ISBN: 978-0-08-097016-5.
- Pacejka, H. B., & Sharp, R. S. (2007). Shear force development by pneumatic tyres in steady state conditions: A review of modelling aspects. *Vehicle System Dynamics*, 20(3–4), 121–175. <https://doi.org/10.1080/00423119108968983>.
- Ran, S. (2016). *Tyre models for shimmy analysis, from linear to nonlinear*. Ph.D. Thesis, TU Eindhoven.
- von Schlippe, B., & Dietrich, R. (1941). *Das flattern eines bepneuten rades*, Bericht 140 der Lilienthal Gesellschaft, NACA TM 1365.
- Takahashi, T., & Pacejka, H. B. (1988). Cornering on uneven roads. *Vehicle System Dynamics*, 17(sup1), 469–480. <https://doi.org/10.1080/00423118808969288>
- TASS International, website: <https://tass.plm.automation.siemens.com/delft-tyre>.
- Zegelaar, P. W. A. (1988). *The dynamic response of tyres to brake torque variations and road unevennesses*. Dissertation, TU Delft.

# Optimal Vehicle Suspensions: A System-Level Study of Potential Benefits and Limitations



Davor Hrovat, H. Eric Tseng and Joško Deur

**Abstract** Fundamental ride and handling aspects of active and semi-active suspensions are presented in a systematic way starting with simple vehicle models as basic building blocks. Optimal, mostly Linear-Quadratic (H2), principles are used to gradually reveal and explore key system characteristics where each additional model Degree-of-Freedom (DoF) brings new insight into potential system benefits and limitations. The chapter concludes with practical considerations and examples including some that go beyond the more traditional ride and handling benefits.

**Keywords** Active and semi-active suspensions • Ride comfort  
LQ control • Preview • Trajectory optimization • Active safety

## 1 Introduction

### 1.1 Goals/Objectives

During the past several decades there was a substantial activity in the area of automotive computer controls and related mechatronics developments. This started in the 1970s with engine controls and later included transmission and overall powertrain controls. Subsequent additions included brake and driveline controls such as four- and all-wheel drives, for example.

While there were substantial evolutionary developments in controls of longitudinal direction or X-dimension of vehicle motion, on the other hand there was relatively less activity and progress in the other two dimensions—lateral or Y and

---

D. Hrovat (✉)  
University of California, San Diego, CA, USA  
e-mail: ddhrovat@gmail.com

H. Eric Tseng  
Ford Motor Company, Dearborn, MI, USA

J. Deur  
University of Zagreb, Zagreb, Croatia

vertical or Z dimension—in terms of actual production applications. This is in particular true for the case of vertical vehicle motion control via appropriate advanced, controllable suspensions. While there were occasional major waves of agitated and at times almost frantic activity in this area in the past, currently the only advanced suspensions that saw some actual market penetration and usage are the so-called semi-active suspensions, which are essentially controllable dampers.

The main objective of these lectures is to present potential benefits and associated requirements and limitations of advanced active and semi-active suspensions. It is hoped that this will lead to additional insight and revived interest towards further developments in the above “forgotten dimension”, which may represent a major yet not fully explored and exploited opportunity. In addition to addressing the opportunities in more traditional areas of improved ride and handling the new class of advanced suspensions may be especially attractive and timely addition to overall vehicle controls in view of ever increasing interests in the areas of active safety, driver assist technologies and autonomous vehicles. The conglomerate of all those benefits may eventually lead to wide-spread production of advanced suspensions benefiting millions of customers.

## 1.2 Basic Definitions

Before proceeding it is necessary to define some basic notions to avoid possible misunderstandings, i.e. so that we are all on the same plane going forward through these notes. In particular, we are concerned with such notions as what sort of vehicle suspensions we are going to deal with in the sequel. The definitions are mainly based on the notion of passivity, which is closely related to energy supplied to or dissipated by the suspension unit.

**Passive suspensions.** They typically consist of shock absorbers and springs and as such they don't require any external energy sources i.e. they dissipate the energy through the process of heating up the shock absorbers or dampers. They are seen on most past and contemporary vehicles in the form of Macpherson struts (seen typically as front suspension on most contemporary vehicles), multilink suspensions (seen on most luxury-type vehicles) and others.

**Active suspensions.** Unlike their passive counterparts, active suspensions do require external sources of energy provided through pumps and electro-motors, for example, to fully achieve their intended function. In turn they result in superior performance at the expense of higher costs, increased complexity, more demanding packaging requirements, and, in general, reduced robustness. In particular, while—as we will see later—the active suspension can result in substantial improvements in ride and handling and other benefits, their implementations also face significant challenges such as containment of the so-called “secondary ride” that is demonstrated through excitation of higher frequencies typically around and above 10–20 Hz. In terms of actual practical implementation through different energy media one distinguishes between:

- Electro-pneumatic active suspensions including Load-Leveling
- Electro-hydraulic active suspension
- Electrical active suspension

Furthermore one can distinguish between single and double acting (i.e. one- or two-sided actuation, where controlling force is acting upon one or both sides of an actuator), and between narrow and wide band actuators depending on the frequency range or “fidelity” of actuator desired force (or velocity/displacement) delivery.

**Semi-Active (SA) suspensions.** As their name implies, SA suspensions fall between active and passive suspensions. They are controllable, “smart” dampers or shock absorbers that require relatively very small amount of energy to modulate their damping parameter and thus perform their desired function—produce the desired force, whenever possible in view of the passivity constraint (to be discussed next). Due to small energy requirements the SA suspensions can be in practice regarded as essentially smart passive devices.

**Mathematical definition of passivity.** The above are more intuitive or practical definitions of passivity and related passive or active suspensions. A more precise definition of passivity follows from similar definitions used in the areas of electrical networks and mathematics (Anderson and Vongpanitlers 1973). Accordingly, an operator  $P$  is passive if there exists some constant  $k$  such that the inner product

$$\langle Pv \mid v \rangle_T \geq k \quad (1)$$

where the inequality must hold for any final times  $T$  and all elements of  $v(\cdot)$  from an extended inner space composed of all functions that do not “explode” i.e. have finite escape time. Associating  $v$  with velocity across actuator and  $Pv$  with corresponding force, then the above inequality reflects the energy conservation (in the case of equality) or dissipation (in the case of inequality) that is characteristic of passive suspensions consisting of a spring and/or damper or shock absorber, respectively. In this particular example the above inner product amounts to time-integration of the product of actuator force and velocity i.e. integration of power across the actuator, which is the energy dissipated or produced by the actuator. With passive suspension this energy is positive and larger or equal the amount of the initial energy contained in the actuator as represented by constant  $k$ ; the inequality must hold for any final time  $T$  and velocity profile  $v(t)$ .

For Linear Time-Invariant (LTI) systems the above passivity constraint with  $k = 0$  is equivalent to a requirement that the associated transfer function matrix  $P(s)$  is Rational Positive Real (RPR) matrix. The RPR matrix  $P(x)$  must satisfy a set of conditions (Anderson and Vongpanitlers 1973) that include  $P(\cdot)$  being analytic in the r.h.s. plane i.e. all elements of  $P$  must have poles where  $\text{Re}(s) \leq 0$ . Thus it can be said that for any passive suspension that can be described by the LTI transfer functions the associated impedance matrix  $P$  must be a RPR matrix. This provides one way of checking if a given suspension constitutive relation can be realized via passive means or it may require an active actuator implementation.

### 1.3 Historical Background

There is a relatively long history of efforts in the area of active suspensions. They have been mentioned and considered already in the 1960s through theoretical studies by Bender (1967a, b), Bender et al. (1967), Karnopp and Trikha (1969), Young and Wormley (1973), Thompson (1971) and others, mostly from MIT. Since then there were numerous studies on potential benefits and limitations of active suspensions in the context of ride and to some extent handling; most of this earlier work is summarized in Sharp and Crolla (1987), Elbeheiry et al. (1995), Hrovat (1997) and more recently in Mastinu and Ploechl (2014), Tseng and Hrovat (2015).

While there was much effort and progress in terms of theoretical analysis and overall insight, the progress in actual production implementation of active suspensions was relatively slow and somewhat sporadic. To this end there was a major wave and push towards the latter during late 1980s and early 1990s. It started with the Lotus efforts aimed towards formula F1 racing. In particular, a special Lotus Esprit experimental vehicle was used through many years of research and development resulting in some very impressive media shows and demonstrations. This is also reflected in the January 21, 1987, *New York Times* article, with citations from different automotive media evaluators ranging from “most impressive thing I’ve ever tried” to “the greatest single advance in car engineering since the war”.

However, it should be pointed out that the most impressive demonstrations were done on special test tracks that amplified large, low frequency road undulations, which were “ideal” for exciting the dominant heave mode of body dynamics. The latter is typically around 1–2 Hz with relatively low damping ratio (Hrovat 1997). In reality, most actual roads are not of this type and ride benefits were then less dramatic.

At the time most automotive OEM’s or companies on practically all continents, but especially in Japan and the US (Akatsu et al. 1990; Goto et al. 1990; Goran et al. 1992), have been heavily involved in R&D towards realizing a practical active suspension that would robustly and reliably deliver most of ride and handling benefits at reasonable cost, weight, packaging and energy requirements. While there was considerable progress in experimental and test vehicle developments of active suspensions only a few such systems saw actual production. This was in the form of limited production series introduced during the 1990s by Nissan in the Infinity Q45a (Akatsu et al. 1990) and Toyota in the 1989 Celica (Goto et al. 1990) which were eventually discontinued. One of the main reasons for this lack of wide-spread usage is that active suspensions at the time did not deliver sufficient value: their performance as measured in terms of ride and handling improvements were not noticeable enough while at the same time their cost was prohibitively high for all but the most luxurious vehicle segments.

Subsequently, for the next two decades the active suspension efforts were mostly limited to further theoretical developments done mostly in academia and few industrial R&D institutions. In particular, the latter include long-standing internal

efforts within Bose in developing their electrical active suspension, which attracted significant media attention at the time (Moran 2004). At present, there is only one significant production application of active suspensions—the so-called ABC, Active Body Control, introduced by Mercedes. This was recently further enhanced under Magic Body Control (MBC) where for the first time the use of road roughness preview ahead of the vehicle has been used based on stereo cameras (Anonymous 2017a; Streiter 2008). It is interesting that the ABC/MBC has been offered by Mercedes as standard equipment on their top line, luxury models.

Last but not necessarily least, it should be mentioned that while active suspensions did not see wide-spread in-vehicle production applications thus far, their SA counterparts did find much larger acceptance and can now be found in many vehicles under different marketing designations such as Continuously Controlled Damping (CCD), Magnetic Ride/MagneRide Control and others. While their performance was in general somewhat inferior to corresponding active suspension performance at the time, their cost, robustness, relative simplicity and lower packaging requirements and parts count all were more favorable. Thus they resulted in higher value and acceptance rates so far.

## 1.4 Motivation

Since the first wave of active suspension efforts dating back to 1980s and 90s did not succeed to bring a widespread production introduction of this high-tech concept it is appropriate to ask—why reconsider it now? While this is a fair question there are a number of factors that evolved during the last couple of decades that warrant re-examination of this relatively dormant field. This includes:

- Further developments and continuous progress in the areas of Control Systems and Optimization, and related Optimal Control methodologies such as Model Predictive Controls (MPC) that are becoming more and more applicable to Automotive Controls (Ulsoy et al. 2012; Rajamani 2012; Hrovat et al. 2011a, b);
- Further developments and progress in computers—both hardware and software, electronics/mechatronics, conventional (passive) suspensions, and electrical machinery;
- Ever increasing emphasis on and importance of Active Safety (van Zanten 2014);
- Recent trends in sensors and infrastructure enhancements; this includes cameras, Lidar, Vehicle to Vehicle (V2V) and Vehicle to Infrastructure (V2I) communications, various forms of mapping including 3D mapping etc. Most of these new technological developments will facilitate highly effective preview controls based on, for example, MPC optimization (Xu et al. 2016; Hrovat et al. 2012);
- Recent developments and widespread efforts in Autonomous Vehicles (AV), which could free many current drivers to do many other tasks and activities such

as writing a report or playing his or her favorite computer game; all this will be much easier to accomplish having an AV with a more steady platform facilitated by a fully active suspension.

## 1.5 Brief Overview of Automotive Controls

As shown in the previous section, the field of automatic controls is central for many of the ongoing activities and developments that are highly relevant for the next possible wave of active suspensions. When speaking of “controls” here we are primarily focusing on *computer* controls, which have been prevalent in the automotive field for more than four decades by now. This implies related areas of control-oriented modeling, which uses appropriately simplified models, along with many computer-assisted control system design, analysis and simulation tools and methods such as MATLAB, for example. The latter include open- and closed-loop control algorithm design and analysis based on both classical as well as so-called “modern” or advanced controls; optimization/optimal control design; signal processing and diagnostics; system identification and estimation; Neural nets, Fuzzy logic controls, and Artificial Intelligence (AI); along with associated architecture, sensors, actuators, processes and embedded real-time software/CAE tools.

The automotive computer controls started in 1970s with the advent of microprocessors, which were first used for engine controls, in particular spark advance control that was prior to this accomplished through hardware means. Since their modest beginnings in early 1970s the computer controls then propagated to all aspects of engine and powertrain operations. This includes: Air-Fuel (A/F) ratio control; Idle Speed Control (ISC); Exhaust Gas Recirculation (EGR) control; Waste Gate (WG) control in case of boosted engines; many features of Automatic Transmission (AT) control; and others (Hrovat et al. 2011a).

In almost all those cases the previous hardware-based controls have been replaced by software. In the process the functionality and complexity of hardware solutions that evolved through decades of ingenious refinements was transferred to software, which grew more and more complex with time. However, one huge advantage of software control implementations is their inherent flexibility: it is much easier to modify computer programs then the corresponding hardware implementations.

Next, the computer or more precisely microcomputer controls propagated to many areas of chassis and overall vehicle dynamics and related functionality. This includes, in a somewhat chronometric order, the following features: ABS brake effectiveness/stopping distance control; Traction Control (TC), which can be viewed as a counterpart of ABS especially helpful when driving on slippery roads; Electronic Stability Control (ESC)—a very effective safety feature helping prevent

many accidents, especially in emergency situations; Load Leveling (LL) used for vehicle posture control; Four Wheel/All Wheel Drive (4WD/AWD) drivetrain control that aims at optimizing traction on all four driven wheels, again especially relevant for driving on slippery, snow- or ice-covered roads; Continuously Controlled Damping (CCD) semi-active suspension control; Adaptive Cruise Control (ACC) sometimes also called Autonomous Cruise Control due to its ability to lock-in behind a leading vehicle and keep the related distance constant in terms of time distance between the two; Electrical Power Assist Steering (EPAS) and numerous forms of EPAS-based vehicle controls such as Active Front Steer (AFS), Four Wheel Steer (4WS), Lane Keeping Aid (LKA), Trailer Backup Assist (TBA), and, more recently various means developed to assist or fully control the parking tasks such as Fully Automated Parking Assist (FAPA) and Remote Parking Assist (RePA).

From the above somewhat lengthy list one can observe that most of the automotive computer controls developed to date have been applied—via powertrain, brake, and 4WD actuation, for example—in the longitudinal or X-direction (or dimension) of vehicle motion. This is visualized in Fig. 1, which displays various functionalities placed at their predominant axis of action. Next comes the lateral or Y-direction, which has seen significant revival of activities lately. On the other hand there is relatively little activity seen along the Z-axis or vertical motion of a vehicle where we see only the Mercedes ABC system as a sole representative of active suspension controls. As we will argue in a sequel, this “forgotten dimension” may represent a major opportunity for further expansion and application of automotive computer controls in the future.

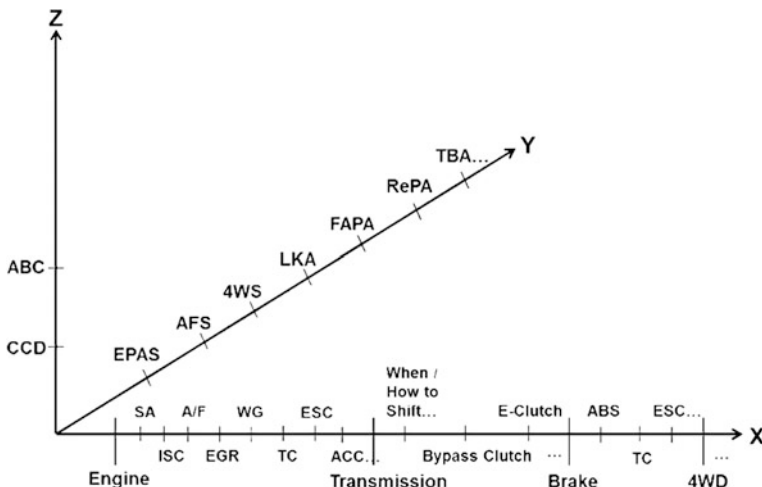


**Fig. 1** 3D representation of various automotive control functionalities

## 1.6 LQ Optimal Control Problem

There are many ways one could design an advanced, active vehicle suspension system. Some of those can be based on different optimization methodologies. In this work we focus on one of the most popular optimization methodologies—the Linear Quadratic (LQ) optimal control techniques, which, as we will see in a sequel, is particularly revealing and well-suited for our vehicle suspension design problem.

**Deterministic LQ problem statement and solution.** Since most of the optimization work pursued in the present study is based on the Linear Quadratic (LQ) optimal control approach (Athans and Falb 1966; Anderson and Moore 1971; Kwakernaak and Sivan 1972; Levine 2011) we will now briefly summarize main characteristics of this by now well-established and quite popular methodology, which years back was referred to as “advanced or modern controls”. As its name implies the LQ technique involves linear vehicle or plant models and quadratic optimization or performance index. The linear models can be either time-varying or time-invariant (LTI); presently we will almost exclusively deal with the latter i.e. LTI models. In addition, we will focus on infinite-time regulator problem that, as we will see below, results in feedback controls with constant control gains. The corresponding deterministic LQ optimal control problem can be stated as minimization of the following Performance Index (PI):

$$\text{Minimize}_{\text{w.r.t.} u} \left[ PI = \int_0^{\infty} (x^T(t) Q x(t) + u^T(t) R u(t) + 2x^T(t) N u(t)) dt \right] \quad (2)$$

subject to LTI vehicle model dynamics

$$\begin{aligned} \frac{dx}{dt} &= Ax + Bu + Gv_d \\ y &= Cx + Du \\ x(0) &= x_0 \end{aligned} \quad (3)$$

where the PI weighting matrices  $R^T = R > 0$ ,  $Q^T = Q \geq 0$ ,  $y$  is the output variable associated with the PI of Eq. (2), and  $v_d$  is a vector of deterministic disturbances. In the present case the latter are typically modeled as unit impulses in ground velocity, which is equivalent to unit steps in ground displacement (in case of more complex ground inputs they can sometimes be captured by expanding the state-space to include the augmented states representing different ground displacement shapes).

Often the above step-like disturbance terms can be fully or partially captured by the equivalent initial condition vector,  $x_0$ . For example, in the simple case of a 1D, 1DoF optimization treated in Sect. 3.1, one can approach the underlying deterministic two-state optimization problem as the one with zero initial conditions and an impulse in ground velocity i.e. step in ground displacement. Alternatively, the same problem can be approached as the one with zero ground input ( $v_d = 0$ ) and

non-zero initial conditions where the first state—the one corresponding to the rattle-space displacement—is initially set to 1 ( $x_1 = 1$ ) to represent the initial compression of the suspension space that is equivalent to the above-mentioned unit step in ground displacement. Later we will discuss another equivalence—the one between the above deterministic LQ results and corresponding stochastic case. But first, let us summarize the general solution to the above optimization problem and then say few words about the important topics of the stability and robustness of the LQ-optimal solution, which is critical for any possible practical implementation of the LQ-like control strategy.

The optimal solution to the above deterministic, infinite-horizon, continuous-time LQ regulator problem is given by following feedback controller:

$$u^* = -Kx \quad (4)$$

where the constant feedback gain matrix  $K$  is given by

$$K = R^{-1} (B^T P + N^T) \quad (5)$$

and  $P$  is obtained by solving the following Algebraic Riccati Equation (ARE)

$$A^T P + PA - (PB + N)R^{-1}(B^T P + N^T) + Q = 0 \quad (6)$$

Now, for the case when  $N = 0$ , which is most often encountered here, if the pair  $(A, B)$  is stabilizable and  $(A, C)$  is observable, where  $Q = C^T C$ , then the above ARE has a unique positive-definitive solution  $P > 0$ , which results in an asymptotically stable, LQ-optimal, closed-loop system. If  $(A, B)$  is stabilizable and  $(A, C)$  is detectable, then the above ARE has a unique positive semi-definitive solution  $P \geq 0$ , which again results in asymptotically stable, LQ-optimal, closed-loop system. When  $N \neq 0$  then the equivalent, more stringent stability conditions can be found in Anderson and Moore (1971).

**Robustness of LQ regulator.** Robustness properties of the deterministic LQ optimal regulator for the nominal or most often cited case when the cross-weighting matrix  $N = 0$ , are well known. Here under “robustness” we refer to system ability to still maintain good performance and stability despite the unavoidable errors due to model mismatch, and many other unpredictable noise factors that typically occur in practice. Assuming that all the states are available the Single-Input-Single-Output (SISO) gain margin is very generous and can range between 6 db and infinity, i.e. the nominal gain of 1 can vary from 0.5 and  $+\infty$ , whereas the associated phase margin is  $60^\circ$ . Similar results apply for each individual control channel of the corresponding Multi-Input-Multi-Output (MIMO) case under some mild additional assumptions as elaborated by Safonov and Athans (1977).

However, as shown by Ulsoy et al. (1994), once the non-zero cross-weighting matrix  $N$  is introduced, the above impressive robustness properties of the “standard” LQ regulator don’t apply anymore and can be significantly reduced. For example, in the context of the present vehicle dynamics ride and handling optimization

problem this situation arises when one augments the actuator-only secondary suspension of a quarter-car setting (see Sect. 3.2 below) with some passive counterparts such as an additional supporting spring and possibly a damper. These passive components could reduce maximum and average force and energy requirements from an active actuator. However, there could be instances when the actuator needs to provide net active power thus requiring total neutralization of the passive elements (or partial reduction of the spring stiffness) and if this action is overdone due to modeling and other errors one could see the potential for significant degradation in system performance including destabilizing effects of ending up with a net negative spring or damper effects, for example.

In addition to the above, the robustness of the LQ solution can be further eroded when not all of the system states are directly measured and available for controls (Ulsoy et al. 1994). Indeed, more often than not this is the case in practice since some state measurements are very difficult to make and some may be too costly. If the system in question is observable then these missing states can be reconstructed via different state estimation techniques, such as Luenberger observer (Levine 2011), for example. However, the additional dynamics and related dynamic delays typically result in further reduction of robustness and associated gain and phase margins. These issues are further amplified in the case when various noises are present—either in the process i.e. model dynamics and/or state or output measurements that will be discussed next.

**Stochastic case—LQG controller.** As described later (Sect. 2.2) most road inputs relevant for vehicle ride dynamics can be described as random, stationary stochastic processes. In this case the above deterministic LQ optimization problem transforms to an equivalent stochastic counterpart with an additional assumption that all random noises are white and of Gaussian character. The resulting optimization problem is then referred to as Linear Quadratic Gaussian (LQG) optimal control problem. In the context of present usage it can be formulated as minimization of the following Performance Index

$$\text{Minimize}_{\text{w.r.t.u}} [PI = E(x^T Qx + u^T Ru + 2x^T Nu)] \quad (7)$$

subject to LTI vehicle dynamics

$$\frac{dx}{dt} = Ax + Bu + Gw_d \quad (8)$$

where the expectation operator  $E(\cdot)$  represents steady-state mean square (co-variance matrix) values of the affected variables. Here  $w_d$  is the system disturbance in the form of aforementioned Gaussian white noise process characterized by

$$\begin{aligned} E[w_d(t)] &= 0 \\ E[w_d(t_1)w_d(t_2)] &= 2\pi W\delta(t_1 - t_2) \end{aligned} \quad (9)$$

with  $\delta(\cdot)$  representing the impulse or Dirac delta function, and  $W$  being the two-sided road (vertical) velocity power spectral density, which is equal to the product of road roughness coefficient and vehicle velocity (see Sect. 2.2 below). Special care should be exercised regarding the factor  $2\pi$  since some road descriptions may imply different factor. This can be traced to different definitions of the associated Fourier transforms (Weisstein 2017). In practice this means that one should be aware of the context how different psd data were obtained, especially when dealing with measured road spectra (Mastinu and Ploechl 2014).

The solution to the stochastic LQG problem is given by the same optimal feedback gain matrix  $K$  as in the corresponding deterministic LQ regulator problem. The only difference is that in the general LQG case one uses Kalman estimate of the state vector  $x$ , which amounts to a linear unbiased minimum error variance estimate obtained via Kalman-Busy optimal filtering (Sage and White 1977; Anderson and Moore 1990; Levine 2011). However, just as in the above deterministic case, the estimation with associated filter dynamics and measurement noises can significantly erode the robustness margins of the LQG controller. Indeed, as shown by Doyle (1978) even a simple two-state example can result in practically zero robustness for sufficiently large measurement noises and state weighting matrix  $Q$ . Another, more practical i.e. physical example was provided by How and Frazzoli (2010) who used an LQG controller to stabilize an inverted pendulum on a cart. It is shown that again one can encounter a situation where vanishingly small robustness margins are present around the nominally stable closed-loop system.

**Calculation of performance metrics.** In order to calculate different rms and mean-square values we use the following Lyapunov-like equation for the closed-loop covariance matrix  $X$

$$(A - BK)X + X(A - BK)^T = -G\Gamma G^T \quad (10)$$

where  $\Gamma$  corresponds to the ground velocity psd quantity  $2\pi W$ . Setting  $\Gamma = 1$  and solving the above equation will then result in normalized covariance matrix, where all relevant entries are normalized by  $2\pi W$ , i.e. the related rms values are normalized by  $\sqrt{2\pi W}$ . This type of normalization will be used through most of the present chapter. Once the covariance matrix  $X$  is known one can then calculate the expected mean-square optimal control input from

$$E(u^2) = KXK^T \quad (11)$$

Other output quantities of interest that are linear functions of states can be calculated in a similar fashion.

**To summarize.** The infinite time deterministic LQ problem and its stochastic LQG counterpart share the same optimal feedback control structure and associated gain matrix  $K$ . In the context of present active suspension study, there are number of equivalent or similar LQ optimization settings that lead to identical control

structure and gains. First, in the case of a deterministic LQ regulator, there is equivalence between appropriately posed initial condition response problem and related step input in ground displacement (or an impulse in ground velocity). Both of those deterministic settings are equivalent to the stochastic LQG problem formulation where ground input is now represented through white-noise in velocity process. In all three optimization cases we end up with the same optimal feedback control structure with the same gain  $K$  as per the above Eq. (5).

Regarding the robustness of the LQ regulator there are two different answers depending on the structure of the problem. In the case when there are no cross-weight terms ( $N = 0$  in PI) and when all the states are available then the LQ regulator results in a robust closed loop system with gain margin of at least 6 db and phase margin of  $60^\circ$ . However, this is in general not the case when  $N \neq 0$  and/or when some of the states have to be estimated—either via an estimator or Kalman-Busy filter. In the present case we will mostly deal with the idealized situation where  $N = 0$  and all the states are available for controls. While this is an idealized assumption the main objective of the present study is to establish best possible performance potentials of active suspensions realizing that eventual actual implementation will result in some degradation of performance and robustness. These are important topics for further investigation along the V-diagram of Fig. 2 that should be pursued in the future once the optimal performance has been identified along with related high-level architecture, bandwidth, and other requirements.

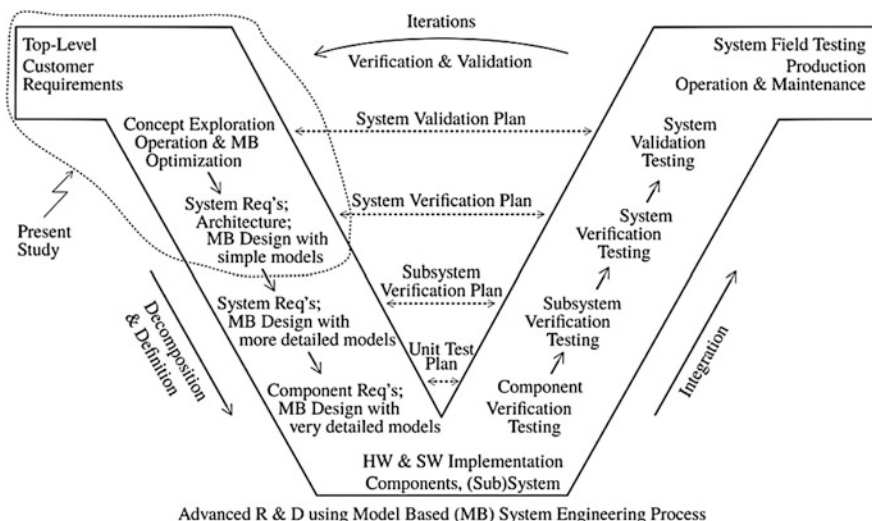


**Fig. 2** V diagram representation of system-engineering approach to advanced suspension design (MB stands for “Model Based”)

## 1.7 System-Level Approach

In order to investigate potential benefits and limitations of active suspensions we propose to start with a system-level (“30,000 ft” or “10,000 m”) study based on simple vehicle models and related requirements and constraints. In particular, it is proposed to start with establishing optimal ride and handling potentials based on a simple, linear one-dimensional (1D) and 2D vehicle models. This is accomplished by using appropriate optimal control tools such as the well-known optimal Linear-Quadratic (LQ) methods, to determine global best possible performance under ideal conditions and constraints.

The rationale being that if we cannot identify sufficient potential benefits within a simple setting under numerous simplifying, mostly favorable assumptions and thus less stringent constraints, there is little incentive to proceed with the study toward more detailed and complex models and optimization settings with many much more stringent constraints. The advantage of this “30,000 ft approach” is that due its simplicity it can cover large territory of potential solutions and produce a *global* view of the potential benefits and limitations. The key word here is “global” since many opportunities may be missed or overstated if one focuses on just one or two isolated points, as is the case with some studies.

On the other hand, depending on the outcome of the above “high-level” global study one can decide whether to proceed toward more detailed (“10,000 ft and below”) studies based on more complex, possibly non-linear models. As such this approach may be viewed as “top-down” as opposed to “bottom-up” approach where one starts with the complex and very detailed models and then gradually simplifies them toward control-oriented models and studies. Each approach has some advantages and disadvantages and may be more or less appropriate depending on a given task at hand.

The above top-down approach is particularly suitable for applying system-engineering principles (Anonymous 2017b) following the Model-based System Engineering V methodology (Anonymous 2017c) shown on Fig. 2. The entry point to the System V is at the upper left brunch of V starting with overall customer-level requirements regarding system functionality and conceptual mode of operations. Starting with overall customer requirements one can then use the above simple models and appropriate optimization tools to establish what are the best possible performance metrics and are they good enough to satisfy top level customer requirements. In addition one can then obtain the outlines of needed architecture and associated design and other engineering constraints such as desired actuator configuration and bandwidth or fidelity. Essentially, such a top-level optimization process uses modeling and related synthesis to produce results that can in turn then be used as requirements and guidance for subsequent more detailed lower-level work based on more detailed models and so on as one proceeds down the left branch of the System V. Eventually the process reverses as one progresses through the r.h.s. branch of V going through verification and validation phases

starting from component tests all the way to validation of the whole system operation and performance.

At this stage, following the above systematic approach we start by specifying the high-level requirements for an advanced, high-performance vehicle suspension. They can be listed as follows:

1. Maintain proper vehicle posture when subject to various inertial and external forces and moments caused by braking, turning, wind gust, and other operational events and disturbances;
2. Provide superior ride comfort (in an optimal sense to be further elaborated in a sequel) when subject to road roughness inputs, which act as a major disturbance to a vehicle;
3. Secure superior road handling (in an optimal sense to be further elaborated in a sequel) and overall vehicle agility;
4. Avoid excessive suspension stroke to avoid hitting jounce and rebound stops (this is the so-called “rattlespace” constraint requirement);
5. Enable additional benefits and functionality that will facilitate enhanced active safety and introduction of new, exciting functionality leading to superior customer experience (the “wow” factor).

In practice, the first requirement is typically best addressed through feed-forward control based on more detailed (possibly non-linear) models since some of the main disturbances regarding posture control come from known sources such as engine and brakes, which are initiated by the driver and thus known in advance to some extent. From the above list we will focus on Ride and Handling requirements 2–4 for most of the subsequent sections with some comments regarding many future exciting potential benefits being discussed in the last part of the chapter.

## 2 Setting up the Stage

In this section we will set the stage for the LQ optimization that will be used in the subsequent section. To this end we will next discuss the appropriate, simple Performance Index (PI) reflecting the above ride and handling requirements along with pertinent constraints. Next, we will address the numerical description and construction of an appropriately simple vertical road input representing the main disturbance acting upon the system. Also, we will address what are the appropriate, simple vehicle models that should be paired with the above. Finally, we will briefly mention many of the underlying assumptions used throughout this chapter.

Note that the key words here are “appropriately simple” since for a global, comprehensive analysis at this high of a level it is imperative to deal with an appropriately simplified setting. This means that all aspects of the problem (PI, constraints, disturbances, models) are in sync as far as the level of complexity is

concerned. Indeed, it would not make much sense nor it would be efficient to have a very detailed, 3D vehicle model but a simple “1D” PI or road description, and vice versa.

## 2.1 Performance Index and Related Constraints

Since one of the main objectives of the present work is to establish ride benefits of advanced active and semi-active suspensions, our first task will be to define an appropriate ride comfort index, which will in turn be used to define the associated optimization Performance Index (PI). This has been a subject of many investigations in the past. In its very nature this is an intrinsically subjective metric and as such may be a subject of many more studies in the future, especially as we face different modes of transportation such as autonomous driving, for example.

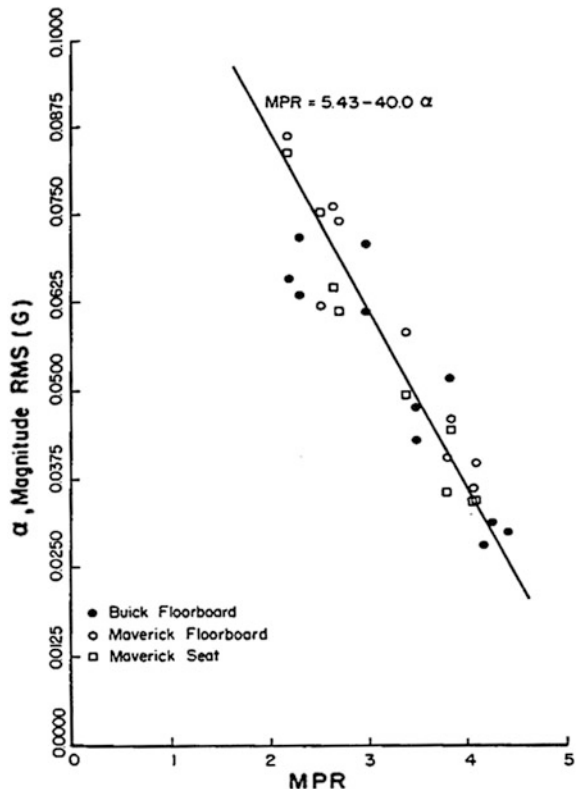
One of the first field-test studies to address the ride comfort metric was done in the 1970s by Smith et al. (1978). The authors used couple of different vehicles driven on 18 different roads with a total of 78 passengers. Their conclusion was that, “excellent correlation was found to exist between the subjective ride ratings and simple root mean square acceleration measurements at either the vehicle floorboard or the passenger/seat interface”. The key results of this study are reproduced in Fig. 3 where the horizontal axis represents the average or mean personal ratings and vertical axis represents rms acceleration measured for combined vertical and lateral directions. Here higher ratings represent better ride comfort. Similar results were obtained for the case limited to vertical accelerations only.

Further refinements of the rms ride comfort PI metric are possible through introduction of the vehicle or seat-track vertical jerk, which is the derivative of the vertical acceleration (Fearnside et al. 1974). The rationale being that the addition of jerk will capture contributions from high-frequency disturbances that are typically part of Noise Vibration and Harshness (NVH) spectrum. We will use this additional jerk term when addressing some elementary ride optimization problem based on simple, 1D vehicle models.

In addition to the above simple rms-based ride metrics there were number of attempts to expand this metric in order to include frequency-dependence of human sensitivity to vibrations. This was captured by the ISO standard 2631, which also takes into account the length of human exposure to vibration (Anonymous 1972). Additional information about various ride metrics and their further enhancements—such as a comprehensive NASA metric applicable to 3D motions—can be found in Hrovat (1993), Tseng and Hrovat (2015) and references therein.

It is interesting that some of the early comparison studies (Smith 1976; Smith et al. 1978) found the simple rms metric comparable to more complex counterparts such as the above ISO standard. Since the usage of proper ride metric depends on the context of its usage and since in the present setting we focus on simple models, optimization methods (LQ), and metrics, in what follows we will exclusively use

**Fig. 3** Least square fit to experimental data by Smith et al. (1978) expressing Mean Personal Rating (MPR) as a function of rms acceleration



the rms ride metrics mentioned above. We remark that, if desired, it is easy to incorporate frequency-weighting into the LQ-type metric by augmenting the state-space model with appropriate filter states associated with the desired frequency shaping. Additional considerations may apply when dealing with future autonomous vehicles where ride sickness effects may be more pronounced due to lack of driving activity (Wada 2016).

At this point it is important to stress that if the ride comfort were the only objective of the optimization then the solution would be simple i.e. to keep the rms acceleration (and jerk) equal to zero for all times by making the total suspension force equal to vehicle weight for all times. This may work fine in isolated cases of driving on flat surfaces. However, the main issue with such a suspension would be that it would require unrealistically large suspension strokes or so-called “rattlespace” to negotiate hills and valleys and similar large road deviations from flat surfaces (in the extreme, one could consider airplanes as limiting case of such “air cushion” vehicles).

In practice, the available suspension stroke is limited as determined by jounce and rebound stops. Although these “bump stops” represent hard constraints they are often approximated by soft constraints in the form of rms or mean-square

limitations on rattlespace. The latter are then appended to the mean-square ride comfort metric to form an overall PI that will be used for LQ or  $H_2$  optimization based on a simplest possible 1D vehicle model to be considered in Sect. 3.1.

In addition to the above rattlespace constraint we will later introduce an additional constraint when dealing with slightly more detailed 1D or quarter-car vehicle models. The main purpose of this additional constraint will be to limit tire wheel-hop, which can be detrimental to vehicle handling as well as ride. This yet another mean-square constraint (this time on tire deflection or relative motion w.r.t. ground) will be addressed in Sect. 3.2.

## 2.2 Road Description

As elaborated in Hrovat (1993) there are two kinds of disturbances that affect vehicle ride and handling. One is caused by road roughness irregularities and the other by different inertial and aerodynamic forces due to braking, turning, and wind gusts, for example. In this paper we focus on road or ground input disturbances, which are the most relevant for present ride studies.

There are many ways to describe road inputs, which can be classified as shocks and vibrations. Shocks are discrete events of short duration and high magnitude, such as encountered while suddenly hitting a pothole or road bump at relatively high speed. On the other hand, vibrations are characterized by prolonged and consistent excitations that are typically encountered during long trips on highways and other roads.

When considering vibration excitation, road roughness is typically described as a stationary random process of a given displacement power spectral density, p.s.d. (Bendat and Piersol 1971). An example of measured displacement or roughness power spectral densities of various roads and terrains from Sevin and Pilkey (1971) is shown in Fig. 4.

Comparing the actual measured traces with the straight line of negative 2:1 slope in the log-log scale one obtains the following often used approximation describing road displacement p.s.d.,  $S(\cdot)$ :

$$S(\Omega) = A/\Omega^n \quad (12)$$

where  $\Omega$  is the spatial frequency in units of “radians per length” (rad/ft in the case of Fig. 4) and  $n \approx 2$ . The above displacement spectra imply that the corresponding vertical velocity spectrum as experienced from a moving vehicle is constant for all frequencies i.e. white noise with intensity of  $A * V$ , where  $V$  is vehicle forward velocity. The white-noise characterization of the road input conveniently matches the well-known LQG (Linear Quadratic Gaussian) optimal control setting, which presupposes the white-noise Gaussian process and measurement noises (see Sect. 1.6).

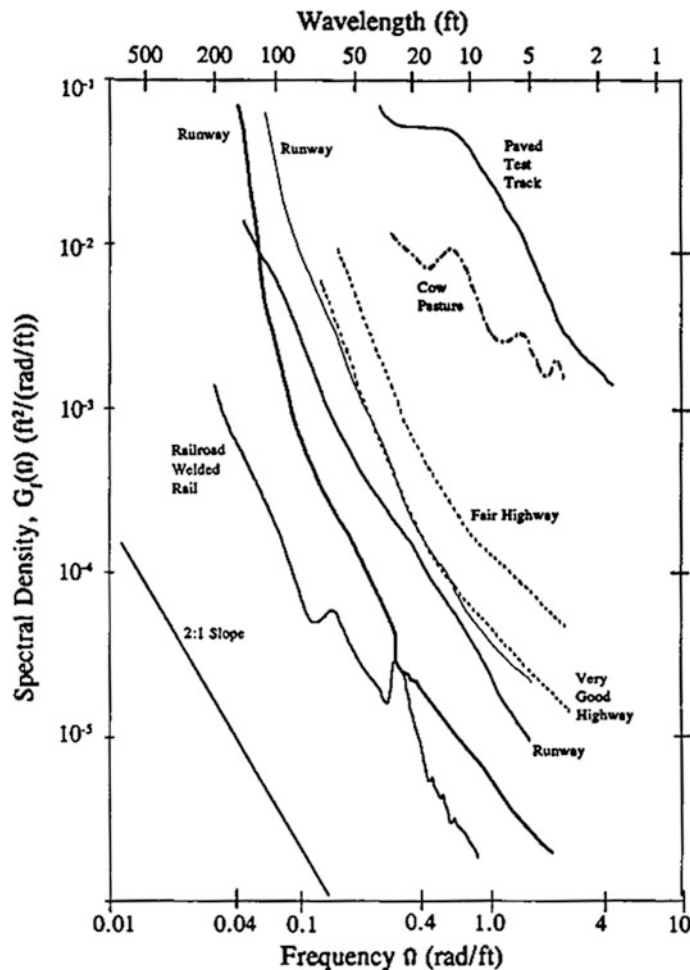


**Fig. 4** Measured power spectral densities of various terrain/road surfaces (according to Sevin and Pilkey (1971) where factor  $1/2\pi$  was used when relating autocorrelation function to psd)

Further reinforcements about the above white character of many measured roads can be seen in Figs. 5 and 6 from Smith (1982).

Additional examples can be found in Hrovat (1993) and references therein where one can also find references to more elaborate and/or multi-dimensional models of road roughness such as discussed by Dodds and Robson (1973) and Rill (1983), for example.

Numerical procedure used to construct an approximate white-in-velocity Gaussian road sequence for usage in simulations is discussed in Hrovat and Margolis (1975). The procedure starts with a sequence of uniformly distributed random numbers with triangular autocorrelation function. The corresponding p.s.d. is then

**Fig. 5** Comparison of best-fit road model with exponent  $n = 2.02$  and measured Road #1 (cf. Hrovat 1997)

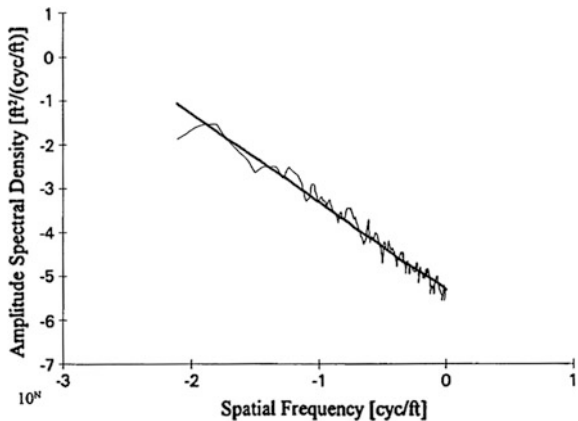
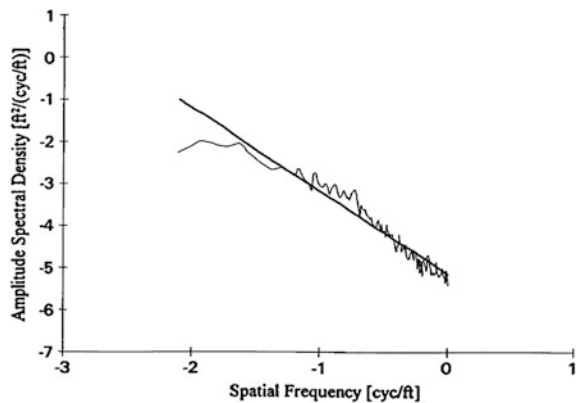


**Fig. 6** Comparison of best-fit road model with exponent  $n = 1.99$  and measured Road #2 (cf. Hrovat 1997)



approximately white up to certain frequency band, which is controlled by the choice of random sequence update rate. The sequence is next passed through appropriate bandpass filter to wash out large road protrusions such as hills and valleys, on the one hand, and high frequency noise that is well beyond the underlying models bandwidth fidelity, on the other. In the final step, the sequence is ensemble averaged to produce the desired Gaussian characteristics.

### 2.3 Vehicle Models

In order to complete the optimization setting we now briefly introduce some of the simple vehicle models to be used in the rest of this work. We start with linear, time invariant models of lowest complexity and gradually add additional dimensions and Degrees-of-Freedom (DoF). The simplest possible model is shown in Fig. 7.

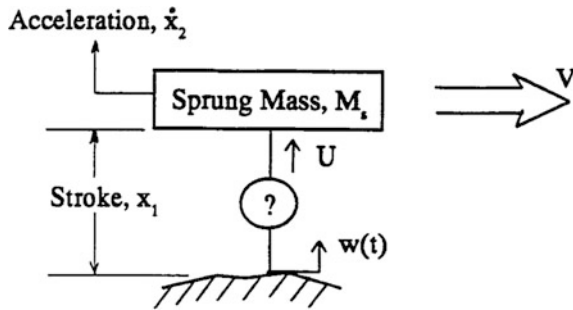


**Fig. 7** Simple 1D, One Degree-of-Freedom (DoF) vehicle model

It consists of only a sprung mass,  $M_s$ , and an active suspension actuator that can produce any desired force  $U$  while supporting vehicle mass  $M_s$ .

The vehicle is assumed to traverse an uneven road with constant velocity  $V$ , which creates a vertical input  $w(t)$  acting upon the lower mounting point of the active suspension actuator. The vertical velocity input  $w(t)$  is proportional to vehicle velocity  $V$  and the spatial slope of the road unevenness. It is in this context that one talks about the “moving ground” when referring to  $w(t)$ . As discussed earlier for the purpose of the present study the spatial slope is approximated by a white-noise process so that  $w(t)$  is also white with p.s.d. intensity proportional to  $V$ .

Next we introduce models resulting from considering only one corner of a vehicle. These are the so-called quarter-car models—some of which are shown in Fig. 8. In addition to the sprung mass  $M_s$ , which is now appropriately proportionated to a given corner, we also have an unsprung mass,  $m_{us}$ , which reflects the wheel/tire subassembly with associated mass components due to steering links, knuckles etc. The unsprung mass is typically only a fraction (one-fifth or less) of the

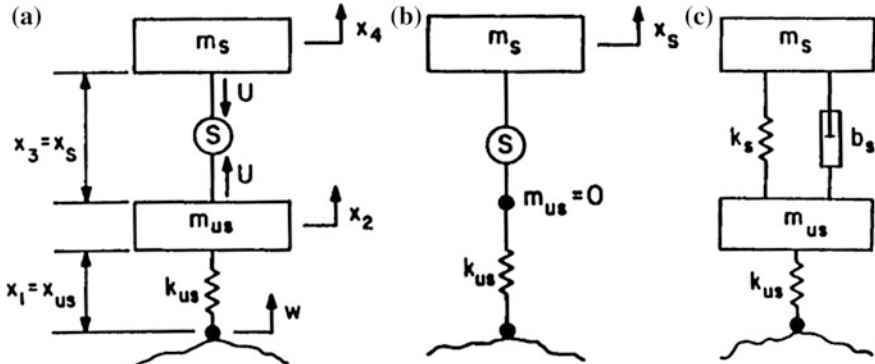


**Fig. 8** Various 1D, 2DoF vehicle models: with active suspension (a); with active suspension and vanishing unsprung mass (b); with passive suspension (c)

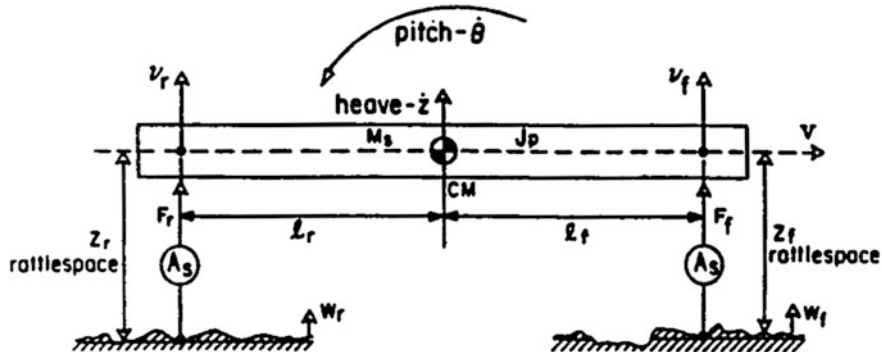


**Fig. 9** Half-car, 2D vehicle model

corresponding sprung mass and is suspended between the primary suspension provided by tire flexibility and secondary suspension that can be passive, active or semi-active. A point-wise tire-road contact is considered, and the tire filtering effect may be included, as needed.

As the next logical step in model complexity, we consider the so-called half vehicle, 2D, models the simplest variant—without unsprung masses—being shown in Fig. 9. It includes vehicle (sprung mass) pitch motion represented by angle  $\theta$ , and vertical or heave motion represented by vertical displacement,  $z$ , of its Center of Mass, CM.

Finally the full 3D models are represented in Fig. 10, which shows the simplest possible 3D model consisting of vehicle heave, pitch and roll modes. Note that again the unsprung masses have been neglected for this lowest-level 3D model; they can be easily added later, as needed.

The above 1D, 2D and 3D model variants are the ones most often used in studies dealing with system-level advanced suspension optimization and synthesis. However, depending on the task at hand one may add some additional elements and components such as subsystems consisting of an engine/powertrain suspended on their mounts, and a driver suspended on a seat. Similar 2D, 6 DoF model has been evaluated through actual vehicle tests and the corresponding results are shown in Figs. 11 and 12. This illustrates that even a relatively simple, linear, time-invariant 2D models can provide good fidelity up to the bandwidth of 10 Hz and more. If further improvements in fidelity are desired then one may have to consider additional modeling details and degrees of freedom and possibly even augment the present lumped parameter models with flexible counterparts, as needed and appropriate. The underlying assumption is that we are dealing with linear vehicle models that are needed for the above LQ optimization approach.

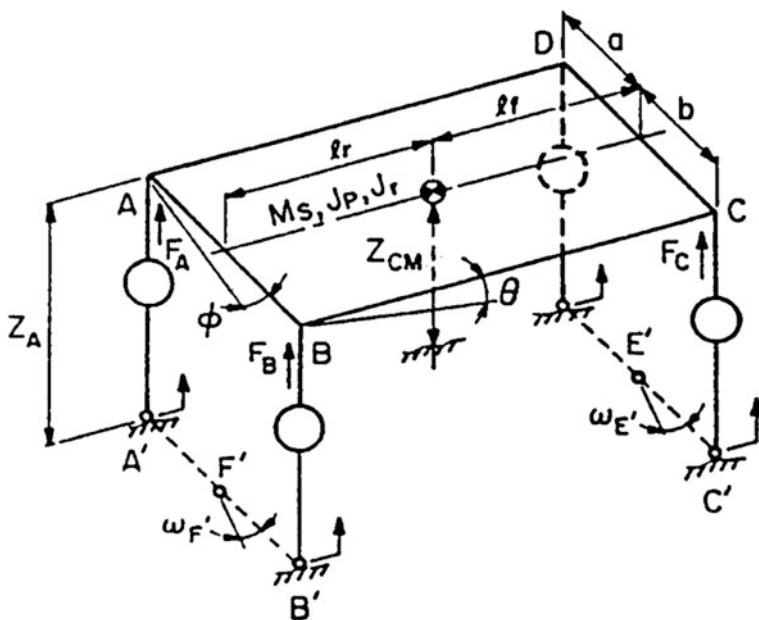


**Fig. 10** Full-car, 3D vehicle model

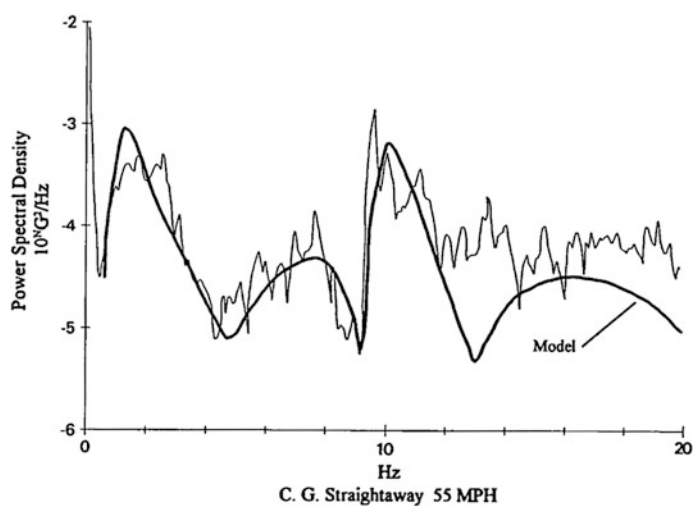


**Fig. 11** Measured and predicted acceleration PSD's at CG for linear 6 DoF, 2D model per Smith and Sigman (1981)

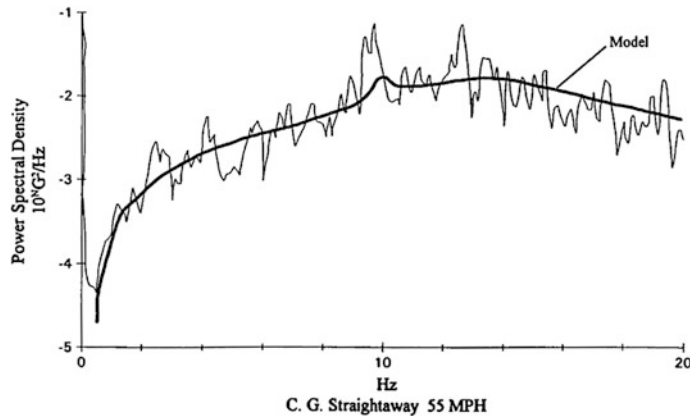


**Fig. 12** Measured and predicted unsprung mass acceleration PSD's for linear 6 DoF, 2D model per Smith and Sigman (1981)

## 2.4 Assumptions

There are many implicit and explicit assumptions used throughout the course of this work. Some of them we have already enumerated in the previous sections when introducing rationale for chosen performance metrics, road disturbance representation, and different simplified vehicle models. Numerous additional assumptions can be found in Hrovat (1997) and references therein such as Hrovat (1988). They include the assumption that in what follows all state variables are available for controls; that—as indicated earlier—all external load effects will be neglected for most of the present study and assumed to be treated separately, mostly in the context of feed-forward controls; and that all actuators are assumed infinitely fast and accurate.

In addition, since one can consider suspension system to be essentially a filter for road roughness induced disturbances, this filtering or attenuation should not include (large) hills and valleys and similar low frequency ground inputs that vehicle should follow. This can be achieved through appropriate signal processing (detrending) of key signals used for control. The latter is especially relevant for so-called “sky-hook” damper and spring implementations to be discussed in a sequel.

## 3 Optimization Results

In this section we proceed with developing optimal control results for different scenarios starting with the simplest possible 1D, 1DoF setting and gradually progressing toward 2D and 3D cases. At each step we build upon the acquired knowledge and insight, which in turn serves as a footing for the next step based on a

more detailed model representation. In the process we reveal essential characteristics of each optimization setup in terms of potential ride and handling benefits, and fundamental constraints—such as different invariant points in key frequency transfer function maps imposed by a given structural constraint, for example. While focusing on best possible performance outcomes, which typically imply an active suspension solution, we will also try to put these optimal results in a proper perspective by comparing them with the corresponding passive suspension counterparts.

### 3.1 Simple 1D, 1DoF Case

**Problem statement.** Referring to Sect. 2, we can now pose the following optimal control problem for the case of a simple, 1D, 1DoF model represented in Fig. 7:

$$\text{Minimize}_{\text{w.r.t.} u} [PI = E(x_1^2 + ru^2)] \quad (13)$$

subject to the following second-order state equations

$$\begin{aligned} dx_1/dt &= x_2 - w \\ dx_2/dt &= u \end{aligned} \quad (14)$$

where as seen from Fig. 7, the states  $x_1$  and  $x_2$  represent suspension rattlespace and sprung mass velocity, respectively, and  $u$  is a normalized force  $U/M_s$ , which in the present case equals to sprung mass acceleration. The PI of Eq. (13) then captures the requirements for smooth ride (low  $u$ ) balanced against the competing requirement for limited rattlespace (low  $x_1$ ). The disturbance  $w$  when seen from a moving vehicle appears as a vertical velocity input caused by road irregularities. It is modeled according to the aforementioned zero-mean, Gaussian white-noise velocity characterization discussed in Sects. 1.6 and 2.2.

**One DoF LQG problem solution—Skyhook structure.** The solution to the above LQG problem follows the procedure outlined in Sect. 1.6. Since we are dealing with a simple second-order system it is now possible to obtain an entirely analytical solution to this problem. We start with the Riccati equation (6)

$$A^T P + PA - (PB + N)R^{-1}(B^T P + N^T) + Q = 0 \quad (15)$$

where in the present case

$$A = \begin{bmatrix} 0 & 1 \\ 0 & 0 \end{bmatrix}, \quad B = \begin{bmatrix} 0 \\ 1 \end{bmatrix}, \quad N = 0, \quad Q = \begin{bmatrix} 0 & 0 \\ 1 & 0 \end{bmatrix}, \quad P = \begin{bmatrix} P_1 & P_2 \\ P_2 & P_3 \end{bmatrix}, \quad R = r \quad (16)$$

Substituting these expressions into the above ARE and solving for  $P$  we get

$$P_1 = \sqrt{2}r^{\frac{1}{4}}, \quad P_2 = \sqrt{r}, \quad P_3 = \sqrt{2}r^{\frac{3}{4}} \quad (17)$$

so that the optimal control gain matrix from Eq. (5) becomes

$$K = \frac{1}{r} [P_2 \quad P_3] = [r^{-\frac{1}{2}} \quad \sqrt{2}r^{-\frac{1}{4}}] \quad (18)$$

Thus the LQ-optimal feedback control  $u_{LQ}$  becomes

$$u_{LQ} = -\frac{1}{r^{1/2}}x_1 - \frac{\sqrt{2}}{r^{1/4}}x_2 \quad (19)$$

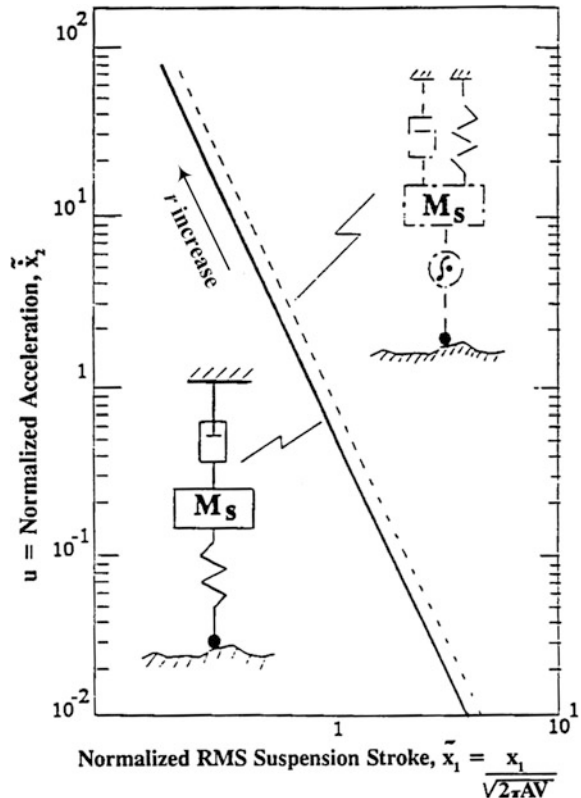
Since  $u$  represents a normalized force, the optimal suspension structure amounts to a spring of normalized spring constant  $r^{-1/2}$ , and a damper with normalized damping constant of  $\sqrt{2}r^{-1/4}$ . While the optimal spring is placed between the vehicle sprung mass and “moving” ground, the optimal damper is placed between the vehicle sprung mass and an *inertial* ground. For this reason the latter configuration is called “skyhook” damper. The optimal skyhook structure is shown in Fig. 13 along with the corresponding optimal performance boundary, both shown as full lines in the figure. Note that this optimal structure could be inferred even before solving the above LQ problem. This follows from the fact that the LQ optimal control amounts to a feedback control based on two states with negative signs resulting from the fact that the closed-loops system is asymptotically stable.

The optimal performance line in Fig. 13 has been calculated using covariance Eq. (10) of Sect. 1.6, where for the sake of efficiency of presentation both states have been normalized w.r.t.  $\sqrt{2\pi AV}$  so that in general traversing rougher roads and/or at higher speeds leads to larger normalized acceleration due to limited available rattlespace. Just as in the case of optimal gain calculation, it has again been possible to analytically determine all PI quantities of interest. Actual calculation steps can be found in the Appendix. The resulting optimal trade-off is given by the following equation

$$u_{LQ, rms, norm} = \frac{3\sqrt{3}}{8x_{1, rms, norm}^3} \quad (20)$$

This is represented in Fig. 13 by solid straight line with a slope of  $-3$  on the log-log scale so that each 10% increase in available rattlespace facilitates 30% decrease in rms acceleration levels. The optimal trade-off line is parameterized by the weighting factor  $r$ . As it can be seen from the above equation for normalized force  $u_{LQ}$ , which in the present case equals sprung mass acceleration—larger weights  $r$  result in softer suspension settings with related smaller accelerations and larger rattlespace requirements.

**Fig. 13** Optimal structure and performance trade-offs for 1 DoF model with PI of Eq. 13 (solid lines) and Eq. 22 (dashed lines)



In terms of actual practical realization, the skyhook damper structure cannot be implemented in the configuration shown in Fig. 13 since an inertial ground is not available from a moving vehicle. Thus in the context of a simple 1D, 1DoF model under consideration, the suspension members can only be placed between sprung mass and a “moving” ground. It is then shown in Hrovat (1982) by using the definition of passivity from Sect. 1.2 that so positioned suspension actuator must be an active device in order to implement the above LQ-optimal control strategy. It is interesting to mention that one “almost” optimal all passive structure was shown in Young and Wormley (1973). It consists of a serial combination of a spring and damper all in series with the sprung mass. However, although such a structure resulted in desired transfer functions there was a pole-zero cancellation corresponding to the unstable pole at zero. This reflects the inability of such a structure to support the sprung mass weight and also it violates the asymptotic stability property of the LQ-optimal solution.

The skyhook structure has a number of advantages. Since the skyhook damper is not in direct contact with the moving ground it can be tuned to higher damping values than its more conventional counterpart placed between the moving ground and sprung mass. Indeed, typical damping ratios for the conventional passive

suspension are in the range of 0.2–0.3. On the other hand from the above equations one can see that the LQ-optimal damping ratio is significantly higher and equals  $\sqrt{2}/2 \approx 0.7$ . The latter leads to more effective containment of sprung mass oscillations especially the ones induced by frequencies around vehicle dominant heave mode of oscillations typically around 1–2 Hz. This is the area where back-to-back comparison between active and passive suspensions is typically the most impressive when performed on a specially constructed test tracks with large, low frequency undulations that can excite the above heave mode at right vehicle speeds.

**Consideration of external loads.** It is interesting that the above elevated damping ratio will also help in containment of load-induced dynamic disturbances due to inertia effects when braking, accelerating, turning and similar (Hrovat 1997). Here it should be reminded that, as explained earlier, load disturbances have not been explicitly considered so far. However, for completeness we briefly mention the work of Young and Wormley (1973) where the authors address simultaneous effects of both road as well as load disturbances. The load disturbances were primarily due to aerodynamic forces acting upon a proposed high-speed ground transportation vehicle. These aerodynamic forces that included wind gust and similar were modeled as a random process in the form of a low-pass filtered white noise. The authors show that large and random load forces can significantly deteriorate the LQG performance from Fig. 13 where, depending on the magnitude of these forces, there could be a significant deviation in the optimal performance line toward saturation in the direction of the lower r.h.s. of the plot. However, these load effects become significant at very high wind speeds w.r.t. vehicles that were travelling at speeds up to 300 mph, such as high-speed trains discussed by Young and Wormley (1973). Another area of relevance is racecars such as Formula 1 vehicles, which are subject to large aerodynamic loads. For most of conventional vehicles this is not the case, and besides, since vehicle speed is known, one could use feed-forward controls to counteract any mean aerodynamic loading (as well as any loading due to inertia forces caused by braking, turning etc.).

**Introduction of Semi-Active (SA) control.** Although as discussed before it is not possible to implement the LQ-optimal skyhook structure using more standard passive components, one can still attempt to approach the LQ-optimal performance by using semi-active dampers (Crosby and Karnopp 1973). One such strategy would be to attempt to reproduce the optimal skyhook damper force whenever possible i.e. whenever there is a passive power required by the SA damper placed between sprung mass and moving ground (in reality this will be between sprung mass and unsprung masses, as discussed in Sect. 3.2 based on quarter-car 2DoF vehicle models). At any instant when this passivity constraint is not satisfied the SA force is turned off since this is in some sense the “closest” that one could get to optimal force at that moment. While not optimal this simple strategy leads to close to optimal performance in practice.

**Inclusion of jerk in PI.** Although the vehicle sprung mass vertical acceleration has been generally accepted as main indicator of passenger ride comfort, some authors (Fearnside et al. 1974) argued that in addition to acceleration one should

also consider jerk—derivative of acceleration—as an additional metric when evaluating ride comfort. This case was elaborated by Hrovat and Hubbard (1981). To this end we expand the original PI of Eq. (13) by one additional term proportional to the mean-square of expected sprung mass jerk. The augmented PI is then

$$PI_j = E \left[ x_1^2 + r_1 u^2 + r_2 (du/dt)^2 \right] \quad (21)$$

This can be next aligned with the standard LQG formulation by defining the normalized force i.e. sprung mass acceleration,  $u$ , as a new state,  $x_3$ , so that the derivative of  $u$ , which is equal to sprung mass jerk, then becomes the new control  $u_1$ . The resulting LQG optimization problem can now be stated as

$$\text{Minimize}_{\text{w.r.t. } u_1} [PI_j = E(x_1^2 + r_1 x_3^2 + r_2 u_1^2)] \quad (22)$$

subject to the following state equations

$$\begin{aligned} dx_1/dt &= x_2 - w(t) \\ dx_2/dt &= u = \hat{x}_3 \\ dx_3/dt &= u_1 \end{aligned} \quad (23)$$

with  $r_1, r_2 \geq 0$ ,  $r_1 + r_2 > 0$ , and the white noise process  $w(t)$  specified as before.

The LQ-optimal solution to this problem is given by the following feedback control law

$$u_{1,LQ} = -Kx(t) = -k_1 x_1 - k_2 x_2 - k_3 x_3 \quad (24)$$

where it was again possible to obtain analytical solutions for control gains  $k_1, k_2$  and  $k_3$  as a function of weighting parameters  $r_1$  and  $r_2$  (Hrovat and Hubbard 1981). Moreover, since the new control,  $u_1$ , i.e. jerk, is equal to derivative of acceleration, and the latter is in turn equal to the original control,  $u$ , one can now write the original optimal control—normalized control force as

$$u_{LQ} = -K \int x(t) dt = -k_1 \int x_1 dt - k_2 \int x_2 dt - k_3 x_2 \quad (25)$$

The first integral term on the r.h.s. equals the integral of rattlespace, second is integral of sprung mass velocity, which is equal to sprung mass position, and the last term involves sprung mass velocity. This leads to a structure depicted through dashed lines in Fig. 13. In addition to the skyhook damper this new LQG-optimal structure includes a skyhook spring and a (possibly fast) load-leveling device acting upon the integral of suspension deflection. Both—the skyhook damper and spring—are attached to an inertial ground that is in practice not available from a moving vehicle. As implied by the assumptions in Sect. 2.4, this “inertial” ground should represent a low-pass filtered or smoothed version of the road that retains large hills,

valleys and similar. In practice this can be achieved through proper signal processing such as, for example, high-pass filtering of vehicle accelerations and velocities that would detrend large, low frequency components. In addition, with current efforts on 3D road mapping, it should be possible to know some portions of the road elevation well in advance thus further facilitating a creation of an appropriate “inertial” ground.

At this stage it is of interest to see how would the jerk-optimal suspension compare w.r.t. more standard acceleration-only case. Relevant analytical calculations have been performed in Hrovat and Hubbard (1981); the results fall in-between the full and dashed lines in Fig. 13. As indicated previously, the full line corresponds to the standard 1DoF case with acceleration-only weighting. The dashed line then represents the other special case when  $r_1 = 0$  so that in this case only the vehicle jerk has been optimized as a measure of ride comfort. For this jerk-only weighting one can analytically express the relations between optimal normalized rms rattlespace and acceleration as

$$x_{3, \text{rms}, \text{norm}} = \frac{\sqrt{1000}}{36x_{1, \text{rms}, \text{norm}}^3} \quad (26)$$

This is plotted in the log-log scale of Fig. 13 as a dashed straight line parallel to the standard case where  $r_2 = 0$ . As it can be seen from Fig. 13 the difference in performance in terms of acceleration-rattlespace trade-off is relatively small in-between the two extreme cases. For example, for the same level of rms suspension stroke the acceleration-only optimal suspension results in up to 26% lower acceleration levels or, equivalently, the jerk-only optimal suspension results in up to 35% higher rms acceleration levels while substantially reducing the related jerk (theoretically, for the standard case of acceleration-only weighting the rms jerk tends toward infinity, which in practice may lead to very large jerk levels).

In addition to the substantial jerk reduction, there are a number of other advantages associated with jerk-optimal suspension. This includes relatively large damping ratios between 0.5 and 0.7, and the presence of integrating, load-leveling component, which can provide good load containment and posture control. As opposed to more traditional load-leveling systems that may take seconds and minutes to establish new level, the present load-leveling system can be fast, depending on the desired overall closed-loop system bandwidth. It should be pointed out that the above skyhook spring-and-damper structure, and the fact that the optimal controller includes load-leveling, imply that—just as in the standard 1DoF case—one will necessarily need an active actuator to implement the jerk-optimal strategy.

**Summary.** While extremely simple the above standard 1D, 1DoF case provides many useful data and insightful information about the structure and key characteristics of an optimal suspension. This includes:

- Special so-called “skyhook” damper that provides superior isolation from road-induced vibrations and shocks;

- Superior heave mode damping with relatively high damping ratio of 0.7 when compared to conventional passive suspension damping, which is typically in the range between 0.2 and 0.3;
- Better dynamic load containment with up to 2–3 times smaller sags due to, for example, sudden braking or cornering (Hrovat 1997);
- Optimal skyhook algorithm points to a practical strategy for semi-active suspension control—today SA suspensions are already widely used in the industry and “skyhook” is one of the most popular approaches for controlling the SA devices.
- As an extension of the above standard 1DoF case one can also consider including jerk as an additional metric of ride (dis)comfort. This naturally leads to concepts of skyhook spring and fast load leveling resulting in substantial jerk reduction and thus further smoothing and filtering of the ground input effects.

It should be stressed again that this simple analysis and synthesis is only the first step in system-engineering based approach to advanced vehicle suspension design. For example, reference (Evers 2010) addresses design of optimized cabin suspensions for commercial trucks by starting with LQ design for the simple, 1 DoF models discussed above. It then introduces much more detailed 4 DoF quarter car models that include engine/powertrain module suspended on engine mounts and some other additional effects. It is interesting that after detailed analysis and appropriate approximations the study concludes that for the quarter-car models under considerations the acceleration- and jerk-optimal controllers based on the simple 1 DoF models perform close to the optimal controllers based on the full eight- and nine-state models, respectively.

It could be said that in terms of the System V diagram from Fig. 2 we are at around the tip of the left branch of V. While in general many more steps still need to follow down the System V diagram, including input signal processing, actuator design, load containment, system diagnostics and similar, nevertheless the above insight serves as a solid “first base” (in the lingo of American baseball) for subsequent R&D steps. At each such step we should gain some unique insight, which will in turn point out to additional tasks and details needed to bring production-worthy advanced active suspension to life.

### **3.2 Quarter-Car, 2DoF Case**

A natural next step when progressing from the above simplest possible 1DoF model is to include the so-called unsprung mass associated with the wheel-tire component and all the related attached masses of steering and suspension subsystems. The resulting “quarter-car” model is shown in Fig. 8. Part (a) from Fig. 8 corresponds to the active suspension model we will be dealing with next, while models from parts

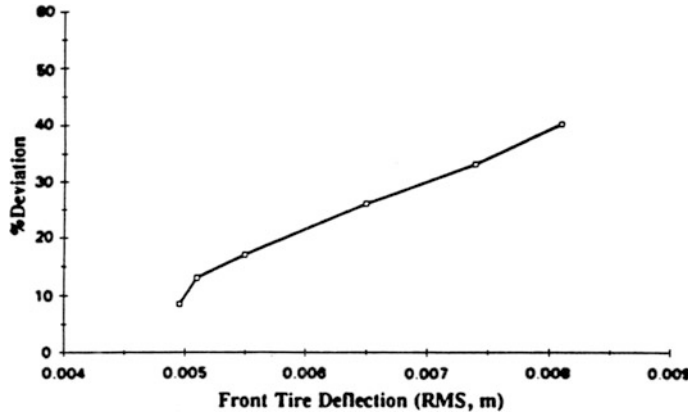


**Fig. 14** Percent path deviation versus change in tire deflection for simulated sudden crosswind disturbance per (Asgari and Hrovat 1991)

(b) and (c) will be used later for comparison purposes in order to put our optimization results in proper perspective.

**Wheel-hop dynamics and related constraint.** Introduction of unsprung mass and tire stiffness brings an additional degree-of-freedom and an additional limitation or constraint upon our system. The constraint comes from the fact that this additional dynamics may lead to wheel-hop oscillations on uneven roads which in turn may lead to some loss of vehicle handling capability. More precisely, excessive wheel hop leads to large variations in tire normal force, which then results in the net loss of average normal force due to tire nonlinearity (concavity). Net effect is some loss of tire tractive and cornering i.e. handling capability. The latter is illustrated in Fig. 14 from Asgari and Hrovat (1991) where it can be seen that there is almost a linear relation between the rms tire deflection due to wheel hop dynamics and the percent deviation from an original, straight path of a vehicle subjected to sudden crosswind disturbance. Thus, as is common in related literature, we will try to limit the undesirable wheel-hop effects by introducing an additional quadratic penalty term for tire deflection in the original performance index, Eq. (13).

**Problem statement.** Based on the above discussion and Fig. 14, we will next define an appropriate performance index for the 2DoF quarter-car problem as

$$\text{Minimize}_{\text{w.r.t.u}} [PI = E(r_1x_1^2 + r_2x_3^2 + u^2)] \quad (27)$$

subject to the following quarter-car dynamics corresponding to Fig. 8a

$$dx_1/dt = x_2 - w \quad (28)$$

$$m_{us}dx_2/dt = -k_{us}x_1 + U \quad (29)$$

$$dx_3/dt = x_4 - x_2 \quad (30)$$

$$m_s dx_4/dt = -U \quad (31)$$

where we have introduced an additional term  $r_1 x_1^2$  in the above PI to penalize excessive tire deflections. The rest of the symbols are self-explanatory:  $m_{us}$  and  $k_{us}$  stand for unsprung mass and (tire) stiffness, respectively;  $w$  is again the white-noise ground velocity input;  $U$  represents the active suspension actuator force, and  $u$  is normalized active force, which again equals sprung mass acceleration,  $u = U/m_s$ .

After normalizing the above set of four state equations one can end up with another set of four with only two physical parameters instead of the original three ( $m_s$ ,  $m_{us}$ ,  $k_{us}$ ). The two normalized parameters are  $\omega_1 = 2\pi f_1 = (k_{us}/m_{us})^{1/2}$ , which is natural “wheel-hop” frequency of the unsprung mass subsystem, and  $\rho = m_s/m_{us}$ . The normalized control,  $u$ , is now again equal to sprung mass acceleration. The resulting LQG problem was solved using control systems CAE/CAD tools such as Matlab and its predecessor Matrixx. Again, we were interested for a global solution that will provide a comprehensive map and insight into the potential benefits and limitations of the proposed active suspension concept. This was very much facilitated by the above tools.

The optimal control solution was in the form of a linear feedback of states, where according to Sect. 2.4 we assume that all four states are known

$$u = - \sum_{i=1}^4 k_i x_i \quad (32)$$

With this control and using the covariance Eq. (10) we can next calculate and plot various performance metrics. The global plot of normalized rms acceleration versus normalized rms rattlespace is shown in Fig. 15, parameterized by weighting factors  $r_1$  and  $r_2$ . The plot has been obtained for the case with  $f_1=10$  Hz and  $\rho = 10$ . From this “tornado-like” plot it can be seen that higher values of  $r_1$  and  $r_2$  result in less comfortable rides. Similar comments apply to Fig. 16, which shows normalized rms acceleration versus corresponding tire deflection.

More precisely, as it can be seen from Fig. 15, higher value of rattlespace penalty,  $r_2$ , results in smaller suspension excursions but larger sprung mass accelerations i.e. less comfortable ride. Similarly, from Fig. 16 it can be seen that higher value of the tire wheel-hop deflection penalty,  $r_1$ , results in smaller tire excursions but larger sprung mass accelerations, and thus better handling but worse ride comfort. The shaded areas in Figs. 15 and 16 correspond to the areas of practical significance for the present vehicle ride optimization problem. The following example from Hrovat (1997) illustrates how could one use the above plots in early phase of an advanced suspension design.

**Illustrative example.** Assume that you have been given a task to perform a preliminary, system-level study of potential benefits of an advanced active suspension applied to an autonomous commuter vehicle. In order to facilitate the

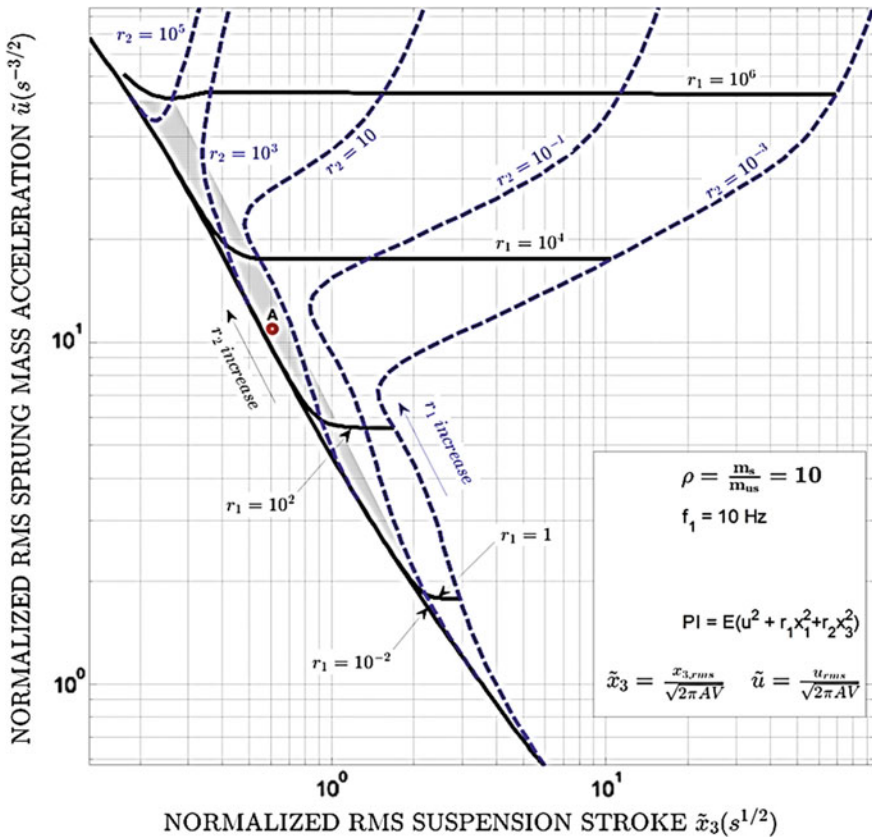


**Fig. 15** Optimal normalized sprung mass acceleration versus rattlespace trade-offs for quarter-car, 2 DoF vehicle model

unhindered activities such as reading, texting, writing and similar, the proposed suspension should deliver best possible ride quality within given design constraints during a typical commute at nominal speed of  $V = 80$  ft/s (88.5 km/h) on a road characterized by road roughness coefficient of  $A = 1.6 \times 10^{-5}$  ft ( $4.9 \times 10^{-6}$  m).

The design constraints are that the rms tire deflection should remain bounded within 1 in. (2.54 cm) from static equilibrium value 99.7% of time, and that the rms of suspension deflection (rattlespace) should remain bounded within 3 in. (7.62 cm) from its static value 99.7% of time. What would be the best possible i.e. the lowest rms acceleration in this case based on the above quarter-car model with  $f_1=10$  Hz,  $\rho = 10$ , and assuming that the road input is characterized by a Gaussian distribution? How realistic is the resulting closed-loop design in terms of underlying dynamics, stability, robustness and bandwidth requirements?

We start by normalizing different constraint variables so that we can then use the global optimal plots of Figs. 15 and 16. Since for most on-road operations the tire (wheel-hop) constraint is more stringent than the rattlespace counterpart we first

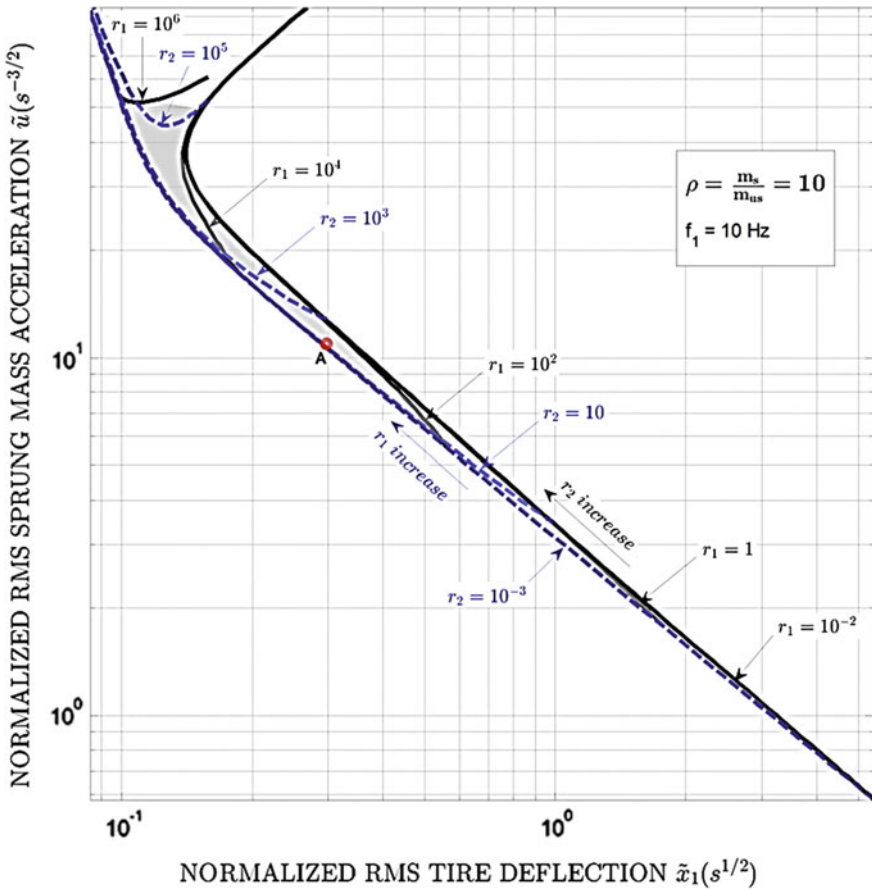


**Fig. 16** Optimal normalized sprung mass acceleration versus tire deflection trade-offs for quarter-car, 2 DoF vehicle model

explore the limiting case of  $x_1$ . The Gaussian assumption and 99.7% time requirement (i.e. the well-known  $3\sigma$  rule) imply that the rms tire deflection must be less than 1/3 in. or 0.85 cm. The normalized rms tire deflection for the above speed and road then must remain within

$$x_{1,rms,norm} < 0.31 \text{ s}^{1/2} \quad (33)$$

Choosing the above as the limiting value we proceed to Fig. 16 from where we obtain the corresponding limiting i.e. smallest possible normalized rms acceleration

$$u_{rms,norm} \approx 10 \text{ s}^{-3/2} \quad (34)$$

Choosing  $u_{rms,norm} = 10.9 \text{ s}^{-3/2}$  results in only 3%g rms acceleration. This particular candidate design is indicated as point A<sub>1</sub> in Fig. 16. Note that this level of rms acceleration is at the lowest r.h.s. end of the scale used for subjective tests in Fig. 3 thus securing highest level of ride comfort.

At this stage we need to check if the rattlespace constraint has been satisfied. To this end we enter the value of  $10.9 \text{ s}^{-3/2}$  into the vertical, normalized rms acceleration axis on Fig. 15 from where, for the aforementioned design point A, we get the normalized rms rattlespace value as

$$x_{3,rms,norm} = 0.605 \text{ s}^{1/2} \quad (35)$$

which then results in actual rms value of only 0.67 in. implying  $3\sigma$  value of 2 in. (5.08 cm). This is well within the required  $\pm 3$  in. constraint thus showing that the most critical constraint in the present example is on tire deflection and related road holding and handling. As indicated earlier, this is usually the case with most on-road operating situations.

For the above design A we can next determine from Fig. 15 the associated PI weights

$$r_1 = 1100, \quad r_2 = 100 \quad (36)$$

With these values one can then obtain the optimal control gains

$$k_1 = 6.084, \quad k_2 = -0.548, \quad k_3 = 10.0, \quad k_4 = 4.438 \quad (37)$$

so that the closed loop system eigenvalues become

$$\epsilon_{1,2} = -2.2 \pm j2.26, \quad \epsilon_{3,4} = -2.75 \pm j62.9 \quad (38)$$

Note that the first set of eigenvalues corresponds to the well-damped oscillatory mode associated with vehicle sprung mass heave or vertical vibration. It is characterized by a natural frequency of only 0.5 Hz with the damping ratio of 0.7, which by now should be well known from our previous 1DoF “skyhook” study (it will be shown later that this 0.7 ratio is also LQ-optimal for vehicle models of higher dimensions, i.e. 2D and 3D models). The relatively low natural frequency of 0.5 Hz falls significantly below most of current vehicle suspensions and is an indication of an overall “softer” suspension setting.

The second oscillatory mode corresponds to the wheel-hop dynamics. It is characterized by natural “wheel-hop” frequency of 10 Hz, and relatively small damping ratio of only 4.4%. Whether this small amount of wheel-hop damping will be sufficient will depend on the operating conditions, particular adaptive optimal control strategy used, and similar factors. For example, this may be acceptable while driving on the long straight stretches of the road where handling may be less critical. On the other hand driving on winding stretches of the road may require much higher wheel hop damping and thus an optimal control strategy that will

adapt to different driving conditions, as needed. We will address this—along with some possible hardware i.e. structural modifications—in more detail in subsequent sections.

Before closing this illustrative example let us summarize how we answered the original inquiries. First, we have succeeded to quantify what is the best possible ride comfort level within given design constraints. Moreover, we have obtained some insight about the resulting closed-loop system dynamics. While stable it did display some potential issues and challenges such as robust containment of relatively low wheel-hop damping. The latter may have to be addressed through software and possibly hardware means, as we will discuss later.

Finally, a word of caution regarding bandwidth requirements of the resulting closed-loop system. On the first glance, based on the above system eigenvalues it would appear that the bandwidth requirements on the actuator force production would extend to 10 Hz and more. However, such relatively high-bandwidth systems can be challenging to implement in practice since they tend to negatively influence so-called “secondary ride” i.e. they tend to transmit high frequency road induced disturbances. This also points out to the fact that force-related bandwidth requirements are only part of the story. Indeed, even if we were required to keep the actuator force constant and equal to vehicle weight (for “bestest” possible ride with zero acceleration) i.e. if we were asked for zero force bandwidth, this task would by no means be trivial due to the fact that our actuator mounting points are subject to constant motion and road-induced disturbance. Some of these important design-related issues will be discussed later and some are beyond the scope of this system-level study at the left-top end of System V diagram of Fig. 2.

**Passive suspension comparison.** It can be shown (Smith and Walker 2000) that the above optimal suspension strategy requires an active device, which is to be expected based on our previous 1DoF results. At this stage it is appropriate to ask how does this active suspension (Fig. 8a) compare with a conventional passive counterpart from Fig. 8c. This is shown in Fig. 17, which focuses on the more critical constraint i.e. tire deflection versus sprung mass acceleration trade-off. For simplicity we show only the limiting curves for  $r_1 \cong 0$ , and  $r_2 \cong 0$ . Superimposed on the figure are traces of passive suspension performance trade-offs for heave mode natural frequencies between 1 and 1.5 Hz, and damping ratios varying between 0.02 and 1.

From Fig. 17 it can be seen that the best passive suspension setting—in terms of present trade-offs between smooth ride and firm handling—corresponds to point  $P_1$  with natural frequency of 1 Hz and damping ratio of 0.3. The latter is typically in the range seen on most conventional vehicles that have been optimized through many generations of iterative work primarily based on experience and intuition. In addition, it can be seen that the best active setting for the same amount of tire deflection corresponds to point  $A_1$ , which is only 11% below the passive counterpart in terms of rms acceleration. Thus if one focuses at only this narrow region (as was the case with prior investigations by some authors) then one would conclude that there is not much potential in active suspensions, especially taking into

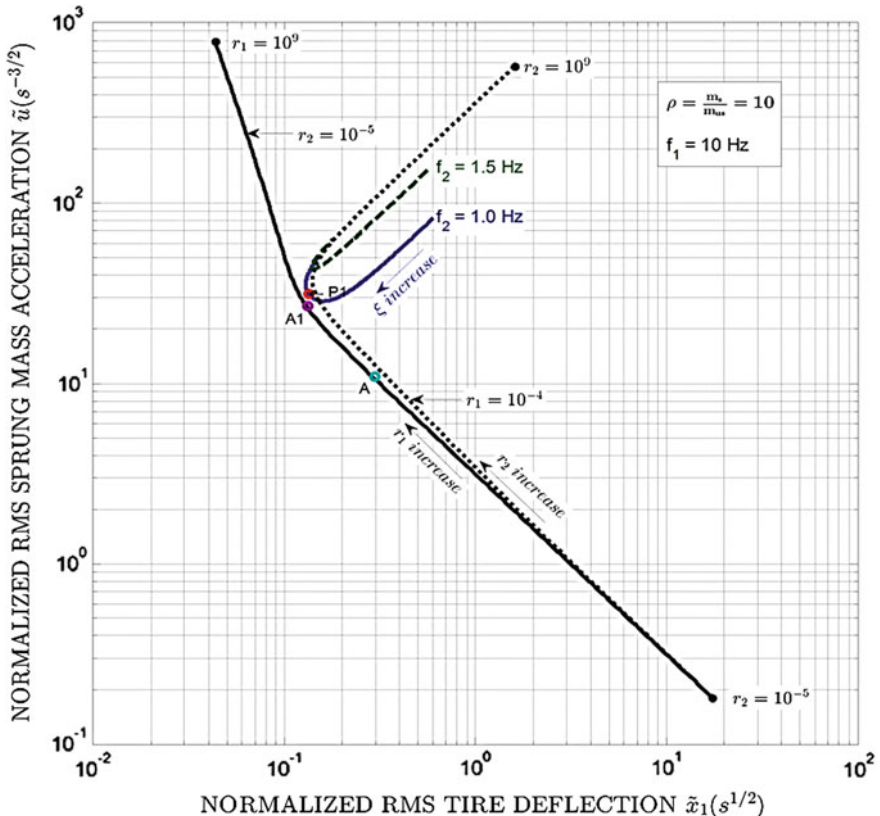


**Fig. 17** Comparison between conventional passive suspension (point P<sub>1</sub>) and optimal active counterparts (points A<sub>1</sub> and A) in terms of ride and handling trade-offs

account that most likely the results of the present simplified high-level study constitute upper bounds of best possible performance.

However, one inherent advantage of active suspensions is that they can adapt to different road/driving conditions so that different control settings can be used on different stretches of the road. In other words, we could move either to the right or left of point A<sub>1</sub> in Fig. 17. Thus on the long straight stretches of a highway, such as exist in Nevada, for example, one could relax the settings to mimic a soft suspension with very smooth ride thus moving to the right of point A<sub>1</sub>. This is shown as point A, which corresponds to our Illustrative Example design. Note that in this case there is a 67% reduction in rms acceleration when compared with the passive case P<sub>1</sub>. According to Fig. 3, such as large reduction can lead to substantial improvement in subjective ride comfort ratings.

Alternatively, on winding roads one can go for much firmer suspension settings for superior road holding and handling. In this case one would move to the left of point A<sub>1</sub> trading improved vehicle agility for reduced ride comfort. This is not

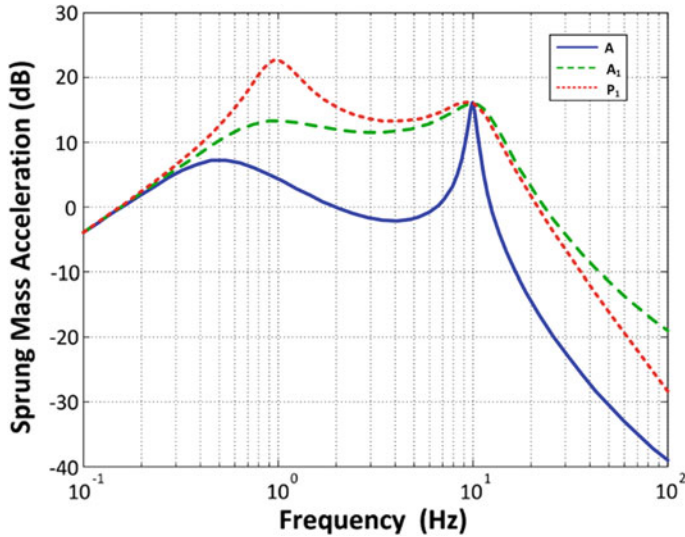


**Fig. 18** Frequency response function of sprung mass acceleration versus ground input velocity for passive and active suspensions from Fig. 17

possible for passive suspensions, which cannot move much farther to the left from point  $P_1$ .

We will next extend our comparison to Frequency Transfer Functions (FTF) between the above three design cases,  $A_1$ ,  $P_1$ , and  $A$ . This is shown in Figs. 18, 19 and 20 for the three PI metrics of primary interest, sprung mass acceleration, tire deflection and suspension stroke, respectively. By associating the rms values of these quantities with the area under different frequency response curves we can clearly see from Fig. 18 that design  $A$  will lead to much smaller rms acceleration. On the other hand from Figs. 19 and 20 we can also see that this design results in a large resonant peak at the tire natural frequency, which will lead to increased wheel hop. This is in accordance with our previous observation that the design  $A$  will result in relatively small wheel-hop damping. From the above FTF's we can make the following additional observations as given in the following paragraph/subsection.

**Invariant Points (IP).** Turning our attention back to Fig. 18 it can be seen that both active suspension settings  $A$  and  $A_1$ , do a good job in reducing the acceleration levels around the dominant, sprung mass heave mode of oscillations in the neighborhood of 1 Hz. However, this is not the case with the second oscillatory mode around the wheel hop frequency of 10 Hz where all three transfer functions seem to pass through the same point. Indeed, it turns out that this is exactly an invariant point for our original quarter-car structure. This was first observed by Thompson (1971) and then extended by Hedrick and Butsuen (1990) to include an additional invariant point at the frequency corresponding to the case of locked secondary suspension i.e. sprung and unsprung masses vibrating in synch on a tire

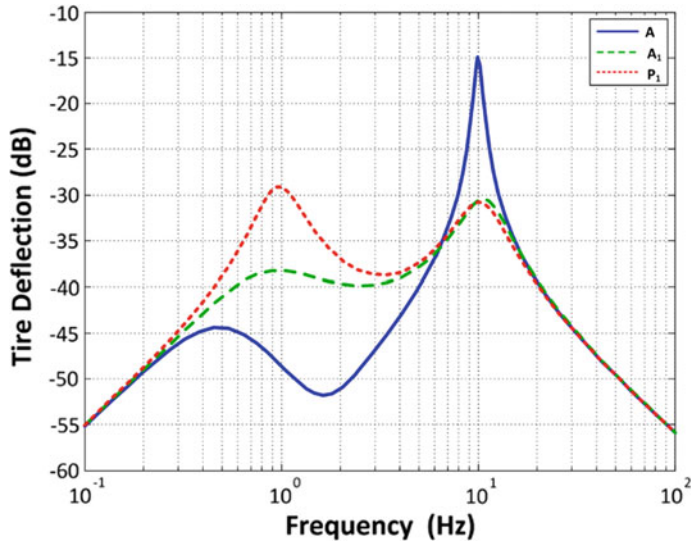


**Fig. 19** Frequency response function of tire deflection versus ground input velocity for passive and active suspensions from Fig. 17

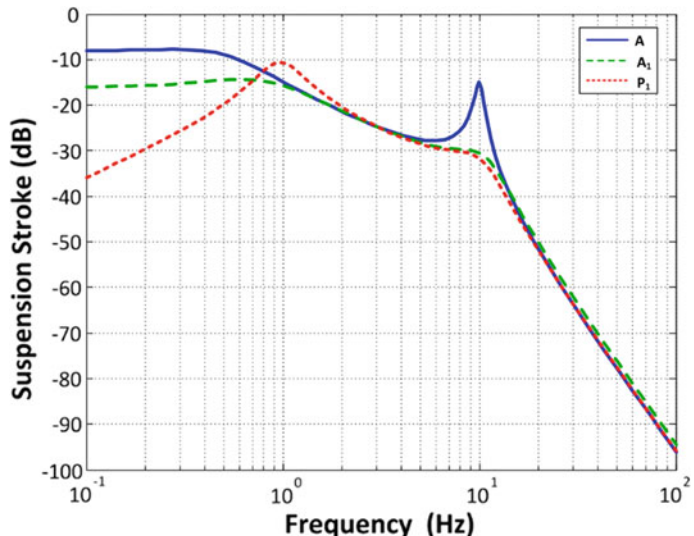


**Fig. 20** Frequency response function of suspension stroke versus ground input velocity for passive and active suspensions from Fig. 17

spring. This can be seen from the following equations where we start with the original set of four state Eqs. (28–31). Summing up second and fourth equation we get the overall momentum-like equation for the two-mass subsystem

$$m_s \frac{dx_4}{dt} + m_{us} \frac{dx_2}{dt} = -k_t x_1 \quad (39)$$

By defining (absolute) displacements of sprung and unsprung masses as  $x_s$  and  $x_{us}$ , and substituting  $x_{us} = x_1 + \int w dt$  in the above equation, the corresponding Laplace transform becomes

$$m_s s X_4(s) + (k_t + m_{us} s^2) X_1(s) = -m_{us} s W(s) \quad (40)$$

Dividing the above equation by road velocity Laplace transform quantity,  $W(s)$ , and defining the three transfer functions associated with the PI acceleration, rattlespace, and tire deflection metrics as

$$G_A(s) = \frac{s X_4(s)}{W(s)}, \quad G_R(s) = \frac{X_3(s)}{W(s)}, \quad G_{TD}(s) = \frac{X_1(s)}{W(s)} \quad (41)$$

after dividing with  $W(s)$  and setting  $s = j\omega$ , we can rewrite the above equation as in Hedrick and Butsuen (1990)

$$m_s G_A(j\omega) + (k_t - m_{us} \omega^2) G_{TD}(j\omega) = -m_{us} j\omega \quad (42)$$

From this equation we can conclude that at the wheel hop natural frequency  $\omega_1 = \sqrt{k_t/m_{us}}$  the sprung mass acceleration transfer function,  $G_A$ , has an invariant point equal to

$$G_A(j\omega_1) = -j \frac{\sqrt{m_{us} k_t}}{m_s} = -j \frac{\omega_1}{\rho} \quad (43)$$

which, for our case with  $\rho = 10$ ,  $f_1 = 10$  Hz, is equal to  $j 2\pi$ . The corresponding gain or magnitude of  $G_A$  is  $2\pi$  or  $15.97$  dB  $\approx 16$  dB (cf. Fig. 18).

Using similar kind of manipulations starting with the above Eq. (39) but this time substituting  $x_s = x_{us} + x_3$ , we end up with the following equation

$$-m_s \omega^2 G_R(j\omega) + [k_t - (m_s + m_{us}) \omega^2] G_{TD}(j\omega) = -(m_{us} + m_s) j\omega \quad (44)$$

From this equation we see that there is now an invariant point at

$$\omega_2 = \sqrt{k_t / (m_{us} + m_s)} = \omega_1 / \sqrt{\rho + 1} \quad (45)$$

where the rattlespace or suspension deflection transfer function,  $G_R$ , has the following constant value

$$G_R(\omega_2) = j \frac{(m_{us} + m_s)}{m_s \omega_2} = j \frac{\rho + 1}{\rho \omega_2} \quad (46)$$

For our case with  $\rho = 10$ ,  $f_1 = 10$  Hz, we have  $\omega_2 = 2\pi 3.02$  and corresponding gain of  $G_R$  is 0.058 or  $-24.7$  dB (cf. Figure 20). As mentioned previously the above invariant point frequency  $\omega_2$  corresponds to natural frequency of a combined sprung and unsprung mass oscillating on tire spring; it is typically in the range between 3 and 5 Hz.

Based on Eqs. (42) and (44) it was observed by Hedrick and Butsuen (1990) that once one of the above three transfer functions is specified the other two follow from the constraint equations. For example, choosing  $G_A(s)$  then implies that  $G_{TD}(s)$  follows from Eq. (42), which in turn fixes  $G_R$  via (44). A physical interpretation of the above invariance is that within the given quarter-car structure of Fig. 8a we observe that a single suspension actuator placed in-between sprung and unsprung masses is asked to perform conflicting tasks of minimizing sprung mass acceleration for improved ride comfort while at the same time providing adequate wheel hop damping and road holding. It should be pointed out that the above invariances and related limitations hold independent of the particular suspension type—passive, active or semi-active—or control strategy used, as long as the fundamental mechanical structure remains the same.

### 3.3 Comparison Between 1DoF and 2DoF Cases

In order to put the above results into proper perspective we next try to compare the two basic active suspension cases studied so far: the simple 1DoF configuration of Fig. 7 and the 2DoF case from Fig. 8a. To this end we overlay the 1DoF optimal trade-offs over the corresponding 2 DoF results as shown in Fig. 21. From this figure we can make two observations. From the lower right side we can see that for the most part the optimal 1 DoF case results are significantly better i.e. below the 2 DoF trade-offs. This is to be expected since the 2 DoF problem introduced one more constraint—tire deflection—that should then lead to less favorable outcome.

On the other hand from the upper left side we see that in some areas the reverse is true i.e. the 1 DoF performance appears even worse than the 2 DoF case! The reason for this apparent discrepancy is that we are not actually comparing apples to apples since on the horizontal axis we are comparing total deflection between sprung mass and ground of the 1 DoF system with the deflection between sprung and unsprung masses of a 2 DoF system. As the rattlespace constraint becomes more and more stringent i.e. as the suspension becomes more and more stiff the advantage of the 2 DoF structure becomes more pronounced due to the ameliorating effects of primary suspension i.e. due to more pronounced contribution from tire deflection.

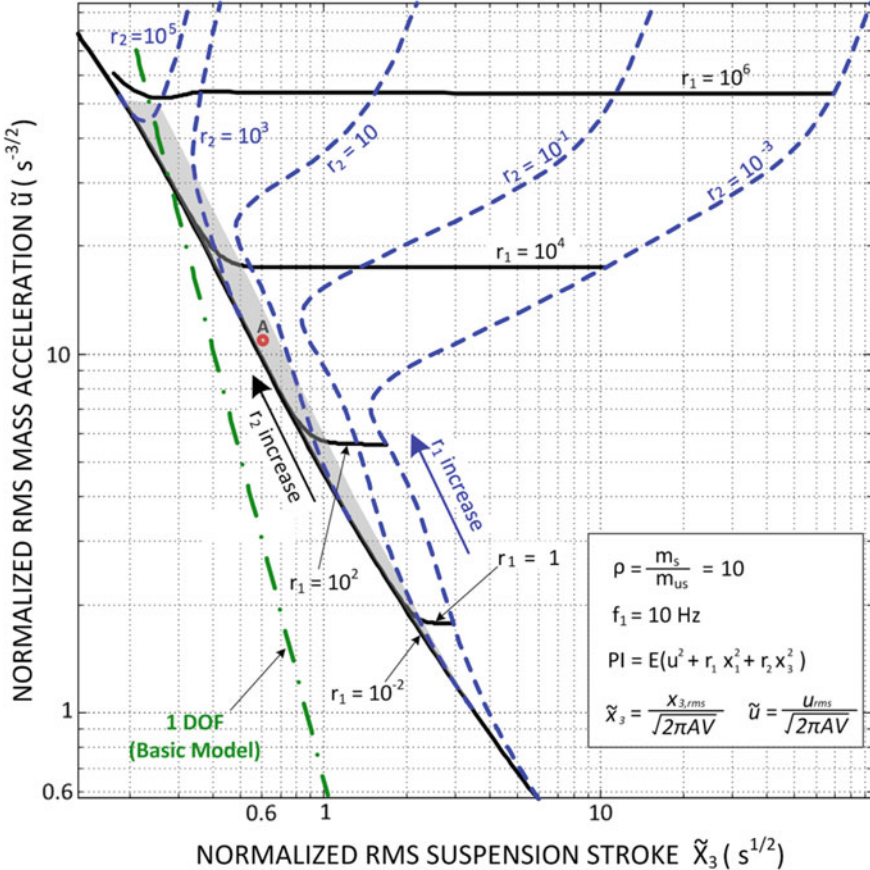


**Fig. 21** Comparison between “basic” 1DoF and 2DoF optimization trade-offs

To rectify this situation and facilitate more appropriate (apples-to-apples) comparison, we introduce a modified 1 DoF model shown in Fig. 8b. It is a limiting case of standard 2 DoF model with unsprung mass reduced to zero. The corresponding optimal trade-offs are shown in Fig. 22, where we can now see—as one would expect—that the upper left side of the plot is close to and below the corresponding 2 DoF line. At the same time the lower right side approaches and merges with the previous “standard” 1 DoF case optimal trade-offs.

The observation that this optimal structure with vanishing unsprung mass,  $m_{us} = 0$ , offers superior performance w.r.t. corresponding 2 DoF counterparts is logical consequence of the fact that reduced unsprung mass for a given sprung mass, i.e. larger  $\rho$ , leads to improved performance trade-offs as shown by Hrovat (1988), for example. In the context of the present problem the new 1 DoF structure can be seen as limiting case of 2 DoF model as unsprung mass becomes smaller and smaller. Another observation from the lower right side of the plot is that for most operations where good ride is of

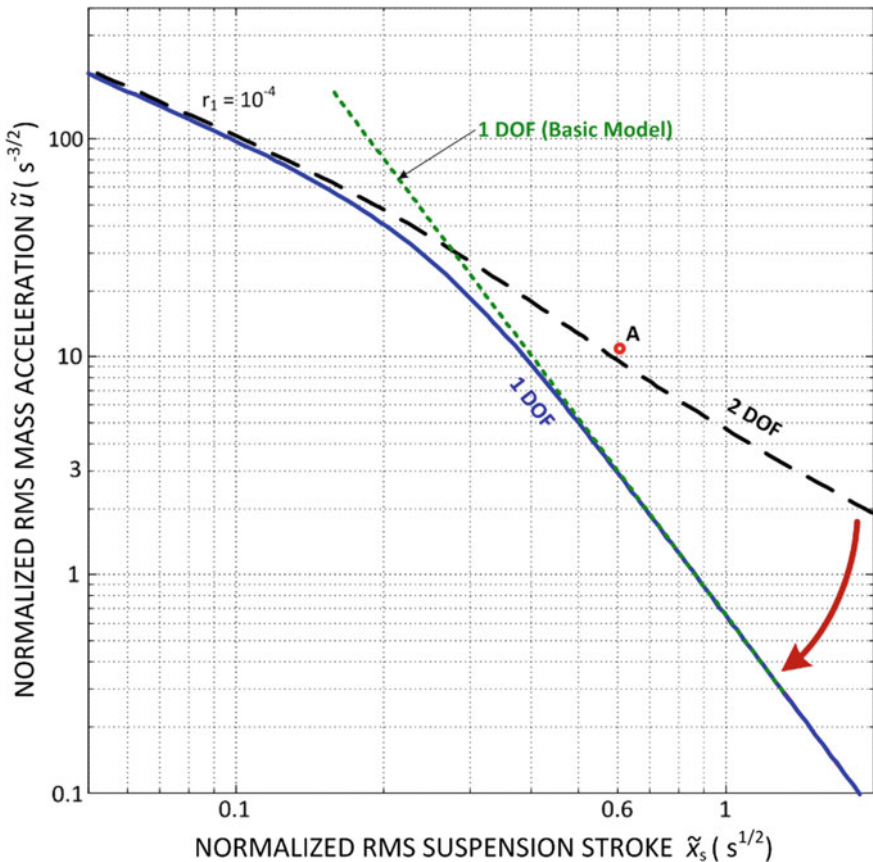


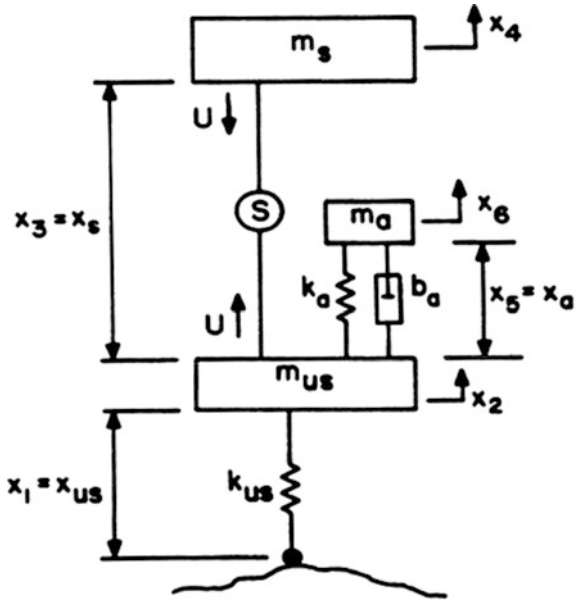
**Fig. 22** Comparison between 2DoF and various 1DoF optimization trade-offs

primary concern, we see that there is a significant loss of performance associated with the 2 DoF models, which is primarily due to the additional, wheel-hop imposed constraint.

### 3.4 Dynamic Vibration Absorber

At this stage it would be natural to inquire how we could recover some of the above lost performance and thus sway the optimal trade-offs in the direction of the arrow in Fig. 22. To address this inquiry we know from the Invariant Points (IP) discussion that this will not be possible within the given 2 DoF structure of Fig. 8a. Thus the answer should be pursued through structural i.e. hardware modification. One logical candidate to consider is tuned mass damper or Dynamic Absorber (DA).

**Fig. 23** Quarter-car 2DoF vehicle model with dynamic vibration absorber (DA)



As we know from the IP subsection, one of the most critical invariant points is at the wheel-hop frequency and associate pronounced resonant peak due to relatively low damping in this mode. Thus, if we could increase this damping *without* negatively influencing sprung mass accelerations we may achieve our goal. This leads us to the modified quarter-car configuration (3 DoF system) shown in Fig. 23 where we use a DA tuned to wheel-hop frequency to alleviate the above issue i.e. increase wheel hop damping without simultaneously increasing sprung mass acceleration. The DA mass was chosen as one tenth of the unsprung mass and corresponding DA damping ratio was chosen as 0.2.

The results of this global study are shown in Figs. 24 and 25. As it can be seen, the DA effectively sways the optimal trade-offs toward the corresponding 1 DoF case, which is especially pronounced in the case of acceleration versus rattlespace trade-off in Fig. 24. This means that with the help of DA, our original smooth ride design point A with very lightly damped wheel-hop mode now transform to point A', where based on Figs. 24 and 25 we can see that both the sprung mass acceleration and tire deflection are further reduced resulting in improved ride comfort *and* handling. From these figures we can conclude that further substantial improvements are possible up to the point where now rattlespace constraint becomes the limiting factor. For example, for design point A'' we see that suspension deflection requirement is the same as for the previous design case A while tire deflection and especially sprung mass acceleration are both reduced.

At this stage to put all this into broader perspective and gain additional insight into DA benefits, it is appropriate to compare performance of the above designs A and A' with design case A<sub>1</sub> and related passive case P<sub>1</sub> discussed in Sect. 3.2

**Fig. 24** Impact of dynamic absorber on ride versus rattlespace trade-offs (Hrovat 1997)

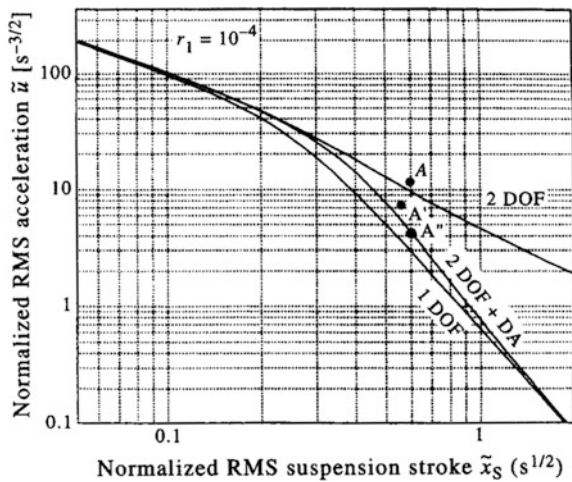
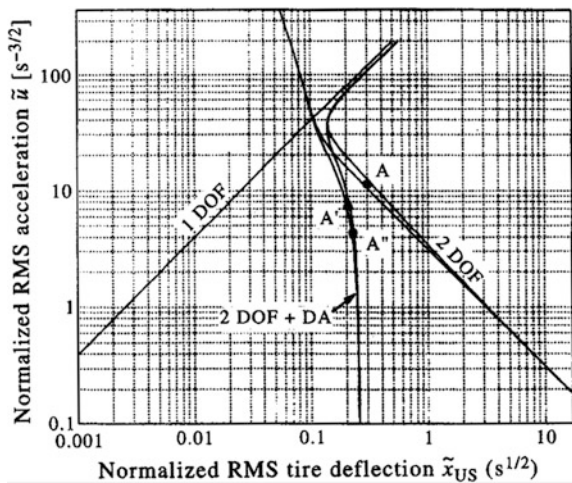


**Fig. 25** Impact of dynamic absorber on ride versus handling/tire deflection trade-offs (Hrovat 1997)



(also see Fig. 17). The corresponding frequency response curves are given in Figs. 26 and 27, which show sprung mass acceleration and tire deflection gain transfer functions, respectively. From Fig. 26 we see that for all three cases,  $P_1$ ,  $A_1$ , and  $A$ , the sprung mass accelerations pass through the invariant point at the wheel-hop frequency of 10 Hz. However, for case  $A'$ , which includes a DA, we see that the invariant peak at 10 Hz has been substantially reduced (by more than 10 dB). This demonstrates that structural changes introduced by DA eliminate this important and detrimental quarter-car constraint. At the same time, from Fig. 27 it can be seen that the strong resonant peak in tire deflection at 10 Hz has been substantially reduced when compared with the soft case  $A'$  with the potential for further reduction at the resonant peak but at the expense of more narrow notch. All

**Fig. 26** Frequency response function of sprung mass acceleration versus ground input velocity for passive and active suspensions with and w/o DA

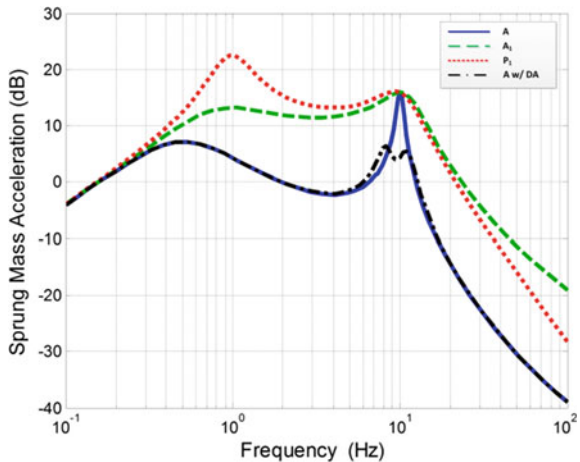
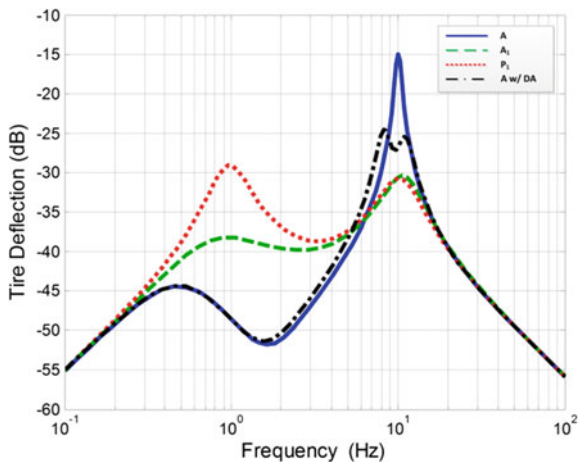


**Fig. 27** Frequency response function of tire deflection versus ground input velocity for passive and active suspensions with and w/o DA



those considerations can also be seen in related time responses where excessive oscillations of the soft suspension case A' have been contained with the help of DA.

The above study demonstrates significant potential benefits of dynamic vibration absorbers. Their main drawback is added weight and more challenging packaging requirements. To date there has been only one widespread, production application of the DA concept. This was implemented in the highly popular Citroen 2CV (sub)compact vehicle that was legendary for its supreme ride, especially for such a small vehicle. According to the June 1987 *Car* magazine article, the 2CV ride was characterized by the following statement, “You will be enjoying the scenery on top of a chassis which, in terms of small car terms, has no peer in ride comfort.”

In closing this section we observe that we did not re-optimize the total 3 DoF system with the DA included. This would lead to further improvements at the

expense of increased complexity since we would be feeding back six states instead of four. Additional refinements are possible by optimizing combined or “hybrid” system consisting of an active actuator and DA with free design parameters (DA mass, damping, stiffness). One could also contemplate an active or at least SA dynamic vibration absorber as proposed by Hrovat (1990). We will later focus on the ultimate i.e. best possible quarter car configuration in the sense of LQG-optimal performance. But first let us introduce an interesting mechanical element that shares some (but not all of) characteristics of dynamic vibration absorber.

### 3.5 Inerter and DA Comparison

Inerter was introduced by Smith (2002) as a mechanical device where inertia-like force is proportional to the *difference* of two accelerations across the device terminals shown in the insert of Fig. 28, i.e.

$$F = M_{\text{eff}} \frac{d(v_L - v_R)}{dt} \quad (47)$$

where  $M_{\text{eff}}$  stands for the effective (linear) inertia due to reflected inertias of the inner rotational masses within the inerter of Fig. 28, and  $v_L$  and  $v_R$  stand for the corresponding left and right terminal velocities, respectively. Note that, in terms of bond graphs, the above device is a one-port with two distinct terminals. Further generalization of this interesting concept might be possible in the form of a two-port

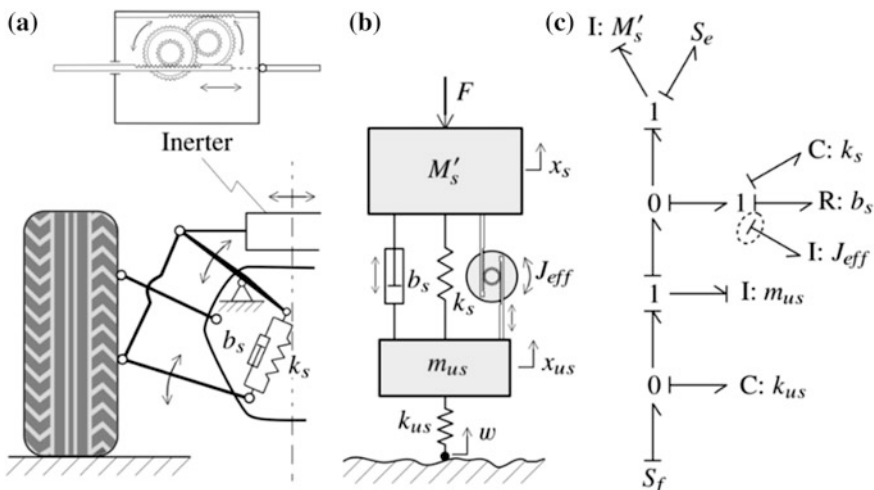


**Fig. 28** Race-car suspension with an inerter: schematic diagram (a); equivalent quarter car schematic (b); and corresponding bond graph (c)

that represents inertia-coupling that is characteristic of planetary transmissions, for example (Hrovat et al. 2000).

It can be said that inerter is in part similar to the more common inertia element where inertia force is proportional to the acceleration of the inertia element or derivative of the associated momentum (Karnopp et al. 2012). Indeed, by grounding one of the two terminals we end up with a standard inertia element.

It is interesting that the (generalized) inerter elements were present for quite some time in different mechanical and hydraulic systems such as differentiators, planetary gears, engine mounts, and hydraulic suspensions, for example. This can also be seen from corresponding bond graphs where inerters can be revealed through non-trivial attachments of inertia elements to a zero junction, where the latter indicates a difference of two speeds or generalized flows (Karnopp et al. 2012; Karnopp and Rosenberg 1970; Hrovat et al. 2000). While some of them may not satisfy somewhat restrictive requirements originally postulated in Smith (2002) they are certainly very useful as demonstrated through millions of vehicles and other devices. In any case, Smith deserves credit for explicitly identifying and promoting this somewhat ubiquitous yet “hidden” structural component, and at the same time devising an interesting practical mechanical inerter device that has found significant applications in the car-racing arena.

The device is sketched in Fig. 28 in the context of a racecar application. Based on available information (Clarke 2012; Smith 2011; Scarborough 2011) the setup seems to consist of a standard mechanical spring and damper configuration augmented with a black-box device placed across the left and right side of a vehicle front suspension elements or rockers. Assuming that the black box device is an inerter without additional internal components and assuming symmetrical road inputs at the left and right side of a vehicle an equivalent quarter car representation and corresponding bond graph model are shown in Fig. 28b and c, respectively.

From the bond graph it can be seen that in this particular case the inerter is represented by an inertia element in differential causality (Karnopp et al. 2012). However, this may not always be the case. For example, inserting an additional spring in series with the current C-R-I suspension setup would remove this constraint. Based on the bond graph of Fig. 28c, it can be deduced that the sprung and unsprung masses effectively act in series with the inerter with the reflected inertia,  $J_{eff}$ . This can be seen directly from the bond graph due to the corresponding 0-junctions.

In reference (Smith 2002) it is shown that under certain conditions the inerter-based suspension structure can produce notch filter-like effect similar to tuned mass dampers or dynamic vibration absorbers (DA). Specifically, this was demonstrated for a single mass case where such mass has been supported by a vibration absorption-type suspension consisting of a parallel combination of inerter and spring, which were in turn placed in series with a parallel combination of another spring and a damper. The underlying assumption was that the mass is subject to the base input oscillations with strong single-component frequency content. It was then shown that by tuning the inerter-spring combination to this

input frequency one could achieve complete disturbance cancellation comparable to similarly tuned DA.

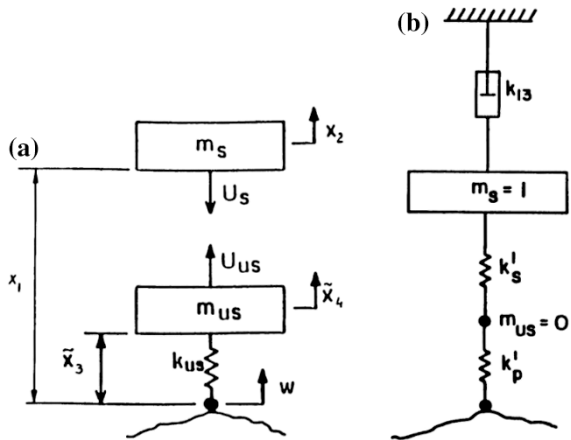
According to available literature the inerter was used to improve wheel adherence to the track with Formula 1 racecars although the quantitative extent of this improvement was not given. It is interesting that a DA-type device used by a competing team was not allowed by the Formula 1 governing body although the effects were apparently similar (Clarke 2012; Scarborough 2011). It is possible that this was due to lack of full understanding of how these two devices operate in the context of car racing.

While there was strong similarity between inerter-based and DA-based vibration isolation in the case of single mass exposed to base oscillation, this similarity seems to break down in the case of a 2DoF quarter car configuration. In particular, note from Fig. 28 that the inerter, as a one-port device, imposes equal forces on the sprung and unsprung masses so that the Invariant Point constraint at the critical wheel-hop frequency still applies (it is interesting that in the case of no system damping this IP constraint reduces to a singularity). This is fundamentally different from the DA structure of Fig. 23. Consequently it is expected that the quarter-car performance will not improve to the degree seen with the DA. Indeed, the available publications (Smith and Wang 2004; Papageorgiou and Smith 2006; Scheibe and Smith 2009) seem to confirm this, although they were based on somewhat localized studies where only one or maximally two attributes were considered at the time. Further extensions could include jerk as component of ride comfort, although this may disadvantage inerter-based suspensions due to their inherent inertia-like effects and potentially less favorable high-frequency roll-off.

### ***3.6 Best Possible Quarter-Car Performance and Related Structure***

Based on encouraging results with DA-enhanced quarter-car structure it was natural to look into different possible extensions and variations of this concept in a search toward best possible quarter-car performance. To this end reference (Hrovat 1990) investigated potential benefits of augmenting the conventional, passive tuned mass damper or DA with an additional active actuator acting in-between the DA and unsprung mass. This lead to up to 35% lower sprung mass acceleration and 26% lower tire deflection w.r.t. previously mentioned LQ optimal case A" with passive DA—see Figs. 24 and 25. At the same time the suspension stroke or rattlespace excursions have been kept almost the same in all cases. Similar results were obtained for the configuration where only the DA-equivalent mass was kept without the accompanying spring and damper so that only an active “unsprung” actuator was used to suspend the DA-equivalent mass. However, the required active actuator energy and force were significantly higher in this case thus confirming the usefulness of a full DA structure even when augmented by an active actuator attached to the DA mass.

**Fig. 29** Formulation of optimal 2DoF two-actuator problem (a), and corresponding best possible, optimal structure (b)



Observing that significant additional benefits in performance resulted from having unequal forces acting upon sprung and unsprung masses facilitated by the DA-like structure, we now pose the following optimization problem as an extension of the previous analysis. The problem setting is illustrated in Fig. 29a. This time we are considering two independent actuators—one acting upon the sprung mass and the other on the unsprung counterpart. Note that while in the previous DA-based setting we were limited how much force could the unsprung actuator impose due to limiting motion capabilities of the DA mass, this sort of constraint is not imposed now.

In addition we make use of the fact that there is a natural two time-scale separation associated with quarter-car problem, where the slow mode corresponds to the sprung mass oscillatory mode around 1–2 Hz and the fast mode corresponds to unsprung mass wheel-hop mode around 8–12 Hz. Anticipating this separation we structure the states as shown in Fig. 29a. The associated PI then has the same three components (weighted means square of sprung mass acceleration and tire and suspension deflection) as before with an additional term penalizing the unsprung force

$$\text{Minimize}_{w.r.t. u_1, u_2} \left[ PI = E \left( u_1^2 + r_1 x_3^2 + r_2 (x_1 - x_3)^2 + r_3 u_2^2 \right) \right] \quad (48)$$

where  $u_1$  is the sprung mass acceleration equal to  $U_s/m_s$ , and  $u_2$  corresponds to normalized unsprung force, i.e.  $u_2 = U_{us}/m_{us}$ . Now letting the penalty  $r_3$  on normalized unsprung force be very small one ends up with the so-called (partially) cheap controls (Saberi and Sannuti 1987). In the process we can think of the cheap control  $u_2$  as an essentially “structure optimizer”. Eventually letting  $r_3$  go toward zero and transforming the cheap control problem to an equivalent singular perturbation problem we end up with the optimal structure depicted in Fig. 29b (Hrovat 1990).

Note that the structure optimizer  $u_2$  was used to effectively eliminate the unsprung mass, which is in accordance with the established fact that reduced unsprung mass helps the overall ride and handling performance (Hrovat 1988). This was also confirmed by our previous analysis from Fig. 22 comparing the optimal 2 DoF and 1 DoF performances. In addition, the structure optimizer i.e. cheap and fast control adjusts the incremental stiffness of primary and secondary suspensions to best accommodate the respective weights  $r_1$  and  $r_3$ , thus resulting in the best possible performance. Once the wheel hop mode has been so contained the sprung mass control  $u_1$  can then be used to contain the slow, sprung mass mode according to the well-known 1 DoF LQ-optimal rules with skyhook damper and an overall damping ratio of 0.7.

The above “most” optimal quarter-car structure results in additional substantial benefits. An illustrative example from Hrovat (1990) shows normalized sprung mass acceleration of only  $1.17 \text{ s}^{-3/2}$ , with well-contained tire and suspension deflections. While it would be difficult to realize such a suspension in practice (e.g. it may require very powerful jets on each, sprung and unsprung masses) these limiting results can serve as a benchmark of best possible performance that any practical suspension realization can be compared against. It also confirms our previous results and intuition about the superiority of a simple 1 DoF structure in the context of a quarter-car vehicle models.

As a final remark in this section we mention that we could also pose the question what is the best possible passive two-port suspension setup as a counterpart to the active setting from Fig. 29a. To this end one could follow similar approach based on passive network optimization and synthesis that was elegantly done in Papageorgiou and Smith (2006) for the case of passive one-port suspension structures. It is expected that some portions of such a two-port extension would contain DA-like components. Further optimal passive extensions could include cross-coupling between left and right as well as front and rear sides of a vehicle, such as can be seen in so-called interconnecting or equalizing-type suspensions first found on Citroen 2 CV (Pevsner 1957), which was well-known for its smooth ride.

### 3.7 2D, Half-Car Models

Since we have pretty much exhausted various quarter-car optimization scenarios the next logical step is to consider the half-car models and related LQ optimization. We start with 2 DoF half-car model shown in Fig. 30. It includes vehicle heave and pitch modes.

This is reflected in the following performance index

$$PI = E \left[ r_1 (d^2 z / dt^2)^2 + r_2 (d^2 \Theta / dt^2)^2 + r_3 z_f^2 + r_4 z_r^2 \right] \quad (49)$$

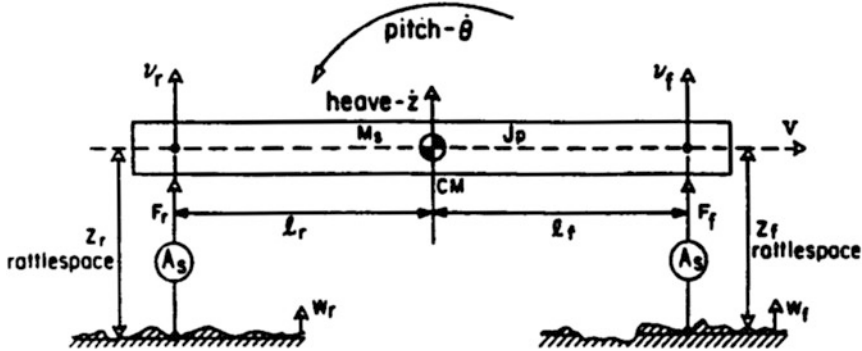


**Fig. 30** Half-car, 2D vehicle model with 2DoF (heave and pitch)

where different quantities have been defined w.r.t. Fig. 30 with  $z_f$  and  $z_r$  standing for the front and rear suspension rattlespace—in the present case where we did not include the unsprung masses, this is the distance between the ground and front and rear end of the sprung mass. Note that this PI could be slightly modified to explicitly include the acceleration at a specific position such as driver's or some (VIP) passenger's seat, for example.

Optimization of the above PI under four state equations representing the simplest possible 2D, Half-car model has been done in Krtolica and Hrovat (1992). It is interesting that in this case it was still possible to analytically solve the LQ optimal problem. The resulting closed-loop control system was again characterized by the optimal damping ratio of 0.7 in both heave and pitch modes. The same reference establishes necessary and sufficient conditions to decouple the original two-dimensional, 2 DoF, half-car LQ optimization problem into two one-dimensional, 1 DoF, quarter-car problems; these conditions are

$$\begin{aligned} M_s \cdot l_f \cdot l_r &= J_p \\ r_1 \cdot l_f \cdot l_r &= r_2 \end{aligned} \quad (50)$$

where  $M_s$  and  $J_p$  are vehicle sprung mass and pitch moment of inertia about the center of mass, CM, and  $l_f$  and  $l_r$  are front and rear distances from CM (see Fig. 30). The first condition depends on vehicle physical parameters and is typically satisfied within 20% by most present vehicles. The second condition depends on the PI weighting parameters  $r_1$  and  $r_2$ , which are at designer's disposal and can often be chosen to satisfy the above constraint while at the same time leading to a reasonable design, i.e. compromise between heave and pitch aspect of ride.

Through the above decoupling one can see the connection between the previously established wealth of results for the simple 1 DoF quarter-car vehicle models and the corresponding 2 DoF, half-car case. This parallel can be extended to more complex 4 DoF, half-car models that include unsprung masses, as shown in Fig. 31.

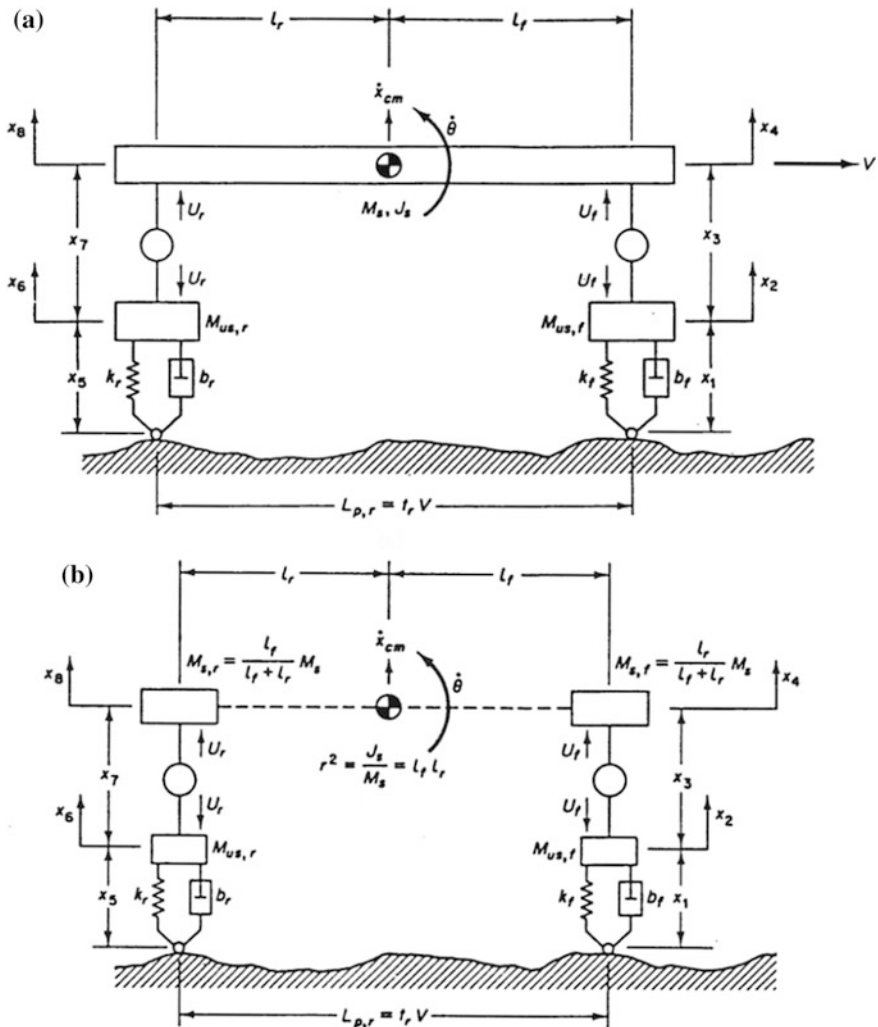


**Fig. 31** Half-car, 4DoF vehicle model (a) and, corresponding decoupled model consisting of two quarter-car, 2DoF sub-models (b)

It turns out that the same decoupling conditions apply in this case as well leading to two decoupled 2 DoF, quarter-car models shown in Fig. 31b. This again establishes the link between more complex half-car models and corresponding quarter-car counterparts for which there is an abundance of previously established results. In practice this means that a reasonable approach to an active suspension system design may start with controlling the corners enhanced with some additional, typically feed-forward action to counteract different pitch disturbance due to braking, accelerating and similar.

At this stage we note that the 2D setup of Figs. 30 and 31 facilitates preview of road ahead of certain points of a vehicle. In particular we see that front wheels could serve as sensors or previewers of road inputs ahead of rear suspension units. In general, having some advance knowledge of the future disturbances may be invaluable in some situations and highly beneficial in many.

While in case of most automobiles this kind of preview may be relatively short and of limited effectiveness, it could be much more pronounced in some other vehicles such as heavy-duty trucks (“18-wheelers”) and especially trains (Karnopp 1968). Similar applies to some more recent transportation paradigms under consideration such as vehicle platooning or convoys of trucks that is becoming more and more realistic proposition due to rapid advances in sensors, actuators and processing intelligence needed for (semi)autonomous driving. This includes preview information provided by on-board cameras, lidars, and availability of 3D road maps and V2V communication, where vehicles ahead may serve as “sensors” for following vehicles.

One of the first studies investigating potential benefits of preview was done by Bender (1967a) who started with logical simplest case of 1 DoF vehicle models. Using the Wiener-Hopf optimization approach (which is similar to—albeit more restrictive than—the hereby pursued LQG approach) the author obtained the global optimal performance maps shown in Fig. 32, where the axes are the same as in Fig. 13 with horizontal axis corresponding to normalized rattlespace (or, more precisely, to the distance between sprung mass and road) and vertical axis corresponding to normalized sprung mass acceleration. The straight line for no preview (i.e. preview time  $T = 0$  s) corresponds to the case studied earlier—this was represented as the full line in Fig. 13.

On the other hand the line with infinite preview ( $T = \infty$ ) indicates the best possible performance under preview. Based on the analysis from Bender (1967a) the optimal infinite preview line in a log-log scale of Fig. 32 can be expressed as

$$u_{rms, norm} = \frac{3\sqrt{3}}{128x_{1, rms, norm}^3} \quad (51)$$

Comparing this expression with the corresponding expression for the 1 DoF case without preview (see Eq. (20) in Sect. 3.1 and Eq. (72) in the Appendix) one can conclude that there is a substantial, 16-fold, potential for reducing the sprung mass acceleration while keeping the overall rattlespace the same. While this requires knowing *all* of the future, from Fig. 32 it can be seen that even knowing only 0.5 s of advanced road ahead could lead to significant benefits in the context of the present 1 DoF problem.

An extension of the above 1 DoF preview case toward the 2 DoF quarter-car counterpart was considered in Hrovat (1991a). The approach taken was to shift the time point of reference so that instead of considering a preview system one ends up with a dynamic system with delays for which there is an abundance of research results (Richard 2003; Fridman 2014). This was achieved by shifting the observer

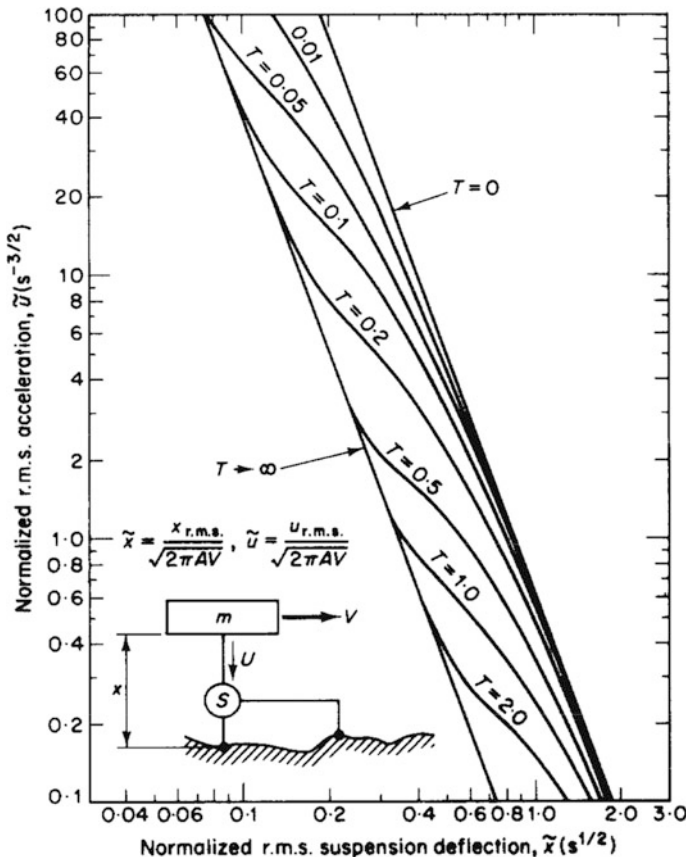


**Fig. 32** Optimal 1DoF active suspension (S) performance for different preview times,  $T$  (Bender 1967)

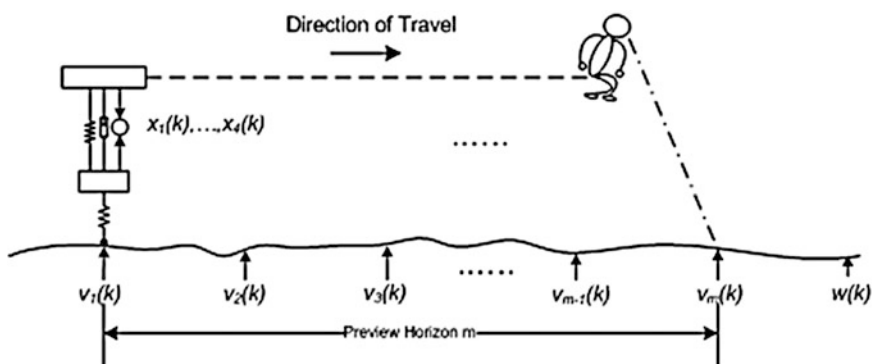


**Fig. 33** Conceptual representation of road preview process

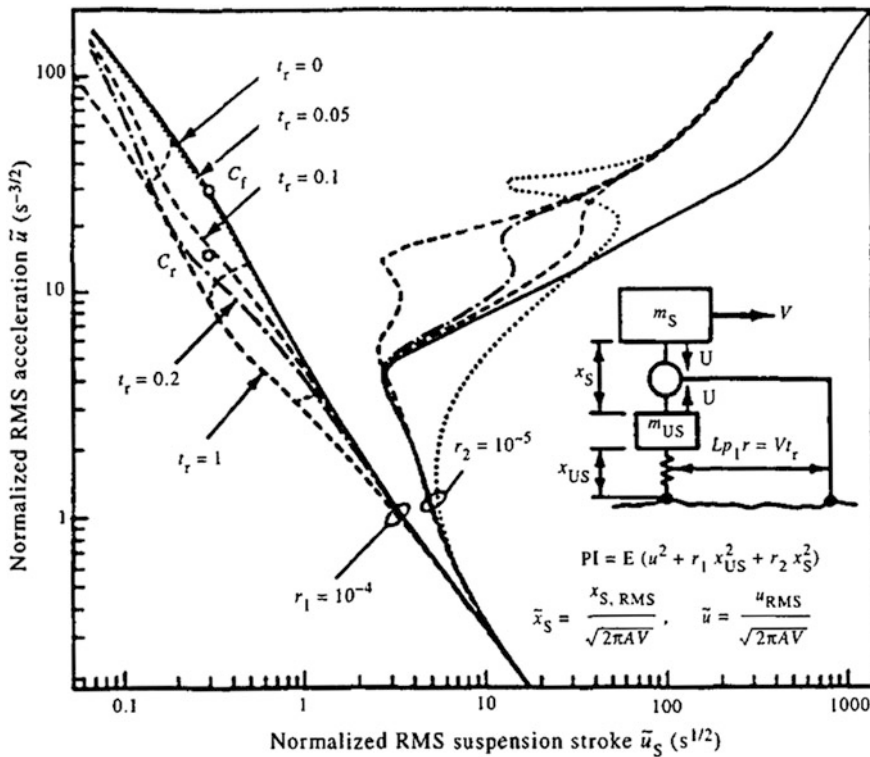


**Fig. 34** Normalized acceleration versus rattlespace trade-offs for quarter-car, 2DoF vehicle model with different preview times,  $t_r$

vantage point from vehicle to some distance ahead of vehicle corresponding to the magnitude of preview. Figure 33 illustrates this graphically.

The resulting carpet plots of normalized rms acceleration versus suspension rattlespace and tire deflection are shown in Figs. 34 and 35, respectively. While, as it might have been expected from previous non-preview analysis, the performance improvements are now less dramatic than for the 1 DoF case of Fig. 32, the plots still reveal opportunities for further significant improvements in both ride as well as handling aspects of vehicle performance. In particular, from Fig. 35 one can see that even a relatively short amount of preview of only 0.1 or 0.2 s can make significant difference in terms of the sprung mass acceleration versus tire deflection trade-offs, which is also a reflection of the fact that this particular trade-off is in good part associated with the fast, wheel-hop mode.

To put this short preview times in proper perspective—a preview of 0.1 s corresponds to traversing the distance of little more than one wheelbase length of Ford Fusion sedan (wheelbase distance between front and rear wheels being 2.84 m in this case) at speeds of 65 mph or 29 m/s. This indicates that one could in theory benefit from even such a short preview times or equivalent distances. However, to

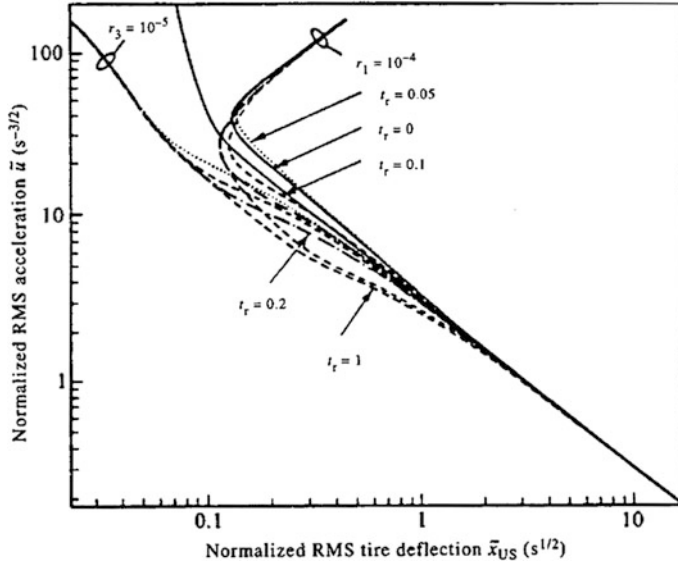


**Fig. 35** Normalized acceleration versus tire deflection trade-offs for quarter-car, 2DoF vehicle model with different preview times,  $t_f$

fully exploit such opportunities one would in practice need very fast and accurate “high-fidelity” actuators and/or some ingenious hardware design measures and innovations. Additional aspects of preview control in the context of quarter-car models, such as bandwidth requirements and frequency responses, can be found in Pilbeam and Sharp (1993), Hac (1992), Hrovat (1997) and references therein.

### 3.8 3D, Full-Car Models

The optimization problem treated thus far for 1D, quarter-car and 2D, half-car models can be naturally extended toward the full 3D setting. Thus, following the above example of 1D–2D extension, one would now add sprung mass roll acceleration to the PI of Sect. 3.7 in addition to rattlespace constraint for each of the four vehicle corners; the resulting PI is given below (see Fig. 10)

$$PI = E \left[ q_A z_A^2 + q_B z_B^2 + q_C z_C^2 + q_D z_D^2 + r_1 (d^2 z / dt^2)^2 + r_2 (d^2 \Theta / dt^2)^2 + r_3 (d^2 \phi / dt^2)^2 \right] \quad (52)$$

Some of the first studies based on the LQG approach were presented in Barak (1985), Chalasani (1986), Barak and Hrovat (1988). The approach taken by Hrovat (1991b) is based on the simplest possible 3D model where one again starts by

neglecting the unsprung masses. For this particular case with some additional mild assumptions on the road roughness characterization, it was possible to obtain an analytical solution even for this 3D problem, as elaborated in Hrovat (1991b).

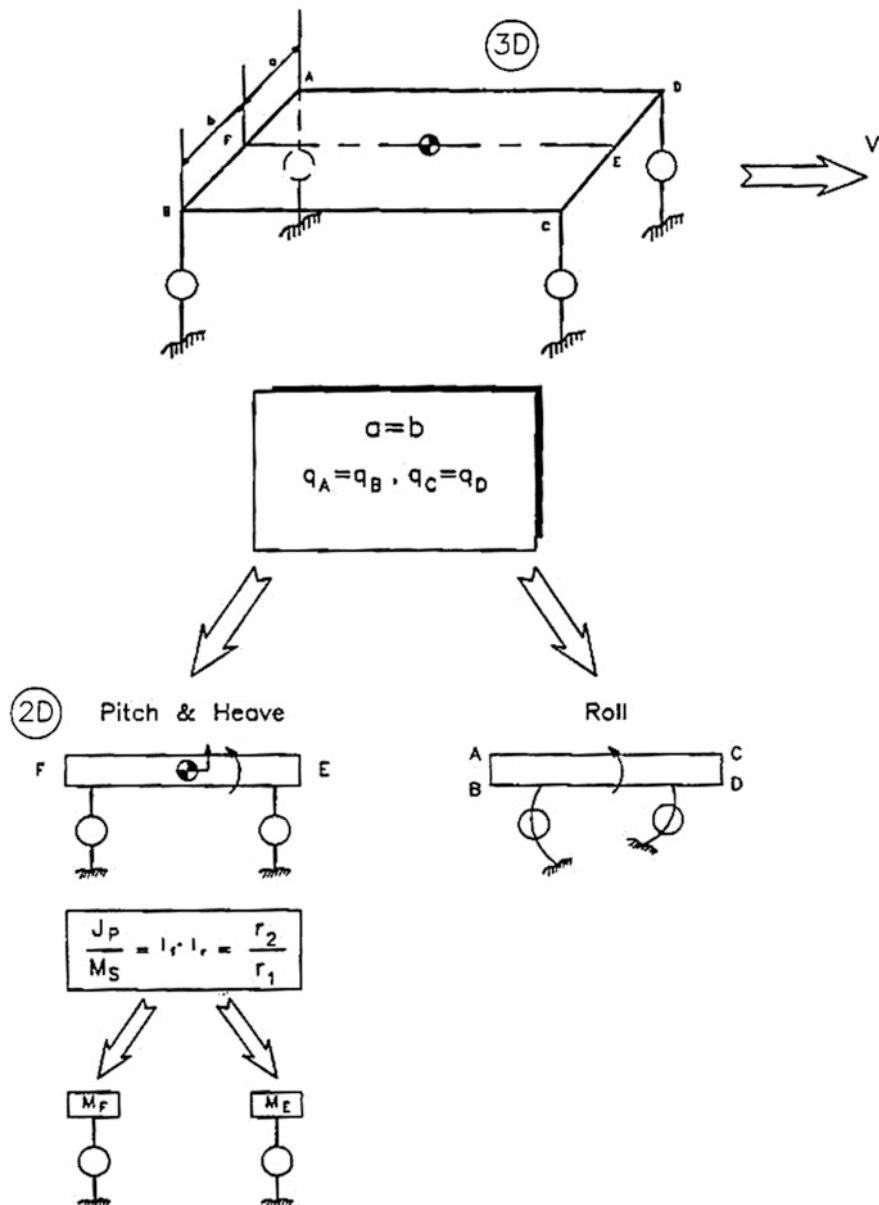


Fig. 36 Full-car, 3D vehicle model and related simplifications

Based on these analytical results it was possible to make a number of observations about the optimal system characteristics. This includes the fact that all three optimal body modes have the highly desirable damping ratio of 0.7, which is an extension of similar results for 1D and 2D cases. In addition, under some mild conditions shown in Fig. 36, the original 3D problem can be decoupled into two subsystems: one being the 2D pitch and heave subsystem, and another being a special roll subsystem as depicted in Fig. 36. Furthermore, if the previously established conditions for 2D decoupling hold (see Fig. 36) then the pitch and heave subsystem can be further decoupled into two basic, 1D optimization problems.

This way the original full car optimization problem has been transformed into much simpler half and quarter car optimization setting. In this manner we have established a link with the previously obtained wealth of results for 1D and 2D optimization cases. Some other approaches and results based on the full 3D model including unsprung masses can be found in Barak (1985), Chalasani (1986), for example. Further extensions of the 3D model are possible to include flexible modes (in case of long trucks and similar vehicles) and flexible guideways, such as long (suspension) bridges and similar structures (Margolis 1978; Karnopp et al. 2012).

## 4 Model Predictive Control (MPC) as an Extension of Preview Control

In this section, we review the usage of Model Predictive Control in suspension control where it can incorporate not only the road preview but the other dynamic considerations including constraints, mode switchings and other non-linearities. Figure 37 illustrates suspension travel limits, bumper nonlinearities, and tire road interaction nonlinearities or constraints.

As indicated earlier (e.g. Sect. 3.1), in semi-active suspension systems, the suspension force can be modulated through a range of damping force within the

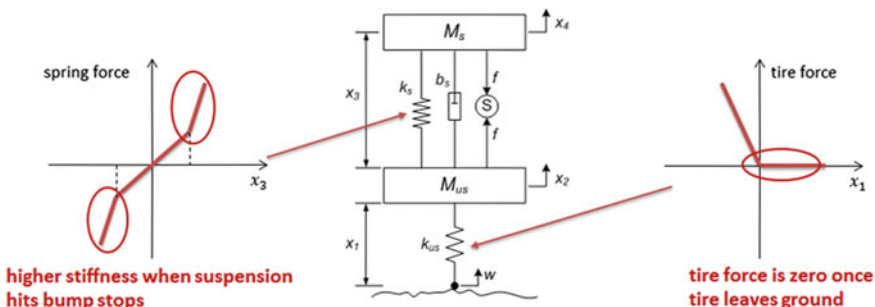


**Fig. 37** Dynamic mode switching, nonlinearities, and constraints

associated passivity constraint. In this case the suspension force cannot track an arbitrary desired force from the unconstrained LQ optimization-derived control law. As a compromise, the semi-active control design typically follows its unconstrained active counterpart when it can, and operates along the passivity envelope when it cannot. For example, the damping force is adjusted to follow the desired suspension force derived from the optimal control law, and set to zero when a negative damping force is required. This control is therefore commonly referred to as “clipped optimal”.

The optimal control law for the semi-active system has been posed as a constrained LQ optimization and solved numerically in Hrovat et al. (1988), Tseng and Hedrick (1994), involving the iterative solution of a time-varying force constraint. A specific example in Tseng and Hedrick (1994) showed that up to a 10% advantage with respect to clipped-optimal can be achieved. However, it also found that the amount of improvement depends on driven scenarios and is usually very limited. A later work (Giorgetti et al. 2006) leveraged the explicit hybrid MPC to confirm analytically the previously obtained numerical finding that clipped optimal is not the optimal control for semi-active suspensions in general.

In practical suspension design, rebound and jounce bumpers are needed within the rattle space to ensure no metal to metal contact when the vehicle encounters a large road disturbance. Since the power and force of an actuator are limited, an optimal active suspension controller may want to take advantage of this passive nonlinearity in the vehicle. A hybrid MPC controller was discussed in Xu et al. (2016) to demonstrate the control’s potential in further enhancing overall suspension performance, given limited actuation force/power. As is well known, the power and force of a hardware actuator are limited since they are tightly correlated to the practical constraints of cost and weight.

Noting that the tire of a vehicle may briefly lose road contact when encountering a large road disturbance such as an abrupt pothole or a brick on the road, a preview-based hybrid MPC can be designed (Xu et al. 2016) to take advantage of the upcoming road profile as well as the knowledge of non-symmetric tire behavior (when leaving the ground).

In a preview-based Model Predictive Control, not only is the vehicle response in the future prediction horizon “simulated and evaluated”, but also is the road profile within the prediction horizon “measured and buffered”. Bringing the future road profile into the augmented system dynamics is a native capability within the MPC framework where the look-ahead road input at each sampling time is measured, if available, and buffered until it reaches the vehicle (See Fig. 33). As such, a road preview MPC can be developed to enhance performance (Xu et al. 2016) using the same framework of MPC without preview.

A benchmark simulation comparison for a quarter car going through a curb with the step change of 0.1 m in road height is illustrated in Fig. 38, where the overall cost function, rms tire deflection, suspension rms deflection, and sprung mass rms acceleration are listed. All the controllers (LQR, MPC, and hybrid MPC) utilized 0.1 s preview, while the LQR controller assumed linear model, the MPC controller constrained the suspension and tire deflection to within their linear and symmetric

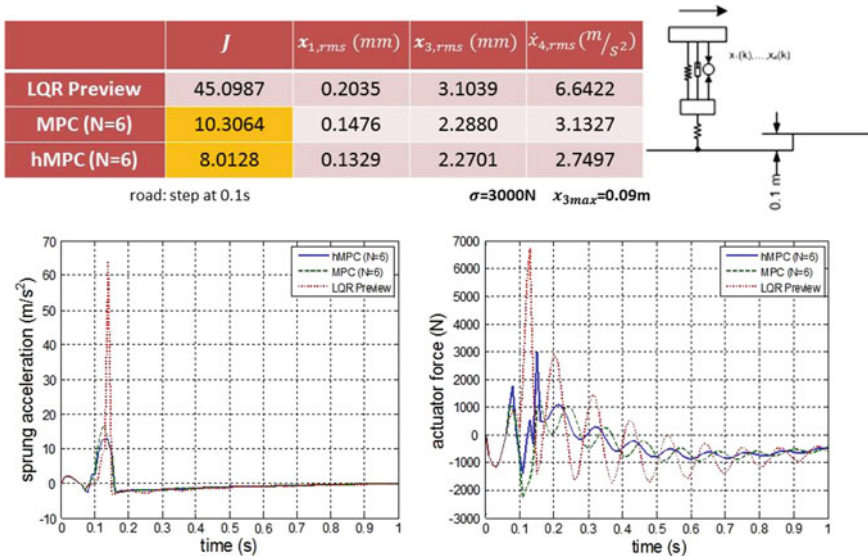


Fig. 38 Benchmark comparison among LQR preview, MPC, and hybrid MPC

region, and the hybrid MPC accounted for more detailed representation of suspension nonlinearities and unsymmetrical tire behavior. Significant improvement can be achieved with MPC and hybrid MPC where the realistic nonlinearity can be predicted and managed to avoid hitting the suspension jounce bumper.

## 5 Other Concepts, Features, and Related Practical Considerations

### 5.1 Other Concepts

As the suspension performance index often includes conflicting terms, multi-objective optimization—symbolic or numeric—has been widely used to systematically manage nonlinearities and constraints (Gobbi and Mastinu 2001; Chatillon et al. 2006; Chen et al. 2003). The solution of a multi-objective optimization finds the best trade-off among the various pre-defined control terms. This is also known as Pareto optimization used in systematic design procedures, which is in many cases similar to the global optimization approach pursued in Sect. 3.

On the other hand, there are approaches with simpler concepts that focus on emulating an ideal damping for the single element in consideration. Among them, one of the most popular approaches is the skyhook concept which is supposed to emulate a damper connected between the sprung mass and the sky or a moving cloud representing an absolute, inertial ground. The skyhook control focuses on

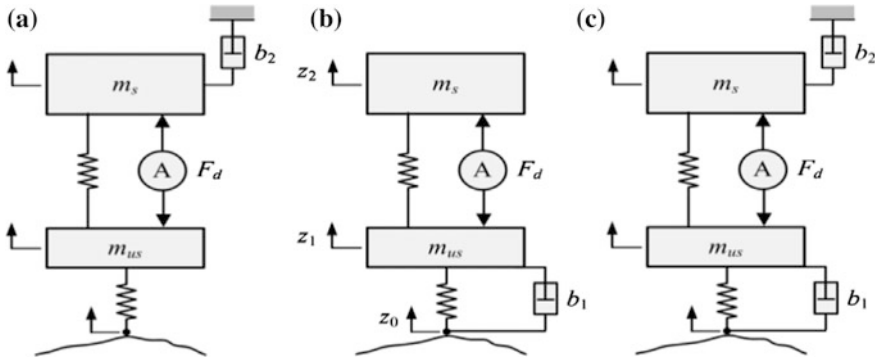


**Fig. 39** Illustration of skyhook, groundhook, and their combination

passenger comfort with proper trade-off between suspension travel and tire force variation. An analogous concept was introduced to focus on the minimization of tire force variation. Instead of putting a damper between the sprung mass and a moving cloud (aka sky or “inertial ground”), it suggests to put a heavy duty damper between the unsprung mass and the moving ground, hence its name “ground hook” (Novak and Valasek 1996; Valasek et al. 1997). In its implementation, the suspension device located between sprung and unsprung mass emulates a damping of the unsprung mass with respect to the ground i.e. road. Its emphasis is on the prevention of road damage and minimization of tire force variations. Practical advantages for road, soil, and bridges have been supported by experimental results with a prototype truck (Valasek et al. 1998, 2003). Figure 39 illustrates the concept of sky hook, ground hook, and their combined implementation.

An attempt to extend the above LQ optimization results to a nonlinear setting is presented in Karlsson et al. (2000, 2001a, b). The idea was to put additional, higher order (e.g. quartic) penalty on the rattle space, which in reality is best represented by hard constraint as opposed to soft constraint representation used in the typical LQ setting of Sect. 3. As a consequence of this increased penalty, there is more efficient utilization of rattle space, especially in case of large bumps and potholes that could otherwise result in unacceptably large impact forces.

## 5.2 Hydraulic Suspensions and Their Brief History

A brief history of hydraulic-based suspensions is illustrated in Fig. 40 where various version of hydraulic and related electro-hydraulic suspensions have been implemented in production vehicles, ranging from low, mid, to high bandwidth, ride height focused to vehicle roll response motivated. Note that the Kinetic Suspension Technology (Sherman 2011) is essentially a semi-active suspension system acting between different corners while Nissan Infinity Q45a (Akatsu et al. 1990)

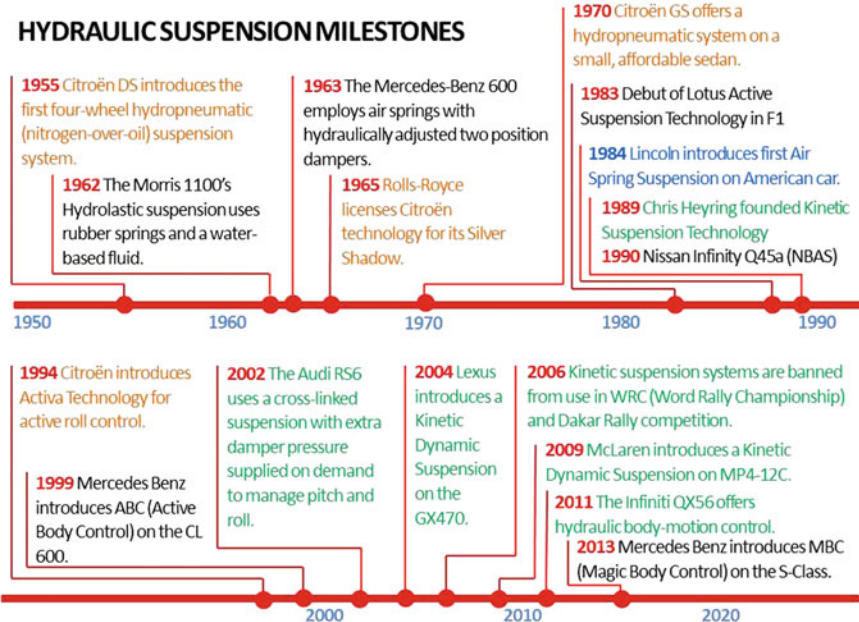


**Fig. 40** Brief history of hydraulic suspensions

and Mercedes ABC (Merker et al. 2002) are narrow bandwidth active suspension (NBAS) systems, to be discussed in Sect. 5.6.

### 5.3 Self-leveling Feature

Various self-leveling systems have been introduced in the market including the ones illustrated in Fig. 40. Notable examples include the Hydropneumatic systems developed by Citroen (Nastasić 2002) and the Electronically-Controlled Air Suspension on Lincoln by Ford Motor Company (Chance 1984). This feature allowed these vehicles to maintain proper ride height and suspension stiffness over a wider range of vehicle loading. It adjusts the vehicle ride height, usually very slowly, in order to balance among (1) soft and comfortable ride from the softer-than-usual passive spring, (2) proper vehicle attitude/stance, and (3) increased rattle space for anticipated or unknown road disturbance ahead. This feature has been implemented in the Lincoln Mark VIII in the 90s and most recently in Tesla Motor Model S (Edmunds 2012; Korosec 2014). It enables the lowering of the vehicle at highway speeds to improve aerodynamics and therefore, better fuel economy and driving range.

## 5.4 Variable Suspension Damping (Semi-active Suspension) Feature

Production semi-active suspension systems are generally constructed using an adjustable damper in parallel with the secondary suspension spring. These are typically constructed from pneumatic and/or hydraulic piston/cylinder combinations with electromechanical control of an orifice. Actuator bandwidth is primarily determined by the reaction time of the controlling valve and associated pressure/force production dynamics. A modern version can be found in Lincoln's Continuous Controlled Damping system introduced in 2006. The Lincoln system uses a suite of sensors that constantly monitor suspension motion, body movement, steering and braking inputs and adjusts the suspension in milliseconds, helping keep the car smoothly on track (See Fig. 41). Specifically, it monitors up to 46 inputs and reacts on average within 20 ms (Nicolas 2014) to reduce roll, pitch, and heave motions, while enhancing driving comfort and dynamics, and isolating the vehicle from road harshness.

Another implementation of adjustable damping is through magneto-rheological (MR) fluids. MR fluid viscosity can be changed electronically, allowing the force across the actuator to change quickly (Bodie and Hac 2000). This method benefits from faster response time, although limited fluid life may contribute to service concerns. One MR damper application is found in the 2002 Cadillac Seville STS and 2003 Chevrolet Corvette whose MR fluid system was co-developed by Delphi and Lord Corporation.

## 5.5 Variable Suspension Geometry/Low Power Low Bandwidth Active Suspension Feature

A variable geometry suspension adjusts the ratio of wheel movement to the deflection of the suspension spring in real-time. By changing the leverage of the passive suspension spring depending on wheel motion, it essentially controls the wheel rate or effective spring stiffness.

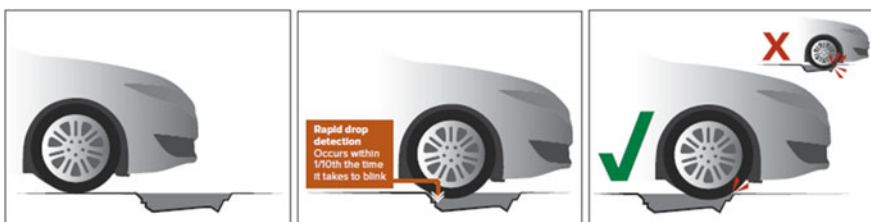


**Fig. 41** Illustration of Lincoln CCD mitigating pothole impact by “stiffening” the damper

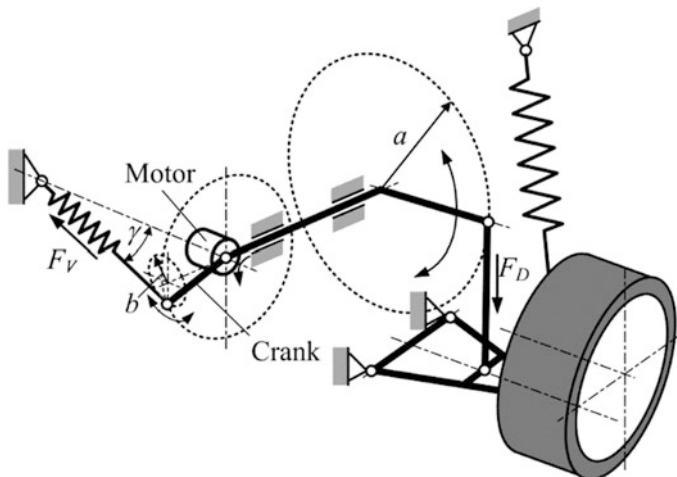


**Fig. 42** Delft active suspension realized with a cone mechanism

Various systems and hardware configurations that provide variable suspension geometry have been proposed in the literature (Venhovens and van der Knaap 1995; Sharp 1998; Watanabe and Sharp 1999; Tumova 2004) including the “Delft Active Suspension” concept that was implemented as a prototype vehicle and demonstrated experimentally.

A specific variable geometry design, the “Delft Active Suspension” (van der Knapp 1989; Venhovens et al. 1992; Evers et al. 2008), is realized with a cone mechanism and illustrated in Fig. 42. This mechanism connects the spring to the car body on one end and to a rotatable crank on the other end. The crank is joint-connected to the suspension/wheel control arm and can be rotated at the joint around the base of the imaginary cone. The cone mechanism serves two purposes; (1) the length of the spring remains the same as the crank rotates, and (2) the ratio of movement between the wheel/tire control arm and the crank changes as the crank rotates (see Fig. 42). The intent is that the power required for geometry variation and the associated force leveraging of wheel rate will be much less than for directly changing the desired force. Ideally, with the configuration, the mechanism would require very low power and low energy. In practice, however, the precise arrangement and alignment could be compromised by suspension motion and deflection, and associated always-present friction.

## 5.6 Narrow Bandwidth Active Suspensions (NBAS)

Narrow bandwidth active suspensions are characterized by relatively low force-production bandwidth of up to few Hertz, which results from an architecture

where the dominant compliance is placed in geometric series with the active force generator. Most of the NBAS implementations thus far have been of electro-hydraulic type. Some representative electro-hydraulic active suspension configurations are shown in Fig. 43. Starting with a general structure shown in Fig. 43a one can use the bond graph of Fig. 43b to derive an equivalent all-mechanical structure shown in Fig. 43c. In the special case when the flow source  $Q_B$  is not present one ends up with the load-leveling-like configuration shown in Fig. 43d where we assumed a very soft, possibly pneumatic or air spring compliance. Finally, if the flow source  $Q_A$  is not present then we end up with the configuration shown in Fig. 43e. This is similar to some NBAS architectures—note in particular the serial arrangement between the dominant spring and the active force

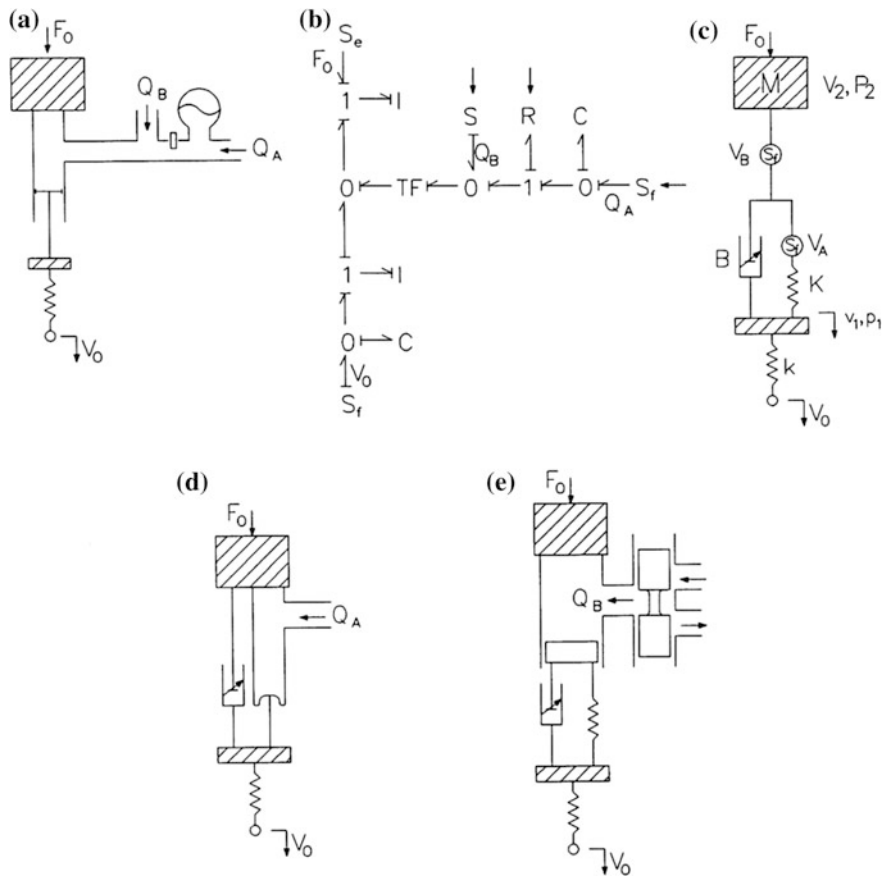


**Fig. 43** Electro-hydraulic suspension configurations: **a** general structure; **b** corresponding bond graph; **c** equivalent mechanical system; **d** typical structure with  $Q_B \equiv 0$ ; **e** typical structure with  $Q_A \equiv 0$  (based on Karnopp 1987)

generator represented by the electro-hydraulic actuator that includes the controlled flow source  $Q_B$ .

As suggested by Hrovat (1997) the above NBAS model could be further enhanced by inclusion of inertia effects due to hydraulic line dynamics, which can be especially relevant in case of relatively long and narrow lines or tubing. This is shown in Fig. 44, where the hydraulic conduit connecting the two flow sources,  $Q_A$  and  $Q_B$ , and suspension cylinder has been modeled as an inerter element represented by a differential causality within the associated bond graph of Fig. 44. A corresponding all-mechanical configuration is also shown in that figure. At this point, it should be mentioned that more recently there were attempts to develop and commercialize the hydraulic inerter (Scarborough 2011) as an alternative to its more common mechanical inerter counterpart. This may have some advantages in terms of packaging and overall design/cost flexibility, depending on particular implementation situation.

Further extensions of the above electro-hydraulic structures are possible by including an additional compliance near the suspension cylinder. This is shown in Fig. 45a along with an associated controlled damping mechanism. In the case that the latter is of an on/off type and neglecting all active sources (i.e. setting  $Q_A$  and  $Q_B$  to zero) one ends up with a semi-passive suspension shown in Fig. 45b. This is similar to Citroen hydro-pneumatic suspension (Carbonaro 1990) where one uses the on-off valve to control the effective suspension stiffness. The bond graph for the generic configuration of Fig. 45a is shown in Fig. 45c. Note in particular, that the inerter element corresponding to fluid line inertia is now in an integral causality with corresponding increase in the number of system states. Based on this bond graph one can easily deduce the corresponding all-mechanical suspension structure shown in Fig. 45d.

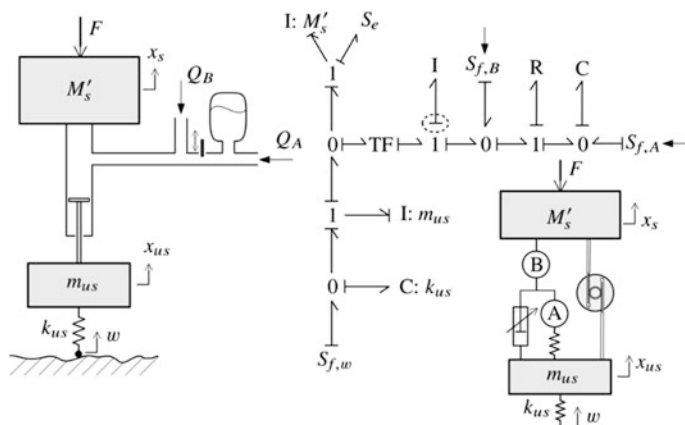


**Fig. 44** Electro-hydraulic suspension model including hydraulic inertia (inerter-like) effects, equivalent bond graph, and all-mechanical counterpart

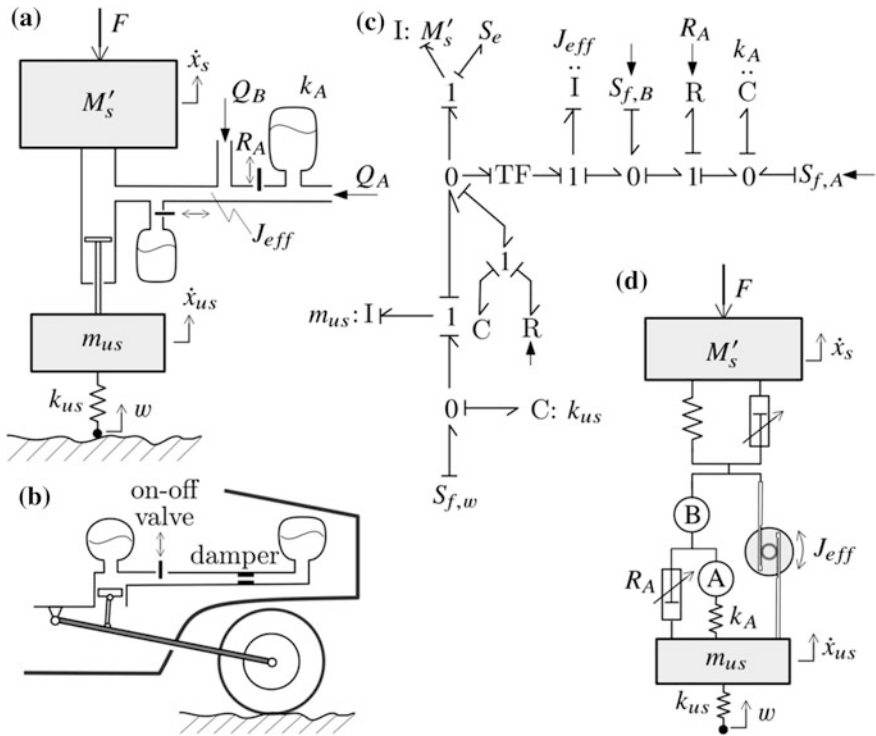


**Fig. 45** Electro-hydraulic suspension configurations including hydraulic inertia (inertier) effects, and additional compliance and controlled (on-off) damping; **a** generic structure; **b** Citroen-like hydro-pneumatic semi-passive equivalent with  $Q_A = Q_B = 0$ ; **c** corresponding generic bond graph; **d** equivalent all-mechanical system

A special case of the generic configuration of a typical electro-hydraulic (semi) active suspension from Fig. 45 is shown in Fig. 46. This is one of the first production implementations of the NBAS system developed by Nissan for their Infinity Q45a luxury vehicle (Akatsu et al. 1990). Note in particular the presence of an accumulator, which effectively acts in series with the actuator thus limiting the actuator bandwidth while at the same time filtering high-frequency road-induced disturbances. This corresponds to the accumulator with stiffness  $k_A$  in Fig. 45a. While the Infinity Q45a system used pressure control valve (Fig. 46a) another alternative would be to use the flow control valve shown in Fig. 46b.

In late 1990s Mercedes introduced their Active Body Control—ABC advanced suspension control system illustrated in Fig. 47 (Merker et al. 2002), which is structurally similar to the NBAS architecture generalized in Fig. 45. However, there is an important practical difference. While Infinity Q45a system used an hydraulic

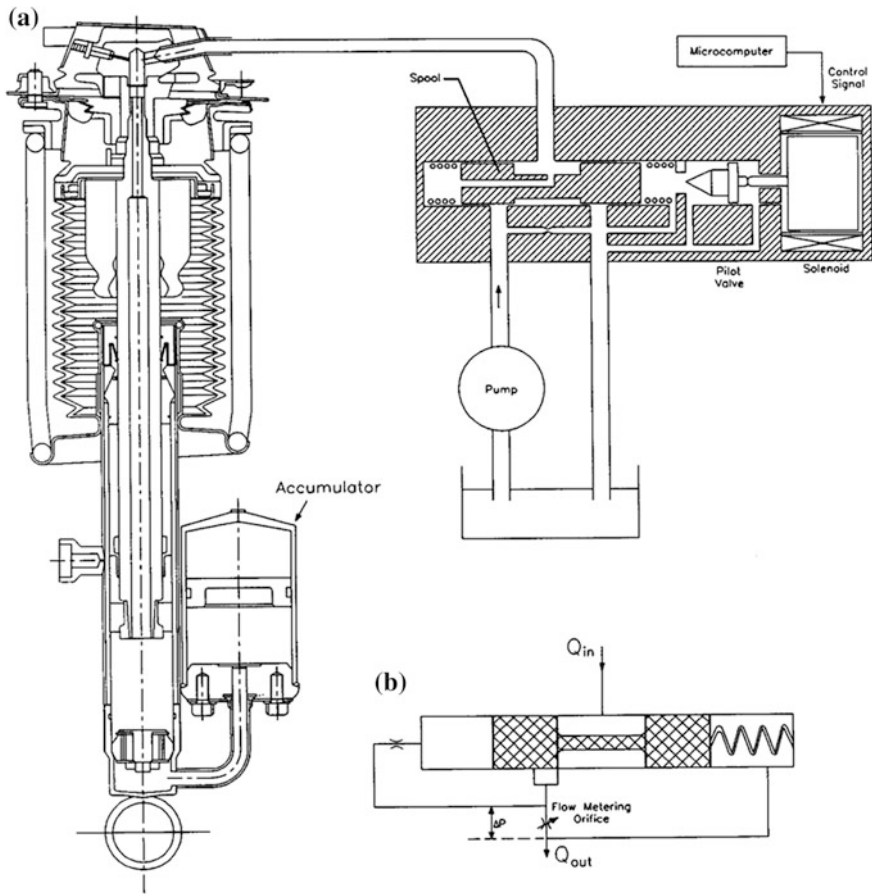
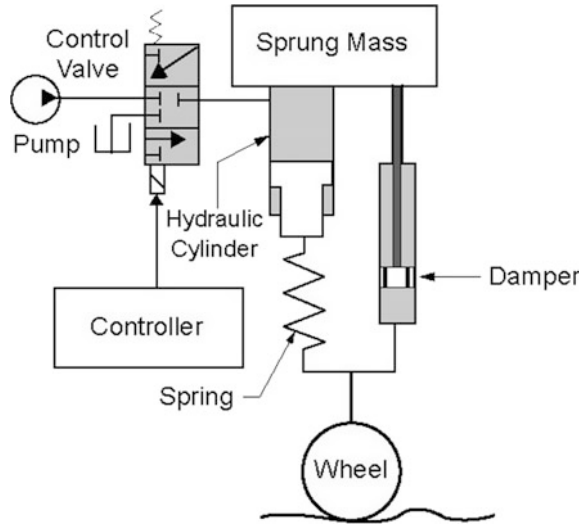


**Fig. 46** Nissan infinity Q45a N-B active suspension

accumulator to implement the above mentioned in-series stiffness  $k_A$ , the Mercedes ABC suspension uses a mechanical counterpart similar to the one shown in Fig. 45d. For most cases the two would be equivalent except in the case when there is significant friction or even stiction within the actuator piston/cylinder combination in which case the mechanical implementation would lead to smaller road-induced disturbances resulting in better ride comfort. Through the years Mercedes has further developed and enhanced their system, which has recently included preview of the road based on stereo cameras. This system is now marketed under Magic Body Control (MBC) on their high-end luxury vehicles (Anonymous 2017a; Streiter 2008).

**Fig. 47** Mercedes ABC system (based on Merker et al. 2002)



### 5.7 Broad Bandwidth Active Suspensions (BBAS)

Broad bandwidth active suspensions are characterized by relatively high force-production bandwidth that may extend up to and beyond the wheel-hop frequencies. This typically implies a very fast actuation and relatively stiff in-series compliance  $k_A$  in Fig. 45. The negative aspect of the latter is that the high-frequency road-induced disturbances are more easily transmitted to the sprung mass resulting in increased NVH (Noise, Vibration and Harshness) i.e. less comfortable secondary ride. While most of the BBAS implementations thus far have been of electro-hydraulic type equipped with high-fidelity servo-valves, there is also a case to be made for all electrical actuation, especially in view of increasing emphasis on Hybrid (HEV) and Battery Electric Vehicles (BEV).

As an example of electro-hydraulic implementation, we will next consider the BBAS prototype system (Fig. 48) that was developed at Ford Research Laboratory in the early nineties and successfully demonstrated in a research vehicle. It consisted of four high-fidelity electro-hydraulic servo actuators, one at each corner, installed onto a 1989 Ford Thunderbird (Goran and Smith 1996). The concept hardware and software not only verified the potential in ride quality improvement but also identified the shortcomings of the implemented hardware structure including actual power consumption, secondary ride harshness, and actuator noise.

The Ford Thunderbird BBAS system was controlled through four-way servo valves, which have high precision and speed of response. In addition, the BBAS actuators were based on double-acting cylinders capable of equally fast rebound and jounce strokes. The vehicle also had one central processor operating at lower

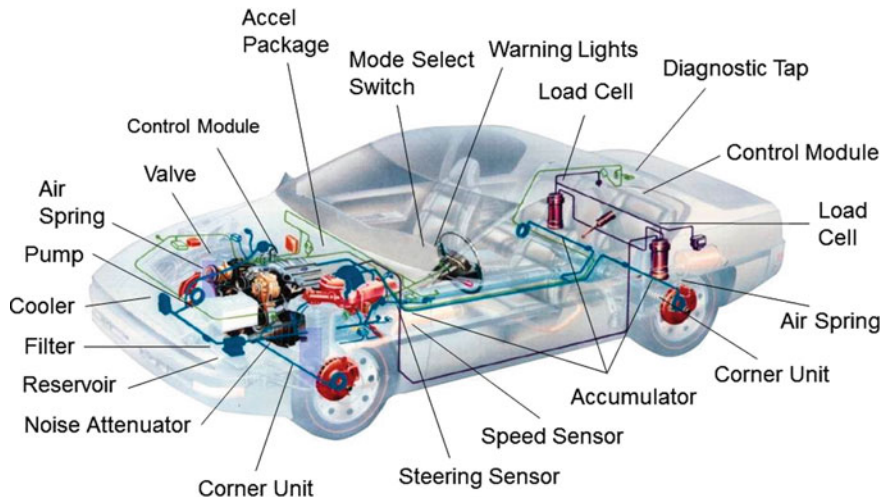


**Fig. 48** Illustration of Ford broadband active suspension prototype

rates, and four corner-unit micro-processors for fast signal/control processing; four actuator displacement sensors and four load cells for internal (force) loop calculations; and four air springs—one at each corner placed in parallel with the BBAS actuators. The air springs serve to support and self-center the vehicle sprung mass as is typical of load leveling systems. At the same time they provide lower sprung mass natural frequency for more comfortable basic ride, which is then appropriately dynamically modified through the BBAS actuators. The system incorporated 26 various sensors, including accelerometers, pressure sensors, vehicle speed sensors and others.

The BBAS control strategy was based on coordinated individual wheel control and consisted of two hierarchical control levels (Goran et al. 1992). The outer loop level operated at a 20 ms rate. It calculated the desired corner forces for the four BBAS actuators, desired operating modes (handling or ride dominated) and checked the overall system integrity. The ride related calculations were based on quarter-car vehicle models aimed at emulating skyhook damping at each corner, which is often very close to the optimal possible ride benefit (Hrovat 2014). Different effective spring and damping rates were used depending on prevailing operating modes, i.e. ride or handling. Additional details about the system and its performance can be found in Goran et al. (1992), Goran and Smith (1996).

An example of an Electrical Active Suspension (EAS) implementation (Davis and Patil 1991) in a prototype Ford vehicle is shown in Fig. 49. An important aspect of this BBAS system development was creation of an appropriate validated model, with special emphasis on actuator model fidelity. The corresponding bond graph model is shown in Fig. 50. This model was validated using bench testing and

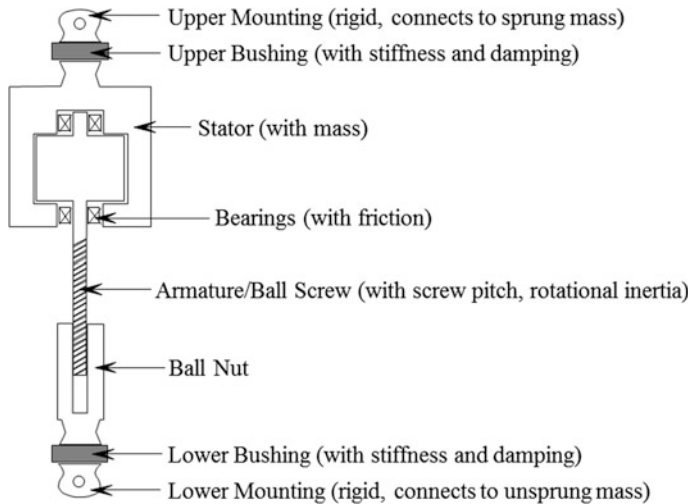


**Fig. 49** Ford broadband electric active suspension (EAS) prototype

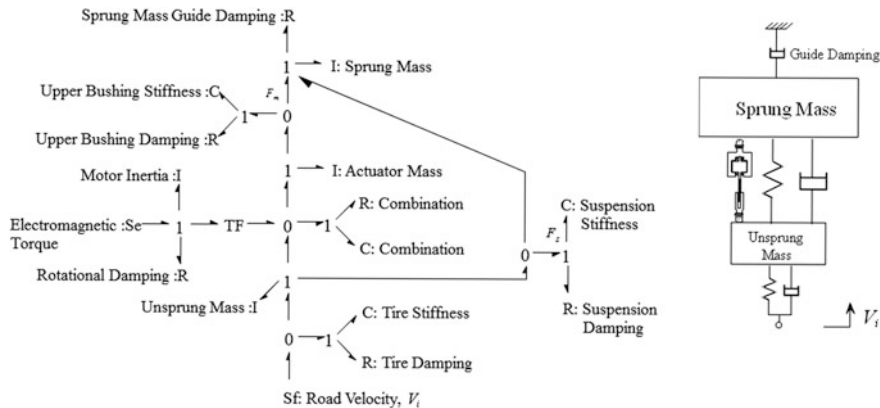


**Fig. 50** Bond graph of Ford EAS broadband active suspension quarter car

the results—in terms of relevant frequency transfer function plots—are shown in Fig. 51. It can be seen that there is in general very good correlation between the model and test data. Once validated, this model was used in the process of this—at the time very novel—BBAS system development, which culminated in successful demonstration in a research vehicle. More recent example of an EAS system development can be seen in Moran (2004), Gysen et al. (2010), Anderson et al. (2013) indicating renewed interest in this promising concept, especially in view of increased emphasis on electric (HEV and BEV) vehicles.

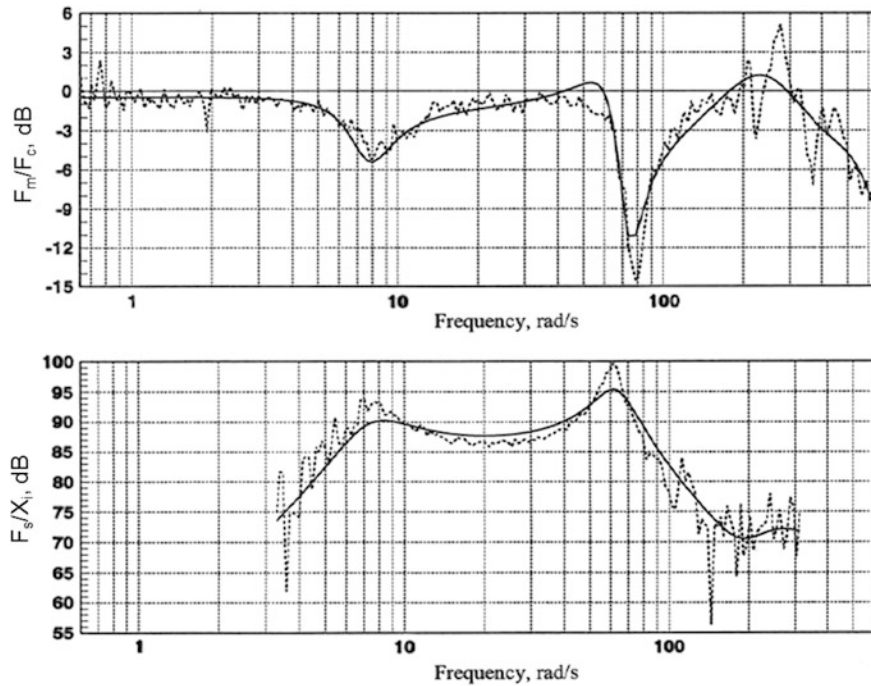


**Fig. 51** Ford EAS actuator model validation

## 6 Optimization-Based Analysis of Active Suspensions for Integrated Vehicle Controls

As discussed in the previous sections, active suspension is commonly considered under the framework of vertical vehicle dynamics control primarily aimed at improvements in ride comfort. In this section, we expand upon this traditional application by introducing some recent developments based on more detailed, non-linear vehicle models and more general optimization methodology. In particular, a collocation-type control trajectory optimization method is used to analyze to which extent the application of fully active suspension (FAS) can be broaden to the tasks of vehicle handling/cornering control and braking distance reduction, as well as enhanced active safety, in general. The analysis is extended to the ride control task for the case of emphasized, discrete road disturbances such as high-magnitude bumps and potholes. The main optimal control objective is to provide a favorable trade-off of ride comfort and road holding capability, as well as a robustness against wheel damage, e.g. at the pothole trailing edge. The presentation is based on the recent papers (Čorić et al. 2016a, b, 2017), which include more details on vehicle modeling, optimization problem formulation, and optimization results and related discussions.

## 6.1 Vehicle Dynamics Model

The conducted optimization study is mostly based on the 10 DOF passenger vehicle dynamics model depicted in Fig. 52a, b (Hancock 2006). The model state variables include longitudinal ( $U$ ), lateral ( $V$ ), and heave ( $W$ ) velocities, and roll ( $p$ ), pitch ( $q$ ), and yaw ( $r$ ) rates, as well as the four state variables related to the rotational speeds  $\omega_i$  of each wheel,  $i = 1, \dots, 4$ . For the ride control optimization task, the simple quarter-car vehicle model shown in Fig. 52c (Hrovat 1997) is mostly used. The 10 DOF model is extended by the unsprung mass dynamics (dashed lines in Fig. 52b) when verifying the basic 10 DOF model-based optimization results, or when using the full vehicle model for ride control optimization.

The variable  $\Delta F_{zi}$  (or  $F_a$  in Fig. 52c) represents the FAS control input to be optimized along with other control inputs such as  $\Delta\delta_1 = \Delta\delta_2$  (for active front steering, AFS) and  $T_i$  (for active brakes, ABS).

The tire is described by the 1994 Magic formula combined-slip model, including the relaxation length dynamics for the lateral DOF (Pacejka 2006). The longitudinal and lateral tire forces are scaled by the tire-road friction coefficient  $\mu$ .

## 6.2 Braking Distance Reduction

The optimization objective is to find the control input vector  $\mathbf{u} = [T_1, \dots, T_4, \Delta F_{z1}, \dots, \Delta F_{z4}]$ , which minimizes the final longitudinal position  $X(t_f)$  of the vehicle on the fixed time interval  $[0, t_f]$ , i.e. the cost function to be minimized is specified as

$$J_0 = X(t_f) \quad (53)$$

The optimization is subject to hard constraints on the tire normal load  $F_{zi}$ ,  $i = 1, \dots, 4$ , the FAS control inputs  $\Delta F_{zi}$ , and the suspension deflection  $z_i$ , see Fig. 52b and Čorić et al. (2017):

$$F_{zi} \geq F_{z\min} \quad (54)$$

$$-\Delta F_{z\max} \leq \Delta F_{zi} \leq \Delta F_{z\max} \quad (55)$$

$$-d_j \leq z_i - z_{0i} \leq d_j \quad (56)$$

In order to provide a well-damped system response, the cost function (53) is extended with additive soft constraint terms of mean-square type on the variables  $\dot{\eta}_i$ ,  $\dot{F}_{zi}$ ,  $\Delta F_{zi}$ , and  $\Delta \dot{F}_{zi}$ , where  $\eta_i$  denotes the tire longitudinal slip. Similarly, to ensure straight ahead motion of the vehicle during the braking maneuver in the case of split- $\mu$  scenario, the mean-square constraints are introduced for the yaw rate ( $r$ ) and the lateral displacement ( $Y$ ) variables, and the active front or rear steering input is added to the control vector to be optimized.

**Fig. 52** 10 DOF vehicle dynamics model (**a**, **b**) and quarter car model (**c**)

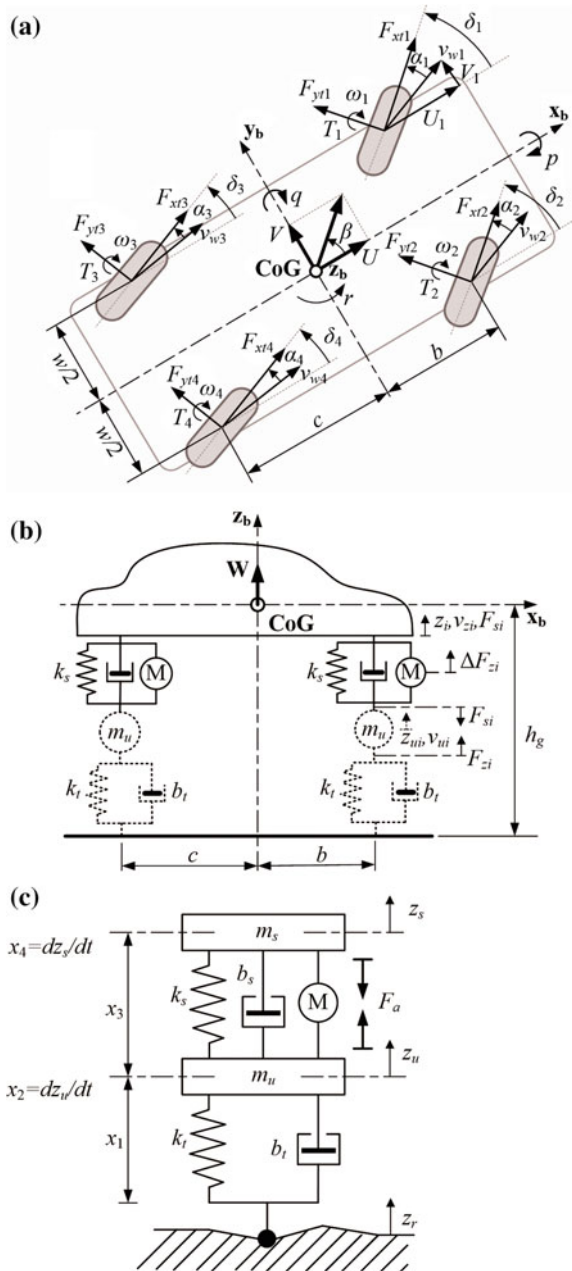
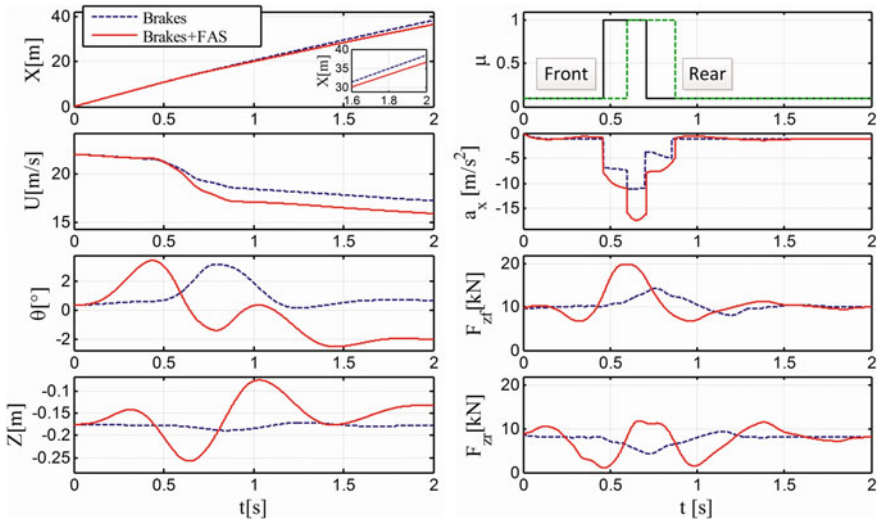


Figure 53 shows the vehicle response for a pulse-type, low-high-low transient- $\mu$  scenario, where the FAS and brake control inputs,  $\Delta F_{zi}$  and  $T_i$ ,  $i = 1, \dots, 4$ , are simultaneously optimized. The FAS provides a load boost on those tires that



**Fig. 53** Comparative Brakes and FAS + Brakes optimization results for pulse-type transient- $\mu$  scenario

experience the high- $\mu$  condition (first front,  $F_{zf} = F_{z1} + F_{z2}$ , and then rear tires,  $F_{zr} = F_{z3} + F_{z4}$ ). This results in a boost of the longitudinal deceleration  $-a_x$ , and finally in reduction of the braking distance by 5.1% (on the given, fixed time horizon).

The side effects of FAS action include excitation of vehicle heave and pitch dynamics. This results in the long stroke in the heave,  $Z$ , direction (approx.  $\pm 10$  cm; which is closely related to the suspension deflection constraint (56), with  $d_j = 10$  cm), and the corresponding heave acceleration peak of 0.69 g. The pitch angle response  $\theta$  includes some more oscillatory content as the results of FAS action.

In order to produce a strong tire load boost during the high- $\mu$  period and at the same time satisfy the suspension stroke constraint, the FAS relaxes the tire load immediately before and after the high- $\mu$  interval (see  $F_{zf}$  and  $F_{zr}$ ). These tire load holes have a weaker effect on the deceleration  $-a_x$  than the load boost, because they occur during the low- $\mu$  intervals.

The analysis is extended in Čorić et al. (2017) for other  $\mu$ -scenarios. The braking distance reduction is lower for the step-type, high-low transient- $\mu$  case (around 2% for the same  $\mu$  levels and time horizon values) and much smaller for the constant- $\mu$  scenario (0.5%). In the latter case, the performance gain is higher (around 2%) if the ABS actuator bandwidth is lower than the FAS bandwidth. This is because the FAS can boost the tire load when the braking torque is being settled i.e. when it is close to maximum, while preparing for the boost through generating the tire load hole in the early stage of braking torque transient.

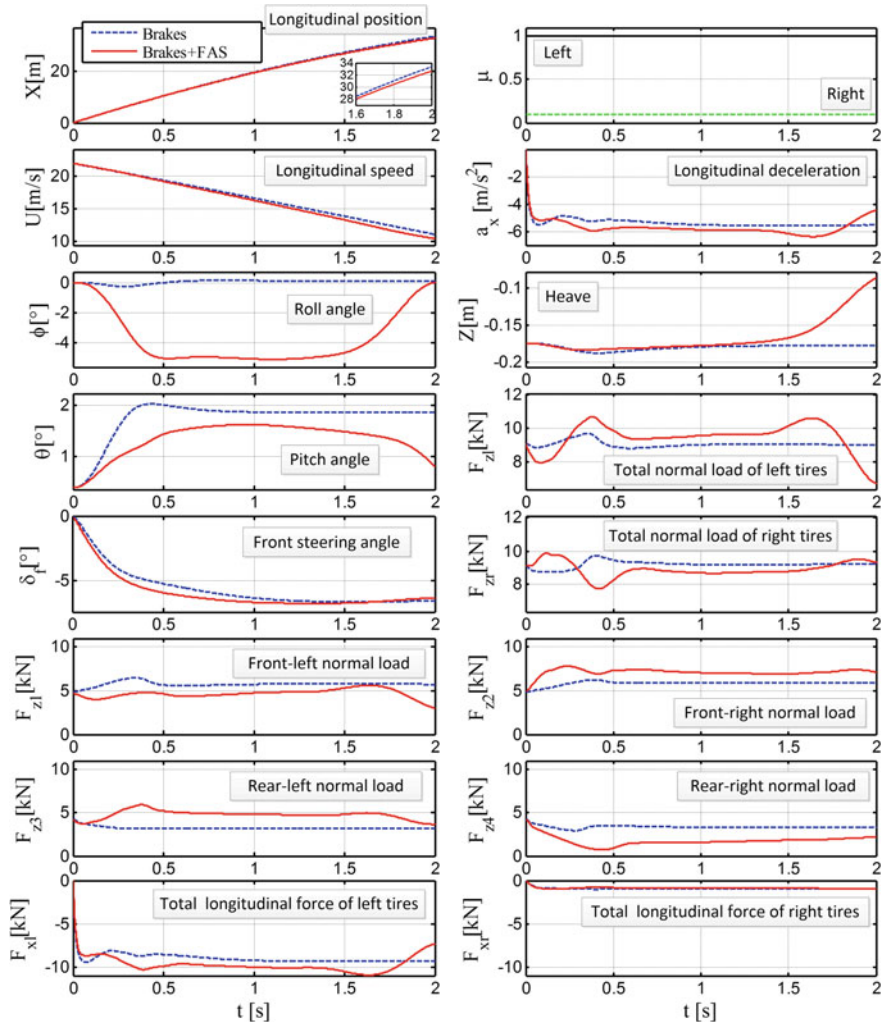


**Fig. 54** Comparative brakes and brakes + FAS optimization results for split- $\mu$  maneuver with included AFS actuator

In the split- $\mu$  scenario ( $\mu_{1,3} = 1$  and  $\mu_{2,4} = 0.1$  in the particular case, Fig. 54), the FAS again transfers the load to the high- $\mu$  tires (the left tires in this case), and the braking distance is reduced by 2.1%. To keep the vehicle moving straight ahead, the optimized active front steering (AFS) input  $\delta_f$  is such to counteract the yaw torque caused by unequal left and right braking forces. Between the high- $\mu$  tires, the load is transferred to the non-steered (left rear) tire, because it has a larger longitudinal force potential according to the friction circle (Pacejka 2006). It is important to note that the overall FAS action is such to form a warp arrangement of the four

FAS forces (see the normal load,  $F_{zi}$ , responses in Fig. 54). In this case the total FAS force  $\Sigma\Delta F_{zi}$  is approximately equal to zero, thus avoiding any notable have motion, and allowing for control of tire load distribution over long steady-state intervals. Namely, the load redistribution occurs during the whole maneuver interval (Fig. 54), unlike in the transient- $\mu$  case where only a temporary load boost (preceded by load hole) was achievable due to the suspension deflection/heave stroke constraint (Fig. 53). It should also be noted that a chassis roll is induced towards the high- $\mu$  wheels.

The constant- $\mu$  scenario has been extended by imposing oscillatory behavior of the longitudinal slip (through an equality constraint), in order to mimic the ABS-inherent limit-cycle behavior. The optimized FAS action is such to increase the tire load in the wheel torque peak periods, thus resulting in a higher tire friction potential in those periods, and finally boosted deceleration. This is in accordance with the FAS + ABS control strategy proposed by Alleyne (1997).

### 6.3 Handling Control—Stabilization

The standardized sine-with-dwell maneuver-based test (Anonymous 2007) is used to evaluate the FAS control authority in stabilizing the vehicle. In this maneuver, a “robot” steering wheel angle (SWA) with the amplitude  $\delta_k$ , the frequency of 0.7 Hz, and the dwelling period of 0.5 s, is applied to a vehicle coasting at the velocity  $U = 80$  km/h for the tire-road friction coefficient  $\mu = 0.9$ . Unlike the original test specification, where repetitive tests with a growing SWA are executed, only the worst-case scenario related to the SWA amplitude  $\delta_k \cong 270^\circ$  is considered in optimization. In order to reflect the test requests on limiting the yaw rate response (stabilization) and maximizing the lateral displacement  $Y$  (responsiveness) during the maneuver interval  $[0, t_f = 4$  s], the following cost function is considered:

$$J = \int_0^{t_f} (r - r_R)^2 dt - k \max(Y) \quad (57)$$

where  $r_R$  is the target yaw rate generated by a vehicle dynamics reference model, and  $k$  is the weighting factor selected to achieve a trade-off between the two conflicting objectives. The optimization is subject to inequality constraints (54)–(56). The optimized control variables are FAS inputs  $\Delta F_{zi}$ ,  $i = 1, \dots, 4$ . A more detailed elaboration of the optimization problem formulation and a more detailed discussion of the optimization results are presented in Čorić et al. (2017).

Figure 55 shows the optimization results for the considered sine-with-dwell maneuver. A typical though simplified feedback-type ESC reference strategy predominantly brakes the outer front wheel ( $F_{x1}$ ) to generate an oversteer compensation (OSC) component of the yaw torque  $M_z$  and stabilize the vehicle (Tseng et al.

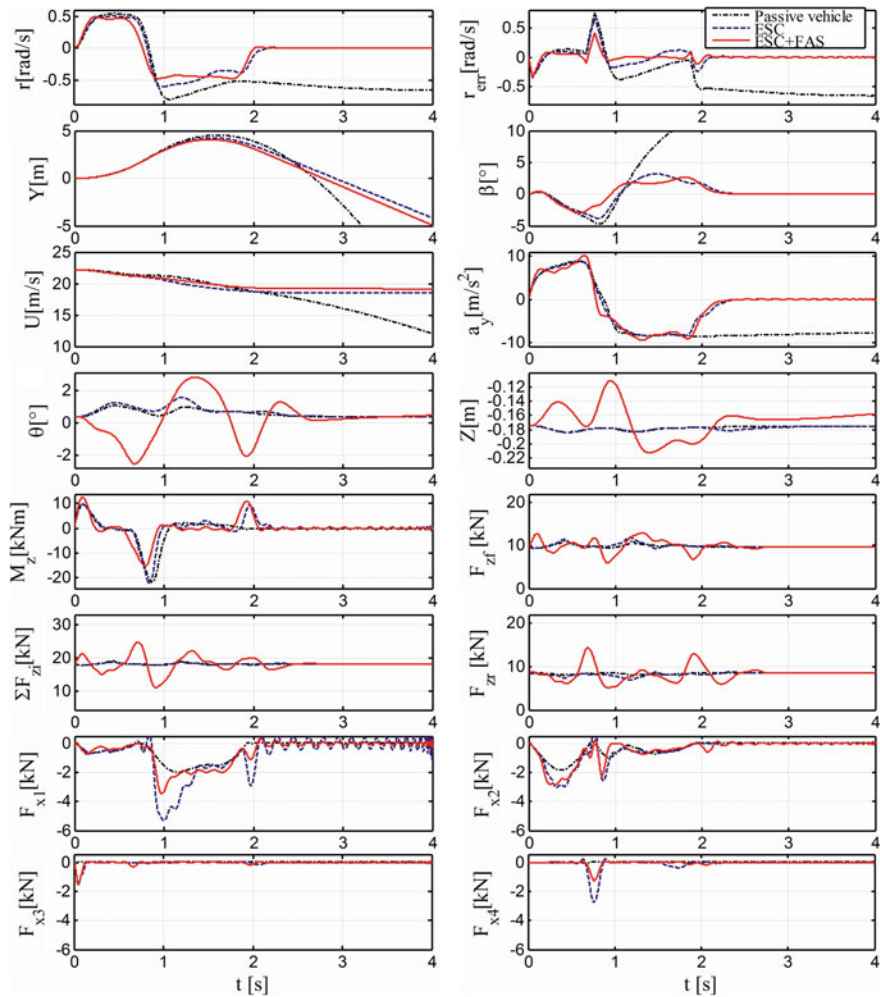


**Fig. 55** Comparative FAS + ESC optimization results for sine-with-dwell maneuver, including comparison with passive vehicle and ESC-only cases

1999). The OSC action is emphasized in the interval around  $t = 1$  s in order to suppress the excursion of sideslip angle  $\beta$  resulting in stabilization effect, as well as around  $t = 2$  s, but to a lower extent.

The ESC + FAS optimization results in Fig. 55 point to a significant yaw rate error reduction leading to 45% lower yaw rate root-mean-square (RMS) error, and also  $\beta$ -peak reduction resulting in a wider stability margin (see the performance indices given in Table 1). This is achieved by two distinct actions that can be observed in Fig. 55: (i) the total tire load boost (see  $\Sigma F_{zi}$  around  $t = 0.7$  s and  $t = 1.3$  s) that increases the lateral acceleration  $a_y$  over its saturation level for

**Table 1** Comparative stability control performance indices for different actuator configurations and FAS control strategies ( $k = 0.01$  in Eq. (57))

Case <sup>a</sup>	$\max(Y)$ (m)	RMS <sup>b</sup> ( $r_{err}$ ) (rad/s)	$ \dot{W} _{\max}$ (m/s <sup>2</sup> )	$ \beta _{\max}$ (°)	$ \theta _{\max}$ (°)	$U(t_f)$ (m/s)
No control	4.51	0.471	0.38	29.63	1.08	11.87
ESC	4.22	0.126	0.33	3.82	1.57	18.48
FAS1	4.21	0.073	5.28	2.85	3.37	19.82
FAS2	3.86	0.077	0.81	2.97	3.09	19.83
FAS3	3.81	0.096	0.33	2.46	1.08	19.88
FAS4	4.33	0.088	7.91	3.16	1.28	19.85
FAS5	4.16	0.083	6.23	3.16	1.23	19.90
FAS6	4.23	0.153	0.33	6.48	0.95	19.35
FAS7	3.69	0.097	0.33	2.78	1.05	19.86
ESC + FAS	4.05	0.070	3.80	2.95	2.85	19.12
Active brakes	3.61	0.074	0.40	3.25	2.00	11.61

<sup>a</sup>FAS1—Full FAS control<sup>b</sup>RMS = Root Mean SquareFAS2—Hard constraint on total actuator force  $\sum F_{zi} = 0$ FAS3—Laterally anti-symmetric force distribution ( $\Delta F_{z1} = -\Delta F_{z2}$ ,  $\Delta F_{z3} = -\Delta F_{z4}$ )FAS4—Longitudinally symmetric force distribution ( $\Delta F_{z1} = \Delta F_{z3}$ ,  $\Delta F_{z2} = \Delta F_{z4}$ )FAS5—Warp-related constraint ( $\Delta F_{z1} = \Delta F_{z4}$ ,  $\Delta F_{z2} = \Delta F_{z3}$ )FAS6—Longitudinally symmetric and laterally anti-symmetric force distribution ( $\Delta F_{z1} = \Delta F_{z3} = -\Delta F_{z2} = -\Delta F_{z4}$ )FAS7—Coupled warp-related constraint ( $\Delta F_{z1} = \Delta F_{z4} = -\Delta F_{z2} = -\Delta F_{z3}$ )

improved handling, and (ii) transfer of load from front to rear tires to generate OSC yaw torque (see  $F_{zf}$  and  $F_{zr}$  around  $t = 0.65$  s and  $t = 1.9$  s). As side effects, the former excites significant heave motion (the heave acceleration peak of 0.38 g, Table 1), while the latter causes emphasized pitch angle magnitudes ( $\theta$ ). The lateral displacement  $Y$  (i.e. the responsiveness) remains largely unaffected. However, the agility is notably improved in the case of integrated control ( $U(t_f)$  is higher,  $t_f = 4$  s), because the ESC + FAS system uses the brakes to a lower extent than in the ESC-only case (see  $F_{x1}, \dots, F_{x4}$ ).

Since the optimization is inherently conducted over the full time window (full-horizon preview is available), the comparison between the optimized FAS control action and the causal ESC action (no preview) is strictly speaking unfair. To provide a more appropriate comparison between the FAS and ESC systems control authorities, the same preview-based optimization approach has been applied in the FAS-only case ( $\Delta F_{zi}$  inputs are optimized) and active brake-only case ( $T_i$  inputs are optimized). The corresponding results given in Table 1 under the labels ‘FAS1’ and ‘Active brakes’ show that the optimized FAS and active brake systems give comparable yaw rate RMS errors. The advantages of FAS control include improved responsiveness (by 17%) and agility (by 40%), while the disadvantages are related

to increased magnitudes of heave acceleration (0.5 g vs. 0.04 g) and pitch angle (3.4° vs. 2°).

In order to investigate if the ultimate FAS performance can be approached by simpler control actions based on lower number of control DOFs, the FAS control input optimization scenarios defined in the legend of Table 1 under the labels ‘FAS2’–‘FAS7’ are also considered. The main conclusions drawn from the corresponding performance indices are as follows: (1) the application of zero total FAS force constraint (FAS2; three control inputs) gives only slight reduction of control performance, with an advantage of no heave motion excitation (no total tire load boost is allowed); (2) in the cases of longitudinally symmetric force constraint and warp-related constraints (FAS4 and FAS5, respectively; two control inputs in both cases), the performance also remains high, the pitch motion excitation is avoided (no front/rear tire load transfer is allowed), but the heave acceleration is excessive; and (3) in the case of coupled warp-related constraint (FAS7; only a single control input), the performance is notably deteriorated, but it is still better than that of the ESC case, and both pitch and heave dynamics excitation is avoided. For the coupled warp-related constraint, the FAS control makes the front tire loads more distinctive from each other and the rear tire loads more balanced, thus providing an oversteer compensation action based on the convexity of the lateral force versus normal load tire curve (Pacejka 2006). At the same time, the total tire load, heave, and suspension deflection are kept approximately constant, so that the control action can be applied during steady-state turns, as well. FAS3 configuration gives comparable performance as in the case of FAS7 configuration, but it includes one control DOF more. FAS6 configuration is inferior to other configuration, because it does not allow for load boost, front/rear load transfer, and different left/right load transfers on the two axles.

## 6.4 Handling Control—Path Following

A path following minimization objective is used along a double lane change maneuver (DLC) to further investigate the FAS control authority, particularly under the conditions of understeer behavior (with respect to reference trajectory). The optimization problem is to find the FAS control inputs  $\Delta F_{zi}(t)$ ,  $0 \leq t \leq t_f$ ,  $i = 1, \dots, 4$ , which minimize the cost function

$$J = \underbrace{\int_0^{t_f} (Y - Y_R(X))^2 dt}_{J_0} + k_1 \int_0^{t_f} \sum_{i=1}^4 (F_{zi} - F_{zi0})^2 dt + k_2 \int_0^{t_f} \theta^2 dt + k_3 \int_0^{t_f} \phi^2 dt + k_4 \int_0^{t_f} \sum_{i=1}^4 \dot{\eta}_i^2 dt \quad (58)$$

subject to inequality constraints similar to those given by Eqs. (54)–(56). In addition to the main, cost function term  $J_0$ , which penalizes the path following error, there are other, soft constraint-related terms penalizing the control effort, pitch and roll magnitudes, and excessive longitudinal slip excursions.

Figure 56 shows the optimization results for the worst-case DLC Maneuver 3. The reference response corresponds to the passive vehicle for  $\mu = 1$ , zero driveline torque, and optimized driver steering input. The achieved vehicle path  $Y(X)$  is used as the reference path for other cases presented in the same figure, where the same driver steering input is applied, but for the reduced tire-road friction coefficient  $\mu = 0.6$  and the driveline input torque  $T_{in} = 250 \text{ Nm}$ . Under these conditions the passive vehicle ('No control' case) becomes unstable (see  $\beta$ ). The optimized active front steering (AFS) control stabilizes the vehicle and provides an accurate path following.

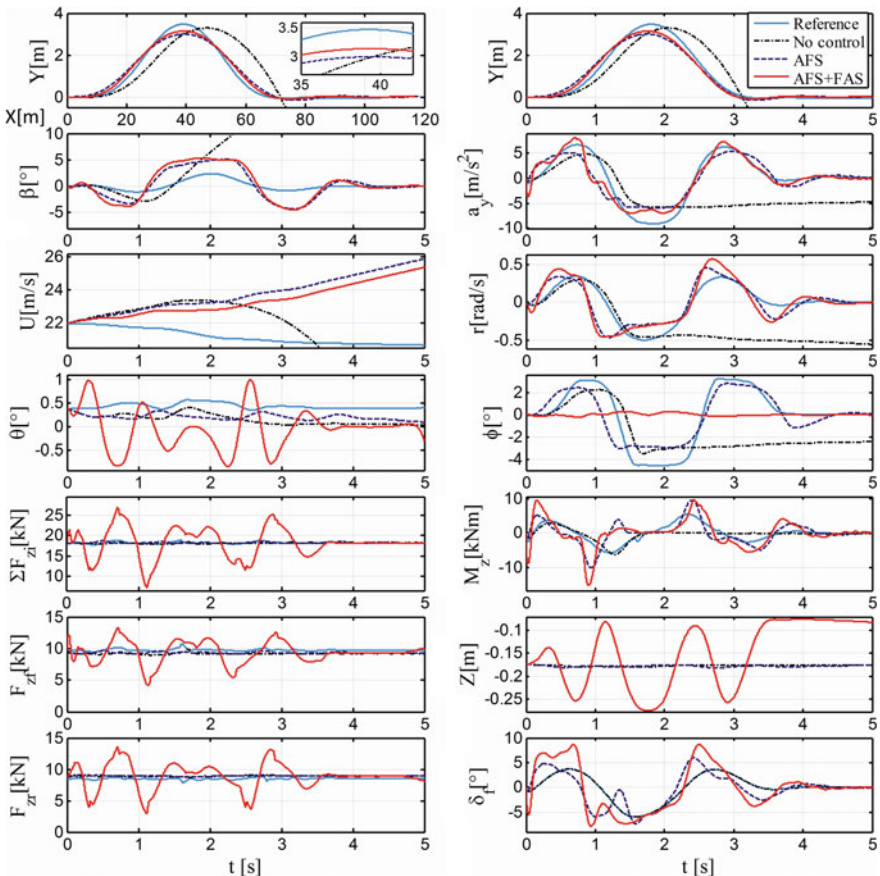


**Fig. 56** Comparative AFS and FAS + AFS optimization results for path following task and Maneuver 3 ( $\mu = 0.6$ ,  $T_{in} = 250 \text{ Nm}$ )

The path following RMS error is further reduced (by 30%) when the integrated AFS + FAS control is applied. Since the AFS has a large control authority over the lateral vehicle dynamics, the FAS action is focused on the effect of boosting the total tire load ( $\Sigma F_{zi}$ ) and, thus, the lateral acceleration ( $a_y$ ) capacity in the critical intervals. The FAS also provides a certain rear-to-front tire load transfer by strongly unloading the rear axle for understeer compensation (USC) around the intervals of 0.3, 1.1, and 2.6 s. The side effects of FAS action are again related to excitation of heave and pitch dynamics: the heave acceleration peak is 0.6 g while the pitch angle amplitude is relatively modest (1°).

Table 2 shows the performance indices related to FAS-only optimization results obtained for Maneuver 1 ( $\mu = 0.6$ ,  $T_m = 0$ ) and different sets of cost function weighting factors given in the table legend. In the unconstrained case (no hard and soft constraints, Case 1), almost ideal path following can be achieved ( $J_0 \rightarrow 0$ ). However, this case is unrealistic due to very high heave peaks required by the strong FAS action (43 cm from the equilibrium  $Z_0$ ), i.e. due to violation of the suspension stroke limits ( $\pm 10$  cm). After adding the hard constraint on suspension stroke (Eq. (56); Case 2), the path following RMS error ( $J_0/t_f$ )<sup>1/2</sup> grows significantly, but it remains substantially lower compared to the no-control case. By adding the soft constraint on control effort (Cases 3 and 4), the FAS control amplitudes become smaller, thus reducing the FAS consumed energy  $E = \int \Delta F_{zi} v_{zi} dt$ , as well as the pitch angle, heave, and heave acceleration magnitudes. This is paid for by reduction of the path following performance, which is more emphasized in the case with higher control effort weighting factor  $k_1$  (Case 4). When compared to the optimization results for Case 5 (considered in Fig. 56; the pitch and roll angle magnitudes are constrained), the less restrictive tuning related to Case 3 provides a significant improvement in the path following performance

**Table 2** Comparative performance indices of FAS optimization results for different sets of constraints and Maneuver 1 ( $\mu = 0.6$ ,  $T_m = 0$ )

Case <sup>a</sup>	$(J_0/t_f)^{1/2}$ (m)	$ \beta _{\max}$ (°)	$X(t_f)$ (m)	$E$ (kJ)	$ \dot{W} _{\max}$ (m/s <sup>2</sup> )	$ \theta _{\max}$ (°)	$ Z - Z_0 _{\max}$ ( $ z_i - z_{i0} _{\max}$ ) (cm)
No control	4.493	8.0	103.1	0	0.3	0.7	0.6 (7.0)
Case 1	0.004	5.5	102.3	22.7	15.3	18.8	43.0 (69.0)
Case 2	0.182	5.2	104.4	7.0	10.1	4.6	10.0 (12.8)
Case 3	0.194	5.0	104.7	5.4	7.7	4.2	8.9 (11.1)
Case 4	0.262	4.4	105.5	3.4	4.3	4.2	2.6 (10.2)
Case 5	0.285	4.1	105.7	1.4	2.8	2.5	9.1 (10.1)

<sup>a1</sup>Unlimited FAS (no hard constraints and  $k_1 = k_2 = k_3 = 0$  in Eq. (58))

<sup>2</sup>Added suspension deflection constraint ( $k_1 = k_2 = k_3 = 0$ )

<sup>3</sup>Added weak constraint on control effort ( $k_1 = 0.001$ ,  $k_2 = k_3 = 0$ )

<sup>4</sup>Added strong constraint on control effort ( $k_1 = 0.01$ ,  $k_2 = k_3 = 0$ )

<sup>5</sup>Added constraints on pitch and roll angle magnitudes ( $k_1 = 0.01$ ,  $k_2 = 0.1$ ,  $k_3 = 0.1$ )

**Table 3** Comparative path following RMS error values (m) for different active steering and FAS configurations and different DLC maneuver types

Maneuver	ARS	FAS	ARS + FAS	AFS	AFS + FAS	4WS	4WS + FAS
1	0.112	0.281	0.077	0.137	0.086	0.091	0.067
2	0.044	0.197	0.025	0.045	0.027	0.030	0.023
3	0.175	0.405	0.141	0.229	0.157	0.163	0.130

Maneuver 1:  $\mu = 0.6$ ,  $T_{in} = 0$

Maneuver 2:  $\mu = 1$ ,  $T_{in} = 350$  Nm

Maneuver 3:  $\mu = 0.6$ ,  $T_{in} = 250$  Nm

(30% lower RMS error). However, the control effort is increased to such extent that the tire load lower amplitudes approach the limit value set to 500 N.

Table 3 shows the path following RMS errors (m) for various single- and multi-actuator configurations, and different DLC maneuver types. Maneuver 1 is similar to the already described Maneuver 3, but the driveline torque is set to zero. Maneuver 2 is executed for the non-reduced friction coefficient ( $\mu = 1$ ) like in the reference case, but with a relatively high driveline torque ( $T_{in} = 350$  Nm). The results in Table 3 indicate that the FAS-only control is inferior to the AFS/ARS control, which may appear to be in contrast with the handling control results from Sect. 6.3, where the FAS was very competitive to active brake control. This is because in the considered control task a strong USC action is required, including the preview action during the initial period when the vehicle moves straight ahead (see  $\delta_f = \delta_1 = \delta_2$  in the AFS case in Fig. 56). The fact that the FAS cannot generate lateral tire force in the absence of tire sideslip angle explains its inferiority compared to AFS. Nevertheless, it effectively stabilizes the vehicle and provides relatively accurate path following.

Table 3 further shows that the ARS is more effective than AFS, because it utilizes a driver-untapped lateral force potential of rear tires (Deur et al. 2014). The FAS action is, thus, less effective when integrated with ARS (than with AFS), and it is reduced solely to the unique ability of FAS to boost the total tire load and the lateral acceleration. This unique control authority explains why the FAS brings more significant improvement to the AFS (in the AFS + FAS configuration) than the ARS does (in the ARS + AFS = 4WS configuration).

There are several other, secondary mechanisms through which the FAS can improve the vehicle handling performance (Čorić et al. 2016b). First, for a throttle-on maneuver and the example of rear-wheel-drive vehicle, the FAS unloads the inner driven tire to increase its longitudinal slip and, thus, weaken its lateral force to provide USC. Next, as already mentioned in Sect. 6.3, the FAS can increase the left-right tire load difference on the front axle and make the tire load more balanced on the rear axle, thus generating OSC yaw torque based on the convexity feature of the tire lateral force versus load static curve. Finally, the FAS can provide the vehicle tilting effect as an USC intervention acting through the front-axle bump steer component of the toe effect.

## 6.5 Ride Comfort and Tire Impact Control for Bumps and Potholes

In the case of bump-type road disturbance and the quarter-car vehicle model given in Fig. 52c, the cost function is defined as (see Sect. 3.2):

$$J = k_{11} \underbrace{\int_0^{t_f} \dot{x}_4^2 dt}_{J_{11}} + k_{12} \underbrace{\int_0^{t_f} (x_1 - x_{10})^2 dt}_{J_{12}} + k_{13} \underbrace{\int_0^{t_f} (x_3 - x_{30})^2 dt}_{J_{13}} + k_{14} \underbrace{\int_0^{t_f} F_a^2 dt}_{J_{14}} \quad (59)$$

where the terms  $J_{11}, \dots, J_{14}$  penalize the ride discomfort, loss of road holding/handling ability, excessive suspension stroke, and control input oscillations, respectively. The only hard constraint applied in the basic optimization case relates to the FAS actuator force limits:  $-2500 \leq F_a [\text{N}] \leq 2500$ .

The dashed-line blue curves in Fig. 57 represent the corresponding optimization results for the case of high-amplitude bump (10 cm), bump length of 0.1 s, and the bump preview time of 0.2 s (see  $z_r$  response). Immediately before the bump occurrence, the FAS generates a positive force  $F_a$ , which tends to lift the tire (see  $x_1$  and  $F_z$ , and also Fig. 52c), thus reducing the strong tire-bump impact. Consequently, the sprung mass acceleration  $d\dot{x}_4/dt$  is suppressed when compared to the passive vehicle, thus resulting in better ride comfort. After the wheel hop peak, occurring around  $t = 0.3$  s (see  $x_1$ ), the FAS abruptly reverses its action ( $F_a < 0$ ) to prevent the strong sprung mass (free) fall that would affect the ride comfort.

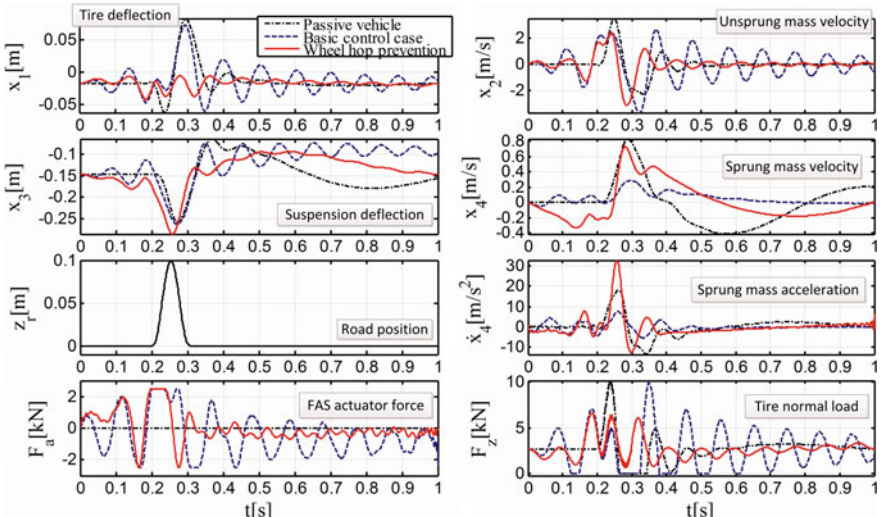


**Fig. 57** Optimization results for emphasized discrete bump-type road disturbance

However, such “bang-bang”-like FAS action excites strong oscillations of the system response, which results in residual wheel hops and related temporary losses of road holding ability ( $F_z = 0$ ). During the bump preview period ( $t < 0.2$  s), the FAS prepares for the tire lift action at the leading bump edge by exciting the unsprung mass oscillations with a proper phase angle.

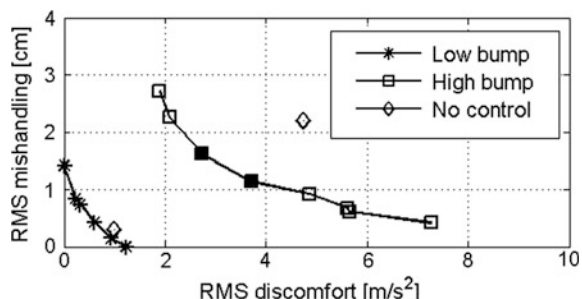
The solid-line red response in Fig. 57 corresponds to the case of imposing the lower-limit constraint on the tire normal load ( $F_z > 1000$  N), and also applying the final time conditions on the state and control variable that are equal to the corresponding initial conditions. The wheel is prevented from hopping (see  $x_1$  and  $F_z$  responses) by generating a strong negative FAS force  $F_a$  after the bump peak ( $0.25 < t$  (s)  $< 0.3$ ), which presses the wheel to the ground. However, the reactive force of the same amount  $F_a$  acts on the sprung mass (see Fig. 52), thus causing a very strong peak of the sprung mass acceleration and affecting the ride comfort. Therefore, there is an evident trade-off between the ride comfort and road holding ability. The summarized performance plot shown in Fig. 58 indicate that the cost function weighting factors can be tuned so that both ride comfort and road holding indices are notably better than in the passive vehicle case, particularly in the high-bump case.

The analysis has been extended to the case of full vehicle model (Fig. 52a, b) with the unsprung mass dynamics included. It has been found that there is an additional cross-axle FAS control mechanism, which reduces variation of the total (four-corner) sprung mass/chassis force for improved ride comfort (Čorić et al. 2016a). This mechanism counteracts the anti-wheel-hop peak of suspension force on the active axle (the one exposed to the bump) by means of suspension force reduction on the inactive axle.

In the pothole case the cost function is formulated as

$$J = \underbrace{\int_0^{t_f} (F_a(x_2 - x_4))^2 dt}_{J_{31}} + k_{32} \underbrace{\int_0^{t_f} \dot{x}_4^2 dt}_{J_{32}} + k_{33} \underbrace{\left( -\min(z_u) \Big|_{t_p}^{\tau_p + T} \right)}_{J_{33}} + k_{34} \underbrace{\int_0^{t_f} F_a^2 dt}_{J_{34}} \quad (60)$$

**Fig. 58** Pareto frontier-like diagram for two main performance indices ( $(J_{12}/t_f)^{1/2}$  versus  $(J_{11}/t_f)^{1/2}$  based on definition in Eq. (59)) and low (2 cm) and high (10 cm) amplitude of bump-type road disturbance



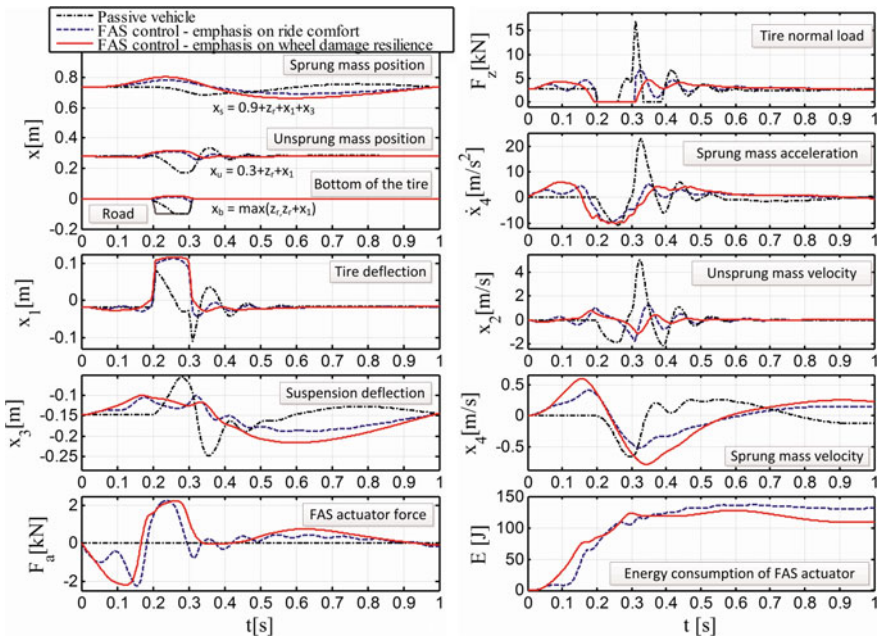


**Fig. 59** Optimization results for emphasized discrete pothole-type road disturbance of square shape

The main difference compared to the cost function (59) relates to two additional terms,  $J_{31}$  and  $J_{33}$ , which penalize the FAS actuator energy consumption and the tire sensitivity to damage during the pothole interval, respectively. The hard constraints include the aforementioned actuator force limit and the state variable boundary condition.

Figure 59 shows the optimization results for the case of square-shape pothole with the depth of 0.1 m, length of 0.1 s, and the preview time of 0.2 s. Regardless of the cost function tuning, the optimal system behavior is such that the wheel hops over the pothole (see  $x_b$ ) to prevent the wheel damage on the pothole trailing edge (see  $x_1$  and  $F_z$  immediately after  $t = 0.3$  s). To effectively prepare for the wheel hop, the FAS first increases the (absolute value of) tire deflection  $x_1$  immediately before the pothole ( $F_a < 0$ ). It then quickly reverses its control action ( $F_a > 0$ ) to lift the wheel near the pothole leading edge ( $t \cong 0.2$  s) with some significant hop-off velocity  $x_2$ . The response of FAS energy consumption  $E$  indicates that the FAS predominantly generates active force ( $dE/dt > 0$ ), where the power peaks equal around 1.5 kW.

The main difference between the two active control responses in Fig. 59 is that the wheel entirely hops over the pothole when the emphasis is on damage prevention (solid red curves) compared to the case when the ride comfort is emphasized (dashed blue curves). In the former case, the FAS action  $F_a$  is stronger (longer) both in the preview phase ( $t < 0.2$  s) and during the pothole period

**Table 4** Comparative performance indices for passive vehicle and three FAS control optimization cases for pothole-type road disturbance

Case	Square-shaped pothole		
Cost	$(J_{32}/t_f)^{1/2}$ (m/s <sup>2</sup> )	$E$ (kJ)	$J_{33}$ (cm)
No control	6.6	–	12.8
Case 1	2.9	0.14	2.5
Case 2	3.5	0.05	3.0
Case 3	4.0	0.12	0.0

In Cases 1, 2, and 3 the emphasis is on ride comfort, energy saving, and wheel damage robustness, respectively

( $0.2 < t$  (s)  $< 0.3$ ), in order to better prepare for the wheel hop and keep the wheel lifted action when hopping over. The post-pothole peak of the normal tire force  $F_z$  is not only lower in that case, but it occurs after the trailing edge, thus reducing further the possibility of wheel damage. However, the ride comfort is reduced (see  $dx_4/dt$ ) due to the stronger FAS activity before and during the pothole period.

Another cost function tuning case is also considered in (Čorić et al. 2016a), where the emphasis is on energy consumption. In this case the FAS action is such that it keeps the suspension deflection  $x_3$  approximately constant during the pothole period (and longer), i.e. no power is consumed in that case (as  $dx_3/dt \cong 0$  holds in that case). This results in halving the energy consumption compared to the previous two cases, but the ride comfort or wheel damage robustness is compromised.

The above results are further illustrated by the performance indices listed in Table 4 based on the definition of the cost function terms in Eq. (60), and for three characteristic sets of weighting functions. In all cases, the FAS improves the wheel damage robustness (see  $J_{33}$ ), and, it also, improves the ride comfort performance ( $J_{32}$ ) when compared to the passive vehicle. In Case 3, the wheel damage is avoided, while the other two cost indices are modestly high. In Case 2 the energy consumption is the lowest, but ride comfort and wheel damage robustness are inferior compared to Case 1.

The case of long pothole is analyzed in (Čorić et al. 2016a), as well. In that case the optimal behavior includes the phases of (i) wheel landing and traveling over the pothole bottom, and (ii) hopping over the pothole trailing edge.

## 6.6 Summary

The presented control variable optimization study has pointed to the unique control authority of FAS, which relates to boosting the tire load for providing an increased tire friction potential and improved vehicle dynamics control (VDC) performance. The tire load boost can be applied under conditions of non-uniform tire friction coefficient  $\mu$  (the load is increased during the high- $\mu$  interval, e.g. for improved ABS performance) or during the critical handling/cornering maneuvers (to increase the lateral acceleration over its  $\mu$ -related saturation level and improve the VDC

performance without affecting the agility). The VDC performance can also be enhanced by the FAS ability to generate oversteer compensation- or understeer compensation-yaw torque by transferring the load to rear or front tires, respectively. There are additional FAS control mechanisms for enhanced VDC, such as those relying on spinning a driven tire by reducing its load, balancing the left-right tire load on an axle to boost its lateral force, and increasing the steering effort through the bump steer component of the toe effect. Finally, in the case of emphasized discrete road disturbances such as high-amplitude bumps and potholes, a proper (optimal) FAS control action can improve both ride comfort and road holding performance. Moreover, in the pothole case, the wheel damage can be prevented by forcing it to hop over the pothole.

However, the FAS control action has certain side effects and limitations. The tire load boost and load transfer actions are directly associated with excitation of heave and pitch dynamics, respectively, thus affecting the driving comfort. Due to the limited suspension stroke, the FAS actions can last only for a relatively short interval, and they would, thus, not be very effective in nearly steady-state turns or transient maneuvers performed at slower rates of change. To emphasize the FAS control effect (e.g. the tire load boost) and satisfy the suspension stroke constraint, the FAS action typically includes a preparatory phase during the preview period (e.g. a tire load hole), and is usually succeeded by a similar relaxation phase. This makes the control system development more challenging, as it would require some kind of on-line optimization that is typically included within the model predictive control framework, and a preview of critical period of maneuver and/or road disturbance. Another limitation relates to the fact that the FAS cannot influence the tire lateral forces unless the tire is subject to non-zero lateral sideslip angle. This affects the effectiveness of understeer compensation, particularly when it is a part of preview control action during straight ahead driving.

There is though a FAS action that is not associated with most of the above side effects. When the tire normal loads are distributed in the warp-like arrangement, the FAS action does not excite the heave and pitch dynamics, and it can be applied during steady-state turns and braking maneuvers in a simplified (more conventional) control law formulation. However, this action has a lower control authority than the load boost and front/rear load transfer actions, thus usually resulting in limited control performance enhancement.

It is believed that the encouraging results of this study may serve as a solid basis and inspiration for future possible extensions, especially when combined with (semi)autonomous vehicles fortified by V2V, V2I, detailed 3D mapping, and similar exciting and promising future developments.

**Acknowledgements** Assistance of Dr. Li Xu and Dr. Mirko Čorić in preparation of these class notes and related slides, and the help of Professor Rill with some figures, is gratefully acknowledged.

## Appendix

In this appendix we establish the LQG-optimal trade-off line for the 1 DoF model of Fig. 7. We start with the covariance (Lyapunov) equation

$$(A - BK)X + X(A - BK)^T = -G\Gamma G^T \quad (61)$$

where in our case  $G^T = [-1 \ 0]$  and  $\Gamma = 1$  since we are dealing with normalized covariance,

$$X = \begin{bmatrix} X_1 & X_3 \\ X_3 & X_2 \end{bmatrix} \quad (62)$$

where,

$$X_1 = (X_{1, rms, norm})^2, \text{ and } X_2 = (X_{2, rms, norm})^2 \quad (63)$$

Define

$$A_{CL} = A - BK = \begin{bmatrix} 0 & 1 \\ -k_1 & -k_2 \end{bmatrix} \quad (64)$$

with optimal control gains

$$k_1 = r^{-1/2}, \quad k_2 = \sqrt{2}r^{-1/4} \quad (65)$$

then the covariance equation becomes

$$A_{CL}X + XA_{CL}^T = -GG^T \quad (66)$$

or

$$\begin{bmatrix} 2X_3 & X_2 - k_1X_1 - k_2X_3 \\ X_2 - k_1X_1 - k_2X_3 & -2k_1X_3 - 2k_2X_2 \end{bmatrix} = \begin{bmatrix} -1 & 0 \\ 0 & 0 \end{bmatrix} \quad (67)$$

Solving for  $X_1$ ,  $X_2$ , and  $X_3$ ,

$$X_1 = \frac{3}{2\sqrt{2}}r^{1/4}, \quad X_2 = \frac{1}{2\sqrt{2}}r^{-1/4}, \quad X_3 = -\frac{1}{2} \quad (68)$$

from where we get the normalized rms rattlespace

$$x_{1, rms, norm} = \sqrt{X_1} = \frac{\sqrt{3}}{\sqrt{2\sqrt{2}}} r^{1/8} \quad (69)$$

The normalized rms sprung mass acceleration then follows from

$$U = K X K^T = \frac{1}{2\sqrt{2}} r^{-3/4} \quad (70)$$

so that

$$U = \frac{27}{64} X_1^{-3} \quad (71)$$

resulting in the normalized rms acceleration versus rattlespace equation

$$u_{rms, norm} = \frac{3\sqrt{3}}{8} x_{1, rms, norm}^{-3} \quad (72)$$

which was used to plot the corresponding optimal trade-off line in Fig. 13.

## References

- Akatsu, Y. N., Fukushima, K., Takahashi, M., Satch, M., & Kawarasaki, Y. (1990). *An active suspension employing an electrohydraulic pressure control systems*. SAE Paper No. 905123.
- Alleyne, A. (1997). Improved vehicle performance using combined suspension and braking forces. *Vehicle System Dynamics*, 27(4), 235–265.
- Anderson, B. D. O., & Moore, J. B. (1971). *Linear optimal control*. London: Prentice-Hall International.
- Anderson, B. D. O., & Vongpanitlers, S. (1973). *Network analysis and synthesis*. Englewood Cliffs, NJ: Prentice Hall.
- Anderson, B. D. O., & Moore, J. B. (1990). *Optimal control*. Englewood Cliffs: Prentice-Hall.
- Anderson, Z. M., Morton, S., Jackowski, Z. J., & Bavetta, R. (2013, March 5). *Inventors; Levant Power Corporation, assignee. System and method for control for regenerative energy generators*. United States patent US 8,392,030.
- Anonymous. (1972). *A guide to the evaluation of human exposure to whole body vibration*. ISO/DIS 2631, International Standard Organization, New York.
- Anonymous. (2007). FMVSS No. 126. *Electronic Stability Control Systems*. National Center for Statistics and Analysis.
- Anonymous. (2017a). [https://en.wikipedia.org/wiki/Active\\_Body\\_Control](https://en.wikipedia.org/wiki/Active_Body_Control).
- Anonymous. (2017b). <http://www.incosse.org/AboutSE/WhatIsSE>.
- Anonymous. (2017c). <https://en.wikipedia.org/wiki/V-Model>.
- Asgari, J., & Hrovat, D. (1991). Bond graph models of vehicle 2D ride and handling dynamics. In *Proceedings of the 1991 ASME Winter Annual Meeting*, Publication DE-Vol. 40 (Advanced Automotive Technologies 1991), Atlanta, December 1991.
- Athans, M., & Falb, P. L. (1966). *Optimal control*. New York: McGraw-Hill.

- Barak, P. (1985). *On a ride control algorithm for heave, pitch and roll motions of a motor vehicle*. Ph.D. Thesis, Wayne State University, Detroit, MI.
- Barak, P., & Hrovat, D. (1988). Application of the LQG approach to design of an automotive suspension for 3D vehicle models. In *Proceedings of the International Conference on Advanced Suspensions*. London, UK: IMECE.
- Bendat, J. S., & Piersol, A. G. (1971). *Random data*. New York: Wiley.
- Bender, E. K. (1967a). *Optimization of the random vibration characteristics of vehicle suspensions using random process theory*. ScD Thesis, MIT, Cambridge, MA.
- Bender, E. K. (1967b). Optimum linear control of random vibrations. In *Proceedings of the JACC* (pp. 135–143).
- Bender, E. K., Karnopp, D. C., & Paul, I. L. (1967). *On the optimization of vehicle suspensions using random process theory*. ASME Paper No. 67-Tran-12.
- Bodie, M. O., & Hac, A. *Closed loop yaw control of vehicles using magneto-rheological dampers*. SAE Technical Paper No. 2000-01-0107.
- Carbonaro, O. (1990). Hydractive suspension electronic control system. SAE Paper No. 905101. In *Proceedings of the 23rd FISITA Congress, Torino, Italy* (pp. 779–783).
- Chalasani, R. M. (1986). Ride performance potential of active suspension systems—Part II: Comprehensive analysis based on full-car model. *ASME Monograph AMD-80, DSC-I*.
- Chance, B. K. (1984). *Continental Mark VII/Lincoln continental electronically-controlled air suspension (EAS) system*. SAE Technical Paper 840342.
- Chatillon, M., Jezequel, L., Coutant, P., & Baggio, P. (2006). Hierarchical optimization of the design parameters of a vehicle suspension system. *Vehicle System Dynamics*, 44(11), 817–839.
- Chen, H., Sun, P., & Guo, K. (2003). A multi-objective control design for active suspensions with hard constraints. *Proceedings of the American Control Conference*, 5, 4371–4376.
- Clarke, P. (2012). *Mass dampers*. Retrieved August 22, 2012, from <https://racemagazine.com.au/editorial/mass-dampers>.
- Crosby, M., & Karnopp, D. C. (1973). The active damper—A new concept for shock and vibration control. *Shock and Vibration Bulletin, Part H* (Washington, D.C.).
- Čorić, M., Deur, J., Xu, L., Tseng, H. E., & Hrovat, D. (2016a). Optimization of active suspension control inputs for improved vehicle ride performance. *Vehicle System Dynamics*, 54(7), 1004–1030.
- Čorić, M., Deur, J., Kasać, J., Tseng, H. E., & Hrovat, D. (2016b). Optimization of active suspension control inputs for improved vehicle handling performance. *Vehicle System Dynamics*, 54(11), 1574–1600.
- Čorić, M., Deur, J., Xu, L., Tseng, H. E., & Hrovat, D. (2017). Optimisation of active suspension control inputs for improved active safety systems performance. *Vehicle System Dynamics*. <https://doi.org/10.1080/00423114.2017.1340652>.
- Davis, R. I. & Patil, P. B. (1991). *Electrically powered active suspension for a vehicle*. US Patent 5,060,959.
- Deur, J., Čorić, M., Kasać, J., Assadian, F., & Hrovat, D. (2014). Application of computational optimal control to vehicle dynamics. In H. Waschl et al. (Eds.), *Optimization and optimal control in automotive systems* (pp. 131–145). Cham: Springer.
- Dodds, C. J., & Robson, J. D. (1973). The description of road surface roughness. *Journal of Sound and Vibration*, 31(2), 175–183.
- Doyle, J. (1978). Guaranteed margins for LQG regulators. *IEEE Transaction on Automatic Control*, 23(4), 756–757.
- Edmunds, D. (2012). *2012 Tesla Model S signature performance suspension walkaround*. [Online]. Retrieved September 26, 2012, from <http://www.edmunds.com/car-reviews/track-tests/2012-tesla-model-s-signature-performance-suspension-walkaround.html>.
- Elbeheiry, S. A., Karnopp, D. C., Elaraby, M. E., & Abdelraouf, A. M. (1995). Advanced ground vehicle suspension systems—A classified bibliography. *Vehicle System Dynamics*, 24, 231–258.
- Evers, W.-J. (2010, May). *Improving driver comfort in commercial vehicles*. Ph.D. Thesis, TU Eindhoven, Eindhoven.

- Evers, W. J., Besselink, I. J. M., van der Knaap, A. C. M., & Nijmeijer, H. (2008). Analysis of a variable geometry active suspension. In *Proceeding of International Symposium on Advanced Vehicle Control (AVEC)* (pp. 350–355).
- Fearnside, J. J., Hedrick, J. K., & Firouztask, H. (1974). Specification of ride quality criteria for transportation systems: The state of the art and new approach. *High Speed Ground Transportation Journal*, 8(2), 125–132.
- Fridman, E. (2014). *Introduction to time delay systems: Analysis and control*. Birkhauser.
- Giorgetti, N., Bemporad, A., Tseng, H. E., & Hrovat, D. (2006). Hybrid model predictive control application towards optimal semi-active suspension. *International Journal of Control*, 79(5), 521–533.
- Gobbi, M., & Mastinu, G. (2001). Analytical description and optimization of the dynamic behaviour of passively suspended road vehicles. *Journal of Sound and Vibration*, 245(3), 457–481.
- Goran, M., & Smith, R. (1996). Insights gained from active suspension development. In *Proceedings of the 26th FISITA Congress* (pp. 2486–2514).
- Goran, M. B., Bachrach, B., & Smith, R. E. (1992). The design and development of a broad bandwidth active suspension concept car. SAE Paper No. 925100. In *Proceedings of the 24th FISITA Congress, London, UK* (pp. 231–252).
- Goto, T., Kizu, R., Sato, H., Ohnuma, T., & Ohno, H. (1990). Toyota active suspension control for the 1989 Celica. In *Proceedings of the 22nd ISATA Conference*, Paper 900007 (pp. 857–864).
- Gysen, B. L., Paulides, J. J., Janssen, J. L., & Lomonova, E. A. (2010). Active electromagnetic suspension system for improved vehicle dynamics. *IEEE Transactions on Vehicular Technology*, 59(3), 1156–1163.
- Hac, A. (1992). Optimal linear preview control of active vehicle suspension. *Vehicle System Dynamics*, 21, 167–195.
- Hancock, M. (2006). *Vehicle handling control using active differentials*. Ph.D. Thesis, University of Loughborough, UK.
- Hedrick, J. K., & Butsuen, T. (1990). Invariant properties of automotive suspensions. *Proceedings of the Institution of Mechanical Engineers*, 204, 21–27.
- How, J. P., & Frazzoli, E. (2010). *Feedback control systems*. On line course, Section 19, at <https://ocw.mit.edu/courses/aeronautics-and-astronautics/16-30-feedback-control-systems-fall-2010/>.
- Hrovat, D. (1982). A class of active LQG optimal actuators. *Automatica*, 18(1), 117–119.
- Hrovat, D. (1988). Influence of unsprung weight on vehicle ride quality. *Journal of Sound and Vibration*, 124(3), 497–516.
- Hrovat, D. (1990). Optimal active suspension structures for quarter-car vehicle models. *Automatica*, 26(5), 845–860.
- Hrovat, D. (1991a). Optimal suspension performance for 2-D vehicle models. *Journal of Sound and Vibration*, 146(1), 93–110.
- Hrovat, D. (1991b, June). Optimal active suspensions for 3D vehicle models. In *Proceedings of the 1991 American Control Conference, Boston* (pp. 1534–1541).
- Hrovat, D. (1993, June) Applications of optimal control to advanced automotive suspension design. Special Issue of the ASME *Journal of Dynamic Systems Measurement and Control* commemorating 50 years of the DSC division.
- Hrovat, D. (1997). Survey of advanced suspension developments and related optimal control applications. *Automatica*, 33(10), 1781–1817.
- Hrovat, D. (2014). Active and semi-active suspension control. In G. Mastinu & M. Plöchl (Eds.), *Road and off-road vehicle system dynamics handbook*. CRC Press.
- Hrovat, D., & Hubbard, M. (1981). Optimum vehicle suspensions minimizing RMS rattle-space, sprung-mass acceleration and Jerk. *ASME Journal of Dynamic Systems, Measurement and Control*, 103(3).
- Hrovat, D., & Margolis, D. L. (1975). Realistic road-track systems simulation using digital computers. In *Proceedings of the Winter Computer Simulation Conference, Sacramento, CA*.

- Hrovat, D., Asgari, J., & Fodor, M. (2000). Automotive mechatronic systems. In C. T. Leondes (Ed.), *Mechatronic systems, techniques and applications: Volume 2—Transportation and vehicle systems* (pp. 1–98). Gordon and Breach Science Publishers, 2000.
- Hrovat, D., Margolis, D. L., & Hubbard, M. (1988, September). An approach toward the optimal semi-active suspension. *ASME Journal of Dynamic Systems, Measurement and Control*, 110(3).
- Hrovat, D., Jankovic, M., Kolmanovsky, I., Magner, S., & Yanakiev, D. (2011a). Powertrain controls. In W. S. Levine (Ed.), *The control handbook: Control system applications* (2nd ed., pp. 2.1–2.48). CRC Press.
- Hrovat, D., Tseng, H. E., Lu, J., Deur, J., Assadian, F., Borrelli, F., & Falcone, P. (2011b). Vehicle controls. In W. S. Levine (Ed.), *The control handbook: Control system applications* (2nd ed., pp. 3.1–3.60). CRC Press.
- Hrovat, D., Di Cairano, S., Tseng, H. E., & Kolmanovsky, I. V. (2012, October). The development of model predictive control in automotive industry: A survey. In *Proceedings of the 2012 IEEE International Conference on Control Applications (CCA), Dubrovnik, Croatia* (pp. 295–302).
- Karlsson, N., Ricci, M., Hrovat, D., & Dahleh, M. (2000). A suboptimal nonlinear active suspension. *Proceedings of the 2000 American Control Conference* (Vol. 6, pp. 4036–4040).
- Karlsson, N., Teel, A., & Hrovat, D. (2001a). A backstepping approach to control of active suspensions. *Proceedings of the 40th IEEE Conference on Decision and Control* (Vol. 5, pp. 4170–4175).
- Karlsson, N., Dahleh, M., & Hrovat, D. (2001b). Nonlinear active suspension with preview. *Proceedings of the 2001 American Control Conference* (Vol. 4, 2640–2645).
- Karnopp, D. C. (1968). Continuum model study of preview effects in actively suspended long trains. *Journal of the Franklin Institute*, 285(4), 251–260.
- Karnopp, D. C. (1987). Active suspension based on fast load levelers. *Vehicle System Dynamics*, 16, 355–380.
- Karnopp, D. C., & Rosenberg, R. C. (1970). Application of bond graph techniques to the study of vehicle drive line dynamics. *ASME Journal of Basic Engineering*, 355–362.
- Karnopp, D. C., & Trikha, A. K. (1969). A comparative study of optimization techniques for shock and vibration isolation. *ASME Journal of Engineering for Industry*, 91(4), 1128–1132.
- Karnopp, D. C., Margolis, D. L., & Rosenberg, R. C. (2012). *System dynamics: A unified approach* (5th ed.). Hoboken, New Jersey: Wiley.
- Korosec, K. (2014). *Potholes and Tesla's Model S: Never the twain shall meet* [Online]. Retrieved September 19, 2014, from <http://fortune.com/2014/09/19/tesla-model-s-suspension-upgrade/>.
- Krtolica, R., & Hrovat, D. (1992, April). Optimal active suspension control based on a half-car model: An analytical solution. *IEEE Transactions on Automatic Control*, (37).
- Kwakernaak, H., & Sivan, R. (1972). *Linear optimal control systems*. New York: Wiley Interscience.
- Levine, W. S. (Ed.). (2011). *The control handbook* (2nd ed.). CRC Press, 2011.
- Margolis, D. L. (1978). Bond graphs, normal modes, and vehicular structures. *Vehicle System Dynamics*, 7(1), 49–63.
- Mastinu, G., & Ploechl, M. (2014). *Road and off-road vehicle system dynamics handbook*, Chapters 22 and 31. CRC Press.
- Merker, T., Gaston, G., & Olaf, T. (2002). *Active Body Control (ABC) the DaimlerChrysler active suspension and damping system*. SAE Technical Paper 2002-21-0054.
- Moran, T. (2004, October 11). A new suspension's magnetic appeal. *New York Times*.
- Nastasić, Ž., & Deák Jahn, G. (2002). *Citroen technical guide* [Online]. <http://www.citroenkerho.fi/xantia/pdf/teknikka/Tekniikkaopas.pdf>.
- Nicolas, R. (2014). *Intelligent suspension system of Lincoln MKZ help mitigating pothole damage* [Online]. Retrieved March 20, 2014, from <http://www.car-engineer.com/intelligent-suspension-system-lincoln-mkz-help-mitigating-pothole-damage/>.
- Novak, M., & Valasek, M. (1996). A new concept of semi-active control of truck's suspension. In *Proceedings of AVEC'96* (pp. 141–152).
- Pacejka, H. B. (2006). *Tyre and vehicle dynamics*. Amsterdam: Elsevier.

- Papageorgiou, C., & Smith, M. C. (2006). Positive real synthesis using matrix inequalities for mechanical networks: Application to vehicle suspension. *IEEE Transactions on Control Systems Technology*, 14(3), 423–435.
- Pevsner, J. M. (1957, January). Equalizing types of suspension. *Automobile Engineer*.
- Pilbeam, R. C., & Sharp, R. S. (1993). On the preview control of limited bandwidth vehicle suspensions. *Proceedings of the Institution of Mechanical Engineers, Part D: Journal of Engineering*, 207(D3), 185–194.
- Rajamani. (2012). *Vehicle dynamics and control* (2nd ed.). Springer.
- Richard, J. P. (2003). Time-delay systems: An overview of some recent advances and open problems. *Automatica*, 39(10), 1667–1694.
- Rill, G. (1983). The influence of correlated random road excitation processes on vehicle vibration. In *Proceedings of the 8th IAVSD Symposium on the Dynamics of Vehicle on Roads and on Railway Tracks, Cambridge, Massachusetts* (pp. 449–459).
- Saberi, A., & Sannuti, P. (1987). Cheap and singular controls for linear quadratic regulators. *IEEE Transaction on Automatic Control*, 32, 208–219.
- Safonov, M., & Athans, M. (1977). Gain and phase margins for multiloop LQG regulators. *IEEE Transactions on Automatic Control*, 22(2), 361–368.
- Sage, A. P., & White, C. C. (1977). *Optimum system control* (2nd ed.). Englewood Cliffs: Prentice-Hall.
- Scarborough, C. (2011). *Lotus Renault GP: Fluid Inerter*. Retrieved November 29, 2011, from <https://scarbsf1.wordpress.com/2011/11/29/lotus-renault-gp-fluid-inerter/>.
- Scheibe, F., & Smith, M. C. (2009). Analytical solutions for optimal ride comfort and tyre grip for passive vehicle suspensions. *Vehicle System Dynamics*, 47(10), 1229–1252.
- Sevin, E., & Pilkey, W. D. (1971). *Optimum shock and vibration isolation*. The Shock and Vibration Information Center, United States Department of Defense.
- Sharp, R. S. (1998). Variable geometry active suspension for cars. *Computing & Control Engineering Journal*, 9(5), 217–222.
- Sharp, R. S., & Crolla, D. A. (1987). Road vehicle suspension design—A review. *Vehicle System Dynamics*, 16(3), 167–192.
- Sherman, D. (2011). *Tenneco's Kinetic Suspension, the Anti Anti-Roll Bar*, Car and Driver. July 2011 issue.
- Smith, C. C. (1976). On using the ISO standard to evaluate the ride quality of broad-band vibration spectra in transportation vehicles. *ASME J. of Dynamic Systems, Measurement, and Control*, 98(4), 440–443.
- Smith, C. C., McGehee, D. Y., Healey, A. J. (1978). The prediction of passenger riding comfort from acceleration data. *ASME Journal of Dynamic Systems, Measurement, and Control*, 100, 34–41.
- Smith, M. C. (2002). Synthesis of mechanical networks: The inerter. *IEEE Transactions on Automatic Control*, 47(10), 1648–1662.
- Smith, M. C. (2011). Control for Formula One. In T. Samad & A. Annaswamy (Eds.), *The Impact of Control Technology*. IEEE Control Systems Society.
- Smith, M. C., & Walker, G. W. (2000). Performance limitations and constraints for active and passive suspensions: A mechanical multi-port approach. *Vehicle System Dynamics*, 33(3), 137–168.
- Smith, M. C., & Wang, F. C. (2004). Performance benefits in passive vehicle suspensions employing inerters. *Vehicle System Dynamics*, 42(4), 235–257.
- Smith, R. E. (1982). *Amplitude characteristics of Dearborn Test Track roadways*. Ford Motor Company memorandum, SRM-82-26, Dearborn, MI.
- Smith, R. E., & Sigman, D. R. (1981). *Experimental verification of a linear rigid body model*. Ford Motor Company Research Report.
- Streiter, I. R. (2008). Active preview suspension system. *ATZ Worldwide*, 110(5), 4–11.
- Thompson, A. G. (1971). Design of active suspensions. *Proceedings of the Institution of Mechanical Engineers*, 185, 553–563.

- Tseng, H. E., & Hedrick, J. K. (1994). Semi-active control laws-optimal and sub-optimal. *Vehicle System Dynamics*, 23(1), 545–569.
- Tseng, H. E., & Hrovat, D. (2015). State of the art survey: Active and semi-active suspension control. *Vehicle System Dynamics*, 53(7), 1034–1062.
- Tseng, H. E., Ashrafi, B., Madau, D., et al. (1999). The development of vehicle stability control at Ford. *IEEE ASME Transaction on Mechatronics*, 4(3), 223–234.
- Tumova, G. (2004). *Delft Active Suspension (DAS-II)*. Research Report OND1281145 [Online]. <http://www.narcis.nl/research/RecordID/OND1281145>.
- Ulsoy, A. G., Hrovat, D., & Tseng, T. (1994). Stability robustness of LQ and LQG active suspensions. *ASME Journal of Dynamic Systems, Measurement and Control*, 116(1), 123–131.
- Ulsoy, A. G., Peng, H., & Cakmakci, M. (2012). *Automotive control systems*. Cambridge University Press.
- van der Knapp, A. (1989). *Design of a low power anti-roll/pitch system for a passenger car*. Delft University of Technology, Vehicle Research Laboratory, Report 89.3VT.2628.
- Valasek, M., Kejval, J., Maca, J., & Smilauer, V. (2003). Bridge-friendly truck suspension. In *Proceedings of the 18th IAVSD Symposium* (vol. 41, pp. 13–22).
- Valášek, M., Novák, M., Šíka, Z., & Vaculin, O. (1997). Extended ground-hook-new concept of semi-active control of truck's suspension. *Vehicle System Dynamics*, 27(5–6), 289–303.
- Valasek, M., Sveda, J., & Šíka, Z. (1998). Soil-friendly off-road suspension. *Vehicle System Dynamics*, 44(sup1), 479–488.
- Venhovens, P. T., & van der Knaap, A. M. (1995). Delft active suspension (DAS) background theory and physical realization. *Smart Vehicles*, 139–165.
- Venhovens, P., van der Knaap, A., & Pacejka, H. (1992). Semiactive vibration and attitude control. In *Proceedings of the International Symposium on Advanced Vehicle Control (AVEC)* (pp. 170–175).
- Wada, T. (2016). Motion sickness in automated vehicles. In *Proceedings of the AVEC '16 Conference, Munich, Germany*.
- Watanabe, Y., & Sharp, R. S. (1999). Mechanical and control design of a variable geometry active suspension system. *Vehicle System Dynamics*, 32(2–3), 217–235.
- Weisstein, E. W. (2017). *Fourier transform. From MathWorld—A Wolfram web resource*. <http://mathworld.wolfram.com/FourierTransform.html>, 2017.
- Xu, L., Tseng, H. E., & Hrovat, D. (2016, July). Hybrid model predictive control of active suspension with travel limits and nonlinear tire contact force. In *Proceedings of the 2016 ACC, Boston, MA*.
- Young, J. W., & Wormley, D. N. (1973). Optimization of linear vehicle suspensions subjected to simultaneous guideway and external force disturbances. *ASME Journal of Dynamic Systems, Measurement, and Control*, 213–219.
- van Zanten, A. (2014). Control of horizontal vehicle motion. In G. Mastinu & M. Ploechl (Eds.), *Road and off-road vehicle system dynamics handbook* (pp. 1094–1174). Boca Raton, FL: CRC Press.

# Active Control of Vehicle Handling Dynamics



Tim Gordon

**Abstract** This chapter provides an overview of the basic lateral control of a road vehicle using actuators such as individually controlled brakes and or rear-wheel steering. The main focus is on linear control system design for cornering, especially for the improvement of stability and manoeuvrability of a passenger car. Steering control is presented in the form of a simple ‘driver model’ that shows the importance of road preview in providing a stable controller. For nonlinear control, anti-lock braking and electronic stability control are described; finally there is an introduction to vehicle motion control at the limits of friction.

**Keywords** Chassis control · Vehicle stability · Rear-wheel steering  
Electronic stability control · Anti-lock braking system · Driver model  
Friction limits

## 1 Overview of Vehicle Control Applications

In recent years, electronic controls have become an integral part of automobile engineering. Starting with electronic engine control and anti-lock braking systems (ABS), the number of electronic functions has expanded almost exponentially over the past decade. However there are relatively few degrees of freedom associated with the primary ride and handling of a rigid vehicle—just six. Compared to this, there may be a large number of actuators available, or at least feasible, for controlling these six degrees of freedom. If we assume a four-wheel rigid vehicle has independent braking/traction at each wheel (drive and brake torque combined together) plus independent suspension and steering, this gives three independent actuation modes per wheel, or 12 actuator degrees of freedom in total. In this case, the ratio of actuators to degrees of freedom is 2:1. Fundamentally the automobile is an *over-actuated* machine.

Not all degrees of freedom may be actively controlled (for example when bounce, pitch and roll are controlled by a standard passive suspension). But even then, a

---

T. Gordon (✉)  
School of Engineering, University of Lincoln, Lincoln, UK  
e-mail: tgordon@lincoln.ac.uk

standard Electronic Stability Control (ESC) system will be over-actuated, having four individual wheel brakes available and only two degrees of freedom to control: yaw and body side-slip. So again, motion control becomes over-actuated and some form of constraint or control allocation is necessary as part of the controller design.

Certain vehicle control modes are more simply described as single-input-single-output (SISO) systems. An example is cruise control, where the vehicle follows a set reference speed; the input is the speed reference, the output is the actual vehicle speed, and a suitable performance index would be the root-mean-square error between the two. Another SISO example is steering control, where lane position is controlled via steering. Although this might be thought of as an ‘advanced’ control function for automated driving, it is so fundamental to the control of a road vehicle that we also analyse the system dynamics when a steering controller is connected to the base vehicle. These notes adopt a similar approach to the book Abe (2015), which is recommended for further reading.

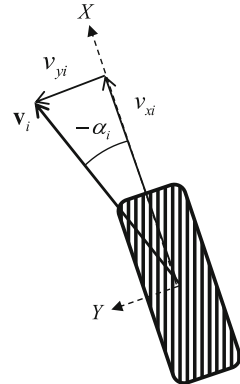
In Sect. 2 we consider the basic linear bicycle handling model and the way its dynamics can be altered by rear-wheel steering. This includes the use of feedforward control to reduce body sideslip, which is a fundamental concern of ESC. Stability, even for the linear model, is a key concern and is covered in some detail. In Sect. 3 we introduce the effects of feedback control, with emphasis on actuation by rear-wheel steering (RWS). But we note that the exact same approaches can be applied to active-front-steering (AFS) and direct yaw moment control (DYC) using active differentials or differential braking. In Sect. 4 we consider the fundamentals of lane keeping, where the system dynamics includes the influence of a steering controller. Finally, Sect. 5 considers the nonlinear control region, which occurs when the limits of friction are approached: ABS, ESC plus an introduction to combined path and speed control at or near the limits of friction.

## 2 Open-Loop Control of Handling Dynamics

### 2.1 Overview

Analogous to the quarter-car model of ride dynamics, we require a simple model for handling dynamics that for control system design, and also as a reference model for closed-loop control. The bicycle handling model is commonly used, being the simplest model that represents the effect of tyre forces on the lateral and yaw motions of the vehicle. Cornering forces are generated either by lateral slip of the tyre (slip angle), by lateral inclination (camber angle), or a combination of the two. The forces due to camber are relatively small, so here we only consider cornering forces generation due to slip angle, as represented in Fig. 1. The slip angle of any individual tyre is analogous to steering angle, except that it measured relative to the velocity of the wheel center over ground, rather than the longitudinal axis of the vehicle body. Typically, rear wheels are not steered, but they experience sideslip in order to gen-

**Fig. 1** Slip angle  $\alpha_i$  at wheel  $i$ , where  $\mathbf{v}_i$  is the velocity vector of the wheel centre relative to the ground.  $(X, Y)$  is the local coordinate frame of the tyre. Slip angle  $\alpha_i$  becomes positive when  $v_{yi} < 0$



erate cornering forces. For either front or rear, the wheel generates cornering force due the component of velocity lateral to the wheel  $v_{yi}$ , and in the opposite direction. In Fig. 1 the  $(X, Y)$  axes are oriented according to the ISO convention, and we consider the positive slip angle  $\alpha_i > 0$  generating cornering force in the  $+Y$  direction; this is a common, but not universal, convention in vehicle dynamics:

$$\tan \alpha = \frac{-v_y}{v_x} \quad (1)$$

Note that when we introduce the bicycle handling model below, the corresponding slip angle  $\beta$  for the vehicle uses the opposite sign convention,  $\beta < 0$  when the body is oriented to the left of the velocity vector; this sign convention is almost universal in the literature.

Friction limits and the complex structure of the pneumatic tyres lead to the non-linear input-output relationship shown in Fig. 2, which displays a linear region for small  $\alpha$ , an adhesion peak at which the maximum force  $F_{yp}$  is achieved, and then a sliding region with reduced force at large slip angles. Under normal driving conditions the tyre remains in the linear region, and hence a satisfactory representation of the tyre mechanics is given by the simple equation

$$F_y = C_\alpha \alpha \quad (2)$$

where  $C_\alpha$  (the *cornering stiffness* of the tyre) is the initial slope of the force-slip curve in Fig. 2. Typically, this linear tyre model is valid for vehicle handling dynamics up to lateral accelerations  $\sim 4 \text{ ms}^{-2}$ .

Note that the cornering stiffness is dependent on many variables: tyre size and type (radial vs. bias construction), number of plies, cord angles, wheel width, and tread design, all of which affect the structural performance of the tyre. For a given tyre, the vertical load and inflation pressure are the main parameters affecting the value of  $C_\alpha$ .

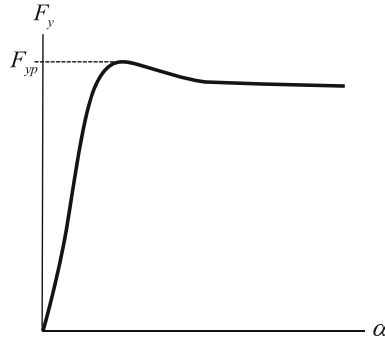


**Fig. 2** Lateral force  $F_y$  versus slip angle  $\alpha$

## 2.2 Linear Bicycle Model

The key dimensions and variables for the bicycle handling model are shown in Fig. 3. Here  $(X_G, Y_G)$  represents the global orientation of the in-plane coordinate axes, relative to which the vehicle body has yaw angle  $\psi$ . Using the sign convention mentioned above, the path angle (i.e. the direction of motion of the vehicle mass centre) equals  $\psi + \beta$ , where  $\beta$  is the body sideslip angle.

The model assumes the vehicle forward speed  $U$  is constant; also the steer angle  $\delta$  is assumed small, so the cornering force at the front axle is considered to act perpendicular to the vehicle longitudinal axis. Then the yaw and lateral motions are controlled by the front and rear lateral tyre forces  $F_{yf}$  and  $F_{yr}$  respectively. The resultant side-force and yaw moment then determine the lateral dynamics of the vehicle. Roughly speaking, the front steering angle  $\delta = \delta_f$  commands the yaw rate, while body sideslip follows from the equilibrium of forces between the front and rear axles.

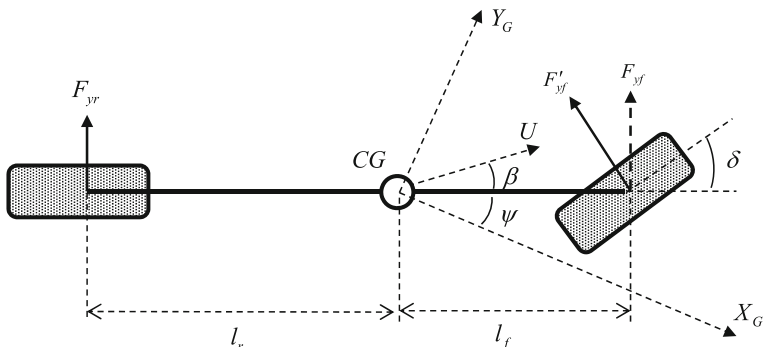


**Fig. 3** Bicycle handling model. The left and right wheels are combined at each axle and the *axle cornering stiffness* is introduced:  $C_{af} = C_{afl} + C_{afr}$ ,  $C_{ar} = C_{arl} + C_{arr}$ . Steer angle  $\delta$  is assumed small, so  $F_{yf} = F'_{yf} \cos \delta \approx C_{af} \alpha_f$

Using coordinates fixed with respect to the vehicle, the equations of motion are:

$$MU \left( \frac{d\beta}{dt} + r \right) = F_{yf} + F_{yr} \quad (3)$$

$$I \frac{dr}{dt} = l_f F_{yf} - l_r F_{yr} \quad (4)$$

Here,  $I$  is the yaw moment of inertia,  $l_f$  and  $l_r$  are the distances of the front and rear wheel axles from the centre of gravity and  $l (= l_f + l_r)$  is the wheelbase. The cornering forces ( $F_{yf}$  and  $F_{yr}$ ) are the axle totals, and are assumed to act in the vehicle lateral direction.

As above, for small tyre slip angles we use the linear approximation and assume small angles:

$$F_{yf} = C_{af}\alpha_f, \alpha_f = \delta_f - \beta - \frac{l_f}{U}r \quad (5)$$

$$F_{yr} = C_{ar}\alpha_r, \alpha_r = -\beta + \frac{l_r}{U}r \quad (6)$$

where  $C_{af}$ ,  $C_{ar}$  refer to the total cornering stiffness at the front and rear axles respectively.

Substituting Eqs. 5 and 6 into Eqs. 3 and 4 we obtain:

$$MU \frac{d\beta}{dt} + (C_{af} + C_{ar})\beta + MUr + \frac{(l_f C_{af} - l_r C_{ar})}{U}r = C_{af}\delta_f \quad (7)$$

$$I \frac{dr}{dt} + (l_f C_{af} - l_r C_{ar})\beta + \frac{(l_f^2 C_{af} + l_r^2 C_{ar})}{U}r = l_f C_{af}\delta_f \quad (8)$$

These are the fundamental equations of vehicle planar motion under the simplifying assumptions stated above. A number of constant parameters repeatedly occur in these equations

$$L_0 = C_{af} + C_{ar} \quad (9)$$

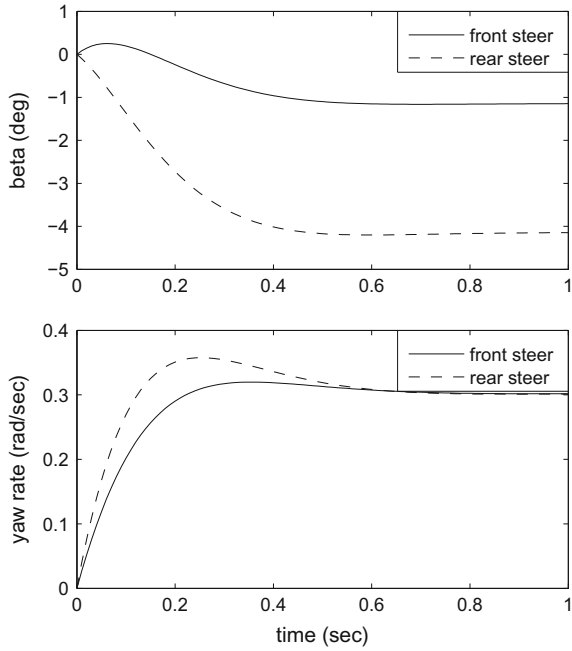
$$L_1 = l_f C_{af} - l_r C_{ar} \quad (10)$$

$$L_2 = l_f^2 C_{af} + l_r^2 C_{ar} \quad (11)$$

these being the  $p$ th moments of cornering stiffness, of the form  $L_p = \sum_i x_i^p C_{ai}$  with summation over all wheels. Then, for example, the state-variable form of the bicycle handling model can be written in a relatively compact form

$$\dot{\mathbf{x}} = A\mathbf{x} + Bu \quad (12)$$

**Fig. 4** Step-steer responses for the linear bicycle handling model, with either front or rear wheel steering as input. For rear-wheel-steer a negative steering ratio is used, so that positive steering induces positive yaw rate. Data: steering ratio: 15:1 (−15:1 for rear wheel steering); vehicle mass:  $M = 1500$  kg; cornering stiffnesses:  $C_{ai} = 1000$  N/deg (each individual tyre); distance from CG to front/rear axles:  $l_f = 1.08$  m,  $l_r = 1.62$  m; radius of gyration for yaw:  $R_g = 1.25$  m; forward speed:  $\dot{U} = 25$  m/s; step-steer angle:  $\delta_0 = 45^\circ$  at the steering wheel



$$A = - \begin{pmatrix} L_0/MU & 1 + L_1/MU^2 \\ L_1/I & L_2/IU \end{pmatrix} \quad (13)$$

$$B = \begin{pmatrix} C_{af}/MU \\ l_f C_{af}/I \end{pmatrix} \quad (14)$$

where  $\mathbf{x} = [x_1, x_2]^T = [\beta, r]^T$ ,  $u = \delta_f$ .

Figure 4 shows (solid lines) the response of the bicycle handling model for a step input at the steering wheel, assuming front-wheel-steer (FWS). The sideslip angle and yaw rate responses are shown. Also shown (dashed lines) are the corresponding responses for rear-wheel-steer (RWS), i.e. when the steering mechanism connects instead to the rear wheels; we return to this aspect in Sect. 2.5. Focusing attention to the FWS results, the vehicle takes around 0.5 s to reach steady state, settling with a negative sideslip angle  $\beta$ .

Note the following simple relationships, which are easily confirmed; they turn out to be useful in the algebraic manipulation of the various transfer functions in the next section:

$$\begin{aligned}
L_2 - l_f L_1 &= ll_r C_{ar} \\
L_2 + l_r L_1 &= ll_f C_{af} \\
-L_1 + l_f L_0 &= lC_{ar} \\
L_1 + l_r L_0 &= lC_{af}
\end{aligned} \tag{15}$$

### 2.3 Transfer Function Analysis

For the transfer function form of the bicycle handling model we may convert from state-space or apply the Laplace transform operator to the original equations of motion, Eqs. 7 and 8. Using  $s$  as the Laplace variable, we obtain:

$$\begin{bmatrix} MUs + L_0 & MU + L_1/U \\ L_1 & Is + L_2/U \end{bmatrix} \begin{bmatrix} \beta(s) \\ r(s) \end{bmatrix} = \begin{bmatrix} C_{af} \\ l_f C_{af} \end{bmatrix} \delta_f(s) \tag{16}$$

where  $\beta(s)$ ,  $r(s)$  and  $\delta_f(s)$  are the Laplace transforms of  $\beta$ ,  $r$  and  $\delta_f$  respectively. The relevant transfer functions are then found. We solve using the inverse-matrix to obtain

$$\begin{bmatrix} \beta(s) \\ r(s) \end{bmatrix} = \Delta(s)^{-1} \begin{bmatrix} Is + L_2/U - (MU + L_1/U) \\ -L_1 & (MUs + L_0) \end{bmatrix} \begin{bmatrix} C_{af} \\ l_f C_{af} \end{bmatrix} \delta_f(s) \tag{17}$$

where  $\Delta(s)$  is the system determinant:

$$\Delta(s) \equiv \begin{vmatrix} MUs + L_0 & MU + L_1/U \\ L_1 & Is + L_2/U \end{vmatrix} \tag{18}$$

System stability is determined from the characteristic equation  $\Delta(s) = 0$ :

$$MIU \left[ s^2 + \frac{ML_2 + IL_0}{MIU} s + \frac{l^2 C_{af} C_{ar}}{MIU^2} - \frac{L_1}{I} \right] = 0 \tag{19}$$

where  $l = l_f + l_r$  is the wheelbase. In the above equations, the term  $L_1 = (l_f C_{af} - l_r C_{ar})$  relates to the imbalance between front and rear axle cornering forces; if this parameter is zero, the resultant yaw moment becomes zero only when the front and rear slip angles are equal, which is the *neutral steer* condition.

Let  $W_f = Mgl_r/l$  and  $W_r = Mgl_f/l$  be the static vertical loads on the front and rear axles respectively. Then the *understeer gradient* (USG)  $K_u$  is defined as:

$$K_u = \frac{W_f}{C_{af}} - \frac{W_r}{C_{ar}} \tag{20}$$

or equivalently

$$K_u = -\frac{MgL_1}{lC_{af}C_{ar}} \quad (21)$$

Hence the characteristic equation, Eq. 19, can be written

$$s^2 + 2Ds + E = 0 \quad (22)$$

where the *damping* and *stiffness* terms are respectively

$$2D = \frac{ML_2 + IL_0}{MIU} \quad (23)$$

$$E = \frac{C_{af}C_{ar}l}{MgIU^2}(gl + K_u U^2) \quad (24)$$

The natural frequency  $\omega_n$  and damping ratio  $\zeta$  of the vehicle response are defined from the characteristic equation coefficients:

$$\omega_n^2 = E \quad (25)$$

$$2\zeta\omega_n = 2D \quad (26)$$

Returning to Eq. 17, after some manipulation we can now obtain the following simplified forms of the input-output transfer functions:

$$\frac{\beta(s)}{\delta(s)} = \frac{K_\beta(s + a_\beta)}{s^2 + 2\zeta\omega_n s + \omega_n^2} \quad (27)$$

where

$$K_\beta = \frac{C_{af}}{MU} \quad (28)$$

$$a_\beta = \frac{ll_r C_{ar} - Ml_f U^2}{IU} \quad (29)$$

Similarly, for the yaw rate  $r(s)$ ,

$$\frac{r(s)}{\delta(s)} = \frac{K_r(s + a_r)}{s^2 + 2\zeta\omega_n s + \omega_n^2} \quad (30)$$

where

$$K_r = \frac{l_f C_{af}}{I} \quad (31)$$

$$a_r = \frac{l C_{ar}}{MUL_f} \quad (32)$$

In either case, the steady-state gain takes the form

$$G(0) = \frac{Ka}{\omega_n^2} \quad (33)$$

which is the input-to-output scaling factor in the steady-state limit. For example, in the case of a step-steer input, when a driver suddenly shifts the steering angle (say from zero to  $\delta_0$ , e.g. in the initial stage of an evasive manoeuvre) the steady-state gain  $K_r a_r / \omega_n^2$  determines the yaw rate achieved, and hence the responsiveness of the vehicle to driver inputs.

Vehicle responsiveness in the step-steer scenario is also measured via the *delay* in achieving steady-state. For a second order transfer function of the type in Eq. 30 this is determined by the time constant

$$T_c = \frac{1}{\zeta \omega_n} = \frac{1}{D} = \frac{2MIU}{ML_2 + IL_0} \quad (34)$$

If  $T_c$  becomes larger, this means the vehicle becomes slow to respond, but if  $T_c$  becomes too small the driver will have greater difficulty in controlling the vehicle. For the step-response in Fig. 4,  $T_c = 0.148$  s (and corresponds to a settling time of around  $3T_c$ , or around 0.45 s in the figure). Eq. 34 shows some simple and natural trends: (i) when vehicle mass increases then so does  $T_c$  (assuming yaw inertia  $I$  also increases with vehicle mass) (ii) the yaw response is slower at higher speeds (iii) increasing tyre cornering stiffness reduces  $T_c$  (the denominator increases in proportion to  $C_\alpha$ ).

## 2.4 Stability

The solutions of Eq. 22 are the system eigenvalues (poles)

$$\lambda = -D \pm \sqrt{D^2 - E} \quad (35)$$

or equivalently

$$\lambda = -\zeta \omega_n \pm j\omega_n \sqrt{1 - \zeta^2} \quad (36)$$

System stability is determined by the condition that the real part of  $\lambda$  should be negative; from Eq. 23 it is clear that the first term in Eq. 35 is strictly negative for all reasonable physical parameters (e.g. positive cornering stiffness). For both solutions of Eq. 35 to have negative real parts, it is seen that the stability condition is simply

$$E > 0 \quad (37)$$

(consider first the case  $E = 0$  and then let  $E$  increase or decrease). If  $U \rightarrow \infty$  in Eq. 24 then the first term tends to zero and the remaining stability condition is that

$$\frac{lC_{af}C_{ar}K_u}{MgI} > 0 \quad (38)$$

or more simply that the vehicle understeers, i.e.  $K_u > 0$ . Thus for a passive vehicle operating in the linear region, the necessary and sufficient condition for handling stability *at all speeds* is that the understeer gradient is positive. An oversteering vehicle ( $K_u < 0$ ) has a critical speed above which the vehicle is unstable—at least if there is no control intervention.

## 2.5 Rear-Wheel Steering

The aim now is to design some simple linear handling control laws—using actuators and feedback control to improve handling via reference model tracking. We assume the actuator is an automated rear-wheel steering system which responds to the driver input at the steering wheel  $\delta(t)$  and/or the vehicle states  $(\beta(t), r(t))$ .

First however we need to revisit the bicycle handling model with a second input, namely the rear steer angle  $\delta_r$ . Referring to Eqs. 5 and 6, we obtain the simple modification

$$F_{yf} = C_{af}\alpha_f, \alpha_f = \delta_f - \beta - \frac{l_f}{U}r \quad (39)$$

$$F_{yr} = C_{ar}\alpha_r, \alpha_r = \delta_r - \beta + \frac{l_r}{U}r \quad (40)$$

Hence it is a simple matter to expand the previous state-space equations to include the second input. The **A** matrix in Eq. 13 is unchanged, while the **B** from Eq. 14 is expanded to

$$B = \begin{pmatrix} C_{af}/MU & C_{ar}/MU \\ l_f C_{af}/I & -l_r C_{ar}/I \end{pmatrix} \quad (41)$$

Here state variables are unchanged, but there are two inputs:  $u_1 = \delta_f$ ,  $u_2 = \delta_r$ . Now, referring once more to Fig. 4, the dashed line represents the use of rear steering, with the front wheels unsteered. As mentioned, a negative RWS steering ratio is used so the vehicle turns in the same direction of the steering wheel. In steady-state, the rate of turn is exactly the same as for FWS. However the yaw rate shows a more oscillatory response, due to the need for a larger body sideslip angle. This is because the front wheels are now ‘steered’ via the yaw angle of the entire vehicle body; contrary to  $\alpha_r$ , yawing motion tends to reduce  $\alpha_f$ , so (negative) body sideslip must be increased to achieve equilibrium. Thus, in practice, a driver will find it harder to

steer a RWS vehicle, even though it is *inherently just as stable* as a FWS vehicle: the values of  $D$  and  $E$  in Eqs. 23 and 24 are independent of which axle is steered.

For transfer function analysis we introduce the transfer function matrix  $[G_{ij}(s)]$ , where  $i$  denotes the output ( $x_i$ ) and  $j$  denotes the input ( $u_j$ ):

$$\begin{bmatrix} \beta(s) \\ r(s) \end{bmatrix} = \begin{bmatrix} G_{11}(s) & G_{12}(s) \\ G_{21}(s) & G_{22}(s) \end{bmatrix} \begin{bmatrix} \delta_f(s) \\ \delta_r(s) \end{bmatrix} \quad (42)$$

All four transfer functions  $G_{ij}(s)$  take the form similar to Eqs. 27 and 30:

$$G_{ij}(s) = \frac{K_{ij}(s + a_{ij})}{s^2 + 2\zeta\omega_n s + \omega_n^2} \quad (43)$$

and in this notation  $K_{11} = K_\beta$  in Eq. 28,  $K_{21} = K_r$  in Eq. 31 and similarly  $a_{11} = a_\beta$ ,  $a_{21} = a_r$ .

For the rear steering input, the corresponding transfer functions may be obtained by setting  $\delta_f = 0$  and using the rear-steer analogue of Eq. 17

$$\begin{bmatrix} \beta(s) \\ r(s) \end{bmatrix} = \Delta(s)^{-1} \begin{bmatrix} Is + L_2/U - (MU + L_1/U) \\ -L_1 & (MUs + L_0) \end{bmatrix} \begin{bmatrix} C_{ar} \\ -l_r C_{ar} \end{bmatrix} \delta_r(s) \quad (44)$$

Following the same type of algebraic manipulation as before, making use of Eq. 15, and gathering front and rear terms together, we obtain the full set of transfer function parameters relating to Eq. 43:

$$[K_{ij}] = \begin{bmatrix} K_{11} & K_{12} \\ K_{21} & K_{22} \end{bmatrix} = \begin{bmatrix} C_{af}/MU & C_{ar}/MU \\ l_f C_{af}/I & -l_r C_{ar}/I \end{bmatrix} \quad (45)$$

$$[a_{ij}] = \begin{bmatrix} (ll_r C_{ar} - MU^2 l_f)/IU & (ll_f C_{af} + MU^2 l_r)/IU \\ l_f C_{af}/MUIl_f & l_r C_{ar}/MUIl_r \end{bmatrix} \quad (46)$$

To emphasize, for both  $K_{ij}$  and  $a_{ij}$ , the first index refers to output (sideslip angle or yaw rate) and the second index refers to input (front or rear steering). The gain and phase plots for these transfer functions (frequency responses, with  $s = j\omega$ ) are shown below in Figs. 5 and 6.

As in Eq. 33, we find the steady-state gain by letting  $s \rightarrow 0$ , i.e.

$$G(0) = \frac{Ka}{\omega_n^2} = \frac{MgIU^2Ka}{lC_{af}C_{ar}} \frac{1}{(gl + K_u U^2)} \quad (47)$$

where for clarity we have omitted the  $ij$  subscript. For example, setting  $i = 2$  (yaw rate),  $j = 1$  (front steer) we obtain

**Fig. 5** Frequency response functions, with input =  $\delta_f$  or  $\delta_r$ , output = yaw rate (rad/sec). Note in the upper plot: steady-state gains are equal; also there is a stronger resonance for  $\delta_r$ . Lower plot: rear steer indicates a steady-state phase lag of  $180^\circ$ , indicating that positive  $\delta_r$  induces negative  $r$

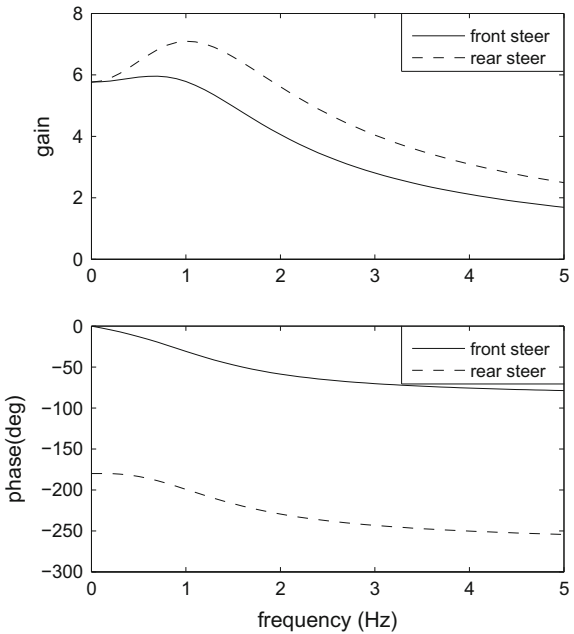
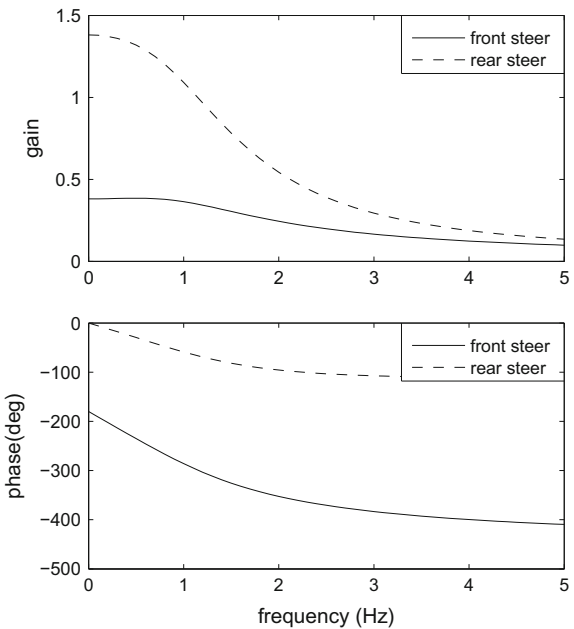


**Fig. 6** Frequency response functions, with input =  $\delta_f$  or  $\delta_r$ , output = body sideslip angle (rad). Note in the upper plot: gain is substantially higher for input  $\delta_r$ . Lower plot: front steer indicates a steady-state phase lag of  $180^\circ$ , indicating that positive  $\delta_f$  induces negative  $\beta$  (Vehicle data: see Fig. 4)



$$G_{21}(0) = \lim_{s \rightarrow 0} \frac{r(s)}{\delta_f(s)} = \frac{gU}{gl + K_u U^2} \quad (48)$$

Interestingly, we also find

$$G_{22}(0) = \lim_{s \rightarrow 0} \frac{r(s)}{\delta_r(s)} = -\frac{gU}{gl + K_u U^2} \quad (49)$$

i.e. the same result but with a negative sign, confirming that a constant positive rear-steer angle produces a negative yaw rate; this is in agreement with the upper plot in Fig. 5 which shows equal gain factors. Thus, if control is applied to make the rear steer angle equal to the front, then the steady-state yaw rate gain is zero. Note however that the transient dynamics will not generally cancel out in this way. Indeed, the gain is higher for the rear-steer (Fig. 5), so the rear input will tend to dominate the response during transient motions of the steering.

Also note that, from the common term  $(gl + K_u U^2)^{-1}$ , instability will result in the case of an oversteering vehicle  $K_u < 0$ ; for all of these transfer functions,  $G_{ij} \rightarrow \infty$  at the critical speed

$$U_c = \sqrt{gl/(-K_u)} \quad (50)$$

In reality, the distinction between stable and unstable behaviour is not a sharp one. A vehicle may become inherently unstable but very slow to respond, and this is what happens when an oversteering vehicle is close to the critical speed. Fortunately, since the unstable response is slow, an experienced driver can make corrections to counteract such instability by ‘counter-steering’, i.e. by steering in the opposite direction to the growing yaw rate. On the other hand, a stable vehicle with fast yaw dynamics ( $T_c$  in Eq. 34 very small) may become unstable in the hands of a novice driver.

## 2.6 Feedforward Control for Zero Body Sideslip

Using the above models it is relatively easy to craft a control transfer function to achieve simple objectives. With rear wheel steering it is clearly possible to adjust body sideslip independent of the yaw rate. For example, if  $\delta_r = \delta_0$  is set to a constant, then to drive in a straight line the driver needs to set  $\delta_f = \delta_0$ , so the front and rear wheels steer at the same angle; the yaw rate will be zero but body sideslip angle  $\beta$  is not—and the vehicle will move with a somewhat crab-like motion. Clearly this is counter-intuitive and would make the vehicle difficult to drive!

On the other hand it may be thought desirable to regulate  $\beta$  to zero under dynamic manoeuvres, so the vehicle is always ‘pointing in the right direction’. To impose this we assume a control law of the form

$$\delta_r(s) = C(s)\delta_f(s) \quad (51)$$

Thus we impose the condition

$$\begin{aligned}\beta(s) &= G_{11}(s)\delta_f(s) + G_{12}(s)\delta_r(s) \\ &= (G_{11}(s) + C(s)G_{12}(s))\delta_f(s) \\ &= 0\end{aligned}$$

According to Eq. 43 we have

$$K_{11}(s + a_{11}) + C(s)K_{12}(s + a_{12}) = 0$$

from which we obtain the required controller transfer function:

$$C(s) = -\frac{K_{11}(s + a_{11})}{K_{12}(s + a_{12})} = -\frac{C_{af}}{C_{ar}} \cdot \frac{s + (ll_r C_{ar} - MU^2 l_f)/IU}{s + (ll_f C_{af} + MU^2 l_r)/IU} \quad (52)$$

This has the form of a standard first order (lead-lag) compensator, and is a familiar type for implementation as a digital controller (once converted to discrete-time form). By definition the transfer function  $\beta(s)/\delta_f(s)$  is zero. Then the transfer function for yaw rate, including the effect of  $C(s)$ , is:

$$\frac{r(s)}{\delta_f(s)} = G_{21}(s) + C(s)G_{22}(s) \quad (53)$$

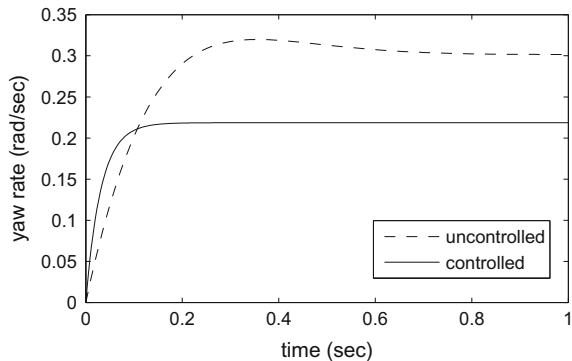
Substitution from Eqs. 43 and 52 yields, after some algebra—which includes cancellation of the term  $(s^2 + 2Ds + E)$ —this reduces to the simple first-order transfer function:

$$\frac{r(s)}{\delta_f(s)} = \frac{l C_{af} C_{ar}}{MIUK_{12}} \cdot \frac{1}{s + a_{12}} \quad (54)$$

As expected, for a first-order transfer function the step-response is non-oscillatory—Fig. 7; the controlled system has a faster response but with reduced steady-state yaw rate.

This is a satisfactory illustration of the capability of a rear-steer actuator, but there are several limitations of the approach, in particular (a) control is open-loop: the controller relies on the bicycle model being an accurate representation of the actual vehicle dynamics; (b) the design objective is somewhat arbitrary and there is no design freedom to choose the target (steady-state) yaw rate or response time. In particular there is considerable steady-state understeer compared with the uncontrolled vehicle. On the other hand, with zero body sideslip the yaw rate becomes directly proportional to both lateral acceleration and path curvature, even under transient conditions. For example the path-lateral acceleration is given by

**Fig. 7** Step response in the case where feedforward control imposes zero body sideslip. Rear wheel steering remains active in steady-state, inducing considerable understeer in the form of reduced yaw rate and increased turning radius



$$\frac{\ddot{y}(s)}{\delta_f(s)} = U \frac{\dot{\psi}(s) - \dot{\beta}(s)}{\delta_f(s)} = U \frac{r(s)}{\delta_f(s)} - U \frac{s\beta(s)}{\delta_f(s)} = U \frac{r(s)}{\delta_f(s)} \quad (55)$$

The net result is to suppress the yaw dynamics and force the vehicle to respond as though it were a simple particle; as to whether this is desirable depends then on ‘human factors’, i.e. whether the coupled vehicle-driver system is a more effective controller. This very interesting question goes beyond the scope of the current analysis however.

## 2.7 Feedforward Control of Yaw Rate

In this case we assume a reference model for how the vehicle ‘ought’ to respond to steering input, which allows the step-steer response to be directly chosen by the designer. By analogy to the previous controller, we will require the yaw velocity to be dominated by a first order response with a specified amplitude and time constant. Of course other choices are possible. The design intent in this example is to choose a time constant  $T_d$  which is smaller than the corresponding time constant  $T_c$  of the passive vehicle (Eq. 34), but with unchanged steady-state gain. The target transfer function is then

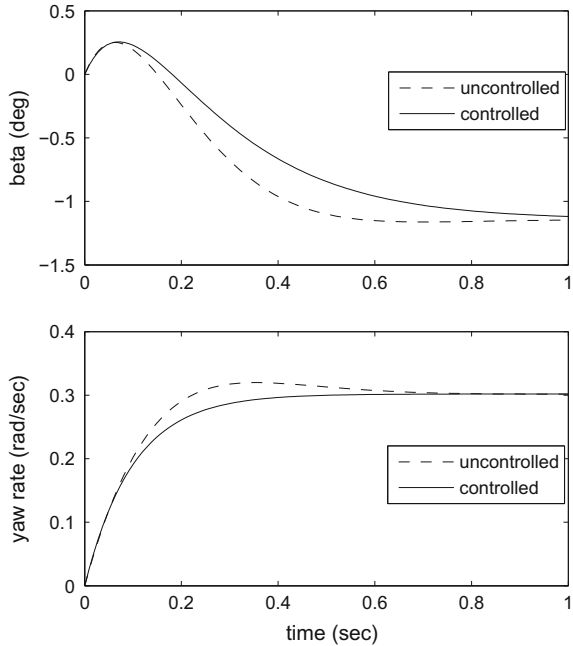
$$r_d(s) = \frac{K_d}{1 + T_d s} \delta_f(s) \equiv G_{21}^d(s) \delta_f(s) \quad (56)$$

where  $G_{21}^d(s)$  is the desired yaw rate transfer function after rear-steer control is applied, and  $K_d$  is the desired steady-state gain. Hence

$$G_{21}^d \delta_f = G_{21} \delta_f + G_{22} \delta_r$$

$$\delta_r = \frac{G_{21}^d - G_{21}}{G_{22}} \delta_f$$

**Fig. 8** Step responses for feedforward control targeting a first-order yaw rate reference (Vehicle data: see Fig. 4)



giving a control law of the same form as Eq. 51, and where the controller transfer function is now second order:

$$C(s) = \frac{K_d(s^2 + 2\zeta\omega_n s + \omega_n^2) - K_{21}(s + a_{21})(1 + T_d s)}{K_{22}(s + a_{22})(1 + T_d s)} \quad (57)$$

For this example,  $T_c = 0.148$  s,  $T_d = 0.1$  s and, in line with the passive vehicle model,  $K_d = 5.77$ . Results are shown in Fig. 8.

The choice of maintaining the same steady-state yaw rate as the passive (uncontrolled) vehicle has the advantage that  $\delta_r \rightarrow 0$  in steady-state, which also explains why body sideslip returns to the passive value. Interestingly, for simple feedforward control,  $\delta_r(s) = C(s)\delta_f(s)$ , there is a direct relationship between the steady state values of  $r(t)$  and  $\beta(t)$ . Considering Eq. 53, together with the analogous expression for  $\beta(s)/\delta_f(s)$ , we set  $s = 0$  in Eq. 43 to obtain the steady-state values:

$$\begin{aligned} \beta_{ss} &= (K_{11}a_{11} + C(0)K_{12}a_{12})\delta_0/E \\ r_{ss} &= (K_{21}a_{21} + C(0)K_{22}a_{22})\delta_0/E \end{aligned} \quad (58)$$

where (recall)  $E = \omega_n^2$ . We illustrate this result in Fig. 9, where the step-steer input  $\delta_0 = 3^\circ$  is again assumed. Irrespective of how the feedforward transfer function  $C(s)$  is designed, the trade-off between steady-state yaw rate and sideslip is fixed. In the upper plot we see that yaw rate decreases as  $C(0)$  increases, while body sideslip has

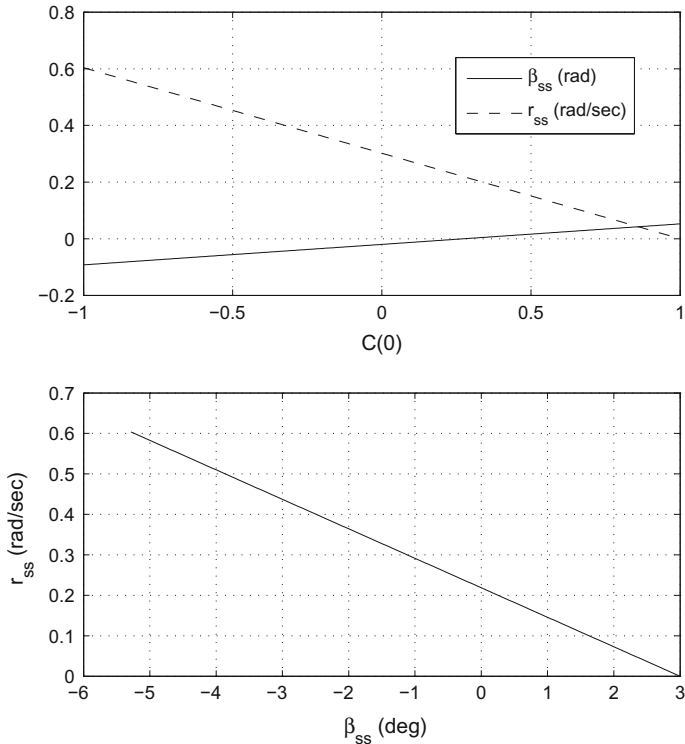


**Fig. 9** Steady-state relationship between body sideslip angle and yaw rate (Vehicle data: see Fig. 4)

the opposite trend. In the lower plot we more clearly see the inverse relationship between  $\beta_{ss}$  and  $r_{ss}$ . The figure clearly shows the reduction in  $r_{ss}$  between the passive case ( $C(0) = 0$  in the upper plot) and zero body sideslip ( $\beta_{ss} = 0$  in the lower plot). These results apply for the feedforward controller, independent of the details of the controller transfer function  $C(s)$ .

### 3 Closed-Loop Control of Handling Dynamics

In the above we presented the open-loop control of the vehicle, and also feedforward control of the lateral dynamics; in these approaches there is no feedback of vehicle states to the controller, and hence no ‘self-correcting’ mechanism. This is needed to ensure robustness in cases when the model is not a sufficiently accurate representation of the actual vehicle. This arises since basic parameters may vary, e.g. the mass  $M$  changes according to the number of passengers, the cornering stiffnesses  $C_{\alpha i}$

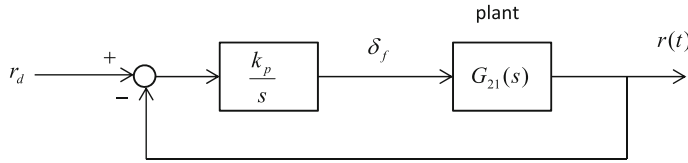


**Fig. 10** Block diagram for closed-loop control of yaw rate in response to a demand input. The closed-loop transfer function is  $\frac{r(s)}{r_d(s)} = \frac{k_p G_{21}(s)}{s + k_p G_{21}(s)}$

vary with inflation pressure, vertical load etc. And the effects of disturbances such as crosswinds are not automatically corrected for in such a controller.

In the absence of electronic control, the only feedback loop is via the driver, adjusting the steering angle to follow a desired path. We consider this type of control in Sect. 4, where the feedback signal comes from the position and motion of the vehicle relative to the road geometry. In that case, for example, the effect of a crosswind disturbance will be corrected by a change in steering wheel angle by the driver.

Electronic feedback control can also be used to improve the robustness and stability of the base vehicle, for example to track a desired yaw rate inferred from the steering wheel angle.

### 3.1 Feedback Control of Yaw Rate

We now introduce feedback control, where the effects of disturbances will be largely rejected, provided there is a sufficiently large gain in the feedback loop. Further, the inclusion of integral control, will remove undesirable steady-state errors (previously seen for example in Fig. 7).

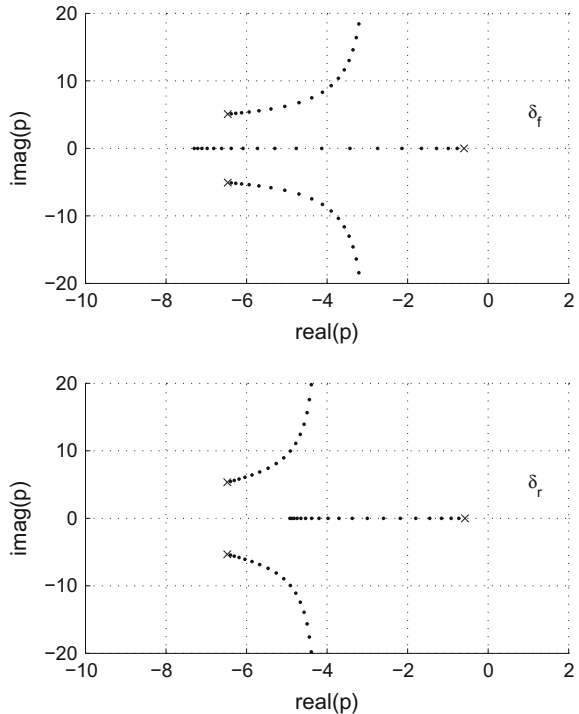
The basic feedback loop is shown in Fig. 10. This is shown using front steering wheel angle to test the approach. Equivalent to the figure, the control equation can be written:

$$\dot{\delta}_f(t) = -k_p(r(t) - r_d(t)) \quad (59)$$

which implies for example that steering angle is increased if the current yaw rate is less than desired,  $r < r_d$ . Clearly, if the yaw rate demand is constant, as would be the case on a road of constant curvature, then steady-state ( $\dot{\delta}_f = 0$ ) will only be achieved once the desired yaw rate is achieved ( $r = r_d$ ). This is the result of the integral control action  $1/s$  in Fig. 10.

The main concern is now the stability of the feedback loop. This is tested (using vehicle parameters previously given) via the root-locus plot in Fig. 11. Here  $k_p$  is systematically increased and the closed-loop poles (eigenvalues) are plotted. Clearly the points all have negative real parts, so the system is stable for all values of  $k_p$ . The corresponding step responses are shown in Fig. 12, where it is seen that all plots tend towards the commanded value  $r_d = 1$ . However, the low gain response is very slow

**Fig. 11** Root locus plot as  $k_p$  is increased over the range  $0.1 \leq k_p \leq 10$  in Fig. 10. The system is third order with one real pole and a pair of complex poles. Point ‘x’ marks the starting point (low-gain limit,  $k_p = 0.1$ ). For RWS (lower plot) the control law is  $\dot{\delta}_r(s) = +k_p(r(s) - r_d(s))$ , the + sign being required for stability



and high gain response is very oscillatory. Hence a compromise case is required, for example the tenth point on the root-locus, corresponding to the thick curve in Fig. 12,  $k_p = 0.9$ .

For rear-wheel steering the results are quite similar, corresponding to the lower half of Fig. 11. The control law is now

$$\dot{\delta}_r(t) = +k_p(r(t) - r_d(t)) \quad (60)$$

where the sign change is needed since positive rear steer angle induces negative yaw rate. Again the closed-loop system is stable for all values of  $k_p$  and again a compromise is required ( $k_p = 0.9$  is again suitable). The closed-loop transfer function is given by

$$\frac{r(s)}{r_d(s)} = \frac{-k_p G_{22}(s)}{s - k_p G_{22}(s)} \quad (61)$$

reflecting the sign change applied to  $k_p$ .

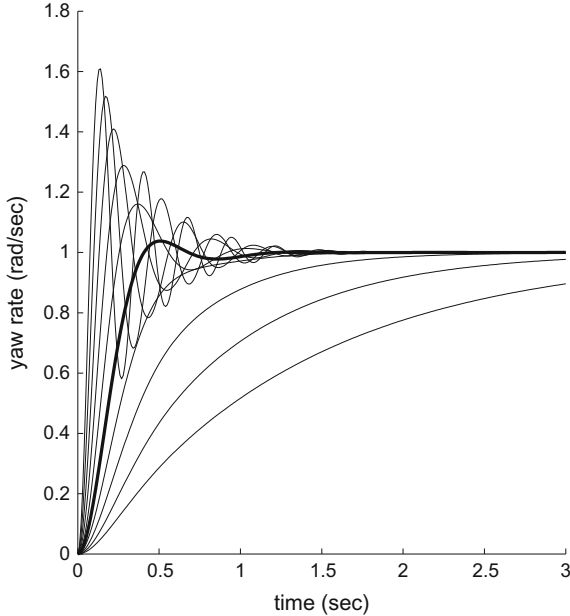


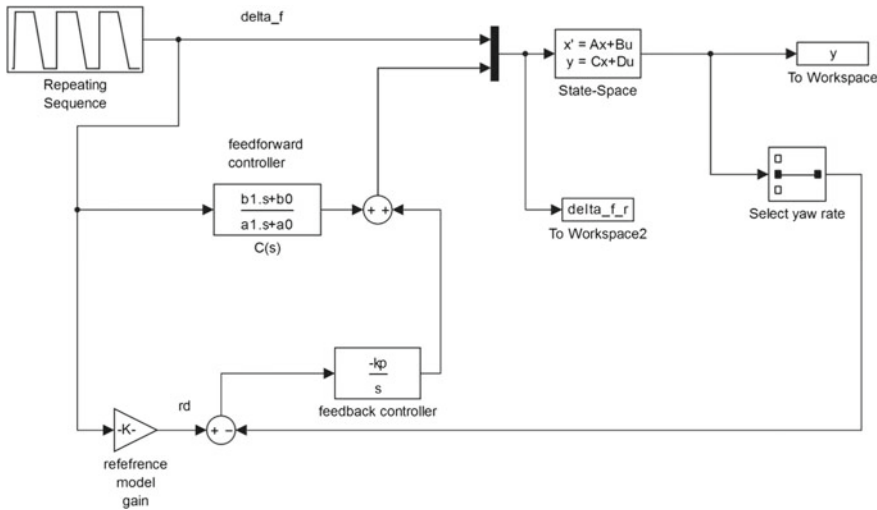
**Fig. 12** Time responses to a step demand in yaw rate corresponding to the upper plot in Fig. 11—front wheel steer. The highlighted curve corresponds to the tenth point of the root locus, with  $k_p = 0.9$

### 3.2 Combined Feedback/Feedforward Control

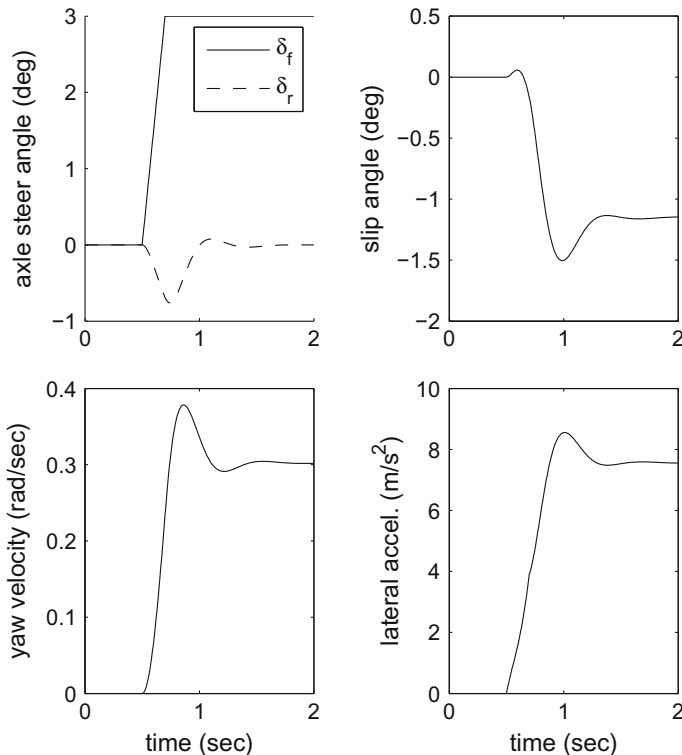
We now combine the feedforward and feedback control schemes, as shown in Fig. 13. Starting in the top left corner, the steering command is realistic form of a step-steer, taking 0.2 s to reach the maximum angle. Across the top and to the right is the basic input to the vehicle, via the first input  $\delta_f$ , and the three outputs are saved to workspace (sidelslip, yaw rate and path-lateral acceleration). Feedforward control is the next component down, where  $C(s)$  from Eq. 52 is used to excite a rear-steer response from the driver input. The lower part of the figure is the yaw rate feedback. Here the target yaw rate, derived from the steady-state gain (Eq. 33) is compared with the actual yaw rate, and using the above integral control (with  $k_p = 0.9$ ) we add feedback and feedforward terms together to complete the control law for rear steer.

Figure 14 shows the step response when the feedforward term is switched off, hence combining front-wheel-steer direct to the vehicle with rear-wheel-steer based on yaw rate tracking. Then in Fig. 15 we see the beneficial effect of including the feedforward term.

The advantage of feedforward control is that there is no ‘waiting time’ for errors to appear before corrections are applied, leaving smaller errors for feedback control to correct. And the advantage of feedback is that it counteracts disturbances and



**Fig. 13** SIMULINK block diagram of a combined feedforward/feedback controller for handling dynamics. The steering wheel angle changes from 0 to 45° in 200 ms, then remains constant



**Fig. 14** Step response in the case where feedforward control is turned off

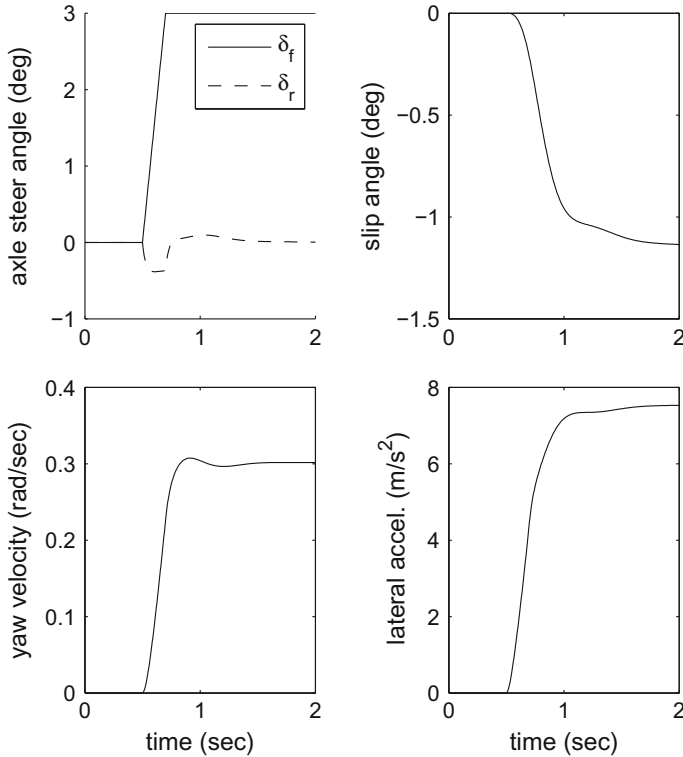


**Fig. 15** Step response in the case where both feedback and feedforward control actions are included. Note that because of the integrator in the feedback control loop, steady-state error is eliminated

can avoid steady-state errors. Figure 15 combines both and overcomes the steady-state error seen previously in Fig. 7. Note however that the same restriction exists as before—in steady state, the rear steer angle tends to zero if the passive yaw velocity gain is to be preserved, and in this case we lose the possibility of cancelling out body sideslip; see the slip angle plot in Fig. 15.

The above methodology can be applied to other types of actuators. One option is active-front-steer (AFS) where the control actuator manipulates the actual front steer angle by controlling an offset relative to the steering wheel, and may be represented as:

$$\delta_f = G^{-1} \delta_s + u_2 \quad (62)$$

where  $G$  is the steering ratio,  $\delta_s$  is the angle commanded by driver at the steering wheel, and  $u_2$  is the offset from the control actuator. In this case the exact same approach can be taken as above, using the same linear bicycle model. Another option is *direct yaw moment control* (DYC) where differences in braking or traction torque

can be applied to affect the yaw response. In this case the equations of motion need to be further expanded (in a very simple way), and a similar controller design approach can be taken.

## 4 Lateral Control

### 4.1 Overview

We normally assess vehicle dynamic performance as something *in the vehicle*. But it is increasingly common (and important) to model and evaluate the interaction between the steering controller and the vehicle particularly because of ‘smart’ driver assistance systems e.g. electronic stability control or lane keeping assistant. Many control tasks in driving are in the form of regulator control:

- maintain the center of the lane
- maintain speed
- maintain following distance
- brake to rest at a stop sign.

These are relatively simple control tasks, where a key component is error correction by feedback—applying steering or speed control (acceleration or braking) to reduce errors between the actual and intended outputs over time.

In some literature on driver modelling (e.g. Jagacinski and Flach 2003; Weir and McRuer 1970) the control regulator task is referred to as *compensatory* control, while the more dynamic components—for example active steering around an obstacle or driving on a curved road—is referred to as *pursuit* control. In the latter type of tracking control there is an element of preview and prediction involved, while in compensatory control the target is reasonably fixed. There is a clear correspondence with *feedback* and *feedforward* control, the former being closely associated with the regulator problem, the latter with pursuit of a ‘moving target’. When the target is the geometry of the road itself, it is a highly predictable target and we expect driving control to make use of *road preview* in this case—see below.

In *low speed driving control* the feedback loop is mostly *position-based* where the priorities (for error correction) are based on

- lateral position (e.g. in lane or parking spot)
- longitudinal position (e.g. moving slowly up to a stop line)
- path curvature (turning into driveway).

Lateral control action can then be based on the kinematics of the steering system, and tyre mechanical properties are hardly involved. This is also the control domain for low-speed mobile robots.

At normal driving speeds, *motion cues* are more important, and the control of the vehicle is more of a challenge, involving visual sensing of motion (foveal and

peripheral vision), acceleration sensing (e.g. from the vestibular system), steering torque feedback, brake pedal force, and more general vehicle response cues, such as pitch and roll motions. Since most control tasks are conducted well within the friction limits of the vehicle, tyre elastic properties become relevant, but linear dynamics can reasonably be assumed.

In *emergency driving* situations, the friction envelope of the vehicle needs to be exploited to the full, and vehicle control is most reliant to commanding path accelerations and using the yaw dynamics of the vehicle to support this in the best way possible. Few, if any, validated (human) driver models exist for this regime, but recent work on friction-limited control does address this area.

## 4.2 Lateral Offset Steering Control

The simplest driver model involves tracking by simple feedback of position. According to the above this is only likely to be relevant for low-speed motion. The control task is to follow a target path and apply steering correction to compensate for lateral deviations from the path. Here we investigate the coupled dynamics using the previously developed linear 2 DOF bicycle handling model for a simple test case: straight-line driving with the target path represented by the  $x$  axis.

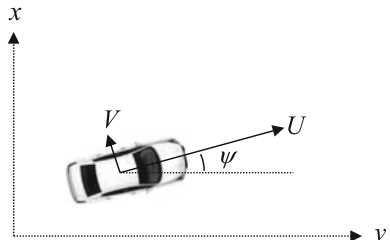
It is necessary to expand the vehicle model to include position variables

$$\begin{aligned}\dot{x} &= U \cos \psi - V \sin \psi \\ \dot{y} &= U \sin \psi + V \cos \psi \\ \dot{\psi} &= r\end{aligned}$$

In the case shown in Fig. 16, the target direction is the  $x$  axis, and the vehicle forward speed  $U$  is assumed constant; thus we may ignore the differential equation for  $\dot{x}$ .

According to the equations of motion of the bicycle handling model in state-space form, Eqs. 12–14, the differential equations for  $x_1 = \beta$ ,  $x_2 = r$  can be rewritten in an expanded state-space form, with the introduction of two further state variables  $x_3 = y$ ,  $x_4 = \psi$ . If we assume small angles, the equations of motion are as follows:

**Fig. 16** Position variables are included within an expanded state-space model



$$\dot{x}_1 = a_{11}x_1 + a_{12}x_2 + b_1\delta_f \quad (63)$$

$$\dot{x}_2 = a_{21}x_1 + a_{22}x_2 + b_2\delta_f \quad (64)$$

$$\dot{x}_3 = Ux_1 + Ux_4 \quad (65)$$

$$\dot{x}_4 = x_2 \quad (66)$$

Here we write  $a_{ij}$  for the components of the  $2 \times 2$  matrix  $\mathbf{A}$  and  $b_i$  are the components of the  $2 \times 1$  matrix  $\mathbf{B}$ ; so for example  $a_{11} = -L_0/MU$  etc.

The simplest possible control law for lane keeping is

$$\delta_f = -k_1y \quad (67)$$

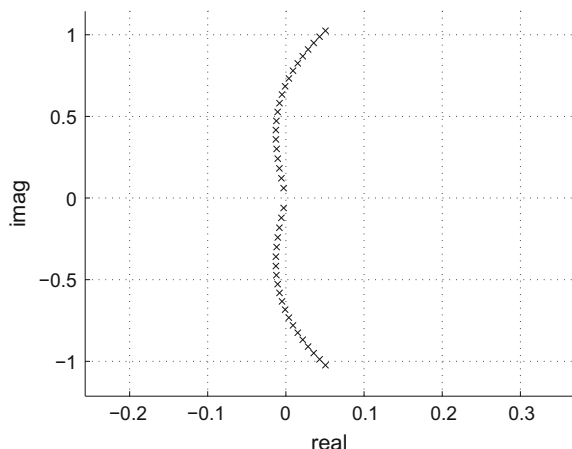
Combining this control law with the state equations we easily determine the resulting system eigenvalues. We omit the analytical details, but using the previous vehicle data it is easy to vary the vehicle speed and control gain and then determine system stability. It turns out that the coupled system can be made stable, but only with low gain and at very low speeds. For example, if we choose  $k_1 = 10^{-3}$  the system remains stable for  $U \leq 12$  m/s.

Figure 17 shows part of the root locus diagram with  $U$  increasing; a complex pair of eigenvalues moves into the right half plane as the speed increases. Note however that, even within the stable speed range, the eigenvalues have very small real parts, indicating that settling to equilibrium will be very slow and any small disturbance will cause considerable drift from the target path.

Clearly some improvement is needed! A modest improvement in stability can be achieved by introducing derivative feedback

$$\delta_f = -k_1y - k_2\dot{y} \quad (68)$$

**Fig. 17** Closed-loop eigenvalue locations for increasing speed. Control gain  $k_1 = 10^{-3}$  is fixed and the vehicle speed is increased from  $U = 1$  m/s in increments of 1 m/s



but realistic driving models require more stability, which can only be achieved using preview of the road ahead.

### 4.3 Preview Steering Control

It is worth noting the destabilizing effect of time delay. A human driver does not react instantaneously to changes in vehicle motion or position, and any performance or stability analysis should take account of delays in human response. The above results assume zero time-delay,  $T_d = 0$ . In the following we should relax this condition and yet have a realistic chance of finding a control law to satisfactorily regulate the lateral position of the vehicle.

The preview control scheme is shown in Fig. 18, where the *previewed* lateral deviation  $\hat{y}(t + T_p)$  is used for feedback control:

$$\delta_f(t + T_d) = -k_1\hat{y}(t + T_p) - k_2\dot{y}(t) \quad (69)$$

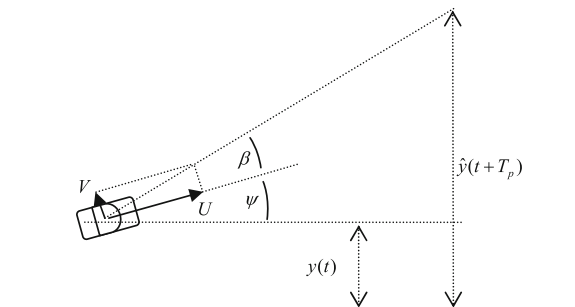
$$\hat{y}(t + T_p) = y(t) + UT_p \sin(\psi(t) + \beta(t)) \quad (70)$$

The resulting driving control is well behaved, provided the control gains ( $k_1, k_2$ ) and preview time  $T_p$  are suitably tuned to provide acceptable tracking and stability performance, and the valid parameter ranges also depend on the vehicle dynamic properties as well as the driver delay time  $T_d$ .

The following results correspond to  $k_1 = k_2 = 0.005$ , with driver time delay  $T_d = 0.25$  s and preview time  $T_p = 0.5$  s (Fig. 19). Starting with an initial lateral deviation of 1 m, the task of the driver model is to return the vehicle to the  $x$ -axis. The system performs the manoeuvre within a few seconds, and is clearly stable and capable of settling back to the desired path. For more complex situations, where there is changing road curvature or obstacles to avoid, we expect that additional feedforward control will be required. However this will take us well beyond the scope of this chapter.

The choice of feedback gains ( $k_1, k_2$ ) can be addressed in a systematic way using a form of root locus for the linearized system. For example, if the system is defined

**Fig. 18** Preview control variables



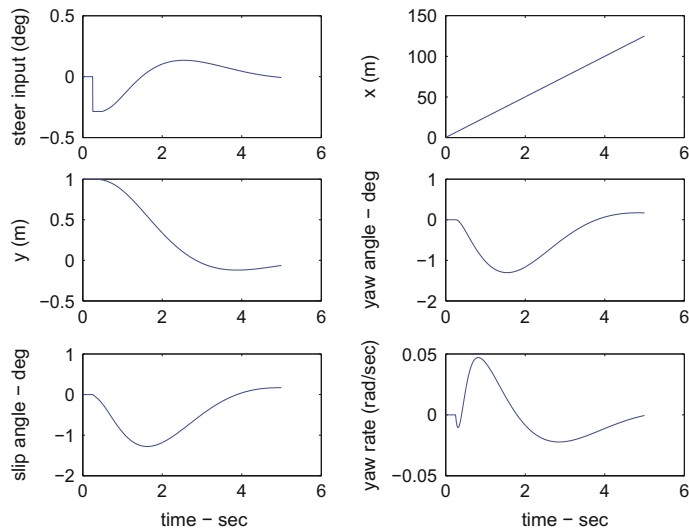


**Fig. 19** Closed-loop responses of the vehicle-driver system. Initial lateral offset  $y(0) = 1$  m. The effect of the driver time delay  $T_d = 0.25$  s is clearly seen in the steering response

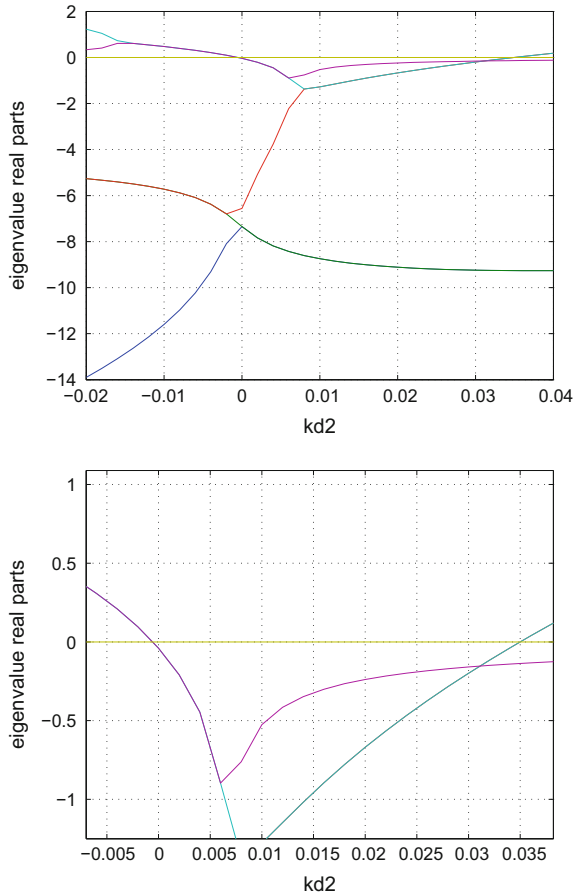
in Simulink, the linearization (including time delay) is easily performed numerically and the eigenvalues determined for each set of chosen gains. Here, starting with the parameters in the above example,  $k_2$  is varied over a range of positive and negative values; the real parts of the system eigenvalues are plotted in Fig. 20. It is seen that, for the particular case,  $k_2 \approx 5 \times 10^{-3}$  gives ‘optimum stability’ meaning that the maximum real part of the eigenvalue set is as negative as possible. Of course this result depends on the other parameters chosen, including the time delay  $T_d$ . Note that the constant zero eigenvalue is related to longitudinal dynamics and can be ignored.

## 5 Control of Nonlinear Handling Dynamics

### 5.1 Overview

Antilock braking and electronic stability control systems (ABS/ESC) operate near the limits of friction. ABS works in a localized way, controlling the dynamics of individual wheels without any significant coordination between them. ESC controls the overall dynamics of the vehicle and hence has a wider scope and somewhat greater sensing requirements. Since neither system can ‘see’ the world outside, there is scope for more capable systems to be developed in the future, to control vehicle motions in emergency situations taking account of the local road geometry, obstacles etc.; this wider aspect is introduced in Sect. 5.4.

**Fig. 20** Stability influence of parameter  $k_2$ . Upper: full-range, lower: zoomed-in. Note One eigenvalue  $\lambda = 0$  is due to a longitudinal speed integrator, and is not relevant to lateral stability



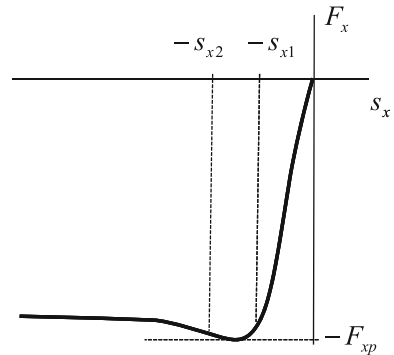
## 5.2 Anti-lock Braking Systems

ABS works by limiting the slip ratio  $s_x$  during severe braking.  $s_x$  defines the relative speed reduction of the wheel during braking, or alternatively the relative speed increase during vehicle acceleration. It is this speed reduction relative to a free-rolling wheel which leads to elastic deformation of the tyre and hence the generation of longitudinal tyre force for braking:

$$s_x = \frac{\omega R - v_x}{v_x} \quad (71)$$

Here  $\omega$  is the wheel angular velocity,  $R$  is the rolling radius of the tyre and  $v_x$  is the longitudinal velocity of the wheel-centre in the local tyre coordinates, and  $s_x < 0$  during braking. Similar to the case with lateral tyre force generation, the braking

**Fig. 21** Tyre force versus slip during braking (plot of braking force vs. slip ratio). To avoid wheel-lock, the ABS control keeps the slip ratio in the range  $-s_{x2} \leq s_x \leq -s_{x1}$



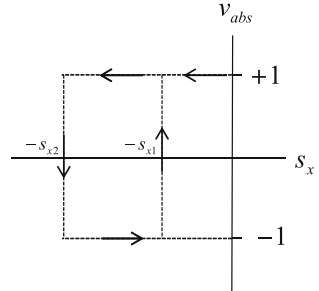
force experiences an adhesion peak—Fig. 21. When the slip ratio goes beyond this adhesion peak, there is a tendency for the wheel to lock up under further braking, which reduces the available braking force and degrades the ability of the (front) tyres to steer the vehicle. ABS is especially important in conditions where road surface friction is reduced (e.g. wet or icy road) but is designed to also operate under hard braking, even when the surface friction is high.

Previously, before ABS became a common feature, the brake pressures on a car would be biased towards the front wheels so that, in the case of severe braking, the front wheels would lock before the rear wheels. A locked wheel has no angular velocity and there is only sliding contact with the road; hence there is a very low cornering stiffness—lateral forces due to slip angle become correspondingly small. According to Eq. 20 the denominator of the first term in the understeer gradient becomes small, so  $K_u \gg 0$  and the vehicle will severely understeer. The alternative, rear wheels locking first, leads to severe oversteer and the vehicle will spin out. While the latter option is clearly worse, severe understeer means that the vehicle tends to straight-line motion even when the driver turns the steering wheel. Hence, to maintain stability with some basic level of steerability, all wheels should be kept from locking.

ABS requires a hydraulic pump and valves (two per wheel) that allow wheel cylinder pressure to: (i) *increase* (inlet open, return valve closed); (ii) *hold* a fixed value (inlet and return valves closed) or (iii) *reduce* hydraulic pressure (inlet is closed, return valve is open). The valves are to be actuated to maintain the slip ratio in a suitable range  $(-s_{x2}, -s_{x1})$  once the lower limit  $-s_{x2}$  is first reached—see Fig. 21. As mentioned, not only does this increase the braking force to some extent (and hence reduce straight-line stopping distance), it also preserves adhesion in the contact patch and hence the generation of cornering forces arising from slip angles. In this way the vehicle can maintain its stability—avoiding oversteer—and at the same time be capable of responding to steering inputs—avoiding excessive understeer.

A simple ABS control strategy is in the form of a switched ('bang-bang') controller. Define the valve states  $v_{abs}$  according the values

**Fig. 22** ABS control by simple hysteresis



$$v_{abs} = \begin{cases} +1 & \text{increase} \\ 0 & \text{hold} \\ -1 & \text{reduce} \end{cases} \quad (72)$$

Then the ABS controller can be defined by a simple hysteresis switching rule, as shown in Fig. 22. This will maintain the slip ratio in the desired range  $(-s_{x2}, -s_{x1})$ . Note that  $v_{abs} = 0$  is not used in this simple function.

However, during a hard braking event, vehicle speed is not easily estimated—once all wheels decelerate under braking, the vehicle speed over ground becomes decoupled from the wheel speeds and there is not enough information to calculate slip ratios. Clearly, uncertainty in the slip ratio is greatly magnified by any uncertainty in the vehicle speed (see Eq. 71). However, since wheel speed itself can be accurately determined, the rate of change of wheel speed can be used as an alternative trigger for controlling the valve state  $v_{abs}$ . This involves using heuristic switching rules, tuned to adapt to different conditions of friction and driving. Wheel accelerations are compared to thresholds to allow valve states to be selected. The basic idea is very simple: a large wheel deceleration cannot arise from a reduction in vehicle speed, and hence the wheel is tending towards a locked condition. On the other hand if, after pressure release, there is a large enough wheel acceleration, it is presumed that the wheel has recovered sufficient rotation to be given another brake actuation.

A typical set of rules are given in Fig. 23. Reading down the first column, brake pressure is allowed to increase until the first threshold is reached,  $\dot{\omega} < -a_1$ . The valve state is set to *hold* ( $v_{abs} = 0$ ) until the second threshold is reached  $\dot{\omega} < -a_2$ , at which point the wheel hydraulic pressure is released ( $v_{abs} = -1$ ). Then, moving up the second column ( $\uparrow$ ) the pressure is held when  $\dot{\omega} > -a_1$  and remains held until  $\dot{\omega} > a_4$ , i.e. there is appreciable wheel acceleration. Now, with pressure allowed to increase the wheel will again decelerate, switching to *hold* when  $\dot{\omega}$  crosses  $a_4$ , to ‘slow increase’ after  $a_3$  and full release after  $-a_1$ . The switching will then cycle through the switching logic of the final two columns of the table ( $\uparrow, \downarrow$ ).

In the following example, the effect of ABS control is demonstrated in the scenario where a steering input is applied during hard braking.

**ABS example** A collision avoidance scenario is defined where the driver applies an intervention with hard braking and simultaneously applies steering to try to

Threshold	First Cycle	$\uparrow$	$\downarrow$
$a_4$	~	1	1
	—	—	—
$a_3$	~	0	0
	—	—	—
$-a_1$	1	0	0.5
	—	—	—
$-a_2$	0	-1	-1
	—	—	—
	-1	-1	-1

**Fig. 23** Switching rules for ABS valve states  $v_{abs}$ —see Eq. 72—based on wheel rotational acceleration thresholds  $a_i$ . State  $v_{abs} = 0.5$  is *slow pressure increase* with states alternating between  $v_{abs} = 0$  and  $v_{abs} = 1$

change lanes. A low-friction surface ( $\mu = 0.4$ ) is assumed, representing for example a smooth wet concrete road surface. Steering is in the form of a sinus steer, of amplitude  $68^\circ$  and duration 1.6 s; this has sufficient amplitude to execute a lane change if there were no braking.

Two cases are simulated using (CarMaker 2014); in case (a) there is no ABS and the wheels lock under hard braking; in (b) the ABS system maintains rotation of all wheels. For both cases, the initial speed is set at 80 km/h and initial lane-keeping is via a driver model; the brake/steer manoeuvre is initiated after 5 s of simulation. Figure 24 shows that in case (a) the (lighter, blue) car has no appreciable lateral deviation; the driver model continues braking to minimize collision speed and the simulation continues until the vehicle stops. In case (b), with ABS enabled, the (darker, red) vehicle is able to respond to steering and, after the 1.6 s avoidance manoeuvre, control is resumed by the driver model and the car is able to return safely to the original lane.

According to Fig. 25 the deceleration advantage of ABS is actually very small—both cars have approximately the same speed profile. The operation of ABS is clearly shown in Fig. 26—during the intervention for (a) all wheels lock (slip ratio = -1)

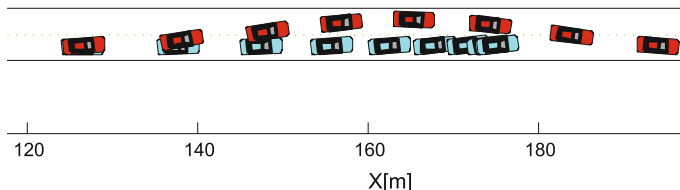


**Fig. 24** Vehicle trajectories for an attempted lane change manoeuvre with hard braking: **a** light (blue) car locks the wheels and stops in the current lane; **b** dark (red) car uses ABS and completes the lane change

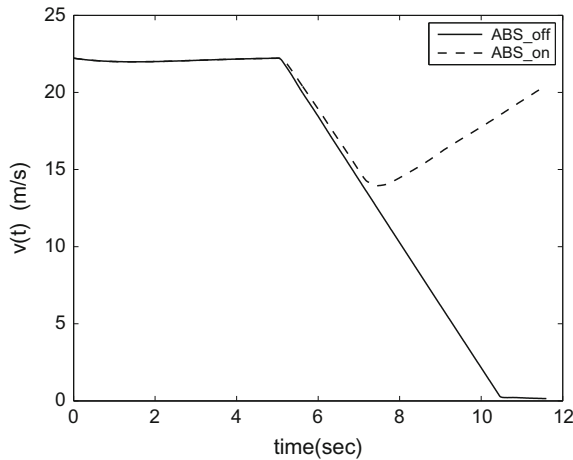


**Fig. 25** Speed profile for: **a** ABS off; **b** ABS on. The whole driving contains three phases: first phase, the vehicle runs for 5 s at speed of 80 km/s; second phase, steering and braking for 1.6 s; third phase **a** the driver continues to brake, or **b** the driver returns to normal speed and steering control

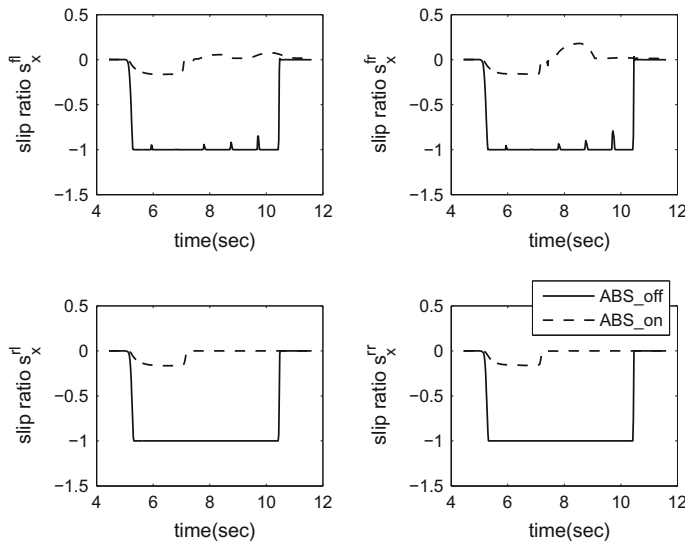


**Fig. 26** Slip ratio of four wheels: without ABS system, the vehicle locks four wheels during lane change and braking phase

while for (b) there is a controlled reduction of wheel speed giving a minimum slip ratio  $\approx -0.15$ . In this scenario it is clear that the major effect of ABS is to provide the driver with continued steering control during braking. Of course, in reality the human driver may not respond in such an ‘optimal’ way, but the point is clear, that ABS enables directional control from the driver even under hard braking on a low-friction surface.

### 5.3 Electronic Stability Control (ESC)

Electronic Stability Control is referred to under many different names and acronyms such as Electronic Stability Program (ESP) and Vehicle Stability Control (VSC). In all cases the basic function is the same: ABS hardware (valves and hydraulic pump) are used to actuate one or more wheel brakes to provide a corrective yaw moment to the vehicle, in order to avoid excessive oversteer or understeer. The crucial difference, compared with ABS, is that the brakes are actuated without the driver pressing the brake pedal. Also, the control reference comes from the vehicle motion rather than simply the rotation of the individual wheel.

Additional sensors are required in the form of (i) a steering wheel angle sensor (ii) a yaw rate sensor. These sensors are relatively inexpensive, and so the development of ESC from ABS is largely a question of the enhanced software. A third sensor, for lateral acceleration, is also required. This is because body sideslip angle  $\beta$  is part of the ESC control algorithm, but there is no affordable sensor to directly measure it. Hence  $\beta$  is to be estimated using other sensors, and the accelerometer helps with the estimation.

ESC is an example of *integrated chassis control* where one or more actuators work together to improve the handling performance of the vehicle as a whole.

**Oversteer correction** Oversteer is commonly characterized by the rear slip angles being larger than at the front, and in *steady-state cornering* this follows directly from the bicycle model equations. Thus, for the case of cornering to the left,  $\delta > 0$ , we expect  $\alpha_r > \alpha_f > 0$  during oversteer. In everyday terms, the rear of the vehicle ‘spins out’ leading to excessive yaw rate and a large (negative) sideslip angle. Given a reference model, such as the bicycle handling model of Sect. 2, the model-reference for these variables may be determined in real-time,  $\mathbf{x}_{ref} = [\beta_{ref}, r_{ref}]^T$  based on the current vehicle speed  $U$  and steering inputs  $\delta(t)$ . Then the oversteer condition is characterized by

$$\beta < \beta_{ref} < 0 \quad (73)$$

$$r > r_{ref} > 0 \quad (74)$$

again for the case of turning to the left, using ISO coordinates.

The situation is shown in Fig. 27; the yaw rate  $r = \dot{\psi}$  is larger than is demanded by the curvature of the intended path; the rear axle loses grip and the tendency to spin

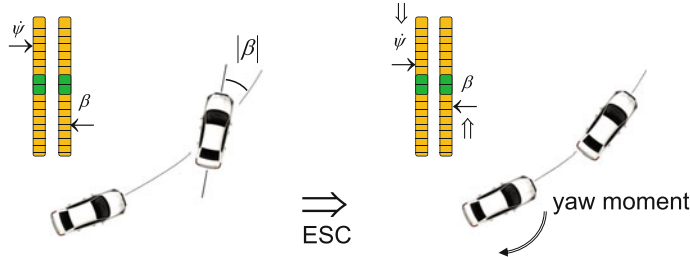


**Fig. 27** ESC intervention to correct oversteer (spin-out). Left figure: without ESC, right figure: with ESC. The yaw moment simultaneously balances excessive positive yaw velocity  $\dot{\psi}$  and negative body sideslip angle  $\beta$

out also leads to an increase in body sideslip. In the case shown, the right-front wheel is braked under ESC control so that the yaw rate is reduced and simultaneously the body sideslip angle is restored towards the reference state (shown as dark green at the center of the vertical bar).

As noted, reference values for  $r$  and  $\beta$  can be obtained from the bicycle handling model. In state-space form (see Eq. 12)  $\dot{\mathbf{x}} = A\mathbf{x} + B\mathbf{u}$  and the reference may be obtained from a steady-state condition.

$$\mathbf{x}_{ref} = -A^{-1}B\mathbf{u} \quad (75)$$

assuming matrix  $A$  is invertible. In fact it is quite common to set the reference side-slip angle to zero (since typically it is small) and allow the controller to apply corrections only when  $|\beta|$  is larger than around  $5^\circ$ . In steady-state the yaw rate reference is obtained from Eq. 48

$$r_{ref}(t) = \frac{gU\delta(t)}{gl + K_u U^2} \quad (76)$$

Because ESC in this instance is intended only for occasional intervention to prevent oversteer, a trigger is also required:

$$\begin{aligned} & \text{if } |r - r_{ref}| > r_0 \\ & \text{and } \left| \frac{r - r_{ref}}{r_{ref}} \right| > p \\ & \text{then } e_r = r - r_{ref} \\ & \text{else } e_r = 0 \end{aligned} \quad (77)$$

The error term  $e_r$  is then used to generate a yaw moment, via braking, for feedback control—but only if the absolute and relative errors are sufficiently high. A similar feedback error is required for body sideslip control:

$$\begin{aligned}
 & \text{if } |\beta| > \beta_0 \\
 & \text{and } \beta \dot{\beta} > 0 \\
 & \text{then } e_\beta = \beta + \tau \dot{\beta} \\
 & \text{else } e_\beta = 0
 \end{aligned} \tag{78}$$

Then, finally, feedback is applied whenever the error terms are non-zero:

$$M_z = -K_r e_r + K_\beta e_\beta \tag{79}$$

The yaw rate feedback is essentially a switched proportional control, while the body side-slip term includes derivative action also via the term  $\tau \dot{\beta}$  in the expression for  $e_\beta$ . The difference of  $\pm$  signs is clear from Fig. 27—a negative yaw moment is required in this case, where  $e_r > 0$  and  $e_\beta < 0$ .

For oversteer correction, the yaw moment  $M_z$  may be obtained by braking the front outer wheel, creating a stabilizing effect as in Fig. 27. The reasoning here is that, for oversteer, the rear tyres are operating beyond their adhesion limits and additional braking will have little effect, so the priority is to brake the relevant front wheel, which is likely to be working below its adhesion limit. In reality, such single-wheel control allocation is overly restrictive, and control may be applied to more than one wheel, depending on the estimated surface friction and vertical tyre loads—for example including braking of the rear outer wheel; it may also be possible to apply traction forces at the inner wheels if there are available actuators such as independent electric drive. On the other hand, single-wheel braking at the outer front wheel is well-known as a simple and effective countermeasure for oversteer. The appropriate algorithms for wheel actuator allocation are vehicle-specific, and the parameter values for  $r_0$ ,  $p$ ,  $\beta_0$ ,  $\tau$ ,  $K_r$  and  $K_\beta$  are obtained by trial-and-error tuning in simulation and track testing.

**Understeer correction** For the understeer case, Fig. 28, the countermeasure can be similar and the same control law, Eq. 79, may be applied. For example, with single-wheel control allocation and for the case shown,  $e_r < 0$ ,  $e_\beta \approx 0$  so the correcting positive yaw moment is applied by braking the rear inner wheel. However, unlike oversteer correction, the yaw moment will typically have an undesirable side-effect for body sideslip, generating an increasingly negative value for  $\beta$  leading to a second (oversteer) ESC correction. Overall there will be a desirable effect, since increasing the magnitude of  $\beta$  will increase the cornering force at the rear axle, hence increasing path curvature, but only temporarily.

In the above ‘classical’ understeer mitigation algorithm, the critical role of vehicle speed is neglected, and it is now known that four-wheel braking can be the most effective intervention for the understeer case—see Sect. 5.4 below. In brief, four-wheel braking has three potential benefits for understeer correction: (a) longitudinal load transfer to the front axle increases its lateral force capacity; (b) speed reduction directly reduces the understeer effect, presented for example in Eq. 48; (c) the limiting path curvature for a given lateral force capacity increases quadratically with the reduction in speed:

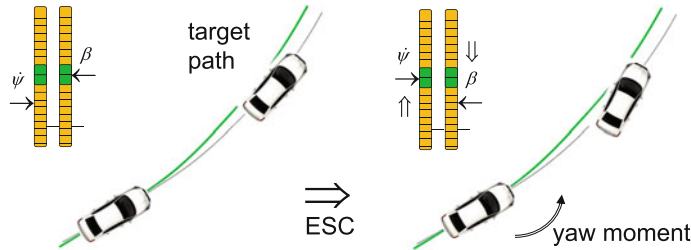


**Fig. 28** ESC intervention to correct understeer. The yaw moment increases yaw velocity  $\psi$  but pushes the body sideslip angle  $\beta$  towards the oversteer condition

$$F_y = \frac{MU^2}{R} \Rightarrow R^{-1} = \frac{F_y}{MU^2} \quad (80)$$

where  $F_y$  represents the overall lateral force capacity of both axles and  $R^{-1}$  is the path curvature. This suggests there should be an optimum balance between the use of available friction to slow the vehicle and also create the necessary lateral forces to promote path curvature.

It is clear from the above that, while oversteer correction is mostly concerned with maintaining the stability of the vehicle so the driver can remain in control, understeer is more concerned with giving the driver-vehicle system the capability of increasing path curvature—for example to prevent run-off-road crashes on tight curves. Thus oversteer mitigation prioritizes yaw moment control for stability, understeer mitigation prioritizes the magnitude and direction of the resultant force at the mass centre.

## 5.4 Motion Control Near the Limits of Friction

When the limits of friction are reached, it is beyond the skill of the average driver to control the path and speed of the vehicle to maintain the stability and safety of the vehicle. We have seen how ABS and ESC can help with lateral stability, but for path and speed control they only assist in an indirect way. In the following we introduce a more sophisticated vehicle control concept which focuses directly on motion control. Consider once again the problem of understeer when a vehicle approaches a curve, and the speed is too high or the road surface friction is too low, so that without intervention a dangerous road or lane departure becomes inevitable. As the driver steers more, the vehicle reaches its overall friction limit and there is no available increase in path curvature: we term this condition *path understeer*, which is similar but distinct from the conventional understeer condition discussed above; conventional understeer is related to the cornering force limit at the single (front) axle, while path understeer relates to the overall force capacity of the vehicle.

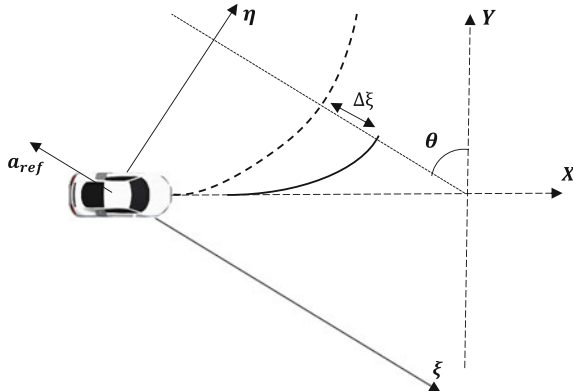


**Fig. 29** Schematic of the PPR target motion with constant  $\theta$  acceleration. The dashed line represents the target path and the aim is to minimize the maximum off-tracking distance  $\Delta\xi$ . This is equivalent to minimizing the distance traveled in the  $\xi$  direction. Hence  $\mathbf{a}_{ref}$  is fixed in the inertial axes. The optimal choice of  $\theta$  depends on initial conditions and surface friction

The problem of path-understeer was addressed in Klomp et al. (2014), where an optimal control problem was formulated with an objective to minimize the maximum off-tracking from the reference path. The optimal combination of braking and cornering forces was found to be a parabolic path associated with a reference CG acceleration vector fixed in inertial coordinates. This is shown in Fig. 29. In the coordinates shown the acceleration vector is  $\mathbf{a}_{ref} = \mu g[-\sin \theta, \cos \theta]^T$  where  $\mu g$  is the limiting acceleration magnitude and  $\theta$  defines the fixed inertial direction. The optimal value of  $\theta$  is chosen so that, at the point of maximum off-tracking,  $\mathbf{a}_{ref}$  is perpendicular to the tangent of the vehicle path. The reference motion is termed the ‘parabolic path reference’, PPR—(Klomp et al. 2014). Note that for the PPR motion, as the vehicle path curves and returns to the direction of the desired path, in vehicle coordinates the acceleration vector changes its bias from combined braking and cornering towards the pure lateral (cornering) direction. Correspondingly, the path curvature reaches a maximum at the point of maximum lateral deviation, which is also the point of minimum vehicle speed.

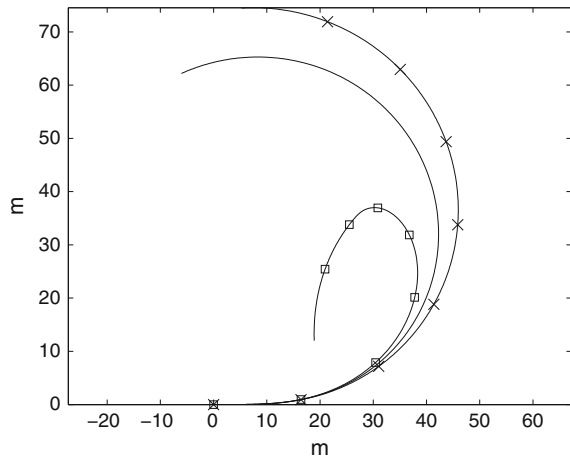
The high level control concept is quite simple, but to implement it requires a nonlinear multivariable brake controller. It is no longer sufficient to use single-wheel braking, and an optimal (or near-optimal) brake force distribution controller is needed. In the papers Gao et al. (2015, 2016b) the *Modified Hamiltonian Algorithm* (MHA) was proposed, and MHA is used in the following. Note, however, that other optimization methods might be used to achieve the same control objective: track the target acceleration vector while maintaining lateral stability.

**Example: path understeer mitigation** This example is due to Yangyan Gao—see Gao et al. (2016a). The aim is to highlight the fundamental distinction between conventional understeer/ oversteer and path understeer. The example is simulation-based and makes use of a high fidelity simulation model in CarMaker (2014). Vehicle parameters are given in Table 1.

**Table 1** Vehicle data

Description	Symbol	Value
Vehicle mass (kg)	$m$	1675
Vehicle moment of inertia ( $\text{kg m}^2$ )	$I_{zz}$	2610
Wheelbase (m)	$l$	2.675
Axle distances from CG (m)	$l_f, l_r$	$0.4l, 0.6l$
Front and rear track width (m)	$l_w$	1.5
Road surface friction coefficient	$\mu$	0.9

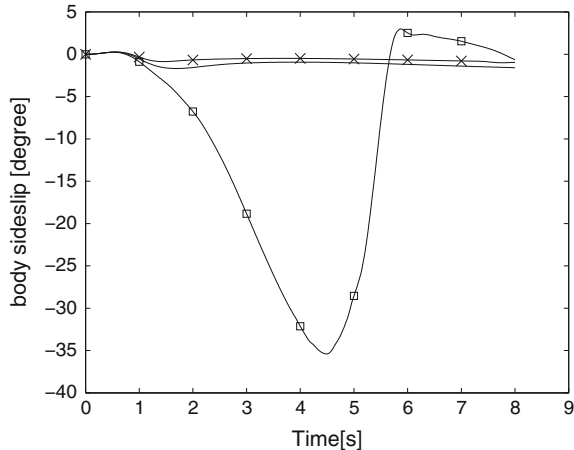
**Fig. 30** Vehicle trajectory of negotiating a curve (target radius  $R = 27 \text{ m}$ ): solid line without marker: standard vehicle; solid line with cross marker: terminal understeer case; solid line with square marker: terminal oversteer



To alter the (classical) understeer/ oversteer characteristics, but otherwise maintain the same overall properties of the reference vehicle, the front and rear anti-roll bar stiffness are varied. A stiffer anti-roll bar at the front promotes load transfer at the front, and results in reduced maximum force at the front axle, giving terminal understeer under severe cornering. On the other hand, increasing the anti-roll bar stiffness at the rear and reducing the anti-roll bar stiffness at the front causes the rear tires to lose maximum force, and therefore promote terminal oversteer. Various simulations were performed for the three vehicle configurations (standard, understeer, oversteer) under both uncontrolled and controlled conditions.

First we present the uncontrolled responses. Figure 30 represents a test condition where a large step-steer input pushes both axles towards their friction limits. It can be seen that the understeer vehicle follows a wider path than the standard vehicle, while the oversteer vehicle follows a tighter curve. In the case of oversteer there is a much larger body sideslip angle—see Fig. 31—which is responsible for a speed reduction and leads to the tighter path. Both terminal understeer and oversteer lead

**Fig. 31** Vehicle body sideslip response: solid line without marker shows the body sideslip of the standard vehicle; solid line with cross marker shows that of understeering vehicle; solid line with square marker shows that of oversteering vehicle



to poorly controlled vehicle motions that endanger the vehicle occupants and other road users.

Turning to the effect of MHA control, a fixed reference  $\theta = 53^\circ$  was tested with initial velocity  $U_0 = 20$  m/s. This value corresponds to surface friction  $\mu = 0.9$  and a desired path curvature  $R = 27$  m.

Overall off-tracking performance is shown for two of the three cases in Fig. 32, giving distance, velocity and acceleration in the direction of interest  $\xi$ . The standard vehicle responses are not shown because they are almost identical to the understeer case.

It is seen that, while there are subtle differences in the acceleration time histories (the oversteer case showing some oscillation), the velocity and distance plots are nearly identical.

Maximum off-tracking is achieved when the velocity reaches zero at the direction of  $\xi$ , as shown by the square markers. Both understeer and oversteer vehicles are controlled in the same way (the MHA algorithm is not ‘told’ anything about the change in configuration) and achieve nearly identical results.

However, since the passive dynamic properties are quite different, we expect some differences when individual braking forces are considered. In Fig. 33 it is seen that while braking forces are similar at the front axle, there are significant differences at the rear axle; in the oversteer case there is more of a bias to the right (outer) wheel braking.

Referring to Fig. 34, the body sideslip turns out to be very similar for both understeer and oversteer configurations. This is completely different from the uncontrolled case in Fig. 31. This emphasizes that optimal (or near-optimal) path understeer mitigation is only mildly affected by differences in yaw stability, provided the controller can stabilize the yaw motion. Hence we expect to see difference in the direct yaw moment from the commanded braking forces. This is seen in Fig. 35. Since the over-

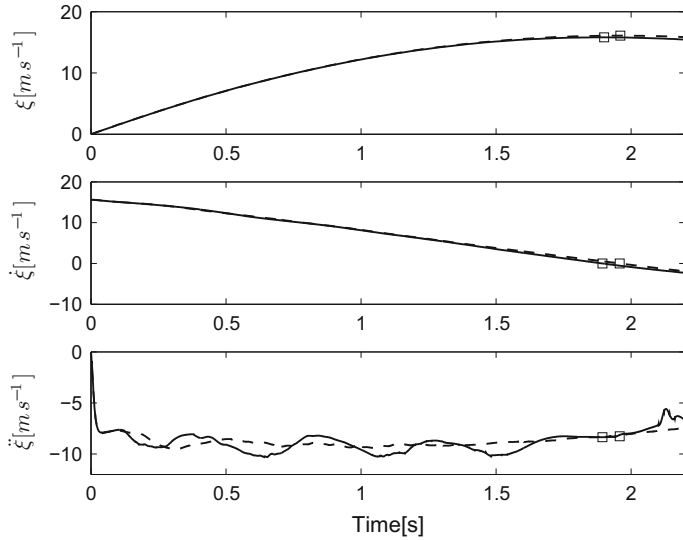


**Fig. 32** Displacement, velocity and acceleration component in the direction of off-tracking  $\xi$ , markers shows point of maximum off-tracking: solid line represents oversteer vehicle response; dashed line represents understeer vehicle

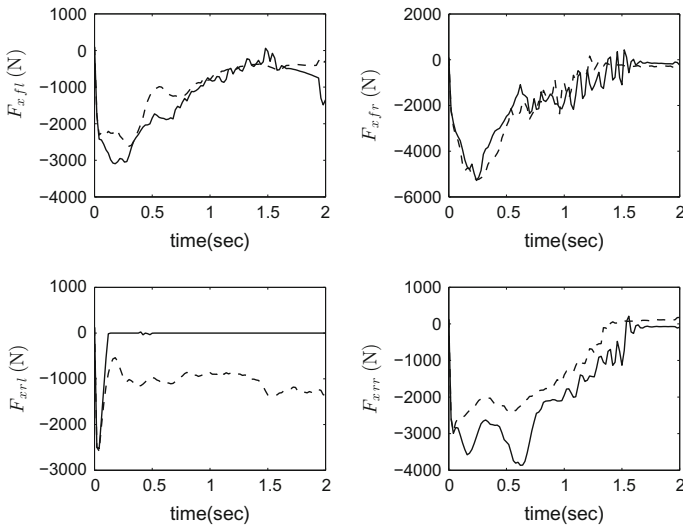


**Fig. 33** Braking force of four wheels: solid line represents oversteering vehicle; dashed line represents understeering vehicle

**Fig. 34** Vehicle body sideslip response during MHA intervention: solid line represents oversteering vehicle; dashed line represents understeering vehicle

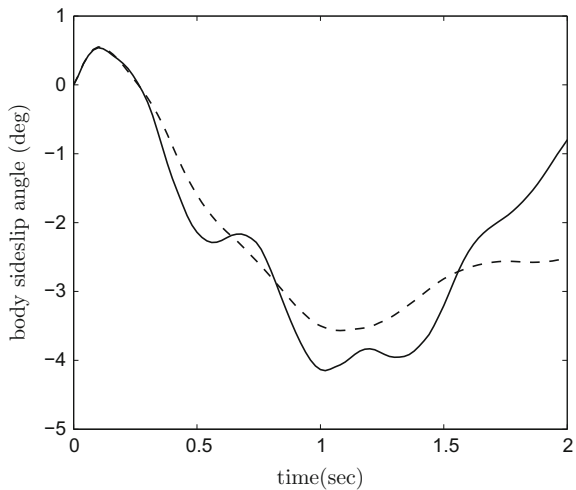
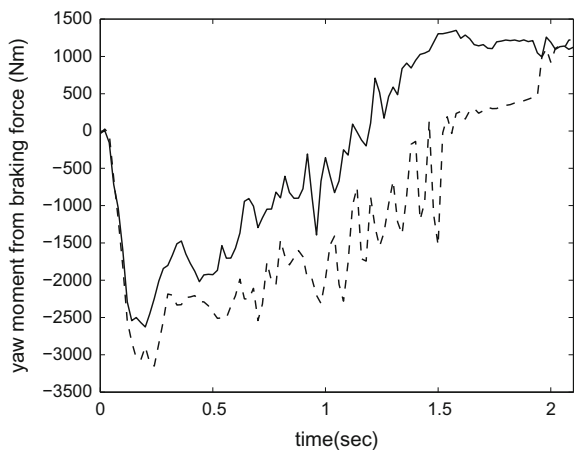


**Fig. 35** Vehicle yaw moment from braking force during MHA intervention: solid line represents the understeering vehicle and the dotted line represents the oversteering vehicle



steer vehicle has a tendency to spin, the turn-out yaw moment should be greater (i.e.  $M_z$  should be more negative) and this is clearly seen in the figure.

We conclude that path understeer compensation via four wheel braking deals with understeering and oversteering configurations in a seamless way—automatically adjusting the yaw moment compensation to suit the particular chassis. Note that in both cases there is a negative direct yaw moment arising from braking, i.e. the effect is a *turning out yaw moment*, contrary to the standard understeer compensation via ESC, described above in Sect. 5.3. Clearly the combined slip condition at the tyres is being taken into account by the controller, and the lateral tyre forces provide sufficient turning-in yaw moment.

More generally we conclude there are sufficient actuator degrees of freedom available from individual wheel braking to deal simultaneously with any inherent *vehicle understeer* or *vehicle oversteer* tendencies, while at the same time addressing *path understeer* using a single integrated chassis control algorithm.

## References

- Abe, M. (2015). *Vehicle handling dynamics: Theory and application*. Butterworth-Heinemann.
- CarMaker, I. P. G. (2014). *Users guide version 4.5. 2*. IPG Automotive, Karlsruhe, Germany.
- Gao, Y., Lidberg, M., & Gordon, M. (2015). Modified Hamiltonian algorithm for optimal lane change with application to collision avoidance. *MM Science Journal MAR*, 576–584.
- Gao, Y., Gordon, T., & Lidberg, T. (2016a). A flexible control allocation method for terminal understeer mitigation. In *International Conference for Students on Applied Engineering (ICSAE)* (pp. 18–23). IEEE.
- Gao, Y., Gordon, T., Lidberg, M., & Klomp, M. (2016b). An autonomous safety system for road departure prevention based on combined path and sideslip control. In *The Dynamics of Vehicles on Roads and Tracks: Proceedings of the 24th Symposium of the International Association for Vehicle System Dynamics (IAVSD 2015), Graz, Austria, 17–21 August 2015* (p. 281). CRC Press.
- Jagacinski, R. J., & Flach, J. M. (2003). *Control theory for humans: Quantitative approaches to modeling performance*. CRC Press.
- Klomp, M., Lidberg, M., & Gordon, T. (2014). On optimal recovery from terminal understeer. *Proceedings of the Institution of Mechanical Engineers, Part D: Journal of Automobile Engineering*, 0954407013511796.
- Weir, D. H., & McRuer, D. T. (1970). Dynamics of driver vehicle steering control. *Automatica*, 6(1), 87–98.

# Advanced Chassis Control and Automated Driving



Masao Nagai and Pongsathorn Raksincharoensak

**Abstract** Recently, various chassis control and preventive safety systems have been developed and applied in modern passenger cars, such as Electronic Stability Systems (ESC), Autonomous Emergency Braking (AEB) etc. This chapter, “*Advanced Chassis Control and Automated Driving*”, describes the theoretical design of Active Rear Steering (ARS), Active Front Steering (AFS) and Direct Yaw-moment Control (DYC) systems for enhancing vehicle handling dynamics and stability. The controller implementation and effectiveness verification using experimental vehicles are also demonstrated. In addition to recently deployed preventive safety systems, Adaptive Cruise Control (ACC) and Lane Keeping Control Systems have been investigated and developed among universities and companies as key technologies for automated driving systems. Here, fundamental theories, principles and applications are mainly presented to give comprehensive understandings in the context of chassis control and automated driving technology.

**Keywords** Chassis control · Control engineering · Active steering  
Direct Yaw moment control · Handling and stability · Automated driving

The main purpose of this chapter is to provide an overview of the advanced chassis control systems aiming for enhancing vehicle handling and stability followed with the automated driving functions of intelligent vehicles in longitudinal and lateral vehicle dynamics.

The first half of this chapter will describe the advanced chassis control systems for enhancing vehicle handling and stability. As the basic performance of current pas-

---

M. Nagai (✉)

Japan Automobile Research Institute, Minato, Tokyo, Japan  
e-mail: mnagai@jari.or.jp

P. Raksincharoensak

Tokyo University of Agriculture and Technology, Koganei, Tokyo, Japan  
e-mail: pong@cc.tuat.ac.jp

senger cars improved, most of drivers feel the need for a quicker response that could control the direction of vehicle as desired with less effort. Based on the constraint that only the front tyres can be steered, the chassis performance is limited to a certain level. Chassis control has objectives to enhance vehicle handling and stability with respect to the steering input from the driver, and to enhance its limit performance avoiding side slip or spin during emergency manoeuvre. Handling and stability performance can be enhanced by controlling lateral and yaw motions of vehicle body, by using front and rear tyre forces in lateral and longitudinal direction. This chapter describes the design of Active Rear Steering (ARS), Active Front Steering (AFS) and Direct Yaw-moment Control (DYC) systems for enhancing vehicle lateral dynamics, i.e. handling and stability. The controlled variables are the vehicle body side slip angle and the yaw rate.

The latter half of this chapter describes the control system design in the context of automated driving vehicles. Automated driving functionalities as Advanced Driver Assistance Systems (ADAS) has been currently developed to prevent traffic accidents as well as fatalities, increase driving convenience as well as comfort and increase traffic and fuel efficiency. A suite of on-board sensors for environment perception such as camera, radar or LiDAR (Light Imaging Detection And Ranging) have been progressively developed and the detection performance has been improved. Actuator technology for steering and braking becomes more advanced and has good control performance.

ADAS assists human drivers to maintain safe driving in the form of (1) information provision, (2) warning by auditory, visual or haptic types and (3) control intervention. ADAS in the context of control intervention can be classified into two types: Co-Pilot (Fig. 1) and Auto-Pilot (Fig. 2). The Co-Pilot type ADAS acts in parallel with the human driver to control the vehicle not to fall into critical situations. The human driver still has a full authority to control the vehicle by steering, accelerating and braking. Co-Pilot ADAS may be able to monitor the human driver behavior in real time in order to adapt the intensity of control intervention. On the other hand, the auto-pilot ADAS replaces the human driver in the vehicle longitudinal and/or lateral control manoeuvre. The human driver has responsibility to monitor the control behavior of the system and it is necessary for the human driver to take over the ADAS in the case that the system cannot handle some difficult situations. In this textbook, the basic control algorithm of the ADAS in longitudinal and lateral control will be described.

**Fig. 1** Schematic of co-pilot type advanced driver assistance system (ADAS)

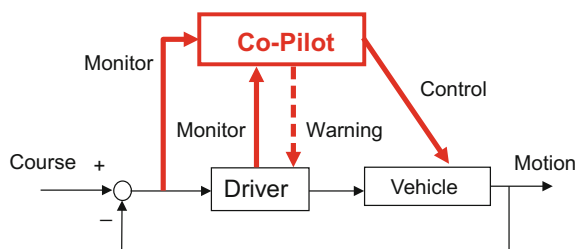
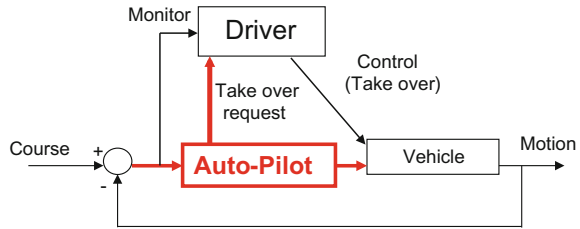


**Fig. 2** Schematic of auto-pilot type advanced driver assistance system



## 1 Active Rear Steering (ARS) Control System for Enhancing Vehicle Handling and Stability

In conventional front wheel steering vehicles, only the front tyres are involved in controlling the side slip angle needed for cornering. The rear tyres generate cornering force only by the resulting side slip angle from the front steering angle input. The rear tyres are not directly involved in controlling the direction of the vehicle. If the rear tyres can be steered together with the front tyres to control the side slip angle, the vehicle lateral dynamics can be changed. The idea of steering the rear tyres simultaneously with the front ones becomes an innovative step forward in the field of vehicle dynamics control (Furukawa et al. 1989). This chapter shows basic control system design of the ARS technology in terms of vehicle dynamics and control techniques (Abe, 2015).

A vehicle which can steer the rear steering angle is called Four-Wheel-Steering Vehicle (4WS). The equations of lateral and yaw motion of vehicle can be written as follows:

$$mV(\dot{\beta} + r) = 2C_f \left( \delta_f - \frac{l_f}{V}r - \beta \right) + 2C_r \left( \delta_r + \frac{l_r}{V}r - \beta \right) \quad (1)$$

$$I_z \dot{r} = 2l_f C_f \left( \delta_f - \frac{l_f}{V}r - \beta \right) - 2l_r C_r \left( \delta_r + \frac{l_r}{V}r - \beta \right) \quad (2)$$

From these equations, we can express the vehicle response in the form of state space equation as follows:

$$\begin{bmatrix} \dot{\beta} \\ \dot{r} \end{bmatrix} = \begin{bmatrix} a_{11} & a_{12} \\ a_{21} & a_{22} \end{bmatrix} \begin{bmatrix} \beta \\ r \end{bmatrix} + \begin{bmatrix} b_{11} & b_{12} \\ b_{21} & b_{22} \end{bmatrix} \begin{bmatrix} \delta_f \\ \delta_r \end{bmatrix} \quad (3)$$

where each element is determined from the equations of motion.

$$\begin{aligned} a_{11} &= -\frac{2(C_f + C_r)}{mV}, \quad a_{12} = -1 - \frac{2(l_f C_f - l_r C_r)}{mV^2}, \\ a_{21} &= -\frac{2(l_f C_f - l_r C_r)}{I_z}, \quad a_{22} = -\frac{2(l_f^2 C_f + l_r^2 C_r)}{I_z V}, \\ b_{11} &= \frac{2C_f}{mV}, \quad b_{12} = \frac{2C_r}{mV}, \quad b_{21} = \frac{2l_f C_f}{I_z}, \quad b_{22} = -\frac{2l_r C_r}{I_z} \end{aligned}$$

From the above state space equation indicated in Eq. (3), by taking Laplace transformation, we can express the vehicle response in the form of transfer function as follows:

[Side slip angle response to the front and rear steering angle]

$$\begin{aligned} \beta(s) &= \frac{b_{11}s + (-b_{11}a_{22} + b_{21}a_{12})}{s^2 + (-a_{11} - a_{22})s + (a_{11}a_{22} - a_{12}a_{21})} \delta_f(s) \\ &\quad + \frac{b_{12}s + (-b_{12}a_{22} + b_{22}a_{12})}{s^2 + (-a_{11} - a_{22})s + (a_{11}a_{22} - a_{12}a_{21})} \delta_r(s) \end{aligned} \quad (4)$$

[Yaw rate response to the front and rear steering angle]

$$\begin{aligned} r(s) &= \frac{b_{21}s + (-b_{21}a_{11} + b_{11}a_{21})}{s^2 + (-a_{11} - a_{22})s + (a_{11}a_{22} - a_{12}a_{21})} \delta_f(s) \\ &\quad + \frac{b_{22}s + (-b_{22}a_{11} + b_{12}a_{21})}{s^2 + (-a_{11} - a_{22})s + (a_{11}a_{22} - a_{12}a_{21})} \delta_r(s) \end{aligned} \quad (5)$$

## 1.1 Front Steering Angle Proportional ARS

The basic idea to control the rear steering angle is to make it steer proportional to the front tyre steering angle which is determined by the driver as the following control law.

$$\delta_r = k\delta_f \quad (6)$$

We can steer the rear steering angle in the same direction with the front steering angle ( $k$  is positive) or in the opposite direction ( $k$  is negative). In the case that the rear steering angle is in the same phase with the front steering angle, it has effect in reducing yaw rate gain and improving vehicle stability in high speed region and reducing the body side slip angle during cornering manoeuvre. In contrast, in the case

that the steering angle is out of phase with the front steering angle, it has effect in increasing yaw rate gain, improving vehicle agility and improving manoeuvrability in low speed region, e.g. reducing the turning radius.

The important effect of the front steering angle proportional rear steering angle is the reduction of the lateral acceleration gain and the phase delay of the lateral acceleration. As can be noticed from Fig. 3, when increasing rear steering angle gain  $k$ , the lateral acceleration gain with respect to the front steering angle is reduced and the phase delay of the lateral acceleration is also reduced.

Next, the effect of rear steering angle on the vehicle body side slip angle is observed. As can be noticed from Fig. 4 increasing the rear steering angle gain  $k$  reduces the body side slip angle gain. This means the vehicle heading direction becomes the same with the vehicle forward direction resulting in easy controllability by the driver.

In the case of front-wheel-steering vehicle (2WS), the vehicle attitude changes depending on the vehicle speed as shown in Figs. 5 and 6. In low speed region, the vehicle body side slip angle is positive indicating that the vehicle is heading outside the corner. In high speed region, the vehicle body side slip angle is negative indicating that the vehicle is heading inside the corner. We can use the side slip angle as the index to determine the proportional gain  $k$  of the rear steering angle in theoretical manner. If the rear steering angle is controlled to regulate the side slip angle in steady state condition (steady state cornering), we can derive the control law as follows:

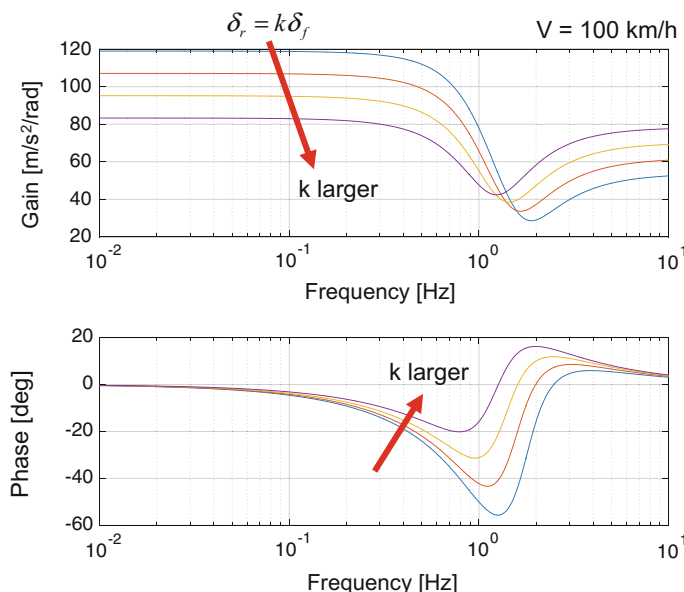


**Fig. 3** Frequency response of lateral acceleration when changing the rear steering control coefficient (velocity = 100 km/h)

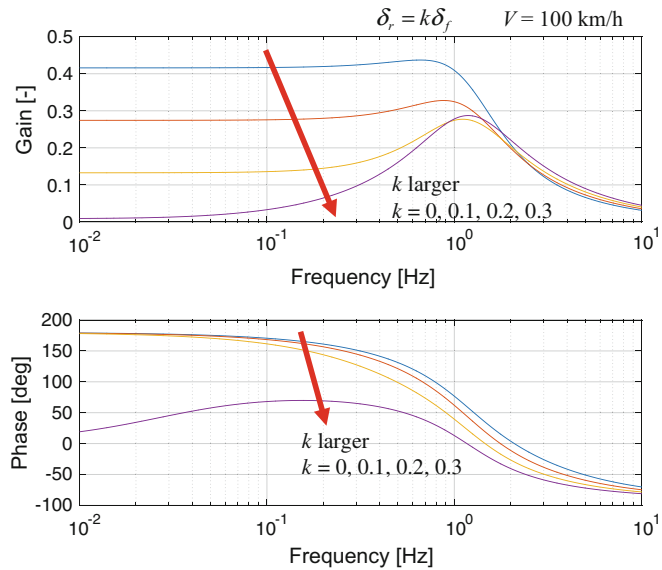


**Fig. 4** Frequency response of body side slip angle when changing the rear steering control coefficient (velocity = 100 km/h)

**Fig. 5** Vehicle attitude during cornering at low speed (positive side slip angle) and high speed region (negative side slip angle)

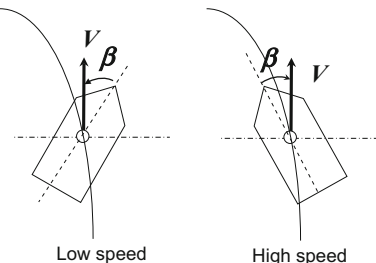


**Fig. 6** Body side slip angle against velocity

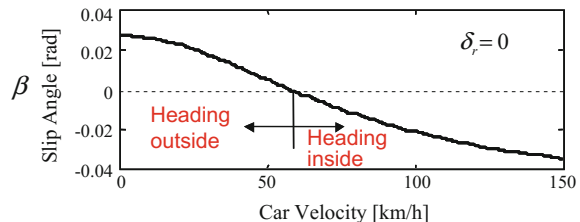
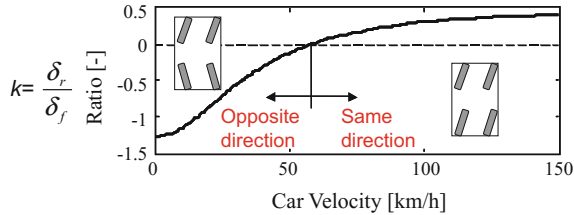


**Fig. 7** Ratio of rear steering angle to front steering angle to realize steady-state zero side-slip-angle



$$\begin{aligned} \beta(s) = & \frac{b_{11}s + (-b_{11}a_{22} + b_{21}a_{12})}{s^2 + (-a_{11} - a_{22})s + (a_{11}a_{22} - a_{12}a_{21})} \delta_f(s) \\ & + \frac{b_{12}s + (-b_{12}a_{22} + b_{22}a_{12})}{s^2 + (-a_{11} - a_{22})s + (a_{11}a_{22} - a_{12}a_{21})} \delta_r(s) \end{aligned} \quad (4)$$

Considering the steady state condition, the Laplace operator  $s = 0$ , the gain  $k$  can be derived as follows:

$$\beta(0) = \frac{(-b_{11}a_{22} + b_{21}a_{12})}{(a_{11}a_{22} - a_{12}a_{21})} \delta_f(0) + \frac{(-b_{12}a_{22} + b_{22}a_{12})}{(a_{11}a_{22} - a_{12}a_{21})} \delta_r(0) = 0 \quad (7)$$

$$\frac{(-b_{11}a_{22} + b_{21}a_{12})}{(a_{11}a_{22} - a_{12}a_{21})} \delta_f(0) + \frac{(-b_{12}a_{22} + b_{22}a_{12})}{(a_{11}a_{22} - a_{12}a_{21})} k \delta_f(0) = 0 \quad (8)$$

$$k = -\frac{-b_{11}a_{22} + b_{21}a_{12}}{-b_{12}a_{22} + b_{22}a_{12}} \quad (9)$$

$$k = -\frac{2ll_r C_f C_r - l_f C_f m V^2}{2ll_f C_f C_r + l_r C_r m V^2} \quad (10)$$

By using zero-side-slip-angle as the control objective, we can derive the speed-dependent control ARS law as indicated in Eq. (10) and Fig. 7.

## 1.2 Dynamic Compensation ARS control

In vehicle planar motion, there are two state variables: side slip angle and yaw rate. Figure 8 shows the block diagram of 2-input 2-output system. In the design of active rear steering angle controller, we need to select the controlled variable that we want to control, as we have only one control input. Generally, it is difficult for human drivers to control the side slip angle. Therefore, in general, most of rear steering angle control laws are designed to directly control the body side slip angle.

### (A) Design by Using Inverse Dynamics

By referring to the linear equation of body side slip angle including dynamic characteristics, if we set the side slip angle response to be zero not only in the steady state steering manoeuvre but also dynamic steering manoeuvre, this results in the control law which generates opposite steering direction of the rear wheel with respect to the front wheel in the initial steering manoeuvre phase.

$$\begin{aligned}\beta(s) = & \frac{b_{11}s + (-b_{11}a_{22} + b_{21}a_{12})}{s^2 + (-a_{11} - a_{22})s + (a_{11}a_{22} - a_{12}a_{21})} \delta_f(s) \\ & + \frac{b_{12}s + (-b_{12}a_{22} + b_{22}a_{12})}{s^2 + (-a_{11} - a_{22})s + (a_{11}a_{22} - a_{12}a_{21})} \delta_r(s)\end{aligned}\quad (4)$$

$$\begin{aligned}0 = & \frac{b_{11}s + (-b_{11}a_{22} + b_{21}a_{12})}{s^2 + (-a_{11} - a_{22})s + (a_{11}a_{22} - a_{12}a_{21})} \delta_f(s) \\ & + \frac{b_{12}s + (-b_{12}a_{22} + b_{22}a_{12})}{s^2 + (-a_{11} - a_{22})s + (a_{11}a_{22} - a_{12}a_{21})} \delta_r(s)\end{aligned}\quad (11)$$

$$\delta_r = -\frac{b_{11}s + (-b_{11}a_{22} + b_{21}a_{12})}{b_{12}s + (-b_{12}a_{22} + b_{22}a_{12})} \delta_f(s)\quad (12)$$

An example of time history of the front and rear steering angles in the case of vehicle running at a velocity of 100 km/h is shown in Fig. 9. As can be noticed from Fig. 9, in the initial phase, the rear steering angle is steered in opposite direction with the front steering angle in order to reduce side slip angle motion as well as improve the yaw responsiveness in the initial phase of steering manoeuvre. Such kind of characteristics is called Non-minimal Phase Delay System which refers to the transfer function which contains the positive zeros in the system.

### (B) Design by Using Inverse Dynamics Model II

There is another design method for active rear steering angle based on two-wheel vehicle model in order to achieve zero-side-slip response. Based on the equations of

**Fig. 8** Structure of 2-input 2-output vehicle planar motion

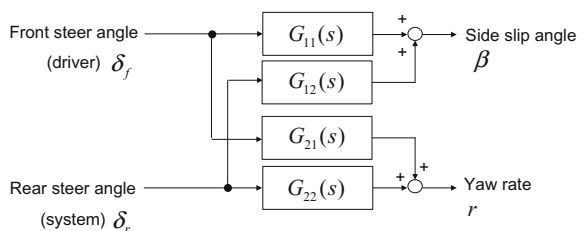
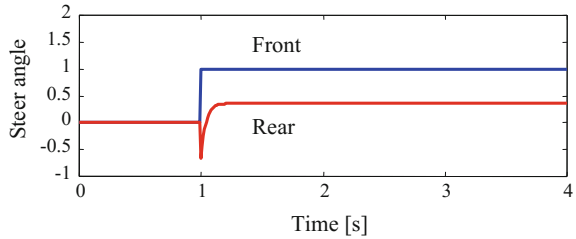


**Fig. 9** Rear steering angle with respect to stepwise front steering angle using inverse dynamics model design method for zero-side-slip-angle ( $V = 100 \text{ km/h}$ )



motion shown below,

$$mV(\dot{\beta} + r) = 2C_f \left( \delta_f - \frac{l_f}{V}r - \beta \right) + 2C_r \left( \delta_r + \frac{l_r}{V}r - \beta \right) \quad (1)$$

$$I_z \dot{r} = 2l_f C_f \left( \delta_f - \frac{l_f}{V}r - \beta \right) - 2l_r C_r \left( \delta_r + \frac{l_r}{V}r - \beta \right) \quad (2)$$

By letting the side slip angle and side slip angular velocity term become zero, and then solving for the control law of active rear steering angle, the following control law can be achieved (Yamamoto, 1991).

$$\delta_r = -\frac{C_f}{C_r} \delta_f + \left( \frac{mV}{2C_r} + \frac{l_f C_f - l_r C_r}{C_r V} \right) r \quad (13)$$

From the above equation, the rear steering angle is determined as function of linear combination of front steering angle and the yaw rate. This control law has yaw rate feedback feature which can compensate the yaw disturbance such as side wind so that the vehicle is more robust to the disturbance.

Next we will see how the yaw rate response changes by applying the control law indicated in Eq. (13). The control law indicated in Eq. (13) is substituted into the equation motion of yaw rate.

$$I_z \dot{r} = (2l_f C_f + 2l_r C_f) \delta_f + \left( -2l_f C_f \frac{l_f}{V} - 2l_r C_r \frac{l_r}{V} - ml_r V - 2l_r \frac{l_f C_f - l_r C_r}{V} \right) r \quad (14)$$

By taking the Laplace transformation to the above equation, we can get the

$$(I_z Vs + (ml_r V^2 + 2ll_f C_f)) r(s) = (2l_f C_f V) \delta_f \quad (15)$$

By rearranging the equation, we can get the modified yaw rate response by the active rear steering angle control as 1st order delay transfer function while in the case of conventional front-wheel-steering (2WS) vehicle has 2nd order delay characteristics. It is known that in the case of high velocity region of conventional front-wheel-

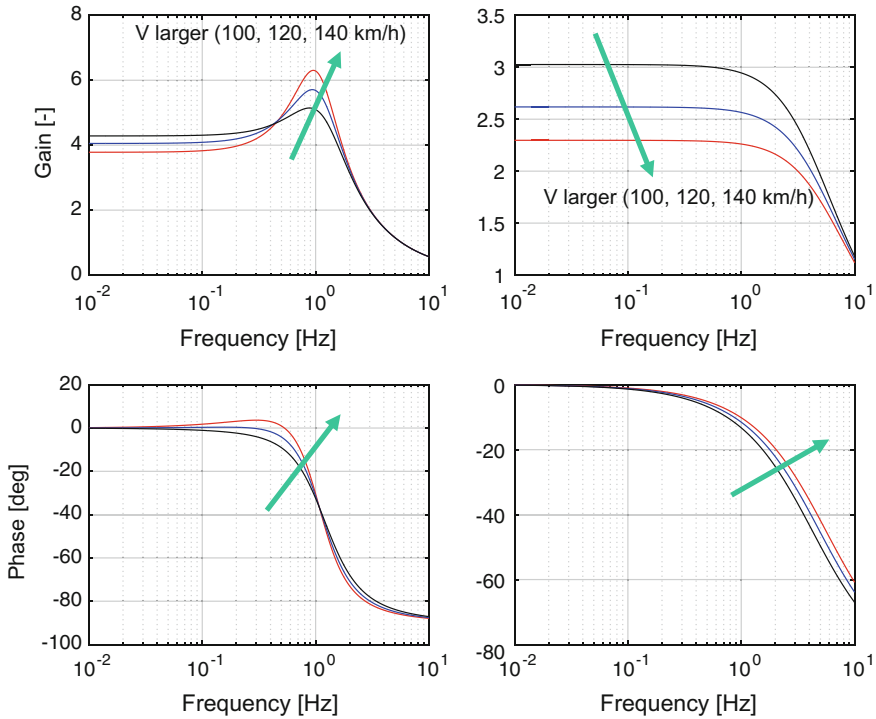


**Fig. 10** Effect of zero-side-slip active rear steering angle control on yaw rate response

steering (2WS) vehicle which the resonance peak of yaw rate is dominant and the damping characteristics is not satisfactory. This bad damping characteristics can be effectively improved by controlling the active rear steering angle which regulates the side slip angle to be zero, as shown in Fig. 10.

$$\frac{r(s)}{\delta_f(s)} = \frac{2lC_fV}{I_zVs + (ml_rV^2 + 2ll_fC_f)} \quad (16)$$

### 1.3 Active Rear Steering Angle Control by Using Model Following Control Theory

Alternative methods to design the controller for the active rear steering angle control system is to apply the model following control theory to the vehicle plant. The model following control theory is a method to make the vehicle response match a desirable response based on 2-degree-of-freedom control system consisting of a feedforward

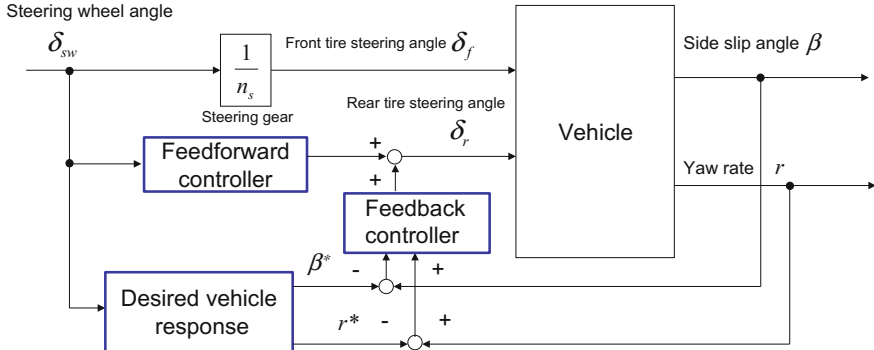


**Fig. 11** Block diagram of model following control ARS

controller and a feedback controller. Generally, the feedforward controller aims to improve the response with respect to the reference signal input and the feedback controller aims to compensate the modeling errors and unexpected disturbances. Both controllers are designed independently so that it is called 2-degree-of-freedom control system. Mostly, the feedforward controller is designed by using inverse dynamics via transfer function method, whereas the feedback controller is designed to compensate the error between the desired response and the actual response by using a classical controller such as PID or a modern controller using LQR control theory and etc. Fig. 11 shows the block diagram of active rear steering angle control system to make the vehicle follow a desired vehicle response model.

If it is possible to control the front steering angle actively using electronic control device, the active four-wheel-steering control (active 4WS) as shown in Fig. 12 can be realized. The authors have proposed a control system which can control the front and rear steering angles by a combination of feedforward and feedback compensation to make the steering response characteristics of vehicle side slip angle and yaw rate follow a virtual vehicle model. A theoretical analysis of a closed-loop driver-vehicle system reveals that the addition of feedback compensation to the control system capabilities ensures superior stability in straight-road driving because the vehicle can respond autonomously to reduce the influence of external disturbance. The effects of errors in vehicle modeling and of changes in parameters for the vehicle or the driver are also studied and the feedback compensation is effective to compensate the error in modeling and secure the control performance. Besides the above design methods, the new variable  $D^*$  which is defined as a linear combination of yaw rate and lateral acceleration is employed as the controlled variable to be followed by using the model following control method. A rear steering angle control can make the quantity  $D^*$  follow the output of the desired reference model.

$$D^* = ka_y + (1 - k) Vr \quad (17)$$

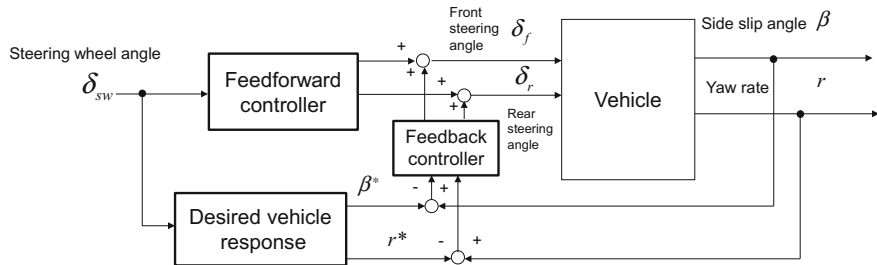


**Fig. 12** Active 4WS for model following control

Moreover, against changes in the state of the vehicle and parameters such as loading condition, road friction or errors due to the nonlinear factors which are not considered in the model for the controller design, a control method that can autonomously adjust the control system parameters to changes of vehicle conditions is required. This method is called “Adaptive Control”.

## 1.4 Summary

This section has described various control laws of Active Rear Steering (ARS) control system. ARS can be classified into two main categories, a feedforward controller type which uses the driver steering wheel angle as input signal and a feedback controller which uses the vehicle state variables as input signal. ARS is effective in controlling the body side slip angle. Extensive researches on ARS by applying modern control theories have been also conducted including the model-matching or model-following control techniques to achieve desired steering response characteristics and there are also further studies on adaptive steering control systems to secure the robustness of the controller against changes in vehicle parameters. As ARS can modify the vehicle steering response characteristics, it is important to know the vehicle steering response characteristics that is easy for drivers to control the vehicle motion. Handling quality objectification is also one of essential issues in this area of study.

## 2 Active Front Steering (AFS) Control System for Enhancing Vehicle Handling and Stability

Since 2000's, Electric Power Steering (EPS) system by using electric motor has been developed instead of the hydraulic system of conventional power steering system for increasing the fuel consumption efficiency. EPS has strong potential to improve the

vehicle stability, the vehicle responsiveness and driving comfort, by reducing steering torque effort in manoeuvreing. As EPS has a mechanical linkage, the relationship between the steering wheel angle and the steering torque cannot be independently designed. Therefore, to enhance both the vehicle stability and the steering feeling in manoeuvreing characteristics is limited under the current mechanical type of steering configuration.

To overcome this problem, Steer-by-Wire (SBW) becomes one of the solutions since the mechanical linkage between the steering wheel and the front tyre as a mechanical constraint in motion does not exist anymore. Typically, SBW system has several merits as follows: (1) Avoiding steering column shaft collision to driver, (2) Flexibility of interior layout and steering situation, (3) Flexibility of steering configuration design, such as joystick, circular wheel, ellipse, bar. Moreover, SBW can control the steering angle automatically to stabilize the vehicle behavior and can control the steering feeling as well as decrease the physical workload, transmit the vehicle behavior and the road information based on front tyre force to the driver. From the viewpoint of human-machine interface (HMI), SBW has structural merits in avoiding interference between the driver and the steering wheel as the mechanical linkage between them is completely replaced by electric wiring, several actuators and controllers.

This section describes a chassis control system utilizing the feature of SBW system based on the model matching control method to improve handling and stability (Shino et al. 2004b; Yoshida et al. 2005). The experiments using an actual test vehicle equipped with SBW, were carried out and the experimental results show the effectiveness of the control system.

## 2.1 Structure of Steer-By-Wire System (SBW)

SBW system consists of a reaction torque generation motor for adjusting steering reaction torque which relates to steering feeling and a front tyre steering actuator for actually steering the front tyres to control the vehicle motion with respect to the driver steering intention. The configuration of SBW is shown in Fig. 13. As a fail safe mechanism when the system error occurs or it is in a malfunction mode, this steering system is also equipped with an electromagnetic clutch between the steering column shaft and the intermediate shaft that connects them together and thus the conventional mechanical linkage of steering can be resumed.

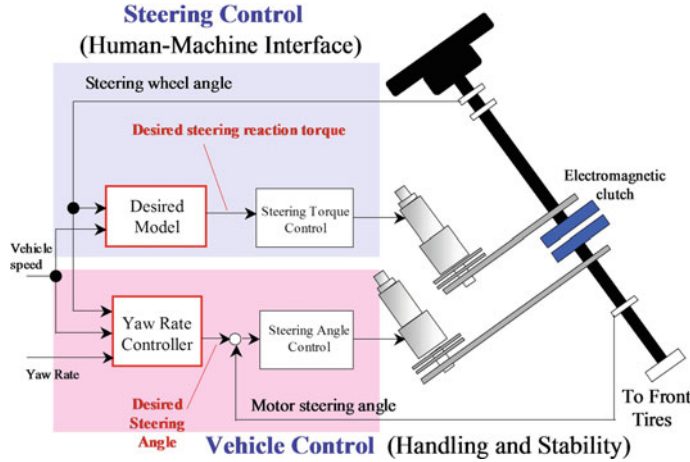
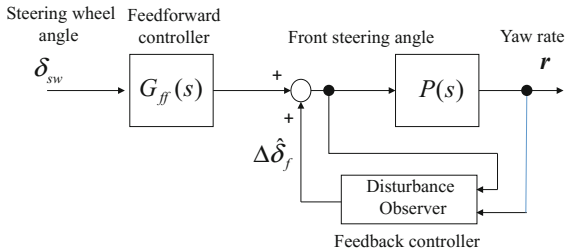


**Fig. 13** Schematic diagram of Steer-By-Wire system

## 2.2 SBW Control System Design

For enhancing the handling and stability of vehicle, the yaw rate of the vehicle is controlled to trace the desired response by using active front steering control input activated by SBW system. Here, the controlled variable is the yaw rate and the control input is the actual front steering angle. The reaction torque for adjusting the steering feeling as an important topic will not be discussed here. With the application of model matching control theory, the control system consists of a feedforward compensator with respect to the steering wheel angle input from the driver and a feedback compensator designed with the application of disturbance observer to reduce the sensitivity to the external disturbances. The proposed SBW control law can be expressed as shown in Fig. 14.

**Fig. 14** Block diagram of Steer-By-Wire control system



## Design of Feedforward Compensator

The inversed dynamics model can be used to design the feedforward compensator to make the yaw rate response of uncontrolled vehicle follow the desired steering response.

The desired yaw rate with respect to the steering wheel angle is assumed to be the first-order delay system as follows:

$$\frac{r(s)}{\delta_{sw}(s)} = G_d = \frac{k_{rd}(V)}{\tau_{rd}(V)s + 1} \quad (18)$$

where,  $k_{rd}$  and  $\tau_{rd}$  are the steady state gain and the time constant of the yaw rate response respectively.

As shown in Fig. 14, the feedforward compensator can be expressed as a transfer function from the steering wheel angle to the front steering angle as follows:

$$\delta_f(s) = G_{ff}(s)\delta_{sw}(s) \quad (19)$$

From the linear two-wheel vehicle model, the transfer function from the front tyre steering angle to the yaw rate can be expressed as follows:

$$\frac{r(s)}{\delta_f(s)} = \frac{a_1 s + a_0}{s^2 + b_1 s + b_0} \quad (20)$$

where, each coefficient in the above transfer function can be expressed as follows:

$$\begin{aligned} a_1 &= \frac{2l_f C_f}{I_z}, \\ a_0 &= \frac{4l C_f C_r}{m I_z V}, \\ b_1 &= \frac{2(C_f + C_r)}{m V} + \frac{2(l_f^2 C_f + l_r^2 C_r)}{I_z V}, \\ b_0 &= \frac{4l^2 C_f C_r}{m I_z V^2} - \frac{2(l_f C_f - l_r C_r)}{I_z} \end{aligned}$$

Moreover, to avoid complexity in the controller design, the transfer function indicated in Eq. (20) is approximated as the first-order delay system with respect to the front steering angle as follows:

$$\frac{r(s)}{\delta_f(s)} = \frac{a_1 s + a_0}{s^2 + b_1 s + b_0} \approx P(s) = \frac{k_r(V)}{\tau_r(V)s + 1} \quad (21)$$

where,  $k_r$  and  $\tau_r$  are the steady state gain and the time constant of yaw rate response respectively and  $P$  indicates the transfer function of the desired steering response. Moreover, by comparing the transfer function of the uncontrolled vehicle indicated in Eq. (20) with the approximated one indicated in Eq. (21), the steady state gain and the time constant of yaw rate response can be obtained as follows:

$$k_r = \frac{a_0}{b_0} = \frac{V}{l \left( 1 - \frac{m}{2l^2} \frac{l_f C_f - l_r C_r}{C_f C_r} V^2 \right)} \quad (22)$$

$$\tau_r = \frac{a_0}{b_0 a_1} = \frac{I_z V}{2l_f l C_f \left( 1 - \frac{m}{2l^2} \frac{l_f C_f - l_r C_r}{C_f C_r} V^2 \right)} \quad (23)$$

Here, by substituting Eq. (19) into Eq. (21), the following equation can be obtained.

$$r(s) = P(s) G_{ff}(s) \delta_{sw}(s) \quad (24)$$

In order to match the actual vehicle yaw rate response with the desired yaw rate response, let the yaw rate in Eq. (21) be equal to the desired yaw rate response indicated in Eq. (18), and the feedforward controller transfer function can be derived as follows:

$$\begin{aligned} G_{ff}(s) &= P^{-1}(s) G_d(s) \\ &= \frac{\tau_r(V)s + 1}{k_r(V)} \cdot \frac{k_{rd}(V)}{\tau_{rd}(V)s + 1} = \frac{k_{rd}(V)}{k_r(V)} \cdot \frac{\tau_r(V)s + 1}{\tau_{rd}(V)s + 1} \end{aligned} \quad (25)$$

Moreover, the above transfer function can be further rearranged as follows:

$$G_{ff}(s) = \frac{\delta_f(s)}{\delta_{sw}(s)} = \frac{k_{rd}(V)}{k_r(V)} \cdot \left[ 1 - \frac{[\tau_r(V) - \tau_{rd}(V)] s}{\tau_{rd}(V)s + 1} \right] \quad (26)$$

From the above equation, it can be interpreted that the first term refers to the steering gear ratio between the steering wheel angle and the front tyre steering angle, and the second term refers to the derivative steering control part, in the other words, the derivative term of the steering angle input from the driver. The feedforward controller transfer function depends on the parameters of the desired yaw rate response model which will be described in the next subsection.

### Desired Yaw Rate Model

As described in the previous section, four wheel steering (abbreviated as 4WS) vehicle improves vehicle handling in the low speed region and vehicle stability in the high speed region. In this paper, the desired yaw rate steering response of zero-side-slip 4WS as the transfer function from the steering wheel angle to the yaw rate can be expressed as follows:

$$\frac{r_d(s)}{\delta_{sw}(s)} = \frac{k_{rd}(V)}{\tau_{rd}(V)s + 1} \quad (27)$$

where,

$$k_{rd} = \frac{V}{l_f n_s \left( 1 + \frac{ml_r}{2ll_f C_f} V^2 \right)} \quad (28)$$

$$\tau_{rd} = \frac{l_z V}{2ll_f C_f + ml_r V^2} \quad (29)$$

In the case without active front steering control, the transfer function from the steering wheel angle to the yaw rate can be expressed as follows:

$$\frac{r(s)}{\delta_{sw}(s)} = \frac{k_{r0}(V)}{\tau_r(V)s + 1} \quad (30)$$

where, the steady state gain of the yaw rate with respect to the steering wheel angle is expressed as follows:

$$k_{r0} = \frac{V}{n_s l \left( 1 - \frac{m}{2l^2} \frac{l_f C_f - l_r C_r}{C_f C_r} V^2 \right)} \quad (31)$$

To discuss the characteristics of feedforward compensator, the case of feedforward controller is compared with the case without control. The parameters used in the calculation is a small-scale electric vehicle. The yaw rate gain and the time constant of yaw rate steering response are shown in Fig. 15 and Fig. 16 respectively. In other words, the equivalent steering gear ratio for Steer-By-Wire system can be expressed as follows:

$$n_{sbw}(V) = \frac{k_r(V)}{k_{rd}(V)} = \frac{1 + \frac{ml_r V^2}{2ll_f C_f}}{1 - \frac{m}{2l^2} \frac{l_f C_f - l_r C_r}{C_f C_r} V^2} \frac{l_f}{l} n_s \quad (32)$$

The above equation shows that this steering gear ratio  $n_{sbw}$  has speed-dependent characteristics as shown in Fig. 17.

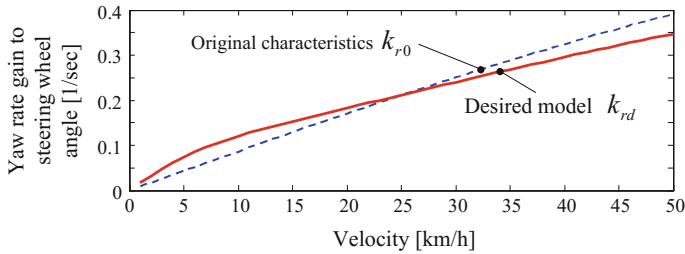


Fig. 15 Yaw rate gain with respect to the steering wheel angle

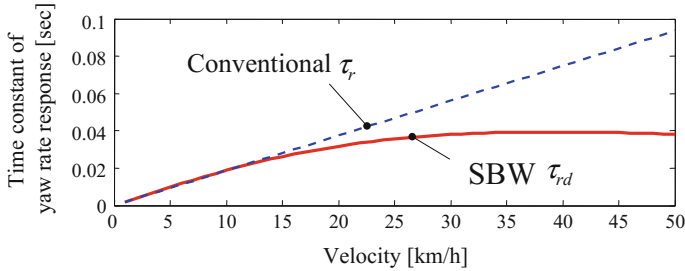


Fig. 16 Time constant of yaw rate response to the steering wheel angle

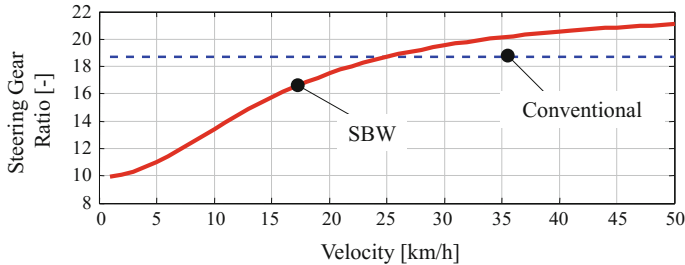
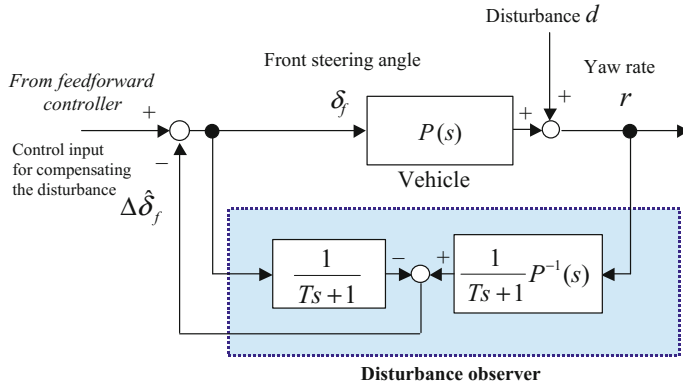


Fig. 17 Steering gear ratio as a function of vehicle velocity

### Design of Feedback Controller

Generally, using only feedforward controller cannot completely secure the vehicle stability against unexpected disturbance, e.g. crosswind, or unexpected vehicle parameter changes, e.g. road friction coefficient. Hence, to enhance the vehicle stability against disturbance, a steering control algorithm of feedback compensator is proposed by using the theory of disturbance observer.

Figure 18 shows the block diagram of the disturbance observer. The front steering angle and the yaw rate are measured in order to estimate the yaw rate disturbance. The relationship between the front steering angle, the vehicle yaw rate and the yaw rate disturbance can be expressed as follows:



**Fig. 18** Block diagram of feedback controller based on disturbance observer

$$\hat{d} = r - P(s)\delta_f \quad (33)$$

The transfer function  $P(s)$  is the approximated yaw rate response model as shown in Eq. 21. To suppress the yaw rate deviation against a disturbance, the active front steering angle input for compensating the disturbance can be expressed as follows:

$$\Delta\hat{\delta}_f = P^{-1}(s)\hat{d} = P^{-1}(s)r - \delta_f \quad (34)$$

In the above equation, the linear inverse function  $P^{-1}(s)$  exists and makes the transfer function of the feedback controller become not proper. In practical cases, some measurement noise in the system might be amplified. A method to solve this problem is to augment a 1st order delay transfer function with the current feedback controller transfer function.

$$\Delta\hat{\delta}_f = \frac{1}{T_{do}s + 1} [P^{-1}(s)r - \delta_f] \quad (35)$$

where,  $T_{do}$  indicates the time constant of disturbance observer. Setting the value of  $T_{do}$  involves the tradeoff relation between the noise problem and disturbance estimation delay. By considering this calculation tradeoff, the value of the time constant is set to 0.01 s heuristically.

## 2.3 Effectiveness of SBW Control system

This section demonstrates the effectiveness of Steer-By-Wire control system on handling and stability of vehicle by using a small-scale electric vehicle equipped with Steer-By-Wire system.

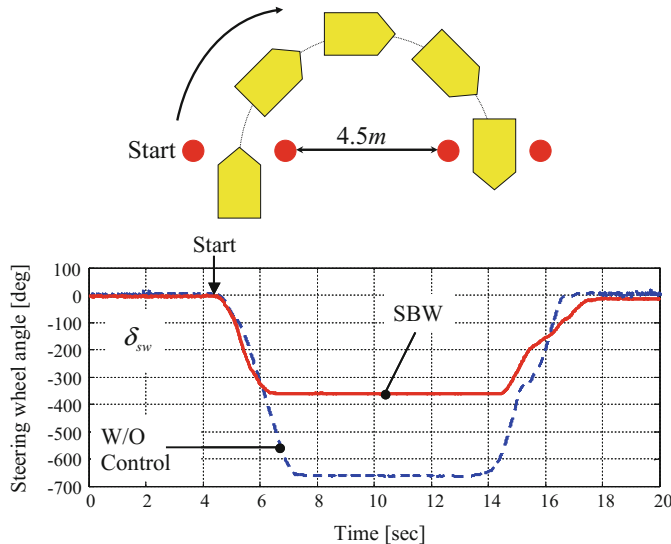


**Fig. 19** Effect of SBW in low speed U-turn manoeuvre

### Effectiveness on Low-Speed Manoeuvre

In low speed manoeuvre such as U-turn manoeuvre, Steer-By-Wire system is very useful in changing the steering gear ratio so that the amount of turning the steering wheel angle becomes less. Figure 19 shows the steering wheel angle in the case with active front steering angle ratio and with the conventional constant gear ratio. It was found that by the usage of Steer-By-Wire with the feedforward controller, the steering wheel angle magnitude is significantly reduced during U-Turn manoeuvre.

### Effectiveness on Lane-Change Manoeuvre

The improvement of vehicle handling quality by using the feedforward controller was investigated in lane-change test as a course indicated in Fig. 20. From the experimental results in Fig. 20, the front steering angle was steered earlier than the steering wheel angle input from the driver. As a result, the phase delay of the yaw rate was effectively reduced with the Steer-By-Wire control system. The main contribution is from the derivative steering term of the feedforward controller. From the investigation of Lissajous diagram between the steering wheel angle and the yaw rate indicated in Fig. 21, the hysteresis of the yaw rate response to the steering wheel angle in the case of control was smaller than that of the vehicle without active front steering control. The feedforward controller can effectively make the yaw rate response to the

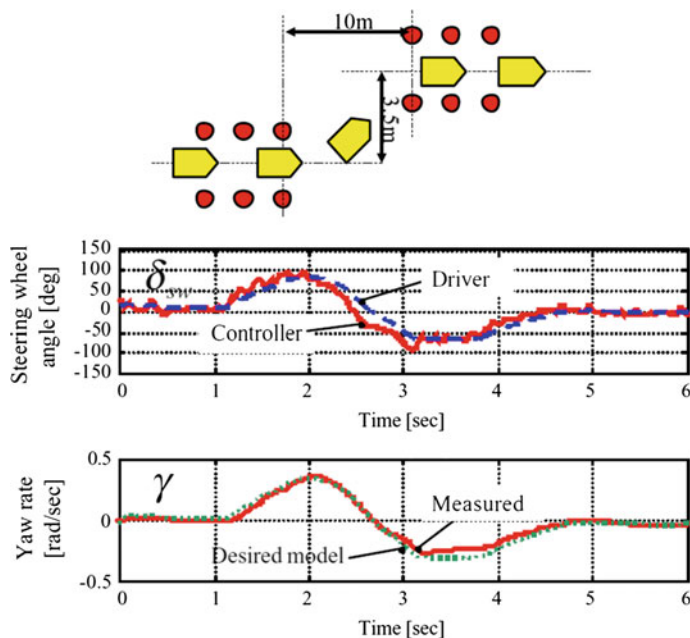
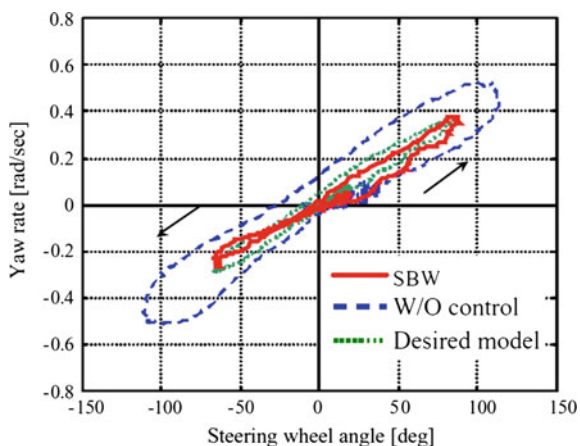


**Fig. 20** Single lane change course and vehicle behavior

**Fig. 21** Lissajous diagram of steering wheel angle and yaw rate



steering wheel angle close to a linear relationship. This implies that Steer-By-Wire control system also significantly enhances vehicle handling so that the driver can steer the vehicle much easier.

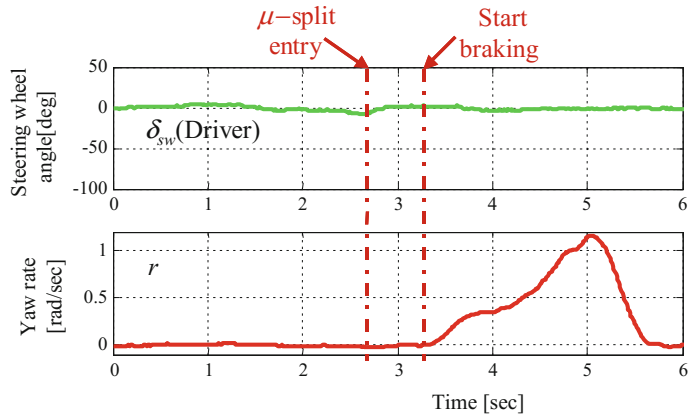


**Fig. 22** Response of uncontrolled vehicle in braking on  $\mu$ -split road

### Effectiveness on $\mu$ -Split Road

The vehicle stability against a yaw moment disturbance caused by asymmetric braking on  $\mu$ -split road was investigated. The effectiveness of the feedback controller with the application of disturbance observer theory was verified. The vehicle ran straight at constant speed of 35 km/h into the  $\mu$ -split road and then conducted full braking by the driver. To verify the effectiveness of the controller, the corrective steering manoeuvre by the driver was not conducted. Figure 22 and Fig. 23 show the experimental results in the case without control and with feedback controller respectively. In the case without control, large yaw rate deviation was generated as a result of yaw moment disturbance due to asymmetric braking on  $\mu$ -split road. On the other hand, in the case with the feedback controller, the control system can effectively suppress the yaw rate deviation by controlling the front tyre steering angle in real time. With the proposed Steer-By-Wire control system, it shows that the vehicle stability can be secured with the application of disturbance observer.

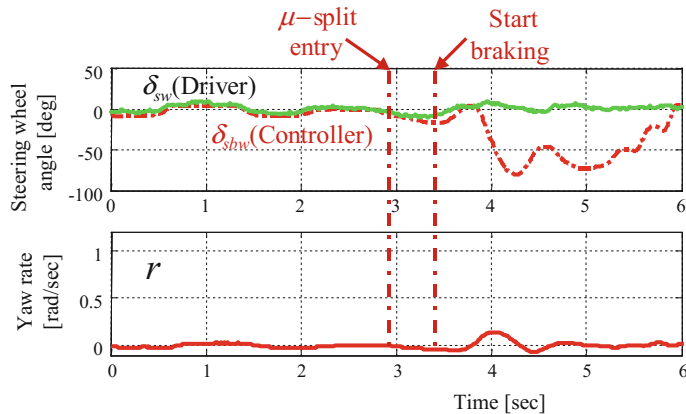


**Fig. 23** Effect of feedback controller of SBW in braking on  $\mu$ -split road

## 2.4 Summary

Steer-By-Wire control system for enhancing handling and stability was presented here. Setting the desired yaw rate response, the feedforward controller of Steer-By-Wire system can be theoretically determined. With the application of disturbance observer, the feedback controller can be designed by measuring the steering wheel angle and the yaw rate. Demonstrations using a small-scale electric vehicle were shown to verify the effectiveness of the proposed active front steering angle control based on Steer-By-Wire structure.

### 3 Direct Yaw-Moment Control System

Active steering control performance for enhancing handling and stability strongly depends on the tyre lateral forces, in a range where the lateral acceleration is comparatively high and the vehicle is near handling limit, the lateral forces become saturated and then the active steering control system cannot perform its control effectively anymore. In such situations, the driver may lose control over his car due to excessive side slip angle together with unbalance of yaw moment on the car. To overcome this problem, a strategy using tyre longitudinal forces to control vehicle lateral motion was proposed, called direct yaw-moment control (DYC). As a common approach for vehicles in productions, by utilizing the existing ABS (Anti-lock Braking System) hardware or traction force distribution control, DYC system can be realized in real applications (Koibuchi et al. 1996; Shibahata et al. 1992; Van Zanten et al. 1996). Nowadays, in the automobile market, DYC is commonly used for the objective of side slip prevention, and also effectively for rollover prevention, especially for commercial vehicles.

This chapter describes a chassis control system utilizing DYC by using a model matching control method to make the steering response of body side slip angle be constantly zero (Shino et al. 2004a). A concept to enhance vehicle stability during cornering is to generate additional yaw moment by transverse distribution of longitudinal forces. As an electric vehicle (EV) has in-wheel-motor structure which the motors can be controlled to generate wheel torques independently of each other, transverse distribution of longitudinal forces (traction or braking forces) can be precisely generated. Furthermore, as the electric motor has comparatively faster torque response, and easy measurability of torque compared with the conventional engine, the individual driving/braking torque control by motors is very attractive for engineers in the field of vehicle dynamics. For realizing the proposed control system using an actual electric vehicle, it is necessary to estimate the side slip angle instead of measuring it directly. A speed-dependent observer is presented here. With the objective of enhancing vehicle stability, the control objective is to obtain desirable steering response by controlling the body side slip angle of the vehicle. Experiments using an actual electric vehicle is carried out to verify the effectiveness of the proposed chassis control system on cornering performance in a J-turn and Lane Change tests.

#### 3.1 Direct Yaw-Moment Control System for Side Slip Angle Regulation

Figure 24 shows the vehicle model used for the controller design. The control objective of DYC system is to make the side slip angle and the yaw rate trace the responses of the desired vehicle model for enhancing handling and stability. The direct yaw moment generated by the traction forces at rear axle is employed as the control input

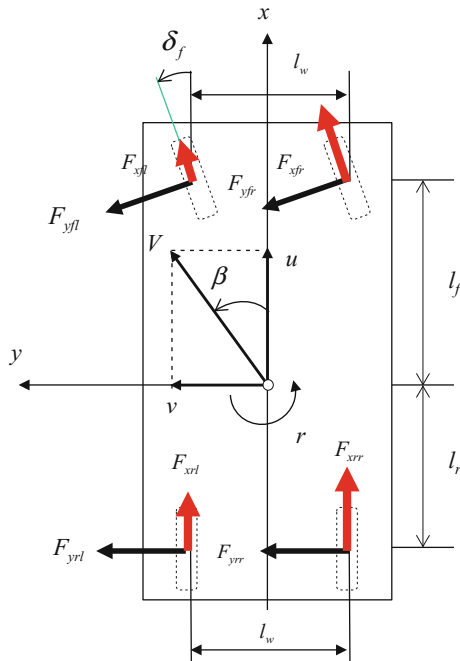


**Fig. 24** Vehicle model in planar motion with DYC input

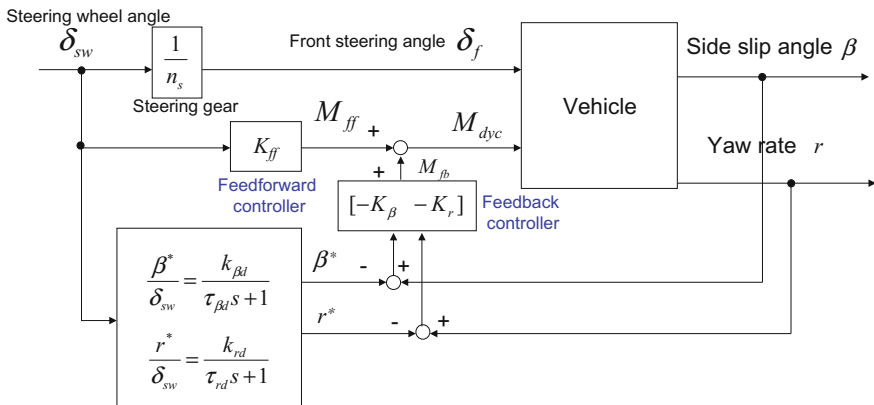


**Fig. 25** Block diagram of Direct Yaw moment Control (DYC) system

to make the actual response trace the desired vehicle response. With the application of model matching control method, the control system consists of a feedforward compensator with respect to the steering angle, and a feedback control compensator depending on the state deviations of the side slip angle and the yaw rate as shown in Fig. 25.

To improve the vehicle stability, the main objective of the control is to make the side slip angle response with respect to the steering wheel angle input be zero. First from the governing equations of the vehicle in planar motion, the state space equation of the vehicle can be written as follows:

$$\dot{X} = AX + BU + H\delta_f \quad (36)$$

$$\begin{bmatrix} \dot{\beta} \\ \dot{r} \end{bmatrix} = \begin{bmatrix} a_{11} & a_{12} \\ a_{21} & a_{22} \end{bmatrix} \begin{bmatrix} \beta \\ r \end{bmatrix} + \begin{bmatrix} b_{11} \\ b_{21} \end{bmatrix} M_{dyc} + \begin{bmatrix} h_{11} \\ h_{21} \end{bmatrix} \delta_f \quad (37)$$

where, each coefficient in the state space equation can be expressed as follows:

$$\begin{aligned} X &= \begin{bmatrix} \beta \\ r \end{bmatrix}, \quad U = M_{dyc}, \\ a_{11} &= -\frac{2(C_f + C_r)}{mV}, \quad a_{12} = -1 - \frac{2(l_f C_f - l_r C_r)}{mV^2}, \\ a_{21} &= -\frac{2(l_f C_f - l_r C_r)}{I_z}, \quad a_{22} = -\frac{2(l_f^2 C_f + l_r^2 C_r)}{I_z V}, \\ b_{11} &= 0, \quad b_{21} = \frac{1}{I_z}, \quad h_{11} = \frac{2C_f}{mV}, \quad h_{21} = \frac{2l_f C_f}{I_z} \end{aligned}$$

Here, the control input is determined to be the direct yaw moment input and the steering angle is treated as an excitation input from the driver. As a part of model matching control system, the feedforward control input is set to be proportional to the steering wheel angle as follows:

$$M_{ff} = K_{ff} \delta_{sw} \quad (38)$$

Considering the steady state of motions, the derivative terms in the state space equation are zero. Then, the feedforward controller gain  $K_{ff}$  can be solved under the condition that the zero side slip angle is achieved.

$$\dot{\beta} = a_{11}\beta + a_{12}r + b_{11} \frac{\delta_{sw}}{n} \quad (39)$$

$$\dot{r} = a_{21}\beta + a_{22}r + b_{21} \frac{\delta_{sw}}{n} + b_{22} (K_{ff} \delta_{sw}) \quad (40)$$

Let the side slip angle term and the derivatives of side slip angle and yaw rate be zero, the following relationship is obtained.

$$0 = 0 + a_{12}r + b_{11} \frac{\delta_{sw}}{n} \quad (41)$$

$$0 = 0 + a_{22}r + \left( \frac{b_{21}}{n} + b_{22}K_{ff} \right) \delta_{sw} \quad (42)$$

Then, the feedforward controller gain  $K_{ff}$  can be solved from the system equation as follows (Fig. 26):

$$0 = 0 + a_{22} \left( \frac{-b_{11}}{a_{12}} \frac{\delta_{sw}}{n} \right) + \left( \frac{b_{21}}{n} + b_{22}K_{ff} \right) \delta_{sw} \quad (43)$$

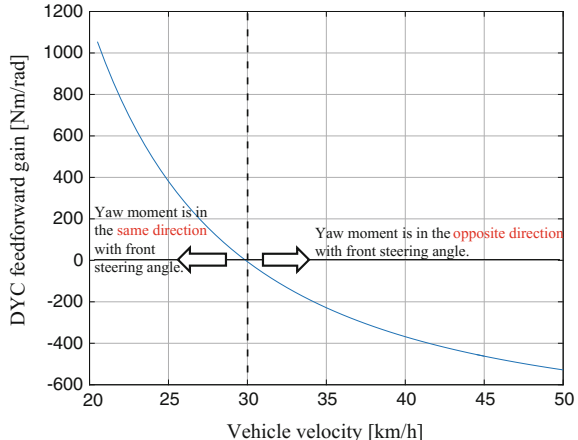
$$K_{ff} = \frac{a_{22}b_{11} - a_{12}b_{21}}{a_{12}b_{22}n} = \frac{4ll_rC_fC_r - 2l_fC_f m V^2}{n(2(l_f C_f - l_r C_r) + m V^2)} \quad (44)$$

By using the feedforward control input for zeroing the side slip angle, the transfer function of the yaw rate with respect to steering angle input can be computed by substituting the relationship between the steering wheel angle and the front tyre steering angle as,  $\delta_{sw} = n\delta_f$ , into Eq. (20) and then the yaw rate  $r(s)$  can be derived as follows:

$$\frac{r(s)}{\delta_{sw}(s)} = \frac{a_1 s + a_0}{s^2 + b_1 s + b_0} \quad (20)$$

where,

**Fig. 26** DYC feedforward gain to realize steady-state zero-side-slip response



$$\begin{aligned}
a_1 &= \frac{4C_f}{I_z} \frac{l_f^2 C_f + l_r^2 C_r}{mV^2 + 2(l_f C_f - l_r C_r)}, \\
a_0 &= \frac{1}{n} \frac{2C_f V}{mV^2 + 2(l_f C_f - l_r C_r)} \left( \frac{4l_f^2 C_f C_r}{mI_z V^2} - \frac{2(l_f C_f - l_r C_r)}{I_z} \right), \\
b_1 &= \frac{2(C_f + C_r)}{mV} + \frac{2(l_f^2 C_f + l_r^2 C_r)}{I_z V}, \\
b_0 &= \frac{4l_f^2 C_f C_r}{mI_z V^2} - \frac{2(l_f C_f - l_r C_r)}{I_z}
\end{aligned}$$

The desired vehicle response embedded in the model matching control system is determined in the way that the side slip angle response is zero and the yaw rate is set to be the first order delay system with respect to the steering wheel angle input as follows:

$$\frac{\beta(s)}{\delta_{sw}(s)} = 0 \quad (45)$$

$$\frac{r(s)}{\delta_{sw}(s)} = \frac{k_{rd}}{\tau_{rd}s + 1} \quad (46)$$

where,  $k_{rd}$  and  $\tau_{rd}$  are the steady state gain and the time constant of the desired yaw rate dynamics respectively. It is important to determine the desired yaw rate dynamics as it strongly relates to the handling dynamics evaluated by human drivers. By comparing the transfer function of the desired yaw rate (Eq. (20)) with the transfer function in Eq. (46), the steady state gain and the time constant of the desired yaw rate dynamics can be determined as follows:

$$k_{rd} = \frac{2C_f V}{mV^2 + 2(l_f C_f - l_r C_r)} \cdot \frac{1}{n} \quad (47)$$

$$\tau_{rd} = \frac{I_z V}{2(l_f^2 C_f + l_r^2 C_r)} \quad (48)$$

To compensate the side slip angle and yaw rate deviations during transient steering manoeuvre, it is necessary to combine the feedback controller with the feedforward controller. Here, the state feedback of side slip angle and yaw rate deviation is presented.

The state deviation between the desired value vector  $X_d$  and the actual value vector  $X$  is defined as follows:

$$E = X - X_d \quad (49)$$

To formulate the optimal regulator problem, the differentiated value of the above equation can be written as follows:

$$\dot{E} = \dot{X} - \dot{X}_d \quad (50)$$

$$\dot{E} = (AX + BM_{fb} + H\delta_f) - (A_d X_d + H_d \delta_f) \quad (51)$$

$$\dot{E} = A(X - X_d) + BM_{fb} + (A - A_d)X_d + (H - H_d)\delta_f \quad (52)$$

$$\dot{E} = AE + BM_{fb} + W \quad (53)$$

where,  $W$  is lumped as a disturbance term of the regulator. The optimal control input is determined to minimize the deviation of each state variable with respect to its desired value as follows:

$$M_{fb} = -K_{fb1}(\beta - \beta_d) - K_{fb2}(r - r_d) \quad (54)$$

where, the feedback gains  $K_{fb1}$ ,  $K_{fb2}$  are determined by the application of optimal linear quadratic regulator (LQR) control theory to minimize the following cost function.

$$J = \int_0^{\infty} \left[ \left( \frac{\beta - \beta_d}{q_1} \right)^2 + \left( \frac{r - r_d}{q_2} \right)^2 + \left( \frac{M_{fb}}{r_{fb}} \right)^2 \right] dt \quad (55)$$

where, the weighting coefficients  $q_1$  and  $q_2$  indicate the maximum allowable values of the state variables and the coefficients  $r_{fb}$  indicates the available yaw moment control input.

To generate the yaw moment control input on the actual electric vehicle, the differential traction forces are exerted on left and rear tyres. With the structural merit of in-wheel-motor electric vehicles, the transverse distribution of the traction forces can be done easily.

Considering the case of rear-wheel-driven electric vehicle and the driving resistance is small. If the longitudinal acceleration given by the driver via the accelerator pedal stroke is given as  $a_x$ , the governing equation of longitudinal dynamics can be expressed as:

$$ma_x = F_{x3} + F_{x4} \quad (56)$$

The yaw moment control input which is determined from the controller is given as follows:

$$M_{dyc} = M_{ff} + M_{fb} = \frac{l_w}{2} (F_{x4} - F_{x3}) \quad (57)$$

By rearranging Eqs. (56) and (57), the command traction force of each tyre can be calculated as follows:

$$\text{Rear left tyre: } F_{x3} = \frac{ma_x}{2} - \frac{M_{dyc}}{l_w} \quad (58)$$

$$\text{Rear right tyre: } F_{x4} = \frac{ma_x}{2} + \frac{M_{dyc}}{l_w} \quad (59)$$

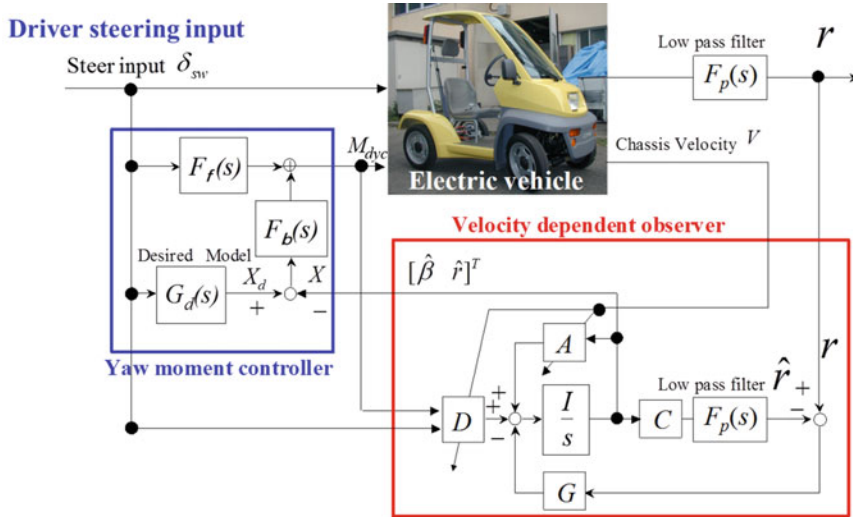


**Fig. 27** Block diagram of Direct Yaw-moment Control and Observer for estimating the side slip angle

### Design of Speed-Dependent Side Slip Angle Observer

For implementing the proposed DYC system on the actual vehicle, it is necessary to estimate the side slip angle instead of direct measurement, as the side slip angle sensor is too expensive to be equipped in production vehicles. According to the theory of observer for state estimation, the side slip angle can be estimated by measuring the steering wheel angle, the yaw rate and the vehicle velocity as shown in the schematic diagram in Fig. 27. As the body side slip angle has speed-dependent characteristics, it is necessary to design the side slip angle observer with variable observer gains depending on the vehicle velocity.

The state space equation of the observer can be written as follows:

$$\dot{\hat{X}} = A\hat{X} + BU + L(Y - C\hat{X}) \quad (60)$$

$$\dot{\hat{X}} = (A - LC)\hat{X} + BU + LY \quad (61)$$

where,  $L$  indicates the observer gain which can be determined by the pole placement theory or Kalman Filtering theory.  $Y$  is the measurement value which is the vehicle yaw rate in this case, so the matrix  $C$  is expressed as:

$$Y = r = CX = \begin{bmatrix} 0 & 1 \end{bmatrix} \begin{bmatrix} \beta \\ r \end{bmatrix} \quad (62)$$

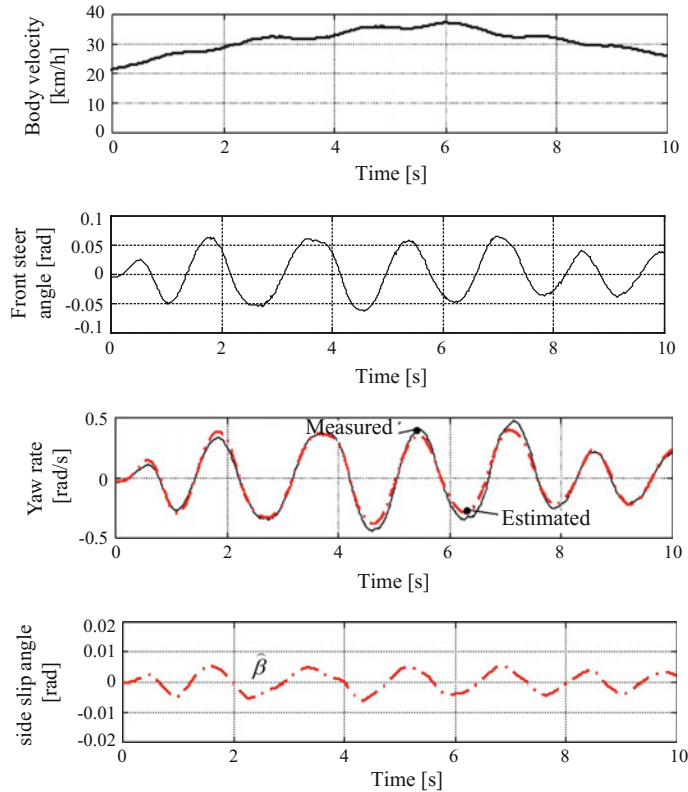


**Fig. 28** Side slip angle estimation results by using the observer

If the error vector of the estimated states is defined as  $E_{ob} = \hat{X} - X$ , the dynamics of the estimated error can be expressed as follows:

$$\dot{E}_{ob} = \dot{\hat{X}} - \dot{X} = [(A - LC)\hat{X} + BU + L(CX)] - [AX + BU] \quad (63)$$

$$\dot{E}_{ob} = (A - LC)E_{ob} \quad (64)$$

Setting the eigenvalues of the matrix  $A - LC$  to be located on the left side of complex plane results in fast convergence of the estimation error to zero which means the estimated state variables will be close to the actual state variables very fast.

For example, by using the pole placement method, the desirable poles of the observer i.e. eigenvalues of the matrix  $A - LC$ , are set to be real numbers ( $\lambda_1, \lambda_2$ ), the observer gains can be calculated as follows:

$$L = \begin{bmatrix} L_1 \\ L_2 \end{bmatrix} = \begin{bmatrix} -\{a_{11}(-a_{11} + \lambda_1 + \lambda_2) - \lambda_1\lambda_2 - a_{12}a_{21}\} / a_{21} \\ a_{11} + a_{22} - (\lambda_1 + \lambda_2) \end{bmatrix} \quad (65)$$

Figure 28 shows the experimental results with respect to the given front steering angle that is equivalent to slalom driving test with variable speed. This study assumes that the body side slip angle is correctly estimated when the estimated yaw rate well matches the measured yaw rate. As a result, Fig. 28 shows that the estimated yaw rate can effectively trace the actual value by the use of the proposed observer against the change in velocity. From repeated experiments, it was verified that the proposed observer is effective against any arbitrary steering inputs.

### **3.2 Effectiveness of DYC**

This section discusses the validity of the proposed DYC system in cornering performance as described in the previous section by experiments using a small-scale electric vehicle. All experiments are conducted under a dry asphalt road. The front steering angle is assumed to be calculated from the measured steering wheel angle divided by the overall steering gear ratio, while neglecting the steering dynamics. The J-turn and lane-change test were conducted to verify the effectiveness on regulating the body side slip angle of the vehicle.

#### **Effectiveness of DYC in J-Turn Test Manoeuvre**

In J-turn test shown in Fig. 29, after the vehicle runs straightly at constant speed of 35 km/h, the front steering angle pattern, as shown in the upper graph of Fig. 29, is executed by the driver. This test is used to investigate the vehicle behavior for transient and steady state steering manoeuvres. Figure 29 shows the vehicle behavior with respect to the given steering manoeuvre input. It was found that, by using DYC, the vehicle body side slip angle was significantly suppressed during the steady state cornering. Figure 29 also shows that the body side slip angle during transient state can be effectively suppressed by using the feedback compensator. Moreover, it was confirmed that the DYC input is realized by controlling each wheel driving torque independently to achieve differential traction in real-time.

#### **Effectiveness of DYC in Double Lane-Change Test Manoeuvre**

In double lane-change test, the front steering angle as shown in Fig. 30, is executed at a vehicle velocity of 35 km/h. The driving course was set up equivalently to an emergency obstacle avoidance manoeuvre at the level of lateral acceleration of 0.5 G. Figure 31 shows the vehicle behavior against the double lane-change steering input which can be treated as continuous steering manoeuvre input. Figure 31 shows that, by using only the feedforward controller, the body side slip angle can be suppressed as it becomes closer to zero, as compared with the uncontrolled vehicle. It is also confirmed that the body side slip angle can be more suppressed by the combination with

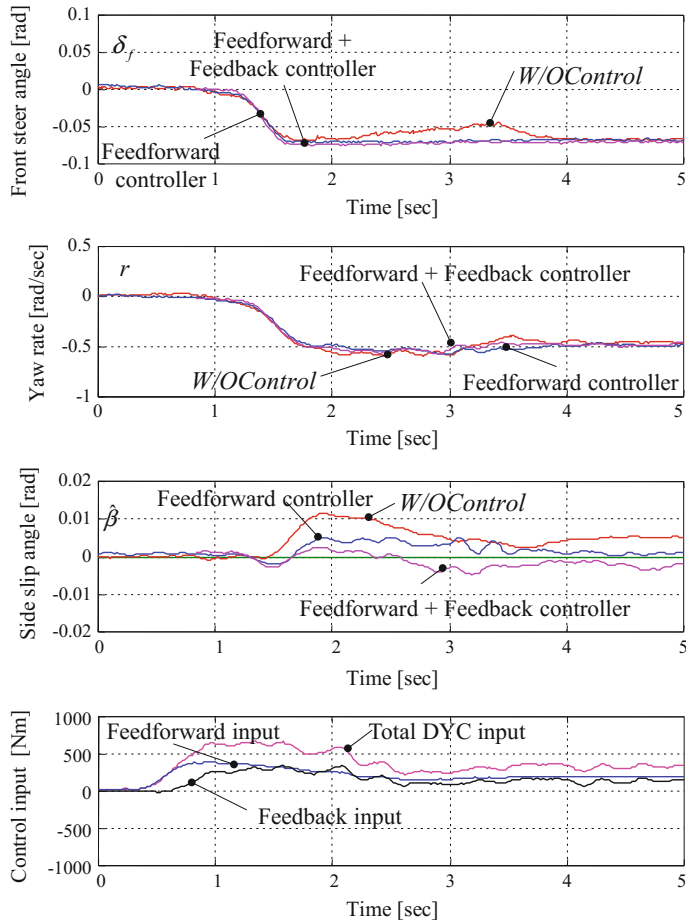


**Fig. 29** Control effectiveness of DYC during J-turn at 35 km/h

the feedback compensator. Moreover, in the case without control, large body side slip angle appeared during the lane-change manoeuvre which causes difficulty for the driver to trace the given course. There were collisions with pylons in some trials during the experiment without DYC. According to the subjective comments from the driver, DYC system significantly enhanced handling performance and vehicle stability so that the driver could steer the vehicle much more easily.

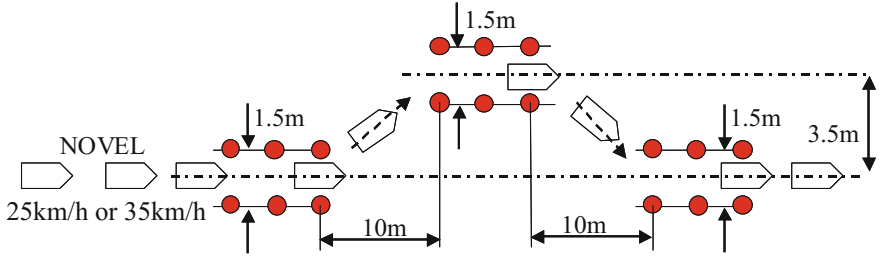


**Fig. 30** Course configuration for double lane change manoeuvre

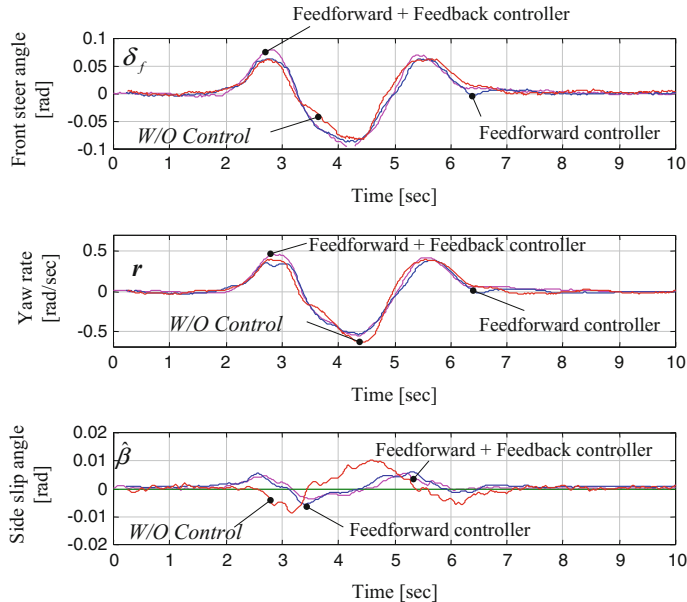


**Fig. 31** Control effectiveness of DYC during double lane change manoeuvre at 35 km/h

### 3.3 Summary

This section has described the feature and the structure of Direct Yaw-moment Control (DYC) especially using the structural merits of in-wheel-motor electric vehicle and its effect on enhancing vehicle handling and stability against various types of steering manoeuvre, step steer and lane change. The control objective of DYC is to regulate the vehicle body side slip angle, i.e. making the vehicle attitude aligned with the vehicle forward direction, with the application of model matching control theory, consisting of feedforward and feedback controllers. An additional remark here is that controlling the side slip angle by DYC when the vehicle is near limits in nonlinear

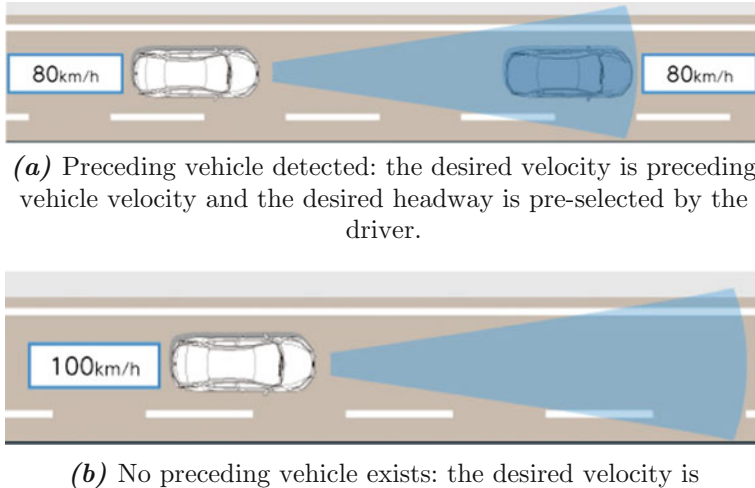


**Fig. 32** Basic function of Adaptive Cruise Control (ACC) System

tyre region is more effective compared to active rear steering angle control system due to limitation of tyre cornering forces.

## 4 Adaptive Cruise Control System (ACC)

The functional purpose of ACC system is to maintain a desired range clearance between an ACC-equipped vehicle and its preceding vehicle, when one is present. If there are no preceding vehicles within a reasonable range, the system performs as a cruise control system to trace a set velocity, for example 100 km/h (Fig. 32).

### 4.1 Governing Equation of Longitudinal Vehicle Dynamics

To design the control algorithm of ACC, the longitudinal vehicle dynamics is used (Rajamani, 2012). The governing equation of longitudinal vehicle motion is expressed as shown in Eq. (66).

$$m\dot{V} = ma_x = \sum_{i=1}^4 F_{xi} - F_R - F_A - F_G \quad (66)$$

where,  $m$  indicates the vehicle mass,  $V$ , the vehicle velocity,  $\Sigma F_x$ , the actuation force (longitudinal tyre force) produced by the engine and drivetrain and the braking system,  $F_R$ , the tyre rolling resistance force,  $F_A$ , the aerodynamic drag,  $F_G$ , the resistance force caused by road gradient.

The entire flow of the vehicle powertrain from the accelerator pedal stroke input to the wheel torque is shown in Fig. 33. The governing equation of the engine and drivetrain is described. To simplify the torque characteristics of the driving source (engine or electric motor in the case of EV), it can be assumed that the engine torque transfer function with respect to the pedal stroke input (or throttle input) is a first-order delay system as follows:

$$\tau_e \dot{T}_e + T_e = K_e P_a \quad (67)$$

$$T_e(s) = \frac{K_e}{\tau_e s + 1} P_a(s) \quad (68)$$

where,  $P_a$  indicates the accelerator pedal stroke input,  $\tau_e$ , the time constant of the torque produced by the driving source,  $T_e$ , the torque produced by the driving source,  $K_e$ , the driving source torque gain.

The governing equation of rotational motion about the engine driveshaft is expressed as follows:

$$I_e \dot{\omega}_e = T_e - T_t \quad (69)$$

where,  $I_w$  indicates the moment of inertia of tyre and wheel  $\omega$  the rotational velocity of the tyre and  $r_w$  the effective radius of the tyre. Next, the governing equation of rotational motion about the transmission shaft is expressed as follows:

$$I_t \dot{\omega}_t = T_t - i_g T_f \quad (70)$$

where  $I_e$  indicates the moment of inertia of the engine,  $\omega_e$  the rotational velocity of the engine, and  $T_t$  the torque on the transmission side. The governing equation of rotational motion about the driving wheel is expressed as follows:

$$I_w \dot{\omega} = T_f - F_x r_w \quad (71)$$

where,  $I_t$  indicates the moment of inertia of the transmission,  $\omega_t$  the rotational velocity of the transmission, i.g. the transmission gear ratio, and  $T_f$  the torque on the driving wheel. The pictorial diagram of the tyre-wheel dynamics is shown in Fig. 34. From the equation of longitudinal vehicle motion indicated in Eq. (66), the required driving force to obtain the desired longitudinal motion can be calculated as follows:

$$\sum_{i=1}^4 F_{xi} = m \ddot{V} + F_R + F_A + F_G \quad (72)$$

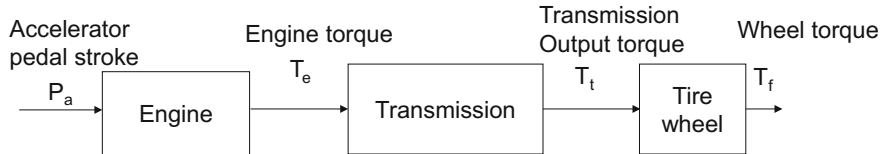
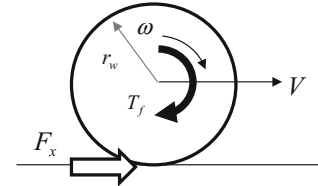


**Fig. 33** Flow of the accelerator pedal stroke to the torque of the driving wheel

**Fig. 34** Rotational motion of driving wheel



If we assume that the slip ratio of the driving wheel is small in normal driving region, the relationship between the forward velocity of the vehicle body and the driving wheel rotational velocity can be written as follows:

$$\dot{V} = r_w \dot{\omega} = r_w i_g \dot{\omega}_e \quad (73)$$

By using the equations of motions indicated in Eqs. (69)–(73), the relationship between the desired vehicle acceleration and the required driving torque can be obtained as shown in the following equation.

$$T_e = \left( I_e + I_t + i_g^2 (I_w + m r_w^2) \right) \frac{\dot{V}}{i_g r_w} + i_g [r_w (F_R + F_A + F_G)] \quad (74)$$

In the above equation, the first term refers to the driving torque to compensate the inertia of the engine and drivetrain and the second term refers to the driving torque to compensate the resistance of the vehicle longitudinal motion.

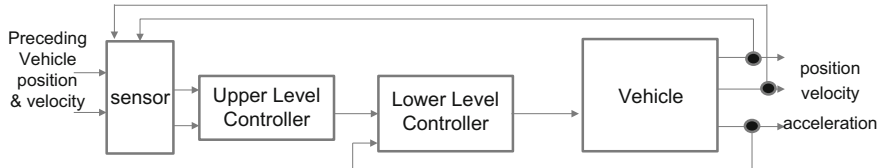


**Fig. 35** Architecture of Adaptive Cruise Control System

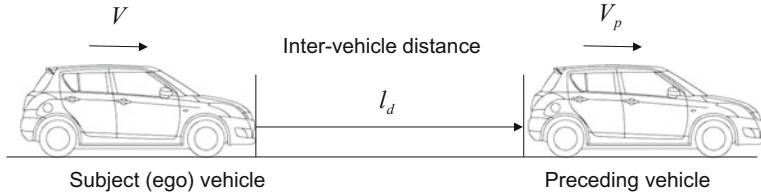


**Fig. 36** Variables used in car-following scene

## 4.2 Basic Function and Characteristics of Adaptive Cruise Control

ACC system design can be divided into two parts: the upper level controller and the lower level controller as shown in Fig. 35. The upper level controller is designed to determine the acceleration that is required to follow the preceding vehicle at a desirable headway distance with zero relative velocity. The lower level controller is designed to determine the amount of the driving or braking torque to realize the demand acceleration required from the upper level controller.

The upper level controller design will be described. The variables used are shown in Fig. 36. From the current positions of the ego vehicle and the preceding vehicle, after  $T_p$  seconds, the error of the headway distance with respect to the desired headway distance can be expressed as the following expression.

$$e = [(x_p + T_p V_p) - (x + T_p V) - l] - T_{hw}^* V \quad (75)$$

$$e = [(x_p - x - l) + T_p (V_p - V)] - T_{hw}^* V \quad (76)$$

$$e = [l_d + T_p \dot{l}_d] - T_{hw}^* V \quad (77)$$

Then, the controller determines the amount of acceleration which is proportional to the error of future headway distance.

$$a_{x\_des} = k_p e = k_p [(l_d + T_p \dot{l}_d) - l_d^*] = k_p (l_d - l_d^*) + k_p T_p \dot{l}_d \quad (78)$$

$$a_{x\_des} = H_R (l_d - l_d^*) + H_V \dot{l}_d \quad (79)$$

where, the coefficient of headway distance error is  $H_R = k_p$  and the coefficient of relative velocity is  $H_V = k_p T_p$ . In the above equation, the first term refers to the feedback of headway distance error and the second term refers to the feedback of relative velocity. Mostly, the desired headway distance can be defined as the function of ego vehicle velocity as follows:

$$l_d^* = T_{hw}^* V + l_{d\_stop} \quad (80)$$

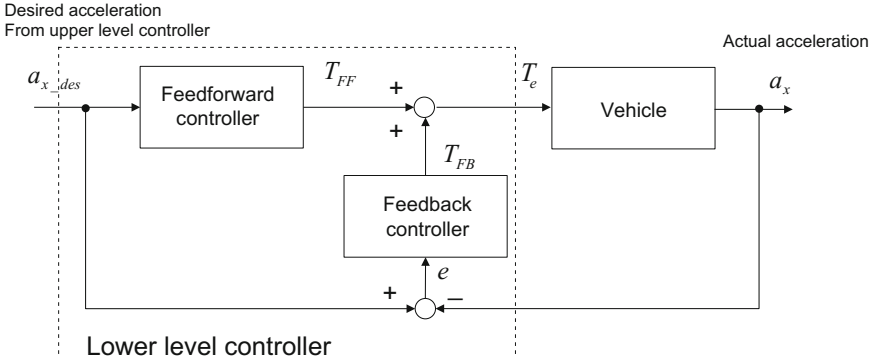


**Fig. 37** Block diagram of lower level controller of ACC system

where,  $l_{d\_stop}$  indicates the headway distance when the vehicle is stopping. In some literatures, a nonlinear function of desired headway distance such as a quadratic function is also employed to express the desired headway distance with respect to the ego vehicle velocity.

The acceleration model following control method can be used to design the lower level controller as shown in Fig. 37. The feedforward controller determines the driving torque based on Eq. (74) and the feedback controller determines the compensatory driving torque by using the acceleration feedback control such as PI Controller. The feedback controller plays a role to reduce the error of acceleration with respect to the desired value when there are unexpected disturbances or modelling error.

$$\begin{aligned}
 T &= T_{FF} + T_{FB} \\
 &= \frac{I_{\text{drivetrain}}}{i_g r_w} a_{x\_des} + i_g [r_w (F_R + F_A + F_G)] \\
 &\quad + K_p (a_{x\_des} - a_x) + \frac{K_i}{s} (a_{x\_des} - a_x)
 \end{aligned} \tag{81}$$

### 4.3 Control Characteristics of ACC

Next, the control characteristics of the ACC-controlled vehicle velocity with respect to the preceding vehicle velocity will be discussed. First, assuming that the lower level controller dynamics, i.e. reference acceleration model following control, can be approximated as first order delay system, the transfer function from the desired acceleration to the actual acceleration can be expressed as follows:

$$\frac{a_x(s)}{a_{x\_des}(s)} = \frac{1}{\tau_c s + 1} \quad (82)$$

Using the relationship,  $a_x = \dot{V}$ ,  $\dot{a}_x = \ddot{V}$ ,  $\dot{l}_d = V_p - V$  and substitute all into Eq. (79), the following equation can be obtained.

$$\ddot{V} = -\frac{1}{\tau_c} \dot{V} + \frac{1}{\tau_c} [H_R(l_d - l_d^*) + H_V(V_p - V)] \quad (83)$$

Then, differentiating the above equation, we get,

$$\ddot{\ddot{V}} = -\frac{1}{\tau_c} \ddot{V} + \frac{1}{\tau_c} [H_R(V_p - V - T_{hw}^* \dot{V}) + H_V(\dot{V}_p - \dot{V})] \quad (84)$$

Then, multiplying the whole equation with  $\tau_c$ , we get,

$$\tau_c \ddot{\ddot{V}} = -\ddot{V} + [H_R(V_p - V - T_{hw}^* \dot{V}) + H_V(\dot{V}_p - \dot{V})] \quad (85)$$

Then, taking Laplace Transformation of the above equation, the following equation can be obtained.

$$\tau_c s^3 V(s) = -s^2 V(s) + [H_R(V_p(s) - V(s) - T_{hw}^* s V(s)) + H_V(s V_p(s) - s V(s))] \quad (86)$$

Rearranging the above equation, the transfer function from the preceding vehicle velocity to the ego vehicle velocity can be achieved as follows:

$$\frac{V(s)}{V_p(s)} = \frac{H_V s + H_R}{\tau_c s^3 + s^2 + (H_V + T_{hw}^* H_R)s + H_R} \quad (87)$$

Figure 38 shows the frequency response of the ego vehicle velocity with respect to the preceding vehicle velocity while changing the value of relative velocity feedback gain  $H_V$ . As can be noticed from Fig. 38, increasing the value of  $H_V$  improves the damping characteristics of the car-following behaviour as the resonance peak around the natural frequency of the closed loop control characteristics is significantly reduced.

Next, Fig. 39 shows an example of time history of car-following behaviour by using the proposed ACC control algorithm when changing the value of relative velocity feedback gain  $H_V$  in the situation that the preceding vehicle brakes with a deceleration of  $2 \text{ m/s}^2$ . As can be noticed from Fig. 39, increasing the value of  $H_V$  results in less undershoot and more responsiveness of vehicle velocity response.

From the above equation, if the time constant of the lower level controller is comparatively smaller than the upper level controller, the transfer function from the preceding velocity to the ego-vehicle velocity can be expressed as follows:

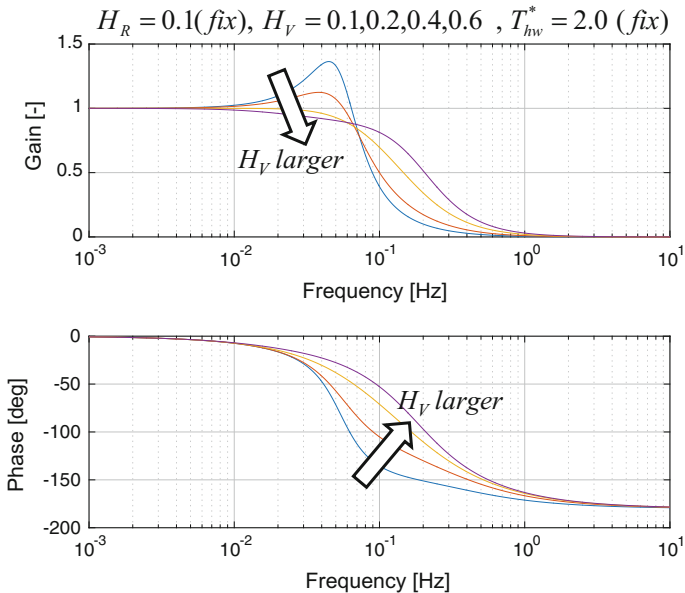


**Fig. 38** Effect of changing relative velocity feedback gain  $H_V$  on frequency characteristics of the ego vehicle velocity response to the preceding vehicle velocity

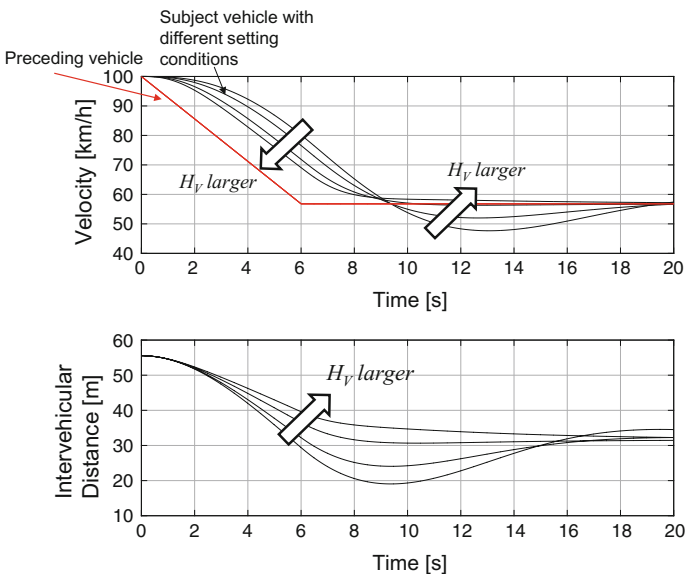


**Fig. 39** Effect of changing relative velocity feedback gain  $H_V$  on time history of the ego vehicle velocity response to the preceding vehicle velocity

$$\frac{V(s)}{V_p(s)} = \frac{H_V s + H_R}{s^2 + (H_V + T_{hw}^* H_R)s + H_R} = \frac{\omega_n^2(Ts + 1)}{s^2 + 2\zeta\omega_n s + \omega_n^2} \quad (88)$$

From the above transfer function, the relationship between the natural frequency of the closed-loop control characteristics and the feedback gain of the driver model can be expressed as follows:

$$\omega_n^2 = H_R \quad \Rightarrow \quad \omega_n = \sqrt{H_R} \quad (89)$$

From the damping term in the characteristic equation, the following relationship can be obtained.

$$2\zeta\omega_n = H_V + T_{hw}^* H_R \quad \Rightarrow \quad \zeta = \frac{H_V + T_{hw}^* H_R}{2\sqrt{H_R}} \quad (90)$$

For example, if the desirable time headway is set at 2 s and the desirable damping ratio of the closed-loop control system is set to be 1.00, the following relationship about the ACC controller gains can be achieved.

$$\zeta = \frac{H_V + T_{hw}^* H_R}{2\sqrt{H_R}} \quad \Rightarrow \quad 2\sqrt{H_R} = H_V + 2H_R \quad (91)$$

$$H_V = 2(\sqrt{H_R} - H_R) \quad (92)$$

Figure 40 shows the simulation result that ACC control system parameters are set in the condition that realizes the critical damping ratio. It can be confirmed from the time history that the ego vehicle can follow the preceding vehicle velocity without undershoot behaviour of vehicle velocity according to the theoretical parameter setting indicated in Eqs. (89) and (92).

#### 4.4 Summary

This section described the theoretical design of Adaptive Cruise Control System (ACC) aiming at controlling the vehicle velocity and following the preceding vehicle at a certain headway distance. In real applications, the headway distance and the relative velocity can be measured by using a millimeter wave radar or a stereo camera. The proposed theoretical control system design can be also applied to a vehicle platooning control. In addition, in the case of curved roadway, if the information of road curvature can be acquired via a navigation system and digital map, the braking manoeuvre before entering the curved road will be also combined in order to get comfortable acceleration during car following situation on curved roadways.

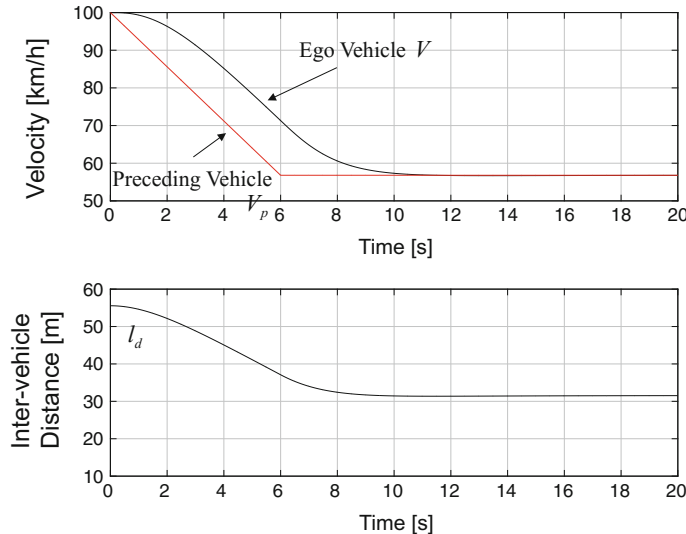


**Fig. 40** Vehicle following behavior when setting the damping ratio at 1.0

## 5 Lane Keeping Control System

An automated steering system is designed to support the driver lateral vehicle control task to keep the vehicle on the desired lane based on using on-board sensor such as a vehicle-mounted camera that detects lane markers ahead of the vehicle. This is a convenience-targeted feature which can potentially reduce driving workload as well as fatigue on long-time highway driving. The basic design requirements of the lane keeping control system are as follows:

- (1) The automated steering control must accomplish lane keeping task without driver's handling manoeuvre.
- (2) The steering actuator provides suitable torque smoothly for lane keeping task.
- (3) The driver can override the steering system easily if necessary.

The control input of such a steering system can be classified into the steering angle input and the steering torque input. This subsection describes the design of lane keeping control based on state-feedback control and investigates the physical characteristics of lane keeping controller using the steering angle and the steering torque as the control input, and compares their differences (Nagai et al. 2002). Generally, most of researches about lane keeping control maneuver deal with steering angle control method due to its excellent robustness to uncertainty in steering nonlinear dynamics. Typically, however, in driving on highways, drivers do not hold steering wheel with strong restraining force to prevent vehicle from course deviation. In contrast, the steering torque control provides some degree of freedom in permitting the driver

to steer the vehicle, thus it has potential for development as a driver assistance system which keeps driver-in-the-loop. Additional intervention, i.e. override by human driver, could be performed when necessary such as emergency avoidance. There are a number of lane keeping control methods such as methods based on geometric and kinematic relationships, feedback control methods based on vehicle-dynamics-model, sliding mode control methods, model predictive control methods and etc. For learning the basic characteristics, the following section will show the design of the lane keeping control system using the steering angle and the steering torque as the control inputs by employing Linear Quadratic (LQ) control theory (Mouri and Furusho 1997).

### 5.1 Governing Equation for Lane Keeping Control System Design

In the design of lane keeping control system, it is important to know the position of the vehicle with respect to the desired lane so it is more reasonable to express the vehicle motion with the earth-fixed coordinate system. Here, the X-Y coordinates are fixed on the ground and the equations of motions are derived based on the lateral position and yaw angle variables. The vehicle model in the earth-fixed coordinate

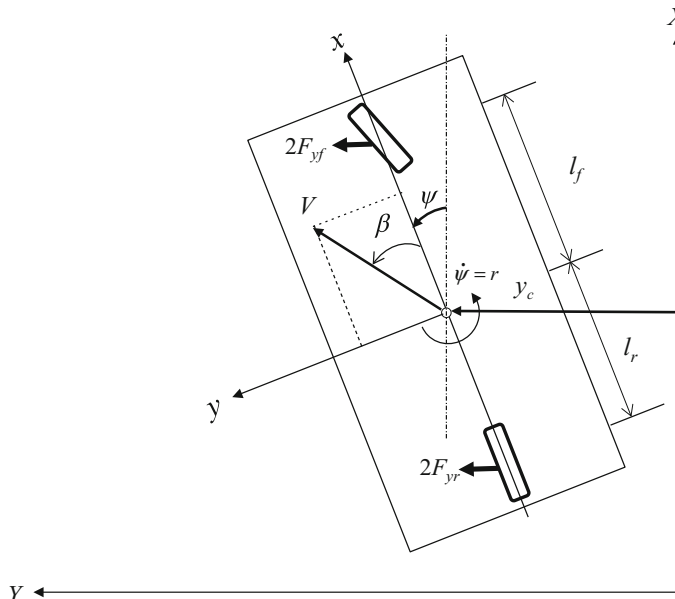


**Fig. 41** Bicycle model in earth-fixed coordinate system

system is shown in Fig. 41. Normally, when considering the motion of the vehicle moving in a straight path and the front steering angle is not large, the direction of the lateral forces acting on the front and rear tyres almost coincides with Y-direction. The vehicle lateral and yaw motions can be expressed as below.

$$m \frac{d^2 y_c}{dt^2} = 2F_{yf} + 2F_{yr} \quad (93)$$

$$I_z \frac{d^2 \psi}{dt^2} = 2l_f F_{yf} - 2l_r F_{yr} \quad (94)$$

The relationship between the lateral velocity and the side slip angle and yaw angle can be expressed as follows:

$$\dot{y}_c = V(\beta + \psi) \quad (95)$$

Therefore, the side slip angle can be rewritten using the variables of lateral velocity and yaw angle as follows:

$$\beta = \frac{\dot{y}_c}{V} - \psi \quad (96)$$

Converting the yaw rate and the side slip angle into the earth-fixed coordinate system variables, the tyre forces can be rewritten as follows:

$$F_{yf} = C_f \left( \delta_f - \frac{l_f}{V} \dot{\psi} - \left( \frac{\dot{y}_c}{V} - \psi \right) \right) \quad (97)$$

$$F_{yr} = C_r \left( \frac{l_r}{V} \dot{\psi} - \left( \frac{\dot{y}_c}{V} - \psi \right) \right) \quad (98)$$

Then, the vehicle motion in the earth-fixed coordinate system can be expressed as follows:

$$m \ddot{y}_c = 2C_f \left( \delta_f - \frac{l_f}{V} \dot{\psi} + \psi - \frac{\dot{y}_c}{V} \right) + 2C_r \left( \frac{l_r}{V} \dot{\psi} + \psi - \frac{\dot{y}_c}{V} \right) \quad (99)$$

$$I_{zz} \ddot{\psi} = 2l_f C_f \left( \delta_f - \frac{l_f}{V} \dot{\psi} + \psi - \frac{\dot{y}_c}{V} \right) - 2l_r C_r \left( \frac{l_r}{V} \dot{\psi} + \psi - \frac{\dot{y}_c}{V} \right) \quad (100)$$

As similar to the previous section, to apply the modern control theory on the vehicle motion control problem, Eqs. (99) and (100) can be arranged in the form of state-space equation comprising of four state variables as follows:

$$\begin{bmatrix} \ddot{\psi} \\ \dot{\psi} \\ \dot{y}_c \\ \ddot{y}_c \end{bmatrix} = \begin{bmatrix} a_{11e} & a_{12e} & a_{13e} & 0 \\ 1 & 0 & 0 & 0 \\ a_{31e} & a_{32e} & a_{33e} & 0 \\ 0 & 0 & 1 & 0 \end{bmatrix} \begin{bmatrix} \psi \\ \dot{\psi} \\ \dot{y}_c \\ y_c \end{bmatrix} + \begin{bmatrix} b_{11e} \\ 0 \\ b_{31e} \\ 0 \end{bmatrix} \delta_f \quad (101)$$

$$\dot{\mathbf{X}} = \mathbf{AX} + \mathbf{B}_f \delta_f, \quad \mathbf{X} = [\psi \ \dot{\psi} \ \dot{y}_c \ y_c]^T \quad (102)$$

where each element in the matrices are shown as follows:

$$\begin{aligned} a_{11e} &= -\frac{2(l_f^2 C_f + l_r^2 C_r)}{I_z V}, \quad a_{12e} = \frac{2(l_f C_f - l_r C_r)}{I_z}, \quad a_{13e} = -\frac{2(l_f C_f - l_r C_r)}{I_z V}, \\ a_{31e} &= -\frac{2(l_f C_f - l_r C_r)}{m V}, \quad a_{32e} = \frac{2(C_f + C_r)}{m}, \quad a_{33e} = -\frac{2(C_f + C_r)}{m V}, \\ b_{11e} &= \frac{2l_f C_f}{I_z}, \quad b_{31e} = \frac{2C_f}{m} \end{aligned}$$

## 5.2 Lane Keeping Control with Steering Angle Input

A lane keeping control system where the steering wheel angle is used as the control input is referred as steering angle control. Using a simplified linear two-wheel model in the planar motion as shown in Fig. 41 and the state space equation in Eq. (101), we can rewrite the state space equation as follows:

$$\begin{bmatrix} \ddot{\psi} \\ \dot{\psi} \\ \dot{y}_{cr} \\ \ddot{y}_{cr} \end{bmatrix} = \begin{bmatrix} a_{11e} & a_{12e} & a_{13e} & 0 \\ 1 & 0 & 0 & 0 \\ a_{31e} & a_{32e} & a_{33e} & 0 \\ 0 & 0 & 1 & 0 \end{bmatrix} \begin{bmatrix} \psi \\ \dot{\psi} \\ \dot{y}_{cr} \\ y_{cr} \end{bmatrix} + \begin{bmatrix} b_{11e}/n \\ 0 \\ b_{31e}/n \\ 0 \end{bmatrix} \delta_{sw} \quad (103)$$

where  $n$  indicates the steering gear ratio. The state variables of the state space equation are the vehicle position and attitude with respect to the desired lane. The subscript  $r$  refers to the relative variables. In the design of lane keeping control, all variables are regulated to zero in the form of general regulator problem. Here, in the case of straight path, the desired lateral displacement is a constant value along the desired lane, thus the lateral deviation is expressed as:

$$y_{cr} = y_c - y_c^* \quad (104)$$

where  $y_c^*$  denotes the desired lateral displacement, and the desired lateral velocity, the desired yaw angle and the desired yaw rate are zero.

An example of lane keeping control algorithm design using an optimal regulator is to determine the steering angle input in a form of full state feedback as follows:

$$\delta_{sw} = -(K_{\dot{\psi}}\dot{\psi} + K_{\psi}\psi + K_{\dot{y}_{cr}}\dot{y}_{cr} + K_y y_{cr}) \quad (105)$$

The feedback gains are determined theoretically in order to minimize the performance index or cost function  $J$  in the form of integral of linear quadratic terms of the steering wheel angle and the state variables indicated in Eq. (106).

$$J = \int_0^{\infty} (q_1\dot{\psi}^2 + q_2\psi^2 + q_3\dot{y}_{cr}^2 + q_4y_{cr}^2 + \delta_{sw}^2) dt \quad (106)$$

where,  $q (i = 1 \sim 4)$  denotes the weighting coefficient of the state variables and  $r$  indicates that of the steering wheel angle input. This control theory is also known as Linear Quadratic (LQ) Regulator. In the simplified case, the cost function on the lateral deviation is the most important in the case of lane keeping control, therefore the cost function can be written as

$$J = \int_0^{\infty} (qy_{cr}^2 + \delta_{sw}^2) dt \quad (107)$$

Larger value of  $q$  results in small lateral deviation during lane keeping. In addition to the weighting coefficient of the lateral deviation, the weighting coefficients of the other state variables can also be added to achieve desirable performance depending on the controller designers.

From the linear quadratic (LQ) control theory, the feedback gains shown in Eq. (105) can be calculated as shown in the following equation.

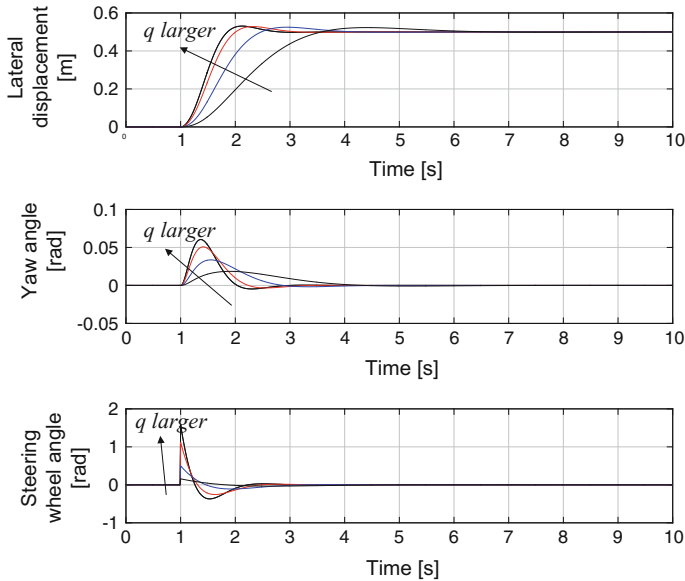
$$K = -R^{-1}B^TP \quad (108)$$

$P$  is the matrix solution of the Riccati equation shown in Eq. (109) based on optimal control theory.

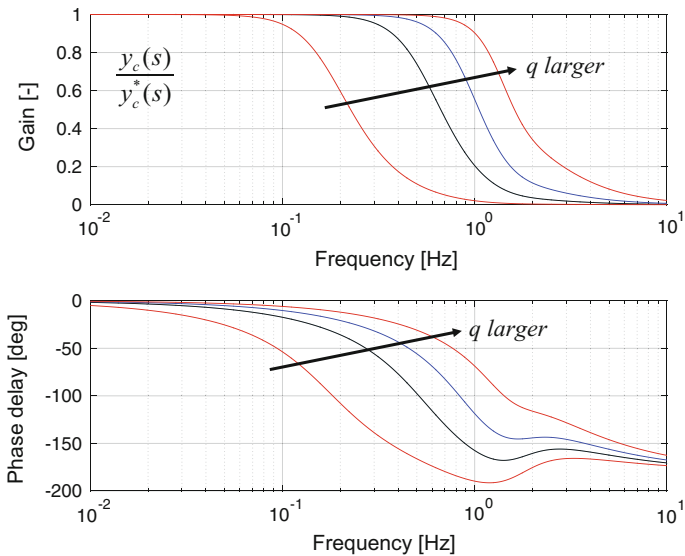
$$PA + A^TP - PBR^{-1}B^TP + Q = 0 \quad (109)$$

Figure 42 shows the simulation results of lane keeping control of a passenger car with respect to the desired step lane given at the time  $t = 1$  s and a velocity of 100 km/h. The control algorithm is LQ regulator, and the linear two-wheel vehicle model is used in the simulation. Increasing the value of weighting coefficient  $q$  provides better lane tracking. On the other hand, the steering wheel angle becomes larger, which means that more energy consumption of steering actuator is needed for lane-tracking performance enhancement.

Figure 43 shows the frequency response of lateral displacement with respect to the desired lane when increasing the value of the weighting coefficient of lateral deviation  $q$ . As can be noticed from Fig. 43, increasing the weighting coefficient of lateral deviation results in better lane keeping performance as the gain is close to 1 up to higher frequency region and the phase delay is also improved.



**Fig. 42** Simulation results of lane keeping control of a passenger car with steering angle input



**Fig. 43** Frequency response of lateral displacement with respect to the desired lane

### 5.3 Lane Keeping Control with Steering Torque Input

A lane keeping control system where the steering torque is used as the control input is referred as steering torque control. In this case, the steering system as shown in Fig. 44 becomes necessary in modeling the vehicle plant. In this paper, the steering system is configured such that the self-aligning torque (abbreviated as SAT) of the front tyre is transmitted directly to the steering wheel via the steering gear. In this case, the governing equation of steering system can be expressed as follows:

$$I_s \ddot{\delta}_{sw} = -C_s \dot{\delta}_{sw} - \frac{2\xi C_f}{n} \left( \frac{\delta_{sw}}{n} - \frac{l_f}{V} \dot{\psi} + \psi - \frac{\dot{\gamma}_{cr}}{V} \right) + T_a \quad (110)$$

where, the left hand side term refers to the inertia, the right hand side terms refers to the viscous damping, the reaction torque from SAT, the steering assist torque supplied by the steering actuator, respectively.

Therefore, the model of the control object becomes the 6th order system as follows:

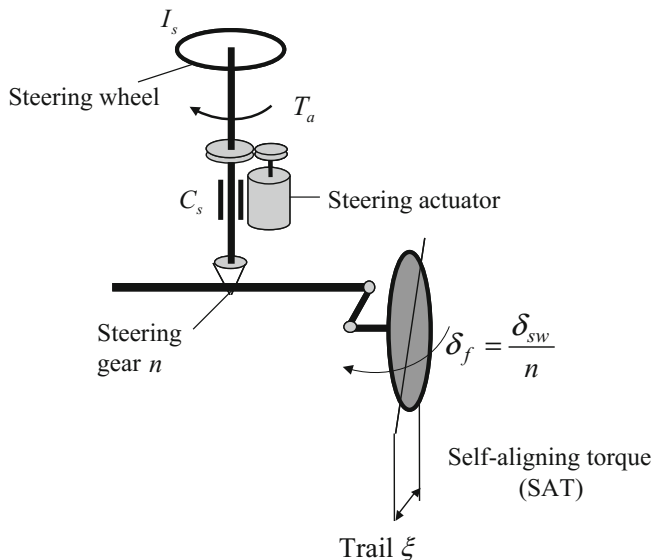


**Fig. 44** Simplified steering model for lane keeping control with steering torque input

$$\begin{bmatrix} \ddot{\psi} \\ \dot{\psi} \\ \ddot{y}_{cr} \\ \dot{y}_{cr} \\ \ddot{\delta}_{sw} \\ \dot{\delta}_{sw} \end{bmatrix} = \begin{bmatrix} a_{11e} & a_{12e} & a_{13e} & 0 & 0 & b_{11e}/n \\ 1 & 0 & 0 & 0 & 0 & 0 \\ a_{31e} & a_{32e} & a_{33e} & 0 & 0 & b_{31e}/n \\ 0 & 0 & 1 & 0 & 0 & 0 \\ a_{51e} & a_{52e} & a_{53e} & 0 & a_{55e} & a_{56e} \\ 0 & 0 & 0 & 0 & 1 & 0 \end{bmatrix} \begin{bmatrix} \dot{\psi} \\ \psi \\ \dot{y}_{cr} \\ y_{cr} \\ \dot{\delta}_{sw} \\ \delta_{sw} \end{bmatrix} + \begin{bmatrix} 0 \\ 0 \\ 0 \\ 0 \\ 0 \\ 0 \end{bmatrix} T_a \quad (111)$$

where, the elements in the fifth row of the state space equation are determined from the governing equation of the steering system as follows.

$$\begin{aligned} a_{51e} &= \frac{2\xi C_f l_f}{I_s n V}, & a_{52e} &= -\frac{2\xi C_f}{I_s n}, & a_{53e} &= \frac{2\xi C_f}{I_s n V}, \\ a_{55e} &= -\frac{C_s}{I_s}, & a_{56e} &= -\frac{2\xi C_f}{I_s n^2}, & b_{51e} &= \frac{1}{I_s} \end{aligned}$$

In this case, for the design of lane keeping controller with steering torque input, the control input can be expressed as the following full state feedback law, including the feedback of steering wheel angular velocity and steering wheel angle.

$$T_a = - (K_\psi \dot{\psi} + K_\psi \psi + K_{\dot{y}} \dot{y}_{cr} + K_y y_{cr} + K_{\dot{\delta}} \dot{\delta}_{sw} + K_\delta \delta_{sw}) \quad (112)$$

Here, as in the same manner with the case of steering angle control, the feedback gains are determined with the application of the optimal control theory, i.e. Linear Quadratic (LQ) regulator, which aims to minimize the following performance index.

$$J = \int_0^\infty (q y_{cr}^2 + T_a^2) dt \quad (113)$$

As same as the case of the steering angle control, the simulation is conducted. Figure 45 shows the simulation results of lane keeping control with steering torque input of a passenger car with respect to the desired step lane given at the time  $t = 1$  s and a velocity of 100 km/h. As similar to the case of lane keeping control with steering angle input, increasing the value of weighting coefficient  $q$  provides better lane keeping performance. On the other hand, the steering torque input becomes larger, which means that more energy consumption from the steering actuator is needed for lane keeping performance enhancement.

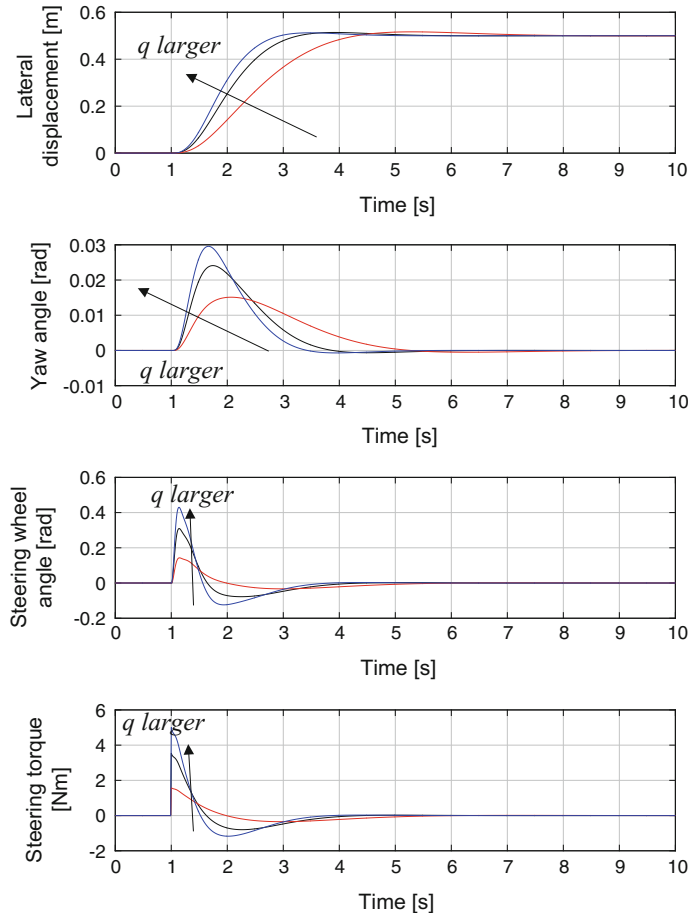


**Fig. 45** Simulation results of lane keeping control of a passenger car with steering torque input

#### 5.4 Comparison of Steering Angle Control and Steering Torque Control

As shown in the previous subsection, both lane keeping control system with steering angle input and steering torque input act on the vehicle in the same way when the lane keeping control maneuver is accomplished with the optimal regulator. However, the control system structure of the two approaches differs from each other. The structures of lane keeping control systems in the case of steering angle and steering torque input are shown in Fig. 46 and Fig. 47 respectively. In the case of lane keeping control with steering angle input, since the actual steering angle must correspond to the command steering angle, the steering wheel angle control unit is designed independently of the vehicle lane keeping control. On the other hand, in the case of

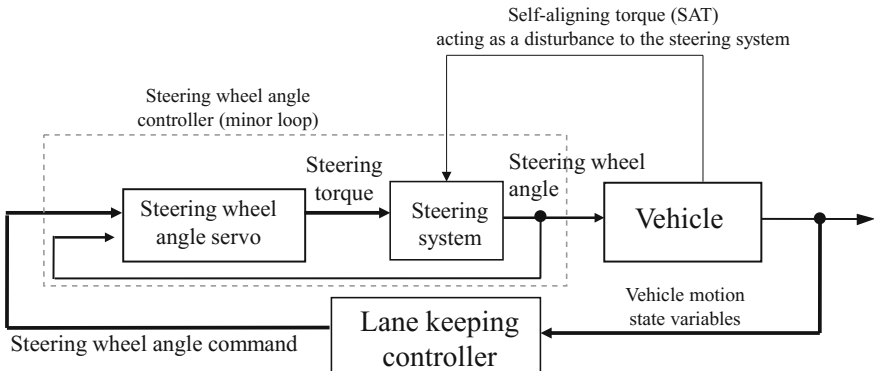


**Fig. 46** Structure of lane keeping control with steering angle input

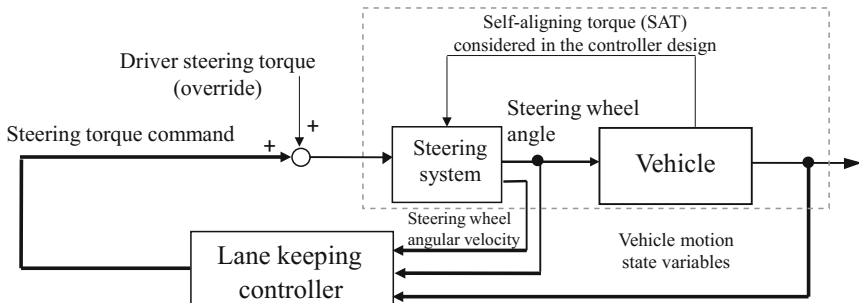


**Fig. 47** Structure of lane keeping control with steering torque input allowing override by driver

steering torque input, the steering angle control and the vehicle motion control for lane keeping are designed together as the steering torque feedback control input is determined based on steering system dynamics including the characteristics of self-aligning torque (SAT). Therefore, in the case of steering angle control, any torques added to the steering system including the SAT and the driver steering torque input are all treated as external disturbances. On the other hand, in the steering torque input, SAT is not treated as an external disturbance, since it has been included in the system modeling when the feedback gains are determined. From the viewpoint of driver assistance systems, the lane keeping control with steering torque input allows the driver to override the automated lane keeping control system such as in the case that the lane-change manoeuvre or obstacle avoidance manoeuvre must be executed by the driver if necessary. However, in real steering systems, there are nonlinear characteristics, such as coulomb friction in the steering and the hysteresis between the lateral acceleration and the steering torque, which are not considered in the model for lane keeping controller design. Therefore, the lane keeping control using steering torque input needs to be carefully designed considering such nonlinear characteristics to secure the lane keeping control performance.

## 5.5 Summary

This section described the design of automated lane keeping control by the front steering input, in the cases of steering angle and steering torque input. It was found that both steering angle control and steering torque control approach equivalent characteristic in lane keeping control via an analysis by using the optimal linear quadratic control theory. From the viewpoint of the control structure, the steering angle control treats self-aligning torque as an unknown disturbance, so the additional minor loop control of steering servo is needed to follow the steering angle command from the upper-level lane keeping controller. On the other hand, the steering torque control approach takes the characteristics of self-aligning torque into account, thus it does not need the minor loop control in the design of lane keeping control. In the case of steering torque input, the driver steering torque is allowed to override the system if necessary, thus the system characteristics fits the specification of a driver assistance system.

## 6 Direct Yaw Moment Control for Lane Keeping Functions

This section presents an alternative function of DYC which plays a role in enhancing vehicle safety. Here, an alternative lane keeping control strategy with direct yaw moment control which utilizes the transverse driving torque distribution will be described (Raksincharoensak et al. 2006). It is presumed that the information of road position can be acquired by current technologies such as a vision system using a CCD camera together with an on-board image processing system. As a feature of the proposed control law, the lateral deviation detected by CCD camera is converted into the desired yaw rate for tracing the desired lane. Then, DYC input is theoretically determined to follow the desired yaw rate. The theoretical analysis of lane keeping control characteristics using the 2-DOF linear vehicle model on planar motion will be presented, and an experimental study using a small-scale electric vehicle will be demonstrated to verify the effectiveness of the proposed strategy.

### 6.1 Introduction

This section describes a new lane keeping control strategy for enhancing active safety of automobiles, as one of advanced driver assistance system functions (ADAS). As one of active chassis control systems to enhance vehicle handling and stability, the individual wheel torque distribution control of electric vehicle by utilizing in-wheel-motors in order to achieve direct yaw moment control (DYC) input has been theoretically studied and experimentally examined as shown the previous section for reducing the vehicle side slip angle. On the other hand, in the field of automated

driving and driver assistance systems, lane keeping control systems to prevent lane departure accidents have been studied extensively. As shown in the previous section, the lane keeping control with the steering angle and the steering torque input can be conducted based on the lane marker position information acquired by a camera. Besides the steering control device, transverse distribution of braking forces as an extension of ABS device has potential to prevent vehicle from lane departure in emergency case by providing yaw moment to change the vehicle orientation and thus reduce the time-to-lane-crossing, i.e. risk of lane departure. This section considers that if DYC with differential driving torques generated by electric motors can be effectively used for lane keeping, the existing hardware of electric vehicle can be used while the steering system remains intact for the driver to have full authority in control. The aspect of lane keeping control system with DYC input is theoretically described and the effectiveness of the proposed control system is verified by the experiments using the small-scale electric vehicle.

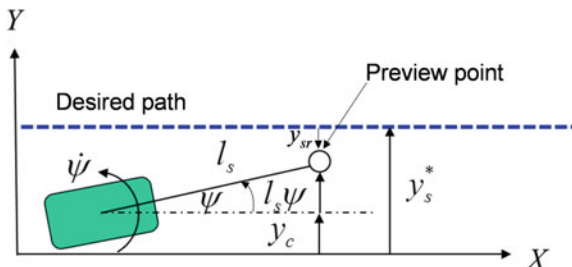
## 6.2 Lane Keeping Control System Design

The control objective of lane keeping is to regulate the lateral deviation of vehicle with respect to the given desired lane. This means that lane keeping control behaviour is equivalent to the lateral acceleration control. However, DYC is practically a strategy, which uses tyre longitudinal forces to directly control yaw motion, thus it is more suitable to control the yaw rate instead of the lateral acceleration. Here an alternative algorithm for lane keeping control by applying yaw rate matching control is proposed to fulfil the task of lane keeping functionality.

Here, the idea of the 2nd order predictive model for calculating the desired yaw rate based on the information from CCD camera is used. As shown in Fig. 48, From Taylor's 2nd order expansion, the predicted lateral displacement at the distance in front of vehicle of  $l_s$  can be expressed as follows:

$$y_c(t + \Delta t) = y_c(t) + \Delta t \cdot \dot{y}_c(t) + \frac{(\Delta t)^2}{2} \cdot \ddot{y}_c(t) \quad (114)$$

**Fig. 48** Vehicle model in earth-fixed coordinate system for control system design



$$\Delta t = \frac{l_s}{V} \quad (115)$$

As the objective of lane keeping control, the desired lateral displacement at preview point and the predicted lateral displacement must be equal ( $y_c(t + \Delta t) = y_s^*(t)$ ). Consequently, the required lateral acceleration for lane keeping can be calculated as follows:

$$\ddot{y}_c(t) = \frac{2V^2}{l_s^2} \left[ y_s^*(t) - \left( y_c(t) + l_s \frac{\dot{y}_c(t)}{V} \right) \right] = -\frac{2V^2}{l_s^2} y_{sr}(t) \quad (116)$$

When the body side slip angle is negligible, the kinematics relationship between yaw rate and lateral acceleration can be expressed as follows:

$$\ddot{y}_c(t) = V(\dot{\beta}(t) + r(t)) \approx Vr(t) \quad (117)$$

By substituting Eq. (117) into Eq. (116), the desired yaw rate for lane keeping control can be obtained as follows:

$$r(t) = -\frac{2V}{l_s^2} y_{sr}(t) \quad (118)$$

In the case of curved lane tracking, the yaw rate according to the road curvature  $\rho$  must be included.

$$\text{Yaw rate at curved lane : } r_c(t) = \frac{V}{\rho(t)} \quad (119)$$

$$\text{Total yaw rate : } r_d(t) = r(t) + r_c(t) = -\frac{2V}{l_s^2} y_{sr}(t) + \frac{V}{\rho(t)} \quad (120)$$

where, the turning radius of the desired path  $\rho$  can be estimated in real time from the vision information and vehicle lateral dynamics model with the application of Kalman filter. To make the vehicle trace the desired yaw rate, the yaw moment controller calculates the direct yaw moment control input by using linear inverse dynamics. The transfer function from the yaw moment input to the yaw rate can be calculated as follows:

$$r(s) = \frac{a_{1M} + a_{0M}}{s^2 + b_1 s + b_0} M_{dyc}(s) \quad (121)$$

where, each coefficient can be expressed as follows:

$$a_{1M} = \frac{1}{I_z}, \quad a_{0M} = \frac{2(C_f + C_r)}{mI_z V},$$

$$b_1 = \frac{2(C_f + C_r)}{mV} + \frac{2(l_f^2 C_f + l_r^2 C_r)}{I_z V}, \quad b_0 = \frac{4l_f^2 C_f C_r}{mI_z V^2} - \frac{2(l_f C_f - l_r C_r)}{I_z}$$

With the inverse transfer function of Eq. (121), the yaw moment input for tracing the desired yaw rate can be theoretically calculated as follows:

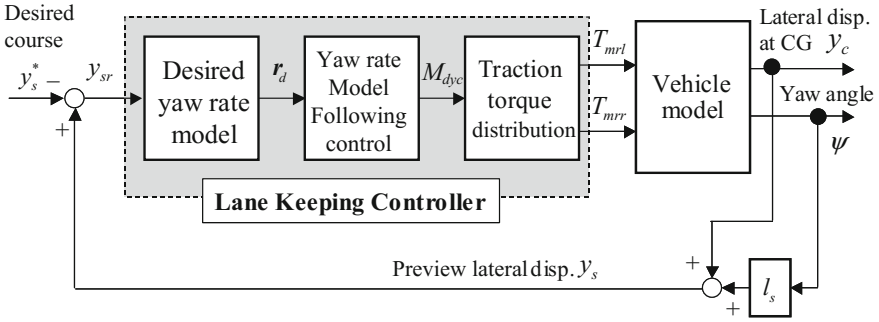


**Fig. 49** Block diagram of lane keeping control system by DYC

$$M_{dyc}(s) = \frac{s^2 + b_1 s + b_0}{(a_{1M}s + a_{0M})(\tau_0 s + 1)} r_d(s) \quad (122)$$

where,  $\tau_o$  denotes the time constant of 1st order lag element to make the transfer function of the controller become proper.

Practically, the yaw moment input is generated by the differential driving torque between left and right wheels. The driving torque of each motor can be calculated as follows:

$$\text{Left wheel : } T_{m3}(t) = T_{st}(t) - \frac{r_w}{l_w} M_{dyc}(t) \quad (123)$$

$$\text{Right wheel : } T_{m4}(t) = T_{st}(t) + \frac{r_w}{l_w} M_{dyc}(t) \quad (124)$$

where,  $T_{st}$  indicates the driving torque required for straight running and  $r_w$  indicates the effective radius of the wheel. The block diagram of the proposed lane keeping control system is shown in Fig. 49.

### 6.3 Experimental Validation

#### Experiments on Straight Roadway

The structure of the electric-vehicle-based experimental vehicle used for lane keeping control system verification is shown in Fig. 50. First, the validity of the proposed lane keeping control system was proved on straight roadway with a small lane change course as shown in Fig. 51. Figure 52 shows the experimental results in the case of straight lane. The vehicle ran straight and accelerated to velocity of 25 km/h and passed through the course shifting region without driver's corrective steering. Figure 52 shows the time history of preview lateral deviation measured from the CCD camera, the vehicle yaw rate, the front steering angle, the DYC input and the

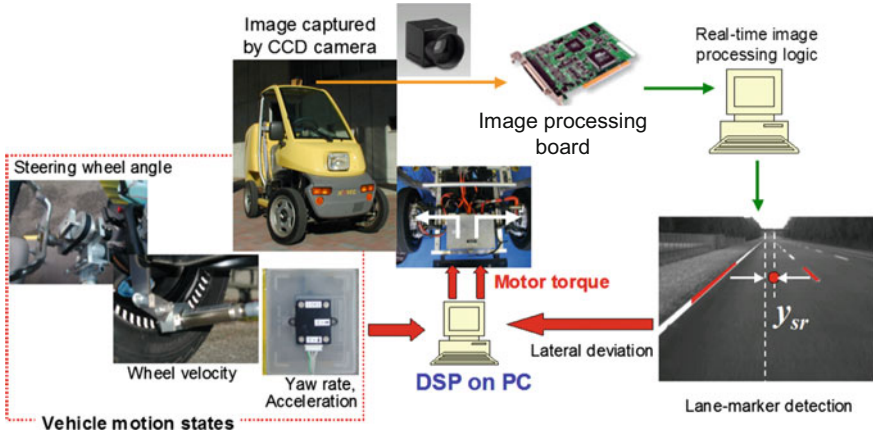


**Fig. 50** System configuration in micro-scale electric vehicle

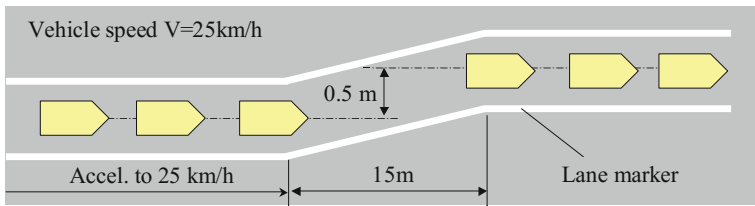


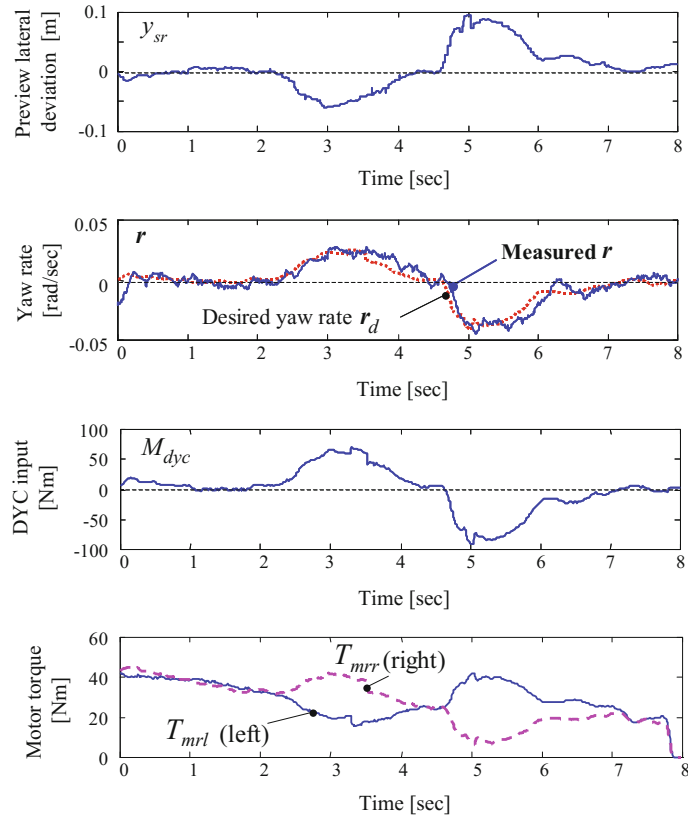
**Fig. 51** Course layout for system validation (straight roadway)

in-wheel-motor torques. The measured yaw rate shows good consistency with the desired yaw rate, which means the yaw moment controller by yaw rate matching control method is effective. The in-wheel-motor torques shows that the individual wheel torque control was actually realized. Figure 53 shows the trajectory of vehicle centre of gravity, which shows that the vehicle actually traced the set course by the proposed DYC.

### Experiments on Curved Roadway

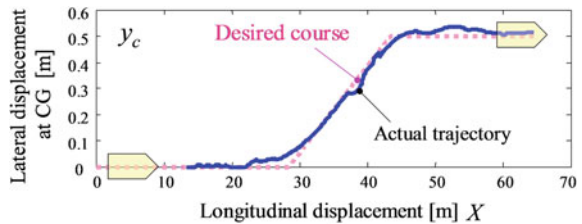
Next, the validity of the proposed lane keeping control system was proved on curved roadway with constant radius of curvature of 100 m at velocity of 35 km/h. During tracing the curved roadway, the driver did not hold the steering wheel. The experimental data is shown in Fig. 54.

Figure 54 shows the time responses of the preview lateral deviation, the vehicle yaw rate, the estimated road curvature, the DYC control input, the in-wheel-motor torques. The lateral deviation was suppressed under 50 cm, which was quite



**Fig. 52** Experimental results of straight lane keeping with DYC ( $V = 25\text{km/h}$ )

**Fig. 53** Vehicle trajectory during lane keeping experiment



satisfactory. The vehicle yaw rate in steady state traced the reference value well. The estimated road curvature was satisfactorily consistent with the reference road curvature.

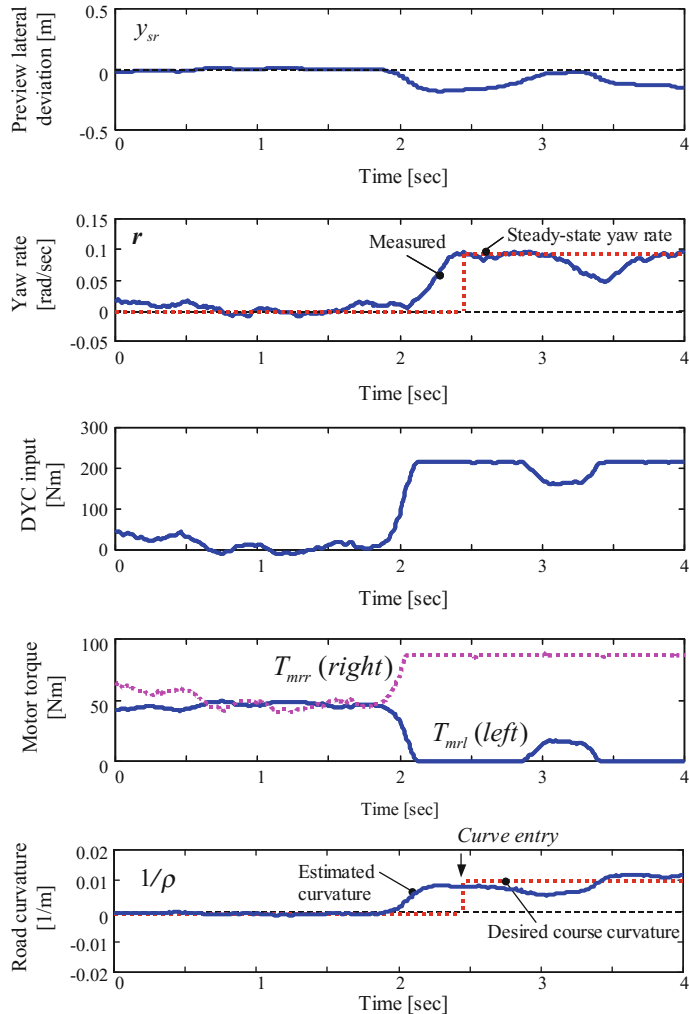


**Fig. 54** Lane keeping result on curved roadway with constant radius of 100 m (velocity = 35 km/h)

## 6.4 Summary

This paper examined the feasibility of the automated lane keeping control strategy with direct yaw moment control (DYC) input generated by differential transverse driving torques of in-wheel-motors, which is a structural merit of electric vehicle. The direct yaw moment control (DYC) system was designed to follow the desired yaw rate, which was determined from lane marker position information acquired by vision system. From the experimental validation, it was proved that the proposed

desired yaw rate determination and the yaw rate model matching control for lane keeping task was valid in actual driving. In addition, in the case of curved lane, since the desired yaw rate must be corrected due to road curvature, so the road curvature is estimated based on the information of preview lateral deviation considering vehicle dynamics in planar motion. As a result, the vehicle can perform lane keeping on curved lane with small lateral deviation.

## 7 Conclusion

As a great progress in automotive electronic control units in production cars, chassis control technology together with automated driving system for driver assistance systems have been developed and put in current production cars. This chapter provided an overview of the advanced chassis control systems aiming for enhancing vehicle handling and stability followed with the automated driving functions of intelligent vehicles in longitudinal and lateral vehicle dynamics, by employing the linear two-wheel vehicle dynamics model. In the controller design, classical control theory based on transfer function method or modern control theory based on optimal linear quadratic (LQ) control theory can be used depending on the control applications. Designing driver-friendly active vehicle dynamics control systems is a very important issue, for example, make the system easy for the driver to override the system or the system can support the driver to control the vehicle easier. Adaptive Human-Machine Interface (HMI) is also required to make man-machine closed-loop characteristics stable and realize good driver acceptance.

## References

- Abe, M. (2015). Vehicle handling dynamics. In *Theory and Application* (2nd ed.). Butterworth-Heinemann, Chapter 8, 8.1–8.5.
- Furukawa, Y., Yuhara, N., Sano, S., Takeda, H., & Matsushita, Y. (1989). A review of four-wheel steering studies from the viewpoint of vehicle dynamics and control. *Vehicle System Dynamics*, 18(1–3), 151–186.
- Koibuchi, K., Yamamoto, M., Fukada, Y., & Inagaki, S. (1996). Vehicle stability control in limit cornering by active brake. *SAE Paper No. 960487* (pp. 163–173).
- Mouri, H., Furusho, H. (1997). Automatic path tracking control using linear quadratic control theory. In *IEEE Conference on Intelligent Transportation Systems*.
- Nagai, M., Mouri, H., & Raksincharoensak, P. (2002). Vehicle lane-tracking control with steering torque input. *Vehicle System Dynamics Supplement*, 37, 267–278.
- Rajamani, R. (2012). *Vehicle Dynamics and Control*. (Vol. 6, pp. 144–145). Springer, Chapter.
- Raksincharoensak, P., Nagai, M., & Shino, M. (2006). Lane keeping control strategy with direct yaw moment control input by considering dynamics of electric vehicle. *Vehicle System Dynamics Supplement*, 43, 192–201.
- Shibahata, Y., Shimada, K., & Tomari, T. (1992). The improvement of vehicle maneuverability by direct yaw moment control. *Proceedings of AVEC'92* (pp. 452–457) Japan.

- Shino, M., Raksincharoensak, P., Kamata, M., & Nagai, M. (2004a). Side slip control of small-scale electric vehicle by DYC. *Vehicle System Dynamics Supplement*, 41, 487–496.
- Shino, M., Watanabe, S., Rokoincharoensak, P., & Nagai, M. (2004b). Vehicle handling and stability control of micro-scale electric vehicle utilizing steer-by-wire system. In *Proceedings of the 7th International Symposium on Advanced Vehicle Control (AVEC)* (pp. 797–802). Arnhems, The Netherlands.
- Van Zanten, A. T., Erhardt, R., Pfaff, G., Kost, F., Hartmann, U., & Ehret, T. (1996). Control aspects of the Bosch-VDC. *Proceedings of AVEC'96* (pp. 573–608).
- Yamamoto, M. (1991). Active control strategy for improved handling and stability. *SAE 1991 Transactions—Passenger Car* (Vol. 100-6, pp. 1–13).
- Yoshida, H., Yamada, M., Nagai, M., & Kamada, T. (2005). Development of active interface vehicle. In *Proceedings of the 19th IAVSD*. Milan, Italy.

# Multibody Systems and Simulation Techniques



Georg Rill

**Abstract** This part begins with an introduction to Multibody Systems (MBS). It presents the elements of MBS and discusses different modeling aspects. Then, different methods to generate the equations of motion are presented. Solvers for ordinary differential equations (ODE) as well as differential algebraic equations (DAE) are discussed. Finally, techniques for “online” and “offline” simulations including real-time applications are presented like necessary for car development. Special examples show the connection between simulation and test results.

**Keywords** Multibody systems • Vehicle models • Equations of motion  
Differential equations • Numerical solution

## 1 Multibody Systems

### 1.1 *The Multibody Systems Approach to Vehicle Dynamics*

For dynamic simulation, vehicles are usually modeled by multibody systems (MBS), Jagt (2000). Typically, the overall vehicle model is separated into different subsystems, Rauh (2003). The components of a passenger car model that can be used to investigate handling and ride properties are shown in Fig. 1. A generic vehicle model consists of the vehicle framework and subsystems for the steering system and the drive train. It must be supplemented by an appropriate model for the tire road interaction. The vehicle framework represents the kernel of the model. It at least includes the module chassis and modules for the wheel/axle suspension systems.

For standard vehicle dynamics analysis, the chassis can be modeled by one rigid body, Blundell and Harty (2004). The first eigenmodes of the chassis consist of torsion and bending. These modes can be approximated by a lumped mass model where the chassis is divided into three parts, Fig. 2. Software packages like MSC.Adams, Simpack or RecurDyn make it possible to describe the chassis by sophisticated Finite

---

G. Rill (✉)

Faculty of Mechanical Engineering, OTH Regensburg, Regensburg, Germany  
e-mail: georg.rill@oth-regensburg.de

**Fig. 1** Structure of a generic vehicle model

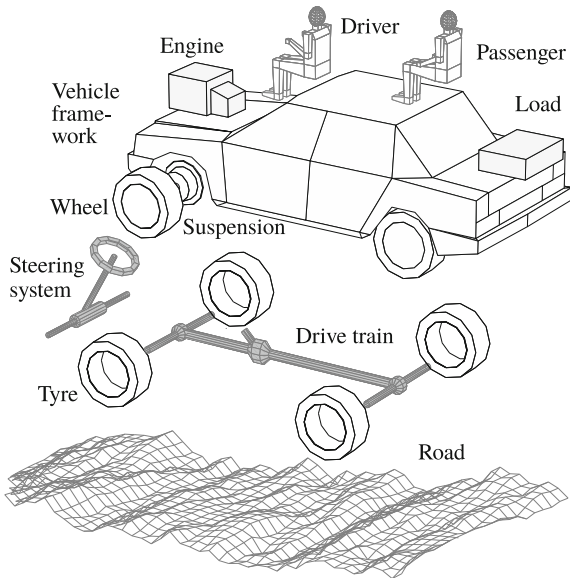
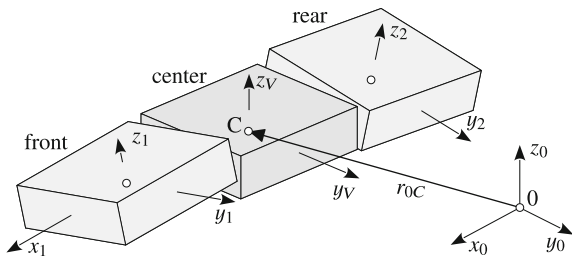


**Fig. 2** Lumped mass chassis model



Element Models. But that requires a detailed knowledge of the internal chassis structure. Hence, for basic studies the rigid body or lumped mass approach will be more appropriate.

Most wheel/axle suspension systems can be described by typical MBS elements such as rigid bodies, links, joints, and force elements, Rill (1994). Analytical models of a double whisbone suspension and a MacPherson axle suspension can be found in Rill (2012) and Rill and Schaeffer (2014). A purely kinematic suspension model consists of ideal joints, rigid links, and force elements describing the coil spring, and the damper, Fig. 3. However, relevant bushing compliances must be taken into account for detailed investigations of handling and ride properties, Seibert and Rill (1998). For that purpose, a hierachic model structure of the wheel suspension may be provided. Depending on the objectives and on the availability of data the user can activate a purly kinematic, a comfort, or a comfort and handling model. The corresponding model types for a quadra-link rear axle suspension system are shown in Fig. 4. On most cars the wheel suspension system is attached to a subframe that is elastically mounted to the chassis, Fig. 5. A double whisbone suspension system

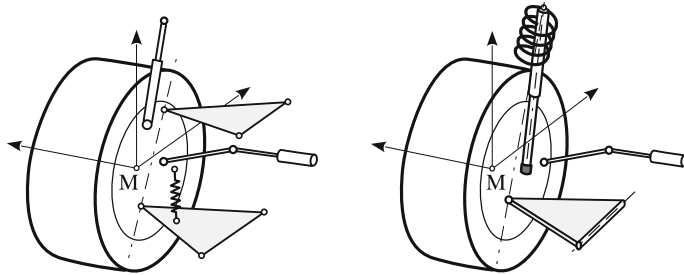


**Fig. 3** Kinematic suspension models

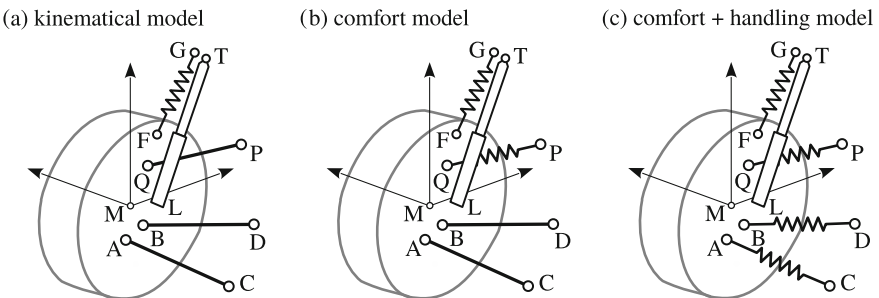


**Fig. 4** Hierarchic structure of a suspension system

then consists of two knuckles, two wheels, two lower and two upper wishbones, and one subframe. These bodies, modeled rigid or flexible, are attached to each other by several bushings. Rubber elements connect the subframe to the chassis. Spring and damper elements control the hub motion of each wheel.

Usually the suspension spring and the suspension damper are modeled as non-linear force elements characterized by

$$F_S = F_S(u) \quad \text{and} \quad F_D = F_D(v) \quad (1)$$

as functions of the spring displacement  $u$  and the damper velocity  $v$  respectively. Depending on the layout of the suspension the spring and/or the damper incorporates bump and rebound stops that are described by additional non-linear force characteristics. Torsional compliances in the bushings between the wishbones and the subframe or the chassis generate additional or parasitic stiffness and damping effects. In most cases the damper is mounted elastically to the chassis. The damper top-mount combination results in a dynamic force characteristic then. Last but not least, the anti-roll bar couples out of phase movements of the left and right knuckle, Fig. 6. Today luxury cars offer active anti-roll bars that increase ride comfort and ride safety simultaneously.

The vehicle framework is supplemented by modules for the load, an elastically suspended engine, passenger/seat models, and optionally a model for the trailer, Rill

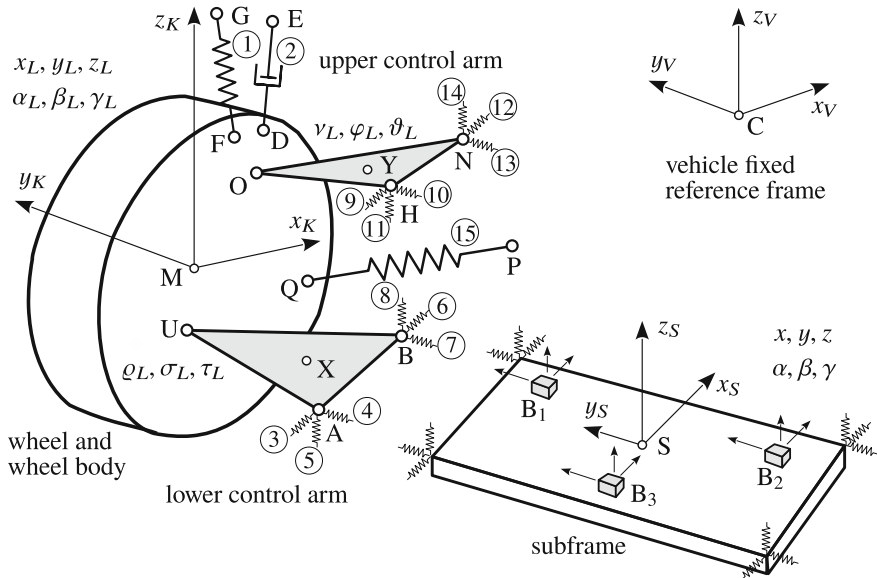
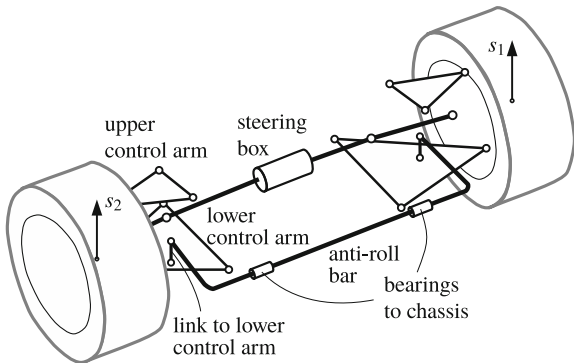


**Fig. 5** Sophisticated model of a double whishbone suspension system

**Fig. 6** Double whishbone suspension system with anti-roll bar



and Chucholowski (2004). A simple load module just takes the mass and inertia properties of the load into account. The subsystems elastically suspended engine and complex passenger/seat models can all be handled by a generic free-body model, Rill (2006a).

The steering system, shown in Fig. 7, consists of the steering wheel, an optional overriding gear, a flexible steering shaft, and the steering box, which may also be power-assisted, Rill and Chucholowski (2005b). A very sophisticated model of the steering system that includes compliances, dry friction, and clearance can be found in Neureder (2002). Today, the power assistance is usually provided by an electric motor.

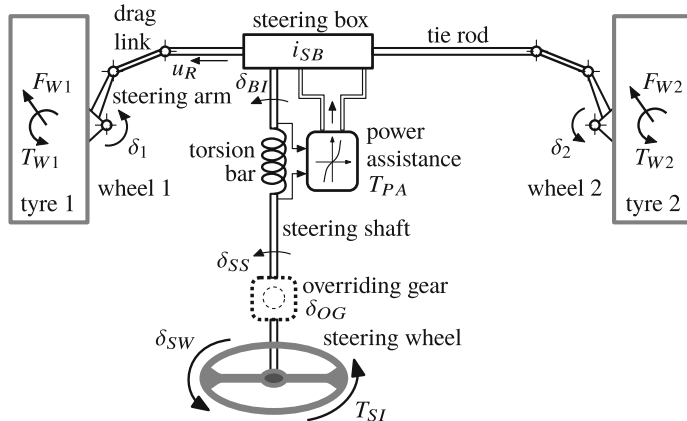


**Fig. 7** Steering model including power assistance

The drive train model described in Rill (2006a) takes lockable differentials into account, and it combines front-wheel, rear-wheel, and all-wheel drive, Fig. 8. The drive train is supplemented by a module describing the engine torque. It may be modeled quite simply by a first-order differential equation or by enhanced engine torque modules.

Tire forces and torques have a dominant influence on vehicle dynamics. In particular the wheel dynamics strongly depends on the tire model, Rill (2007). Usually, semi-empirical tire models are used for vehicle handling analysis. They combine a reasonable computer runtime performance with sufficient model accuracy. Complex tire models are valid even for high frequencies and on really rough roads. But, they are computer time consuming and therefore used in special investigations only. The “Tyre Model Performance Test (TMPT)” provides information about the efficiency and problems of tire modeling and parameterization as well as the integration in standard multibody system program codes, Lugner and Plöchl (2007). The semi-empirical tire model “TMeasy” that is part of the Simpack Automotive package meets the requirements of both user friendliness and sufficient model accuracy, Rill (2013a).

Road irregularities and variations in the coefficient of friction present significant impacts on the vehicle. Therefore a road model must at least provide the road height and the local friction coefficient, Butz et al. (2004).

Besides that, a driver model is needed to operate the vehicle. Even rather simple driving maneuvers, like a step-steer input or braking in a turn, require at least a simple drive torque controller to maintain the given speed. The maneuvers steady state cornering, lane change, double lane change, or driving along a given path, demand for a driver model that controls the steer input and the drive torque simultaneously.

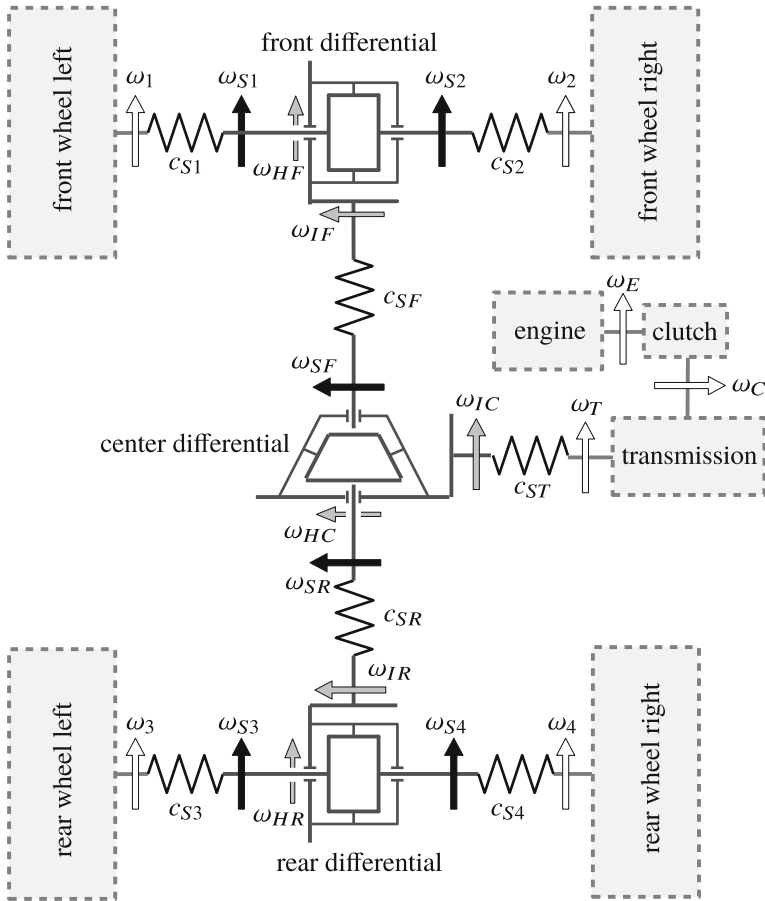
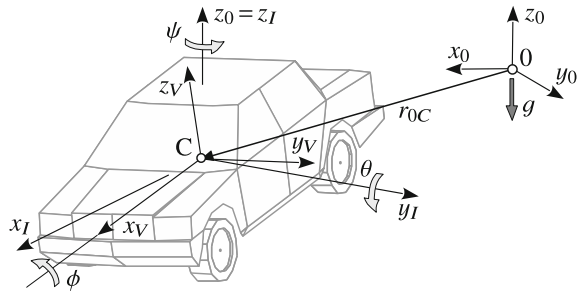


**Fig. 8** Generic drive train model

## 1.2 Position and Orientation

If the chassis is supposed to be a rigid body, one coordinate system fixed to the vehicle body will be sufficient to describe the overall motions of the vehicle, Fig. 9. The vehicle-fixed system  $V$  is located in the center  $C$  in general. Its  $x_V$ -axis points forward, the  $y_V$ -axis to the left, and the  $z_V$ -axis upward, which will correspond with the definitions in the ISO 8855 directive. In complex vehicle models it is often more convenient to attach the vehicle-fixed axis system  $V$  to a representative chassis point rather than to the center of gravity of the vehicle, because the latter will change with different loading conditions. The earth-fixed system  $0$  with the axis  $x_0, y_0, z_0$  serves as inertial reference frame. Its origin  $0$  lies in a reference ground plane and its  $z_0$ -axis

**Fig. 9** Position and orientation of the vehicle body



will point in the opposite direction of the gravity vector  $g$ . The vector  $r_{0C}$  pointing from 0 to C describes the momentary position of the vehicle then.

The orientation of the vehicle-fixed axis system  $V$  with respect to the inertial frame 0 can be described by a rotation matrix  $A_{0V}$  that is defined by a sequence of three elementary rotations. In vehicle dynamics the angles  $\psi$ ,  $\theta$ , and  $\phi$  which represent the yaw, the pitch, and the roll motion of the vehicle body are used for that purpose.

The first rotation about the  $z_0 = z_I$ -axis defines the intermediate axis system with  $x_I$  and  $y_I$  parallel to the horizontal ground.

The wheel consists of the tire and the rim. Handling tire models simplify the contact patch by a local plane, which is represented by the contact point P and an unit vector  $e_n$  perpendicular to this plane. The rim is mounted at the wheel carrier or knuckle. The suspension system, consisting of force and guidance elements, attaches the wheel carrier to the chassis. Depending on the type of suspension system, the wheel carrier and the attached wheel can perform a hub motion  $z$  and optionally a steering motion  $\delta$ , Fig. 10.

To describe the position and orientation of the wheel carrier or knuckle and the wheel, a reference frame with the axes  $x_K$ ,  $y_K$ ,  $z_K$  is fixed to the wheel carrier. The origin of this axis system is supposed to coincide with the wheel center M. The position and the orientation of the wheel carrier depend on the hub motion  $z$  and optionally on the steer motion  $\delta$ . In design position, the corresponding axes of the

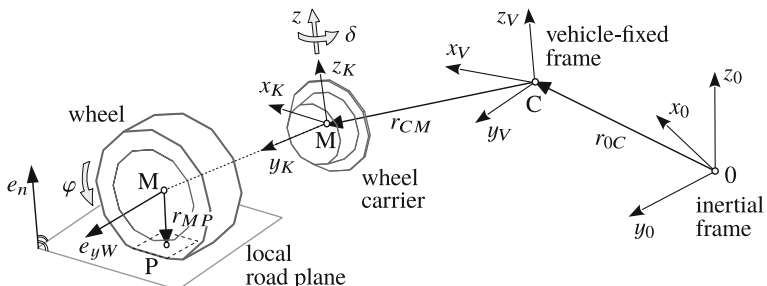
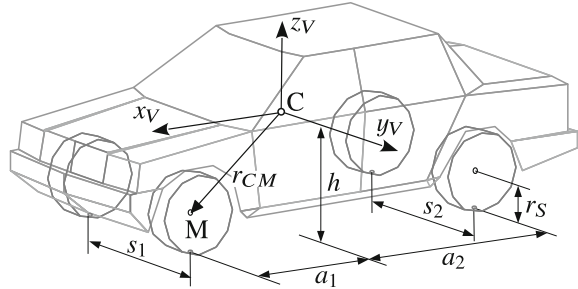


**Fig. 10** Position and orientation of wheel carrier and wheel

**Fig. 11** Design position of wheels



frames  $K$  and  $V$  are supposed to be parallel. The wheel itself rotates with the angle  $\varphi$  about an axis that is determined by the unit vector  $e_{yW}$ , Fig. 10.

### 1.3 Design Position

The design position of a wheel center  $M$  is roughly<sup>1</sup> determined by the wheelbase  $a = a_1 + a_2$  and the track widths  $s_1, s_2$  at the front and rear axles, Fig. 11. If left/right symmetry is assumed, then the position vector

$$\mathbf{r}_{FM,D} = \begin{bmatrix} a_1 \\ s_1/2 \\ -h + r_S \end{bmatrix} \quad (2)$$

denoted in the vehicle-fixed reference frame  $V$  will define the design position of the front left wheel center  $M$  relative to the vehicle center  $C$ . Here,  $h$  denotes the height of the vehicle center  $C$  above the ground and  $r_S$  names the static tire radius, which takes the tire deflection caused by the weight of the vehicle into account. By changing the sign in the second component ( $s_1/2 \rightarrow -s_1/2$ ), Eq. (2) applies for the right front wheel too. Finally, the design position of the rear wheels is obtained by replacing  $a_1$  and  $s_1$  by  $-a_2$  and  $s_2$ , respectively.

Usually, the wheel rotation axis, which is described by the unit vector  $e_{yW}$ , will not coincide with the  $y_K$ -axis, which is part of the corresponding axis system located in the wheel center  $M$  and fixed to the knuckle, Fig. 12. The orientation of the unit vector  $e_{yW}$  can be defined either by the angles  $\delta_0$  and  $\gamma_0$ , or by  $\delta_0$  and  $\hat{\gamma}_0$ , where  $\delta_0$  is the angle between the  $y_V$ -axis and the projection line of the wheel rotation axis into the  $x_V y_V$ -plane. The angle  $\hat{\gamma}_0$  describes the angle between the  $y_V$ -axis and the projection line of the wheel rotation axis into the  $y_V z_V$ -plane, whereas  $\gamma_0$  is the angle between the wheel rotation axis  $e_{yW}$  and its projection into the  $x_K y_K$ -plane. Toe-in and a positive camber angle are indicated by  $\delta_0 > 0$  and  $\gamma_0 > 0$  or  $\hat{\gamma}_0 > 0$  at the

<sup>1</sup>Note: The track width is defined as the distance of the contact points at an axle. On cambered wheels, the distance of the wheel centers is slightly different.

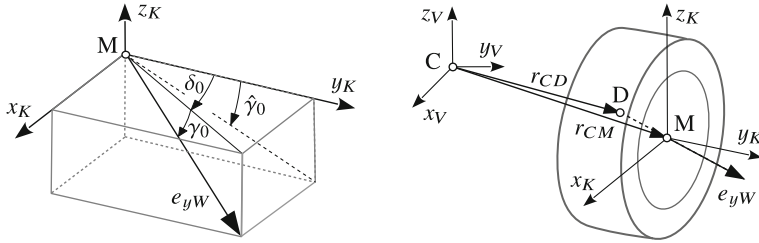


**Fig. 12** Design position of wheel rotation axis

left wheel. In the design position, where the corresponding axis of the vehicle-fixed axis system  $V$  and the knuckle-fixed coordinate system  $K$  are parallel, one gets by inspecting Fig. 12,

$$e_{yW,V} = e_{yW,K} = \frac{1}{\sqrt{\tan^2 \delta_0 + 1 + \tan^2 \hat{\gamma}_0}} \begin{bmatrix} \tan \delta_0 \\ 1 \\ -\tan \hat{\gamma}_0 \end{bmatrix} \quad (3)$$

On the other hand, applying a series of elementary rotations results in

$$e_{yW,V} = e_{yW,K} = \begin{bmatrix} \sin \delta_0 \cos \gamma_0 \\ \cos \delta_0 \cos \gamma_0 \\ -\sin \gamma_0 \end{bmatrix} \quad (4)$$

On a flat and horizontal road where the track normal  $e_n$  points in the direction of the vertical axis  $z_K = z_V$ , the angles  $\delta_0$  and  $\gamma_0$  correspond to the toe angle and the camber angle, respectively. To specify the difference between  $\gamma_0$  and  $\hat{\gamma}_0$ , the ratio between the third and second component of the unit vector  $e_{yW}$  is considered now. Equations (3) and (4) deliver

$$\frac{-\tan \hat{\gamma}_0}{1} = \frac{-\sin \gamma_0}{\cos \delta_0 \cos \gamma_0} \quad \text{or} \quad \tan \hat{\gamma}_0 = \frac{\tan \gamma_0}{\cos \delta_0} \quad (5)$$

Hence, for small angles  $\delta_0 \ll 1$ , the difference between the angles  $\gamma_0$  and  $\hat{\gamma}_0$  is hardly noticeable. Kinematics and compliance test machines usually measure the angle  $\hat{\gamma}_0$ . That is why the automotive industry mostly uses this one instead of  $\gamma_0$  to determine the orientation of the wheel rotation axis in the design position.

Often the position of the wheel rotation axis is defined by the wheel center  $M$  and an additional point  $D$  which is called “wheel alignment point”. If this point is located inside the wheel center, then the unit vector pointing in the direction of the wheel rotation axis is given by

$$e_{yW,V} = \frac{r_{CM,V} - r_{CD,V}}{|r_{CM,V} - r_{CD,V}|} \quad (6)$$

where the vectors  $r_{CM,V}$  and  $r_{CD,V}$  describe the design position of the wheel center M and the wheel alignment point D relative to the origin C of the vehicle-fixed reference frame V.

## 1.4 Kinematics

According to Fig. 10, the absolute position of the wheel carrier or knuckle is defined by the vector

$$r_{0M,0} = r_{0C,0} + A_{0V} r_{CM,V} \quad (7)$$

where the vector  $r_{0C,0}$  and the rotation matrix  $A_{0V}$  define the momentary position of the chassis center C and the orientation of the vehicle-fixed frame V with respect to the inertial frame 0. The vector  $r_{CM,V}$  describes the momentary position of the knuckle fixed reference point M with respect to C and its components are expressed the vehicle-fixed frame V which is indicated by the corresponding comma separated index. The multiplication with the rotation matrix  $A_{0V}$  transforms a vector via

$$r_{CM,0} = A_{0V} r_{CM,V} \quad (8)$$

from the system V into the system 0. As the rotation matrix is orthonormal

$$A_{0V}^T A_{0V} = A_{0V} A_{0V}^T = I \quad \text{and} \quad A_{0V}^{-1} = A_{0V}^T \quad (9)$$

will hold, where  $I$  denotes the corresponding matrix of identity.

Even if the knuckle performs only hub motions relative to the chassis the suspension kinematics will cause the knuckle to rotate as more or less requested. Hence, the absolute orientation of the knuckle-fixed reference frame is defined by the rotation matrix

$$A_{0K} = A_{0V} A_{VK} \quad (10)$$

where the rotation matrix  $A_{VK}$  defines the orientation of the knuckle-fixed system K relative to the vehicle-fixed frame V.

A three-dimensional vehicle model consists at least of the chassis, 4 knuckles and 4 wheels. The chassis has 6 degrees of freedom, each knuckle can perform at least a hub motion and each wheel an angular rotation. Describing the steering motions at the front and optionally at the rear axle by the rack displacements at front and rear, the three-dimensional vehicle model has  $f = 6 + 4 + 4 + 2 = 16$  degrees of freedom then. The generalized coordinates that are required to describe the free motions are usually collected in the vector  $y$ . Then

$$r_{0i,0} = r_{0i,0}(y) \quad \text{and} \quad A_{0i} = A_{0i}(y) \quad (11)$$

will hold for body  $i$  of the vehicle model or a multibody system in general.

The velocity with which body  $i$  is moving relative to the inertial system 0 is determined by the time derivative of the position vector defined in Eq. (11)

$$v_{0i,0} = \frac{d}{dt} r_{0i,0}(y) = \dot{r}_{0i,0}(y) = \sum_{m=1}^f \frac{\partial r_{0i,0}(y)}{\partial y_m} \dot{y}_m = v_{0i,0}(y, \dot{y}) \quad (12)$$

where

$$\frac{\partial r_{0i,0}(y)}{\partial y} = \left[ \frac{\partial r_{0i,0}(y)}{\partial y_1} \frac{\partial r_{0i,0}(y)}{\partial y_2} \dots \frac{\partial r_{0i,0}(y)}{\partial y_f} \right] \quad (13)$$

denotes the  $3 \times f$ -Jacobian matrix of the translational motion of body  $i$ .

The time derivative of the rotation matrix multiplied by its transposed results in a skew-symmetric matrix

$$\tilde{\omega}_{0i,0} = \frac{d}{dt} (A_{0i,0}(y)) A_{0i,0}^T(y) = \sum_{m=1}^f \frac{\partial A_{0i,0}(y)}{\partial y_m} \dot{y}_m A_{0i,0}^T(y) = \tilde{\omega}_{0i,0}(y, \dot{y}) \quad (14)$$

Its essential components

$$\tilde{\omega}_{0i,0} = \begin{bmatrix} 0 & -\omega_{0i,0}(3) & \omega_{0i,0}(2) \\ \omega_{0i,0}(3) & 0 & -\omega_{0i,0}(1) \\ -\omega_{0i,0}(2) & \omega_{0i,0}(1) & 0 \end{bmatrix} \quad (15)$$

define the vector of the angular velocity  $\omega_{0i,0} = [\omega_{0i,0}(1), \omega_{0i,0}(2), \omega_{0i,0}(3)]^T$  with which the body-fixed axis system  $i$  rotates relative to the earth-fixed axis system 0. A direct calculation shows that

$$\tilde{\omega}_{0i,0} r_{,0} = \omega_{0i,0} \times r_{,0} \quad (16)$$

holds for any vector  $r_{,0}$ , which means that the multiplication of the skew-symmetric matrix of the angular velocities can be replaced by the corresponding vector- or cross-product.

Depending on the kind of constraints, the algebraic representation of the velocity vector  $v_{0i,0} = v_{0i,0}(y, \dot{y})$  and the vector of the angular velocities  $\omega_{0i,0} = \omega_{0i,0}(y, \dot{y})$  may become very complex. However, significant simplifications are possible if the time derivative of the vector of the generalized coordinates  $\dot{y}$  is replaced via

$$\dot{y} = K(y)z \quad (17)$$

by a corresponding vector of generalized velocities  $z$ . Then, the algebraic representation for the resulting velocities and angular velocities

$$v_{0i,0}(y, \dot{y}) \Rightarrow v_{0i,0}(y, z) \quad \text{and} \quad \omega_{0i,0}(y, \dot{y}) \Rightarrow \omega_{0i,0}(y, z) \quad (18)$$

will be less complicated. In many cases a simple inspection of the resulting velocity terms already leads to appropriate generalized velocities and automatically delivers the kinematical matrix  $K = K(y)$ , Kane and Levinson (1980). The trivial choice

$$\dot{y} = z \quad (19)$$

is always possible. Here, the kinematical matrix simplifies to the corresponding matrix of identity.

The time derivatives of the velocities and the angular velocities finally result in the corresponding accelerations

$$\begin{aligned} a_{0i,0} &= \frac{d}{dt} v_{0i,0}(y, z) = \sum_{m=1}^f \frac{\partial v_{0i,0}(y, z)}{\partial y_m} \dot{y}_m + \sum_{m=1}^f \frac{\partial v_{0i,0}(y, z)}{\partial z_m} \dot{z}_m \\ a_{0i,0} &= \frac{d}{dt} \omega_{0i,0}(y, z) = \sum_{m=1}^f \frac{\partial \omega_{0i,0}(y, z)}{\partial y_m} \dot{y}_m + \sum_{m=1}^f \frac{\partial \omega_{0i,0}(y, z)}{\partial z_m} \dot{z}_m \end{aligned} \quad (20)$$

## 1.5 Forces and Torques

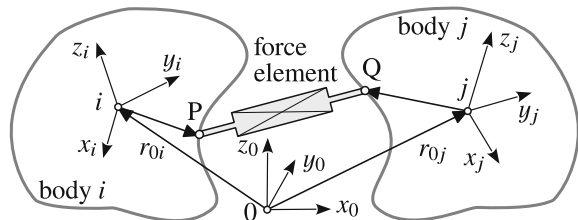
**Point-to-Point Force Elements:** Usually, mounts connecting springs, dampers, and actuators to different bodies can be regarded as ball joints, Fig. 13. Then, the action line of the force generated by the element that is mounted between the points P and Q is defined by the unit vector

$$e_{PQ,0} = \frac{r_{PQ,0}}{|r_{PQ,0}|} = \frac{r_{0Q,0} - r_{0P,0}}{|r_{0Q,0} - r_{0P,0}|} \quad (21)$$

where

$$L = |r_{PQ,0}| = \sqrt{r_{PQ,0}^T r_{PQ,0}} \quad (22)$$

**Fig. 13** A point-to-point force element attached between two bodies



defines the actual length of the force element in addition. The point P is attached to body  $i$  and point Q to body  $j$ . The vectors  $r_{0i,0}$ ,  $r_{0j,0}$  and the rotation matrices  $A_{0i}, A_{0j}$  describe the momentary position and orientation of axis systems fixed in the center of each body with respect to the earth-fixed reference frame 0. Then, the position of the attachment points is defined by

$$\begin{aligned} r_{0P,0} &= r_{0i,0} + \underbrace{A_{0i} r_{iP,i}}_{r_{iP,0}} \quad \text{and} \quad r_{0Q,0} = r_{0j,0} + \underbrace{A_{0j} r_{jQ,j}}_{r_{jQ,0}} \end{aligned} \quad (23)$$

where the vectors  $r_{iP,i}$ ,  $r_{jQ,j}$  characterize the position of P and Q with respect to the corresponding body-fixed axis systems. The deflection of the force element is just given by

$$s = L_0 - L \quad (24)$$

where  $L_0$  denotes the length of the force element in the design position and the actual length  $L$  is defined by Eq. (22).

It is common practice to describe spring forces via  $F_S = F_S(s)$  as functions of the force displacement  $s$  and dampers via  $F_D = F_D(v)$  as functions of the damper velocity  $v$ . The time derivative of the force element deflection  $s$  given in Eq. (24) delivers the damper velocity at first as

$$v = \dot{s} = \frac{d}{dt} (L_0 - L) = -\dot{L} \quad (25)$$

By using Eq. (22) it results in

$$v = -\frac{2 r_{PQ,0}^T \dot{r}_{PQ,0}}{2 \sqrt{r_{PQ,0}^T r_{PQ,0}}} = -\frac{r_{PQ,0}^T}{|r_{PQ,0}|} \dot{r}_{PQ,0} = -e_{PQ,0}^T (\dot{r}_{0Q,0} - \dot{r}_{0P,0}) \quad (26)$$

where Eq. (21) was used to re-insert the unit vector  $e_{PQ}$  and to put the time derivative of the vector  $r_{PQ}$  down to the time derivatives of the position vectors  $r_{0Q}$  and  $r_{0P}$ . According to Eq. (23), the time derivatives of the position vectors are given by

$$\dot{r}_{0P,0} = v_{0i,0} + \omega_{0i,0} \times r_{iP,0} \quad \text{and} \quad \dot{r}_{0Q,0} = v_{0j,0} + \omega_{0j,0} \times r_{jQ,0} \quad (27)$$

where  $v_{0i,0} = \dot{r}_{0i,0}$ ,  $v_{0j,0} = \dot{r}_{0j,0}$  name the absolute velocities of the body centers and  $\omega_{0i,0}, \omega_{0j,0}$  denote the absolute angular velocities of the bodies. In particular dampers are designed nonlinear at least by distinguishing between the rebound and compression mode.

Finally, the force acting in an arbitrary point-to-point force element can be described by

$$F = F(s, \dot{s}, u, x) \quad (28)$$

where the dependency on a control signal  $u$  will include actuators and the vector  $x$  collects internal states that are required when dynamic force elements are modeled.

**Enhanced Dry Friction Model:** The braking torque applied to the wheel usually is generated by friction, Fig. 14. However, a simple dry friction model will cause severe numerical problems because it is not defined in a locking situation ( $\Delta\Omega = 0$ ). The regularized model that is mostly used in commercial software packages avoids this problem but becomes less accurate when approaching the locking situation. The enhanced dry friction model avoids the jump at  $\Delta\Omega = 0$  and provides an appropriate locking torque, Rill (2006b). So, the braking torque will here be modeled by

$$T_B = T_B^{st} + d_N \Delta\Omega \quad \text{and} \quad |T_B| \leq T_B^{mx} \quad (29)$$

where  $T_B^{st}$  names the static or locking torque,  $d_N > 0$  is a constant with the dimension of Nm/(rad/s),  $T_B^{mx}$  denotes the maximum braking torque, and

$$\Delta\Omega = \Omega - \omega_K \quad (30)$$

describes the relative angular velocity between the wheel and the body where the brake caliper is mounted. Usually this will be the knuckle.

The static part provides a steady-state locking torque when the relative angular velocity is vanishing,  $T_B^{st}(\Delta\Omega = 0) = T_B^{st}$ . In the steady state when  $\dot{\Omega} = 0$  holds in addition, The torque balance at one wheel delivers

$$0 = T_D - T_B^{st} - r F_x \quad (31)$$

where  $T_D$  names the drive torque,  $r$  is the radius of the wheel, and  $F_x$  describes the longitudinal tire force. The rolling restiniance torque and additional friction torques in the wheel bearing are neglected, here. Hence, the static braking torque

$$T_B^{st} = T_D - r F_x \quad (32)$$

will counteract appropriately the resulting torque applied to the wheel, namely consisting of the driving torque  $T_D$  and the torque  $r F_x$  generated by the longitudinal

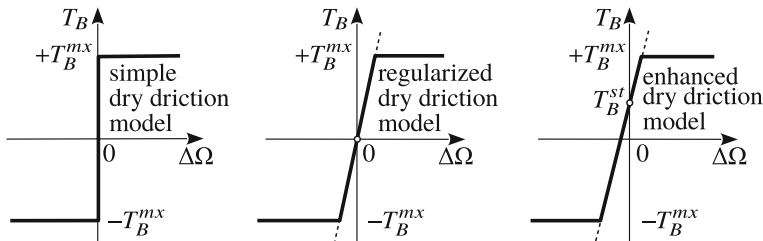
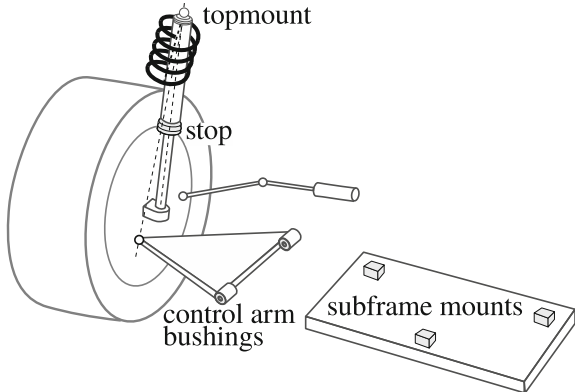


**Fig. 14** Coulomb dry friction model and enhanced brake torque model

**Fig. 15** Rubber elements in vehicle suspension



tire force. Just like the overall braking torque  $T_B$ , the steady-state part is bounded to the maximum braking torque

$$|T_B^{st}| \leq T_B^{mx} \quad (33)$$

As shown in Rill (2012) the numeric constant  $d_N$  can be chosen such that the dynamics of a fully braked and freely rolling wheel will be similar.

**Rubber Elements:** Force elements made of natural rubber or urethane compounds are used in many locations on the vehicle suspension system, Fig. 15. Those elements require no lubrication, isolate minor vibration, reduce transmitted road shock, operate noise-free, offer high load carrying capabilities, and are very durable.

During suspension travel, the control arm bushings provide a pivot point for the control arm. They also maintain the exact wheel alignment by fixing the lateral and vertical location of the control arm pivot points. During suspension travel, the rubber portion of the bushing must twist to allow control arm motion. Thus, an additional resistance to suspension motion is generated.

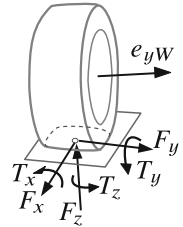
Bump and rebound stops limit the suspension travel. The compliance of the topmount avoids the transfer of large shock forces to the chassis. The subframe mounts isolate the suspension system from the chassis and allow elasto-kinematic steering effects of the whole axle.

It turns out that those elastic elements can hardly be described by simple spring and damper characteristics,  $F_S = F_S(u)$  and  $F_D = F_D(v)$ , because their stiffness and damping properties change with the frequency of the motion. Here, more sophisticated dynamic models are needed.

**Tire Forces and Torques:** Tires are very complex. They combine dozens of components that must be formed, assembled, and cured together. In normal driving situations the tire is in contact to the road. The forces and torques transmitted in this rather small contact area must support and guide the vehicle, Fig. 16. Handling tire models, like TMeasy, describe the steady state forces and torques as functions of the longitudinal, the lateral and the turn slip at first. Then, dynamic effects caused

**Fig. 16** Contact forces and torques

$F_x$	longitudinal force
$F_y$	lateral force
$F_z$	vertical force or wheel load
$T_x$	tilting torque
$T_y$	rolling resistance torque
$T_z$	self-aligning and turn torque



by the tire compliance are taken into account, Rill (2013a). Within TMeasy a set of first order differential equations is generated that describe the dynamic tire forces and torques by using internal tire states that describe the tire deflections in longitudinal, lateral, and torsional directions, Rill (2007). For instance, the dynamic force in longitudinal direction  $F_x$  is thus defined by

$$\begin{aligned} (v_{Tx}^* d_x + f_G) \dot{x}_e &= -v_{Tx}^* c_x x_e - f_G (v_x - r_D \Omega) \\ F_x &= c_x x_e + d_x \dot{x}_e \end{aligned} \quad (34)$$

where  $c_x$  and  $d_x$  describe the stiffness and damping properties of the tire in longitudinal direction. The internal tire state  $x_e$  characterizes the circumferential tire deflection,  $v_x$  defines the longitudinal velocity component of the wheel center,  $r_D$  is the dynamic rolling radius,  $\Omega$  represents the angular wheel velocity, and  $v_{Tx}^*$  names a modified transport velocity with which the tread particles are transported through the contact patch. Finally,  $f_G = F_G/s_G$  is the global derivative of the generalized tire characteristics  $F_G = F_G(s_G)$  with respect to the generalized slip  $s_G$  that vectorially combines the slips in longitudinal, lateral, and torsional directions, Rill (2013b).

## 1.6 Equations of Motion

Each body in a multibody system is exposed to applied and constraint forces and torques. Then, the linear and angular momentum may be written as

$$m_i a_{0i,0} = F_{i,0}^a + F_{i,0}^c \quad (35)$$

$$\Theta_{Si,0} \alpha_{0i,0} + \omega_{0i,0} \times \Theta_{Si,0} \omega_{0i,0} = T_{i,0}^a + T_{i,0}^c \quad (36)$$

where  $m_i$ ,  $\Theta_{Si,0}$  describe the mass and inertia properties of body  $i$ ,  $F_{i,0}^a$ ,  $T_{i,0}^a$  are the applied forces and torques, and  $F_{i,0}^c$ ,  $T_{i,0}^c$  denote the constraint forces and torques generated by links and joints.

To combine and solve the equations of motion for a multibody system consisting of  $i = 1(1)k$  bodies, the constraint forces and torques have either to be

eliminated or the set of dynamic equations must be supplemented by algebraic constraint equations.

The principle of virtual work (D'Alembert's Principle) or the principle of virtual power (Jourdain's principle) eliminate all constraint forces and torques very effectively. The principle of virtual power, for example, states that the virtual power of the constraint forces and torques must vanish, because each constraint force or torque generated by a link or a joint points into a direction that is blocked by this link or joint. Hence, for a system with  $k$  rigid bodies

$$\sum_{i=1}^k \left\{ \delta v_{0i,0}^T F_{i,0}^c + \delta \omega_{0i,0}^T T_{i,0}^c \right\} \quad (37)$$

must hold. The virtual velocity and the virtual angular velocity of body  $i$  are defined by

$$\delta v_{0i,0} = \frac{\partial v_{0i,0}}{\partial z} \delta z \quad \text{and} \quad \delta \omega_{0i,0} = \frac{\partial \omega_{0i,0}}{\partial z} \delta z \quad (38)$$

where the  $f \times 1$ -vector  $\delta z$  collects the variations of the  $f$  generalized velocities  $\delta z_1, \delta z_2, \dots, \delta z_f$  that are required to describe the motions of the multibody system. The partial derivatives simply named as partial velocities and partial angular velocities may be arranged in the  $3 \times f$ -Jacobian matrices of translation and rotation

$$\frac{\partial v_{0i,0}}{\partial z} = \left[ \frac{\partial v_{0i,0}(y, z)}{\partial z_1}, \frac{\partial v_{0i,0}(y, z)}{\partial z_2}, \dots, \frac{\partial v_{0i,0}(y, z)}{\partial z_f} \right] \quad (39)$$

$$\frac{\partial \omega_{0i,0}}{\partial z} = \left[ \frac{\partial \omega_{0i,0}(y, z)}{\partial z_1}, \frac{\partial \omega_{0i,0}(y, z)}{\partial z_2}, \dots, \frac{\partial \omega_{0i,0}(y, z)}{\partial z_f} \right] \quad (40)$$

Using the Jacobian matrices, the accelerations provided by Eq. (20) can be written as

$$a_{0i,0} = \frac{\partial v_{0i,0}}{\partial z} \dot{z} + a_{0i,0}^R \quad \text{and} \quad \alpha_{0i,0} = \frac{\partial \omega_{0i,0}}{\partial z} \dot{z} + \alpha_{0i,0}^R \quad (41)$$

where  $\dot{z}$  is the time derivative of the vector of generalized velocities and

$$a_{0i,0}^R = \sum_{m=1}^f \frac{\partial v_{0i,0}(y, z)}{\partial y_m} \dot{y}_m \quad \text{and} \quad \alpha_{0i,0}^R = \sum_{m=1}^f \frac{\partial \omega_{0i,0}(y, z)}{\partial y_m} \dot{y}_m \quad (42)$$

abbreviates the remaining terms in the accelerations. By combining Eq. (37) with Eqs. (35) and (36), one is able to put the constraint forces and torques down to dynamic terms and the applied forces and torques. Using the notation in Eqs. (41) and (42), Jourdain's principle reads as

$$\sum_{i=1}^k \left\{ \frac{\partial v_{0i,0}^T}{\partial z} \begin{bmatrix} m_i \frac{\partial v_{0i,0}}{\partial z} \dot{z} + m_i a_{0i}^R - F_{i,0}^a \\ \Theta_{i,0} \frac{\partial \omega_{0i,0}^T}{\partial z} \dot{z} + \Theta_{i,0} \alpha_{0i}^R + \omega_{0i,0} \times \Theta_{i,0} \omega_{0i,0} - T_{i,0}^a \end{bmatrix} \right\} \delta z = 0 \quad (43)$$

The variations of the generalized velocities  $\delta z$  are arbitrary. Hence, the expression in the braces must vanish. The resulting first-order differential equation can be written as

$$M(y) \dot{z} = q(y, z) \quad (44)$$

where the  $f \times f$ -mass-matrix is defined by

$$M(y) = \sum_{i=1}^k \left[ \frac{\partial v_{0i,0}^T}{\partial z} m_i \frac{\partial v_{0i,0}}{\partial z} + \frac{\partial \omega_{0i,0}^T}{\partial z} \Theta_{i,0} \frac{\partial \omega_{0i,0}^T}{\partial z} \right] \quad (45)$$

and the  $f \times 1$ -vector of generalized forces

$$q(y, z) = \sum_{i=1}^k \left[ \frac{\partial v_{0i,0}^T}{\partial z} (F_{i,0}^a - m_i a_{0i,0}^R) + \frac{\partial \omega_{0i,0}^T}{\partial z} (T_{i,0}^a - \Theta_{i,0} \alpha_{0i,0}^R - \omega_{0i,0} \times \Theta_{i,0} \omega_{0i,0}) \right] \quad (46)$$

combines the inertia and gyroscopic forces and torques with the applied forces and torques. The equations of motion result in a set of two first-order ordinary differential equations (ODEs). The definition of generalized velocities which is done by Eq. (17) or in the trivial form by Eq. (19) represent the first set and the dynamic equation defined in Eq. (44) the second one. Usually, a multibody systems contains dynamic force elements too. Then, the set of ODEs

$$\begin{aligned} \dot{y} &= K(y) z \\ M(y) \dot{z} &= q(y, z, s) \\ \dot{s} &= h(s, y, z, u) \end{aligned} \quad (47)$$

describes the dynamics of a general multibody system, where the vectors  $s$  und  $u$  collect the states of the dynamic force elements und the external inputs, like the road roughness. Finally, one will end up in a set of Differential-Algebraic-Equations (DAEs) of index 3

$$\begin{aligned} \dot{y} &= K z \\ M(y) \dot{z} &= q^a + J_g^T \lambda \\ \dot{s} &= h(s, y, z, u) \\ 0 &= g(y) \end{aligned} \quad (48)$$

if only some or none at all constraint forces and torques were removed. In this simple approach,  $q = q^a + q^c$  separates the generalized force vector into parts of applied and constraint generalized forces and torques. According to Lagrange<sup>2</sup> it is possible to reduce the unknown vector of generalized constraint forces and torques via

$$q^c = J_g^T \lambda \quad \text{where} \quad J_g = \frac{dg(y)}{dy} K \quad (49)$$

to the vector of Lagrange multipliers  $\lambda$  that correspond in its dimension with the number of constraint equations and just require the derivative of the constraint equations  $g(y)$  with respect to the vector of generalized coordinates  $y$  and the kinematical matrix  $K$  in addition. Finally, the vector function  $g(y)$  summarizes the (remaining) constraint equations.

The DAE of index 3 in (48) can be reduced step by step to a DAE of index 1. For that purpose the constraint equation is replaced by its time derivatives. Making use of the kinematical differential equation, the first equation in (48), one gets

$$0 = \dot{g} \quad \text{or} \quad 0 = \frac{dg}{dt} = \frac{dg}{dy} \frac{dy}{dt} = \frac{dg}{dy} \dot{y} = \frac{dg}{dy} K z = J_g z \quad (50)$$

In general, the Jacobian of the constraint equations  $J_g$  is not constant, therefore the second derivative results in

$$0 = \ddot{g} \quad \text{or} \quad 0 = \frac{d^2g}{dt^2} = \frac{d}{dt} \left( \frac{dg}{dt} \right) = \frac{d}{dt} (J_g z) = J_g z + J_g \dot{z} \quad (51)$$

The dynamic differential equation, the second equation in (48), delivers

$$\dot{z} = M^{-1} (q^a + J_g^T \lambda) \quad (52)$$

Inserting this relationship into the constraint equation on acceleration level (51) results in

$$0 = J_g z + J_g M^{-1} (q^a + J_g^T \lambda) \quad (53)$$

and yields the Lagrange multipliers as

$$\lambda = - \left( J_g M^{-1} J_g^T \right)^{-1} (J_g M^{-1} q^a + J_g z) \quad (54)$$

Hence, replacing the original constraint equations  $0 = g$  by  $0 = \ddot{g}$  delivers the Lagrange multipliers explicitly and thus reduces the DAEs to

---

<sup>2</sup>Joseph-Louis de Lagrange (25 January 1736–10 April 1813).

$$\begin{aligned}\dot{y} &= K z \\ M(y) \dot{z} &= q^a - J_g^T \left( J_g M^{-1} J_g^T \right)^{-1} \left( J_g M^{-1} q^a + J_g z \right) \\ \dot{s} &= h(s, y, z, u)\end{aligned}\quad (55)$$

This set of equations has the same structure as the ODEs provided in (47). However, the numerical solution requires a special treatment. Besides that, the matrix  $J_g M^{-1} J_g^T$  must be invertible, demanding at least for constraint equations that are free of redundancies.

## 1.7 A Quarter Car Model

**Modeling Concept:** The quarter car model shown in Fig. 17 consists of the chassis, a trailing arm that is rigidly attached to the knuckle, and the wheel. The model represents a quarter car on a hydropulse test rig. That is why, the chassis is supposed to perform vertical motions only. Revolute joints in B and W connect the trailing arm with the chassis and the trailing arm with the wheel. The position of the actuator that supports the wheel is controlled to follow a prescribed displacement time history,  $u = u(t)$ .

A quarter car model is quite a good but surely limited approximation of real vehicle dynamics. So, the simplification that the wheel center W, the center of the knuckle and trailing arm K, and the joint in B are arranged in a straight line will correspond to the overall model quality. In addition, the chassis is supported by a torsional spring and damper combination for the sake of simplicity.

The parameter for a quarter car model that may represent the rear suspension of a small front wheel driven car are listed in Table 1.

**ODE Kinematical Model:** The vertical chassis motion  $z_C$  as well as the rotation angles  $\beta_K$ , and  $\varphi_W$  are sufficient to describe the momentary position and orientation of the  $k = 3$  model bodies chassis, trailing arm with knuckle, and wheel. The vectors

**Fig. 17** Quarter car model with trailing arm suspension

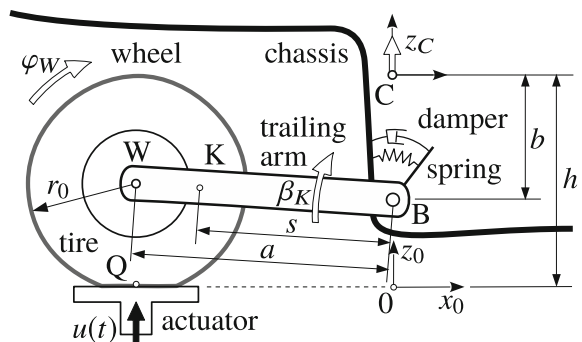


**Table 1** Parameter for the quarter car model

$s = 0.250 \text{ m}$	Joint B to center of knuckle/trailing arm
$a = 0.400 \text{ m}$	Joint B to center of wheel M
$b = 0.310 \text{ m}$	Vertical distance chassis center C to joint B
$h = 0.600 \text{ m}$	Height of chassis center C
$r_0 = 0.305 \text{ m}$	Tire radius
$m_C = 200 \text{ kg}$	Corresponding chassis mass (quarter car)
$m_K = 35 \text{ kg}$	Mass of knuckle/trailing arm
$m_W = 15 \text{ kg}$	Mass of wheel (rim and tire)
$\Theta_K = 0.6 \text{ kg m}^2$	Inertia of knuckle/trailing arm
$\Theta_W = 1.0 \text{ kg m}^2$	Inertia of wheel
$T_S^0 = 1200 \text{ Nm}$	Pre-tension torque in torsional spring
$c_S = 10\,000 \text{ Nm}$	Torsional suspension spring rate
$d_S = 800 \text{ Nm s}$	Torsional suspension damping
$c_x = 180\,000 \text{ Nm s}$	Longitudinal tire stiffness
$c_z = 220\,000 \text{ N/m}$	Vertical tire stiffness
$d_x = 1200 \text{ Ns/m}$	Longitudinal tire damping
$dF_x^0 = 90\,000 \text{ N}/-$	Initial inclination longitudinal force
$v_N = 0.01 \text{ m/s}$	Fictitious velocity

$$r_{0C,0} = \begin{bmatrix} 0 \\ 0 \\ h + z_C \end{bmatrix}, \quad r_{0K,0} = \begin{bmatrix} -s \cos \beta_K \\ 0 \\ h - b + s \cos \beta_K \end{bmatrix}, \quad r_{0W,0} = \begin{bmatrix} -a \cos \beta_K \\ 0 \\ h - b + a \cos \beta_K \end{bmatrix} \quad (56)$$

describe the momentary position and the angles  $\beta_K$ ,  $\varphi_W$  define the rotation of the trailing arm with knuckle and the wheel about the  $y_0$ -axis. A detailed model description, the derivation of the equations of motion, as well as the replacement of this simple torsional spring/damper combination by a point-to-point force element can be found in Rill (2012).

Applying Jourdain's principle the dynamics of this quarter car model is defined by

$$\dot{y} = z \quad \text{and} \quad M \dot{z} = q \quad (57)$$

where  $y$  collects the generalized coordinates  $z_C$ ,  $\beta_K$ ,  $\varphi_W$  and the vector  $z$  defines trivial generalized velocities. The Eqs. (45) and (46) deliver the mass matrix and the vector of the generalized forces and torques as

$$M = \begin{bmatrix} m_C + m_K + m_W & (s m_K + a m_W) \cos \beta_K & 0 \\ (s m_K + a m_W) \cos \beta_K & \Theta_K + s^2 m_K + a^2 m_W & 0 \\ 0 & 0 & \Theta_W \end{bmatrix} \quad (58)$$

$$q = \begin{bmatrix} F_z - (m_C + m_K + m_W) g + (s m_K + a m_W) \sin \beta_K \dot{\beta}_K^2 \\ T_S - (s m_K + a m_W) \cos \beta_K g + a (F_x \sin \beta_K + F_z \cos \beta_K) \\ -r_S F_x \end{bmatrix} \quad (59)$$

The torsional spring damper combination acting at the revolute joint in B generates a torque that can be modeled as a function of the knuckle rotation angle  $\beta_K$  and its time derivative. Assuming linear spring and damper characteristics one gets

$$T_S = c_S \beta_K + d_S \dot{\beta}_K + T_S^0 \quad (60)$$

where  $c_S$  and  $d_S$  name the torsional spring and damper constants and  $T_S^0$  describes the pre-tension torque that determines the steady state position of the trailing arm.

In a first approximation, the vertical tire force is given by

$$F_z = \begin{cases} 0 & \text{if } r_S \geq r_0 \quad (\text{lift off}) \\ c_T (r_0 - r_S) & \text{if } r_S < r_0 \end{cases} \quad (61)$$

where  $c_T$  names the radial tire stiffness and  $r_0$  describes the unloaded tire radius. The loaded tire radius is provided by

$$r_s = h + z_C - b + a \sin(\beta_K) - u(t) \quad (62)$$

where the distances  $a$ ,  $b$  and  $h$  are defined in Fig. 17. According to (34) the longitudinal tire force is defined by

$$F_x = c_x x_e + d_x \dot{x}_e \quad (63)$$

where  $c_x$ ,  $d_x$  describe the stiffness and damping properties of the tire in the longitudinal direction and the internal tire state  $x_e$  is defined by an additional differential equation

$$\dot{x}_e = \frac{-v_{Tx}^* c_x x_e - f_G (v_x - r_D \Omega)}{v_{Tx}^* d_x + f_G} \quad (64)$$

where the dynamic rolling radius may be approximated via  $r_D = \frac{2}{3}r_0 + \frac{1}{3}r_S$  by a weighted combination of the unloaded and loaded tire radius. The global derivative of the generalized tire characteristics can be approximated by the initial inclination of the longitudinal tire characteristics  $f_G \approx dF_x^0$  because no large longitudinal forces will occur in this particular case. The wheel angular velocity is simply given by  $\Omega = \dot{\phi}_W$  and the longitudinal component of the contact point velocity as well as the modified transport velocity are defined by

$$v_x = a \sin \beta_K \dot{\beta}_K \quad \text{and} \quad v_{Tx}^* = |r_D \dot{\phi}_W| + v_N \quad (65)$$

where  $v_N > 0$  is a small fictitious velocity that is introduced to avoid singularities in stand still situations.

Hence, the dynamics of the quarter car model described by (57) and (64) corresponds to the typical set of ODEs defined in (47).

**DAE Model:** Each body is now supposed to move freely in the  $x_0$ - $z_0$ -plane, Fig. 18. Then, the vectors

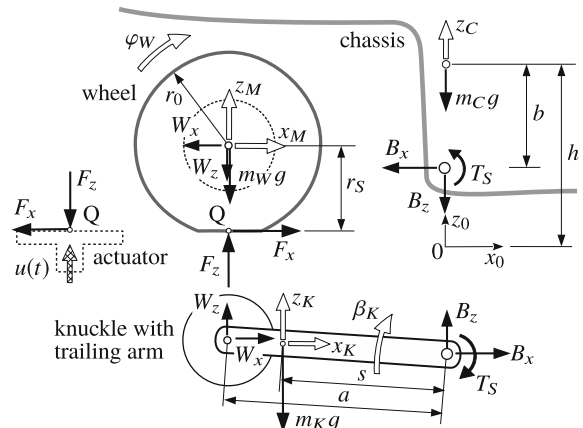
$$\begin{aligned} r_{0C,0} &= \begin{bmatrix} 0 \\ 0 \\ z_C \end{bmatrix}, & r_{0K,0} &= \begin{bmatrix} x_K \\ 0 \\ z_K \end{bmatrix}, & r_{0W,0} &= \begin{bmatrix} x_W \\ 0 \\ z_W \end{bmatrix} \end{aligned} \quad (66)$$

simply define the position of the chassis center C, the knuckle center K, and the wheel center W. The chassis is still supposed to perform vertical motions only and the angles  $\beta_K$  and  $\varphi_W$  describe as before the rotations of the knuckle and the wheel about the  $y_0$ -axis. The equations of motion will then read as

$$\begin{aligned} m_C \ddot{z}_C &= -m_C g - B_z \\ m_K \ddot{x}_K &= B_x + W_x \\ m_K \ddot{z}_K &= -m_K g + B_z + W_z \\ \Theta_K \ddot{\beta}_K &= T_S - B_x s \sin \beta_K - B_z s \cos \beta_K + W_x w \sin \beta_K + W_z w \cos \beta_K \\ m_W \ddot{x}_W &= F_x - W_x \\ m_W \ddot{z}_W &= -m_W g + F_z - W_z \\ \Theta_W \ddot{\varphi}_W &= -r_S F_x \end{aligned} \quad (67)$$

where the abbreviation  $w = a - s$  describes the distance from the knuckle center K to the wheel center W and  $B_x, B_z, W_x, W_z$  denote the reaction forces acting in the

**Fig. 18** Free body diagram of quarter car model



revolute joints where the knuckle is attached to the chassis and the wheel to the knuckle.

Collecting the generalized coordinates in the vector

$$\mathbf{y} = [z_C \ x_K \ z_K \ \beta_K \ x_W \ z_W \ \varphi_W]^T \quad (68)$$

and defining by

$$\dot{y} = z \quad (69)$$

trivial generalized velocities makes it possible to describe the dynamics of the quarter car model by the matrix differential equation

$$\mathbf{M}\dot{\mathbf{z}} = q^a + q^c \quad (70)$$

where

$$\mathbf{M} = \text{diag} [m_C \ m_K \ m_K \ \Theta_K \ m_W \ m_W \ \Theta_W] \quad (71)$$

defines the mass matrix and

$$q^a = [-m_C g \ 0 \ -m_K g \ T_S \ F_x \ -m_W g + F_z \ -r_S F_x]^T \quad (72)$$

collects the applied forces.

However, the differential equation (70) can not be solved because the reaction forces  $B_x$ ,  $B_z$ ,  $W_x$ ,  $W_z$  are not defined or known yet. In this particular case the constraint forces were modeled explicitly. This is possible for rather simple models but extremely cumbersome for complex models. The use of Lagrange multipliers will be more appropriate then. At first the constraint equations are required. A revolute joint that connects body  $i$  to body  $j$  at a specific point prevents body  $i$  to perform any displacement relative to body  $j$  at this very point. Hence, the revolute joints in B and W deliver the constraint equations as

$$\begin{aligned} 0 &= x_K + s \cos \beta_K \\ 0 &= z_K - s \sin \beta_K - (z_C - b) \quad \Rightarrow \quad 0 = g(y) \\ 0 &= x_K - w \cos \beta_K - x_W \\ 0 &= z_K + w \sin \beta_K - z_W \end{aligned} \quad (73)$$

where the abbreviation  $w = a - s$  was used again and  $a$ ,  $s$ ,  $b$ ,  $h$  are constant model parameter defined in Fig. 17. Taking (68) into account, the partial derivative of the constraint equations yields the Jacobian as

$$J_g = \frac{dg}{dy} = \begin{bmatrix} 0 & 1 & 0 & -s \sin \beta_K & 0 & 0 & 0 \\ -1 & 0 & 1 & -s \cos \beta_K & 0 & 0 & 0 \\ 0 & 1 & 0 & w \sin \beta_K & -1 & 0 & 0 \\ 0 & 0 & 1 & w \cos \beta_K & 0 & -1 & 0 \end{bmatrix} \quad (74)$$

The trivial choice of generalized velocities realized in (69) results in a kinematical matrix  $K$  that simply equals the matrix of identity. Then Eq. (49) delivers the vector of the generalized constraint forces as

$$q^c = J_g^T \lambda = \begin{bmatrix} 0 & -1 & 0 & 0 \\ 1 & 0 & 1 & 0 \\ 0 & 1 & 0 & 1 \\ -s \sin \beta_K & -s \cos \beta_K & w \sin \beta_K & w \cos \beta_K \\ 0 & 0 & -1 & 0 \\ 0 & 0 & 0 & -1 \\ 0 & 0 & 0 & 0 \end{bmatrix} \lambda \quad (75)$$

where  $\lambda$  denotes the Lagrange multipliers. In this particular and in similar cases, the Lagrange multipliers  $\lambda$  will coincide with the constraint forces in  $B$  and  $W$ . Depicting the vector of the generalized forces from (67) and rearranging the terms results in

$$q^c = \begin{bmatrix} 0 & -1 & 0 & 0 \\ 1 & 0 & 1 & 0 \\ 0 & 1 & 0 & 1 \\ -s \sin \beta_K & -s \cos \beta_K & w \sin \beta_K & w \cos \beta_K \\ 0 & 0 & -1 & 0 \\ 0 & 0 & 0 & -1 \\ 0 & 0 & 0 & 0 \end{bmatrix} \begin{bmatrix} B_x \\ B_z \\ W_x \\ W_z \end{bmatrix} \quad (76)$$

which compared to (75) delivers by inspection  $\lambda = [B_x \ B_z \ W_x \ W_z]^T$ . In more general cases, the Lagrange multipliers  $\lambda$  will just correspond with the constraint forces and torques but will not necessarily equal them.

The torque  $T_S$  generated by the torsional spring damper combination, the vertical tire force  $F_z$ , and the dynamic tire force in longitudinal direction  $F_x$  are still provided by (60), (61) and (63) in combination with (64). But the loaded tire radius is now simply given by

$$r_s = z_W - r_0 - u(t) \quad (77)$$

and the longitudinal component of the contact point velocity as well as the modified transport velocity are defined by

$$v_x = \dot{x}_W \quad \text{and} \quad v_{Tx}^* = |r_D \dot{\phi}_W| + v_N \quad (78)$$

where  $\Omega = \dot{\phi}_W$  provides as before the angular wheel velocity and the dynamic tire radius  $r_D$  was defined in the text subsequent to Eq. (64).

Hence, the dynamics of the quarter car model described by (69), (67), (64), and (74) represents a typical set of DAEs defined in (48).

A index reduction makes it possible to transfer DAEs into a set of ODEs. However, the calculation of the Lagrange multipliers via (54) will then require the time derivative of the Jacobian  $J_g$  in addition. The Jacobian  $J_g$  for the quarter car model is provided by (74). Its time derivative simply results in

$$\frac{dJ_g}{dt} = \begin{bmatrix} 0 & 0 & 0 & -s \cos \beta_K \dot{\beta}_K & 0 & 0 & 0 \\ 0 & 0 & 0 & s \sin \beta_K \dot{\beta}_K & 0 & 0 & 0 \\ 0 & 0 & 0 & w \cos \beta_K \dot{\beta}_K & 0 & 0 & 0 \\ 0 & 0 & 0 & -w \sin \beta_K \dot{\beta}_K & 0 & 0 & 0 \end{bmatrix} \quad (79)$$

**Free Body Model:** The equations of motion provided by (67) hold for a system of free bodies, that consists here of the chassis, the trailing arm with knuckle and the wheel. The bodies were assembled to a quarter car by constraints that reduce the number of degrees of freedom in case of the kinematical ode approach or require additional constraint equations in case of the DAE model. But there is also another model approach possible if joints and links are modeled by introducing real or fictitious compliances.

Within this planar quarter car model the revolute joints in B and W may be supplemented by bushings providing forces in longitudinal and vertical directions that act opposite to the bushing displacements. Introducing the parameter  $c_{Bx}$ ,  $c_{Bz}$ ,  $c_{Wx}$ ,  $c_{Wz}$  that describe the stiffness properties of the bushings in B and W in longitudinal and vertical directions, the bushing forces will simply be provided by

$$F_B = \begin{bmatrix} B_x \\ B_z \\ W_x \\ W_z \end{bmatrix} = - \begin{bmatrix} c_{Bx} & 0 & 0 & 0 \\ 0 & c_{Bz} & 0 & 0 \\ 0 & 0 & c_{Wx} & 0 \\ 0 & 0 & 0 & c_{Wz} \end{bmatrix} g \quad (80)$$

where  $g = g(y)$  defined by the constraint equation in (73) provides the bushing displacements. Adding appropriate damping effects is straight forward and will just require the time derivative  $\dot{g}(y)$  that Eq. (50) defines in general. Finally, the vector of the generalized “constraint” forces will then be given by

$$q^c = J_g^T F_B \quad (81)$$

which is the result of comparing Eq. (76) with Eq. (75).

However, many joints and links are very stiff in practice. That is why, this rather simple approach may cause severe problems within the numerical solution. In addition, if the stiffness of a bushing is not known, an estimated bushing stiffness may cause unrealistic and unpredictable dynamic effects.

## 2 Numerical Methods

### 2.1 Ordinary Differential Equations

**Overview:** Ordinary differential equations (ODEs) like the ones defined in (47) are usually transferred to a state equation in the form of

$$\dot{x} = f(t, x) \quad (82)$$

where the state vector  $x$  collects the generalized coordinates  $y$  and velocities  $z$  as well as additional states  $s$ . For the numerical time integration of ordinary differential equations (ODEs) numerous methods with one-step and multi-step algorithms are known, see e.g. Nørsett et al. (2008). The commercial software package Matlab® for instance offers seven solvers:

**ode23** is a one-step solver. Based on an explicit Runge-Kutta (2,3) pair of Bogacki and Shampine. It may be more efficient than ode45 at crude tolerances and in the presence of mild stiffness.

**ode45** is a one-step solver. Based on an explicit Runge-Kutta (4,5) formula, the Dormand-Prince pair. It is a one-step solver—in computing, it needs only the solution at the immediately preceding time point. In general, ode45 is the best function to apply as a “first try” for most problems.

**ode113** Variable order Adams-Basforth-Moulton PECE solver. It may be more efficient than ode45 at stringent tolerances and when the ODE function is particularly expensive to evaluate. ode113 is a multistep solver—it normally needs the solutions at several preceding time points to compute the current solution.

**ode15s** Variable-order solver based on the numerical differentiation formulas (NDFs). Optionally it uses the backward differentiation formulas, BDFs, (also known as Gear’s method). Like ode113, ode15s is a multistep solver. If you suspect that a problem is stiff or if ode45 failed or was very inefficient, try ode15s.

**ode23s** Based on a modified Rosenbrock formula of order 2. Because it is a one-step solver, it may be more efficient than ode15s at crude tolerances. It can solve some kinds of stiff problems for which ode15s is not effective.

**ode23t** An implementation of the trapezoidal rule using a “free” interpolant. Use this solver if the problem is only moderately stiff and you need a solution without numerical damping.

**ode23tb** An implementation of TR-BDF2, an implicit Runge-Kutta formula with a first stage that is a trapezoidal rule step and a second stage that is a backward differentiation formula of order 2. Like ode23s, this solver may be more efficient than ode15s at crude tolerances.

The performance of these solvers were benchmarked in Rill and Schiehlen (2009) on a complex planar model. It turned out, that for low accuracies and/or real time simulations a semi-implicit Euler code is an interesting alternative. Applied to a set of ODEs as defined in (47) one gets

$$\begin{aligned}
 s^{k+1} &= s^k + \Delta t h(s^k, y^k, z^k, u^{k+1}) \\
 z^{k+1} &= z^k + \Delta t M^{-1}(y^k) q(y^k, z^k, s^{k+1}) \\
 y^{k+1} &= y^k + \Delta t K(y^k) z^{k+1}
 \end{aligned} \tag{83}$$

where  $\Delta t$  denotes the integration step size and the superscripts  $k$  and  $k+1$  characterize the states at  $t$  and  $t + \Delta t$  respectively. The input signals  $u^{k+1} = u(t + \Delta t)$  are computed here at time  $t + \Delta t$  in order to achieve a slightly more implicit touch. The semi-implicit character comes from the multi-tiered algorithm that makes it possible to use the implicit states  $s^{k+1}$  and  $z^{k+1}$  in the subsequent equations. This implicit terms improve the stability of the integration formulas a lot.

**Euler Semi-Implicit Versus ode23:** The semi-implicit Euler integration formula (83) was applied to the quarter car model. The predefined movements of the hydraulic piston  $u = u(t)$  represent the vertical excitation of the wheel when a vehicle is driven with a constant velocity of  $v = 100$  km/h across a country road. The simulation results are plotted in Fig. 19 where the lower right graph shows the the piston movements  $u = u(t)$  that represent the road profil. To assess the quality of this simple integration formula the results are compared to a simulation performed with the Matlab solver ode23. The default accuracy of the ode23 solver was reduced to  $ABSTOL = 0.0001$  and  $RELTOL = 0.001$  in order to achieve a “fair” comparison. In particular, the vertical chassis motion  $z_C$  and the rotation of the trailing arm  $\beta_K$  are in

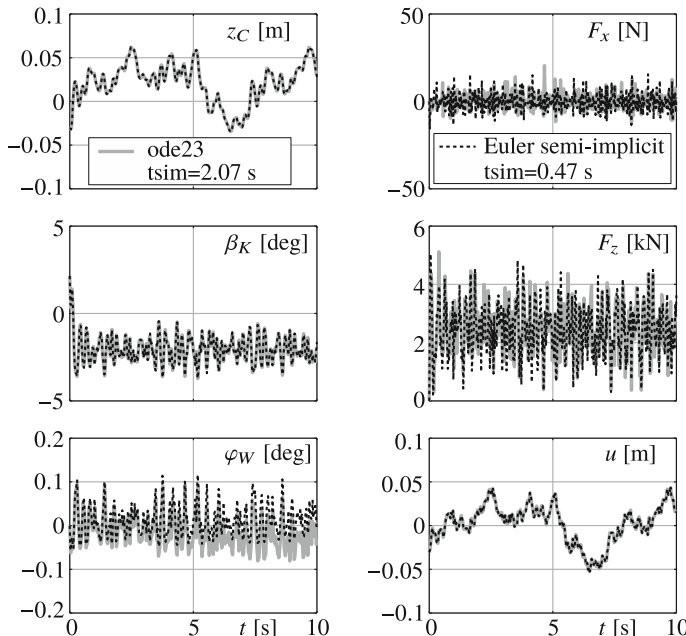
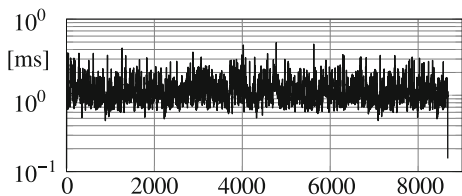


**Fig. 19** Semi-implicit Euler compared to ode23

**Fig. 20** Integration stepsizes automatically chosen by ode23



very good conformity. The stepsize of the ode23 solver is automatically adjusted in order to meet the error tolerances. Figure 20 shows, that its mean value is slightly larger than 1 millisecond (ms). That is why, the stepsize of the semi-implicit Euler formula was fixed to 1 ms. As the accuracy of the semi-implicit Euler formulas is limited, the time histories of the wheel rotation  $\varphi_W$  and the tire forces  $F_x$  and  $F_z$  deviate a little from the corresponding signals calculated with the ode23 solver. But, the semi-implicit Euler generates the results four times faster than the ode23 solver.

**Stiff Problems:** At the end of Sect. 1.7 a quarter car model is presented that describes the bearings in B and W by compliant bushings rather than by ideal revolute joints. Many rear wheel suspension systems based on a trailing arm assemble a bushing at B that provides a significant compliance in longitudinal direction. This “comfort” bearing allows the wheel to run more smoothly across bumps. If both bearings in B and W are modeled with compliant bushings then a simple extension of the DAE quarter car model delivers the corresponding equations of motion.

The stiffness properties of the bearing in B listed in Table 2 correspond to a real layout. The stiffness properties for the bushing in W are chosen significantly larger and equal in the lateral and the vertical directions. Corresponding to the stiffness properties the bushing displacements in B and W differ a lot in longitudinal direction ( $x$ -displacements), left graph in Fig. 21. In total, the vertical excitation of the quarter car model results in bushing displacements in  $z$ -direction that are an order of magnitude greater than the displacements in  $x$ -direction. The hard bushings in W result in “stiff” differential equations that require a special treatment while solved numerically. Figure 22 shows the results of the stiff free body model generated with the stiff Matlab solver ode23tb compared to the results of the kinematical model produced with the ode23 solver.

The longitudinal compliance in Bushing B results in larger variations of the longitudinal force  $F_x$  that infect the wheel rotation angle  $\varphi_W$  in addition. Differences in the vertical chassis motion  $z_C$  and the rotation of the trailing arm  $\beta_K$  are hardly

**Table 2** Stiffness properties of compliant bushings in B and W

$c_{Bx} = 500\,000 \text{ N/m}$	Bushing B: longitudinal stiffness
$c_{Bz} = 200\,000 \text{ N/m}$	Bushing B: vertical stiffness
$c_{Wx} = 5\,000\,000 \text{ N/m}$	Bushing W: longitudinal stiffness
$c_{Wz} = 5\,000\,000 \text{ N/m}$	Bushing W: vertical stiffness

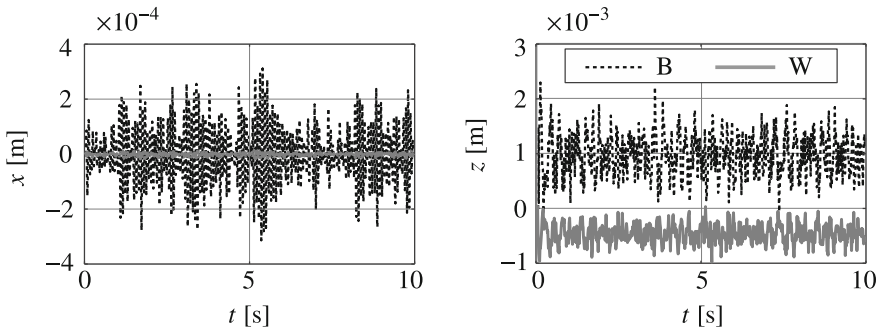


**Fig. 21** Bushing displacements  $B_x$ ,  $W_x$  and  $B_z$ ,  $W_z$  while running across a country road at a velocity of  $v = 100$  km/h

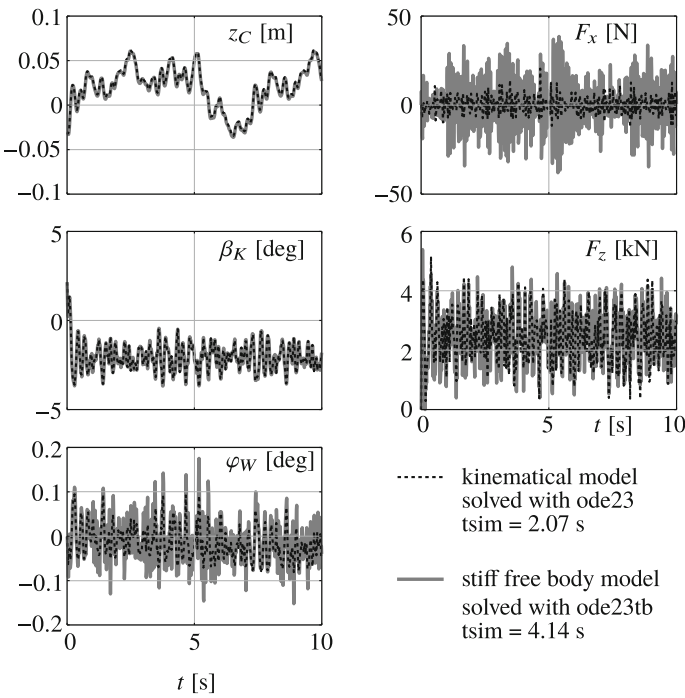


**Fig. 22** Model with bushings compared to kinematical model

noticeable. However, the implicit solver ode23tb needs double the computing time of the explicit ode23 solver.

## 2.2 Differential Algebraic Equations

**General Remarks:** As shown in Sect. 1.6 a system of differential algebraic equations (DAEs) can be reduced to a set of ordinary differential equations (ODEs). If the resulting ODEs are summarized in the state equation (82), a large variety of solvers<sup>3</sup> can be applied, then. Sophisticated solvers like DASSL<sup>4</sup> start from the more general residual form of the state equation

$$\phi(t, x, \dot{x}) = 0 \quad (84)$$

that corresponds for  $\phi(t, x, \dot{x}) = \dot{x} - f(t, x)$  with (82), but optionally allows the use of very efficient residual formalisms. The commercial software package SIMPACK uses the DASSL based integrator SODASRT as the default solver.

An extensive overview of different solvers and applications in multibody dynamics can be found in Arnold et al. (2011).

A direct index 3 solver that processes the DAEs provided by (48) is implemented in the commercial software packages MSC.ADAMS and RecurDyn. This implicit solver called HHT or g-alpha is described in Negruț et al. (2006).

**Index Reduction:** Applying the index reduction technique to the quarter car model produces the results plotted in Fig. 23. The solver ode23 takes now more time because the index reduction of the DAEs to the ODEs were performed by simply executing all the matrix operations provided in Eq. (55) whereas the ODEs of the kinematical model were provided as analytical expressions. Again, the vertical chassis motion  $z_C$  and the rotation of the trailing arm  $\beta_K$  are in very good conformity. But, the time history of the wheel rotation  $\varphi_W$  shows a tendency to drift off from the kinematical solution when time goes on. That drift is the result of the index reduction where the original constraints defined by  $g = 0$  were replaced by  $\dot{g} = 0$ . So, the numerical solver controlling the error of the constraints at acceleration level will automatically result in an increasing constraint violation on position level due to numerical round-off errors, Fig. 24. Of course, the magnitude of the drift can be reduced by more stringent error tolerances. But it cannot be avoided in general by this simple DAE to ODE conversion.

There are several methods available to reduce or avoid this drift. Two of them are discussed in the following, Gear et al. (1985) and Baumgarte (1972).

**Gear-Gupta-Leimkuhler Stabilization:** Extending the DAEs in Eq. (48) with fictitious Lagrange multipliers  $\mu$  in the kinematical differential equation and adding the constraint equation on velocity level results in a DAE of index 2

---

<sup>3</sup>Several free solvers are provided at <http://www.unige.ch/~hairer/software.html>.

<sup>4</sup>freely available at <http://www.netlib.org/ode/>.

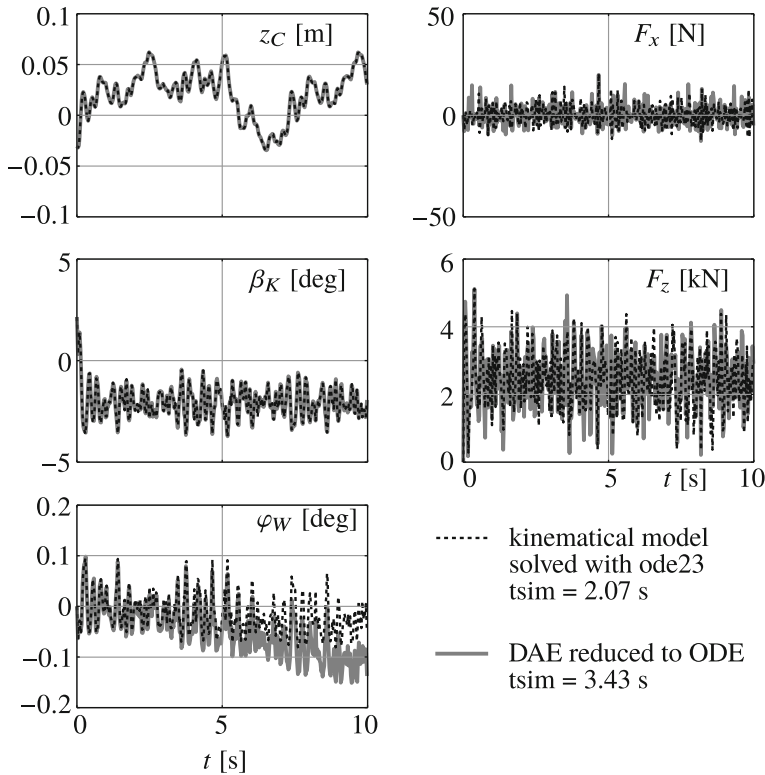


**Fig. 23** DAE model reduced to ODE compared to kinematical model

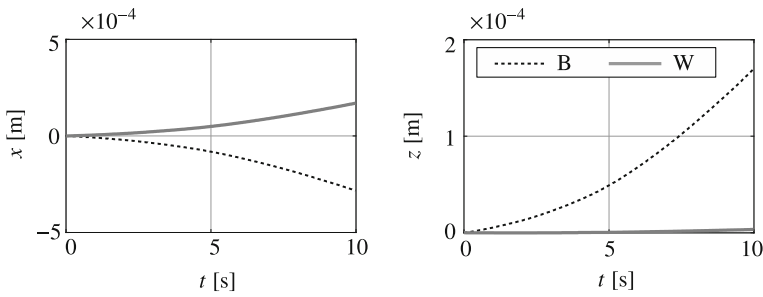


**Fig. 24** Constraint violations in solution of DAE reduced to ODE

$$\begin{aligned}
\dot{y} &= K \left( z + J_g^T \mu \right) \\
M(y) \dot{z} &= q^a + J_g^T \lambda \\
\dot{s} &= h(s, y, z, u) \\
0 &= g(y) \\
0 &= \dot{g}(y)
\end{aligned} \tag{85}$$

Now, the constraint equation on velocity level results in

$$\dot{g} = \frac{dg}{dy} \dot{y} = \frac{dg}{dy} K \left( z + J_g^T \mu \right) = J_g \left( z + J_g^T \mu \right) = 0 \tag{86}$$

which immediately delivers the fictitious Lagrange multipliers as

$$\mu = - \left( J_g J_g^T \right)^{-1} J_g z \tag{87}$$

A index reduction of (85) finally results in a set of ordinary differential equations (ODEs) that in extension to (55) are provided now by

$$\begin{aligned}
\dot{y} &= \left( K - \left( J_g J_g^T \right)^{-1} J_g \right) z \\
M(y) \dot{z} &= q^a - J_g^T \left( J_g M^{-1} J_g^T \right)^{-1} \left( J_g M^{-1} q^a + J_g z \right) \\
\dot{s} &= h(s, y, z, u)
\end{aligned} \tag{88}$$

This slight modification hardly increases the computing time but results in a much smaller drift, Fig. 25. Even after  $t = 10$  s simulation time the constraint violation is below  $5 \times 10^{-7}$  m which in comparisson to Fig. 24 is a reduction of three orders of magnitude. Now, the constraint equation on velocity level  $\dot{g} = 0$  are controlled by the solver too. Of course the overall drift cannot be avoided by this technique completely.

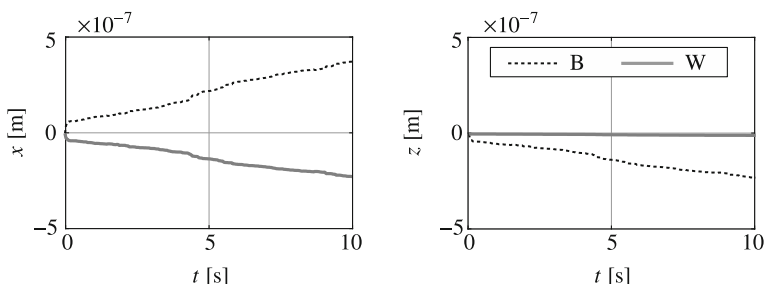


**Fig. 25** Drift in constraints with Gear-Gupta-Leimkuhler stabilization

But, more stringent error tolerances or more sophisticated solvers will produce in most cases neglectable remaining drifts in the constraint equations.

**Baumgarte Stabilization:** In this approach the constraint equation on acceleration level provided by (51) is extended by penalty terms that are proportional to the constraint equation on velocity and position level

$$\ddot{g} + \alpha \dot{g} + \beta g = 0 \quad (89)$$

where  $\alpha$  and  $\beta$  serve as weighting coefficients. Finding appropriate values for  $\alpha$  and  $\beta$  is the problem in this approach. But, Eq. (89) has the form of a single mass oscillator. By introducing the undamped frequency  $\omega_0$  and the viscous damping  $\zeta$  Eq. (89) can be written as

$$\ddot{g} + 2\zeta\omega_0\dot{g} + \omega_0^2 g = 0 \quad (90)$$

So, the constraint equations will perform damped oscillation about the steady state solution that is defined by the original constraint equation  $g(y) = 0$ . From a practical point of view, this oscillations should be damped properly. A viscous damping rate of  $\zeta = 0.5$  will grant an optimal decay of the oscillations. To avoid problems in the numerical solution, the undamped frequency should be choosen not too high, because then the set of the resulting ordinary differential equations will become stiff.

Usually, the multibody approach to vehicle dynamics is valid up to frequencies of 20 to 30 Hz. That is why, besides the viscoous damping of  $\zeta = 0.5$ , the undamped frequency of  $\omega_0 = 2\pi \cdot 30 \text{ Hz} = 188.5 \text{ rad/s}$  was choosen for the Baumgarte stabilization in the case of the quarter car model.

Now, the time histories of the vertical chassis displacement  $z_C$ , the rotation of the trailing arm  $\beta_K$ , as well as the rotation of the wheel  $\varphi$  are in very good conformity to the results of the kinematical model, Fig. 26. Only small differences show up in the time histories of the tire forces  $F_x$  and  $F_z$ .

As can be seen from Fig. 27, the drift in the constraints is for sure sufficient small and remains small. The Baumgarte simulation with appropriate stabilization parameter has nearly no influence on the computing time and is therefor a good choice for vehicle simulations.

## 2.3 Real-Time-Simulations

Using a modified implicit Euler algorithm makes it possible to solve the dynamic equations for vehicles in real time even if axle suspensions with compliances and dry friction in the damper elements are taken into consideration. Real-time-simulations of large vehicle systems are possible too, Rill (1997), Rill and Chucholowski (2005a), and Rill (2006b).

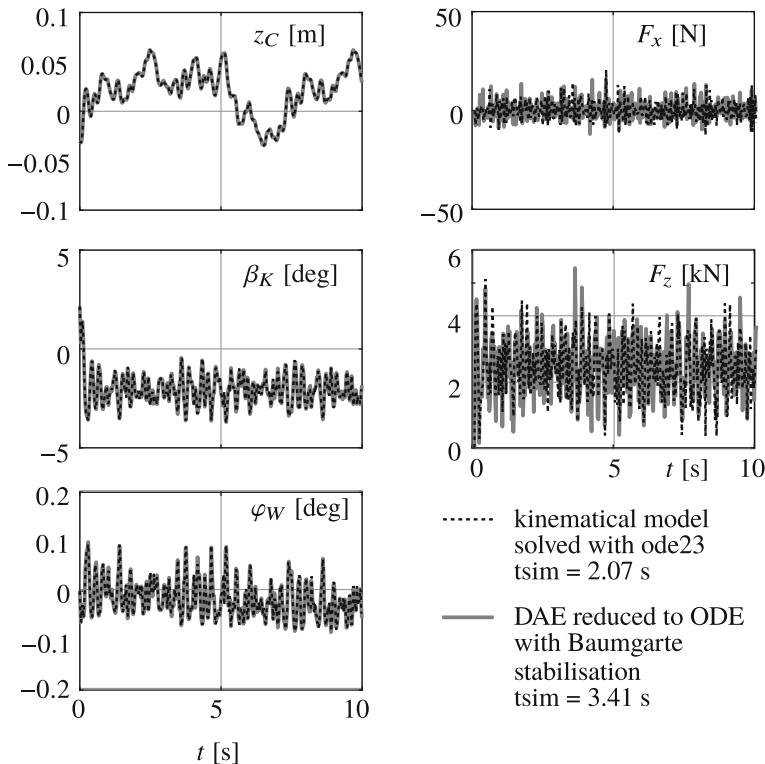


**Fig. 26** Baumgarte stabilization compared to kinematical model

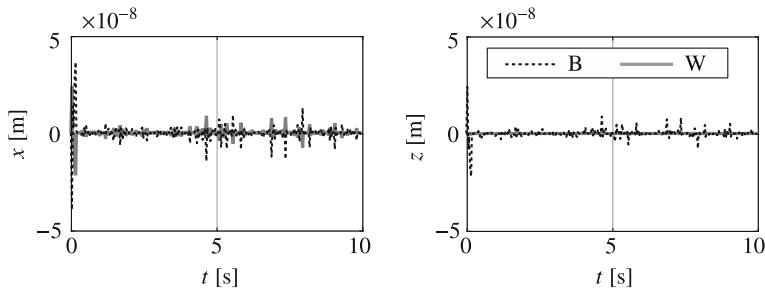


**Fig. 27** Drift in constraints with Baumgarte stabilization

### 3 A Three-Dimensional Vehicle Model

#### 3.1 Model Structure

The vehicle framework of a fully three-dimensional vehicle model consists at least of  $k = 9$  rigid bodies: four knuckles, four wheels, and the chassis, Fig. 28. The vehicle-fixed axis system  $V$  is located now in the middle  $F$  of the front wheel centers. As before, the  $x_V$ -axis points forward, the  $y_V$ -axis to the left, and the  $z_V$ -axis upward.

#### 3.2 Position and Orientation

According to Sect. 1.2 the momentary position and orientation of the vehicle-fixed coordinate system  $V$  with respect to the inertial frame  $0$  is defined by the position vector

$$\mathbf{r}_{0F,0} = [x \ y \ z]^T \quad (91)$$

expressed in the inertial frame  $0$  and the rotation matrix

$$A_{0V} = \begin{bmatrix} c_\psi & -s_\psi & 0 \\ s_\psi & c_\psi & 0 \\ 0 & 0 & 1 \end{bmatrix} \begin{bmatrix} c_\theta & 0 & s_\theta \\ 0 & 1 & 0 \\ -s_\theta & 0 & c_\theta \end{bmatrix} \begin{bmatrix} 1 & 0 & 0 \\ 0 & c_\phi & -s_\phi \\ 0 & s_\phi & c_\phi \end{bmatrix} \quad (92)$$

that is defined by a sequence of elementary rotations about the corresponding  $z$ -  $y$ - and  $x$ -axes. Abbreviations like  $c_\psi = \cos \psi$  and  $s_\psi = \sin \psi$  were used to shorten the expressions. The three components  $x$ ,  $y$ ,  $z$  of the position vector  $\mathbf{r}_{0F,0}$ , and the three rotation angles  $\phi$ ,  $\theta$ ,  $\psi$  define a first set of generalized coordinates.

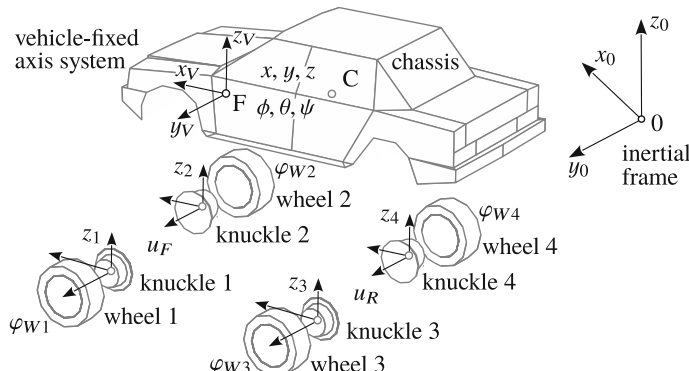


**Fig. 28** Modell bodies of a three-dimensional vehicle model

Now, the position of the chassis center C and the orientation of the chassis are simply given by

$$r_{0C,0} = r_{0F,0} + A_{0V} r_{FC,V} \quad \text{and} \quad A_{0C} = A_{0V} \quad (93)$$

where the vector  $r_{FC,V}$ , that describes the position of the chassis center relative to the vehicle-fixed axis system, is constant and defined by the mass distribution of the chassis.

Each wheel is supposed to be fully balanced. Then, its center is located on the rotation axis. In addition, it is assumed that the center of the corresponding knuckle will be sufficiently close by or will even coincide with the wheel center. As a consequence, the position of each knuckle, and simultaneously of each wheel, is defined by the vector

$$r_{0i,0} = r_{0F,0} + A_{0V} r_{Fi,V}, \quad i = 1(1)4 \quad (94)$$

If the rotation matrices  $A_{Vi}$ ,  $i = 1(1)4$  describe the orientation of each knuckle-fixed axis system relative to the vehicle-fixed axis system, then the rotation matrices

$$A_{0i} = A_{0V} A_{Vi}, \quad i = 1(1)4 \quad (95)$$

will define their orientation with respect to the earth-fixed axis system. A purely kinematic suspension model describes the position and orientation of each knuckle as a function of the jounce and rebound motion as well as the steering motion. The vertical motion  $z_i$  of each knuckle  $i = 1(1)4$  relative to the chassis may be used to characterize the jounce and rebound motion.

Assuming a rack and pinion steering system at both axles, the rack movements  $u_F$  and  $u_R$  at the front and rear axle will fully describe the steering motion at the corresponding axle. Then, the position and orientation of each knuckle and wheel center relative to the vehicle-fixed axis system are defined by

$$r_{Fi,V} = r_{Fi,V}(z_i, u_i), \quad A_{Vi} = A_{Vi}(z_i, u_i), \quad i = 1(1)4 \quad (96)$$

where  $u_1 = u_2 = u_F$  and  $u_3 = u_4 = u_R$  denote the rack displacements at the front and the rear axle respectively.

Finally, the angles  $\varphi_{Wi}$ ,  $i = 1(1)4$  describe the rotation of each wheel relative to the corresponding knuckle.

The generalized coordinates, describing the position and orientation of the  $k = 9$  bodies are now collected in the  $16 \times 1$  position vector

$$\mathbf{y} = [x, y, z, \phi, \theta, \psi, z_1, z_2, u_F, z_3, z_4, u_R, \varphi_{W1}, \varphi_{W2}, \varphi_{W3}, \varphi_{W4}]^T \quad (97)$$

### 3.3 Velocities

Expressing the absolute velocity and the absolute angular velocity of the vehicle-fixed axis system in this axis system results in

$$v_{0F,V} = A_{0V}^T \dot{r}_{0F,0} = A_{0V}^T \begin{bmatrix} \dot{x} \\ \dot{y} \\ \dot{z} \end{bmatrix} \quad (98)$$

$$\begin{aligned} \omega_{0V,V} &= \begin{bmatrix} \dot{\phi} \\ 0 \\ 0 \end{bmatrix} + A_\phi^T \left\{ \begin{bmatrix} 0 \\ \dot{\theta} \\ 0 \end{bmatrix} + A_\theta^T \begin{bmatrix} 0 \\ 0 \\ \dot{\psi} \end{bmatrix} \right\} \\ &= \begin{bmatrix} 1 & 0 & -\sin \theta \\ 0 & \cos \phi & \sin \phi \cos \theta \\ 0 & -\sin \phi \cos \phi \cos \theta & \end{bmatrix} \begin{bmatrix} \dot{\phi} \\ \dot{\theta} \\ \dot{\psi} \end{bmatrix} = K_V \begin{bmatrix} \dot{\phi} \\ \dot{\theta} \\ \dot{\psi} \end{bmatrix} \end{aligned} \quad (99)$$

where the components of  $v_{0F,V}$  and  $\omega_{0V,V}$  will be used as generalized velocities further on. As a consequence, the absolute velocity and the angular velocity of the chassis are simply defined by

$$v_{0C,V} = v_{0F,V} + \omega_{0V,V} \times r_{FC,V} \quad \text{and} \quad \omega_{0C,V} = \omega_{0V,V} \quad (100)$$

The time derivative of Eq. (94) provides the velocities of the knuckle and wheel centers as

$$\underbrace{\dot{r}_{0i,0}}_{v_{0i,0}} = \underbrace{\dot{r}_{0F,0}}_{v_{0F,0}} + \omega_{0V,0} A_{0V} r_{Fi,V} + A_{0V} \dot{r}_{Fi,V}, \quad i = 1(1)4 \quad (101)$$

The transformation into the vehicle-fixed axis system V yields

$$v_{0i,V} = v_{0F,V} + \omega_{0V,V} r_{Fi,V} + \dot{r}_{Fi,V}, \quad i = 1(1)4 \quad (102)$$

where the velocity state of the vehicle-fixed axis system, characterized by  $v_{0F,V}$  and  $\omega_{0V,V}$ , is defined in Eqs. (98) and (99). The time derivatives of the position vectors provided by Eq. (96) result in

$$\dot{r}_{Fi,V} = \frac{\partial r_{Fi,V}}{\partial z_i} \dot{z}_i + \frac{\partial r_{Fi,V}}{\partial u_i} \dot{u}_i = t_{zi,V} \dot{z}_i + t_{ui,V} \dot{u}_i \quad (103)$$

where  $t_{zi,V}$  and  $t_{ui,V}$ ,  $i = 1(1)4$  abbreviate the corresponding partial velocities and  $\dot{u}_1 = \dot{u}_2 = \dot{u}_F$  as well as  $\dot{u}_3 = \dot{u}_4 = \dot{u}_R$  name the time derivatives of the rack displacements. Similary, the angular velocities of the knuckles may be written as

$$\omega_{0Ki,V} = \omega_{0V,V} + d_{zi,V} \dot{z}_i + d_{ui,V} \dot{u}_i, \quad i = 1(1)4 \quad (104)$$

where  $d_{zi,V}$  and  $d_{ui,V}$ ,  $i = 1(1)4$  abbreviate the corresponding partial angular velocities. Finally, the absolute angular velocity of each wheel is given by

$$\omega_{0Wi} = \omega_{0V,V} + d_{zi,V} \dot{z}_i + d_{ui,V} \dot{u}_i + A_{Vi} e_{yWi,i} \dot{\phi}_{Wi}, \quad i = 1(1)4 \quad (105)$$

where the unit vectors  $e_{yWi,i}$ ,  $i = 1(1)4$ , describe the orientation of the wheel rotation axis in the design position. They are defined by a wheel alignment point or via the toe and the camber angles respectively.

The partial velocities and the partial angular velocities of the vehicle model consisting of  $k = 9$  model bodies are collected in the Tables 3 and 4, where  $I$  denotes the  $3 \times 3$  matrix of identity, and the cross-products in the velocity equations are substituted via  $\omega \times r = -r \times \omega = -\tilde{r}\omega = \tilde{r}^T\omega$  by multiplication with the corresponding skew symmetric matrices. In this model approach it is assumed that the centers of each knuckle and wheel will coincide. That is why knuckle and wheel are summarized to one body in Table 3. The components  $v_x$ ,  $v_y$ ,  $v_z$  of the velocity  $v_{0F,V}$  and the components  $\omega_x$ ,  $\omega_y$ ,  $\omega_z$  of the angular velocity  $\omega_{0V,V}$ ; the time derivatives of vertical wheel center displacements  $\dot{z}_1$  to  $\dot{z}_4$ ; the time derivatives of the lateral rack movements  $\dot{u}_F$  and  $\dot{u}_R$  as well as the wheel angular velocities  $\dot{\phi}_{Wi}$ ,  $i = 1(1)4$  are used as generalized velocities here. The three-dimensional vehicle model then has  $f = 3 + 3 + 4 + 2 + 4 = 16$  degrees of freedom. All partial velocities and all inertia tensors are expressed in the vehicle-fixed reference frame.

The partial velocities and the partial angular velocities can be calculated analytically as done in Sect. 3.5 for the multi-link axle suspension. Alternatively, the position and orientation of each knuckle may be provided via look-up tables. A spline interpolation will then provide the partial velocities too.

### 3.4 Accelerations

Now, the absolute acceleration of the chassis, expressed in the vehicle-fixed axis system, is obtained as

$$a_{0C,V} = \dot{v}_{0F,V} + \dot{\omega}_{0F,V} \times r_{FC,V} + \omega_{0V,V} \times v_{0C,V} \quad (106)$$

where the fact that the vector  $r_{FC,V}$  is constant was already taken into account. The last term, which does not depend on the time derivatives of the generalized velocities  $\dot{v}_{0F,V}$  or  $\dot{\omega}_{0F,V}$  represents the remaining term  $a_{0C,V}^R$  here. The absolute angular acceleration, expressed in the vehicle-fixed axis system, is given by

$$\alpha_{0C,V} = \dot{\omega}_{0C,V} + \omega_{0V,V} \times \omega_{0C,V} = \dot{\omega}_{0F,V} + \omega_{0V,V} \times \omega_{0V,V} = \dot{\omega}_{0F,V} \quad (107)$$

**Table 3** Partial velocities: three-dimensional vehicle model

**Table 4** Partial angular velocities; three-dimensional vehicle model

Body name/inertia	Partial angular velocities $\partial\omega_{0i,V}/\partial z_j$	Vehicle	Front Susp.	Rear Susp.	Wheels
$v_{0F,V}$	$\omega_{0V,V}$	$\dot{z}_1$	$\dot{z}_2$	$\dot{u}_F$	$\dot{z}_3$
$v_x, v_y, v_z$	$\omega_x, \omega_y, \omega_z$	$d_{z1}$	0	$d_{ul}$	0
Knuckle 1 $\Theta_{K1}$	0	$I$	$d_{z1}$	0	0
Wheel 1 $\Theta_{W1}$	0	$I$	$d_{z1}$	$d_{ul}$	0
Knuckle 2 $\Theta_{K2}$	0	$I$	0	$d_{uz}$	0
Wheel 2 $\Theta_{W2}$	0	$I$	0	$d_{uz}$	0
Knuckle 3 $\Theta_{K3}$	0	$I$	0	0	$d_{u3}$
Wheel 3 $\Theta_{W3}$	0	$I$	0	$d_{z3}$	0
Knuckle 4 $\Theta_{K4}$	0	$I$	0	0	$d_{u4}$
Wheel 4 $\Theta_{W4}$	0	$I$	0	0	$d_{u4}$
Chassis $\Theta_C$	0	$I$	0	0	0

and will contain no remaining acceleration terms,  $\alpha_{0C,V}^R = 0$ . The absolute acceleration of the knuckles and wheel centers,  $i = 1(1)4$ , are obtained by

$$\begin{aligned} a_{0i,V} = & \dot{v}_{0F,V} + \dot{\omega}_{0F,V} \times r_{Fi,V} + t_{zi,V}\ddot{z}_i + t_{ui,V}\ddot{u}_j \\ & + \omega_{0V,V} \times \dot{r}_{Fi,V} + \dot{t}_{zi,V}\dot{z}_i + \dot{t}_{ui,V}\dot{u}_j + \omega_{0V,V} \times v_{0i,V} \end{aligned} \quad (108)$$

The absolute angular acceleration of the knuckles,  $i = 1(1)4$ , is given by

$$\begin{aligned} \alpha_{0Ki,V} = & \dot{\omega}_{0F,V} + d_{zi,V}\ddot{z}_i + d_{ui,V}\ddot{u}_j \\ & + \dot{d}_{zi,V}\dot{z}_i + \dot{d}_{ui,V}\dot{u}_j + \omega_{0V,V} \times \omega_{0Ki,V} \end{aligned} \quad (109)$$

and the absolute angular acceleration of the wheels,  $i = 1(1)4$ , reads as

$$\begin{aligned} \alpha_{0Wi,V} = & \dot{\omega}_{0F,V} + d_{zi,V}\ddot{z}_i + d_{ui,V}\ddot{u}_i + A_{Vi}e_{yWi,i}\ddot{\phi}_{Wi} \\ & + \dot{d}_{zi,V}\dot{z}_i + \dot{d}_{ui,V}\dot{u}_i + \omega_{Fi,V} \times A_{Vi}e_{yWi,i}\dot{\phi}_{Wi} + \omega_{0V,V} \times \omega_{0Wi,V} \end{aligned} \quad (110)$$

The lateral rack movements were abbreviated by  $u_i$ , where  $u_i = u_F$  holds at the front axle ( $i = 1, 2$ ) and  $u_i = u_R$  at the rear axle ( $i = 3, 4$ ). Each second line in Eqs. (108), (109), and (110) represents the remaining acceleration terms  $d_{0Ki,V}^R$ ,  $d_{0Wi,V}^R$ , and  $\alpha_{0Ki,V}^R$ ,  $\alpha_{0Wi,V}^R$ , respectively. Which in the case of the wheel angular acceleration include the gyroscopic torques generated by the wheel rotation.

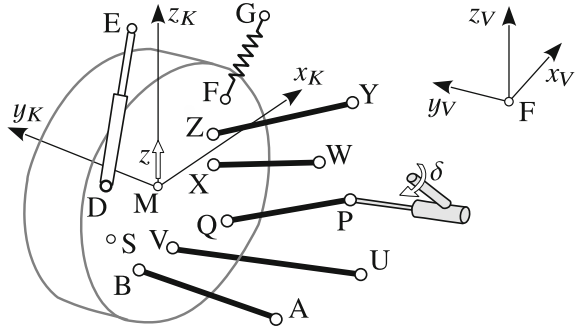
The parts in the remaining accelerations, which are generated by the time derivatives of the partial velocities and partial angular velocities, are small compared to the other parts in vehicle dynamics and may thus be neglected. This makes it possible to describe the kinematics of suspension systems very efficiently because complicated second order derivatives are not required. The kinematics of a Double Wishbone axle suspension and of a MacPherson axle suspension are described in detail in Rill (2012) and Rill and Schaeffer (2014). The kinematics of a multi-link axle suspension will be presented in the following.

### 3.5 Kinematics of a Multi-Link Axle Suspension

**Model Structure:** Figure 29 shows the model of a multi link axle suspension. The guidance of the knuckle is done by 5 rigid links A–B, U–V, W–X, Y–Z and P–Q. By connecting one of the joints A, U, P, W, or Y to a steering linkage, here point P is used for that purpose, the knuckle and the wheel will perform hub and steer motions.

The force elements, like spring (F–G), damper (D–E), and anti-roll bar (S) may be attached to the knuckle or to one of the links. The multi-body suspension represents a generic axle suspension that will include a double wishbone, a central control axle, or a Short-Long-Arm (SLA) axle.

**Fig. 29** Multi-link axle model



**Position and Orientation:** The motion of the wheel center M and the orientation of the knuckle-fixed frame  $x_K, y_K, z_K$  can be described by a single coordinate, for instance the hub motion  $z$ . If the axle is steered, one of the links is attached to the steering linkage; here the link P–Q is chosen. Thus, the momentary position of P depends on the steering angle  $\delta$  or the rack displacement  $u$  respectively

$$r_{MP,V} = r_{MP,V}(\delta) \quad (111)$$

Now, the position and the orientation of the wheel body depend on two coordinates, the hub and the steer motion.

The position of the knuckle center M is described by the position vector

$$r_{FM,V} = r_{FM,D} + \begin{bmatrix} x \\ y \\ z \end{bmatrix} \quad (112)$$

where  $F$  denotes the origin of the vehicle-fixed reference frame and  $r_{FM,D} = \text{const.}$  describes the knuckle center  $M$  in the design position. In the design position the axes of all coordinate systems are parallel per definition. So, no additional rotation matrices are required. As done here, all position vectors defined in the design position are characterized by appending  $_D$  to the subscript.

The orientation of the knuckle-fixed coordinate system  $x_K, y_K, z_K$  with respect to the vehicle-fixed reference frame  $x_V, y_V, z_V$  is defined by the rotation matrix

$$A_{VK} = \begin{bmatrix} 1 & 0 & 0 \\ 0 & \cos \alpha & -\sin \alpha \\ 0 & \sin \alpha & \cos \alpha \end{bmatrix} \begin{bmatrix} \cos \beta & 0 & \sin \beta \\ 0 & 1 & 0 \\ -\sin \beta & 0 & \cos \beta \end{bmatrix} \begin{bmatrix} \cos \gamma & -\sin \gamma & 0 \\ \sin \gamma & \cos \gamma & 0 \\ 0 & 0 & 1 \end{bmatrix} \quad (113)$$

that is composed of three elementary rotations with the angles  $\alpha$ ,  $\beta$ , and  $\gamma$ .

**Constraints:** The vertical displacement of the wheel center, the hub motion  $z$  and the steer angle  $\delta$  are chosen as generalized coordinates. Hence, the longitudinal and lateral motion of the wheel center  $x = x(z, \delta)$ ,  $y = y(z, \delta)$  and the angles  $\alpha = \alpha(z, \delta)$ ,

$\beta = \beta(z, \delta)$ ,  $\gamma = \gamma(z, \delta)$  are defined by the constraint equations

$$\frac{1}{2} r_{ij,V}^T r_{ij,V} = \frac{1}{2} l_{ij}^2, \quad \begin{array}{l} i = A, U, W, Y, P \\ j = B, V, X, Z, Q \end{array} \quad (114)$$

where  $l_{ij}$  denote the lengths of the links and the factor  $\frac{1}{2}$  will simplify the calculation of derivatives later on. The link vectors can be calculated from

$$\begin{aligned} r_{AB,V} &= r_{FM,V} + A_{VK} r_{MB,D} - r_{FA,D} \\ r_{UV,V} &= r_{FM,V} + A_{VK} r_{MV,D} - r_{FU,D} \\ r_{WX,V} &= r_{FM,V} + A_{VK} r_{MX,D} - r_{FW,D} \\ r_{YZ,V} &= r_{FM,V} + A_{VK} r_{MZ,D} - r_{FY,D} \\ r_{PQ,V} &= r_{FM,V} + A_{VK} r_{MQ,D} - r_{FP,V} \end{aligned} \quad (115)$$

where the position vector of the wheel center  $r_{FM,V}$  and the rotation matrix of the knuckle  $A_{VK}$  follow from (112) and (113). The vectors  $r_{MB,D}$  to  $r_{MQ,D}$  as well as  $r_{FA,D}$  to  $r_{FY,D}$  are defined by the design position and given by data. If the axle is steered, the vector from C to P depends on the steering angle  $r_{FP,V} = r_{FP,D}(\delta)$  otherwise it is simply defined by the design position  $r_{FP,V} = r_{FP,D}$  and given by data. The coordinates  $x, y, \alpha, \beta$  and  $\gamma$  that depend on the hub motion  $z$  and the steering angle  $\delta$  are now grouped into a vector

$$\xi = [x, y, \alpha, \beta, \gamma] \quad (116)$$

Then, the constraint equations (114) can be written as a nonlinear vector equation of type

$$f(\xi, z, \delta) = 0 \quad (117)$$

The Newton-Raphson algorithm leads to an iterative solution. Starting with  $\xi_0 = 0$  at each step  $k = 0, 1, 2, \dots$  a better approximation is given by

$$\frac{\partial f}{\partial \xi} (\xi_{k+1} - \xi_k) = -f(\xi_k) \quad (118)$$

where the Jacobi matrix is given by

$$\frac{\partial f}{\partial \xi} = \left[ \begin{array}{ccccc} r_{AB}^T \frac{\partial r_{AB}}{\partial x} & r_{AB}^T \frac{\partial r_{AB}}{\partial y} & r_{AB}^T \frac{\partial r_{AB}}{\partial \alpha} & r_{AB}^T \frac{\partial r_{AB}}{\partial \beta} & r_{AB}^T \frac{\partial r_{AB}}{\partial \gamma} \\ \vdots & \vdots & \vdots & \vdots & \vdots \\ r_{PQ}^T \frac{\partial r_{PQ}}{\partial x} & r_{PQ}^T \frac{\partial r_{PQ}}{\partial y} & r_{PQ}^T \frac{\partial r_{PQ}}{\partial \alpha} & r_{PQ}^T \frac{\partial r_{PQ}}{\partial \beta} & r_{PQ}^T \frac{\partial r_{PQ}}{\partial \gamma} \end{array} \right] \quad (119)$$

The subscript  $,V$  denoting that a vector is expressed in the vehicle-fixed frame V was omitted here. The vector  $r_{FM,V}$  depends on  $x, y$  and  $z$  of course. That is why

$$\frac{\partial r_{AB,V}}{\partial x} = \begin{bmatrix} 1 \\ 0 \\ 0 \end{bmatrix} \quad \dots \quad \frac{\partial r_{PQ,V}}{\partial x} = \begin{bmatrix} 1 \\ 0 \\ 0 \end{bmatrix} \quad (120)$$

$$\frac{\partial r_{AB,V}}{\partial y} = \begin{bmatrix} 0 \\ 1 \\ 0 \end{bmatrix} \quad \dots \quad \frac{\partial r_{PQ,V}}{\partial y} = \begin{bmatrix} 0 \\ 1 \\ 0 \end{bmatrix} \quad (121)$$

will hold. The rotation matrix  $A_{VK}$  is determined by the angles  $\alpha$ ,  $\beta$ , and  $\gamma$ . As a consequence, the corresponding partial derivatives are defined by

$$\frac{\partial r_{AB,V}}{\partial \alpha} = d_{\alpha,V} \times r_{MB,V} \quad \dots \quad \frac{\partial r_{PQ,V}}{\partial \alpha} = d_{\alpha,V} \times r_{MQ,V} \quad (122)$$

$$\frac{\partial r_{AB,V}}{\partial \beta} = d_{\beta,V} \times r_{MB,V} \quad \dots \quad \frac{\partial r_{PQ,V}}{\partial \beta} = d_{\beta,V} \times r_{MQ,V} \quad (123)$$

$$\frac{\partial r_{AB,V}}{\partial \gamma} = d_{\gamma,V} \times r_{MB,V} \quad \dots \quad \frac{\partial r_{PQ,V}}{\partial \gamma} = d_{\gamma,V} \times r_{MQ,V} \quad (124)$$

where the position vectors

$$r_{RB,V} = A_{VK} r_{MB,D}, \quad \dots \quad r_{RQ,V} = A_{VK} r_{MQ,D} \quad (125)$$

are defined in (115) and the rotation vectors are given by

$$d_{\alpha,V} = \begin{bmatrix} 1 \\ 0 \\ 0 \end{bmatrix} \quad d_{\beta,V} = \begin{bmatrix} 0 \\ \cos \alpha \\ \sin \alpha \end{bmatrix} \quad d_{\gamma,V} = \begin{bmatrix} \sin \alpha \\ -\sin \alpha \cos \beta \\ \cos \alpha \cos \beta \end{bmatrix} \quad (126)$$

**Velocities:** The angular velocity of the knuckle fixed reference frame K with respect to the body fixed reference frame V can be derived from the rotation matrix (113). Using the rotation vectors from (126) one gets

$$\omega_{VK,V} = d_{\alpha,V} \dot{\alpha} + d_{\beta,V} \dot{\beta} + d_{\gamma,V} \dot{\gamma} \quad (127)$$

The velocity of the wheel center M follows from (112)

$$\dot{r}_{FM,V} = \begin{bmatrix} 1 \\ 0 \\ 0 \end{bmatrix} \dot{x} + \begin{bmatrix} 0 \\ 1 \\ 0 \end{bmatrix} \dot{y} + \begin{bmatrix} 0 \\ 0 \\ 1 \end{bmatrix} \dot{z} \quad (128)$$

As  $x, y$  as well as  $\alpha, \beta, \gamma$  depend on the generalized coordinates  $z$  and  $\delta$

$$\begin{aligned}\dot{x} &= \frac{\partial x}{\partial z} \dot{z} + \frac{\partial x}{\partial \delta} \dot{\delta}, \\ \vdots &\quad \vdots \\ \dot{\gamma} &= \frac{\partial \gamma}{\partial z} \dot{z} + \frac{\partial \gamma}{\partial \delta} \dot{\delta}\end{aligned}\tag{129}$$

will hold. The partial derivatives of the constraint equation (117) with respect to  $z$  and  $\delta$  result in

$$\frac{\partial f}{\partial \xi} \frac{\partial \xi}{\partial z} + \frac{\partial f}{\partial z} = 0 \quad \text{and} \quad \frac{\partial f}{\partial \xi} \frac{\partial \xi}{\partial \delta} + \frac{\partial f}{\partial \delta} = 0\tag{130}$$

which represent two linear matrix equations that will deliver the partial derivatives  $\partial \xi / \partial z$  and  $\partial \xi / \partial \delta$ . The Jacobian  $\partial f / \partial \xi$  is given by (119) and according to (116)

$$\frac{\partial \xi}{\partial z} = \begin{bmatrix} \partial x / \partial z \\ \vdots \\ \partial \gamma / \partial z \end{bmatrix} \quad \text{and} \quad \frac{\partial \xi}{\partial \delta} = \begin{bmatrix} \partial x / \partial \delta \\ \vdots \\ \partial \gamma / \partial \delta \end{bmatrix}\tag{131}$$

will hold. Finally, the constraint equations (114) deliver

$$\frac{\partial f}{\partial z} = \begin{bmatrix} r_{AB,V}^T \frac{\partial r_{AB,V}}{\partial z} \\ \vdots \\ r_{PQ,V}^T \frac{\partial r_{PQ,V}}{\partial z} \end{bmatrix} = \begin{bmatrix} r_{AB,V}^{(3)} \\ \vdots \\ r_{PQ,V}^{(3)} \end{bmatrix} \quad \text{and} \quad \frac{\partial f}{\partial \delta} = \begin{bmatrix} 0 \\ 0 \\ 0 \\ 0 \\ r_{PQ,V}^T \frac{\partial r_{FP,V}}{\partial \delta} \end{bmatrix}\tag{132}$$

where the partial derivative  $\partial r_{FP,V} / \partial \delta$  results from the steering linkage.

Now, the angular velocity of the knuckle is defined by

$$\omega_{VK,V} = \underbrace{\begin{bmatrix} \frac{\partial \alpha}{\partial z} + \sin \beta \frac{\partial \alpha}{\partial \delta} \\ \cos \alpha \frac{\partial \beta}{\partial z} - \sin \alpha \cos \beta \frac{\partial \gamma}{\partial z} \\ \sin \alpha \frac{\partial \beta}{\partial z} - \cos \alpha \cos \beta \frac{\partial \gamma}{\partial z} \end{bmatrix}}_{d_{Kz,V}} \dot{z} + \underbrace{\begin{bmatrix} \frac{\partial \alpha}{\partial \delta} + \sin \beta \frac{\partial \alpha}{\partial \delta} \\ \cos \alpha \frac{\partial \beta}{\partial \delta} - \sin \alpha \cos \beta \frac{\partial \gamma}{\partial \delta} \\ \sin \alpha \frac{\partial \beta}{\partial \delta} - \cos \alpha \cos \beta \frac{\partial \gamma}{\partial \delta} \end{bmatrix}}_{d_{K\delta,V}} \dot{\delta}\tag{133}$$

and the velocity of the knuckle center is given by

$$\dot{r}_{MR,V} = \underbrace{\begin{bmatrix} \frac{\partial x}{\partial z} \\ \frac{\partial y}{\partial z} \\ 1 \end{bmatrix}}_{t_{Kz,V}} \dot{z} + \underbrace{\begin{bmatrix} \frac{\partial x}{\partial \delta} \\ \frac{\partial y}{\partial \delta} \\ 0 \end{bmatrix}}_{t_{K\delta,V}} \dot{\delta} \quad (134)$$

where the vectors  $d_{Kz,V}, t_{Kz,V}$  and  $d_{K\delta,V}, t_{K\delta,V}$  describe the momentary direction of the knuckle rotations and the wheel center motions due to the generalized coordinates  $z$  and  $\delta$ .

**Orientation of Link A–B:** The link vector  $r_{AB,V}$  is defined in (115). Introducing the rotation matrices

$$A_\varphi = \begin{bmatrix} 1 & 0 & 0 \\ 0 & \cos \varphi & -\sin \varphi \\ 0 & \sin \varphi & \cos \varphi \end{bmatrix}; \quad A_\psi = \begin{bmatrix} \cos \psi & -\sin \psi & 0 \\ \sin \psi & \cos \psi & 0 \\ 0 & 0 & 1 \end{bmatrix} \quad (135)$$

$$r_{AB,V} = A_\varphi A_\psi r_{AB,D} = A_{VL} r_{AB,D} \quad (136)$$

holds in addition, where  $r_{AB,D}$  is given by data and  $A_{VL}$  describes the orientation of the link. Using (135) the first part of (136) can be written as

$$\begin{bmatrix} 1 & 0 & 0 \\ 0 & \cos \varphi & \sin \varphi \\ 0 & -\sin \varphi & \cos \varphi \end{bmatrix} r_{AB,V} = \begin{bmatrix} \cos \psi & -\sin \psi & 0 \\ \sin \psi & \cos \psi & 0 \\ 0 & 0 & 1 \end{bmatrix} r_{AB,D} \quad (137)$$

The first and third line of these vector equation

$$\begin{aligned} r_{AB,V}^{(1)} &= r_{AB,D}^{(1)} \cos \psi - r_{AB,D}^{(2)} \sin \psi \\ -r_{AB,V}^{(2)} \sin \varphi + r_{AB,V}^{(3)} \cos \varphi &= r_{AB,D}^{(3)} \end{aligned} \quad (138)$$

provide trigonometric equations that deliver the angles  $\varphi$  and  $\psi$ .

**Angular Velocity of Link A–B:** The roation matrix  $A_{VL}$  defined in (136) is composed of two elementary rotations. The unit vectors

$$e_{\varphi,V} = \begin{bmatrix} 1 \\ 0 \\ 0 \end{bmatrix} \quad \text{and} \quad e_{\psi,V} = \begin{bmatrix} 0 \\ -\sin \varphi \\ \cos \varphi \end{bmatrix} \quad (139)$$

define the corresponding rotation axis. Then, the angular velocity of link A–B is determined by

$$\omega_{VL,V} = \left\{ e_{\varphi,V} \frac{\partial \varphi}{\partial z} + e_{\psi,V} \frac{\partial \psi}{\partial z} \right\} \dot{z} + \left\{ e_{\varphi,V} \frac{\partial \varphi}{\partial \delta} + e_{\psi,V} \frac{\partial \psi}{\partial \delta} \right\} \dot{\delta} \quad (140)$$

According to (115) the left side of (136) delivers

$$\frac{\partial r_{AB,V}}{\partial z} = t_{Kz,V} + d_{Kz,V} \times r_{MB,V} \quad \text{and} \quad \frac{\partial r_{AB,V}}{\partial \delta} = t_{K\delta,V} + d_{K\delta,V} \times r_{MB,V} \quad (141)$$

where  $r_{MB,V} = A_{VK} r_{MB,D}$  and  $t_{Kz,V}$ ,  $t_{K\delta,V}$  and  $d_{Kz,V}$ ,  $d_{K\delta,V}$  are defined in (128) and (127). The right side of (136) results in

$$\frac{\partial r_{AB,V}}{\partial z} = e_{\varphi,V} \times r_{AB,V} \frac{\partial \varphi}{\partial z} + e_{\psi,V} \times r_{AB,V} \frac{\partial \psi}{\partial z} \quad (142)$$

$$\frac{\partial r_{AB,V}}{\partial \delta} = e_{\varphi,V} \times r_{AB,V} \frac{\partial \varphi}{\partial \delta} + e_{\psi,V} \times r_{AB,V} \frac{\partial \psi}{\partial \delta} \quad (143)$$

Combining (141) with (142) and (143) the partial derivatives are defined as

$$\frac{\partial \varphi}{\partial z} = \frac{e_{\psi}^T (t_{Rz,V} + d_{Rz,V} \times r_{RB,V})}{e_{\psi}^T (e_{\varphi} \times r_{AB,V})}; \quad \frac{\partial \psi}{\partial z} = \frac{e_{\varphi}^T (t_{Rz,V} + d_{Rz,V} \times r_{RB,V})}{e_{\varphi}^T (e_{\psi} \times r_{AB,V})} \quad (144)$$

$$\frac{\partial \varphi}{\partial \delta} = \frac{e_{\psi}^T (t_{R\delta,V} + d_{R\delta,V} \times r_{RB,V})}{e_{\psi}^T (e_{\varphi} \times r_{AB,V})}; \quad \frac{\partial \psi}{\partial \delta} = \frac{e_{\varphi}^T (t_{R\delta,V} + d_{R\delta,V} \times r_{RB,V})}{e_{\varphi}^T (e_{\psi} \times r_{AB,V})} \quad (145)$$

**Force Element Attached to Knuckle:** The momentary position of a force element  $ij$  that is attached to the knuckle at  $i$  and to the chassis at  $j$  is given by

$$r_{ij,V} = r_{Fj,D} - r_{Fi,V} = r_{Fj,D} - (r_{FM,V} + r_{Mi,V}) \quad (146)$$

Then, the actual length and the unit vector into the direction of the element are defined by

$$u_{ij}^a = \sqrt{r_{ij,V}^T r_{ij,V}} \quad \text{and} \quad e_{ij,V} = \frac{r_{ij,V}}{u_{ij}^a} \quad (147)$$

If  $u_{ij}^0$  denotes the initial length of the force element, the actual displacement is given by

$$u_{ij} = u_{ij}^0 - u_{ij}^a \quad (148)$$

To calculate the generalized forces the partial derivatives of  $u_{ij}$  with respect to each generalized coordinate  $y_k$  are needed

$$\begin{aligned} \frac{\partial u_{ij}}{\partial y_k} &= -\frac{\partial u_{ij}^a}{\partial y_k} = -\frac{2 r_{ij,V}^T \frac{\partial r_{ij,V}}{\partial y_k}}{2 \sqrt{r_{ij,V}^T r_{ij,V}}} = -e_{ij,V}^T \left( -\frac{\partial r_{Mi,V}}{\partial y_k} \right) \\ &= e_{ij,V}^T \left( \frac{\partial r_{FM,V}}{\partial y_k} + \frac{\partial r_{Mi,V}}{\partial y_k} \right) = e_{ij,V}^T (t_{Ky_k,V} + d_{Ky_k,V} \times r_{Mi,V}) \end{aligned} \quad (149)$$

where the partial angular velocities  $d_{Ky_k,V}$  or  $d_{Kz,V}$  and  $d_{K\delta,V}$  respectively and the partial velocities  $t_{Ky_k,V}$  or  $t_{Kz,V}$  and  $t_{K\delta,V}$  respectively are defined in (133) and (134) in this particular case.

**Force Element Attached to Link A–B:** In general, force elements will not be attached to a link that is part of the steering system, like the link P–Q here. The momentary position of a force element  $ij$  that is attached to one of the remaining links, e.g. link A–B, at  $i$  and to the chassis at  $j$  is given by

$$r_{ij,V} = r_{Fj,D} - (r_{FA,D} + A_{BL} r_{Ai,D}) = r_{Aj,D} - r_{Ai,V} \quad (150)$$

where the rotation matrix  $A_{BL}$ , is defined in (136) and  $r_{Aj,D}$  and  $r_{Ai,D}$  are defined by data. The partial derivative of the spring deflection defined via (148) and (147) with respect to each generalized coordinate  $y_k$  now leads to

$$\frac{\partial u_{ij}}{\partial y_k} = -\frac{\partial u_{ij}^a}{\partial y_k} = -\frac{2 r_{ij,V}^T \frac{\partial r_{ij,V}}{\partial y_k}}{2 \sqrt{r_{ij,V}^T r_{ij,V}}} = -e_{ij,V}^T \left( -\frac{\partial r_{Ai,V}}{\partial y_k} \right) = e_{ij,V}^T \frac{\partial r_{Ai,V}}{\partial y_k} \quad (151)$$

The partial derivatives of the link vector  $r_{Ai,V}$  with respect to each generalized coordinate  $y_k$  follow from

$$\frac{\partial r_{Ai,V}}{\partial y_k} = \frac{\partial (A_\varphi A_\psi r_{Ai,D})}{\partial y_k} = \begin{bmatrix} 1 \\ 0 \\ 0 \end{bmatrix} \times r_{Ai,V} \frac{\partial \varphi}{\partial y_k} + \begin{bmatrix} 0 \\ -\sin \varphi \\ \cos \varphi \end{bmatrix} \times r_{Ai,V} \frac{\partial \psi}{\partial y_k} \quad (152)$$

where  $A_{BL} = A_\varphi A_\psi$  was used and the partial derivatives  $\partial \varphi / \partial y_k$  and  $\partial \psi / \partial y_k$  or  $\partial \varphi / \partial z$  to  $\partial \psi / \partial \delta$  respectively are defined in (144) and (145).

**Anti-roll Bar:** In general, a vertical drop-link connects the anti-roll bar to the control arm or to a link, Fig. 6. The vertical displacement of the drop link attachment point determines the torsional deflection of the anti-roll bar in a first approximation.

In some cases, the anti roll bar is attached at  $i = S$  to the knuckle. Then, the third component of (146) provides the vertical displacement

$$z_S = r_{Fj,D}^{(3)} - (r_{FM,V}^{(3)} + r_{Mi,V}^{(3)}) \quad (153)$$

and (149) delivers the partial derivatives with respect to the generalized coordinates  $y_1 = z$  and  $y_2 = \delta$  as

$$\frac{\partial z_S}{\partial y_k} = t_{K\beta,V}^{(3)} + d_{K\beta,V}^{(1)} r_{Mi,V}^{(2)} - d_{K\beta,V}^{(2)} r_{Mi,V}^{(1)} \quad (154)$$

where  $e_{ij,V}^T = [0 \ 0 \ 1]$  was applied to realize the assumed vertical orientation of the drop link and the numbers in brackets indicate the vector components.

If the anti roll bar is attached at  $i = S$  to link A–B then (150) and (151) deliver the vertical displacement of the anti roll bar and the partial derivatives of  $z_S$  with respect to  $y_1 = z$  and  $y_2 = \delta$  as

$$z_S = r_{Aj,D}^{(3)} - r_{Ai,V}^{(3)} \quad \text{and} \quad \frac{\partial z_S}{\partial y_k} = \frac{\partial r_{Ai,V}^{(3)}}{\partial y_k} \quad (155)$$

where  $e_{ij,V}^T = [0 \ 0 \ 1]$  was applied again to realize the assumed vertical orientation of the drop link.

### 3.6 Applied and Generalized Forces and Torques

The principle of virtual power processes the applied forces and torques via (46) to the vector of generalized forces and torques. This method is applied here to the weight and inertia forces and to the gyroscopic torques only. In particular, the contribution of the inertia forces and the gyroscopic torques of body  $i$  to the vector of generalized forces and torques is then given by

$$q_{(i)} = \frac{\partial v_{0i,V}^T}{\partial z} \left( m_i g_{,V} - m_i a_{0i,V}^R \right) + \frac{\partial \omega_{0i,V}^T}{\partial z} \left( -\Theta_{i,V} \alpha_{0i,V}^R - \omega_{0i,V} \times \Theta_{i,V} \omega_{0i,V} \right) \quad i = 1(1)k \quad (156)$$

where the gravitational force  $m_i g_{,V}$  was processed too. The three-dimensional model for the vehicle framework consists here of  $k = 9$  bodies, which in the case of translational motions are reduced to five bodies by combining each knuckle and wheel into one body. All terms are expressed in the vehicle-fixed axis system now. The applied torque  $T_{i,V}^a$  is omitted, and the applied force  $F_{i,0}^a$  is just replaced by the body weight  $G_{i,V} = m_i g_{,V}$ , where  $g_{,V}$  denotes the gravity vector expressed in the vehicle-fixed axis system.

All other applied forces and torques are transformed according to generalized ones by applying the principle of virtual power separately. Each force element is characterized by its force  $F$  and its displacement  $u_F$  that depends on the generalized

coordinates  $y$ . Then, the variation of the force element velocity  $v_F = \dot{u}_F(y)$  is given by

$$\delta v_F = \frac{\partial u_F}{\partial y} \delta y = \frac{\partial u_F}{\partial y} K \delta z \quad (157)$$

where  $K$  denotes the kinematical matrix. Finally, the contribution to the vector of generalized forces and torques is defined by

$$q_F = \left( \frac{\partial u_F}{\partial y} K \right)^T F \quad (158)$$

Handling tire models like TMeasy summarize the forces and torques generated in the contact patch in a resulting force vector  $F_T$  applied at the center of the wheel M and in a resulting torque vector  $T_T$ . Then

$$q_{Ti} = \left( \frac{\partial v_{0i}}{\partial z} \right)^T F_{Ti} + \left( \frac{\partial \omega_{0Ki}}{\partial z} \right)^T T_{Ti} \quad (159)$$

provide the corresponding contribution of tire  $i$  to the vector of generalized forces and torques. The partial derivatives of the velocity  $v_{0i}$  and the angular velocity  $\omega_{0Ki}$  of the knuckle are defined in Tables 3 and 4.

The general layout of the drive train generates braking torques between knuckle and wheel and transmits driving torques via half-shafts from the chassis-mounted differentials to the wheels. In this model approach, the wheels are described relative to the knuckle and those relative to the vehicle (chassis). Then, the driving and braking torques  $T_{Di}$ ,  $T_{Bi}$ ,  $i = 1(1)4$ , will act directly as generalized torques here in the components  $q(13)$  to  $q(16)$ . Beyond that, the driving torques  $T_{Di}$ ,  $i = 1(1)4$ , will generate the reaction terms  $d_{zi}^T e_{yWi} T_{Di}$ ,  $i = 1(1)4$ , in the components  $q(7)$ ,  $q(8)$ ,  $q(10)$ ,  $q(11)$ , which are related to the jounce and rebound motions  $z_1$  to  $z_4$  here.

### 3.7 Model Inputs

Depending on the purpose of investigation the fully nonlinear and three-dimensional vehicle model may be supplemented by appropriate subsystems for the drive train and the steering system. Then, the torque at the hand-wheel, the position of the gas, clutch, and brake pedal will serve as model inputs. However, in many cases the rack displacements as well as the driving and braking torques may be provided as pre-defined time histories or generated by an appropriate driver model. Besides that, for basic studies the complex vehicle model may be substituted by simple model that are tailored to the specific task.

## 4 From Complex to Simple Models

### 4.1 Simple Maneuverability Model

Handling analysis is mostly performed on nearly horizontal road surfaces. Hence, the overall performance of the vehicle is mainly characterized by the longitudinal, the lateral and the yaw motion. The simple track model, shown in Fig. 30, is based on the Ackermann geometry. The Ackermann geometry holds in a very low acceleration range where the side slip at the wheels is neglectable small and all wheel move strictly into their circumferential directions. The vehicle turns around a pivot point P if the wheels are steered properly. Applied to fictitious center wheels the Ackermann geometry delivers then

$$\tan \delta_A = \frac{a}{R} \quad \text{and} \quad \tan \beta_A = \frac{a_2}{R} \quad (160)$$

where  $\delta_A$  denotes the Ackermann steering angle at the fictitious front center wheel,  $\beta_A$  defines the Ackermann side slip angle at the vehicle's center of gravity C,  $a$  is the wheelbase,  $a_2$  denotes the distance of the center of gravity to the rear axle, and  $R$  describes the momentary turning radius. In this simple case the rear wheels remain unsteered.

The position and orientation of the vehicle in the  $x_0$ - $y_0$ -plane may be fixed by the coordinates  $x$  and  $y$  that define the center of the fictitious rear wheel and the yaw angle  $\psi$ . Then, the Ackermann geometry provides a set of first order differential equations

$$\dot{x} = v \cos \psi, \quad \dot{y} = v \sin \psi \quad \text{and} \quad \dot{\psi} = \frac{v}{a} \tan \delta_A \quad (161)$$

**Fig. 30** Track model

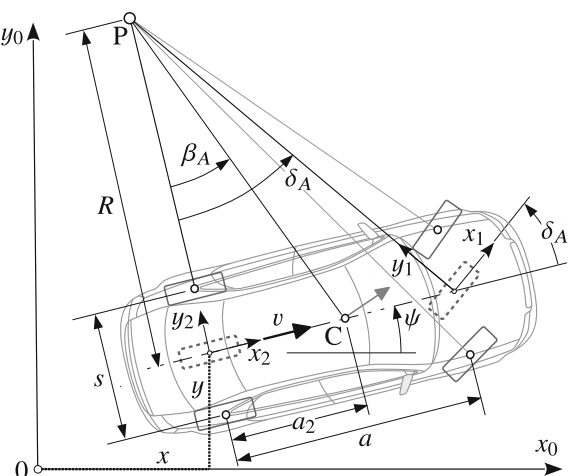
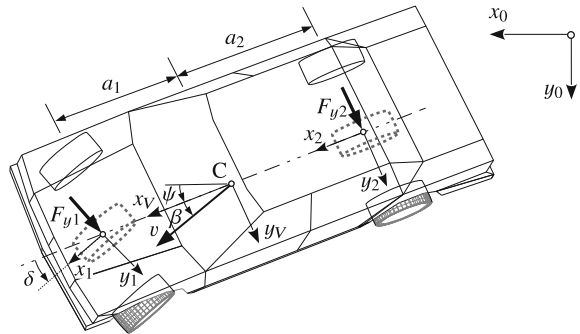


**Fig. 31** Simple handling model



that can be solved numerically if the velocity  $v$  of the vehicle, measured at the fictitious rear wheel, and the Ackermann steering angle  $\delta_A$  are provided as functions of the time  $t$ . In particular, the space requirement of vehicles at parking maneuvers can be investigated by this approach.

## 4.2 Simple Handling Model

Within a simple handling model<sup>5</sup> the side slip angle  $\beta$  and the distances  $a_1, a_2$  that determine the position of the center of gravity within the wheelbase  $a = a_1 + a_2$  are introduced in addition, Fig. 31. The lateral forces applied to the fictitious center wheels are approximated by

$$F_{y1} = c_{S1} s_{y1} \quad \text{and} \quad F_{y2} = c_{S2} s_{y2} \quad (162)$$

where  $c_{S1}, c_{S2}$  denote the cornering stiffness at the front and the rear axle. The lateral slips are defined by

$$s_{y1} = -\beta - \frac{a_1}{|v|} \dot{\psi} + \frac{v}{|v|} \delta \quad \text{and} \quad s_{y2} = -\beta + \frac{a_2}{|v|} \dot{\psi} \quad (163)$$

where a small yaw velocity  $| (a_1 + a_2) \dot{\psi}| \ll |v|$  as well as small angles  $\delta \ll 1$  and  $\beta \ll 1$  were assumed. The dynamics of this simple handling model is then defined by two first order differential equation that can be written as

---

<sup>5</sup>This simple planar model, often called the “bicycle model,” was first published by P. Riekert and T. E. Schunck: Zur Fahrmechanik des gummitireiften Kraftfahrzeugs, Ingenieur-Archiv, 11, 1940, S. 210-224. It is still used for fundamental studies or the basic layout of control systems.

$$\underbrace{\begin{bmatrix} \dot{\beta} \\ \dot{\omega} \end{bmatrix}}_{\dot{x}} = \underbrace{\begin{bmatrix} -\frac{c_{S1} + c_{S2}}{m|v|} & \frac{a_2 c_{S2} - a_1 c_{S1}}{m|v||v|} - \frac{v}{|v|} \\ \frac{a_2 c_{S2} - a_1 c_{S1}}{\Theta} & -\frac{a_1^2 c_{S1} + a_2^2 c_{S2}}{\Theta|v|} \end{bmatrix}}_A \underbrace{\begin{bmatrix} \beta \\ \omega \end{bmatrix}}_x + \underbrace{\begin{bmatrix} \frac{v}{|v|} & \frac{c_{S1}}{m|v|} \\ \frac{v}{|v|} & \frac{a_1 c_{S1}}{\Theta} \end{bmatrix}}_B \underbrace{\begin{bmatrix} \delta \end{bmatrix}}_u \quad (164)$$

where  $\omega = \dot{\psi}$  denotes the yaw velocity,  $m$  specifies the mass of the vehicle, and  $\Theta$  represents the inertia with respect to the center of gravity about an axis perpendicular to the  $x_0$ - $y_0$ -plane. This linear state equation can now be used to investigate the stability of the vehicle, calculate the steady-state or the transient response, and apply classic control methods. In particular the steady state response delivers the steering angle

$$\delta = \underbrace{\frac{a_1 + a_2}{R}}_{\delta_A} + \underbrace{m \frac{a_2 c_{S2} - a_1 c_{S1}}{c_{S1} c_{S2} (a_1 + a_2)}}_{\text{steering tendency } k} a_y \quad (165)$$

and the side slip angle measured at the center of gravity

$$\beta_{st} = \frac{v}{|v|} \left( \frac{a_2}{R} - m \frac{a_1}{c_{S2}(a_1 + a_2)} a_y \right) \quad (166)$$

as functions of the lateral acceleration  $a_y = v^2/R$ . The vehicle has an understeer tendency ( $k > 0$ ) and will be stable at forward drive when the relationship  $a_2 c_{S2} - a_1 c_{S1} > 0$  applies. On forward drive ( $v > 0$ ), the steady state slip angle decreases with increasing lateral acceleration. It changes sign at

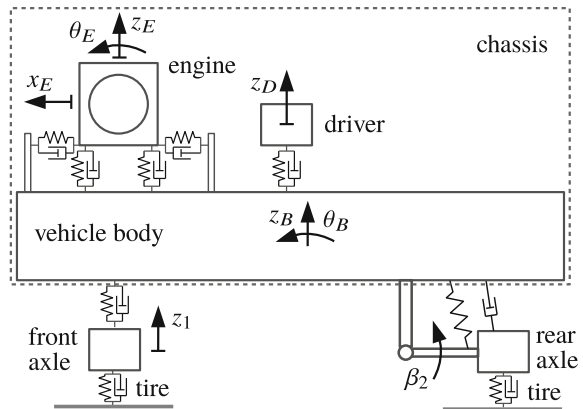
$$a_y^{\beta_{st}=0} = \frac{a_2 c_{S2} (a_1 + a_2)}{a_1 m R} \quad (167)$$

The sign change depends on the position  $a_1, a_2$  of the center of gravity, the mass  $m$  of the vehicle, and the magnitude of the cornering stiffness  $c_{S2}$  at the rear axle, in particular.

### 4.3 Comfort Models of Different Complexity

Much simpler models can be used, however, for fundamental studies of ride comfort and ride safety. If the vehicle is mainly driving straight ahead at constant speed, the hub and pitch motion of the chassis as well as the vertical motion of the axles will dominate the overall movement. Then, planar vehicle models can be used. A nonlinear planar model consisting of five rigid bodies with eight degrees of freedom is discussed in Rill and Schiehlen (2009). The model, shown in Fig. 32, considers

**Fig. 32** Sophisticated planar vehicle model



nonlinear spring characteristics of the vehicle body and the engine suspension, as well as degressive characteristics of the shock absorbers. Even the suspension of the driver's seat is taken into account here. Planar vehicle models suit perfectly with a single track road model.

In a further simplification, the chassis is considered as one rigid body. The corresponding simplified planar model has four degrees of freedom then, which are characterized by the hub and pitch motion of the chassis  $z_C$ ,  $\theta_C$ , and the vertical motion of the axles  $z_{A1}$  and  $z_{A2}$ , Fig. 33. Assuming small pitch motions ( $\theta_C \ll 1$ ) the equations of motion for this simple planar vehicle model read as

$$M \ddot{z}_C = F_1 + F_2 - M g, \quad (168)$$

$$\Theta \ddot{\theta}_C = -a_1 F_1 + a_2 F_2, \quad (169)$$

$$m_1 \ddot{z}_{A1} = -F_1 + F_{T1} - m_1 g, \quad (170)$$

$$m_2 \ddot{z}_{A2} = -F_2 + F_{T2} - m_2 g, \quad (171)$$

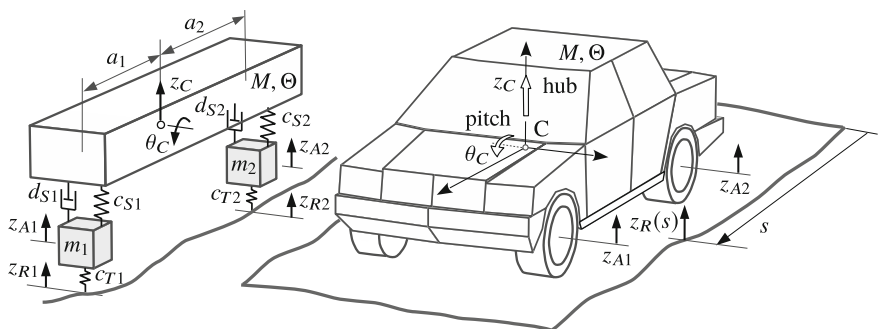


**Fig. 33** Simple planar vehicle model for basic studies

where  $M, m_1, m_2$  denote the masses of the chassis, the front, and the rear axle. The inertia of the chassis around an axis located in the chassis center C and pointing into the lateral direction is described by  $\Theta$  and  $a_1, a_2$  represent the distances of the chassis center C to the front and rear axle. Finally,  $F_1, F_2$  name the suspension forces and  $F_{T1}, F_{T2}$  the tire forces. The restrictions  $F_{T1} \geq 0$  and  $F_{T2} \geq 0$  will take tire lift-off into account.

The hub and pitch motion of the chassis can be combined to two new coordinates

$$\begin{aligned} z_{C1} &= z_C - a_1 \theta_C & \text{or} & \\ z_{C2} &= z_C + a_2 \theta_C & \left[ \begin{array}{c} z_{C1} \\ z_{C2} \end{array} \right] &= \underbrace{\left[ \begin{array}{cc} 1 & -a_1 \\ 1 & a_2 \end{array} \right]}_{T_C} \left[ \begin{array}{c} z_C \\ \theta_C \end{array} \right] \end{aligned} \quad (172)$$

which describe the vertical motions of the chassis in the front and in the rear, Fig. 34. Then, the Eqs. (168) and (169) arranged in matrix form

$$\left[ \begin{array}{cc} M & 0 \\ 0 & \Theta \end{array} \right] \left[ \begin{array}{c} \ddot{z}_C \\ \ddot{\theta}_C \end{array} \right] = \left[ \begin{array}{c} F_1 + F_2 - Mg \\ -a_1 F_1 + a_2 F_2 \end{array} \right] \quad (173)$$

can be written as

$$\left[ \begin{array}{cc} M & 0 \\ 0 & \Theta \end{array} \right] \underbrace{\frac{1}{a_1 + a_2} \left[ \begin{array}{cc} a_2 & a_1 \\ -1 & 1 \end{array} \right]}_{T_C^{-1}} \left[ \begin{array}{c} \ddot{z}_{C1} \\ \ddot{z}_{C2} \end{array} \right] = \underbrace{\left[ \begin{array}{cc} 1 & 1 \\ -a_1 & a_2 \end{array} \right]}_{T_C^T} \left[ \begin{array}{c} F_1 \\ F_2 \end{array} \right] + \left[ \begin{array}{c} -Mg \\ 0 \end{array} \right] \quad (174)$$

where the inverse of the transformation matrix  $T_C$  defined in Eq. (172) was used to replace the chassis hub and pitch accelerations by the vertical accelerations of chassis points located above the front and rear axle. It can be seen also that the

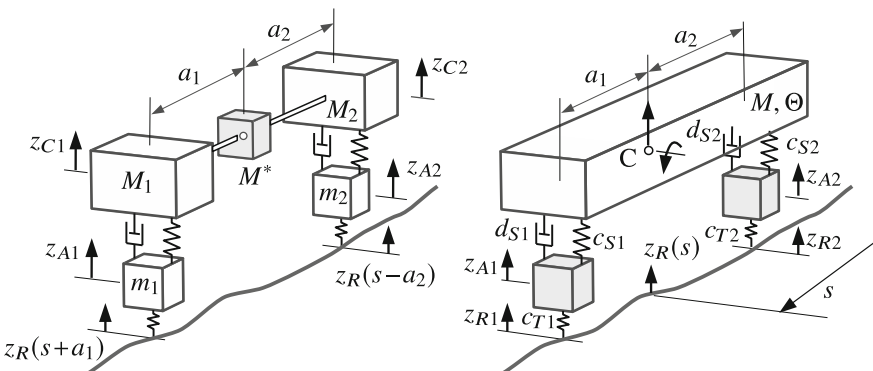


**Fig. 34** Chassis split into three point masses

distribution matrix for the suspension forces  $F_1$  and  $F_2$  is defined by the transposed of the transformation matrix. Multiplying Eq. (174) with the inverse of  $T_C^{-1}$  finally results in

$$\frac{1}{(a_1 + a_2)^2} \begin{bmatrix} Ma_2^2 + \Theta & Ma_1a_2 - \Theta \\ Ma_1a_2 - \Theta & Ma_2^2 + \Theta \end{bmatrix} \begin{bmatrix} \ddot{z}_{C1} \\ \ddot{z}_{C2} \end{bmatrix} = \begin{bmatrix} F_1 \\ F_2 \end{bmatrix} + \frac{1}{a_1 + a_2} \begin{bmatrix} -a_2 Mg \\ -a_1 Mg \end{bmatrix} \quad (175)$$

The off-diagonal elements in the mass matrix, given by  $Ma_1a_2 - \Theta$ , generate a coupling between the chassis acceleration  $\ddot{z}_{C1}$  and  $\ddot{z}_{C2}$  that are induced by the suspension forces  $F_1$ ,  $F_2$  and the corresponding parts of the chassis weight  $Mg$ . If the inertia of the vehicle happens to satisfy the relation

$$\Theta = Ma_1a_2 \quad (176)$$

then, the remaining mass diagonal elements

$$M_1 = \frac{Ma_2^2 + \Theta}{(a_1 + a_2)^2} = \frac{Ma_2^2 + Ma_1a_2}{(a_1 + a_2)^2} = \frac{Ma_2}{a_1 + a_2} \quad (177)$$

and

$$M_2 = \frac{Ma_1^2 + \Theta}{(a_1 + a_2)^2} = \frac{Ma_1^2 + Ma_1a_2}{(a_1 + a_2)^2} = \frac{Ma_1}{a_1 + a_2} \quad (178)$$

spread the chassis mass to the front and rear according to the distribution of the chassis weight. In this particular case, the equations of motion for the front and rear chassis parts are decoupled and simply read as

$$M_1 \ddot{z}_{C1} = F_1 - \frac{Mg a_2}{a_1 + a_2} \quad \text{and} \quad M_2 \ddot{z}_{C2} = F_2 - \frac{Mg a_1}{a_1 + a_2} \quad (179)$$

These equations supplemented by the corresponding differential equations for the axles provided by the Eqs. (170) and (171) represent two separate models with two degrees of freedom that describe the vertical motions of the axle and the corresponding chassis mass on top of each axle.

The mass and inertia properties of the chassis may also be judged by three point masses  $M^*$ ,  $M_1$ ,  $M_2$ , which are located in the chassis center C and on top of the front and the rear axle, left image in Fig. 34. The point masses must satisfy the relations

$$M_1 + M^* + M_2 = M, \quad a_1^2 M_1 + a_2^2 M_2 = \Theta, \quad a_1 M_1 = a_2 M_2 \quad (180)$$

that ensure the same chassis mass, the same inertia, and the same location of the center of gravity. Resolved for the point masses one gets

$$M_1 = \frac{\Theta}{a_1(a_1 + a_2)} \quad \text{and} \quad M_2 = \frac{\Theta}{a_2(a_1 + a_2)} \quad (181)$$

as well as

$$M^* = M \left( 1 - \frac{\Theta}{M a_1 a_2} \right) \quad (182)$$

It can be seen that the coupling mass vanishes if  $\Theta = M a_1 a_2$  will hold. This relation coincides with Eq. (176) exactly.

Hence, a vanishing ( $M^* = 0$ ) or at least a neglectible coupling mass ( $M^* \ll M_1, M_2$ ) indicates a specific chassis mass distribution that makes it possible to split the planar model with four degrees of freedom into two separate models with two degrees of freedom describing the vertical motions of the axle and the corresponding chassis mass on top of each axle. By using half the chassis and half the axle mass, we finally end up in quarter car models.

Finally, the function  $z_R(s)$  provides road irregularities in the space domain, where  $s$  denotes the distance covered by the vehicle and measured at the chassis center of gravity. Then, the irregularities at the front and the rear axle are given by  $z_R(s + a_1)$  and  $z_R(s - a_2)$ , respectively, where  $a_1$  and  $a_2$  locate the position of the chassis center of gravity C in the longitudinal direction. A quarter car model with a trailing arm suspension was presented in Sect. 1.7. For most vehicles the axle mass is much smaller than the corresponding chassis mass,  $m_i \ll M_i$ ,  $i = 1, 2$ . Hence, for a first basic study, axle and chassis motions can be investigated independently. Now, the quarter car model is further simplified to two single mass models, Fig. 35. The chassis model neglects the tire deflection and the inertia forces of the wheel. For the high frequent wheel motions, the chassis can be considered fixed to the inertia frame. The equations of motion for the chassis and the wheel model read as

$$M \ddot{z}_C + d_S \dot{z}_C + c_S z_C = d_S \ddot{z}_R + c_S z_R \quad (183)$$

$$m \ddot{z}_W + d_S \dot{z}_W + (c_S + c_T) z_W = c_T z_R \quad (184)$$

where  $z_W$  and  $z_C$  define the vertical motions of the wheel mass and the corresponding chassis mass with respect to the steady-state position. The constants  $c_S, d_S$  describe

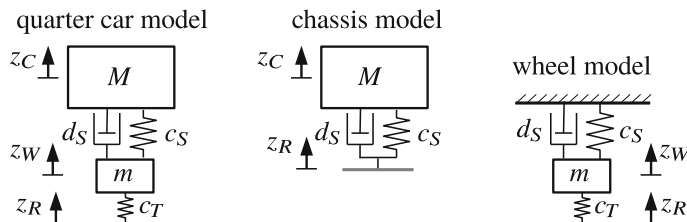


**Fig. 35** Simple vertical vehicle models

the suspension stiffness and damping. The dynamic wheel load is calculated by

$$F_T^D = c_T (z_R - z_W) \quad (185)$$

where  $c_T$  is the vertical or radial stiffness of the tire and  $z_R$  denotes the road irregularities. In this simple approach the damping effects in the tire are not taken into account.

## 5 Applications

### 5.1 Vehicle Parameter

The fully nonlinear and three-dimensional model described in Sect. 3 requires many parameters. At first the mass, the inertia, and the design position of each model body is required. The kinematics of the axle suspension system is characterized by its type (Double Wishbone, MacPherson, Multi-link, ...) and the design position of the joints (hardpoints). The force elements (spring, damper, anti-roll bar, stops) are defined by their characteristics and the design position of the attachment points. A left/right symmetry of the axle layout reduces the number of parameters significantly. Then, the parameter of the tire model must be specified of course. The TMeasy tire model of version 5 requires 52 parameters in total. The main advantage of TMeasy is, that its model parameter can easily be identified by measurements or set properly by an Engineer's guess, if no or not all measurements are available, Rill (2015). Adding subsystems (steering system, drive train, engine suspension, ...) demands for more model parameter. Finally, the environment must be characterized too. At least the road surface must be defined by its profile (flat or uneven) and friction property (dry, wet,  $\mu$ -split). Some applications require aero-dynamic properties (drag coefficient, center of pressure) too.

### 5.2 Vehicle Handling

**Vehicle Model:** To investigate the handling properties of a vehicle, the chassis can be regarded as one rigid body. However, the suspension system as well as the tire must be modeled completely nonlinear and in detail. This kind of vehicle models may be set up as described in Sect. 3 or by using commercial software packages, Hirschberg et al. (2009). The characteristic data for typical fullsize and midsize cars are provided in Tables 5 and 6.

The fullsize car is equipped with rear wheel and the midsize car with front wheel drive. That is why, a MacPherson suspension that leaves enough space for the transversely mounted engine is used at the front axle of the midsize car.

**Table 5** Characteristic parameter of a fullsize car

Wheel base	2.900 m
Track width front   rear	1.530 m   1.524 m
Height of CoG	0.54 m
Total mass and inertia	2140 kg and $\begin{bmatrix} 600 & 0 & 0 \\ 0 & 3100 & 0 \\ 0 & 0 & 3350 \end{bmatrix}$ kg m <sup>2</sup>
Axle load front   rear	10.75 kN   10.25 kN
Suspension front   rear	double wishbone   double wishbone
Tire front   rear	265/40 R18   265/40 R18

**Table 6** Characteristic parameter of a midsize car

Wheel base	2.600 m
Track width front   rear	1.5244 m   1.4878 m
Height of CoG	0.515 m
Total mass and inertia	1450 kg and $\begin{bmatrix} 425 & 0 & 0 \\ 0 & 1800 & 0 \\ 0 & 0 & 2020 \end{bmatrix}$ kg m <sup>2</sup>
Axle load front   rear	8.0 kN   6.2 kN
Suspension front   rear	MacPherson   multi-link
Tire front   rear	205/50 R15   205/50 R15

**Steady State Cornering:** The steering tendency of a vehicle is determined by the driving maneuver called steady-state cornering. The maneuver is performed quasi-static. The driver tries to keep the vehicle on a circle with the given radius  $R$ . He slowly increases the driving speed  $v$  and, due to  $a_y = v^2/R$ , also the lateral acceleration until reaching the limit. Characteristics signals, like the steering wheel angle and the side slip angle, are plotted versus the lateral acceleration, Fig. 36. Both vehicles show moderate understeer tendencies ( $11^\circ/g$  and  $21^\circ/g$ ) in the lower acceleration range. As typical for most front wheel driven cars, the midsize car has a stronger understeer tendency as the rear wheel driven fullsize car. Starting at  $a_y \approx 0.4g$  the understeer tendencies become stronger and stronger while finally approaching the limit range at  $a_y^{max} \approx 0.85g$  for the fullsize and  $a_y^{max} \approx 0.9g$  for the midsize car respectively.

At very low accelerations  $a_y \approx 0$  the Ackermann geometry will apply. Hence, the steering angle as well as the side slip angle correspond with the purely kinematical values determined by the wheel base and the curve radius. According to the axle loads and the wheel bases provided by the Tables 5 and 6 the distances of the centers of gravity to the rear axle are defined by

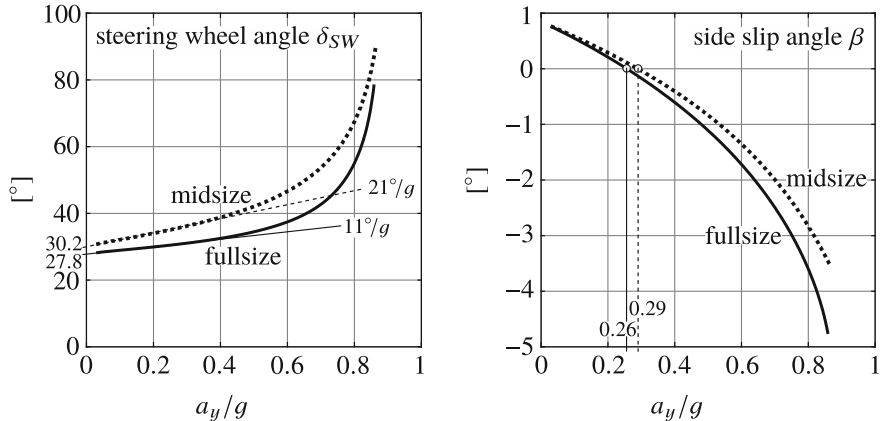


**Fig. 36** Steady state cornering results for a typical fullsize and a midsize car at a curve radius of  $R = 100$  m

$$a_2^F = \frac{2.9 * 10.75}{2140 * 9.81} = 1.485 \text{ m} \quad \text{and} \quad a_2^M = \frac{2.6 * 8.0}{1450 * 9.81} = 1.462 \text{ m} \quad (186)$$

where the superscripts  $F$  and  $M$  indicate fullsize and midsize. The second part of Eq. (160) delivers the Ackermann side slip angles as

$$\beta_A^F = \arctan \frac{1.485}{100} = 0.85^\circ \quad \text{and} \quad \beta_A^M = \arctan \frac{1.462}{100} = 0.84^\circ \quad (187)$$

These values conform quite well with the results of the three-dimensional vehicle model, when the graphs in the right plot of Fig. 36 are extrapolated to  $a_y \rightarrow 0$  by a simple inspection.

The accelerations  $0.26g$  for the fullsize and  $0.29g$  for the midsize car where the slip angle  $\beta$  changes the sign are in the lower acceleration range. Hence, the relationship (167) derived for the linear handling model will apply and deliver the cornering stiffness at the rear axle. The vehicle for the fullsize and the midsize car result in

$$c_{S2}^F = \frac{a_1 R}{a_2 (a_1 + a_2)} m a_y^{\beta_{sr}=0} = \frac{1.415 \cdot 100}{1.485 \cdot 2.9} \cdot 2140 \cdot 0.26 \cdot 9.81 \approx 180 \text{ kN/-} \quad (188)$$

$$c_{S2}^M = \frac{a_1 R}{a_2 (a_1 + a_2)} m a_y^{\beta_{sr}=0} = \frac{1.138 \cdot 100}{1.462 \cdot 2.6} \cdot 1450 \cdot 0.29 \cdot 9.81 \approx 124 \text{ kN/-} \quad (189)$$

The steering tendency

$$k = \frac{\delta}{a_y} = m \frac{a_2 c_{S2} - a_1 c_{S1}}{c_{S1} c_{S2} (a_1 + a_2)} \quad (190)$$

defined in (165) can now be used to determine the cornering stiffness  $c_{S1}$  at the front axle. In the linear range where the handling model applies the steering wheel angle  $\delta_{SW}$  and the steering angle  $\delta$  at the fictitious front wheel are related by the steering ratio  $i_S = \delta_{SW}/\delta$ . The first part of Eq. (160) delivers the Ackermann steering angles when the fullsize and the midsize cars are driven at vanishing lateral acceleration on a radius of  $R = 100$  m

$$\delta_A^F = \arctan \frac{2.9}{100} = 1.6611^\circ \quad \text{and} \quad \delta_A^M = \arctan \frac{2.6}{100} = 1.4897^\circ \quad (191)$$

The left plot in Fig. 36 delivers the steering wheel angles at  $a_y \rightarrow 0$  and makes it possible to calculate the steering ratios

$$i_S^F = \frac{27.8^\circ}{1.6611^\circ} = 16.74 \quad \text{and} \quad i_S^M = \frac{30.2^\circ}{1.4897^\circ} = 20.28 \quad (192)$$

Now, the steering tendencies derived from the graphs can be matched with the one that holds for the simple handling model. One gets

$$k^F = \frac{11/16.74}{9.81} \frac{\pi}{180} = 0.00117 \quad \text{and} \quad k^M = \frac{21/20.27}{9.81} \frac{\pi}{180} = 0.00184 \quad (193)$$

Resolving (190) for the cornering stiffness at the front axle results in

$$c_{S1} = \frac{m a_2}{m a_1 + k c_{S2} (a_1 + a_2)} c_{S2} \quad (194)$$

and delivers the values

$$c_{S1}^F \approx 157 \text{ kN/-} \quad \text{and} \quad c_{S1}^M \approx 117 \text{ kN/-} \quad (195)$$

In case of the fullsize car where  $a_1^F \approx a_2^F$  holds the light understeer tendency is achieved by a smaller cornering stiffness at the front axle  $c_{S1}^F < c_{S2}^F$ . Whereas the stronger understeer tendency of the midsize car is the result of  $a_1^M < a_2^M$ .

The parameter  $k$  that determines the steering tendency of the vehicle is related to the stability of the vehicle. That is why  $k > 0$  implying stability and an understeer tendency is applied at most vehicles.

**Dynamic Maneuvers:** Step like or sinusoidal steer inputs are used to judge the dynamic reactions of a vehicle. Here, the dynamics of the tires as well as elastic properties of the wheel axle suspension have to be taken into account. The closed loop performance of driver and vehicle is tested in double lane change maneuvers. Simulation results of autonomous obstacle avoidance maneuvers including off-road scenarios are published in Castro et al. (2017).

**Critical Maneuvers:** Braking in a corner or at  $\mu$  split may cause critical situations. Different braking scenarios, including no braking at all, are shown in Fig. 37. At the

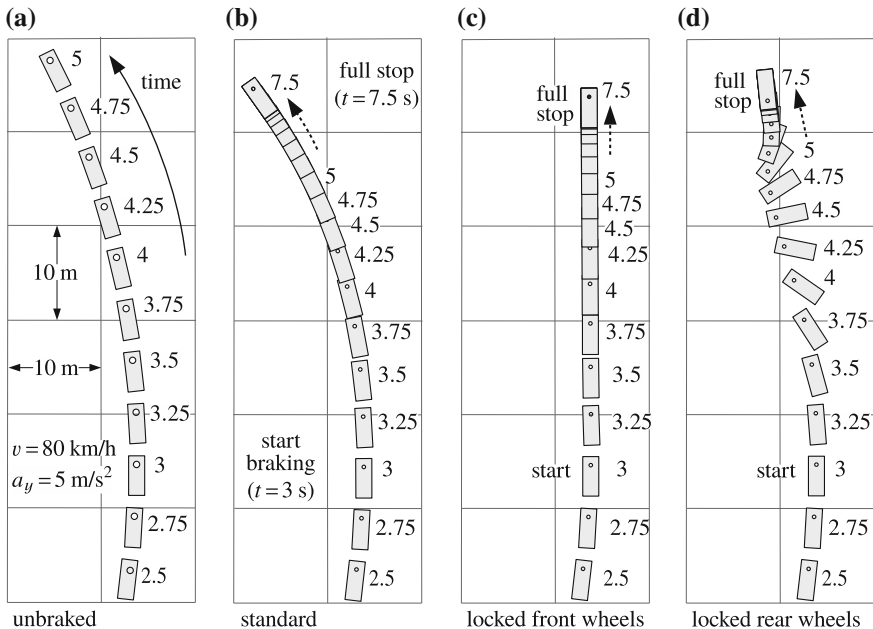


**Fig. 37** Braking in a turn with different scenarios

beginning, the vehicle, a standard passenger car, is cornering with a driving velocity of  $v = v_0 = 80 \text{ km/h}$  on a radius of  $R \approx 100 \text{ m}$ , which results in a lateral acceleration of  $a_y \approx (80/3.6)^2/100 = 4.94 \text{ m/s}^2$ . All braking scenarios start at  $t = 3 \text{ s}$ . In the standard case, the braking torques at the front wheels are raised within 0.1 s to 900 Nm and at the rear wheels to 270 Nm, which stops the vehicle in barely 4 s. If large braking torques of 1500 Nm are applied only at the front wheels, the vehicle will stop in nearly the same time. But, the front wheels will lock now and cause the vehicle to go straight ahead instead of further cornering. If the same braking torques are put on the rear wheels only, the vehicle becomes unstable, rotates around, is then stabilized by the locked rear axle, which has come to the front, and finally comes to a stand still.

If a vehicle without an anti-lock system is braked on a  $\mu$ -split surface, then the wheels running on  $\mu_{low}$  will lock in an instant, thus providing small braking forces only. The wheels on the side of  $\mu_{high}$ , however, generate large braking forces that generate a severe yaw impact. The rear wheel on  $\mu_{low}$  is locked and provides no lateral guidance at all. At full braking, the rear wheel on  $\mu_{high}$  is close to the friction limit and therefore is not able to produce a lateral force large enough to counteract the yaw impact. As a consequence, the vehicle starts to spin around the vertical axis. Screen shots of a commercial trailer from the company Robert Bosch GmbH, explaining the need for controlled systems<sup>6</sup> compared with the results of a simulation with a full

<sup>6</sup>Anti-Lock-System (ABS) or Electronic Stability Program (ESP).

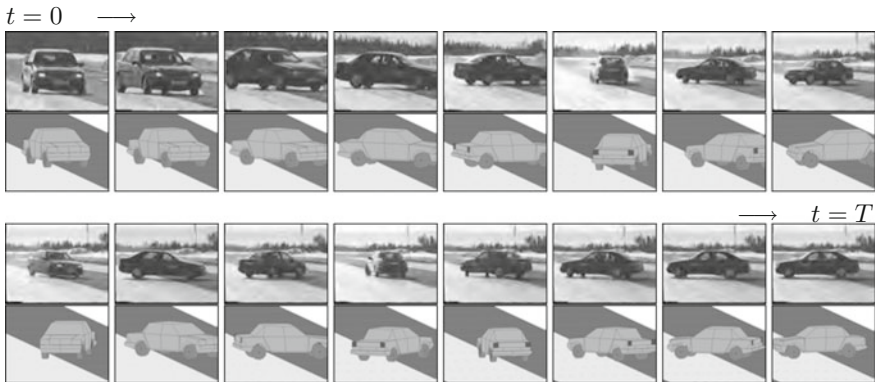


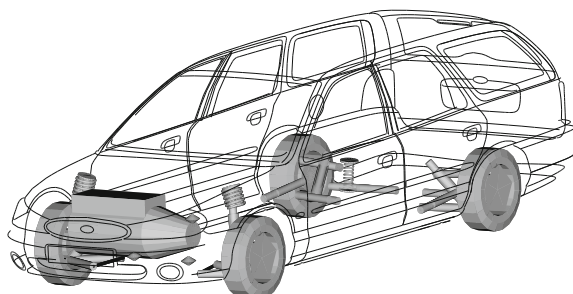
**Fig. 38** Braking on  $\mu$ -split: Field test and simulation results taken from Rill and Chucholowski (2004)

vehicle model are shown in Fig. 38. Despite different vehicles and estimated friction coefficients for the dry ( $\mu_{high} = 1$ ) and the icy part ( $\mu_{low} = 0.05$ ) of the test track, the simulation results are in good conformity with field tests. Whereas the reproducibility of field tests is not always given, a computer simulation can be repeated exactly with the same environmental conditions.

### 5.3 Vehicle Handling and Comfort

For detailed investigations of ride safety and ride comfort, sophisticated road and vehicle models are needed, Seibert and Rill (1998). The three-dimensional and fully nonlinear vehicle model, shown in Fig. 39, includes an elastically suspended engine and dynamic seat models. The elasto-kinematics of the wheel suspension was described as fully nonlinear. In addition, dynamic force elements for the damper topmount combination and the hydro-mounts are used. Such sophisticated models

**Fig. 39** Complex vehicle model for handling and comfort analysis



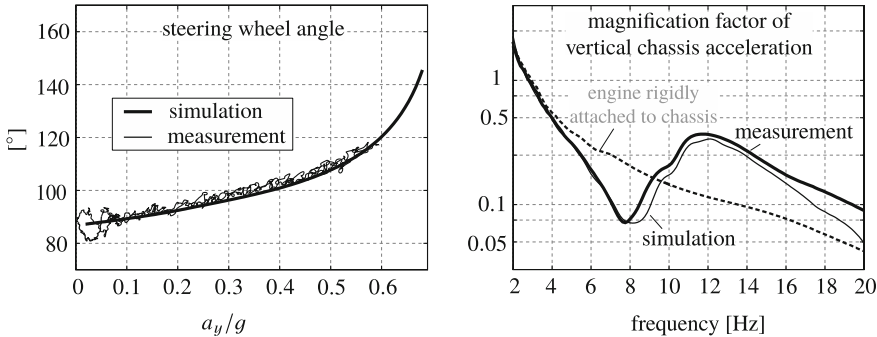


**Fig. 40** Measurements and simulation results to asses handling properties and ride comfort taken from Seibert and Rill (1998)

provide simulation results with one set of parameter that are in good conformity to measurements in a wide range of applications, Fig. 40. Whereas in the simulation a perfectly flat road is easily realized, field test, will usually be characterized by slight disturbances induced by a nonperfect road surface. As can be seen in the left plot of Fig. 40 the measured steering angle is a little bit noisy. Measurements and simulation results conform very well. Again, the understeer tendency, indicated by the slope of the graph steering angle versus lateral acceleration, increases with the lateral acceleration. The simulation results indicate a maximum acceleration of approximately  $0.75g$  here.

In a hydropuls test the simulation results are also very close to the measurements, left plot of Fig. 40. The magnification factor of the vertical chassis acceleration is a sensitive signal to assess the ride comfort of a vehicle. To achieve this good conformity between measurements and simulation even the dry friction in the suspension system had to be taken into account. Of course, the engine suspension plays a mature part here. Attaching the engine rigidly to the chassis produces the broken line in the right graph of Fig. 40. This broken line generated by a simpler model deviates a lot from the measurements and can not be used to predict the ride comfort of a vehicle seriously.

## References

- Arnold, M., Burgermeister, B., Führer, C., Hippmann, G., & Rill, G. (2011). Numerical methods in vehicle system dynamics: State of the art and current developments. *Vehicle System Dynamics*, 49, 1159–1207.
- Baumgarte, J. (1972). Stabilization of constraints and integrals of motion in dynamical systems. *Computer Methods in Applied Mechanics and Engineering*, 1, 1–16.
- Blundell, M., & Harty, D. (2004). *The multibody system approach to vehicle dynamics*. Elsevier Butterworth-Heinemann Publications.

- Butz, T., Ehmann, M., & Wolter, T.-M. (2004). A realistic road model for real-time vehicle dynamics simulation. *Society of Automotive Engineers, SAE Paper 2004-01-1068*.
- Castro, A., Basilio, R., Chaves, Rill, G., & Weber, H. I. (2017). Use of integrated control to enhance the safety of vehicles in run-off scenarios. In P. R. G. Kurka, A. T. Fleury, D. A. Rade (Eds.), *Proceedings of the XVII International Symposium on Dynamic Problems of Mechanics (DINAME 2017)*, São Paulo, SP, Brasil, ABCM.
- Gear, C. W., Gupta, G. K., & Leimkuhler, B. (1985). Automatic integration of euler-lagrange equations with constraints. *Journal of Computational Mathematics*, 12(13), 77–90.
- Hirschberg, W., Palacek, F., Rill, G., & Sotnik, J. (2009). Reliable vehicle dynamics simulation in spite of uncertain input data. In *Proceedings of 12th EAEC European Automotive Congress*, Bratislava.
- Kane, R. T., & Levinson, D. A. (1980). Formulation of equations of motion for complex spacecraft. *Journal of Guidance and Control*, 3(2), 99–112.
- Lugner, P., & Plöchl, M. (2007). *Tire model performance test (TMPT)*. Taylor and Francis.
- Negrut, D., Ottarsson, G., Rampalli, R., & Sajdak, A. (2006). *On an implementation of the Hilber-Hughes-taylor method in the context of index 3 differential-algebraic equations of multibody dynamics*. <http://homepages.cae.wisc.edu/~negrut/PDFpapers/hhtJCND.pdf>.
- Neureder, U. (2002). Untersuchungen zur Übertragung von Radlastschwankungen auf die Lenkung von Pkw mit Federbeinvorderachse und Zahnstangenlenkung, volume 12(518) of *Fortschritt-Berichte VDI*. VDI-Verlag, Düsseldorf.
- Nørsett, S. P., Hairer, E., & Wanner, G. (2008). *Solving Ordinary Differential Equations I, Nonstiff Problems I, Nonstiff Problems*. Berlin: Springer.
- Rauh, J. (2003). Virtual development of ride and handling characteristics for advanced passenger cars. *Vehicle System Dynamics*, 40(1–3), 135–155.
- Rill, G. (1994). *Simulation von Kraftfahrzeugen*, Braunschweig. <https://hps.hs-regensburg.de/rig39165>.
- Rill, G. (2007). Wheel dynamics. In *Proceedings of the 12th International Symposium on Dynamic Problems of Mechanics (DINAME 2007)*.
- Rill, G. (2012). *Road vehicle dynamics*. CRC Press.
- Rill, G. (2013a, February 17–22). TMeasy—The handling tire model for all driving situations. In M. A. Savi (Ed.), *Proceedings of the 15th International Symposium on Dynamic Problems of Mechanics (DINAME 2013)*, Buzios, RJ, Brazil.
- Rill, G. (2013b, August 19–23). TMeasy—A Handling Tire Model based on a three-dimensional slip approach. In W. Zhang & M. Gong (Eds.), *Proceedings of the 23rd International Symposium on Dynamic of Vehicles on Roads and on Tracks (IAVSD 2013)*. Qingdao, China.
- Rill, G. (2015). An engineer's guess on tyre parameter made possible with TMeasy. In P. Gruber & S. Robin Sharp (Eds.), *Proceedings of the 4th International Tyre Colloquium in*. University of Surrey, GB. <http://epubs.surrey.ac.uk/807823>.
- Rill, G., & Chucholowski, C. (2004). A modeling technique for fast computer simulations of configurable vehicle systems. In *Proceedings of the 21st International Congress of Theoretical and Applied Mechanics (ICTAM)*, Warsaw, Poland.
- Rill, G., & Chucholowski, C. (2005a). Modeling concepts for modern steering systems. In *ECCOMAS Multibody Dynamics*. Madrid, Spain.
- Rill, G., & Chucholowski, C. (2005b). Modeling concepts for modern steering systems. In *ECCOMAS Multibody Dynamics*. Madrid, Spain.
- Rill, G., & Schaeffer, Th. (2014). *Grundlagen und Methodik der Mehrkörpersimulation*. Springer.
- Rill, G., & Schiehlen, W. (2009). Performance assessment of time integration methods for vehicle dynamics simulation. In K. Arczewski & J. Fraczek (Eds.), *Multibody Dynamics 2009 (ECCOMAS Thematic Conference, Warsaw, Poland, 29 June–2 July 2009)*. Faculty of Power and Aerospace Engineering: Warsaw University of Technology. ISBN 978-83-7207-813-1.pdf.
- Rill, G. (1997). Vehicle modeling for real time applications. *Journal of the Brazilian Society of Mechanical Sciences - RBCM*, 19(2), 192–206.

- Rill, G. (2006a). Vehicle modeling by subsystems. *Journal of the Brazilian Society of Mechanical Sciences and Engineering - ABCM*, 28(4), 431–443.
- Rill, G. (2006b). A modified implicit euler algorithm for solving vehicle dynamic equations. *Multibody System Dynamics*, 15(1), 1–24.
- Seibert, Th., & Rill, G. (1998). Fahrkomfortberechnungen unter Einbeziehung der Motorschwingungen. In *Berechnung und Simulation im Fahrzeugbau*, VDI-Bericht 1411, Düsseldorf, VDI.
- van der Jagt, P. (2000). *The road to virtual vehicle prototyping; New CAE-models for accelerated vehicle dynamics development*. Tech. Univ. Eindhoven. ISBN 90-386-2552-9 NUGI 834.